New EU data regulations, global research implications *pp. 467 & 496*

Sexual harassment allegations roil the Salk Institute *p. 480*

Targets for malaria mutagenesis *pp. 490 & 506*

Science

$15
4 MAY 2018
sciencemag.org

AAAS

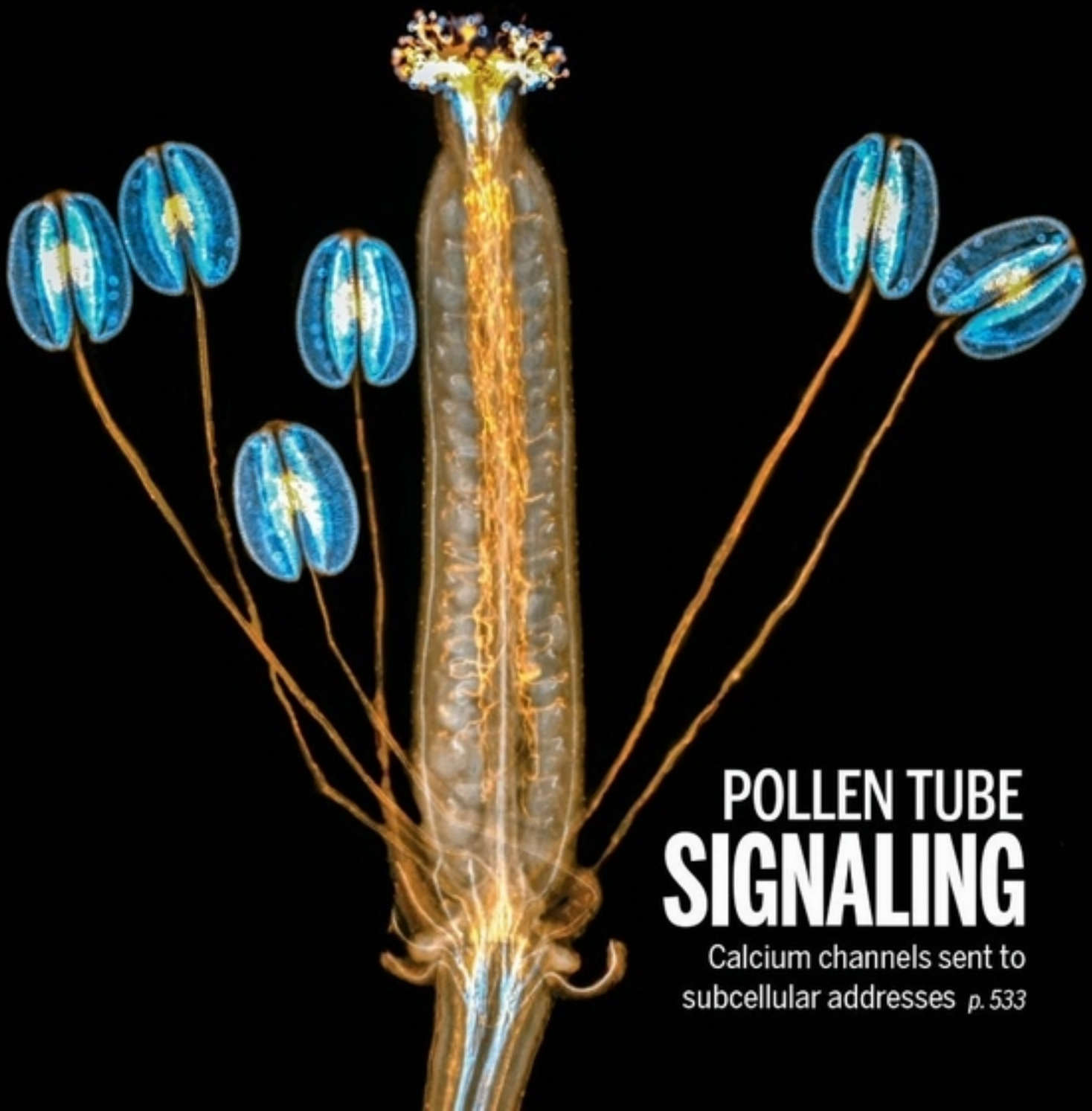

POLLEN TUBE SIGNALING

Calcium channels sent to subcellular addresses *p. 533*

CONTENTS

4 MAY 2018 • VOLUME 360 • ISSUE 6388

486 Global plan for biodiversity

480 Harassment allegations at the Salk Institute

NEWS

IN BRIEF

IN DEPTH

FEATURE

INSIGHTS

PERSPECTIVES

POLICY FORUM

BOOKS *ET AL.*

Published by AAAS

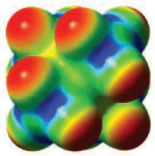

489
Ultrasonic processing of silanes

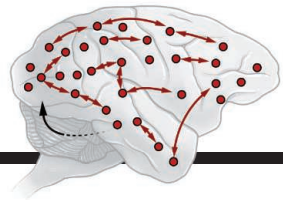

493 & 537
Conscious perception of stimuli

ON THE COVER

Fluorescence microscopy composite image of an *Arabidopsis* flower with six male organs (anthers) bearing pollen grains (blue dots inside) and the central female organ (ovary) bearing two lines of ovules (light blue) targeted by pollen tubes (orange lines). Wudick *et al.* describe a specific protein family's role in sorting and transporting glutamate receptor–like channels, which drive calcium currents and thus affect pollen tube growth and seed production. See page 533.
Image: Pedro Lima and José Feijó

SCIENCE (ISSN 0036-8075) is published weekly on Friday, except last week in December, by the American Association for the Advancement of Science, 1200 New York Avenue, NW, Washington, DC 20005. Periodicals mail postage (publication No. 484460) paid at Washington, DC, and additional mailing offices.

Domestic individual membership, including subscription (12 months): $165 ($74 allocated to subscription). Domestic institutional subscription (51 issues): $1808; Foreign postage extra: Mexico, Caribbean (surface mail) $55; other countries (air assist delivery): $89. First class, airmail, student, and emeritus rates on request. Canadian rates with GST available upon request, GST #125488122. Publications Mail Agreement Number 1069624. **Printed in the U.S.A.**
Change of address: Allow 4 weeks, giving old and new addresses and 8-digit account number. **Postmaster:** Send change of address to AAAS, P.O. Box 96178, Washington, DC 20090–6178. **Single-copy sales:** $15 each plus shipping and handling; bulk rate on request. **Authorization to reproduce** material for internal or personal use under circumstances not falling within the fair use provisions of the Copyright Act is granted by AAAS to libraries and others who use Copyright Clearance Center (CCC) Pay-Per-Use services provided that $35.00 per article is paid directly to CCC, 222 Rosewood Drive, Danvers, MA 01923. The identification code for *Science* is 0036-8075. *Science* is indexed in the *Reader's Guide to Periodical Literature* and in several specialized indexes.

Science
AAAS
1200 New York Avenue, NW, Washington, DC 20005
Clarendon House, Clarendon Road, Cambridge, UK CB2 8FH

SUBSCRIPTION SERVICES For change of address, missing issues, new orders and renewals, and payment questions: 866-434-AAAS (2227) or 202-326-6417, FAX 202-842-1065. Mailing addresses: AAAS, P.O. Box 96178, Washington, DC 20090-6178 or AAAS Member Services, 1200 New York Avenue, NW, Washington, DC 20005

INSTITUTIONAL SITE LICENSES 202-326-6730 **REPRINTS:** Author Inquiries 800-635-7181 **COMMERCIAL INQUIRIES** 803-359-4578 **PERMISSIONS** 202-326-6765, permissions@aaas.org **AAAS Member Central Support** 866-434-2227 www.aaas.org/membercentral.

INFORMATION FOR AUTHORS See www.sciencemag.org/authors/science-information-authors

Published by AAAS

EDITORIAL

Global data meet EU rules

We are at the beginning of the "fourth industrial revolution," with unprecedented capabilities to acquire, process, and communicate data. As with all revolutions, it holds great promise as well as dangers. Outrage at large-scale privacy breaches demonstrates the perils of taking protection of personal data lightly and reminds us that technological progress challenges policies, values, and approaches to ethics. The European Union (EU) General Data Protection Regulation (GDPR) that takes effect on 25 May offers never-before-seen protections and control by individuals of their personal data, including many provisions for research. Although this should increase public trust and therefore propensity to share data, many implementation details and safeguards have yet to be established. It is clear, however, that interoperability of policies will be essential to promote data sharing across research communities within the EU and globally.

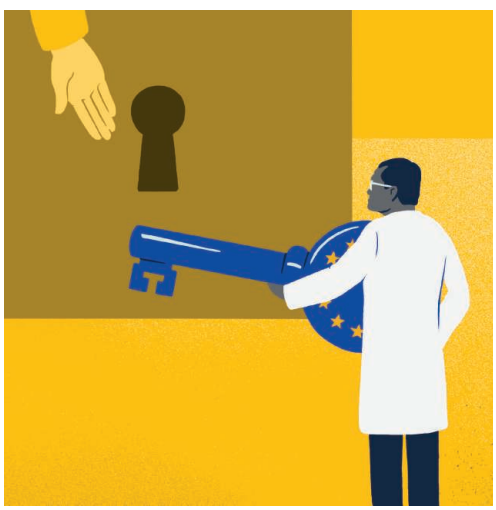

"...interoperability of policies will be essential to promote data sharing..."

The GDPR promulgates "privacy by design," improves data custodianship, establishes rights of data erasure and portability, and specifies that consent to collect and use data must be given by clear affirmative action. It establishes that EU protection follows EU individuals' data even if the data leave the EU. The GDPR includes provisions that ensure personal data protection without undue impact on research and innovation. For example, personal data may be used for research purposes that are not identical with those at the time of their initial collection; under certain conditions, personal data may be processed for research without prior consent, and the rights of an individual to object to processing or request erasure may be overridden. Provisions are made for sensitive data, such as genetic, biometric, and health data, or data revealing racial or ethnic origin and political or religious beliefs.

The GDPR sets basic rules and conditions for personal data in research, but provides flexibility for EU member states to legislate many safeguards and conditions. EU states thus must be vigilant that discretion given to them by the GDPR does not undermine interoperability. Legislation is already adopted or in preparation in some EU states, such as the German Data Protection Amendment Act or the UK Data Protection Bill. Interoperability is equally important at the global level; rules for personal data in research in one country may affect use of data from another.

A basic aspect of interoperability is the ability to transfer data. The European Commission has already deemed some non-EU countries' protections adequate under GDPR, including Argentina, Israel, New Zealand, and the United States (limited to Privacy Shield Framework participants), meaning that personal data may be transferred from the EU without authorization or further safeguards.

The research community has a strong interest in promoting consistent regulatory approaches to facilitate access and legal interoperability, including when data are federated in cloud computing environments and access is provided from anywhere in the world. The GDPR has modernized the EU regulatory framework, but international coordination is needed to seek legal interoperability across countries and regions. This must link to efforts resolving technical and organizational barriers to interoperability and to data initiatives like the European Open Science Cloud or the Helix Nebula project. Coordination may be effected in global forums such as the Research Data Alliance, which with the Committee on Data for Science and Technology and the National Information Standards Organization has been looking at legal interoperability, and in community-led initiatives, such as the Innovative Medicines Initiative, which has already launched key projects in this area.

GDPR is a landmark, but sharing of personal data for research across borders on a global scale will remain a technical, legal, and governance challenge—and opportunity—for the global science community.

–Kostas Glinos

Kostas Glinos is Visiting Fellow at Lee Kuan Yew School of Public Policy, National University of Singapore. He is on sabbatical from the Directorate-General for Research and Innovation, European Commission. kostas.glinos@gmail.com

10.1126/science.aat9878

> “What if [a site] was called Police Genealogy? People wouldn’t do it.”
>
> **Geneticist Yaniv Erlich**, who predicted in a 2014 journal article that police could use genealogy databases to identify suspects, as they did with the alleged Golden State Killer last week, raising privacy concerns.

IN BRIEF

Edited by **Jeffrey Brainard**

CLIMATE SCIENCE

Plans laid to study imperiled glacier

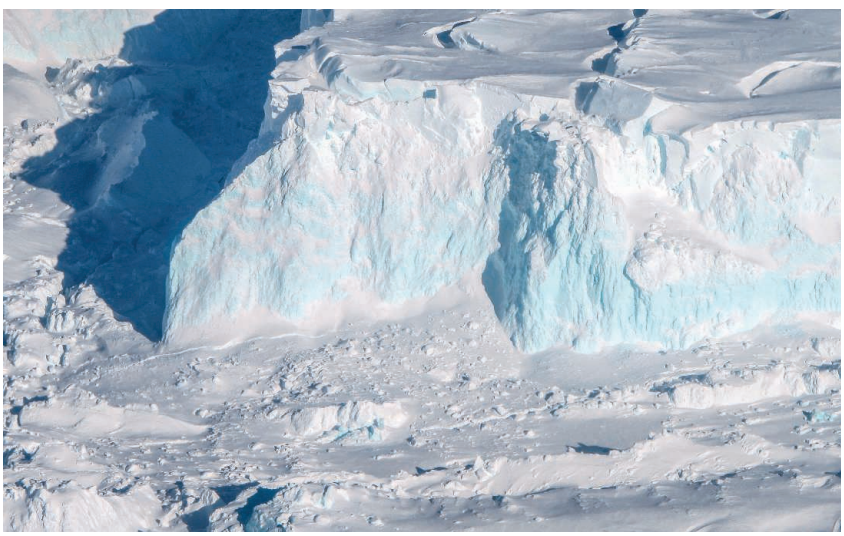

Collapse of the Thwaites glacier could trigger dramatic sea-level rise.

U.S. and U.K. science agencies announced last week a joint, $50 million plan to study the Thwaites glacier in West Antarctica, the continent’s ice sheet most at risk of near-term melting. Thwaites covers 182,000 square kilometers on the Amundsen Sea and acts as a plug, blocking the rest of the West Antarctic Ice Sheet from flowing into the ocean. If the entire ice sheet collapses, it could raise sea levels by several meters over centuries or millennia. To get a better handle on what might happen, the International Thwaites Glacier Collaboration will deploy 100 scientists in six teams to the remote area, 1600 kilometers from the nearest research station. Working mostly during the Antarctic summers of 2019–20 and 2020–21, they will apply a variety of research tools, including seismographs and instrument-carrying seals. Scientists will drill holes through the ice to measure warm ocean water intruding below and to examine whether the glacier has retreated in the past. Seismic surveys will probe the composition of the bedrock and the glacier’s bonds to neighboring ice sheets. Underwater robots will explore the grounding line, the point where ice meets the sea floor. Two other teams will channel these data into global models, with hopes of better understanding just how long Thwaites might remain intact.

Regular antibiotics save children

PUBLIC HEALTH | Giving children in sub-Saharan Africa prophylactic antibiotics could save tens of thousands of lives, a study has found. Researchers gave azithromycin, a broad-spectrum antibiotic, or a placebo twice a year for 2 years to nearly 200,000 infants and toddlers from Malawi, Niger, and Tanzania. Overall, the antibiotics slashed death rates by nearly 14%; for 1- to 5-month-olds, mortality rates plummeted 25%, researchers reported in the 26 April issue of *The New England Journal of Medicine*. Although they did not assess how the azithromycin doses saved lives, the antibiotic likely reduced cases of diarrhea and pneumonia, both major causes of death for newborns. Now, the World Health Organization will begin a review process to decide whether to advise routinely giving antibiotics prophylactically and under what circumstances. Some experts are concerned about the emergence of antibiotic-resistant bacteria. “Giving antibiotics to healthy children is, at best, a stopgap measure to use only in areas with extremely high childhood mortality rates,” said Ramanan Laxminarayan, director of the Center for Disease Dynamics, Economics & Policy in Washington, D.C.

EU expands pesticide ban

AGRICULTURE | The European Union has expanded a controversial ban of neonicotinoid pesticides, long under scrutiny for potentially harming pollinators. They may still be used in permanent greenhouses. In 2013, the European Commission forbade the use of the three neonicotinoids in flowering crops, such as oilseed rape, that appeal to honey bees and other pollinating insects. Last year, the commission proposed extending the ban to all field crops because of growing evidence that the pesticides can harm domesticated honey bees—impairing memory and navigation, for example—and wild pollinators. Representatives of 16 member states voted for the ban on 27 April, after struggling for several months to achieve a majority; five countries opposed the ban, and 13 abstained. Some farming groups warned that neonicotinoids will be replaced with sprays that are more harmful

PHOTO: NASA ICE/JAMES YUNGEL

Removing trees—through fire or deliberate thinning—reduces demands on groundwater.

CONSERVATION

From forest fires, a paradoxical bounty of water

Forest fires could help relieve water shortages in the western United States, a new study shows. When trees are lost to fires, water stays in their watersheds rather than evaporating from leaves to the atmosphere. Between 1990 and 2008, more than 76 billion liters were saved this way across two river basins in California totaling almost 10,000 square kilometers, researchers reported last week in *Ecohydrology*. Hydrologist Roger Bales from the University of California, Merced, and his colleagues studied evaporation rates before and after natural wildfires, using a combination of satellite data and towers that measure water evaporating from trees in forests. Because managers have worked for a century to suppress forest fires, western forests are dense and susceptible to uncontrollable wildfires, Bales says. Thinning forests by cutting down smaller trees or using controlled burns would reduce wildfire risk and, by increasing water yield from these areas, help pay for itself, he notes.

to pollinators. Pollinator experts cautioned that the ban doesn't include other kinds of systemic pesticides, which, like the neonicotinoids, spread through entire plants. They also say more action is needed to protect pollinators from other threats, including introduced parasitic mites, the loss of diverse flowers to feed on, and destruction of nesting habitat.

Scientists dive into podcasting

SCIENCE MEDIA | Scientists have hosted about two-thirds of the nearly 1000 English-language podcasts about science produced since 2004. That data point comes from a study of 952 shows by Lewis MacKenzie of Durham University in the United Kingdom, in an 11 April preprint on bioRxiv. About half of those shows are still active. Most shows (76%) had no apparent revenue source. A majority were framed for nonspecialist audiences; formats included chats, dramas, even comedy. Most did not post episodes on a regular schedule, and a third featured 10 or fewer episodes. Who listens? MacKenzie says data about podcast listeners weren't available, but he thinks the topic deserves follow-up study.

Top 10 podcast topics, 2004–2018

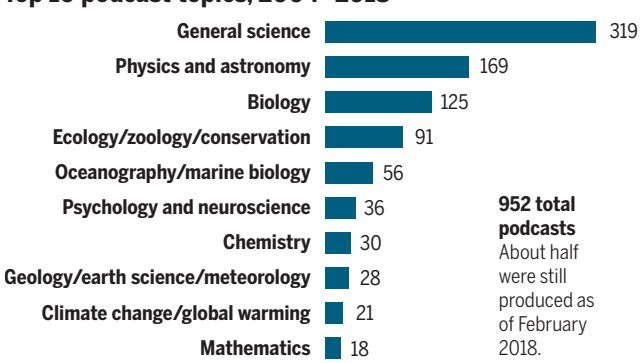

Precision medicine study launches

BIOMEDICINE | The U.S. National Institutes of Health detailed its plans to open national enrollment for a massive study of personalized medicine on 6 May, with a goal of enlisting 1 million people. Proposed in 2015 by then-President Barack Obama, the All of Us project will explore links between genes, lifestyle, and disease by following participants' health for 10 years. After enrolling 26,000 people in a pilot effort, the study will now ramp up the recruiting of more volunteers, 18 years or older, through 17 health provider organizations and a website: joinallofus.org. Participants will be asked to share their electronic medical records, and some will be invited to give blood and urine samples and wear a Fitbit-like device that gathers health data. The study aims to ensure that 70% to 75% of participants are from groups traditionally underrepresented in medical research.

Revamped collider starts up

PARTICLE PHYSICS | It took about 5 years longer than once hoped, but physicists in Japan have started up their revamped particle collider, SuperKEKB, at KEK, the High Energy Accelerator Research Organization, in Tsukuba. An upgrade of the KEKB collider, which ran from 1999 to 2010, the new accelerator began smashing electrons into positrons last week, lab officials announced. Like its predecessor, SuperKEKB will produce particles called B mesons. KEKB helped show that B mesons and their antimatter counterparts decay in slightly different ways, as predicted. Over the next 10 years, SuperKEKB will produce 50 times more data than KEKB, which may reveal additional differences in B meson decays—potential clues to explain why the universe contains more matter than antimatter.

Researchers think the killings may have been a ritualistic plea to stop extreme weather.

ARCHAEOLOGY

Largest mass child sacrifice found in Peru

Around the year 1450 C.E., at least 140 children and 200 baby llamas were killed in Peru, the largest mass child sacrifice discovered to date, archaeologists say. The site is on the country's northern coast, near the city of Chan Chan, the capital of the Chimú empire, which ruled the region from about 1000 C.E. to 1470 C.E. "I see [child sacrifice] as a particularly important, valuable sacrifice," says John Verano, an archaeologist at Tulane University in New Orleans, Louisiana, who helped excavate the site. He and his colleagues hypothesize that the sacrifice could have been a plea to the gods to stop extreme weather. The graves were dug into a thick layer of mud, a likely sign of a flash flood brought on by a strong El Niño event, Verano says. All the human and animal victims were killed with a horizontal cut across the sternum, which was used to open the chest and remove the heart, evidence of an intentional ritualistic sacrifice. Most of the children were between the ages of 8 and 12. The excavations were funded by the National Geographic Society, which exclusively reported the discovery on 26 April (see https://scim.ag/NatGeoPeru).

Seismic ship to be sold

GEOPHYSICS | Marine seismologists are decrying a move by the U.S. National Science Foundation (NSF) to sell its only ship capable of imaging geological structures below the sea floor, such as the boundaries between colliding tectonic plates that drive large earthquakes. For the past few years, NSF has sought a new business model for the *R/V Marcus G. Langseth* to close an annual $3.5 million funding gap. No palatable fix has been found, the agency said in April, which means it will sell the ship and scientists will have to arrange their own survey trips aboard private-sector vessels. The sale amounts to a "loss of trust" and should be delayed until NSF finds a long-term solution, the leaders of the Incorporated Research Institutions for Seismology wrote in a 26 April letter to NSF. Otherwise, they say, scientists may be forced to tag along on survey ships used by oil and gas companies, which could slant research toward questions of interest to industry.

A bid to make virus-proof cells

BIOTECHNOLOGY | The synthetic biology initiative known as Genome Project–write (GP-write) announced plans this week to rally its international group of scientists, ethicists, and policymakers around a "community-wide project"—engineering virus-resistant cells. The goal, described by GP-write's leadership at a 1 May meeting in Boston, is more narrowly focused than the project's original ambition—to design and assemble from scratch a full human genome. But the work, which project organizers hope to complete within 10 years, could be useful in drug manufacturing, where cells producing therapeutic proteins sometimes get contaminated with viruses. GP-write organizers are also considering other "ultrasafe" cell features, such as resistance to cancerous mutations and the effects of radiation and freezing. Its leaders hope the safer cells effort will encourage researchers to develop new tools for redesigning entire genomes. For now, though, GP-write isn't offering its participants any funding.

Estimated autism rate rises

PUBLIC HEALTH | The U.S. Centers for Disease Control and Prevention (CDC) last week revised upward its estimated rate of autism among children, saying the rise was caused in part by increased awareness of the condition and more diagnoses, especially among black and Latino children who were underrepresented in previous federal counts. Based on school and medical records of 8-year-olds in 11 states, CDC found that one in 59 fit the criteria for an autism spectrum disorder in 2014, up from one in 68 in 2012. As in past studies, boys were about four times more likely than girls to be diagnosed. CDC says the biennial study is not nationally representative because of limitations in its design, but that variations in estimated rates across states and among racial and ethnic groups can help guide public awareness campaigns.

Plant palace to reopen

BOTANY | When Kew Gardens' Temperate House opened in Richmond, U.K., in 1863, it was the largest greenhouse in the world, an innovative architectural showpiece designed to help attract crowds from nearby London and introduce them to the growing importance of plant science. On 5 May, the iconic structure is scheduled to reopen after a 5-year, £41 million overhaul. Workers replaced most of the 16,000 panes of glass. Exhibits include about 1000 rare and threatened plants grown by conservation biologists at Kew's Millennium Seed Bank from its vast collections. These will also be available for study and sampling; Kew's Plant and Fungal Trees of Life project is already sequencing the genomes of some species to clarify evolutionary relationships.

SCIENCEMAG.ORG/NEWS
Read more news from *Science* online.

PHOTO: GABRIEL PRIETO/NATIONAL GEOGRAPHIC

PHOTO: IM_PHOTO/SHUTTERSTOCK.COM

U.S. REGULATORY POLICY

Critics see hidden goal in EPA data access rule

They say new policy aims to weaken air pollution regulations by barring key studies

By **Warren Cornwall**

When Scott Pruitt, administrator of the U.S. Environmental Protection Agency (EPA) in Washington, D.C., announced last week that the agency plans to bar regulators from considering studies that have not made their underlying data public, he said it was to ensure the quality of the research used to shape new rules. "The era of secret science at EPA is coming to an end," Pruitt said at a 24 April event (which was closed to the press) unveiling the proposed "transparency" rule.

But longtime observers of EPA, including former senior agency officials, see a more troubling and targeted goal: undermining key studies that have helped justify stricter limits on air pollution. In particular, they say, the new policy is aimed at blocking EPA consideration of large epidemiological studies that have highlighted the health dangers of tiny particles of soot and other chemicals less than 2.5 microns in diameter. Those studies, which rest in part on confidential health information that is difficult to make public, have been under attack for decades from some industry groups and Republican lawmakers in Congress, who argue that the confidentiality masks flaws in the studies. The same interests lobbied heavily for the new EPA rule, and critics of the policy say it is just new clothing for an old—and largely discredited—argument.

"It just keeps coming back in different forms. … It's like malaria. Or maybe herpes would be a better analogy," says toxicologist Dan Costa of Chapel Hill, North Carolina, who recently retired after leading EPA's air research program for 14 years.

At the heart of the fight is a type of pollution scientists believe is particularly lethal, but relatively costly to control: tiny particles of soot and other chemicals produced by burning oil, coal, gasoline, wood, and other fuels, which can lodge deep in the lungs. In the mid-1990s, two major epidemiological studies—known as the Harvard Six Cities and American Cancer Society (ACS) studies—tracked the medical histories of thousands of people exposed to different levels of air pollution. The studies found that exposure to even relatively low particulate levels increased premature deaths. Further studies have linked the pollution to other problems including asthma, heart disease, and heart attacks.

> ***"It just keeps coming back in different forms. … It's like malaria. Or maybe herpes would be a better analogy."***
>
> **Dan Costa**, former Environmental Protection Agency official

In response, EPA began tightening clean air regulations—and affected industries began to attack the findings. Industry representatives also urged Congress to pass legislation that would bar EPA from using nonpublic data in crafting regulations. In recent years that legislation, championed by Representative Lamar Smith (R–TX), head of the House of Representatives's science committee, failed to gain approval. But after the election of President Donald Trump, Smith and his allies found a receptive audience in Pruitt, who agreed to implement similar policies as an EPA rule.

In the meantime, an array of studies, including a government-sponsored reanalysis of the original particulate data, has generally validated the findings (see sidebar, p. 473). "The bottom line is the results don't go away. They're real," says C. Arden Pope III, one of the lead researchers on the Six Cities and ACS studies and now an epidemiologist at Brigham Young University in Provo, Utah.

In 2013, that scientific consensus prompted EPA to reduce allowable particulate levels to 12 micrograms per cubic meter of air, down from an earlier standard of 15 micrograms. At the same time, the agency calculated that the benefits of even tighter

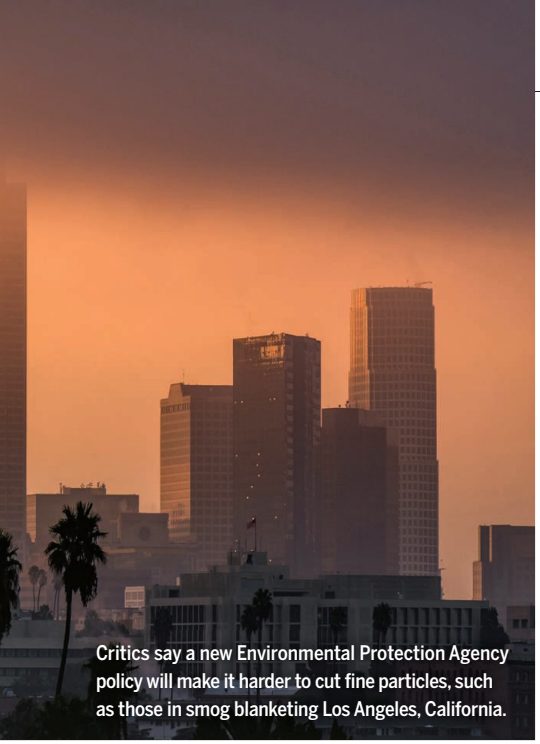

Critics say a new Environmental Protection Agency policy will make it harder to cut fine particles, such as those in smog blanketing Los Angeles, California.

standards would outweigh the costs. Lowering the standard to 11 micrograms would increase pollution-control costs by as much as $1.35 billion in 2020, analysts estimated, but the health gains and lives saved would be worth as much as $20 billion a year.

That cost-benefit ratio is "an inconvenient fact if you're someone who doesn't like air pollution regulations," says Gretchen Goldman, an analyst and former pollution scientist in the Washington, D.C., office of the Union of Concerned Scientists, which opposes the new EPA rule.

The timing of the rule—which observers expect EPA to adopt once a public comment period closes—is no coincidence, Goldman and others believe. The agency is about to embark on a periodic review of key air pollution limits, including those governing particulates. Even seemingly modest changes in how the agency evaluates the science could lead to lower estimates of the health benefits of tighter standards.

"If stakeholders can change the ground rules so that the EPA can't look at that [health] data, that kind of takes away the foundation on which to quantify the adverse effects of exposure," says environmental engineer Chris Frey of North Carolina State University in Raleigh. Frey previously chaired EPA's Clean Air Scientific Advisory Committee (CASAC) and now serves on an agency panel that reviews particulate pollution science.

The current head of EPA's CASAC, however, says the agency will still have good science to draw on. Anthony Cox, a statistician and risk analyst based in Denver, whom Pruitt appointed to lead the panel last year, says there are ways to analyze confidential health data without disclosing identities. He's confident that the agency and his committee will "act with integrity and intelligence in using the best available science" when reviewing air pollution standards. (EPA did not respond to a request for comment.)

A first test could come later this year, when EPA researchers expect to finalize a report on the latest particulate science. Cox's committee would then review the report, which would underpin any agency decision about where to set new pollution thresholds.

In the meantime, Frey questions whether the new rule, which would apply only to "significant" regulations judged to cost $100 million or more, will survive an expected court challenge. In particular, he wonders how EPA will meet its legal obligation, spelled out by Congress, to base regulations on the "best available science" if it tries to disregard a large body of accepted research. "I don't see how," he says, "EPA could defend that in court." ■

Clever use of public data could sidestep new rule

By **Susan Cosier**

Critics of the Environmental Protection Agency's (EPA's) move last week to limit the agency's use of nonpublic data say it is a thinly veiled effort to prevent regulators from drawing on public health studies that have proved pivotal to justifying tougher air pollution limits (see main story, p. 472).

Recently, however, one research team has demonstrated what could be a way around the policy. They used publicly available data to produce high-quality findings on the ills of pollution that EPA's new policy might not be able to quash.

"This is a very highly contentious political climate, and we are taking the extra step to be as transparent as we can be," says biostatistician Francesca Dominici of the Harvard T. H. Chan School of Public Health in Boston, who led the studies. In one, published in *The New England Journal of Medicine* in June 2017, she and her colleagues used publicly accessible air pollution data and records compiled by the federal government's Medicare health insurance program to show that even modest pollution reductions could save more than 10,000 lives per year. In another, published in *JAMA* last December, they linked short-term exposure to air pollution levels below current limits to premature death among the elderly.

Previous studies suggesting that current levels of U.S. air pollution cause avoidable health problems and deaths typically relied on private health information painstakingly collected from a relatively limited group of participants. In contrast, Dominici's team tapped anonymized Medicare data on 60 million enrollees over 12 years. It revealed where people lived, their age, race, hospital visits, and when they died. The researchers also collected weather, pollution, census information, and other public records from EPA and other agencies. They then divided the United States into a 1-kilometer-by-1-kilometer grid and used a computer model to see how levels of pollution compared with the health trajectories of the Medicare enrollees, taking into account confounding factors such as poverty and smoking.

The result is one of the largest and most statistically sophisticated studies of dirty air's health impacts, says air pollution specialist C. Arden Pope III of Brigham Young University in Provo, Utah. Pope helped lead earlier landmark air pollution studies relying on confidential data. Dominici's team, he says, "is taking a brand new cohort, and a huge one at that, and replicating the results" of previous studies. And anyone can download the same data and reanalyze the results, Dominici says—the exact goal EPA says it wants to achieve.

Public data can't be used to answer every important question about how pollution affects people, Dominici emphasizes. "I cannot look at pulmonary function or the thickness of your artery," she says. "Very well designed cohort studies are extremely important to scientific advancement, and when you're looking at the history of individuals, you have to maintain their confidentiality."

Still, EPA could soon be giving her team's studies a close look, because the agency is undertaking a periodic review of key air quality standards. Supporters of EPA's new data access policy have said they want to rid the regulatory process of potentially flawed "secret science." Now, the question is whether they will also object to EPA considering analyses of public data that, like previous studies, suggest tightening the standards would benefit public health.

Susan Cosier is a journalist based in Chicago, Illinois.

SCIENCE POLICY

Europe moves to compete in global AI arms race

With €1.5 billion for artificial intelligence, European Commission pins hopes on ethics

By **Tania Rabesandratana**

Europe is trying to catch up to the United States and China in an artificial intelligence (AI) arms race. The European Commission announced last week that it would devote €1.5 billion to AI research funding through 2020. It also said it would present ethical guidelines for AI development by the end of the year, suggesting that Europe could become a precautionary counterweight to its global rivals as fears are raised about a lack of fairness and transparency in the quickly advancing field.

Both the United States and China practice "permissionless innovation: Break things as you go and go fast," says Eleonore Pauwels, an ethics researcher at United Nations University in New York City. In contrast, Europeans "are betting on being the good guy," she says. This could mean, for instance, developing AI systems that require smaller data sets, enhance privacy and trust, and are more transparent than their competitors', Pauwels says. But it remains to be seen whether Europe can make this noble vision a reality, she adds.

> ***"Europeans are betting on being the good guy."***
> **Eleonore Pauwels**, United Nations University

The commission says it will fund basic research as well as research that could be spun off into the market, and it intends to help member states set up joint research centers across Europe. It also plans to update rules to ease the reuse of public sector information—including available research data. Large data sets are critical for training AIs.

Jeffrey Ding, who studies AI governance at the University of Oxford in the United Kingdom and monitors the AI potential of different countries, says Europe has strong AI research, but a weak AI industry, in part because its AI startups attract far less venture capital funding than those in the United States and China do. Ding also rates the United States as a tougher competitor than China, which he says trails the United States in every factor except access to data.

Stéphan Eloïse Gras, a French digital humanities researcher at New York University (NYU) in New York City, adds that Europe's ambitions are hindered by outdated industrial policies that provide too much support to big, risk-averse firms and not enough for risky startups. Astronomical industry salaries have also lured away talent from European universities, says Jean Ponce, an artificial vision researcher at France's École Normale Supérieure, who spent 22 years working in the United States and is now working on a French-U.S. AI agreement at NYU.

The funding push and the forthcoming ethical guidelines could help nurture what Bernhard Schölkopf, a machine learning researcher at the Max Planck Institute for Intelligent Systems in Tübingen, Germany, calls a "European angle on AI" that values privacy, transparency, and fairness. "However, it would be short-sighted for Europe to only focus on potential problems and let others push the boundaries of knowledge," Schölkopf adds. "We do not yet understand well how to make [AI] systems robust, or how to predict the effect of interventions."

The commission says it will now work with member states to take concrete steps to realize the continent's AI ambitions. The European measures come 1 month after France presented its own AI intentions, and a week after a U.K. Parliament report urged the government to help the country become an AI leader. On 10 April, 25 European countries signed a statement of principles, in which governments agreed to work together on AI and to consider AI research funding "as a matter of priority."

On 24 April, a group of nine prominent AI researchers, including Schölkopf, took matters into their own hands in an open letter urging governments to set up an intergovernmental European Lab for Learning & Intelligent Systems (ELLIS), inspired by the European Molecular Biology Laboratory. ELLIS would be a "top employer in machine intelligence research," and on par with leading world universities, the letter says, offering attractive salaries and "outstanding academic freedom and visibility." ■

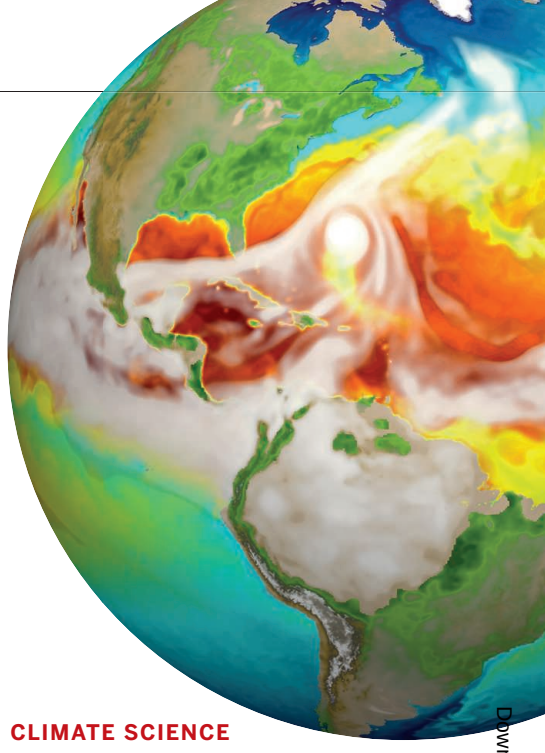

IMAGE: MATHEW MALTRUD, LOS ALAMOS NATIONAL LABORATORY ON BEHALF OF THE E3SM PROJECT (LA-UR-18-23682)

CLIMATE SCIENCE

DOE unveils climate model in advance of global test

Model made for exascale computers is focused on energy infrastructure

By **Gabriel Popkin**

The world's growing collection of climate models has a high-profile new entry. Last week, after nearly 4 years of work, the U.S. Department of Energy (DOE) released computer code and initial results from an ambitious effort to simulate the Earth system. The new model is tailored to run on future supercomputers and designed to forecast not just how climate will change, but also how those changes might stress energy infrastructure.

Results from an upcoming comparison of global models may show how well the new entrant works. But so far it is getting a mixed reception, with some questioning the need for another model and others saying the $80 million effort has yet to improve predictions of the future climate. Even the project's chief scientist, Ruby Leung of the Pacific Northwest National Laboratory (PNNL) in Richland, Washington, acknowledges that the model is not yet a leader. "We really don't expect that our model will be wowing

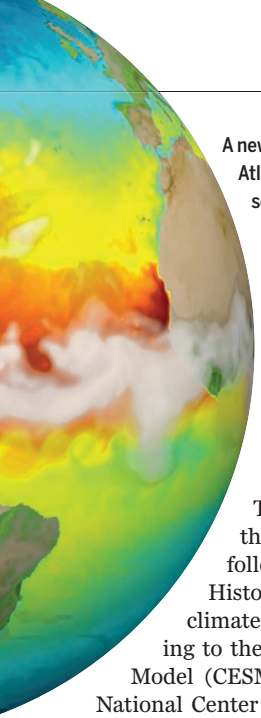

A new model simulates a North Atlantic hurricane and the cold seas (yellow) left in its wake.

the world," she says.

Since the 1960s, climate modelers have used computers to build virtual globes. They break the atmosphere and ocean into thousands of boxes and assign weather conditions to each one. The toy worlds then evolve through simulated centuries, following the laws of physics. Historically, DOE's major role in climate modeling was contributing to the Community Earth System Model (CESM), an effort based at the National Center for Atmospheric Research (NCAR) in Boulder, Colorado. But in July 2014, DOE launched its Accelerated Climate Model for Energy (*Science*, 13 September 2013, p. 1160). The goal was to predict how storms and rising seas could affect power plants, dams, and other energy infrastructure, and to focus on regions such as North America or the Arctic. DOE officials also wanted a model that could run on a generation of megapowerful "exascale" computers expected to turn on around 2021.

The project pulled in researchers from eight DOE national labs. It began as a carbon copy of the CESM and retains similar atmosphere and land models, but includes new ocean, sea-ice, river, and soil biochemistry simulations. The DOE team doubled the number of vertical layers, extended the atmosphere higher, and adopted a number-crunching method that is computationally intensive but may be easier to break into chunks and run in parallel on the anticipated exascale machines. "For them, it makes a lot of sense to go in that direction," says Richard Neale, a climate scientist at NCAR.

In 2017, after President Donald Trump took office and pulled the nation out of the Paris climate accords, DOE dropped "climate" from the project name. The new name, the Energy Exascale Earth System Model (E3SM), better reflects the model's focus on the entire Earth system, says project leader David Bader of Lawrence Livermore National Laboratory in California.

The E3SM's first results highlight its potential; they include model runs with ultrasharp, 25-kilometer-wide grid cells—fine enough to simulate small-scale features such as ocean eddies and mountain snow packs. But this sharp picture is still too coarse to resolve individual clouds and atmospheric convection, major factors limiting models' precision. And some scientists doubt it will improve forecasts. The last intercomparison effort, which ended in 2014, included 26 modeling groups—nine more than the previous round—yet yielded collective predictions that were no more precise. "Just having more models—I don't think there's any evidence that that's key to advancing the field," says Bjorn Stevens, a climate scientist at the Max Planck Institute for Meteorology in Hamburg, Germany, and co-leader of the new intercomparison, code-named CMIP6.

Gavin Schmidt, who heads NASA's Goddard Institute for Space Studies in New York City, which also produces a global climate model, questions the new model's rationale, given that DOE's exascale computers do not yet exist. "No one knows what these machines will even look like, so it's hard to build models for them ahead of time," he wrote on Twitter. And the computational intensity of the E3SM has drawbacks, says Hansi Singh, a PNNL climate scientist who uses the CESM for her research. The sheer number of calculations needed to get a result with the E3SM would overwhelm most university clusters, limiting outside scientists' ability to use it.

One preliminary result, on the climate's sensitivity to carbon dioxide (CO_2), will "raise some eyebrows," Bader says. Most models estimate that, for a doubling of CO_2 above preindustrial levels, average global temperatures will rise between 1.5°C and 4.5°C. The E3SM predicts a strikingly high rise of 5.2°C, which Leung suspects is due to the way the model handles aerosols and clouds. And like many models, the E3SM produces two bands of rainfall in the tropics, rather than the one seen in nature near the equator.

The first test of the E3SM will be its performance in CMIP6. Nearly three dozen modeling groups, including newcomers from South Korea, India, Brazil, and South Africa, are expected to submit results to the intercomparison between now and 2020. Each group will devote thousands of computer-hours to standard scenarios, such as simulating the impact of a 1% per year CO_2 increase and an abrupt quadrupling of it.

But given the plodding rate of improvement since previous intercomparisons, few are expecting the E3SM or any other model to yield revolutionary insights. Stevens hopes to revise the exercise to encourage innovations, such as modeling the climate at the 1-kilometer resolution needed to make out individual clouds, or campaigns to gather new kinds of data. "The whole premise of CMIP is trying to get everyone to do the same thing," he says. "Everyone knows that breakthroughs come from getting people to do different things." ■

Gabriel Popkin is a journalist based in Mount Rainier, Maryland.

SCIENCE AND DIPLOMACY

Korean thaw raises hopes for scientific cooperation

Public health and ecology are among the areas targeted for joint efforts

By **Dennis Normile**

South Korea's scientists are welcoming the outcome of last week's historic summit with North Korea, which has raised hopes for a permanent peace treaty between the longtime foes. The joint statement signed by North Korea's Kim Jong Un and South Korean President Moon Jae-in calls for "more active cooperation, exchanges, visits and contacts at all levels." It does not mention science. But researchers are confident that the sentiments apply to research, too.

"Surely the agreement between Mr. Moon and Mr. Kim creates an opportunity to restart talks over cooperative research," says Ryu In-Chang, a geologist at Kyungpook National University in Daegu, South Korea. Nascent collaborations have been cut short in the past. But given the dramatic shift from confrontation to diplomacy, including an upcoming summit between Kim and U.S. President Donald Trump, "I think the current situation is different," says computer scientist Park Chan-Mo. Park, a former president of South Korea's Pohang University of Science and Technology and a veteran of North-South scientific exchanges (*Science*, 14 April 2006, p. 172).

One area of potential cooperation is public health. At an 18 April forum sponsored by the Korea Federation of Science and Technology Societies in Seoul, Shin Hee Young, a Seoul National University Hospital pediatric oncologist, described an analysis of North Korean scientific publications indicating that the north is struggling to contain multidrug-resistant tuberculosis and parasitic diseases rarely seen in the south. The study "can be used to develop strategies for North-South Korea cooperation," Shin and colleagues recently wrote in the *Journal of Preventive Medicine & Public Health.*

The rapprochement also brightens prospects for restarting stalled cooperative

studies of Mount Paektu, an active volcano straddling the border between North Korea and China. Paektu unleashed a massive eruption 1000 years ago, and seismic rumblings beneath the mountain in the mid-2000s led North Korea to reach out to geologists in the south and elsewhere for help in analyzing the threat. After several false starts, a pair of researchers from the United Kingdom visited Paektu in 2011 (*Science,* 4 November 2011, p. 584). But South Korean geologists were not invited on that trip.

Over the past year, scientists from South Korea and five other countries have been developing a proposal for installing a monitoring array in deep boreholes on Paektu to capture physical and chemical signals that might presage an eruption. So far, North Korean scientists have not taken part in the planning, says Lee Youn Soo, a geologist at the Korea Institute of Geoscience and Mineral Resources in Daejeon, South Korea. But in late March, with the help of AAAS (which publishes *Science*), the group approached a Pyongyang-based nongovernmental organization (NGO) that works to arrange scientific exchanges with North Korea. Lee hopes joint research on Paektu will be a priority in negotiations to follow the recent summit.

There is one place where scientists would like closer ties to keep things just as they are: the demilitarized zone (DMZ) between the two adversaries. Off-limits since the armistice ending hostilities in the Korean War was signed in 1953, the DMZ has become a 250-kilometer-long, 4-kilometer-wide biodiversity hot spot. It hosts an estimated 3500 plant and animal species, including endangered red-crowned cranes and rare Asiatic black bears. "Both war and peace could make this accidental paradise a zone of total destruction or a zone of overdevelopment," says Seung-ho Lee, a co-founder of the East Meadow, New York–based DMZ Forum, an NGO that hopes to turn at least part of the zone into a nature conservation area.

Hall Healy, an American conservationist who coordinates activities on the Korean peninsula for the International Crane Foundation, based in Baraboo, Wisconsin, says joint ecological studies in the DMZ could later be extended to other areas of the north. And optimists think North Korea is already showing signs of an interest in conservation: Last month the East Asian–Australasian Flyway Partnership—a network of governments and NGOs that works to preserve habitat for migratory birds—announced that North Korea will be its newest member. ■

With reporting by Ahn Mi-Young in Seoul.

PHOTO: BLOOMBERG/GETTY IMAGES

ENERGY POLICY

Bucking global trends, Japan again embraces coal power

Plans for new coal plants imperil efforts to cut emissions

By **Dennis Normile**

Most of the world is turning its back on burning coal to produce electricity, but not Japan. The nation has fired up at least eight new coal power plants in the past 2 years and has plans for an additional 36 over the next decade—the biggest planned coal power expansion in any developed nation (not including China and India). And last month, the government took a key step toward locking in a national energy plan that would have coal provide 26% of Japan's electricity in 2030 and abandons a previous goal of slashing coal's share to 10%.

The reversal is partly a result of the 2011 disaster at the Fukushima Daiichi Nuclear Power Station, which punctured public support for atomic energy. Critics say it also reflects the government's failure to encourage investment in renewable energy. The coal revival, they say, has alarming implications for air pollution and Japan's ability to meet its pledges to cut greenhouse gas emissions, which account for 4% of the world's total. If all the planned coal plants are built, it will "be difficult for us to meet our emissions reduction goals," Minister of the Environment Masaharu Nakagawa noted earlier this year.

Not long ago, coal was on its way out in Japan. In 2010, coal plants accounted for 25% of Japan's electricity, but the powerful Ministry of Economy, Trade and Industry (METI) planned to reduce that share by more than half over 20 years. The ministry counted on nuclear power to pick up the slack, with its share of the nation's electricity set to increase from 29% in 2010 to 50% by 2030.

But the 2011 Fukushima nuclear accident forced a reassessment. All 54 of Japan's reactors were shut down pending compliance with new safety standards. Just seven have restarted. Utilities have turned to liquefied natural gas and coal, which surged to provide 31% of the country's electricity in 2014.

In many other nations, natural gas has replaced coal as a fuel source because gas costs less. But in Japan, "coal is cheap," says Takeo Kikkawa, an energy economist at Tokyo University of Science and a member of an METI advisory council on energy. That's because the nation must import natural gas in its relatively expensive liquefied form.

The new energy plan would cement coal's central role. Endorsed on 26 March by an METI advisory council, and likely to be adopted by the Cabinet later this year, it calls for nuclear plants to be restarted, boosting their share of electricity generation to between 20% and 22% by 2030. Renewable energy's share would rise slightly, to between 22% and 24%, with solar energy alone accounting for 7%. But fossil fuels—coal, oil, and natural gas—would provide 56%.

That reliance on coal will make it difficult for Japan to fulfill its pledge to cut greenhouse gas emissions by 26% below 2013 levels by 2030, and by 80% by 2050. Those cuts will be even harder to achieve if now-shuttered nuclear power plants aren't restarted.

Power industry officials, however, claim

Coal awaits transport at a Japanese port. Almost all of the nation's supply is imported.

they can limit emissions by building so-called clean coal plants and systems for capturing carbon. As an example, they point to Unit 2 at the Isogo Thermal Power Station in Yokohama. Completed in 2009, it uses a so-called ultrasupercritical cycle, which generates steam at very high heat and pressure, boosting the plant's efficiency to 45%, compared with 30% to 35% for conventional plants. The result is the world's lowest emissions per unit of power, according to the International Energy Agency's Clean Coal Center in Paris.

But such plants are costly. And critics note that more than half of the proposed coal stations will use more conventional—and polluting—technologies. The environment ministry projects that if all the planned plants are built, by 2030 coal's carbon emissions would more than offset the cuts Japan wants to make elsewhere. A yet-to-be-published Greenpeace study concludes that if the plants operate for 40 years, they would also emit pollutants that would cause more than 60,000 premature deaths.

Public opposition and projections of declining electricity demand have some utilities rethinking plans for new plants. The Electric Power Development Company of Tokyo announced last week that it is abandoning plans for two new 600-megawatt coal plants near Kobe. In all, companies have now canceled six planned coal plants announced since 2012, according to the environmental group Kiko Network in Kyoto.

Japan's turn to coal represents a missed opportunity for renewable energy, says Tomas Kåberger, an energy specialist at Chalmers University of Technology in Gothenburg, Sweden, and chair of the Tokyo-based Renewable Energy Institute. After the Fukushima accident, he notes, the government adopted incentives for renewable power and started to tweak energy markets to make renewables more competitive. The moves led to a surge of investment in solar power.

But Kåberger says under current rules, Japan's 10 regional utilities can still give their own generating plants priority access to transmission lines, which they also control. This creates uncertainty for those trying to sell renewable power into the grid. Such issues, together with subsidy cuts and other policy changes, last year led to a 32% decline in investment in solar power, says Hisayo Takada, Japan energy project leader for Greenpeace Japan in Tokyo. As a result, Minister of Foreign Affairs Taro Kono said at a symposium last month in Tokyo, "The situation in our solar energy sector today can only be described as lamentable." ■

IMAGE: MICHAEL HANSON AND BHART-ANJAN S. BHULLAR

PALEONTOLOGY

Fossils reveal how ancient birds got their beaks

3D scan of fossil still in rock uncovers agile, toothed beak, and illuminates evolutionary steps to modern birds

By **Gretchen Vogel**

As every schoolchild now knows, birds are dinosaurs, linked to their extinct relatives by feathers and anatomy. But birds' beaks—splendidly versatile adaptations that allow their owners to grasp, pry, preen, and tear—are nothing like stiff dinosaurian snouts, and how they evolved has been a mystery. Now, 3D scans of new fossils of an iconic ancient bird capture the beak just as it took form.

"This region of the [bird family] tree is populated almost exclusively by flattened specimens," in which delicate features of the skull are lost, says Amy Balanoff, a paleontologist at Johns Hopkins University in Baltimore, Maryland, who was not involved in the research. By bringing details from multiple specimens together, the new scans offer an early glimpse of key features of bird skulls, including a big brain and the movable upper jaw that helps make beaks so nimble.

Cretaceous *Ichthyornis* had teeth as well as a beak that could grasp prey like a modern bird's.

Ichthyornis, an ancient seabird from about 90 million years ago, has long been famous for having a body like a modern bird, with a snout lined with teeth like a dinosaur. Paleontologists studying the first *Ichthyornis* fossil, discovered in the 1870s in Kansas, initially thought the body came from a small bird and the jaw from a marine reptile. Further excavation convinced them that the pieces belonged to the same animal. In 1880, Charles Darwin wrote that *Ichthyornis* was among "the best support for the theory of evolution" since *On the Origin of Species* was published 2 decades earlier.

But in the original *Ichthyornis* fossil, the upper jaw is missing, and the toothed lower jaw resembles that of other dinosaurs. So paleontologists assumed that early birds made do with a fixed upper jaw, like most other vertebrates.

In 2014, paleontologists in Kansas found a new specimen of *Ichthyornis*. They shared the fossil with Bhart-Anjan Bhullar at Yale University and his colleagues.

Instead of extracting the fossil from the limestone in which it is embedded, the researchers used computerized tomography to scan the entire block of rock. Then they scanned three previously unrecognized specimens that they found in museum collections, and combined all the scans into a complete model of *Ichthyornis*'s skull. They also re-examined the original fossil from the 1870s, housed at Yale's Peabody Museum of Natural History. Among unidentified pieces stored with the fossil, they found a small fragment that, when scanned, turned out to contain two key bones from the upper snout—bones that were missing in the new specimens.

The resulting 3D model captures *Ichthyornis*'s transitional position between modern birds and other dinosaurs, Bhullar and colleagues report this week in *Nature*. Despite its dinosaurlike teeth, *Ichthyornis* had a hooked beak, likely covered by a hard layer of keratin, on the tip of its snout. It also could move both top and bottom jaws independently like modern birds.

That means beaks appeared earlier than thought, perhaps around the same time as wings, Bhullar says. The agile jaw probably allowed the bird to preen its feathers and gave it a pincerlike grasp. At the same time, *Ichthyornis* retained powerful jaw muscles. "more similar to what you'd see in velociraptor than what you'd see in living birds," says Daniel Field, a paleontologist at the University of Bath in the United Kingdom who helped lead the work.

This mosaic of dinosaurian and avian characteristics shows birds in the act of evolutionary transformation, says Patrick O'Connor, a paleontologist at Ohio University in Athens—and offers a reminder that evolution rarely takes a straight path. ■

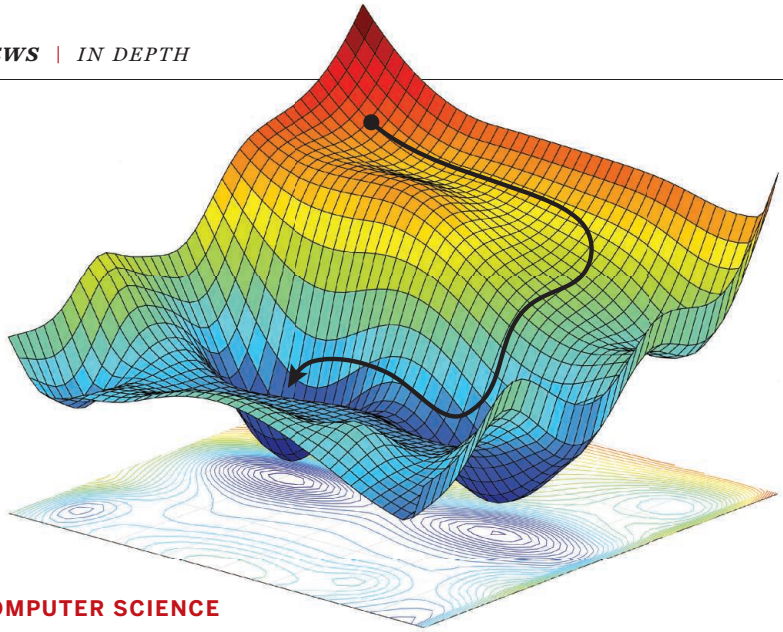

Gradient descent relies on trial and error to optimize an algorithm, aiming for minima in a 3D landscape.

COMPUTER SCIENCE

Has artificial intelligence become alchemy?

Machine learning needs more rigor, scientists argue

By **Matthew Hutson**

Ali Rahimi, a researcher in artificial intelligence (AI) at Google in San Francisco, California, took a swipe at his field last December—and received a 40-second ovation for it. Speaking at an AI conference, Rahimi charged that machine learning algorithms, in which computers learn through trial and error, have become a form of "alchemy." Researchers, he said, do not know why some algorithms work and others don't, nor do they have rigorous criteria for choosing one AI architecture over another. Now, in a paper presented on 30 April at the International Conference on Learning Representations in Vancouver, Canada, Rahimi and his collaborators document examples of what they see as the alchemy problem and offer prescriptions for bolstering AI's rigor.

"There's an anguish in the field," Rahimi says. "Many of us feel like we're operating on an alien technology."

The issue is distinct from AI's reproducibility problem (*Science*, 16 February, p. 725), in which researchers can't replicate each other's results because of inconsistent experimental and publication practices. It also differs from the "black box" or "interpretability" problem in machine learning: the difficulty of explaining how a particular AI has come to its conclusions (*Science*, 7 July 2017, p. 22). As Rahimi puts it, "I'm trying to draw a distinction between a machine learning system that's a black box and an entire field that's become a black box."

Without deep understanding of the basic tools needed to build and train new algorithms, he says, researchers creating AIs resort to hearsay, like medieval alchemists. "People gravitate around cargo-cult practices," relying on "folklore and magic spells," adds François Chollet, a computer scientist at Google in Mountain View, California. For example, he says, they adopt pet methods to tune their AIs' "learning rates"—how much an algorithm corrects itself after each mistake—without understanding why one is better than others. In other cases, AI researchers training their algorithms are simply stumbling in the dark. For example, they implement what's called "stochastic gradient descent" in order to optimize an algorithm's parameters for the lowest possible failure rate. Yet despite thousands of academic papers on the subject, and countless ways of applying the method, the process still relies on trial and error.

Rahimi's paper highlights the wasted effort and suboptimal performance that can result. For example, it notes that when other researchers stripped most of the complexity from a state-of-the-art language translation algorithm, it actually translated from English to German or French better and more efficiently, showing that its creators didn't fully grasp what those extra parts were good for. Conversely, sometimes the bells and whistles tacked onto an algorithm are the only good parts, says Ferenc Huszár, a machine learning researcher at Twitter in London. In some cases, he says, the core of an algorithm is technically flawed, implying that its good results are "attributable entirely to other tricks applied on top."

Rahimi offers several suggestions for learning which algorithms work best, and when. For starters, he says, researchers should conduct "ablation studies" like those done with the translation algorithm: deleting parts of an algorithm one at a time to see the function of each component. He calls for "sliced analysis," in which an algorithm's performance is analyzed in detail to see how improvement in some areas might have a cost elsewhere. And he says researchers should test their algorithms with many different conditions and settings, and should report performances for all of them.

Ben Recht, a computer scientist at the University of California, Berkeley, and coauthor of Rahimi's alchemy keynote talk, says AI needs to borrow from physics, where researchers often shrink a problem down to a smaller "toy problem." "Physicists are amazing at devising simple experiments to root out explanations for phenomena," he says. Some AI researchers are already taking that approach, testing image recognition algorithms on small black-and-white handwritten characters before tackling large color photos, to better understand the algorithms' inner mechanics.

Csaba Szepesvári, a computer scientist at DeepMind in London, says the field also needs to reduce its emphasis on competitive testing. At present, a paper is more likely to be published if the reported algorithm beats some benchmark than if the paper sheds light on the software's inner workings, he says. That's how the fancy translation algorithm made it through peer review. "The purpose of science is to generate knowledge," he says. "You want to produce something that other people can take and build on."

Not everyone agrees with Rahimi and Recht's critique. Yann LeCun, Facebook's chief AI scientist in New York City, worries that shifting too much effort away from bleeding-edge techniques toward core understanding could slow innovation and discourage AI's real-world adoption. "It's not alchemy, it's engineering," he says. "Engineering is messy."

Recht sees a place for methodical and adventurous research alike. "We need both," he says. "We need to understand where failure points come so that we can build reliable systems, and we have to push the frontiers so that we can have even more impressive systems down the line." ■

Matthew Hutson is a journalist based in New York City.

IMAGE: ALEXANDER AMINI, DANIELA RUS, MASSACHUSETTS INSTITUTE OF TECHNOLOGY. ADAPTED BY M. ATAROD/*SCIENCE*

A HIDDEN HISTORY

As cancer scientist Inder Verma's career soared, female colleagues allege that a parallel tale of sexual harassment unfolded over 4 decades

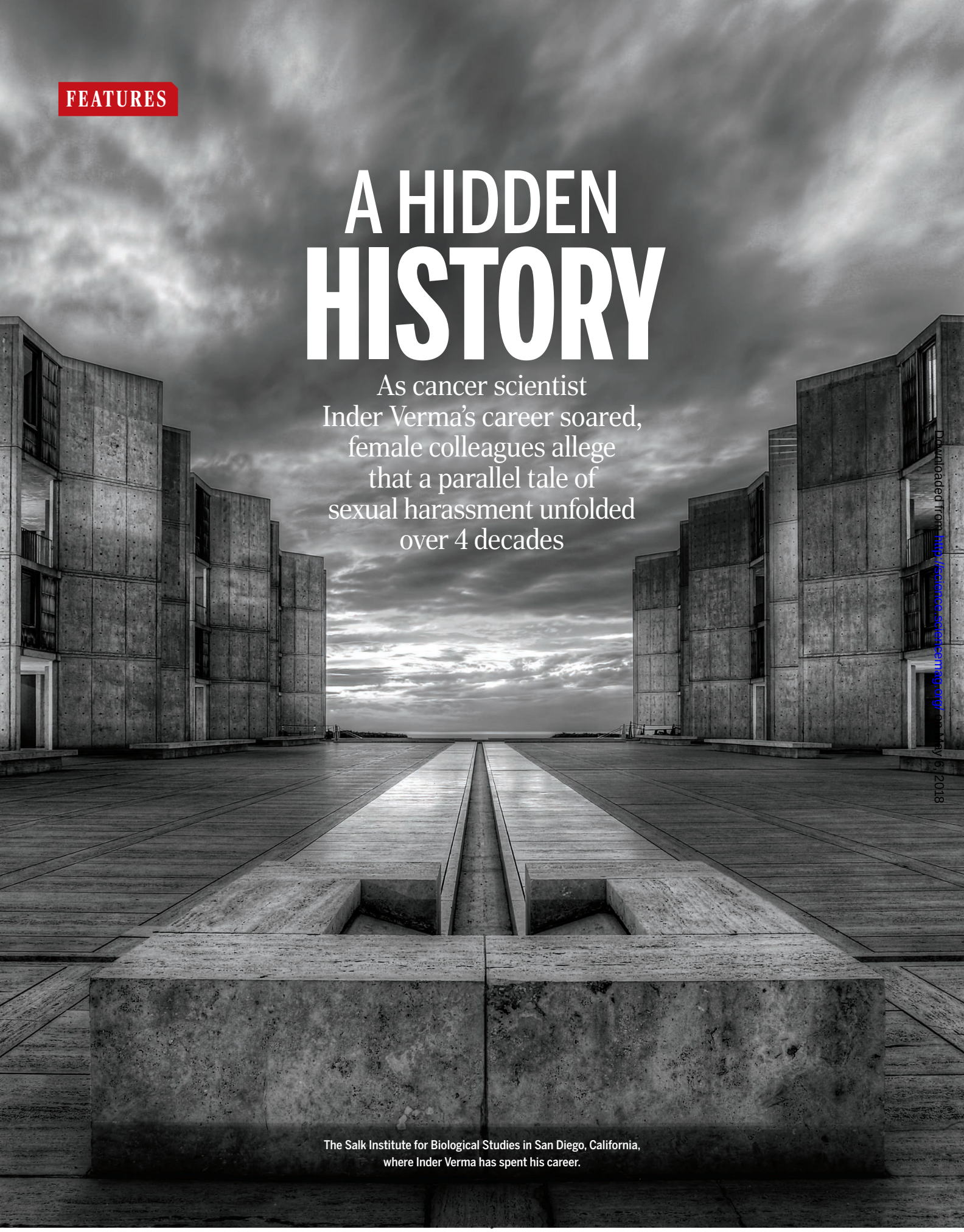

The Salk Institute for Biological Studies in San Diego, California, where Inder Verma has spent his career.

Inder Verma, pictured in a Salk laboratory in 2016, conducted research that helped power the institute's reputation for outstanding science.

By **Meredith Wadman**

Inder Verma, the prominent geneticist and cancer scientist who has made his mark on U.S. research for decades, has sexually harassed women for just as long, according to allegations from eight women.

Verma, 70, led key studies of genes and cancer, pioneered gene therapy techniques, and was editor-in-chief of a major journal and a leader at scientific societies (including AAAS, *Science*'s publisher). He has spent his career at the storied Salk Institute for Biological Studies in San Diego, California.

In reports stretching from 1976 to 2016, women allege, variously, that he grabbed their breasts, pinched their buttocks, forcibly kissed them, propositioned them, and repeatedly commented on their physical attributes in professional settings. The allegations come from a Salk lab technician, a postdoctoral researcher, other Salk staffers and faculty, and women outside of the institute, including a potential faculty recruit.

Five women in their 50s and 60s in secure scientific positions agreed to be named in this story. Three younger women requested anonymity, fearing repercussions to their careers. They cited Verma's power at Salk and the reach of his influence, including his connections to Nobel laureates, National Institutes of Health (NIH) peer-review committees, and journal editorial boards.

On 20 April, Salk's board of trustees put Verma on administrative leave, 2 days after receiving a list of questions from *Science* concerning the allegations and the institute's responses to previous complaints about Verma's behavior.

Science's questions about harassment caused Salk to expand an existing investigation of Verma, board Chairman Dan Lewis told Salk employees in an email on 21 April. The institute had launched an internal investigation in February and hired a law firm on 12 March to conduct an external probe, Salk told *Science* in a separate statement.

For decades, women at Salk have warned female colleagues not to be alone with Verma. "It was on everybody's mouth that he was a harasser," says Monica Zoppè, now a molecular and cell biologist at the Institute of Clinical Physiology in Pisa, Italy. As a brand-new postdoc in Verma's lab in 1992, she had not yet heard the warnings when Verma forcibly grabbed and kissed her, a few weeks after she had arrived from Italy, she alleges.

Salk administrators have received at least two formal complaints and three additional

reports about Verma's behavior since the late 1970s, and they had hired an outside investigator to probe a complaint about him at least once before last month. They also have repeatedly protected him, say women who formally complained and other people with knowledge of the institute's actions. Zoppè, for example, alleges that after she formally complained about Verma's behavior, Salk administrators told her not to speak to anyone about the incident.

The allegations reported to *Science* are not as egregious as some examples of harassment in the scientific world (*Science*, 13 October 2017, p. 162). And many women who worked with Verma at Salk say he treated them with respect. "I found him to be an honorable and very supportive supervisor," says Jane Visvader, a leading breast cancer researcher at the Walter and Eliza Hall Institute of Medical Research in Parkville, Australia, who was a postdoc in Verma's lab in the late 1980s. Visvader was one of 15 women *Science* contacted who said they experienced no harassment when working with or for Verma; another 12 women ignored or declined repeated interview requests. Among Verma's backers, several praised his mentoring and described his kindness.

Yet some women who allege harassment say that after the incidents, they made career choices that would allow them to dodge Verma's influence, or at least his presence. "I have been avoiding him for 30 years," says Pamela Mellon, a neuroscientist at the University of California, San Diego (UCSD). She was an assistant professor at Salk in the mid-1980s when, she says, Verma grabbed her breasts during a party at his home.

Outside experts say that if the decades-long pattern of alleged advances is true, "he's a textbook sexual harasser," as Ann Olivarius, a senior partner at McAllister Olivarius in Saratoga Springs, New York, puts it. Olivarius, who specializes in sexual harassment cases, reviewed the eight women's allegations at *Science*'s request. "When you touch in the way that has been described in these examples," she says, "under the law, these are called assault."

Cathy Young, a media fellow at the Cato Institute, a libertarian think tank in Washington, D.C., also reviewed the allegations. "I have raised questions about some #MeToo accounts in the media that I think are overreactions," she says. "But once you start making surprise, aggressive advances, especially toward people of lower status, especially if they're at the same institution—that clearly crosses the line."

Verma declined to answer a list of questions from *Science*, but he issued a general denial in a statement released after Salk suspended him last month: "I have never used my position at the Salk Institute to take advantage of others. I have also never engaged in any sort of intimate relationship with anyone affiliated with the Salk Institute. I have never inappropriately touched, nor have I made any sexually charged comments, to anyone affiliated with the Salk Institute. I have never allowed any offensive or sexually charged conversations, jokes, material, etc., to occur at the Salk Institute."

Citing legal and privacy constraints, Salk declined to answer *Science*'s questions about certain specific allegations. It would not say how many complaints about sexual harassment by Verma it has received, nor what discipline, if any, it has imposed on him. However, its statement to *Science* said, "Salk has not condoned—and will not condone—any findings of inappropriate conduct in the workplace, regardless of one's stature or influence." It continued: "Salk has had, and has enforced, policies prohibiting sexual harassment for decades. … These policies are reviewed regularly and have been updated numerous times over the years." The institute also noted that it "requires that employees periodically attend anti-harassment and discrimination training."

> ***"I have never inappropriately touched, nor have I made any sexually charged comments, to anyone affiliated with the Salk Institute."***
>
> **Inder Verma**, Salk Institute for Biological Studies

The allegations come as the research institute, founded in 1960 by polio vaccine inventor Jonas Salk, defends itself against gender discrimination lawsuits filed last summer by three of its senior female scientists. The scientists allege that they were denied lab space and personnel, career advancement, and funding opportunities because they are women. Two lawsuits accuse Verma by name. In December 2017, he was suspended as editor-in-chief of the *Proceedings of the National Academy of Sciences* (*PNAS*) until issues raised by the lawsuits are resolved.

Verma—the highest-paid scientist at Salk in its 2015 fiscal year, earning $406,000—remained a power there until last month. He chaired and served on faculty promotion and search committees. He exerted influence on internal funding decisions. On 20 April, he was slated to be on a panel at Salk with former Vice President Joe Biden, promoting a Salk cancer research initiative—but he was dropped at the last moment.

"They used to call Salk 'Inder's institute,'" recalls a young woman who alleges that she experienced unwanted touching and sexual comments from Verma when she worked at Salk during the past 10 years.

THE LAB TECH

Verma, a native of Sangrur, India, was hired by Salk in 1974, at age 26, after completing a Ph.D. at the Weizmann Institute of Science in Rehovot, Israel, and a postdoctoral fellowship in the lab of David Baltimore, who was then at the Massachusetts Institute of Technology in Cambridge.

During Verma's first 4 years at Salk, he published 16 papers, many reporting discoveries about reverse transcriptase, the enzyme that enables retroviruses to insert their genetic material into cells' DNA. Eight were co-authored with Baltimore, who shared the 1975 Nobel Prize in Physiology or Medicine for his discovery of the enzyme. Verma was promoted to associate professor in 1979, one step short of earning tenure in the Salk system.

In May 1976, Leslie Jerominski, now a senior laboratory specialist at the University of Utah Hospitals and Clinics in Salt Lake City, got a job as a technician in Verma's lab. She was 24.

Within a couple months of hiring her, Jerominski says, Verma asked her to play tennis at nearby UCSD. After their match, Jerominski says, she stood preparing to change in a common break room with a private bathroom at Salk. She alleges that Verma grabbed her, hugged her, tried to kiss her—she turned her head aside—and asked her out to dinner.

"I told him to quit," she recalls. "I felt scared, angry, and disappointed."

Jerominski did not report the incident, which was not repeated. "I was very young and I felt really privileged to be working at the Salk Institute. So I kind of let it go."

But she remained on the alert until she left Salk in October 1977. "I never put myself in a position when I was alone in a room with him ever again. … I hated the fact that I always had to be on guard."

Another technician in Verma's lab in that era remembers being warned by other women not to be alone with him. "It was a culture of 'Be careful,'" she says. "It was understood."

A female trainee in a different Salk lab at the time recalls, "He had a habit of following women into the darkroom. I made sure when I was going in, he didn't know."

THE JUNIOR CANCER BIOLOGIST

By the mid-1980s, Verma's lab was a world

leader in its field. Verma had assembled a small, talented group of scientists who uncovered the structure of certain retroviruses and revealed how they co-opted oncogenes to cause cancer. The team also led the development of retroviruses as vectors to deliver DNA for gene therapy. In 1984 alone, Verma published nine papers in *Cell*, *Science*, and *Nature*, and was senior author on five of them. In 1985, Salk promoted him to full professor.

In 1987, the year Verma turned 40, the National Cancer Institute asked him and Jean Wang, then a 35-year-old assistant professor studying cancer biology at UCSD, to help review a program at the Dana-Farber Cancer Institute in Boston. Verma chaired the site review team. Thrilled to be selected as a reviewer, Wang wore her favorite professional dress from Talbots. It was calf length and blue, with irregular white dots and a white Peter Pan collar.

The group stayed at an Embassy Suites hotel on the Charles River, she recalls. After an intense, daylong assessment at Dana-Farber, Wang had just returned to her room when the phone rang. It was Verma, she says, asking her to come to his room to discuss an important matter regarding the site visit.

When Verma opened the door, Wang says, she saw champagne chilling on ice beyond him. She alleges that Verma closed the door behind her, sat on a couch in the front room of the suite and asked her to sit on his lap. Stunned and fearful of angering him, she complied. "He started to ask me about my ex-boyfriend, my sex life, who I was going out with," she says. She parried with pointed questions about his wife and daughter, whom she had met at a party at his home not long before. She told him repeatedly that she would like to leave and after about 5 minutes, she did so.

Back in her room, she took a long shower. "I wanted to wash away the humiliation," Wang says. She threw the dress in the trash in disgust, knowing she would not wear it again.

When she returned to San Diego, "I didn't say a word," Wang says. She blamed herself for going to Verma's hotel room, and she feared both others' judgment of her and retaliation by Verma. She was an obscure, nontenured assistant professor. She remembers thinking that if she told others, "He's going to hurt me. I need grants."

Wang did, however, begin counseling female UCSD students who proposed to do research at Salk, 2 kilometers away, not to work with Verma. In the mid-1990s, she told her husband, Richard Kolodner, about the incident. (He confirmed that report to *Science*.) And whenever she ran into Verma at seminars and meetings, "I actively avoided him each time and made sure that I showed my disgust with my body language," Wang says.

Wang is now a distinguished professor emeritus in the department of medicine at UCSD. Three decades later, she still feels shame and anger about that 5-minute episode. She is speaking up now, she says, because "I just can't keep it in anymore. The #MeToo movement opened my wound. I had to take this opportunity to tell my story so that I could hopefully close that wound and forgive myself."

Inder Verma at a meeting at Cold Spring Harbor Laboratory in New York in 1986, the year after he was promoted to full professor at the Salk Institute. Two women allege he made unwanted physical advances around this time.

PHOTO: COLD SPRING HARBOR LABORATORY

THE SALK ASSISTANT PROFESSOR

Verma and his wife (he has been married since 1973) have long been known as congenial, generous hosts. In the 1980s, they often invited Salk colleagues to their spacious home in suburban Solana Beach, California. At one hot, crowded party there in the late 1980s, Pamela Mellon, an assistant professor at Salk who was studying how gene transcription is regulated, stepped into the dark, quiet backyard to cool off. Mellon, then in her mid-30s, was standing with her back to the house admiring the hilly vista when, she says, Verma's arms suddenly encircled her from behind, pinning her arms to her side as he grabbed her breasts. "I was shocked and struggled to get rid of his arms," Mellon says. That failed, she says. Next, "I just kicked him in the shin backwards. And he let go."

Upset, she left the party immediately. She told no one about the incident and dealt with it by avoiding Verma, who was not in her department and had no direct authority over her. But a year or two later, Verma was appointed chair of the committee deciding whether Mellon should be promoted from assistant to associate professor. Distraught that the man whose advances she had rebuffed would be chairing that committee, she took her situation to the director of human resources. She recalls him telling her that she needed counseling, and refusing to take up the incident with Verma. (That now-retired Salk staffer did not respond to two letters and a phone message requesting an interview.)

Salk wrote in an email last week: "The Institute does not have a record of any report given to Human Resources of this nature during [Mellon's] employment at Salk." It added: "When Salk officials have been made aware of allegations of inappropriate conduct by an employee, the Institute has investigated and responded, as appropriate."

Next, Mellon turned to Salk professor Tony Hunter, whom she knew from shared interests in whitewater rafting and retrovirology. She implored him to remove Verma from the promotion committee. Without asking her why she was so uncomfortable with Verma in that role, Mellon recalls, Hunter arranged to take Verma's place as chair of the committee.

"Tony took me seriously and he fixed it," Mellon says. (Hunter declined repeated interview requests.)

Mellon was promoted. In 1992, she left Salk for a tenured position at UCSD, where today she studies how the brain controls reproduction.

One woman who worked at Salk at the time, who declined to be named for fear of career repercussions, says she recalls the day Verma told her that Mellon had left Salk.

"He was, like, 'Mellons has left.' And I said, 'Mellons?' And he said, 'Pam Mellon, you know, her big breasts look like watermelons?'"

"I was just in shock," says the woman, who adds that she felt too intimidated to respond with anything but silence.

THE POSTDOCTORAL STUDENT

Monica Zoppè was 31 years old when she became a postdoc in Verma's lab late in 1992. A newcomer to the United States, she was excited to work in the lab of a pioneer in gene transfer.

A few weeks after her arrival, Verma offered her a ride home. She didn't have a car and gratefully accepted. "During the trip, he said, 'I don't know what I'm going home to do, nobody is there,'" Zoppè recalls. Pleased with the chance to discuss her research with him, she invited him in for a cup of tea.

Zoppè shared the house with two roommates. Neither was home. "As soon as he stepped in the house he tried to kiss me very, very abruptly," Zoppè says. Shocked and outraged, she shoved him away. Struggling for words in her uncertain English, she said at first, "Let's go!" Verma's face lit up, Zoppè recalls. She corrected herself: "You go!" He went.

The next day, Zoppè confronted Verma, she says. In a statement she set down 3 years later when she briefly considered taking legal action against Salk or Verma, she wrote, "He assured me that he had never done anything like this before and he would never do it again. … [He] asked me not to talk to anybody about this 'incident.'"

Because she had taken Salk's sexual harassment training, which urged reporting of such incidents, Zoppè says, she complained to human resources at Salk a few days later. (A former Salk employee who declined to be named confirmed the complaint and the subsequent investigation to *Science*.) Zoppè says Salk offered to move her to a lab at UCSD; she refused, feeling that if anyone should move it should be Verma.

Several days later, she recalls, the human resources director—the same man whom Mellon had approached a few years earlier—called her at home to tell her she should stay home that day, and continue to stay home until she heard back from human resources, because Verma was going to be told of her complaint and would be angry.

Within another few days, Zoppè says, Verma "apologized very coldly for what he did. He assured me he was not mad at me, which was clearly a lie."

In her statement from the mid-1990s, Zoppè adds that human resources "told me that [Verma] would be requested to undergo psychological counseling … and that, if anybody asked, I should say I know nothing about it." (As with all specific allegations about its handling of complaints, Salk had no comment on the details of Zoppè's account.)

According to Zoppè, Verma routinely disparaged her science after she complained. "If an experiment didn't work, I was incompetent. Any time I would say something in a lab meeting, according to Inder I was wrong." Another postdoc in Verma's lab at the time, who declined to be named for fear of professional retaliation, confirmed to *Science* that after the complaint, Verma "was overly and openly aggressive in criticizing" Zoppè at a lab meeting.

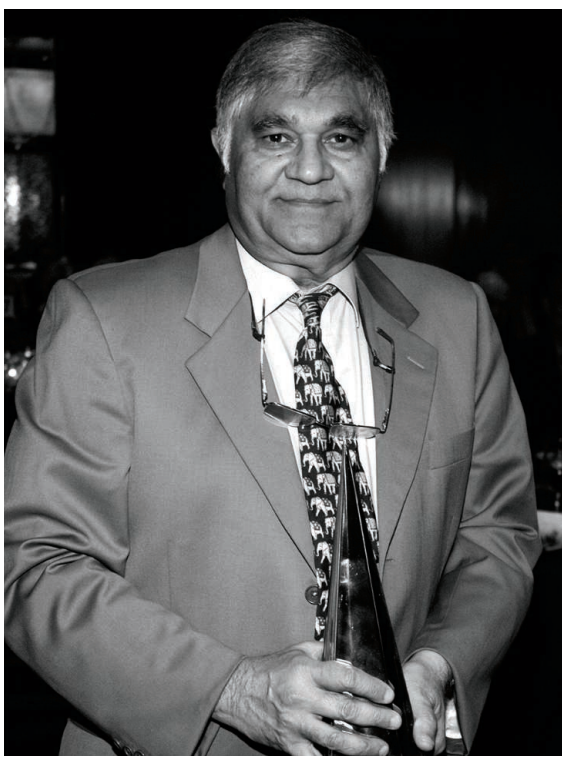

Inder Verma receives a $100,000 prize from The Vilcek Foundation in New York City in 2008. The award honors outstanding contributions to biomedical research by immigrants to the United States.

PHOTO: MATT CARASELLA/PATRICK MCMULLAN VIA GETTY IMAGES

Paolo Remondelli, now a cell biologist at the University of Salerno in Fisciano, Italy, was working in a UCSD lab in the early 1990s and shared a house with Zoppè for 18 months beginning soon after the alleged incident. In an interview with *Science*, he recalled what he described as Zoppè's "distress" about her relationship with Verma after she complained about him to Salk.

"It was clearly something that compromised her relationship with him," Remondelli said. "She didn't work with calm. She was not quiet. It was damaging. It was compromising her career."

Zoppè completed her postdoc, she says, because she had strong support from others in Verma's lab. She left in 1996 for a position in Milan, Italy.

THE SENIOR SALK COLLEAGUE

Verma's career continued to soar. In 1988, he won an "Outstanding Investigator" award from NIH, which steered $12.8 million to Verma and Salk for cancer research over the next 13 years. In 1990, Verma was awarded a coveted American Cancer Society professorship, which funded his work with hundreds of thousands of dollars until 2012. His laboratory pressed ahead with pioneering work developing gene therapy vectors and made key discoveries about cancer-causing genes such as the breast cancer gene *BRCA1*. He was visible in public and policy circles, chairing a committee that examined NIH oversight of gene therapy clinical trials and co-chairing the government's Recombinant DNA Advisory Committee.

In 1997, the year he turned 50, Verma was elected to the National Academy of Sciences (NAS) and 2 years later, to the Institute of Medicine, part of NAS that advises the government on key issues in medicine and health. In 2001, he joined the editorial board of *PNAS*.

One evening in September 2001, Beverly Emerson, then 49, a molecular biologist Salk had hired in 1986 and promoted to full professor in 1999, was working at the photocopier, deep in the Salk library stacks. No one else was around. She didn't hear Verma approach. Suddenly, she says, he was beside her; he grabbed her and kissed her on the mouth.

"Yes?" he asked.

"No!" she remembers responding, in shock. He backed away and left.

The incident, Emerson says, "left me feeling physically vulnerable because Dr. Verma snuck up on me—and at risk of losing lab resources and professional opportunities at Salk" because of Verma's power and influence at the institute. (Emerson, 66, is one of the plaintiffs in the current gender discrimination lawsuits. In December 2017, 5 months after the lawsuits were filed, Salk declined to renew her contract, saying that she failed to bring in 50% of her salary from external sources, as required. *Science*, 22 December 2017, p. 1510.)

Emerson did not report the incident because, she says, "he didn't do it again." If he had, she says she would have reported it not to human resources, but to the institute's president. "I had the sense that human resources had no real power to discipline or take corrective action over Dr. Verma."

THE RECRUIT

In the first years of this century, Salk's scientific ranks were sorely lacking in women. In 2003, seven of 52 faculty members were women, and the trend wasn't improving: Only one of the 11 assistant professors was a woman. The institute did seek to hire women. Between 2000 and 2003, it offered faculty positions to 14 outsiders, five of them women; none of the five accepted a position.

One potential faculty recruit, who declined to be named for fear of retaliation, visited Salk during that period. She noted that several female professors pointedly sought privacy during conversations with her by closing their office doors; one insisted on talking with her in the women's bathroom. One woman, who had published in *Nature* and *Cell*, confided that she was not going to get promoted.

"I looked at her résumé and thought, 'How is that possible?'" the recruit recalls.

She also met with Verma in his office and discussed her research and the institute's. As he escorted her to her next interview, she says, Verma volunteered that, if she had a husband, Salk would not be able to hire him as well. She replied that she wasn't married. At that point, she alleges, Verma reached behind her and pinched her buttocks.

"It wasn't a pat on the butt, it was a pinch," she says.

She declined Salk's job offer. "I was very disturbed by my experience there," she says.

Two people—her faculty mentor and a postdoc at her institution at the time—confirmed in interviews with *Science* that she told them of that incident soon after it happened.

THE JUNIOR SALK COLLEAGUES

One night during the past decade, a young female Salk research assistant, her boss (a Salk professor), and Verma attended a dinner at a San Diego restaurant with pharmaceutical company executives. The research assistant was the only woman present. As the dinner adjourned, she says, Verma "put his arm around my waist and said, 'You are always so beautiful. You are like a beautiful starlet.'"

The woman exchanged a glance with her boss, who "had this, like, 'uh-oh' look on his face," she recalls. She quickly disentangled herself and walked away.

Verma continued to make sexual comments about her to others at Salk, that woman says; those comments found their way back to her and made her feel that "attractiveness was apparently what I was there for. Not doing science."

She went out of her way to avoid Verma. "You knew not to complain to human resources about it. You don't want to be on Verma's bad side. I wanted to keep my job."

Another young woman working at Salk in 2016 reports that after a meeting, she extended her hand to Verma to shake. He took it and pulled her into a half-hug, she says. She alleges that he then put his hand on her cheek and said, "I should probably not say this, but you are so pretty." He went on to compare her to his daughter, she says.

The young woman says she told Elizabeth Blackburn, then Salk's president, about the incident, and that Blackburn reported it to human resources. (Blackburn, who resigned in December 2017, did not respond to repeated requests for comment about the incident.)

Human resources brought in Ken Rose, principal of The Rose Group, a San Diego law firm—the same firm it hired in March to investigate Verma—to investigate.

Rose determined that no sexual harassment had occurred, the woman says. She adds that he concluded by telling her, "'You need to go tell him you thought it was inappropriate.' … But I never confronted him, mostly because I didn't want to be alone with him and I was afraid of retaliation." Rose declined to comment.

> ***"When you touch in the way that has been described in these examples, under the law, these are called assault."***
>
> **Ann Olivarius**, McAllister Olivarius law firm

From then on, she warned new female employees not to be alone with Verma.

During *Science's* 4-month investigation, some women who worked with Verma over the years offered a counternarrative to his portrayal as a sexual harasser, and they praised his actions as a mentor.

In Verma's lab, "women were treated equal to men," says Virginie Bottero, a Verma postdoc from 2002 to 2006 who is now a lecturer at Lake Forest College in Illinois. "I was never subjected to harassment of any sort. I did not witness any harassment and I did not hear about anyone who could have been a target." She called the lab "a fantastic place to work and grow scientifically."

Dinorah Friedmann-Morvinski, an assistant professor at Tel Aviv University in Israel who was a Verma postdoc from 2005 to 2015, wrote in an email, "When my husband lost his job and Inder heard about it, he not only raised my salary but also helped [connect] my husband with relevant people he knew in his field." She added, "During my maternity leave, he assigned a technician to help me with my ongoing experiments and she kept helping me when I returned full time to the lab."

When Verma was elevated to become editor-in-chief of *PNAS* 7 years ago, Ralph Cicerone, then NAS president, lauded Verma as "the ideal person" for the job. "Dr. Inder Verma is known worldwide for his scientific creativity and for his conscientiousness and fair-mindedness," Cicerone said. Other leading science organizations also have sought him out, including AAAS, where Verma served on the board of directors from 2011 to 2015.

Last October, at a gala at the Beverly Hills Hotel in Los Angeles, California, the American Cancer Society honored Verma as a "Giant of Science." In November 2017, he opined on the virtues of preprint servers in *PNAS*. In March—with NAS President Marcia McNutt, *The New England Journal of Medicine* Editor Jeffrey Drazen, *Science*'s Executive Editor Monica Bradford, and others—he co-authored a *PNAS* article urging changes to standardize journals' authorship policies.

Research under Verma also continued, until last week. He was a coauthor on three new scientific papers in the first quarter of this year. In February, he and his team at Salk won a $1.2 million award from the W. M. Keck Foundation to develop living mammalian tissues that are transparent to light microscopy.

Salk said in a statement on 25 April that Hunter will oversee all ongoing research programs in the Verma lab "during Dr. Verma's leave" and that "the Institute expects all research to continue as normal during this period." It added that Salk has contacted the foundations and funding agencies that support Verma's work "to assure them the research they are sponsoring will continue without disruption."

Can outstanding science redeem harassment? "It's the old 'great man' theory of the universe: 'Look what he has done in science,'" says Olivarius, the sexual harassment lawyer. "Instead, look at how many careers he has hurt."

Jennifer Freyd, a research psychologist at the University of Oregon in Eugene, notes that Verma's alleged harassment occurred at an institution where women also contend that they have been shut out of power. "Sexual harassment really reinforces the male power structure and keeps women in their place and terrified. But also, any kind of gender inequity gives more permission to sexually harass. So they are mutually reinforcing. They do go together." ■

This story was supported by the Science *Fund for Investigative Reporting.*

INSIGHTS

PERSPECTIVES

BRIDGE: CLIMATE AND BIODIVERSITY

How to pay for saving biodiversity

Can private sector involvement in a global agreement help to conserve global biodiversity?

By **Edward B. Barbier,[1] Joanne C. Burgess,[1] Thomas J. Dean[2]**

The 1992 Convention on Biological Diversity (CBD) was one of the first international environmental agreements negotiated. In the same year, the Global Environment Facility (GEF) for funding biodiversity conservation in developing countries was launched. Yet 25 years later, biological populations and diversity continue to decline both on land (*1*) and in the oceans (*2*). The main reasons are chronic underfunding of global biodiversity conservation; the lack of incentives for global cooperation; and the failure to control habitat conversion, resource overexploitation, species invasions, and other drivers of biodiversity loss. Dinerstein *et al.* recently called for a global deal, complementing the 2015 Paris Climate Change Agreement, for conserving half of the terrestrial realm for biodiversity by 2050 (*3*). Here, we explore how such a deal might be implemented to overcome the funding problem in biodiversity protection.

As with any public good, biodiversity conservation suffers from a free-riding problem, in which governments have an incentive to provide less than the optimal level of funding in the hope that others will cover the costs. This is especially pertinent when the benefits of such payments accrue to other countries. In particular, global funding to support conservation efforts in developing countries, which host most biodiversity, is woefully inadequate to prevent habitat loss and overexploitation. The global benefits of biodiversity conservation are much greater than the benefits accruing to developing countries. Left on their own, the latter countries will preserve insufficient biodiversity. Existing international institutions and funding mechanisms, including the CBD and GEF, have boosted conservation efforts but failed to deliver enough funding to where it is most needed. As a result, global conservation falls far short of what is required to attain safe biodiversity levels.

A GLOBAL AGREEMENT FOR BIODIVERSITY

Governments around the world have agreed to the Aichi Biodiversity Targets, which include the goal of conserving at least 17% of terrestrial and inland water habitats and 10% of coastal and marine areas by 2020 (*4*). However, the existing Aichi Biodiversity Targets are widely seen as too modest in scale to save global biodiversity (*1*–*3*). Scientists are increasingly calling for an expanded goal of saving half the terrestrial realm, which could cost up to $80 billion annually (*3*). If a new biodiversity agreement also extends the Aichi Target of conserving 10% of coastal and marine areas (*4*) to 50%, an additional $19 billion could be required each year (*3*). This suggests a total annual biodiversity conservation bill

[1]*Department of Economics and School of Global Environmental Sustainability, Colorado State University, Fort Collins, CO 80253-1771, USA.* [2]*College of Business and School of Global Environmental Sustainability, Colorado State University, Fort Collins, CO 80253-1201, USA. Email: edward.barbier@colostate.edu*

of $100 billion. For comparison, the international community currently spends only $4 billion to $10 billion each year (*3*, *5*, *6*).

The flexible architecture of the Paris Agreement is ideally suited to a biodiversity accord. Under the Paris Agreement, a global target was agreed to, but countries made individual pledges to meet the goal. Negotiated within the United Nations Framework Convention on Climate Change, the Paris Agreement is based on all 195 signatory countries reaching a consensus on a few key goals: limiting global warming to 2°C, substantially reducing greenhouse gas emissions by 2050, and having rich countries assist poor nations in abating emissions. The accord allowed individual countries to pledge their own national targets, abatement policies, and timelines for emission reductions, subject to 5-year review. In addition, wealthy countries have pledged $100 billion a year in climate finance for developing countries by 2020 and have pledged to continue raising $100 billion a year until 2025.

Similar to the Paris Agreement, a global agreement for biodiversity would address the loss of uncertain but potentially irreversible and essential global ecosystem benefits. As the governing body of the CBD, the Conference of the Parties (COP) would be well placed to initiate negotiations for such a global agreement. Like the Paris Agreement, the key objective should be agreeing on a global target, with countries making voluntary pledges to meet the goal. The broad goal and time frame could extend one or more of the existing Aichi Biodiversity Targets (*4*), for example, to conserve at least 50% of terrestrial, inland water, coastal, and marine habitats by 2050, as proposed in (*3*). However, establishing an overall target for the global agreement for biodiversity is only a first step. As in the Paris Agreement, all countries should declare their own national targets, policies, and timelines, subject to 5-year review, for attaining the overall target. For wealthier countries, these targets and timelines should also include financial and technological commitments to assist conservation in developing countries through the GEF, other international bodies, or bilateral pledges.

GOING BEYOND NATIONAL PLEDGES

A Paris-style agreement among countries would raise current global biodiversity conservation toward safer levels. However, national governments are unlikely to provide sufficient funds to enable global conservation to reach safe levels of biodiversity. Again, the Paris Agreement is instructive. Current national pledges, if fulfilled, will limit greenhouse gas emissions substantially by 2050, but unless pledges are amended to be more ambitious, the aggregate reduction will fall short of limiting global warming to 2°C. Although some corporations have announced voluntary pledges and low-carbon strategies to comply with the Paris Agreement, the private sector does not participate formally in the accord, nor do corporations contribute to its climate financing. A recent proposal advocates that the Paris Climate Change Agreement should add a formal mechanism to allow corporations, cities, and other nonstate actors to formally join the accord (*7*).

We should expect a similar outcome from any new global agreement on biodiversity that relies just on targets and funding by governments. Overcoming the critical funding gap and extending the Aichi Targets for saving global biodiversity thus requires not only a Paris-style deal but also the direct involvement of the private sector. Cities, nongovernmental organizations, and other nonstate actors could also have a role, as proposed for the Paris Agreement (*7*). Corporations in key sectors—such as seafood, forestry, agriculture, and insurance—have a considerable financial stake in global biodiversity conservation and thus should be able to formally join the global agreement. As full participants, companies would declare their own corporate targets, policies, and timelines, subject to 5-year review, for attaining the overall goal of conserving at least 50% of terrestrial, inland water, coastal, and marine habitats by 2050. In addition, corporate participants should provide financial and technological assistance for conservation in developing countries, through international bodies such as the GEF.

RATIONALE FOR CORPORATE INVOLVEMENT

Corporations that undertake climate change mitigation may not gain financially from their actions. Instead, the benefits from averting global warming occur only over the long term and are shared widely. By contrast, certain industries—such as seafood, forestry, agriculture, and insurance—can benefit directly from supporting biodiversity conservation. For example, conserving marine stocks could increase annual profits of the seafood industry by more than $50 billion (*8*); similarly, protecting coastal wetlands could save the insurance industry $52 billion annually through reducing flood damage losses (see the table) (*9*). The inclusion of corporations alongside governments in the design and implementation of a global agreement for biodiversity could help coordinate and align incentives to support greater and more effective conservation. This is especially important for agricultural concerns, which if they agree to join the global agreement for biodiversity could curtail global land-use change that is threatening terrestrial biodiversity (*1*, *3*). For

example, agriculture has an incentive to protect habitats of wild pollinators, who along with managed populations enhance global crop production by $235 billion to $577 billion annually (*10*). The distinctive partnership between countries and companies may also create new marketing opportunities, such as certified and legitimate product and labeling schemes, further boosting benefits from biodiversity conservation and creating additional incentives to support a global agreement for biodiversity.

Some leading corporations and industries in natural resource–based sectors are already taking concrete steps toward conserving biodiversity. For example, 10 of the 13 seafood companies that control up to 16% of the global marine catch and 40% of the largest and most valuable stocks (*11*) have committed to the Seafood Business for Ocean Stewardship initiative for more sustainable management of seafood resources and the oceans (*12*). Similarly, in 2006 the International Council of Forest & Paper Associations, which represents the global forest products industry, committed itself to improving energy efficiency, reducing emissions of greenhouse gases and other pollutants, increased recycling, controlling illegal logging, and sustainable forest management (SFM) certification (*13*). Between 2000 and 2015, the total SFM-certified area supplying the forest products industry increased from 62 million hectares (Mha) (12% of the total forest area) to 310 Mha (54% of the total forest area) (*13*).

Financial benefits from biodiversity conservation

Examples of biodiversity financial benefits and potential investments by key global industries

INDUSTRY	ANNUAL REVENUES	BENEFITS FROM BIODIVERSITY CONSERVATION	BIODIVERSITY CONSERVATION TARGET	POTENTIAL FINANCIAL INVESTMENT
Seafood	$252 billion (*11*)	Increase in annual profits by $53 billion (*8*)	Increase marine biomass stocks	$5–10 billion annually*
Forest products	$300 billion (*14*)	Attain sustainable forest management goal (*13*)	Increase area of protected forests	$15–30 billion annually†
Insurance	$4300 billion (*15*)	Reduce estimated global flood damage losses of $52 billion annually (*9*)	Increase area of protected coastal wetlands	$5–10 billion annually‡

*Based on 10 to 20% of potential benefits from biodiversity conservation.
†Based on 5 to 10% of annual revenues of $300 billion, which are the global earnings of the 100 largest forest, package, and paper companies (*14*).
‡Based on 10 to 20% of potential benefits from biodiversity conservation.

DESIGNING A GLOBAL AGREEMENT FOR BIODIVERSITY

The first step in designing a global agreement for biodiversity would be for the COP of the CBD, which comprises solely national governments, to begin negotiating such an agreement. The key objectives of the COP should be to establish a global target—such as conserving at least 50% of terrestrial, inland water, coastal, and marine habitats by 2050—and an overall financing goal, such as providing $100 billion annually to assist conservation in developing countries.

The agreement should also include a mechanism for corporate leaders to formally commit their organizations to the accord's global conservation target and financing goals. Individual corporations and industrial organizations can then be invited to accept, or accede to, the negotiated agreement. By joining the global agreement for biodiversity, companies and associations could cooperate with governments to establish well-defined, quantifiable conservation goals for critical habitats and determine the financing targets and timelines for providing assistance to developing countries.

For example, if they join the accord, leading corporations and associations in the seafood, forestry, agricultural, and insurance industries should be involved in establishing the targets for marine, terrestrial, and coastal habitat and biodiversity conservation that are consistent with the overall global conservation goal and timeline. These targets could include specific objectives relevant to each industry, such as increases in marine stocks for seafood companies, forest area protection for forestry industries, and coastal wetland habitats for insurers (see the table). Furthermore, as part of the global agreement for biodiversity, individual companies should pledge their own business targets, policies, and timelines for attaining the overall industry goal.

Participating corporations could also partner with governments in providing financial and technical assistance for conservation in developing countries. Because much of the world's remaining biodiversity habitat is in tropical zones, there is a direct financial benefit to natural resource–based companies that assist developing countries in protecting this habitat. For example, if the seafood, forestry, and insurance industries allocated just a small fraction of the likely revenues and profits they earn from conservation to assist developing countries, this could raise $25 billion to $50 billion annually in additional funding (see the table).

Such a corporate contribution would mean that these industries would share with governments in meeting the estimated $100 billion annual funding needed to protect biodiversity (*3*). The financial commitment could be even larger if other major global industries and corporations with a stake in biodiversity conservation, such as the food and beverage industry and other agricultural concerns, also agreed to join the global agreement for biodiversity and contribute to its funding objectives. For example, if agriculture contributed 10% of the estimated $235 billion to $577 billion that it receives annually in wild and managed pollination services (*10*) to the agreement in order to conserve, create, and restore wild pollinator habitats, this would amount to about $20 billion to $60 billion per year in additional financing.

A global agreement for biodiversity would engage government and industry, and hopefully other nonstate actors, in a manner unparalleled in the history of conservation. In addition, the current global biodiversity crisis is in large part due to the lack of international commitment and funding over the past 25 years. A global agreement for biodiversity would also overcome these shortcomings. Ensuring safe levels of global biodiversity will require the corporations that can benefit financially from conservation to join efforts in order to avoid continued irreversible loss of biodiversity. ■

REFERENCES

1. G. Ceballos, P. R. Ehrlich, R. Dirzo, *Proc. Natl. Acad. Sci. U.S.A.* **114**, E6089 (2017).
2. B. Worm *et al.*, *Science* **314**, 787 (2006).
3. E. Dinerstein *et al.*, *BioScience* **67**, 534 (2017).
4. Convention on Biological Diversity, "Strategic Plan for Biodiversity 2011–2020, including Aichi Biodiversity Targets" (2010); www.cbd.int/sp.
5. E. B. Barbier, *Resources* **180**, 25 (2012); www.rff.org/research/publications/challenge-rio20-funding.
6. Global Environment Facility; www.thegef.org/about-us.
7. D. C. Esty, P. Boyd, *Yale Environ. 360*, 20 March 2018; https://e360.yale.edu/features/to-move-paris-accord-forward-bring-cities-and-companies-on-board.
8. C. Costello *et al.*, *Proc. Natl. Acad. Sci. U.S.A.* **113**, 5125 (2016).
9. C. S. Colgan, M. W. Beck, S. Narayan, *Financing Natural Infrastructure for Coastal Flood Damage Reduction* (Lloyd's Tercentenary Research Foundation, 2017).
10. S. G. Potts *et al.*, *Nature* **540**, 220 (2016).
11. H. Österblom *et al.*, *PLOS ONE* **10**, e0127533 (2015).
12. Seafood Business for Ocean Stewardship; http://keystonedialogues.earth.
13. International Council of Forest & Paper Associations, *Sustainability Information* (2006); www.icfpa.org/resource-centre/sustainability-information.
14. PricewaterhouseCoopers, *Global Forest, Paper & Packaging Industry Survey—2016 edition survey of 2015 results*; www.pwc.com/gx/en/industries/assets/pwc-annual-fpp-industry-survey-2016-10.pdf.
15. Ernst & Young, *Global insurance trend analysis 2016* (2017); www.ey.com/Publication/vwLUAssets/ey-global-insurance-trends-analysis-2016/$File/ey-global-insurance-trends-analysis-2016.pdf.

10.1126/science.aar3454

SILICON MATERIALS

Sonochemistry of silicon hydrides

Ultrasonic treatment of silanes opens a path to new silicon compounds and materials

By **Bernhard Hidding**

Silicon hydrides (silanes) are key precursors for electronic- and solar-grade silicon and silicon nanoparticles, and are used in various other applications. Conversion of silanes to Si and hydrogen is an energy-intensive process. For example, epitaxial Si production from silanes or Si colloid production requires high temperatures (many hundred kelvin), high pressures (a few hundred bar), or both (*1*), which is a cost driver and limits the growth rates in methods such as chemical vapor deposition. Although trisilane (Si_3H_8) allows an order-of-magnitude higher Si deposition rate for semiconductor applications when compared to SiH_4 at comparably low temperatures, down to ~400°C (*2*), solution processing of silanes (*3, 4*) is desirable to avoid high vacuum, temperature, and pressure. In a series of studies, Cádiz Bedini *et al.* (*5*–*8*) have shown that applying ultrasound to liquid silicon hydrides such as Si_3H_8 and cyclopentasilane (Si_5H_{10}) opens a path toward tunable synthesis of silicon nanoparticles, silicon polymers, as well as higher silanes at ambient temperature and pressure conditions.

Relative to alkanes, silanes are highly energetic and reactive substances. For example, linear silanes are pyrophoric at ambient conditions up to heptasilane. The high vapor pressures of lower silanes cause them to ignite in air spontaneously, whereas alkanes require an ignition spark to burn. This difference in reactivity arises from the different atomic and covalent bond radii and electronegativity of silicon (1.7 for Si, versus 2.2 for H and 2.5 for C) that results in polarization inversion and diametrically opposed enthalpies of formation (see the figure).

Heating of silanes can induce disproportionation reactions and is used, for example, to produce trisilane and further longer-chained silanes. Generally, lower silanes are volatile but relatively stable up to elevated temperatures in inert atmospheres. Cádiz Bedini *et al.* applied ultrasound (26-kHz frequency) to liquid trisilane diluted in cyclooctane (*5*). In such a mixture, the sound waves are expected to give rise to acoustic cavitation and microbubbles, which upon collapse produce local temperatures on the order of thousands of kelvin and pressures of several hundred bar. Such conditions naturally trigger various decomposition and polymerization processes, especially given the highly reactive nature of silicon radicals and fast decomposition kinetics of silanes (*9*). The ultrahigh heating and cooling rates in these bubbles, however, avoid substantial macroscopic heating. The conditions are not unlike those in large shock tubes, but are confined to the microscopic scale. With this simple setup, Cádiz Bedini *et al.* produced silicon nanoparticles with sizes tunable from 1.5 to 50 nm by varying the ultrasound sonotrode tip amplitude, the trisilane concentration, or both.

> ***"Cádiz Bedini et al. show that ultrasonic treatment efficiently achieves polymerization in the absence of any photolytic or 'macropyrolytic' effects..."***

The combination of the high transient temperatures and pressures of sonochemistry (*10*) and the exothermic decomposition nature of silanes appears to be a perfect match to induce ultrafast silicon radical and silicon nanoparticle formation, and opens a path to many applications, for example, in biophysics, in drug development based on silicon nanoparticles, and in nanophotonics (*11*). Hydrogenated noncrystalline amorphous semiconducting films have device applications, and nanoporous silicon materials may find use in lithium-ion batteries.

Ultrasound treatment is a cost-effective and simple technique that complements other manipulation techniques such as pyrolysis, photolysis, and electric discharge treatment of silanes. Indeed, Cádiz Bedini *et al.* showed (*6*) that the ultrasound-initiated polymerization of trisilane in combination with ultraviolet irradiation produced a polymer ink of silicon nanoparticles that could prove useful for production of high-quality hydrogenated amorphous silicon films. For example, these materials can be spin-coated onto substrates, or they can be deposited by using related spray-on methods or atmospheric-pressure chemical vapor deposition (*8*).

Silicon hydrides decompose in collapsing microbubbles

The high enthalpy of formation of silanes promotes decomposition and polymerization in ultrasound-driven cavitational collapse.

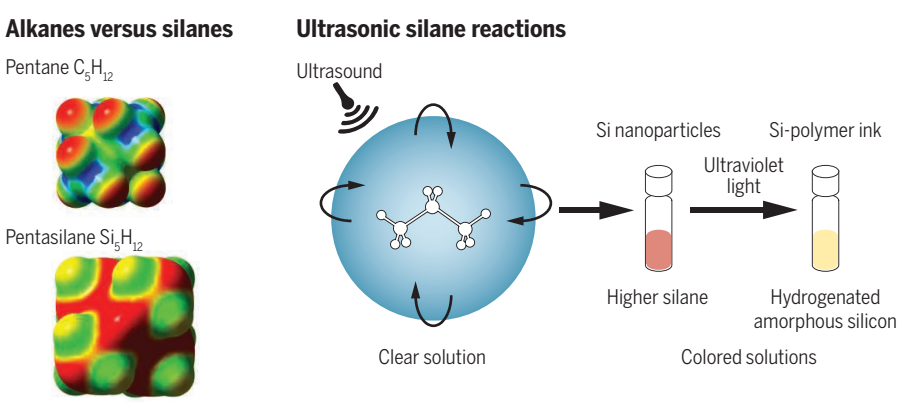

The electronegativity of C vs. Si leads to polarization inversion: e.g., pentasilane is characterized by high electron density (yellow) at the exterior of the molecule.

Ultrasound drives bubble formation, growth, and collapse in liquid silane mixture, where the silane is subject to transient hot spots with temperatures >1000 K and pressures >100 bar.

The ultrafast decomposition kinetics of silanes give rise to Si radicals, nanoparticles, and polymers, which can be further polymerized by ultraviolet light.

GRAPHIC: N. DESAI/*SCIENCE*

Scottish Centre for the Application of Plasma-based Accelerators, University of Strathclyde, Glasgow G4 0NG, UK. Email: bernhard.hidding@strath.ac.uk

Trisilane is a colorless liquid with poor coupling to ultraviolet irradiation. The ultrasound-initiated formation of silicon and silicon polymers acts as a photosensitizer seed and allows strongly enhanced photolytic polymerization, including the formation of higher silanes up to octasilane. Cyclopentasilane, in contrast to trisilane, is ultraviolet photosensitive. This property allows this compound to undergo ring-opening polymerization and production of "printable" semiconductor electronics (*4, 5*). Cádiz Bedini *et al.* show that ultrasonic treatment efficiently achieves polymerization in the absence of any photolytic or "macropyrolytic" effects, which supports the interpretation of ultrasound-driven synthesis via microscopic bubble formation and implosion.

Efficient handling, processing, and synthesis methods of silicon hydrides and derived products have been sought since the first production of silanes by Wöhler and Buff in the 1850s. The approach adopted by Cádiz Bedini *et al.* of using ultrasound is an elegant and, retrospectively, an obvious one: The high energy content of silanes allows them to decompose rapidly. For this reason, silanes are used as piloting gas and propellants in rockets and supersonic combustion engines (*12*). However, the inherently high sonochemical cooling rates confine radicalization and polymerization to microscopic length scales. Using the more readily available trisilane instead of having to rely on the more-difficult-to-synthesize cyclopentasilane at ambient conditions of temperature and pressure has far-reaching technological and cost advantages. The comparable ease with which Cádiz Bedini *et al.* achieve tunable formation of silicon nanoparticles, hydrogenated amorphous silicon, and higher silanes when adopting the sonochemical approach, indicates the great potential of this technique for introducing silicon materials into new applications. ■

REFERENCES

1. L. E. Pell, A. D. Schricker, F. V. Mikulec, B. A. Korgel, *Langmuir* **20**, 6546 (2004).
2. S. G. Thomas, M. Bauer, M. Stephens, C. Ritter, J. Kouvetakis, *Solid State Technol.* **52**, 12 (2009).
3. T. Shimoda *et al.*, *Nature* **440**, 783 (2006).
4. L. Rosenberg, *Nature* **440**, 749 (2006).
5. A. P. Cádiz Bedini *et al.*, *Ultrason. Sonochem.* **39**, 883 (2017).
6. A. P. Cádiz Bedini *et al.*, *Macromol. Chem. Phys.* **217**, 1655 (2016).
7. A. P. Cádiz Bedini *et al.*, *Ultrason. Sonochem.* **34**, 289 (2017).
8. A. P. Cádiz Bedini *et al.*, *Sol. RRL* **1**, 1700030 (2017).
9. J. G. Martin, H. E. O'Neal, M. A. Ring, *Int. J. Chem. Kinet.* **22**, 613 (1990).
10. K. S. Suslick, *Science* **247**, 1439 (1990).
11. I. Staude, J. Schilling, *Nat. Photonics* **11**, 274 (2017).
12. B. Hidding *et al.*, *Acta Astronaut.* **63**, 379 (2008).

10.1126/science.aap8005

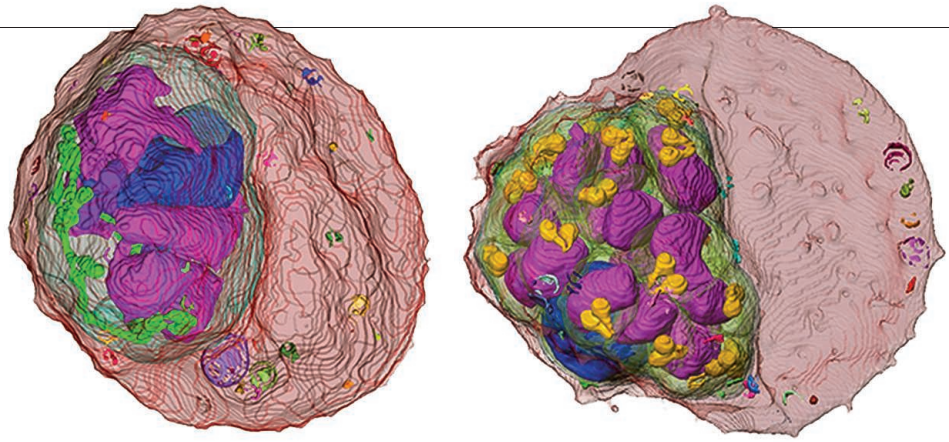

CREDITS: (RENDERING) KAZUYOSHI MURATA/NATIONAL INSTITUTE FOR PHYSIOLOGICAL SCIENCES AND MIAKO SAKAGUCHI/INSTITUTE OF TROPICAL MEDICINE (NEKKEN), NAGASAKI UNIVERSITY; M. SAKAGUCHI *ET AL.* (*16*); (GRAPHIC) OPPOSITE PAGE

MICROBIOLOGY

Indispensable malaria genes

A critical assessment of new opportunities for drug discovery to treat malaria

By **John White** *and* **Pradipsinh K. Rathod**

Malaria parasites, carried by mosquitoes and transmitted to humans, infect ~200 million individuals and cause ~500,000 deaths each year (*1*). Fifteen years after identifying the genome sequence of a malaria-causing parasite, *Plasmodium falciparum*, malaria treatments still rely heavily on chemicals derived from natural products that were used centuries ago (*2*). With cell-based functional assays, the gap between genome sequences of *Plasmodium* spp. and the identification of valuable new therapeutics may be reduced by determining which genes are essential for parasite propagation in the disease-causing blood stage of the parasite life-cycle. The most potent and clinically useful antimalarial drugs rapidly eliminate parasites growing in red blood cells (RBCs). On page 506 of this issue, Zhang *et al.* (*3*) report a mutagenesis screen on *P. falciparum* cultured in human RBCs, identifying 2680 indispensable parasite genes, which may contain antimalarial drug targets. However, it is important to critically assess what fraction of these essential genes will be good drug targets and how one should prioritize such targets for drug discovery.

The technical effort, patience, and care required to identify essential genes for the blood-stage forms of human malaria parasites cannot be overstated. Even the most experimentally tractable species of human malaria parasites, *P. falciparum*, grows ~100 times slower than other microorganisms, such as *Escherichia coli*. Previous efforts to identify essential genes—through random insertions of disabling pieces of DNA into malaria parasite genes—were inefficient, with success rates near one per million parasites in culture. The *piggyBac* transposition mutagenesis system used by Zhang *et al.* allows for at least one insertion in a random location per parasite genome. Combining this controlled mass mutagenesis with parasite pooling strategies, deep DNA sequencing, and bioinformatics, Zhang *et al.* now provide a reliable list of nonessential genes. When insertions occur in nonessential genes, parasites grow successfully. It is assumed that parasites with insertions in essential genes will not grow and survive the screening process.

Zhang *et al.* found that of 5380 malaria parasite genes, nearly 50% are essential for growth in the blood stage of the malaria parasite life cycle (see the table). This estimate of essential genes may also apply to other species of human malaria. Interestingly, a distant mouse malaria parasite (*Plasmodium berghei*), which does not infect humans, has a high fraction of essential genes for growth in RBCs (*4*). Within the list of essential *P. falciparum* genes may lie our best hopes for identifying good targets for the most clinically relevant part of the parasite life cycle. Even if the malaria research community, within a decade or two, finds that only 10% of the 2680 identified essential malaria genes are high-value targets for drug development, this screening approach will be considered successful.

There are several reasons for setting modest expectations. The essentiality of a gene is not likely to be sufficient for the gene prod-

NIH International Center of Excellence for Malaria Research (South Asia), Department of Chemistry, University of Washington, Seattle, WA, USA. Email: rathod@uw.edu

P. falciparum in a red blood cell generates an early multi-nucleated schizont (left) and can release infectious merozoites (right) (*16*).

uct to be a high-value target for cellular pharmacology. High-value drug targets are truly rare. Global small-molecule screens involving more than 2 million different drug-like organic compounds directed at blood-stage malaria parasites have identified very few new druggable targets (*2*, *5*, *6*) compared with the number of essential genes we now know of (*3*) and the number of genes known to be actively expressed in human malaria parasites (*7*, *8*). Furthermore, even small chemical libraries directed at single purified protein targets routinely generate dozens of potent inhibitors (*2*, *6*). In parasite cell assays, not only are good inhibitors rare, but many structurally distinct potent inhibitors of parasite cell proliferation converge on the same ~12 targets (*6*, *9*), most of which have already been identified. Furthermore, not all enzymes—even in essential metabolic pathways—are equally druggable. In the essential, linear, pyrimidine biosynthesis pathway in malaria parasites, only a few enzymes are good targets in an intact cell (*10*, *11*).

Last, to be prioritized for drug development, a small-molecule inhibitor must rapidly kill parasites probably without achieving total inhibition of target activity. Inside a cell, even a potent enzyme inhibitor faces competition from accumulating substrates and from synthesis of replacement target proteins. Select enzyme targets do trigger cell death even after partial inhibition. Such targets repeatedly appear as high-value druggable targets, regardless of whether one is interrogating parasites, bacteria, or cancer cells. For example, the nucleotide synthesis–supporting enzyme dihydrofolate reductase (DHFR) is a proven target in the treatment of malaria (with the drugs pyrimethamine and proguanil), bacterial infection (with the antibiotic trimethoprim), and cancer (with the chemotherapeutic methotrexate, which is also an immunosuppressant used to treat autoimmune diseases) (*12*). These cells are also highly vulnerable to inhibitors of metabolically related thymidylate synthase (TS). It is now understood that even partial inhibition of DHFR or TS leads to a buildup of the nucleotides deoxyuridine monophosphate (dUMP) and deoxyuridine triphosphate (dUTP) and incorporation of unwanted uridine residues into DNA, DNA strand fragmentation, and cell death (*13*). In malaria parasites, inhibitors of DHFR or TS act selectively, partly because of host-parasite variations in active sites of the target enzyme but also partly owing to parasite-specific variations in regulatory responses to such inhibitors (*14*). As parasites become highly resistant to existing drugs, such as pyrimethamine, the hunt for new high-value targets is important.

Overall, the study by Zhang *et al.* offers a powerful start for identifying rare, high-value, potentially druggable processes in human malaria parasites. It will inspire other complementary analyses of the data and also new functional screens. For instance, detailed bioinformatics will reveal which essential genes are specific to parasite biology and—later, if found druggable—will offer clearer paths to selective and safe pharmacology. The extension of insertional mutagenesis screens to other stages of the parasite life cycle, beyond the blood stage, should help generate inhibitors suited for broader community-wide malaria prevention campaigns that control the disease before there are clinical symptoms. Improvements in conditional CRISPR-dCas, and related genomic technologies that allow down-regulation of specific genes without cutting DNA, should help identify genes that trigger parasite death after even partial loss of target activity (*15*). For these reasons, the continued evolution of malaria genomic tools is expected, which will accelerate discovery of high-value drug targets in the parasite genome. ■

REFERENCES AND NOTES

1. World Health Organization (WHO), *WHO World Malaria Report* (WHO, 2017).
2. M. A. Phillips *et al.*, *Nat. Rev. Dis. Primers* **3**, 17050 (2017).
3. M. Zhang *et al.*, *Science* **360**, eaap7847 (2018).
4. E. Bushell *et al.*, *Cell* **170**, 260 (2017).
5. W. A. Guiguemde *et al.*, *Chem. Biol.* **19**, 116 (2012).
6. W. C. Van Voorhis *et al.*, *PLOS Pathog.* **12**, e1005763 (2016).
7. A. J. Reid *et al.*, *eLife* **7**, e33105 (2018).
8. A. S. Tarun *et al.*, *Proc. Natl. Acad. Sci. U.S.A.* **105**, 305 (2008).
9. A. N. Cowell *et al.*, *Science* **359**, 191 (2018).
10. L. Jiang *et al.*, *Antimicrob. Agents Chemother.* **44**, 1047 (2000).
11. M. A. Phillips *et al.*, *Sci. Transl. Med.* **7**, 296ra111 (2015).
12. G. H. Hitchings Jr., Nobel Lecture (1988); www.nobelprize.org/nobel_prizes/medicine/laureates/1988/hitchings-lecture.pdf.
13. N. J. Curtin *et al.*, *Cancer Res.* **51**, 2346 (1991).
14. K. Zhang *et al.*, *Science* **296**, 545 (2002).
15. B. E. Housden *et al.*, *Nat. Rev. Genet.* **18**, 24 (2017).
16. M. Sakaguchi *et al.*, *J. Struct. Biol.* **193**, 162 (2016).

ACKNOWLEDGMENTS

The authors are supported by United States National Institutes of Health (NIH) grants AI089688 and AI093380.

10.1126/science.aat5092

The highly active genome of malaria parasites

Malaria parasites activate a large part of their genome in each life-cycle stage, but high-throughput screens with millions of small molecules reveal few druggable targets.

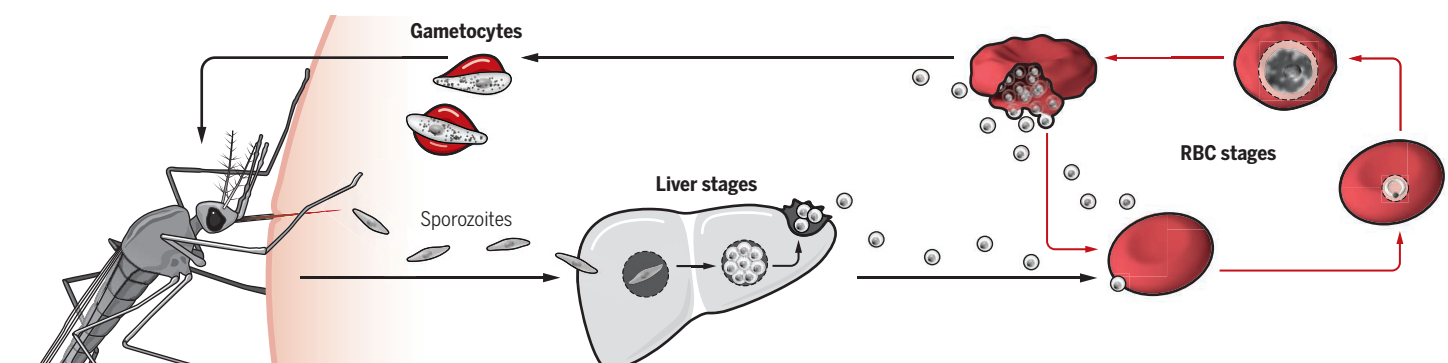

TOTAL GENES (*3*)	STAGE	CLINICAL SYMPTOMS	TRANSCRIPTS IDENTIFIED (*7*, *8*)	PROTEINS EXPECTED (*7*, *8*)	ESSENTIAL GENES (*3*)	POTENT SELECTIVE INHIBITORS (*2*, *5*)	TARGET INHIBITOR PAIRS (*6*, *9*)
5438	**RBC**	Yes	4871	2415	2680	250	25
	Gametocyte	–	4478	2270	?	5	3
	Liver	–	1985	712	?	10	5

Numbers in this table are an approximation from references cited in the top row.

NEUROPHYSIOLOGY

A cellular mechanism for age-induced itch

Age-induced loss of touch signaling causes mechanical itch

By **Amanda H. Lewis** *and* **Jörg Grandl**

It is well known that aging is accompanied by the death of specific cell types that function as sensors of outside signals and that this cell death leads to deficits in our ability to detect these signals. For example, age-associated loss of sensory hair cells and/or spiral ganglia neurons in the inner ear leads to progressive hearing loss, particularly of high frequencies (*1*). Similarly, death of photoreceptors in the retina of the eye is a key aspect of the pathogenesis of age-related macular degeneration, the leading cause of vision impairment in individuals older than 60 years of age (*2*). On page 530 of this issue, Feng *et al.* (*3*) identify an unusual link between age-related loss of a sensory cell type and aberrant sensory processing: During aging, the loss of specialized skin cells called Merkel cells results in alloknesis, the pathological sensation of itch in response to innocuous mechanical stimuli.

Merkel cells aggregate in small clusters called touch domes in the skin, as well as at the base of whisker follicles in rodents (*4*). The first step of detecting touch can originate in Merkel cells when a mechanical stimulus activates the mechanosensitive ion channel Piezo2 in these cells. Activating Piezo2 channels causes them to open, which depolarizes the cell, in turn activating voltage-gated calcium channels. This is thought to eventually lead to the release of neurotransmitters. Merkel cells thus transmit the presence of a mechanical stimulus to their nearby innervating low-threshold mechanoreceptors (LTMRs), which are nerve fibers known to respond to light mechanical stimuli (*5*–*8*). Detection of light touch requires this pathway, as chemical or genetic ablation of either Merkel cells or Piezo2 channels leads to deficits in the ability to detect low-force, but not high-force, stimuli, the latter of which are sensed by an unknown protein (*7*). Consistent with their role in light touch, in humans, Merkel cells are greatly enriched in highly sensitive skin areas, such as the fingertips and lips (*4*).

The fascinating study of Feng *et al.* finds that, in addition to their critical role in light touch, Merkel cells also play an unexpected protective role against alloknesis. Mechanical itch is thought to be a protective response that results from aversive and potentially damaging stimuli, such as a scratchy sweater or a pesky mosquito. However, in the presence of chronic itch (for example, resulting from a rash), stimuli that would otherwise be perceived as harmless, such as light stroking of the skin, can also induce a severe feeling of itch (alloknesis). This is often provoked by dry skin and is particularly prevalent in the elderly. To investigate a possible mechanism for age-induced alloknesis, the authors observed that aged mice (>24 months old) had bouts of scratching when touched lightly with a small nylon hair, whereas younger mice (2 months old) did not exhibit this behavior. Importantly, increased itching occurred selectively in response to light mechanical touch, as older mice did not differ from younger mice in how they responded to chemically induced itch or to aversive mechanical or thermal stimuli. Alloknesis in older mice was also accompanied by a selective decrease in firing rates of LTMRs but not other nerve fibers, suggesting that LTMRs might play an integral role in this phenomenon.

The decreased firing rates of LTMR nerve fibers led the authors to investigate Merkel cells, which are immediately upstream of LTMRs. In aged skin, whereas the number of touch domes was unchanged, there were fewer Merkel cells per touch dome than in skin from younger animals (see the figure). Importantly, the link between this reduction in Merkel cell number and increased mechanical itch was causal, as both genetic ablation of the Merkel cells and chemical ablation, through an acetone treatment to mimic dry skin, also robustly induced alloknesis.

Further, Piezo2 was required for protection against alloknesis, as mice with Merkel cell–specific ablation of the *Piezo2* gene showed increased mechanical itch behavior, similar to that of Merkel cell–deficient mice. Perhaps most promising for future development of therapeutics to treat alloknesis, the authors activated Merkel cells with DREADDs (designer receptors exclusively activated by designer drugs). Activation of Merkel cells with DREADDs suppressed alloknesis in the acetone-treated mice, suggesting that increased activity of the few cells spared by the treatment was sufficient to protect against mechanical itch.

The finding that Merkel cells normally protect against mechanical itch is notable because it is initially counterintuitive. Whereas in other sensory modalities (for example, vision and hearing), a reduction in sensory cell number as a result of cell death leads to a detrimental reduction in sensation, here, death of Merkel cells leads to an increase in unwanted sensation; that is, an otherwise nonaversive stimulus is perceived as potentially harmful. Notably, this pathway has previously been proposed for itch: In 2015, a population of inhibitory interneurons in the spinal cord that express neuropeptide Y (NPY$^+$) was

Itching from loss of touch sensors

Aged skin is associated with the loss of light touch–sensing Merkel cells and an increase in itching sensation.

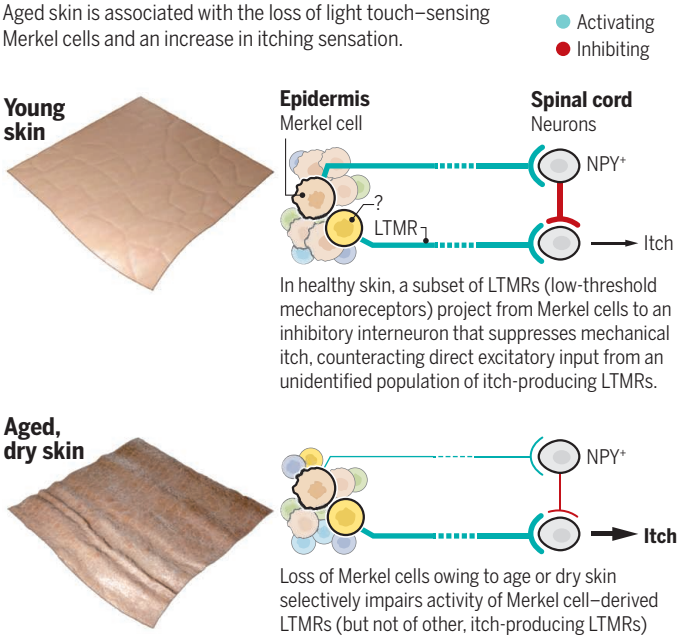

GRAPHIC: V. ALTOUNIAN/*SCIENCE*

Duke University Medical Center, Durham, NC 27710, USA.
Email: grandl@neuro.duke.edu

identified as a gate controlling mechanical itch (*9*). Consequently, ablation or silencing of the NPY$^+$ neurons leads to disinhibition of unidentified excitatory neurons, resulting in mechanical itch through a pathway distinct from that which produces chemical itch.

Together, these studies suggest a mechanism by which Merkel cell signaling modulates itch: Normally, LTMR nerve fibers that receive input from Merkel cells form excitatory synapses onto NPY$^+$ interneurons, counteracting the direct excitatory input from LTMRs and other nerve fibers onto excitatory itch-transmitting interneurons. Similar to the well-established gate theory for pain (*10*), increasing direct excitatory input to the inhibitory NPY$^+$ neurons, through increased recruitment of LTMRs by means of painful scratch, would inhibit this circuit, reducing itch. Conversely, loss of Merkel cell–derived LTMR activity (here, through loss of Merkel cell number) would lead to disinhibition of the inhibitory pathway and result in alloknesis.

Several questions remain, particularly in the context of treating human disease. Is the loss of Merkel cells with age conserved in humans, and, if so, how can this be prevented? Itching is the most common skin complaint among elderly patients and is frequently associated with dry skin (*11*). The current study suggests a mechanism by which painful scratch temporarily alleviates itch, by inducing enough activity through remaining Merkel cells to favor the inhibitory pathway of the gate. Enticing therapeutic routes for treating alloknesis involve either finding a way to prevent Merkel cell loss in the first place or noninvasively increasing activity in remaining Merkel cells, thus avoiding the damage that results from the painful itch-scratch cycle. It is also unknown whether this pathway is a potential avenue for the treatment of other itch disorders involving dry skin, such as eczema. Finally, what is the identity of the excitatory itch-transmitting interneuron? Completing our understanding of this circuit by identifying this excitatory neuron as well as the nerve fibers that innervate it is a necessary first step toward selectively silencing them for the treatment of itch. ■

REFERENCES

1. P. Perez, J. Bao, *Aging Dis.* **2**, 231 (2011).
2. X. Ding *et al.*, *Prog. Retin. Eye Res.* **28**, 1 (2009).
3. J. Feng *et al.*, *Science* **360**, 530 (2018).
4. V. E. Abraira, D. D. Ginty, *Neuron* **79**, 618 (2013).
5. B. Coste *et al.*, *Science* **330**, 55 (2010).
6. R. Ikeda *et al.*, *Cell* **157**, 664 (2014).
7. S.-H. Woo *et al.*, *Nature* **509**, 622 (2014).
8. S. Maksimovic *et al.*, *Nature* **509**, 617 (2014).
9. S. Bourane *et al.*, *Science* **350**, 550 (2015).
10. R. Melzack, P. D. Wall, *Science* **150**, 971 (1965).
11. L. Garibyan *et al.*, *Dermatol. Ther.* **26**, 92 (2013).

10.1126/science.aat5617

NEUROSCIENCE

The controversial correlates of consciousness

New data suggest that the prefrontal cortex ignites networks supporting consciousness

By **George A. Mashour**

The mechanism of consciousness is one of the most fundamental, exciting, and challenging pursuits in 21st-century science. Although the field of consciousness studies attracts a diverse array of thinkers who posit myriad physical or metaphysical substrates for experience, consciousness must have a neural basis. But where in the brain is conscious experience generated? It would seem that, given this remarkable era of technical and experimental prowess in the neurosciences, we would be homing in on the specific circuits or precise neuronal subpopulations that generate experience. To the contrary, there is still active debate as to whether the neural correlates of consciousness are, in coarse terms, located in the back or the front of the brain (*1*, *2*). On page 537 of this issue, van Vugt *et al.* (*3*) provide evidence that the prefrontal cortex is one of the brain regions that mediates visual consciousness. Additionally, Joglekar *et al.* (*4*) provide evidence that the prefrontal cortex is important for igniting neural networks that contribute to visual signal processing. Both studies support a model for consciousness that involves distributed and reciprocal interactions across the cortex.

The investigation of nonhuman primates by van Vugt *et al.* was motivated by a joint consideration of signal detection theory and global neuronal workspace theory. Signal detection theory attempts to explain the processing of stimuli that are around the threshold of perception and the reasons why sometimes we perceive such stimuli and other times we do not. Global workspace was originally a psychological framework for consciousness that has, in the past decade, become more neurobiologically informed (*5*). Global neuronal workspace theory posits that a subset of excitatory neurons and long-range tracts in the cortex, including prominent involvement of the prefrontal cortex, amplify, sustain, and broadcast specific representations for widespread cognitive processing.

Van Vugt *et al.* hypothesized that the threshold required for signal detection and the neural activity required for the broadcasting of information through the neuronal workspace would be the same. Neuronal activity in the visual cortex (areas V1 and V4, in the back of the brain; see the figure) and dorsolateral prefrontal cortex (in the front of the brain) of awake monkeys was recorded to establish neural correlates of visual stimuli that were perceived and reported with a specific eye movement. Reported stimuli were associated with strong and sustained prefrontal cortex activity, whereas nonreported stimuli were associated with weak and transient prefrontal activity. The investigators also assessed where information was lost for nonreportable stimuli and found that propagation failures could occur at various stages in the feedforward pathways en route to the front of the brain. It was concluded that stimuli cross the threshold for reportable signal detection when a critical trigger (or "ignition") for broadcasting occurs in the prefrontal cortex. This empirical conclusion was supported by a model in which reciprocal activity between frontal and parietal cortices enables the signal to become a self-sustained representation.

> ***"...there is still active debate as to whether the neural correlates of consciousness are, in coarse terms, located in the back or the front of the brain."***

But how do the long-range excitatory neurons of the global neuronal workspace amplify sensory signals without corrupting them or leading the brain into unbridled activation? Joglekar *et al.* examined

Center for Consciousness Science, Department of Anesthesiology, Neuroscience Graduate Program, University of Michigan Medical School, University Hospital, 1H247, 1500 East Medical Center Drive, SPC-5048, Ann Arbor, MI 48109-5048, USA. Email: gmashour@med.umich.edu

Processing consciousness

Visual processing (left) becomes consciously accessible (right) after "ignition" in the frontal cortex leads to reciprocal interactions that allow the representation of a stimulus to become self-sustaining and widely broadcast.

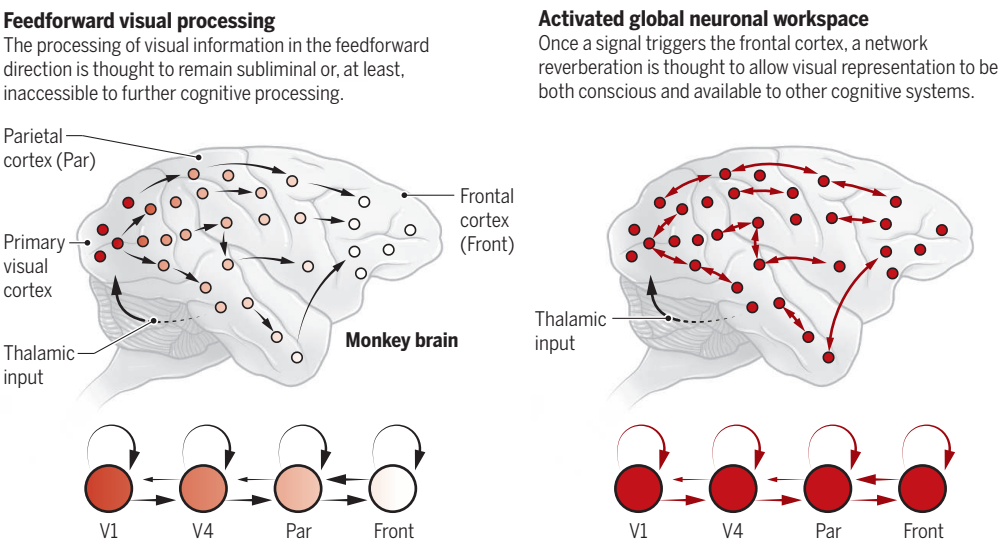

a model of feedforward (back-to-front) and feedback (front-to-back) processing in nonhuman primate brain networks. They demonstrate that excitatory feedback connections can amplify signals but are balanced by local inhibitory processes. This "global balanced amplification" fits current empirical data and is novel because it integrates local, feedforward, and feedback processing as well as the inhibitory neuronal brakes that appropriately constrain the network. Furthermore, Joglekar *et al.* modeled sensory input to area V1 in the visual cortex and found that weak signals activate local cortex whereas stronger signals lead to activation of prefrontal cortex and a reverberation of cortical networks, all of which are consistent with global neuronal workspace theory. These modeling data support the hypothesis of van Vugt *et al.* that the threshold of signal detection is the same threshold that activates prefrontal cortex and ignites a reciprocally connected cortical network.

How do these data inform the current controversy regarding the location of the neural correlates of consciousness? To answer this question, it is necessary to consider the distinction between phenomenal consciousness and access consciousness (*6*). Phenomenal consciousness is the purely qualitative aspect of experience, whereas access consciousness shares that experience with other cognitive systems for further action (for example, memory, motor activity, or report). The empirical data of van Vugt *et al.* were focused explicitly on reportable conscious events and provide further support to the hypothesis that the prefrontal cortex is important for access consciousness. The study does not speak directly to the question of phenomenal consciousness, but the authors do allude to evidence that prefrontal cortical neurons can represent consciously perceived visual stimuli even in the absence of report (*7*). Furthermore, a recent study on dreaming found that, although the neural correlates of phenomenal consciousness appeared to be primarily in the posterior cortex, dreaming during rapid eye movement sleep was also associated with high-frequency activity in the frontal and prefrontal cortices (*8*). In other words, anterior cortex might also contribute to the pure experience that constitutes phenomenal consciousness.

"The studies... help to explain a related and long-standing scientific issue, namely, the mechanisms of general anesthetics."

The studies of van Vugt *et al.* and Joglekar *et al.* also help to explain a related and long-standing scientific issue, namely, the mechanisms of general anesthetics. Models in which a reciprocally interacting frontal and parietal cortex is deemed necessary for access consciousness align with the finding that diverse general anesthetics depress metabolism and/or disrupt connectivity in frontal-parietal networks (*9*). Indeed, there is evidence that diverse general anesthetics preferentially suppress feedback connectivity from the frontal cortex in humans (*10*), potentially representing a failure of ignition. General anesthetics also show dose-dependent effects on local and long-range processing, two critical elements of global balanced amplification. At lower doses, local network connectivity is enhanced while the long-range connections of the global neuronal workspace are disrupted; higher anesthetic doses suppress both local and long-range connectivity (*11*). Thus, general anesthetics could prevent ignition in the prefrontal cortex while mitigating signal strength, depending on the dose. This independent line of investigation on the neural correlates of unconsciousness provides further evidence supporting the conclusions of the two studies.

Many questions remain. How do the studies of van Vugt *et al.* and Joglekar *et al.* apply to sensory processing outside of the visual system or to endogenous experiences (such as dreams) that do not require external sensory input at all? How does this work in nonhuman primates translate to humans or to animals that have a less developed prefrontal cortex? Further, how do these presumed correlates of consciousness inform the actual causes of consciousness? Solving—or dissolving—controversies related to the neural correlates will require transparent definitions of consciousness (access, phenomenal) and carefully designed paradigms (report, no report) as well as techniques that causally manipulate neural circuits with the dependent variable being a principled, possibly behavior-independent measure of consciousness. Only rigorous neuroscientific investigation will be able to reveal if the brain can ultimately explain both itself and its most precious function. ■

REFERENCES

1. M. Boly *et al.*, *J. Neurosci.* **37**, 9603 (2017).
2. B. Odegaard *et al.*, *J. Neurosci.* **37**, 9593 (2017).
3. B. van Vugt *et al.*, *Science* **360**, 537 (2018).
4. M. R. Joglekar *et al.*, *Neuron* **98**, 222 (2018).
5. S. Dehaene, J.-P. Changeux, *Neuron* **70**, 200 (2011).
6. N. Block, *Trends Cogn. Sci.* **9**, 46 (2005).
7. T. I. Panagiotaropoulos *et al.*, *Neuron* **74**, 924 (2012).
8. F. Siclari *et al.*, *Nat. Neurosci.* **20**, 872 (2017).
9. G. A. Mashour, A. G. Hudetz, *Trends Neurosci.* **41**, 150 (2018).
10. U. Lee *et al.*, *Anesthesiology* **118**, 1264 (2013).
11. Z. Huang *et al.*, *J. Neurosci.* **38**, 2304 (2018).

10.1126/science.aat5616

RETROSPECTIVE

Louise M. Slaughter (1929–2018)

Trailblazing congresswoman and women's rights advocate

By **Florence Haseltine**

Elected to the U.S. 100th Congress in 1986, Representative Louise M. Slaughter (D–NY) fought for the health and safety of all Americans, with a special dedication to women's issues. She died on 16 March at age 88, the oldest sitting member of Congress, serving her 16th term in the House of Representatives.

Slaughter was born in Harlan County, Kentucky. She graduated from the University of Kentucky with a bachelor's degree in microbiology in 1951 and a master's degree in public health in 1953. Her academic choices were said to be a response to the death of her sister from pneumonia as a young child. Slaughter served in the local county legislature and New York State Assembly before she was elected to Congress.

An outstanding advocate for women, Slaughter coauthored many pieces of legislation to confront and rectify inequities in women's health, safety, and job security. At a hearing of the House Subcommittee on Health and the Environment on 18 June 1990, the General Accounting Office provided overwhelming evidence that the National Institutes of Health (NIH) was not including women in clinical trials. In response, Slaughter helped draft the National Institutes of Health Revitalization Act, which provided for the establishment of the NIH Office of Research on Women's Health and guidelines for the inclusion of women and minorities in clinical research. She made a well-informed and forceful effort to persuade research communities to include women in clinical trials, a necessity for improving the health of women. The law was not passed under the George H. W. Bush administration but was quickly enacted in early 1993 under President Bill Clinton.

In 1994, Slaughter coauthored the Violence Against Women Act, which aimed to combat all forms of violence toward women, including stalking and physical and sexual abuse. In another forward-looking step, Slaughter began in 1995 to press for the Genetic Information Nondiscrimination Act, which aimed to prevent employers and insurers from discriminating based on predispositions to diseases identified by genetic tests. The law was finally enacted in 2008.

Slaughter was a member of the House Budget Committee and rose to be chair of the powerful Rules Committee. In 1991 and 1992, she was the only Democratic woman on either of these committees, and she worked in conjunction with women's groups to get women's health research funded. Her persistence ensured that in 1996, more than $526 million was earmarked for women's health, especially breast cancer research. Slaughter joined the bipartisan Congressional Caucus for Women's Issues in her first term and became chair of its Task Force on Women's Health in 1993. She was serving as cochair of the Congressional Pro-Choice Caucus when she died.

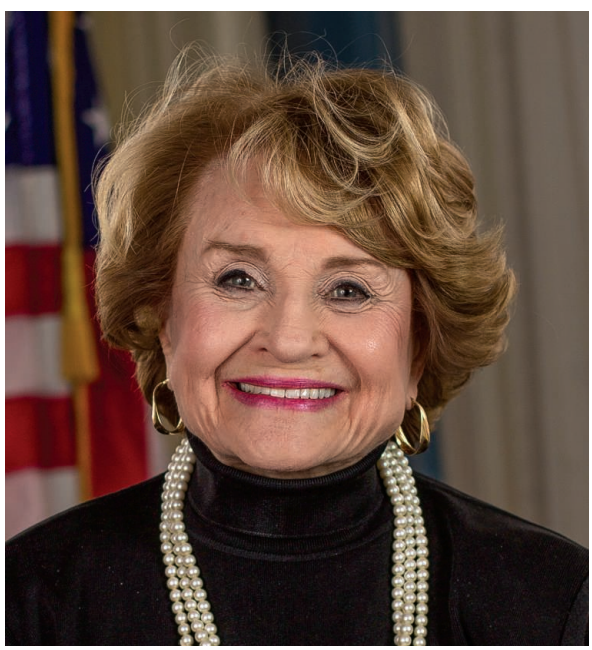

PHOTO: UNITED STATES CONGRESS/WIKIMEDIA COMMONS

Slaughter was a passionate advocate of Title IX and challenges faced by women in the military. She never wavered in her support of Title IX of the Education Act and issues related to girls and women in athletic activities. As recently as last year, she introduced legislation to strengthen Title IX. The legislation created a series of steps to handle gender issues in federally funded institutions. Starting in 2009, my organization—the Society for Women's Health Research (SWHR)—worked with Slaughter on health care for U.S. servicewomen. In 2013, she introduced an important piece of legislation: The Military Access to Reproductive Care and Health (MARCH) for Military Women Act. If passed, the legislation would help female military personnel by abolishing the ban on abortions at military hospitals.

I first met Slaughter in 1990 when I was working with others passionate about women's health to form SWHR. We met with the Congressional Caucus for Women's Issues and had many working lunches during which we exchanged information and views. A good and active listener, she would quickly summarize the information, ask pointed questions, and indicate where she thought legislation could help, always with a twinkle in her eye. She knew I worked at NIH on reproductive health issues and frequently asked about what NIH was doing to fund exciting research in that area. Slaughter knew everyone who was working for women's health. She always greeted me as though I were her best friend, and although I knew she had many "best friends," I was touched. As a woman physician, a specialist in obstetrics and gynecology, and a scientist and researcher, I was committed to improving women's health, but it was unusual and heartening to meet a legislator who felt the same way. Slaughter gave her full support to SWHR, along with many other advocacy organizations. She worked with us to push Congress for more funding, often asked for our input, and facilitated fruitful alliances among organizations seeking to improve women's health.

The legacy of Representative Louise McIntosh Slaughter is broad and significant, and SWHR, the National Breast Cancer Coalition, and many others owe her a large debt. Her personal success in Congress, her deep understanding of the importance of health issues, and her commitment to women's health have changed our nation for the better.

It is a tragedy that Slaughter fell at home and died days later. The Centers for Disease Control and Prevention says that falls are a leading cause of injury and death in older Americans and that women fall more often than men. It is up to us to fight for more research into the cause and prevention of falls in our senior population because, as Representative Slaughter would have said, it is the "smart thing to do." ■

Emerita Scientist, Eunice Kennedy Shriver National Institute of Child Health and Human Development; Founder, Society for Women's Health Research, Washington, DC, USA. Email: florence@swhr.org

10.1126/science.aat8795

POLICY FORUM

DATA GOVERNANCE

Scrutinizing the EU General Data Protection Regulation

How will new decentralized governance impact research?

By **Luca Marelli**[1]* *and* **Giuseppe Testa**[1,2]

On 25 May 2018, the European Union (EU) regulation 2016/679 on data protection, also known as the General Data Protection Regulation (GDPR), will take effect. The GDPR, which repeals previous European legislation on data protection (Directive 95/46/EC) (*1*), is bound to have major effects on biomedical research and digital health technologies, in Europe and beyond, given the global reach of EU-based research and the prominence of international research networks requiring interoperability of standards. Here we describe ways in which the GDPR will become a critical tool to structure flexible governance for data protection. As a timely forecast for its potential impact, we analyze the implications of the GDPR in an ongoing paradigmatic legal controversy involving the database originally assembled by one of the world's first genomic biobanks, Shardna.

The GDPR set out to harmonize data protection legislation in the EU, with the twofold aim of affording citizens increased protection and empowerment over personal data [Art. 1(2)], while also enhancing the circulation of those data within the EU [Art. 1(3)]. This is geared to provide regulatory support for the establishment of a full-fledged Digital Single Market—a policy cornerstone of the European Commission under President Jean-Claude Juncker. At its core, along with conferring new rights to data subjects [such as the "right to be forgotten" (Art. 17) and the right to data portability (Art. 20)], the GDPR adopts a risk-based, context-specific approach meant to ensure that appropriate data-protection measures are designed and implemented throughout the entirety of the processing activities (as enshrined in the "data protection by design and by default" principle, Art. 25). To this end, the GDPR promotes the responsibility of data controllers [Arts. 5(2) and 24], and it introduces new, decentralized modes of accountability (Art. 40). Additionally, the GDPR lays down specific provisions for the processing of sensitive data (Art. 9) for scientific research purposes (Art. 89), requiring organizational and technical safeguards, such as data pseudonymization, and mandating the designation of a data protection officer in case large-scale and systematic processing of sensitive data occurs (Arts. 37 to 39).

[1]*Department of Experimental Oncology, European Institute of Oncology, 20139 Milan, Italy.* [2]*Department of Oncology and Hemato-Oncology, University of Milan, 20122 Milan, Italy.*
**Present address: Marie Skłodowska-Curie Fellow, Centre for Sociological Research, KU Leuven, 3000 Leuven, Belgium.*
Email: luca.marelli@ieo.it; giuseppe.testa@ieo.it

GOVERNING "BIG-DATA" BIOMEDICINE

Regulatory challenges of big-data biomedicine pivot around (i) the inherently open-ended potential of data, whose digital compatibility makes them valuable for research pursuits that may be wholly disjoined from the original project within which samples or data were gathered, thus undermining the classical rationale for "informed consent"; and (ii) the increasing resolution and scope of data across the full range of digitized human features (from genomes to social networks' logs), with the ensuing and often self-proclaimed erosion of privacy (*2*). Responses have come broadly in two flavors, both aiming for technical fixes, though at different levels of technological engagement.

The first includes attempts to solve the conundrums of the digital age by resorting to yet more complex digitization, as in the recent example of secure multiparty computation that enabled genomic diagnosis while preserving participants' privacy (*3*). The second resorts instead to one of the defining human technologies of our time, that is, governance, meant as the reconfiguration of power structures through procedural architectures and distributed agency (*4*), as in the proposal of trust-building techniques to skirt the zero-sum game of data privacy versus data utility by shifting emphasis from the issue of privacy, per se, to the acquisition of control over data and trust in their holders (*5*).

As one of us has empirically shown (*4*), governance mechanisms have been central to the rise of contemporary biomedicine, as well as to the shaping of European science policy (*6*), by virtue of their mutually reinforcing constitutive tenets: (i) a partial retreat of state powers and governing bodies vis-à-vis the advance of market forces and a plurality of heterogeneous "stakeholders," ushering in a substantial reshaping of decision-making ("decentralization"); and (ii) the increased reliance on soft-rule instruments—such as standards, codes of conduct, and ethical thresholds—in place of more rigid forms of legislative interventions ("standardization"). Both of these features, in turn, have been integral to the structuring of the GDPR.

DECENTRALIZATION

Notwithstanding its binding nature and heavy sanctionatory regime [up to 20 million Euros, or 4% of a company's yearly global revenues, in case of noncompliance (Art. 83)], the GDPR decentralizes by delegating responsibility from national and EU authorities to data controllers (that is, the persons, companies, associations, or other entities that are in control of personal-data processing). As enshrined in the "accountability principle" [Arts. 5(2) and 24], controllers are required to adopt a proactive approach toward data protection and are responsible for the ex ante assessment, the implementation, and the post hoc verification of appropriate measures to ensure and demonstrate that data processing complies with the GDPR.

In providing coarse-grained guidance as to what measures fulfill a controller's obligations, and in making the determination of those measures dependent on the "nature, scope, context and purposes" of the relevant processing (Art. 24), the GDPR is set to promote a controller-based, case-sensitive, and context-specific approach to data protection. This marks a transition from a "paternalistic" to an "autonomy-based" regime in European data protection—in a fashion anecdotally best captured by the remark, overheard at a meeting on privacy law, that "with the GDPR, the EU is living the 1960s of data protection."

The shift toward a decentralized, controller-anchored, and accountability-based model gains salience with respect to secondary research, especially considering the emergence of "dynamic knowledge repositories" proposed as key enablers of "high definition medicine" (*7*). Article 5(1)(b) states that further data processing for scientific research "shall not be considered to be incompatible with the initial purposes" for which personal data were originally collected. In addition, the GDPR introduces criteria for compatibility assessment [Art. 6(4)], to be carried out by the data controller, which aims at ascertaining, on a case-by-case basis,

ILLUSTRATION: SÉBASTIEN THIBAULT

whether the further processing of personal data (without the data subject's consent), is compatible with the initial purpose for which data were originally collected. Factors to be taken into account for this "compatibility test" include "the nature of the personal data, in particular whether special categories of personal data are processed" [Art. 6(4)(c)]; "any link between the purposes for which the personal data have been collected and the purposes of the intended further processing" [Art. 6(4)(a)]; "the reasonable expectations of data subjects on the basis of their relationship with the controller as to their further use" (Recital 50); and "the context in which the personal data have been collected" [Art. 6(4)(b)].

STANDARDIZATION

Such flexibility in data processing extends to the foundational tenet of human biomedical research—informed consent. Although the GDPR requires "specific [and] informed" consent of the data subject [Art. 6(1)(a) and Recital 32], it recognizes that researchers may face the impossibility of fully identifying all potential future research purposes at the time of data collection. Accordingly, Recital 33 states that, if too specific a consent would impinge on the purpose of research, "data subjects should be allowed to give their consent to certain areas of scientific research when in keeping with recognized ethical standards for scientific research."

This key provision, which intersects still unsettled bioethical debates on the appropriate modes of informed consent, has two major implications. First, dispelling concerns voiced in relation to previous drafts of the GDPR suggesting otherwise (*8*, *9*), it lends the full legislative weight of the GDPR in support of broad consent whenever the criterion of specific consent for specific research use at the moment of data collection proves impossible to satisfy, as in the case of biobanking.

Interestingly, the Article 29 Working Party (the current EU data protection advisory body) recently issued further clarifying guidelines on the notion of consent in the GDPR (*10*). These guidelines reaffirm, as the default option, the requirement for specific consent. At the same time, they avoid a collision course with Recital 33 by treading a thin line between research purposes that, while being required to be "well-described," ought not always be "fully specified." In such cases, additional safeguards that could offset the lack of a specified purpose are recommended (such as provision of a comprehensive research plan before commencement of a project and/or increased transparency on its development to allow participants to exercise their right to withdraw consent). While submitting the flexible approach of Recital 33 to a "stricter interpretation" and "high degree of scrutiny," this interpretative guidance paves the way for controllers to avail themselves of broad consent whenever required by the intended research purposes.

Second, the provision contained in Recital 33 bestows on institutionalized ethics (that is, ethics committees' guidelines, along with other soft-law instruments such as professional codes of conduct, compare also Art. 40) an enhanced role in defining the scope of data processing for scientific research. More broadly, this role is enhanced in establishing general standards of practice that research with human biospecimens has been (as of yet) largely eschewing, given the absence of binding legislative requirements comparable to those regulating clinical research.

This is likely to heighten the relevance of the crucial, though still scholarly undertheorized, policy-making role of review boards and ethics committees. It also places increased emphasis on the ongoing effort lead by BBMRI-ERIC (the EU Biobanking and BioMolecular resources Research Infrastructure–European Research Infrastructure Consortium), involving major research organizations, patient advocacy groups, and industrial representatives, to develop a comprehensive code of conduct for the processing of personal data in health research (http://code-of-conduct-for-health-research.eu/). This code is envisioned as the reference standard in the field, enabling international harmonization in the EU and possibly beyond. However, it remains to be seen whether the concrete implementation of the GDPR will allow such sweeping reach by a single code of conduct. Or whether, on the contrary, the GDPR's enhanced investment in institution-

alized ethics will end up promoting regulatory fragmentation through a proliferation of approaches by local ethics committees.

TESTING THE GDPR

For the data protection–versus–data utility conundrum, the implementation of a flexible regime of governance for European data protection, in place of rigid homogenizing provisions (and notwithstanding the possibility that Member States introduce further provisions for the processing of genetic and health-related data [Art. 9(4)], has ambivalent implications.

On one hand, in addition to controllers' discretionary prerogatives, the GDPR upholds a far-reaching "research exemption" to the strict limitations otherwise imposed on the processing of sensitive data, relaxing requirements for consent [Art. 9(2)(j)], further processing [Art. 5(1)(b)], and data storage [Art. 5(1)(e)] (*11*). The reach of this research exemption is magnified by the adoption, as per Recital 159, of an exceedingly broad definition of activities falling under the rubric of "scientific research," including "technological development and demonstration," "applied research," and "privately funded research." Through the combination of these provisions, controllers such as pharmaceutical, direct-to-consumer genetic testing, and digital technologies companies, claiming to process (sensitive) personal data within the scope of scientific research activities, stand to benefit directly from a major regulatory leeway in favor of data controllers over data subjects (*11*).

On the other hand, the context-sensitive approach entailed by mechanisms such as the compatibility test, as well as the enhanced role assigned to institutionalized ethics, could be seen—and harnessed accordingly—as laying down the conditions for increased protection of data subjects and the promotion of their substantive, rather than merely tokenistic, engagement in research.

This can be exemplified in reference to the landmark first-instance ruling of the Tribunal of Cagliari (Italy) (*12*) that overturned a decision by the Italian Data Protection Authority (DPA) (*13*)—the first time ever by an Italian court—that had halted the activities of the United Kingdom–based Tiziana Life Sciences Plc. with the Shardna SpA database. Shardna was an Italian genomic biobank that stored genetic, health, and genealogical data (the latter collected from municipal and parish records archived over 4 centuries) of around 12,000 genetically interrelated residents from Ogliastra, an isolated region in Sardinia, Italy, known for being one of the world's few "blue zones," areas with a high prevalence of centenarians. Shardna was purchased by Tiziana in 2016 amid arguments in local communities, including research participants seeking to halt the foreign and for-profit acquisition of Shardna's database (*14*).

The decision of the Italian DPA to impose an interim block to Tiziana's processing was made on the basis that Tiziana, as the new data controller, had to (i) inform data subjects "of the change of data controller, and the further data processing for scientific research purposes in the field of medical genetics that the new controller may intend to carry out" and (ii) recollect consent from all data subjects whose information was stored in the Shardna database (*13*). The Tribunal of Cagliari instead ruled such a provision "exorbitant" given that the new data controller "pursues the same purposes of Shardna," namely, "scientific research purposes for which consent had been given" (*12*).

Although both the decision of the DPA and the ruling that overturned it unfolded with Italian data protection legislation still in place (*15*), the appeal judgment is expected to occur under the GDPR regime. Though full disentanglement of its legal complexity is beyond the scope of this paper, we argue that adjudication of this case is poised to revolve around the assessment of whether the change in data controller entails (i) a further processing of personal data, (ii) whose scope is not compatible with the original purpose for which consent had been obtained. Such assessment will arguably lead to the conclusion that it is highly implausible that Tiziana will not conduct further processing on the data set originally assembled by Shardna to advance its own research programs in oncology and immunology, irrespective of whether it (dis)continues the lines of research originally initiated by Shardna.

Assessing the compatibility of such further processing will require unpacking the abstract notion of scientific research (the stated purpose of the processing carried out by both Shardna and Tiziana). This will involve scrutinizing the research endeavors pursued by the two organizations, recognizing the substantial differences not only in their research programs and goals but also in terms of their respective governance arrangements, values, and aspirations. Shardna was established as a locally owned and governed biobank, strongly rooted in Ogliastra's communities (the name itself recalls the Shardana population inhabiting Sardinia in the Bronze Age). As such, it was able to achieve high recruitment rates in the local population (*14*) for its research programs focused on the genetics of multifactorial diseases typical of Ogliastra, and thus of primarily, albeit not exclusively, local relevance (*12*). By contrast, Tiziana is an international, profit-oriented biotech company with a distinct research focus, with feeble ties to the local communities engaged in research. Consequently, irrespective of how "broad" the original consent given to Shardna was, a cogent case could be made that the relationship between data subjects and the controller—a key criterion identified by the GDPR to determine compatibility of further processing—has been considerably altered upon the change in data controller. This could be argued to make further processing incompatible with the original purpose, thus requiring reconsenting of research participants.

Whatever its outcome, this case is an exemplary testing ground because its adjudication is bound to set jurisprudence for two central issues in contemporary biomedicine that the GDPR, in its bottom-up valorization of context, leaves open to interpretive ingenuity: the reuse of personal data upon a change in the property of biobanks and data repositories and what the relevant demarcations to be traced are, in the age of big data, within the category of scientific research in its ever increasing interdependence with other socioeconomic domains. Collective engagement with the versatility of this legislative tool by European scientists and citizens will thus be key to ensure its impact is scientifically and socially robust.

In conclusion, translating into practice the tensions between greater freedom and greater accountability of research defines the very scope of the GDPR and, more broadly, of the EU's experimenting with the governance of technoscience. ■

REFERENCES AND NOTES

1. Regulation (EU) 2016/679 (General Data Protection Regulation) of the European Parliament and of the Council of 27 April 2016 on the protection of natural persons with regard to the processing of personal data and on the free movement of such data, which repeals Directive 95/46/EC; www.eugdpr.org/.
2. Y. Joly *et al.*, *Cell* **167**, 1150 (2016).
3. K. A. Jagadeesh *et al.*, *Science* **357**, 692 (2017).
4. H. Nowotny, G. Testa, *Naked Genes* (MIT Press, 2011).
5. Y. Erlich *et al.*, *PLOS Biol.* **12**, e1001983 (2014).
6. S. Jasanoff, *Designs on Nature* (Princeton Univ. Press, 2005).
7. A. Torkamani *et al.*, *Cell* **170**, 828 (2017).
8. D. Hallinan, M. Friedewald, *Life Sci. Soc. Policy* **11**, 1 (2015).
9. J. Kaye *et al.*, *Eur. J. Hum. Genet.* **23**, 141 (2014).
10. Article 29 Working Party, Guidelines on Consent under Regulation 2016/679, WP259; http://ec.europa.eu/newsroom/article29/item-detail.cfm?item_id=615239.
11. K. Pormeister, *Int. Data Privacy Law* **7**, 137 (2017).
12. Tribunal of Cagliari, Sentenza n. 1569 (6 June 2017).
13. Italian Data Protection Authority, Garante per la protezione dei dati personali, Provvedimento n. 389 (6 October 2016); www.garanteprivacy.it/web/guest/home/docweb/-/docweb-display/docweb/5508051.
14. S. Kirchgaessner, "Ethical questions raised in search for Sardinian centenarians' secrets," *The Guardian* (12 August 2016).
15. Decreto legislativo n. 196 (Italy, 30 June 2003).

ACKNOWLEDGMENTS

This work was supported by the EPIGEN Flagship Project of the Italian National Research Council (CNR) (L.M. and G.T.) and the Italian Ministry of Health (Ricerca Corrente to G.T.).

10.1126/science.aar5419

BOOKS *et al.*

PHOTO: ISTOCKPHOTO.COM/JORDANLYE

PHYSICS

Deconstructing time

A quantum physicist reveals why time is not as simple as it seems

By **Conor Purcell**

Carlo Rovelli, best-selling author of *Seven Brief Lessons on Physics*, is back with a new book, *The Order of Time*. This latest venture offers insight into the notion of time, including narratives on how our understanding of the concept has changed from antiquity to the present, as well as a concise update on how time is understood today through the lens of quantum mechanics.

Ordered into three parts in which Rovelli, a theoretical physicist and philosopher, gradually deconstructs and rebuilds our picture of time, the book is a nice follow-up to his last title, *Reality Is Not What It Seems*. In that book, the author briefly explored what his work on quantum gravity implies about the concept of time but left the topic open for further thought.

This book leads on by tackling some of the most fundamental questions one could ask about the nature of the universe: "Why do we remember the past and not the future? Do we exist in time, or does time exist in us? What does it really mean to say that time 'passes'?"

From Aristotle and Newton to Einstein, who first made the connection between space-time and the gravitational field, Rovelli explains that there can be no clear concept of the present everywhere in the universe. "There is no special moment on Proxima b that corresponds to what constitutes the present here and now," he writes. "In my opinion, [this] is the most astounding conclusion arrived at in the whole of contemporary physics."

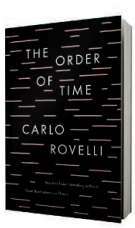

The Order of Time
Carlo Rovelli
Riverhead Books, 2018. 250 pp.

In an interview with the author, conducted for this review, he summarized the take-home message of the book as follows: "Time is not a single notion; it is multifaceted, and to study it scientifically, we must disentangle it." As a means of doing so, Rovelli takes readers on a journey into the field of quantum gravity, his own area of expertise. His ideas are both built on Einstein's but also—because of the nature of quantum mechanics—somewhat in rejection of them.

The reviewer is a science journalist and founding editor of www.wideorbits.com. He can be found on Twitter at @ConorPPurcell. Email: purcelcp@tcd.ie

Einstein's exposure to railway clock synchronization patents may have informed his later theories.

Rovelli maintains that our experience of time owes to a blurred, macroscopic perspective of the world that we encounter as human beings. "The distinction between past and future is tied to this blurring and would disappear if we were able to see the microscopic molecular activity of the world," he argued during our interview. In other words, the past and the future are equally determinable at the molecular level.

In an interesting chapter entitled "The inadequacy of grammar," Rovelli looks at how language has affected the way we think about time. "We say that an event 'is,' or 'has been,' or 'will be,'" he writes. "We do not have a grammar adapted to say that an event 'has been' in relation to me but 'is' in relation to you." Rejecting the notion of an "objective global present," he argues that if grammar is too imprecise to describe reality, we must change it.

Rovelli also looks in detail at the nature of entropy, arguing that it, too, is multifaceted and should be considered relativistically. "The entropy *of the world* does not depend *only* on the configuration of the world," he writes in a chapter entitled "Perspective." "[I]t also depends on the way in which we are blurring the world, and this depends on what the variables of the world are that *we* interact with."

Where other writers struggle to get their complex ideas across, Rovelli introduces profound notions with ease, using simple but evocative language. "The absence of time does not mean … that everything is frozen and unmoving," he writes, for example, in chapter 6. "It means that the incessant happening that wearies the world is not ordered along a time line, is not measured by a gigantic ticktocking."

He also has a knack for mixing his serious enterprise with a sense of humor. "The events of the world do not form an orderly queue, like the English," he writes. "They crowd around chaotically, like Italians."

Ultimately, Rovelli believes that the multifaceted nature of time will become a universally acknowledged truth and that our current conceptions of time will be cast aside. "One after another," he writes, "the characteristic features of time have proved to be approximations, mistakes determined by our perspective, just like the flatness of the Earth or the revolving of the sun."

Like most astounding truths that have been revealed, these new ideas will likely be hard to accept at first, too. ■

10.1126/science.aat2751

MUSEUM SCIENCE

Irreplaceable avian specimens, ransacked

A fly-tying flutist's bizarre theft highlights the importance of natural history collections

By **Christopher Kemp**

On 23 June 2009, after closing time, Edwin Rist broke a pane of glass at the back of the Natural History Museum at Tring, in Hertfordshire, U.K., and lowered himself into the quiet, darkened building. Within a few hours, he had hauled armfuls of bird skins—some of which had been collected more than a century earlier—from drawers and stowed them in a cavernous suitcase on wheels. Rist walked through the darkness to the train station, caught the 3:54 a.m. train to London, and disappeared. *The Feather Thief* by Kirk Wallace Johnson is a true and carefully researched account of Rist's incredible theft and what came afterward.

In 2011, Johnson was fly-fishing for trout in the Sangre de Cristo mountains of New Mexico when his guide told him about the bird heist. A few years before, while working for the U.S. Agency for International Development, Johnson had overseen the postwar reconstruction of Fallujah, in Iraq. After falling from a window in a posttraumatic stress disorder–induced dream state, he returned to the United States to recover, later establishing the List Project—a nonprofit effort to relocate Iraqis who had assisted the U.S. forces in Iraq.

Johnson was tired and frustrated and needed a distraction. Enter Edwin Rist, an odd, lanky American flute prodigy.

The avian collection at the Natural History Museum at Tring is vast. It contains almost a million bird skins, 15,000 skeletons, 17,000 birds preserved in fluid, 4000 bird nests, and about 400,000 eggs. Rist's theft wasn't even discovered for a month.

Increasingly, natural history collections have to find newer and more sophisticated ways to protect their holdings. In 2016, more than a dozen members of the Dead Zoo Gang were convicted in British courts of selling rhinoceros horns stolen from museums on the black market. Elsewhere, irreplaceable fossils have disappeared; rare bird eggs have been taken; shell collections have been ransacked.

Brightly colored and endangered in life, the specimens Rist took—299 in total— were irreplaceable. Many of them had been collected by Alfred Russel Wallace in the 1850s: birds of paradise, red-ruffed fruitcrows, spangled cotingas, resplendent quetzals.

Feathers from rare birds are prized in some fly-fishing communities.

A contemporary of Charles Darwin's, Wallace had dodged death countless times for the birds. But their theft was made worse by what Rist intended to do with them: He planned to dismantle them.

This is where the story takes an unexpected and entertaining swerve. Rist, we learn, planned to sell the feathers into the strange shadowy world of Victorian fly-tying to be used as raw materials.

Years earlier, as a teenager in upstate New York, Rist—homeschooled and socially awkward—had become a world-renowned fly-tyer. He videotaped himself creating his elaborate patterns, posting them online to global oohs and aahs. He was invited to conventions to tie flies before rapt audiences. In that world, he was a global star.

The feathers Rist extracted from the specimens he stole eventually made it across the world—via eBay, through online bulletin boards, and sold in person at fly-tying conventions. Once they were separated from their biodata, the birds became worthless to science.

But a determined Johnson spent years trying to track down the remaining intact birds and their feathers, a tattered list of which he always kept in his pocket. Perhaps, he thought, if he found specimens with their labels attached, he could return them to the museum.

Johnson is a careful guide. He attends the fly-tying conventions. He meets the tight-lipped men who want the feathers. He flies to Dusseldorf and Sweden to interview fly-tyers, and some of Rist's possible accomplices, all with his list in his pocket.

Rist had performed at the London Royal Academy of Music hours before the break-in on 23 June. He intended to buy a new flute with the proceeds from the sale of the feathers. Instead, he received a 12-month suspended prison sentence and was fined £125,150 under the Proceeds of Crime Act. He avoided harsher punishment with a somewhat controversial defense: that he has autism spectrum disorder. (Not all were convinced.)

Out on the fringes of modern society, there are strange worlds that most of us don't glimpse. The world of fly-tying is one of them; the quiet monastic storage rooms of natural history collections are another. The people who populate these spaces are shadows to us, too, until someone like Johnson lifts the veil.

The Feather Thief is an uncommon book. It could have been about nothing more than an ill person who did an odd thing. But it's not. It entertains while it educates. It informs and enlightens. It's a heist story that manages to underline the enduring and continuing importance of natural history collections and their incredible value to science. We need more books like this one. ■

10.1126/science.aas9050

The Feather Thief
Beauty, Obsession, and the Natural History Heist of the Century
Kirk Wallace Johnson
Viking, 2018. 336 pp.

The reviewer is the author of The Lost Species: Great Expeditions in the Collections of Natural History Museums *(University of Chicago Press, Chicago, 2017). Email: cjkemp@gmail.com*

Edited by **Jennifer Sills**

The sugar industry's influence on policy

In the Policy Forum "Was there ever really a 'sugar conspiracy'?" (16 February, p. 747), D. M. Johns and G. M. Oppenheimer based their criticism of our research on news stories, press releases, a podcast, and a commentary, not our peer-reviewed papers (*1*, *2*). Contrary to their assertions, our publications do indeed "focus on the evidence" and "follow the data."

Our *JAMA Internal Medicine* paper (*1*) demonstrated that Harvard nutrition researchers McGandy, Hegsted, and Stare used a double standard when critiquing the epidemiologic, experimental, and mechanistic evidence linking sugar to heart disease in their Sugar Research Foundation (SRF)–funded 1967 *New England Journal of Medicine* review (*3*, *4*). Hegsted's beliefs and publications that were unfavorable to his meat and dairy industry sponsors have no bearing on our conclusions about the bias in his review on the health effects of sugar. Johns and Oppenheimer attempt to put the research in the context of the time, but "logic and tools" and "norms and standards" have always called upon scientists to apply objective criteria when evaluating evidence.

We did not conclude that McGandy *et al.*'s review "meaningfully shaped the course of dietary science and policy," as asserted by Johns and Oppenheimer. Rather, we concluded that the sugar industry's sponsorship of this review, together with other historical and current evidence (*5*–*8*), suggests that the industry may have a long history of influence. Our recent *PLOS Biology* paper (*2*) further documented how SRF terminated funding for and failed to disclose or follow up on preliminary data in the 1970s that strengthened the emerging case—borne out by subsequent research (*9*)—that elevated triglycerides are a cardiometabolic risk factor and that sugar raises triglycerides.

Efforts to understand the impact of SRF's research program, which dates to 1943 (*10*), are hardly "ahistorical," a "conspiratorial narrative," or a "fallacy of emphasizing the machinations of one commodity sector." Rather, they are a necessary step to providing critical context about these industries, which is currently missing from historical accounts and policy discussions.

C. Kearns,[1,2*] L. Schmidt,[1,3,4] D. Apollonio,[1,5,6,7] S. Glantz[1,3,6,7,8]
[1]Philip R. Lee Institute for Health Policy Studies, University of California, San Francisco, San Francisco, CA 94118, USA. [2]Department of Preventive and Restorative Dental Sciences, School of Dentistry, University of California, San Francisco, San Francisco, CA 94143, USA. [3]Department of Medicine, School of Medicine, University of California, San Francisco, San Francisco, CA 94131, USA. [4]Clinical and Translational Science Institute, University of California, San Francisco, San Francisco, CA 94143, USA. [5]Department of Clinical Pharmacy, School of Pharmacy, University of California, San Francisco, San Francisco, CA 94143, USA. [6]Center for Tobacco Control Research and Education, University of California, San Francisco, San Francisco, CA 94117, USA. [7]Helen Diller Family Comprehensive Cancer Center, University of California, San Francisco, San Francisco, CA 94115, USA. [8]Cardiovascular Research Institute, University of California, San Francisco, San Francisco, CA 94158, USA.
*Corresponding author.
Email: cristin.kearns@ucsf.edu

PHOTO: BERT HARDY ADVERTISING ARCHIVE/GETTY IMAGES

In 1961, when this photo was taken, the relative health risks of sugar and fat remained unclear.

Response

Kearns *et al.* suggest that our critique is based on news stories rather than their peer-reviewed papers, and they claim that they did not conclude that a sugar industry–backed review published by Harvard nutritionists in 1967 meaningfully shaped the course of dietary science and policy. Our Policy Forum is based on archival research, secondary sources, and oral history and is a response to a newly popular narrative suggesting that the low-fat campaign of the 1980s was shaped by corrupt industrial and scientific forces—a revisionist depiction to which the publications of Kearns *et al.* have notably contributed (*1*, *2*). In interviews (*3*) and comments to journalists, Kearns *et al.* have suggested repeatedly that the Harvard scientists' "very influential review" (*4*) helped to "derail the discussion about sugar for decades" (*5*) and "delayed the development of a scientific consensus on sugar-heart disease for decades" (*6*). We think that authors are responsible for their own words, regardless of where they appear.

Kearns *et al.* argue that the Harvard nutritionists used a "double standard" when reviewing the evidence linking sugar and heart disease, and they assert that the beliefs and track records of the Harvard scientists have "no bearing" on their conclusion that the review was "biased." But as our Policy Forum demonstrated, the sponsored review emerged directly from a landmark study the Harvard scientists had just completed, with support from the dairy industry, that confirmed their longstanding beliefs that

REFERENCES

1. C. E. Kearns, L. A. Schmidt, S. A. Glantz, *JAMA Intern. Med.* **176**, 1680 (2016).
2. C. E. Kearns, D. Apollonio, S. A. Glantz, *PLOS Biol.* **15**, e2003460 (2017).
3. R. B. McGandy, D. M. Hegsted, F. J. Stare, *New Engl. J. Med.* **277**, 186 (1967).
4. R. B. McGandy, D. M. Hegsted, F. J. Stare, *New Engl. J. Med.* **277**, 242 (1967).
5. C. E. Kearns, S. A. Glantz, L. A. Schmidt, *PLOS Med.* **12**, e1001798 (2015).
6. G. Taubes, C. K. Couzens, "Big sugar's sweet little lies: How the industry kept scientists from asking, does sugar kill?," *Mother Jones* (November/December, 2012).
7. The Sugar Association, "Sugar and heart health: What are the facts?" (2015); www.sugar.org/sugar-heart-health-facts/.
8. Office of Disease Prevention and Health Promotion, "Sugar Association comment ID #22978 submitted 05/07/2015" (2015); https://health.gov/dietaryguidelines/dga2015/comments/readCommentDetails.aspx?CID=22978.
9. Dietary Guidelines Advisory Committee, "Scientific report of the 2015 Dietary Guidelines Advisory Committee" (U.S. Department of Health and Human Services and U.S. Department of Agriculture, Washington, DC, 2015).
10. D. W. Cheek, *Sugar Research, 1943–1972* (International Sugar Research Foundation, 1974).

10.1126/science.aat3763

saturated fats were the central dietary risk factor in heart disease and that sugar had little effect. It was this data-driven perspective—which ran against the interests of their dairy industry sponsors—that subsequently attracted the attention of the sugar industry.

It would be surprising if the Harvard nutritionists' scientific perspective on the health risks of fat and sugar did not pervade their own narrative review. The Institute of Medicine has recognized that "intellectual preconceptions and previously stated positions" can shape expert analyses (*7*). The very rationale advanced by pioneers in the "evidence-based" movement for replacing narrative reviews with systematic reviews was that narrative reviews tended to reflect the intellectual commitments of their authors (*8*–*10*). A typical narrative review dating from the mid-1960s would combine findings from published research with expert opinion. Yet Kearns *et al.* have chosen to dismiss the expert beliefs, scientific track records, and other funders of the Harvard investigators as having no relevance, while narrating in detail any interactions with the sugar industry. Here is a double standard—a one-sided and ahistorical appraisal. Kearns *et al.* have presented no evidence showing that the Harvard group's review would have been different in the absence of sugar industry support, particularly in light of their previous documented willingness to produce findings unfavorable to their sponsors.

We agree with Kearns *et al.* that analyses of the legacy of the sugar industry's research program are needed. However, insights gained from archival documents that provide only a "narrow window" (*1*) into the activities of one commodity sector must be weighed alongside evidence from other commercial, nonprofit, and governmental actors and carefully contextualized within the period under study. Our analysis shows that industry-academy collaborations were normative in the mid-1960s. The American Heart Association had already told all Americans to limit intake of saturated fat, whereas the sugar theory had barely gotten off the ground. Cross-sectional analyses of narrow slices of the past do not provide an adequate basis for historical interpretation.

D. M. Johns[1]* and G. M. Oppenheimer[2]
[1]Center for the History and Ethics of Public Health, Columbia University Mailman School of Public Health, New York, NY 10032, USA. [2]School of Public Health, City University of New York, New York, NY 10027, USA.
*Corresponding author.
Email: dmj2119@columbia.edu

REFERENCES

1. C. E. Kearns, L. A. Schmidt, S. A. Glantz, *JAMA Intern. Med.* **176**, 1680 (2016).
2. C. E. Kearns, D. Apollonio, S. A. Glantz, *PLOS Biol.* **15**, e2003460 (2017).
3. S. A. Glantz, M. Nestle, "Podcast: Food industry funding of nutrition research," *JAMA Intern. Med.* (2016); http://jamanetwork.com/learning/audio-player/13460555.
4. K. McEvers, "Sugar industry manipulated research about health effects, study finds," *National Public Radio* (2016); www.npr.org/2016/09/13/493801090/sugar-industry-manipulated-research-about-health-effects-study-finds.
5. A. O'Connor, "How the sugar industry shifted blame to fat," *New York Times* (2016); www.nytimes.com/2016/09/13/well/eat/how-the-sugar-industry-shifted-blame-to-fat.html.
6. M. Bailey, Sugar industry secretly paid for favorable Harvard research," *STAT* (2016); www.statnews.com/2016/09/12/sugar-industry-harvard-research/.
7. Institute of Medicine, *Conflict of Interest in Medical Research, Education, and Practice*, B. Lo, M. J. Field, Eds. (National Academies Press, 2009).
8. R. J. Light, D. B. Pillemer, *Summing Up: The Science of Reviewing Research* (Harvard University Press, 1984).
9. C. D. Mulrow, *Ann. Intern. Med.* **106**, 485 (1987).
10. G. V. Glass, *Educ. Res.* **5**, 3 (1976).

10.1126/science.aat5208

Linguistics' role in the right to education

In primary schools across the world, 40% of students must learn all academic subjects, including how to read, in a language that they do not speak fluently (*1*). Excluding students' native languages from the classroom leads to academic failure for hundreds of millions of children throughout the world (*1*), contributes to their communities' socioeconomic underdevelopment (*2*), and violates their human rights (*3*).

Postcolonial communities in the Caribbean, Latin America, Africa, Asia, and the Pacific are most likely to subject their students to instruction in a non-native language (*4*). This correlation is no accident: The exclusion of noncolonial languages in education is one of the most insidious tools of class-based and geopolitical power struggles in colonial and postcolonial societies (*5*). In Haiti, for example, French is spoken fluently by no more than 5% of the population (*6*), whereas Haitian Creole ("Kreyòl") is spoken by virtually everyone. Yet French is the primary language of formal education. This language barrier has handicapped generations of students who speak only Kreyòl and has contributed to Haiti's status as one of three countries with the highest levels of inequity in the world (*7*).

Hawaii can serve as a model for a way forward. Hawaii has a successful language-immersion program with high enrollment of indigenous children whose first language is Hawaiian (*8*). The immersion schools have enhanced the students' learning gains, including the learning of second languages such as English (*8*). Through recent legislation that strengthens education in noncolonial languages (*9*), the United States is expanding language-immersion and dual-language education to include Native American and other minority languages (*10*). These models should be extended to communities worldwide. One crucial step is to develop high-quality active-learning methods and resources for teaching in every student's native language [e.g., (*11*)].

Access to education in all languages, including those of disadvantaged communities whose languages have been excluded in education, will allow everyone to "enjoy the benefits of scientific progress and its applications," as provided by Article 15 of the International Covenant on Economic, Social, and Cultural Rights (*12*). To accomplish this goal, we need more research and international collaboration among linguists, scientists, mathematicians, engineers, and educators. Together, we can work to include noncolonial languages in the design of high-quality educational resources that enhance active learning and are anchored in local culture and local needs. Academic and government leaders, as well as granting agencies and international organizations, can help encourage and fund such research.

Michel DeGraff
Department of Linguistics and Philosophy, Massachusetts Institute of Technology, Cambridge, MA 02139, USA. Email: degraff@mit.edu

REFERENCES

1. UNESCO, "If you don't understand, how can you learn?" (Global Education Monitoring Report, Policy Paper 24, 2016); http://unesdoc.unesco.org/images/0024/002437/243713E.pdf.
2. S. L. Walter, in *The Handbook of Educational Linguistics*, B. Spolsky, F. M. Hult, Eds. (Blackwell Publishing, 2008), ch. 10.
3. R. Phillipson *et al.*, *Linguistic Human Rights: Overcoming Linguistic Discrimination* (De Gruyter Mouton, 1994); www.worldcat.org/oclc/979913240.
4. S. L. Walter, C. Benson, in *The Cambridge Handbook of Language Policy*, B. Spolsky, Ed. (Cambridge University Press, 2012), ch. 14.
5. M. DeGraff, *Lang. Soc.* **34**, 533 (2005).
6. M. Saint-Germain, *Rev. Sci. Educ.* **23**, 10.7202/031954ar (1997) [in French].
7. "Inequality index: where are the world's most unequal countries?" *The Guardian* (26 April 2017).
8. W. H. Wilson, K. Kamanā, in *Literacy in the Early Years, Vol. 17*, C. McLachlan, A. Arrow, Eds. (Springer, 2017), pp. 133–150.
9. S.1177: Every Student Succeeds Act (2015).
10. J. Vaznis, "A Haitian Creole program for preschoolers arrives in Mattapan," *Boston Globe* (7 September 2017).
11. The MIT-Haiti Initiative: An International Engagement (2016); http://web.mit.edu/fnl/volume/291/miller.html.
12. United Nations Human Rights, "International Covenant on Economic, Social and Cultural Rights" (1976); www.ohchr.org/EN/ProfessionalInterest/Pages/CESCR.aspx.

10.1126/science.aat5532

EDITOR'S NOTE

"Joint statement on EPA proposed rule and public availability of data" by J. Berg, P. Campbell, V. Kiermer, N. Raikhel, D. Sweet, *Science* **360**, eaau0116 (2018). Published online 4 May 2018 (First Release 30 April 2018); 10.1126/science.aau0116

Cite as: J. Berg., P. Campbell, V. Kiermer, N. Raikhel, D. Sweet, *Science* 10.1126/science.aau0116 (2018).

Joint statement on EPA proposed rule and public availability of data

Jeremy Berg,[1]* Philip Campbell,[2] Veronique Kiermer,[3] Natasha Raikhel,[4,5] Deborah Sweet[6]

[1]Editor-in-Chief, *Science* family of journals, Washington, DC 20005, USA. [2]Editor-in-Chief, *Nature*, London, N1 9XW, UK. [3]Executive Editor, *Public Library of Science* (*PLOS*) Journals, San Francisco, CA 94111, USA. [4]Interim Editor-in-Chief, *Proceedings of the National Academy of Sciences (PNAS) of the United States of America*, Washington, DC 20001, USA. [5]Distinguished Professor of Plant Biology, University of California, Riverside, Riverside, CA 92507, USA. [6]Vice President of Editorial, Cell Press, and Acting Editor-in-Chief, *Cell*, Cambridge, MA 02139, USA.

*Corresponding author. Email: jberg@aaas.org

We are writing in response to a proposed rule announced by the Environmental Protection Agency (EPA) in a 24 April 2018 press release (*1*). The release reads, "The rule will ensure that the regulatory science underlying Agency actions is fully transparent, and that underlying scientific information is publicly available in a manner sufficient for independent validation."

Data sharing is a feature that contributes to the robustness of published scientific results. Many peer-reviewed scientific journals have recently adopted policies that support data sharing, consistent with the Transparency and Openness Promotion (TOP) standards. These standards, however, recognize the array of workflows across scientific fields and make the case for data sharing at different levels of stringency; in not every case can all data be fully shared. Exceptional circumstances, where data cannot be shared openly with all, include data sets featuring personal identifiers.

We support maintaining the rigor of research published in our journals and increasing transparency regarding the evidence on which conclusions are based. As part of these goals, we require that all data used in the analysis must be available to any researcher for purposes of reproducing or extending the analysis. Importantly, the merits of studies relying on data that cannot be made publicly available can still be judged. Reviewers can have confidential access to key data and as a core skill, scientists are trained in assessing research publications by judging the articulation and logic of the research design, the clarity of the description of the methods used for data collection and analysis, and appropriate citation of previous results.

It does not strengthen policies based on scientific evidence to limit the scientific evidence that can inform them; rather, it is paramount that the full suite of relevant science vetted through peer review, which includes ever more rigorous features, inform the landscape of decision making. Excluding relevant studies simply because they do not meet rigid transparency standards will adversely affect decision-making processes.

REFERENCE

1. U.S. Environmental Protection Agency, News Releases, "EPA Administrator Pruitt proposes rule to strengthen science used In EPA regulations" (2018); www.epa.gov/newsreleases/epa-administrator-pruitt-proposes-rule-strengthen-science-used-epa-regulations.

Published online 30 April 2018
10.1126/science.aau0116

RESEARCH

DASH/Dam1c makes rings around microtubules

Jenni and Harrison, p. 552

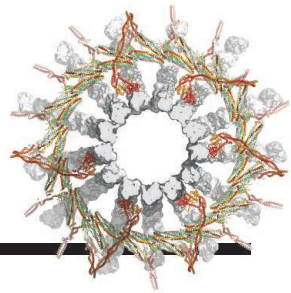

IN *SCIENCE* JOURNALS

Edited by **Caroline Ash**

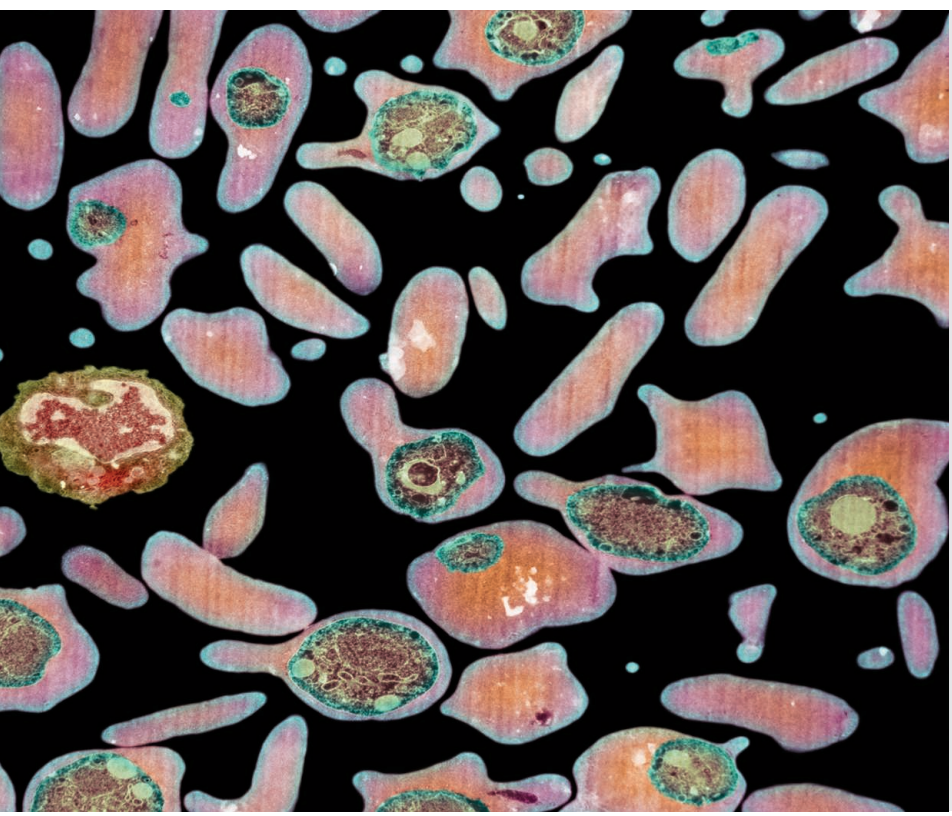

Red blood cells infected by malaria parasites

MALARIA

Saturating malaria mutagenesis

Malaria is caused by eukaryotic *Plasmodium* spp. parasites that classically infect red blood cells. These are difficult organisms to investigate genetically because of their AT-rich genomes. Zhang *et al*. have exploited this peculiarity by using *piggyBac* transposon insertion sites to achieve saturation-level mutagenesis for identifying and ranking essential genes and drug targets (see the Perspective by White and Rathod). Genes that are current candidates for drug targets were identified as essential, in contrast to many vaccine target genes. Notably, the proteasome degradation pathway was confirmed as a target for developing therapeutic interventions because of the several essential genes involved and the link to the mechanism of action of the current frontline drug, artemisinin. —CA

Science, this issue p. 506; see also p. 490

NANOMATERIALS

Retrosynthesizing complex nanostructures

The solution synthesis of complex and asymmetric nanostructures is still challenging. For many applications, it will be important to gain simultaneous control over particle size and morphology, constituent materials, and internal interfaces. Fenton *et al*. have developed a strategy that mimics chemical retrosynthesis, starting with simple nanoparticle synthons—in this case, $Cu_{1.8}S$ nanoparticles, nanorods, and nanosheets. Various types of interfaces and junctions can be introduced, for example, by cation substitution. This intervention breaks the symmetry of the synthons and assembles them into higher-order structures. The nanostructures can thus be formed with asymmetric, patchy, porous, or sculpted regions. —PDS

Science, this issue p. 513

MEMBRANES

Turing structures at the nanoscale

Turing structures arise when imbalances in diffusion rates make a stable steady-state system sensitive to small heterogeneous perturbations. For example, Turing patterns occur in chemical reactions when a fast-moving inhibitor controls the motion of a slower-moving activator. Tan *et al*. grew polyamide membranes by using interfacial polymerization, where the reactions occur at the interface between oil and water layers. The addition of polyvinyl alcohol to the aqueous phase reduced the diffusion of the monomer. This process generates membranes with more bumps, voids, and islands, which prove to be better for water desalination. —MSL

Science, this issue p. 518

SIV

Emptying the reservoir

Antiretroviral therapy can halt HIV-1 replication but cannot clear the hidden reservoirs of latent virus. Lim *et al*. treated simian immunodeficiency virus (SIV)–infected rhesus macaques on antiretroviral therapy with up to 19 doses of the Toll-like receptor 7 agonists GS-986 or GS-9620. By the third dose, all macaques experienced transient SIV plasma viremia within 48 hours. Dosing was also associated with activation of lymphocytes and reductions in SIV DNA in cells from the peripheral blood, lymph nodes, and gastrointestinal tract. When antiretroviral therapy ceased, two of nine treated macaques did not suffer rebound of virus and remained apparently virus-free and disease-free for more than 2 years. —OMS

Sci. Transl. Med. **10**, eaao4521 (2018).

CREDITS: (FROM TOP) S. JENNI AND S. C. HARRISON; LONDON SCHOOL OF HYGIENE & TROPICAL MEDICINE/SCIENCE SOURCE

PALEOGENOMICS

Relationships among North Africans

The general view is that Eurasians mostly descend from a single group of humans that dispersed outside of sub-Saharan Africa around 50,000 to 100,000 years ago. Present-day North Africans share a majority of their ancestry with present-day Near Easterners, but not with sub-Saharan Africans. To investigate this conundrum, Van de Loosdrecht *et al*. sequenced high-quality DNA obtained from bone samples of seven individuals from Taforalt in eastern Morocco dating from the Later Stone Age, about 15,000 years ago. The Taforalt individuals were found to be most closely related to populations from the Near East (Natufians), with a third of their ancestry from sub-Saharan Africa. No evidence was found for introgression with western Europeans, despite attribution to the Iberomaurusian culture. None of the present-day or ancient Holocene African groups are a good proxy for the sub-Saharan genetic component. —LMZ

Science, this issue p. 548

IMMUNOLOGY

PTEN prevents the cytokine storm

An uncontrolled infection leads to sepsis, in which excessive production of proinflammatory cytokines, or a "cytokine storm," can cause potentially fatal tissue damage and organ failure. Sisti *et al*. found that septic mice had increased expression of the mRNA encoding the lipid and protein phosphatase PTEN. Mice lacking PTEN in myeloid cells showed greater inflammation, tissue injury, and mortality from sepsis. PTEN activity in the nucleus of macrophages induced the production of microRNAs that targeted *Myd88* mRNA, which encodes an adaptor protein required for cytokine production. —JFF

Sci. Signal. **11**, eaai9085 (2018).

SYSTEMS BIOLOGY

How to build a better morphogen gradient

To translate insights in developmental biology into medical applications, techniques are needed to ensure correct cell localization. Morphogen gradients allow precise and highly reproducible pattern formation during development. Through in vitro experiments and modeling, Li *et al*. tested the effects of unusual properties of Hedgehog (HH) signaling. The HH morphogen's receptor, Patched (PTCH), sends an inhibitory signal when no ligand is bound, which is relieved by ligand binding. PTCH also regulates spatial distribution of the signal by sequestering the HH ligand. Furthermore, signaling through the receptor promotes synthesis of more inhibitory receptor. These characteristics help speed gradient formation and explain the robustness of the system to changes in the rate of morphogen production. —LBR

Science, this issue p. 543

PLANT SCIENCE

Multiple, diverse, and complex

Calcium currents characterize the developing pollen tube in the small mustard plant *Arabidopsis* and correlate with growth at the tip of the pollen tube. This system constitutes a practical model for screening for Ca^{2+}-signaling mechanisms in plants. Wudick *et al*. analyzed multiple variants of glutamate receptor–like (GLR) channels and discovered that some work alone and others work in pairs or trios. Subcellular localization of GLRs is a complex response to CORNICHON sorting proteins, which leave some GLRs at the plasma membrane and ferry others to internal calcium reservoirs. The calcium current at the tip of the growing pollen tube apparently integrates multiple intracellular currents. —PJH

Science, this issue p. 533

IN OTHER JOURNALS

Edited by **Sacha Vignieri** *and* **Jesse Smith**

PHOTO: NICK PECKER/SHUTTERSTOCK.COM

IMMUNOLOGY

Watching the clock in asthma

Asthma symptoms often show variations based on circadian rhythms. Ehlers *et al*. report that mice missing a functional circadian clock (*Bmal1*$^{-/-}$) are more susceptible to acute bronchiolitis and chronic asthma-like inflammation after infection with Sendai virus. Similar, though less potent, effects were observed when wild-type mice were subjected to a chronic jet lag model. Concordantly, airway cells from human asthmatics show altered clock gene expression patterns. The disruption of circadian rhythms alters interferon-related antiviral responses and enhances the M2 macrophage phenotype. Thus, one way that the circadian clock may play a role in some forms of asthma is by regulating immune responses to respiratory viral infections. Still uncertain is the role of these genes in other forms of the disease, including atopic asthma. —STS

Mucosal Immunol. **11**, 97 (2018).

NEUROSCIENCE

Synaptic downscaling during "up" states

During slow-wave sleep, cortical networks oscillate between periods of high activity, known as "up" states, and quieter periods, known as "down" states. González-Rueda *et al*. compared synaptic plasticity during up and down states in the mouse barrel cortex during slow-wave sleep–like cortical dynamics. They studied connections between cortical layers 4 and 2/3 in young animals at postnatal days 16 to 21. This age corresponds to the end of the critical period of development of these synapses. Plasticity rules were modulated by up states: Spike timing–dependent synaptic potentiation was absent, and active synapses failing to contribute to postsynaptic spiking were selectively depressed. This synaptic downscaling mechanism promotes the elimination of weak and the preservation of strong synapses, thus enhancing the signal-to-noise ratio. —PRS

Neuron **97**, 1244 (2018).

Changes in climate affect the abundance of red-legged kittiwakes.

FORAGING ECOLOGY

Winter can be hard

The largest breeding colony of the red-legged kittiwake, an Arctic seabird, has undergone drastic declines and recovery over the past 40 years. It has been assumed that these changes have been driven by climate-induced shifts in food supply during breeding. Will *et al.* examined feathers collected from living birds and museum specimens to characterize isotopic signatures (which give a picture of food intake) and corticosterone levels (which relate to stress) over a 100-year period. They found that birds were less stressed when oceanic conditions in the eastern Pacific were warmer in both summer and winter and when sea ice was less extensive in the winter. Further, during years with more extensive ice, nitrogen isotope levels were higher, potentially indicating a higher reliance on energy stores. These results suggest that climate variability can directly affect population size and persistence and that winter conditions are important to reproductive success. —SNV

Mar. Ecol. Prog. Ser. 10.3354/meps12509 (2018).

CELL BIOLOGY

Mitochondria fight *Toxoplasma* for fat

Mitochondria provide platforms for innate immunity. The intracellular parasite *Toxoplasma gondii* infects almost 50% of individuals in western countries and up to 90% in developing countries. Pernas *et al.* wanted to understand the role of mitochondrial morphology in the control of *Toxoplasma* growth. They discovered that parasite-infected cells displayed a marked reduction in host lipid droplets caused by *Toxoplasma*-induced droplet autophagy (lipophagy). Fatty acid flux analysis revealed the path of fatty acids from the droplets to the *Toxoplasma*-containing vacuole. Elongated mitochondria congregated around the vacuole and competed with *Toxoplasma* for the lipophagy-liberated fatty acids. When mitochondria could not fuse and elongate, or could not oxidize fatty acids, parasite growth was enhanced. —SMH

Cell Metab. **27**, 886 (2018).

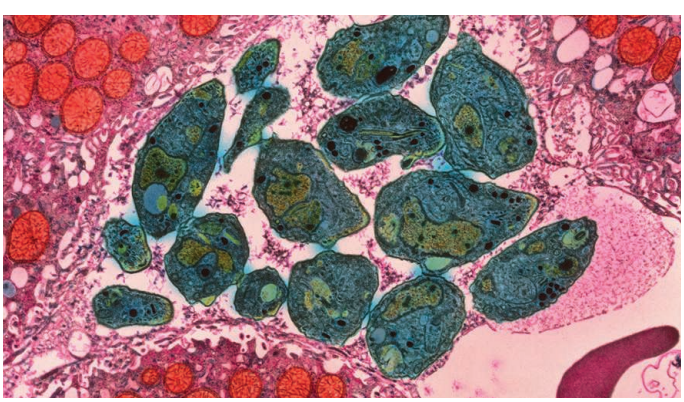

CREDIT: MOREDUN SCIENTIFIC LTD./SCIENCE SOURCE

***Toxoplasma* parasites (blue), shown here in their encysted stage within liver tissue, compete with mitochondria for lipids.**

EDUCATION

You can't be what you can't see

Identity-based motivation theory, which explains how people's identities motivate them, is relevant in science, technology, engineering, and mathematics (STEM) education because the STEM professoriate traditionally leans male. Most research on this topic focuses on student achievement outcomes. Solanki and Xu instead examined the relationship between instructor gender and student nonperformance outcomes, such as behavioral engagement, academic self-efficacy, interest, and utility value. Pre- and post-experience surveys from STEM gateway courses were analyzed, revealing a reduction in the gap between female and male students' course engagement and attitudes toward a STEM subject when a course was taught by a female instructor. Additionally, both female and male students were found to respond to instructor gender. Future studies should focus on understanding the variables underlying these behaviors. —MMC

Am. Educ. Res. J. 10.3102/0002831218759034 (2018).

POROUS MATERIALS

Metallacycles in carbon supports

Metallacycles are large organometallic rings in which metal complexes coordinate ligand assembly. The assembly process is dynamic, so, although convenient, these compounds can reassemble into larger, unwanted aggregates. Chen *et al.* found that a metallacycle formed from an acceptor ligand bearing platinum end groups and a donor bearing a porphyrin group was more stable when assembled within a mesoporous carbon material. The dispersion of the metallacycle was evidenced by a sixfold increase in singlet oxygen production for the porphyrin group compared with the free metallacycle in solution. —PDS

J. Am. Chem. Soc. 10.1021/jacs.8b02386 (2018).

CHEMISTRY

Reusable protein-based sensors

Targeted sensors for ions, molecules, proteins, or DNA can be made by immobilizing specific biomolecules onto a surface. However, it can be difficult to control the surface patterning or reversibly deposit the target molecules, which would allow for reusable surfaces. Ananth *et al.* selectively immobilized proteins onto silica-covered flat or porous surfaces, with control over orientation and surface density, by incorporating polyhistidine tags into the target proteins. The anchoring is reversible, as demonstrated by real-time switching. For devices that contain both gold and silica surfaces, the authors show that they can passivate the gold by using thiol chemistry while selectively coating the silica with the desired target molecules. —MSL

Small 10.1002/smll.201703357 (2018).

ALSO IN *SCIENCE* JOURNALS

Edited by **Caroline Ash**

STRUCTURAL BIOLOGY

How calcium gates a potassium channel

Small-conductance Ca^{2+}-activated K^+ (SK) channels are expressed throughout the nervous system and affect both the intrinsic excitability of neurons and synaptic transmission. An increase in the concentration of intracellular calcium opens the channels to conduct potassium across the cell membrane. Lee and MacKinnon report cryo–electron microscopy structures of human SK4-calmodulin channel complexes. Activation occurs when calcium binds to calmodulin, a protein with two lobes, known as C and N, separated by a flexible region. Each monomer in the channel tetramer binds constitutively to the C-lobe of calmodulin. The N-lobe of calmodulin is reasonably unconstrained until it binds calcium. With calcium bound, it then binds to the channel and induces conformational changes that open the pore. —VV

Science, this issue p. 508

METALLURGY

Smaller but more thermally stable

Synthesizing metals with extremely small (nanoscale) grain sizes makes for much stronger materials. However, very small–grained materials start to coarsen at relatively low temperatures, wiping out their most desirable properties. Zhou *et al*. discovered a way to avoid this problem by mechanically grinding copper and nickel at liquid nitrogen temperatures. The processing method creates low-angle grain boundaries between the nanograins, which promotes thermal stability. —BG

Science, this issue p. 526

NEUROSCIENCE

Loss of touch receptors leads to itch

Itch in response to light touch of the skin is an aging-associated problem. This phenomenon is called alloknesis and can become a major medical condition associated with dry skin. Feng *et al*. discovered that loss or dysfunction of Merkel cells causes scratching in mice (see the Perspective by Lewis and Grandl). Reduction of Merkel cell numbers results in reduced firing patterns and frequencies and changes the activation thresholds of slowly adapting afferent nerve fibers. Like hair cells, Merkel cells are lost with age. A painful scratch will temporarily alleviate itch because it induces enough activity through the remaining Merkel cells. —PRS

Science, this issue p. 530; see also p. 492

NEUROSCIENCE

Setting conscious perception alight

What are the neuronal mechanisms that enable conscious perception? Why do some images remain subliminal? Van Vugt *et al*. trained monkeys to detect low-contrast images and compared neuronal activity in brain areas V1, V4, and the dorsolateral prefrontal cortex. Some stimuli made it into consciousness, and others were subliminal depending on their propagation, which can be variable for weak stimuli (see the Perspective by Mashour). Strongly propagated stimuli initiated a state in the higher brain areas called "ignition" that caused information about a brief stimulus to become sustained and broadcasted back through recurrent interactions between many brain areas. —PRS

Science, this issue p. 537; see also p. 493

IMMUNOLOGY

Complement is a $CD8^+$ T cell metabolic rheostat

Systemic lupus erythematosus (SLE) is associated with deficiencies in the complement protein C1q. Although C1q plays a role in the clearance of apoptotic cells, there are several redundant clearance pathways. Disruption of one pathway does not lead to an autoimmune defect. In a chronic graft-versus-host disease model of SLE, Ling *et al*. show that C1q dampens $CD8^+$ T cell responses to self-antigens. C1q modulates metabolism through the mitochondrial cell-surface protein p32/gC1qR. The lack of C1q during a viral infection also enhances $CD8^+$ T cell responses. Thus, C1q plays a role as a "metabolic rheostat" for effector $CD8^+$ T cells. —STS

Science, this issue p. 558

BIODIVERSITY

Financing biodiversity conservation

Global funds for protecting biodiversity are too low to prevent wildlife populations from falling and species extinctions from increasing. In a Perspective, Barbier *et al.* call for a Global Agreement for Biodiversity modeled on the Paris Climate Agreement, with national targets, policies, and timelines. The overall goal is ambitious: to conserve at least 50% of terrestrial, inland water, coastal, and marine habitats by 2050. Formal involvement of the private sector, particularly in areas such as seafood, forestry, agriculture, and insurance, will be crucial to raise the necessary funds. —JFU

Science, this issue p. 486

IMMUNOGENOMICS

Establishing NK cell identity

The transcription factor ID2 is required for normal differentiation of all innate lymphoid cells. ID2 supports full maturation of natural killer (NK) cells into cytotoxic effectors. To investigate the transcriptional programming steps that underpin NK cell differentiation, Zook *et al*. characterized ID2-deficient NK cells. ID2 limited chromatin accessibility at multiple lymphocyte-associated genes to enable an effector-gene program to take hold. —IW

Sci. Immunol. **3**, eaao2139 (2018).

SURFACE CHEMISTRY

Direct plasmon chemistry

Light can excite plasmons at a metal surface, which can then decay and create hot electrons that induce chemical reactions of adsorbed molecules. Kazuma *et al*. used a scanning tunneling microscope (STM) to induce and map out the surface dissociation of a dimethyl disulfide molecule on silver and copper surfaces. A silver STM tip created localized plasmons at different distances from the molecule. The plasmons drove the reaction directly by exciting the valence electrons of the molecule into unoccupied states and cleaving the sulfur-sulfur bond. —PDS

Science, this issue p. 521

BIOMATERIALS

Curving bones

On larger length scales, bone is known to have a hierarchical structure in which small crystals of calcium phosphates arrange themselves around helices of collagen. These make up larger structures, such as the osteons found in compact bone. However, at smaller lengths, does the hierarchical structure persist? By combining three-dimensional electron tomography with two-dimensional electron

microscopy, Reznikov *et al*. observed structural ordering from the nanoscale upward. At the smallest scale, needle-shaped mineral units form platelets that organize into stacks bridging multiple collagen units. —MSL

Science, this issue p. 507

STRUCTURAL BIOLOGY

Staying attached through division

When a cell prepares to divide, it copies its DNA into pairs of each chromosome, called chromatids. Microtubules attach to the chromosome pairs through protein complexes called kinetochores. During cell division, microtubule depolymerization pulls the chromatids apart. Jenni and Harrison describe the structure of an essential component of the yeast kinetochore, the DASH/Dam1c complex, that forms a ring around a microtubule. The structure shows how the DASH/Dam1c ring interacts with the microtubule and kinetochore components so that the kinetochore can track to the end of the microtubule through cycles of growth and shrinkage. —VV

Science, this issue p. 552

Corrected 3 May 2018. See full text.

RESEARCH ARTICLE SUMMARY

MALARIA

Uncovering the essential genes of the human malaria parasite *Plasmodium falciparum* by saturation mutagenesis

Min Zhang, Chengqi Wang, Thomas D. Otto, Jenna Oberstaller, Xiangyun Liao, Swamy R. Adapa, Kenneth Udenze, Iraad F. Bronner, Deborah Casandra, Matthew Mayho, Jacqueline Brown, Suzanne Li, Justin Swanson, Julian C. Rayner,* Rays H. Y. Jiang,* John H. Adams*

INTRODUCTION: Malaria remains a devastating global parasitic disease, with the majority of malaria deaths caused by the highly virulent *Plasmodium falciparum*. The extreme AT-bias of the *P. falciparum* genome has hampered genetic studies through targeted approaches such as homologous recombination or CRISPR-Cas9, and only a few hundred *P. falciparum* mutants have been experimentally generated in the past decades. In this study, we have used high-throughput *piggyBac* transposon insertional mutagenesis and quantitative insertion site sequencing (QIseq) to reach saturation-level mutagenesis of this parasite.

RATIONALE: Our study exploits the AT-richness of the *P. falciparum* genome, which provides numerous *piggyBac* transposon insertion targets within both gene coding and non-coding flanking sequences, to generate more than 38,000 *P. falciparum* mutants. At this level of mutagenesis, we could distinguish essential genes as nonmutable and dispensable genes as mutable. Subsequently, we identified 2680 genes essential for in vitro asexual blood-stage growth.

RESULTS: We calculated mutagenesis index scores (MISs) and mutagenesis fitness scores (MFSs) in order to functionally define the relative fitness cost of disruption for 5399 genes. A competitive growth phenotype screen confirmed that MIS and MFS were predictive of the fitness cost for in vitro asexual growth. Genes predicted to be essential included genes implicated in drug resistance—such as the "*K13*" Kelch propeller, *mdr*, and *dhfr-ts*—as well as targets considered to be high value for drugs development, such as *pkg* and *cdpk5*. The screen revealed essential genes that are specific to human *Plasmodium* parasites but absent from rodent-infective species, such as lipid metabolic genes that may be crucial to transmission commitment in human infections. MIS and MFS profiling provides a clear ranking of the relative essentiality of gene ontology (GO) functions in *P. falciparum*. GO pathways associated with translation, RNA metabolism, and cell cycle control are more essential, whereas genes associated with protein phosphorylation, virulence factors, and transcription are more likely to be dispensable. Last, we confirm that the proteasome-degradation pathway is a high-value druggable target on the basis of its high ratio of essential to dispensable genes, and by functionally confirming its link to the mode of action of artemisinin, the current front-line antimalarial.

ON OUR WEBSITE

Read the full article at http://dx.doi.org/10.1126/science.aap7847

CONCLUSION: Saturation-scale mutagenesis allows prioritization of intervention targets in the genome of the most important cause of malaria. The identification of more than 2680 essential genes, including ~1000 *Plasmodium*-conserved essential genes, will be valuable for antimalarial therapeutic research. ■

The list of author affiliations is available in the full article online.
*Corresponding author. Email: jadams3@health.usf.edu (J.H.A.); jiang2@health.usf.edu (R.H.Y.J.); jr9@sanger.ac.uk (J.C.R.)
Cite this article as M. Zhang *et al.*, *Science* **360**, eaap7847 (2018). DOI: 10.1126/science.aap7847

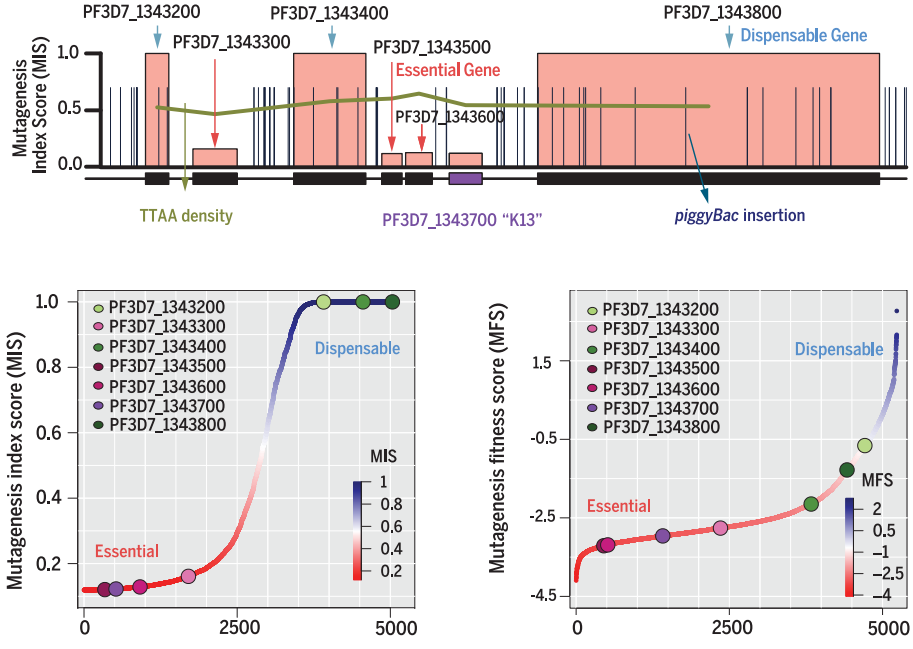

Saturation-scale mutagenesis of *P. falciparum* reveals genes essential and dispensable for asexual blood-stage development. (Top) A high-resolution map of a ~50-kb region of chromosome 13 depicts an essential gene cluster, including K13, that lacks insertions in the coding DNA sequence (CDS) but is flanked by dispensable genes with multiple CDS-disrupting insertions. (Left) The MIS rates the potential mutability of *P. falciparum* genes based on the number of recovered CDS insertions relative to the potential number that could be recovered through large-scale mutagenesis. (Right) The MFS rates the relative fitness of *P. falciparum* genes based on QIseq scores of transposon insertion sites in each gene.

Corrected 3 May 2018. See full text.

RESEARCH ARTICLE

MALARIA

Uncovering the essential genes of the human malaria parasite *Plasmodium falciparum* by saturation mutagenesis

Min Zhang,[1]* Chengqi Wang,[1]* Thomas D. Otto,[2]† Jenna Oberstaller,[1] Xiangyun Liao,[1] Swamy R. Adapa,[1] Kenneth Udenze,[1] Iraad F. Bronner,[2] Deborah Casandra,[1] Matthew Mayho,[2] Jacqueline Brown,[2] Suzanne Li,[1] Justin Swanson,[1] Julian C. Rayner,[2]‡ Rays H. Y. Jiang,[1]‡ John H. Adams[1]‡

Severe malaria is caused by the apicomplexan parasite *Plasmodium falciparum.* Despite decades of research, the distinct biology of these parasites has made it challenging to establish high-throughput genetic approaches to identify and prioritize therapeutic targets. Using transposon mutagenesis of *P. falciparum* in an approach that exploited its AT-rich genome, we generated more than 38,000 mutants, saturating the genome and defining mutability and fitness costs for over 87% of genes. Of 5399 genes, our study defined 2680 genes as essential for optimal growth of asexual blood stages in vitro. These essential genes are associated with drug resistance, represent leading vaccine candidates, and include approximately 1000 *Plasmodium*-conserved genes of unknown function. We validated this approach by testing proteasome pathways for individual mutants associated with artemisinin sensitivity.

Malaria caused by *Plasmodium falciparum* remains an insidious global health problem, with hundreds of thousands of deaths each year. Recently, there have been substantial reductions in disease intensity, in part through concerted recent use of artemisinin-combination therapies, but these gains are now threatened by emerging artemisinin-based combination therapy (ACT) treatment failures spreading across South East Asia (*1*, *2*). If ACT resistance reaches Africa, a devastating rebound of disease is expected, as occurred with chloroquine resistance in the 1970s. The development of new antimalarial therapies, and identification and prioritization of new targets, is a priority. More than a decade after the completion of the *P. falciparum* genome, a substantial fraction of its genome still lacks functional annotation (*3*). Although CRISPR-Cas9 and other targeted endonucleases will accelerate functional genomics studies (*4*–*6*), their usefulness for genome-scale applications is restricted by the absence of nonhomologous end joining in *Plasmodium* parasites and by the extreme AT-richness of the *P. falciparum* genome, which reduces guide RNA target site abundance. Therefore, a critical need remains for large-scale genetic analysis to systematically identify essential genes and prioritize parasite metabolic pathways for drug discovery (*7*).

Large-scale genetic screening methods in model organisms rely on efficient scalable methods for genome engineering. Transposon mutagenesis using the *piggyBac* transposon, which preferentially inserts at the tetranucleotide target sequence TTAA, has been used to carry out whole-genome loss-of-function screens in many organisms (*8*–*11*). The highly skewed nucleotide composition of the *P. falciparum* genome, with >81% AT content, is an advantage for the application of *piggyBac* mutagenesis. The skewed composition results in a high density of TTAA sites, averaging one site per 70 base pairs (bp) over both coding and noncoding regions, in theory allowing systematic and saturation-level mutagenesis of the whole genome. Although *piggyBac* mutagenesis has been developed and optimized for *P. falciparum*, and previously used for small-scale phenotypic screens and functional characterization of loss-of-function mutants, it has not been used for large-scale screening (*12*–*16*). To scale up *piggyBac* mutagenesis in *P. falciparum*, we developed high-throughput transfection mutagenesis methods that mostly create a single insertion per genome and combined them with an Illumina-based sequencing method for identifying transposon insertion sites (*17*, *18*). This approach, known as quantitative insertion-site sequencing (QIseq), thus allowed whole-genome experimental mutagenesis analysis of *P. falciparum* (fig. S1, A and B).

Achieving saturation-level mutagenesis

In a preliminary study, we carried out large-scale transfections followed by short-term in vitro growth of mixed pools of drug-selected *P. falciparum* parasites and identified insertion sites with QIseq. This pilot identified a total of 3651 insertions across the *P. falciparum* genome (table S1) (*17*, *19*). On the basis of the density and distribution of those insertions modeled by a negative binomial distribution, we predicted that recovery of ≥33,000 insertions would be sufficient to achieve saturation-level mutagenesis in the compact genome of the malaria parasite (fig. S1, C to F); this number is sufficient for there to be a high probability that multiple transposon insertions would occur within the coding DNA sequence (CDS) of every protein-coding gene larger than 500 bp. We therefore scaled our transfection methods to achieve this number of insertions. Transfected parasite populations were drug-selected briefly so as to isolate only mutant parasites with integrated *piggyBac* elements carrying the drug-resistance gene *hdhfr*, before insertion-site locations were identified with QIseq. Computational analyses were used to verify the sequence reads of the QIseq libraries and the consistency of the raw data (fig. S2, A to F); nearly all QIseq-defined insertions occurred at the characteristic TTAA target sequence. All insertion sites that were not flanked by the consensus TTAA (2.49%) insertion sites were removed from subsequent analysis (fig. S2A). Previously validated individual *piggyBac* mutant clones were included in each QIseq run in order to act as a control for the accuracy and sensitivity of each insertion-site identification run (fig. S3, A to C, and table S2).

The saturation mutagenesis approach identified ~38,000 independent *piggyBac* insertions at distinct TTAA target sites, covering 5399 nuclear protein-coding genes across all 14 chromosomes of the *P. falciparum* genome (Fig. 1A and table S3). These randomly distributed insertions exceeded those predicted to be required to achieve saturation-level mutagenesis (Fig. 1A), but there were numerous genes and regions encompassing several genes that had significantly fewer insertions than would be expected purely on the basis of the distribution of TTAA sites across the genome (Fig. 1, B, C, and D). As well as discrepancies in nonrandom spatial distribution, coding regions overall lacked insertions compared with intergenic regions ($P < 2.2 \times 10^{-16}$, Fisher test) (Fig. 1D). A more detailed analysis of *piggyBac* insertion density within transcriptional units revealed that insertions in CDS were 75% less common than in flanking intergenic regions, and even within intergenic regions, insertion-site density decreased with proximity to CDS (Fig. 1E). This significant bias toward recovering intergenic insertions in surviving blood-stage parasites, with many CDS having no insertions, are indications that genes lacking insertions are lethal when disrupted by *piggyBac* insertion.

[1]Center for Global Health and Infectious Diseases, Department of Global Health, University of South Florida, 3720 Spectrum Boulevard, Suite 404, Tampa, FL 33612, USA. [2]Malaria Programme, Wellcome Trust Sanger Institute, Genome Campus, Hinxton Cambridgeshire CB10 1SA, UK.
*These authors contributed equally to this work.
†Present address: Centre of Immunobiology, Institute of Infection, Immunity and Inflammation, College of Medical, Veterinary and Life Sciences, University of Glasgow, Glasgow, UK.
‡Corresponding author. Email: jadams3@health.usf.edu (J.H.A.); jiang2@health.usf.edu (R.H.Y.J.); jr9@sanger.ac.uk (J.C.R.)

Corrected 3 May 2018. See full text.

Defining gene dispensability by using mutagenesis index scores

Although there was a bias against insertions in CDSs, 2042 genes were disrupted by at least one *piggyBac* insertion (~38% of genes in the *P. falciparum* genome) (Fig. 1F). The remainder, 3357 genes (~62% of the genome) had no insertions in their CDSs, and some of these were also completely devoid of insertions in the surrounding intergenic regions (2.9% of genes) (Fig. 1C, fig. S4A, and table S4). In the 2042 mutable genes, insertion sites were distributed uniformly along the gene body CDSs, indicating that all disruptions have equivalent consequences for the disrupted gene (Fig. 1E). The uniform distribution

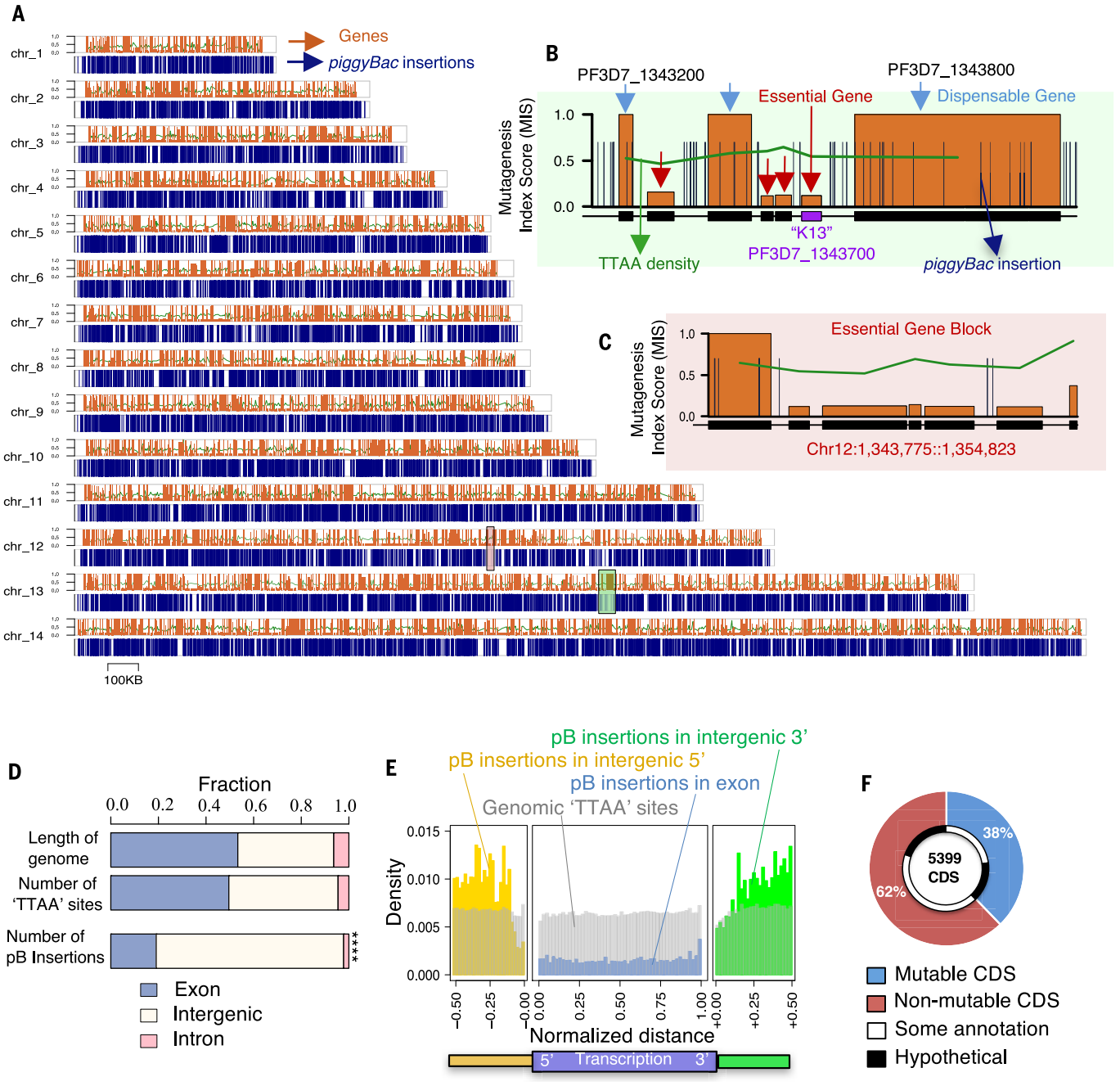

Fig. 1. A genome-wide saturation mutagenesis screen for *Plasmodium falciparum*. (**A**) Chromosomal map displays 38,173 *piggyBac* insertion sites from all mutants evenly distributed throughout the genome. (**B**) High-resolution map of a ~50-kb region of chromosome 13 depicts an essential gene cluster, including K13, flanked by dispensable genes with multiple CDS-disrupting insertions. (**C**) High-resolution map of a ~20-kb region without insertions includes three conserved genes of unknown function (*PF3D7_1232700*, *PF3D7_1232800*, and *PF3D7_1232900*) and a putative nucleotidyltransferase (*PF3D7_1232600*) (fig. S5). (**D**) A plot of all *piggyBac* insertions revealed that significantly fewer insertions were recovered from exon-intron regions compared with the proportion of available TTAA sites (fig. S1D) ($P < 2.2 \times 10^{-16}$, Fisher's exact test). (**E**) Density of *piggyBac* insertion-site distribution revealed 75% fewer insertions recovered in transcriptional regions (blue) than intergenic 5′ (yellow) and 3′ (green) regions, depicted as relative distance upstream and downstream to a gene, respectively. (**F**) This study determined that under ideal culture conditions for asexual blood-stage growth, 38% of genes in the *P. falciparum* genome have mutable CDSs, whereas 62% of genes have nonmutable CDSs, which includes 12% with tentative classification.

of transposon insertions throughout the genome is independent from chromatin structure and gene locations (fig. S4B). We therefore reasoned that the recovery of one or more insertions within the CDS of disrupted genes was an indicator of gene dispensability for in vitro asexual blood-stage growth. Therefore, mutable genes are subsequently referred to as dispensable, whereas the absence of any insertions in the CDS could be considered an indicator that disruptions are lethal, and subsequently, these genes are referred to as essential. However, the essential classification of 677 genes without insertions, which are small or with lower TTAA, is tentative because they are below the average distance between recovered insertions [<613 nucelotides (nt)] (table S5). To quantify the evidence for dispensability or essentiality of each gene, we developed a mutagenesis index score (MIS) based on the number of identified *piggyBac* insertions relative to the number of available TTAA target sites within that gene (Fig. 2A and table S5). Genes with a higher MIS (on a scale of 0 to 1) were considered to have a higher possibility of dispensability, whereas those with a lower MIS were considered to have a higher possibility of essentiality. The 2000 genes with highest and lowest MISs represent mutability characterization with the strongest confidence.

Biological processes identified as dispensable and essential

Mutants in the lowest MIS quartile were enriched in core metabolic processes shared across eukaryotes, which would be predicted to be essential. Mutants in the highest MIS quartile were enriched in parasite-specific multigene families that interact directly with the host and that are known to be partially functionally overlapping and contain many redundant genes (Fig. 2B). This screen was carried out by using in vitro cultured parasites, and many of these in vitro dispensable genes, such as those for antigenic variation and cytoadherence, have greater importance in vivo in human infections. The dispensability of parasite processes involved in host-parasite interactions contrasted with the essentiality of internal parasite processes, such as those associated with RNA metabolism (Fig. 2, C and D; fig. S6; and table S6). *RNase II*, a gene implicated in a posttranscriptional regulatory mechanism relevant to severe malaria, is an example with a low MIS, which is consistent with previous reports of the locus being refractory to disruption (*20*). Other genes involved in general RNA metabolism that have low MISs include both widely conserved RNA-binding proteins (such as *PABP*) and apicomplexan-specific RNA-binding proteins likely to have more specific, mostly unidentified, regulatory targets. The *P. falciparum* genome has an abundance of RNA-binding proteins that are largely functionally uncharacterized, and our analysis suggests that many of these genes are likely to be essential.

MIS therefore correlates with what is known broadly about the importance or redundancy of metabolic pathways. To further validate that MIS is a good predictor of essentiality, we analyzed genes that have been the focus of drug or vaccine development. Genes strongly predicted to be essential based on MIS included the "*K13*" Kelch propeller implicated in artemisinin resistance, as well as other genes implicated in drug resistance, such as *DHFR-TS*, *MDR*, and *AAC2*, which are involved in pyrimethamine, mefloquine and atovaquone reistance, respectively. Other genes classified as essential based on MIS included ones considered high-priority blood-stage drug targets such as *PKG* and *CDPK5* (fig. S5). By contrast, most blood-stage vaccine candidates were dispensable, with the notable exception of *RH5*. Not unexpectedly, sporozoite vaccine candidates CSP and TRAP, which are essential for sporozoite development in mosquitoes but are not required in blood-stage development (*21*), had high MIS. By contrast, the gene for pore-forming protein cell traversal of ookinetes and sporozoites (CelTOS) had a low MIS. CelTOS is important for these parasite migratory phases and is emerging as a pre-erythrocytic-transmission–blocking vaccine candidate; its low MIS indicates it may also have an essential function in blood-stage infections, making it a potential multistage vaccine target. MIS analysis also revealed likely essential genes that are specific to human *Plasmodium* parasites but absent from rodent-infective species, such as the lipid metabolic genes (*PCD* and *PMT*) that are crucial in the development of mosquito-transmissible sexual stages in *P. falciparum* (*22*, *23*).

Mutant growth fitness as a measure of gene dispensability

We previously developed a phenotyping method in which a pool of *piggyBac* mutants were grown as mixed-mutant pools over multiple generations, and the number of reads for each *piggyBac* insertion site was quantified by using next-gen sequencing in order to measure parasite growth rates (*17*). We adapted this method to generate a second quantitative measure of gene dispensability independent from MIS, by comparing the normalized number of reads from each insertion site to the total pool of reads across all *P. falciparum* mutants in the saturation mutagenesis screen (Fig. 2E and table S5). This mutagenesis fitness score (MFS) serves as a proxy for mutant growth fitness. MFSs strongly correlated with MISs, despite the fact that they are independent of each other (Fig. 2F). The MFS of mutable genes was high, in keeping with the MIS prediction of dispensability, whereas predicted essential nonmutable genes had a low MFS (Fig. 2G). Intermediate MISs and MFSs were weakly correlated, in keeping with the lower confidence that we can place on the essentiality or dispensability of genes with these intermediate scores.

We used a competitive in vitro growth screen (*17*) to phenotype four separate pools of mixed-mutant populations so as to provide additional validation of the correlation between MIS and a gene's importance for growth fitness. Mutable genes with high MISs and low or minimal fitness cost were competitive growth "winners," whereas growth fitness "losers" had relatively low MISs (Fig. 3A and table S7). Relatively few mutations had little or no fitness cost, as measured with MFS, resulting in a disproportionate number of mutant losers (Fig. 3B). Overall, both the MIS and MFS were predictive of the fitness cost for in vitro asexual growth (Fig. 3C), and between these metrics, we were able to predict separate 5399 genes in the *P. falciparum* genome into nonmutable and mutable categories (Fig. 3, D and E).

Association of essentiality with genome structure and transcription patterns

Dispensable and essential genes rarely occurred as single isolated genes but rather occurred as multigene clusters reminiscent of conserved syntenic blocks (Fig. 1, A and C, and fig. S4A) (*24*). We therefore assessed the relationship between evolutionary conservation of genome structure and essentiality or dispensability by using previously defined syntenic relationships between *Plasmodium* spp. (*25*). Syntenic genes indeed had lower MISs, suggesting conserved essential functions across *Plasmodium* spp.; conversely, nonsyntenic genes were more likely to be dispensable (Fig. 4A). Mapping chromosomal regions with synteny breaks, which typically harbor gene duplications and paralogs, showed patterns of clustering of essential and dispensable genes in syntenic and nonsyntenic chromosomal regions, as seen in examples for chromosomes 13 and 10 (Fig. 4, B to E).

Transcription metrics for each gene based on maximum FPKM (fragments per kilobase of exon per million fragments mapped) values (*26*) were examined for correlations with essentiality and dispensability (Fig. 5A). This analysis showed that essential genes are expressed at significantly ($P = 2.2 \times 10^{-16}$) higher levels throughout both the asexual and sexual life cycle phases, indicating that they may have critical functional roles throughout both the mosquito and human stages and therefore represent potential multistage drug targets (Figs. 5, B and C). Within the intraerythrocytic cycle, genes with peak expression during the trophozoite stage were more likely to be essential than those expressed during other stages (Fig. 5C). During the trophozoite stage, *P. falciparum* must acquire nutrients from the host and remodel the infected erythrocyte to avoid host defenses, such as clearance by the spleen. By contrast, dispensable processes were enriched at either end of intraerythrocytic development, reflecting parasite stages with a greater need for functional redundancy, such as those involved in host interaction (such as erythrocyte invasion and antigenic variation), and are hence more likely to undergo duplication or paralog evolution. Not unexpectedly, ~41% of the dispensable genes are predominantly expressed in sexual stages (Fig. 5C). These genes may be essential for transmission to or from the mosquito but do not appear to have an essential function for asexual blood-stage development. The high coverage of sexual-stage genes in this screen emphasizes the potential for

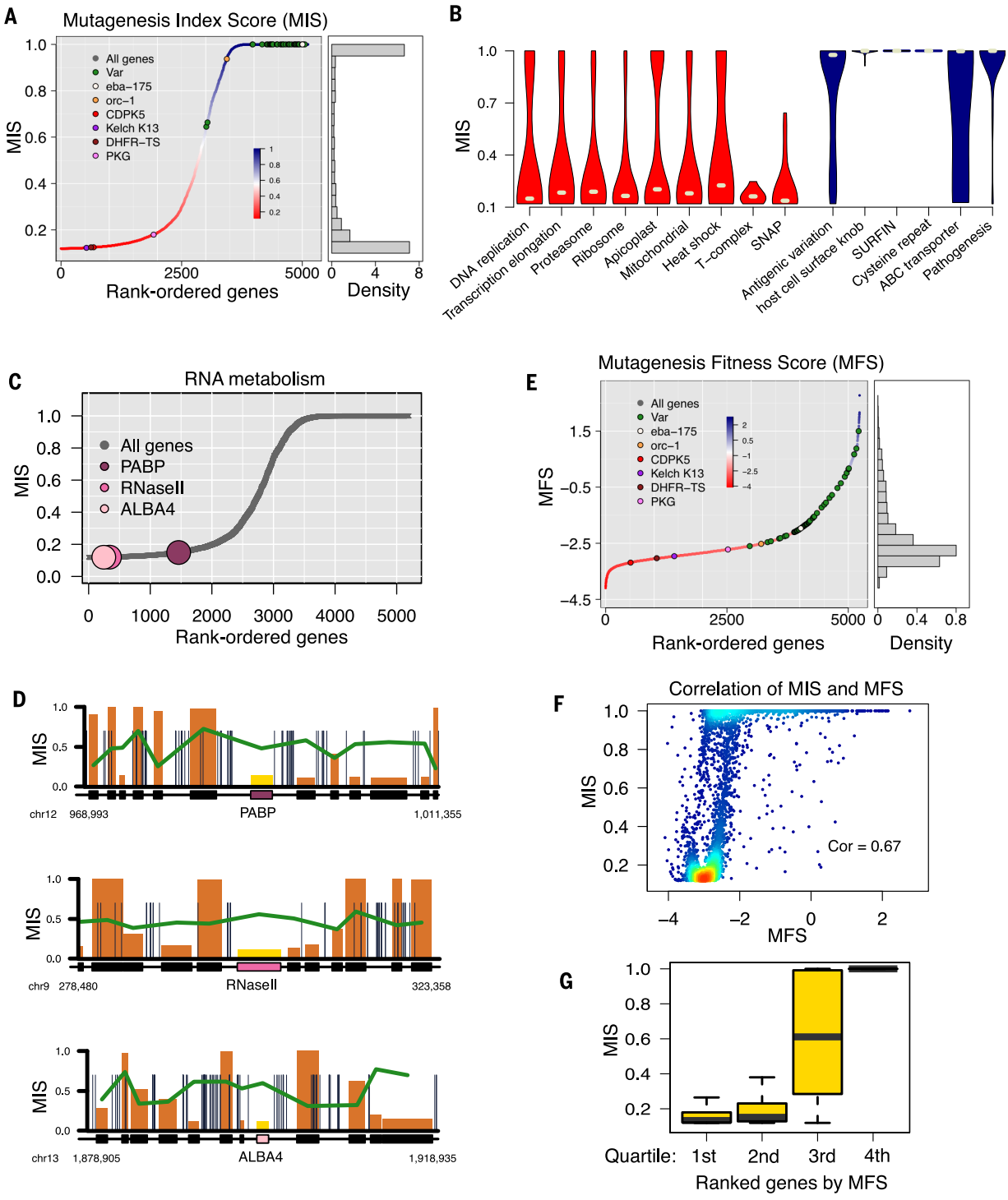

Fig. 2. Identification of dispensable and essential genes through MIS and MFS. (**A**) The MIS rates the potential mutability of *P. falciparum* genes based on the number of recovered CDS insertions relative to the potential number that could be recovered. Genes known as dispensable or essential are highlighted. (**B**) MIS violin plots of GO processes grouped from lowest to highest dispensability, according to gene functional annotations. (**C**) MIS plots and (**D**) high-resolution chromosome maps highlighting important genes of interest for RNA metabolism (−20 kb, +20 kb) (MIS plots of other genes of interest are provided in fig. S4). (**E**) The MFS estimates the relative growth fitness cost for mutating a gene based on its normalized QIseq sequencing reads distribution. (**F**) MIS has significant correlation to MFS (Pearson's $R = 0.67$, $P < 2.2 \times 10^{-16}$ compared with permutation). (**G**) The first and second MFS quartiles were composed primarily of nonmutable genes, the fourth quartile was composed mostly of mutable genes, and the third quartile had nearly equal numbers of both.

Corrected 3 May 2018. See full text.

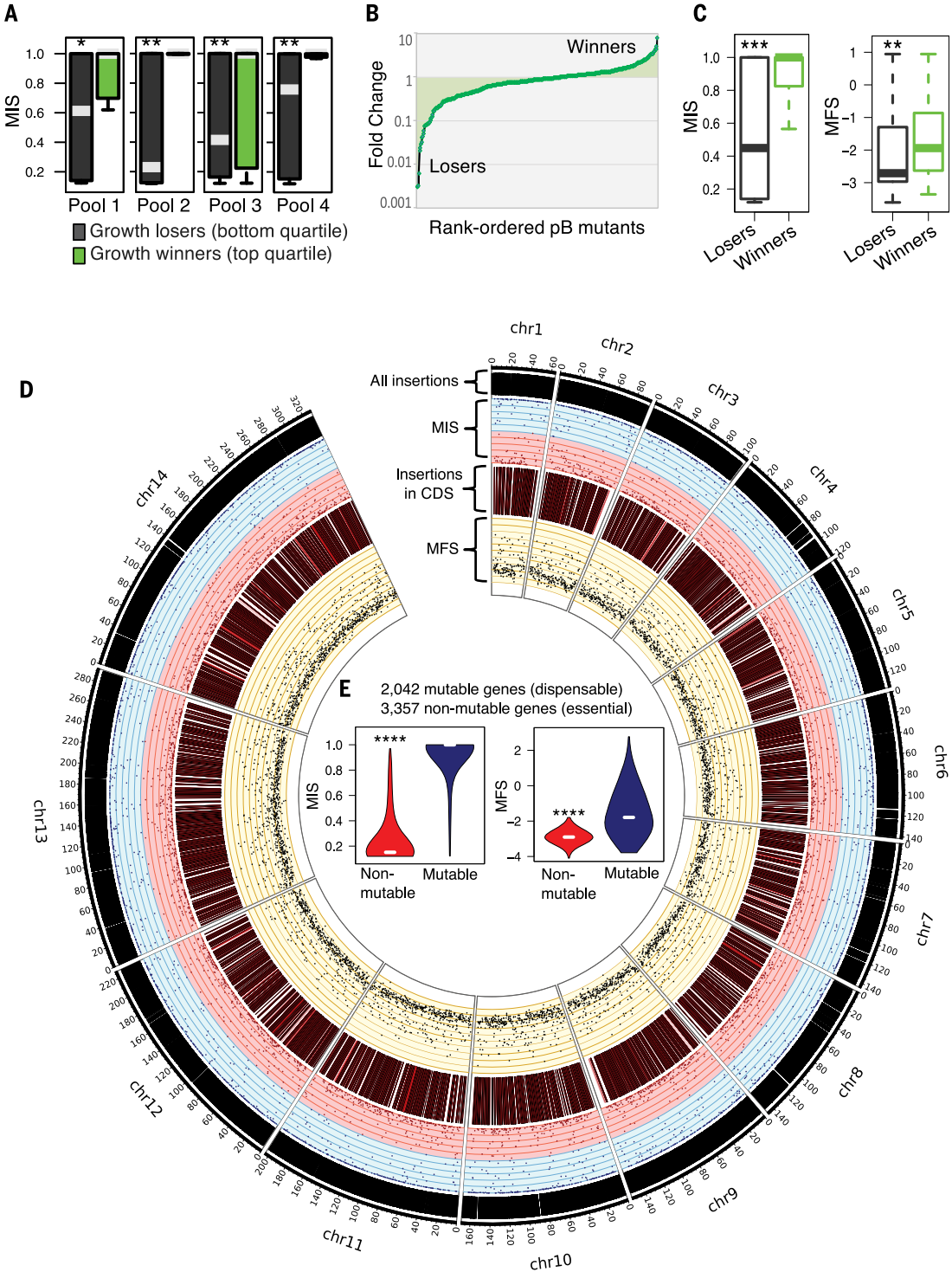

Fig. 3. Validation of mutagenesis score through phenotype screen. (**A**) Competitive growth assays of asexual blood-stage growth under ideal in vitro culture conditions. Phenotypes of four independent mixed-population pools grown for three cycles confirmed that losers (left, bottom quantile) and winners (right, top quartile) had significantly different MIS. (**B**) Overall rank-ordered plot of competitive growth phenotypes shows losers and winners. (**C**) Competitive growth losers had significantly lower MISs and MFSs, respectively, validating MIS and MFS as predictors of gene essentiality and dispensability. (**D**) Circos plot from outer to inner shows the distribution of all *piggyBac* insertions, MIS (pink indicates MIS < 0.5, and blue indicates MIS > 0.5), CDS insertions, and MFS along each chromosome of *P. falciparum* genome. (**E**) Violin plots indicate nonmutable genes had significantly lower MIS and MFS (Wilcoxon, $^{****}P < 2.2 \times 10^{-16}$).

piggyBac-based screens for identifying sexual phenotypes.

Evolutionary conservation of apicomplexan gene essentiality

We compared the data from our genome-wide saturation screen with data from large-scale genome-sequencing studies of *P. falciparum*, as well as data from recent large-scale mutagenesis studies of apicomplexan genomes (*6*, *18*, *27*–*29*), to evaluate the conservation of gene essentiality across the organisms' lineages. Essential *P. falciparum* genes were more highly conserved across *Plasmodium* spp. (Fig. 5D and fig. S8A), are less likely to have a paralog (Fig. 5E and fig. S8B), and encode genes with less genetic variation among *P. falciparum* clinical isolates (Fig. 5F and fig. S8C). Of the *P. falciparum* genes studied here, 2083 and 1998 have orthologs in the more distantly related parasites *Toxoplasma gondii* (*6*) and *P. berghei* (*29*), respectively. Overall, there was a strong correlation in gene function between species, particularly with genes predicted as essential (Fig. 5, G and H, and fig. S8, D and E). Genes that are dispensable in *P. falciparum* were also more likely to be dispensable in *P. berghei*. By contrast, the correlation between the dispensable

Corrected 3 May 2018. See full text.

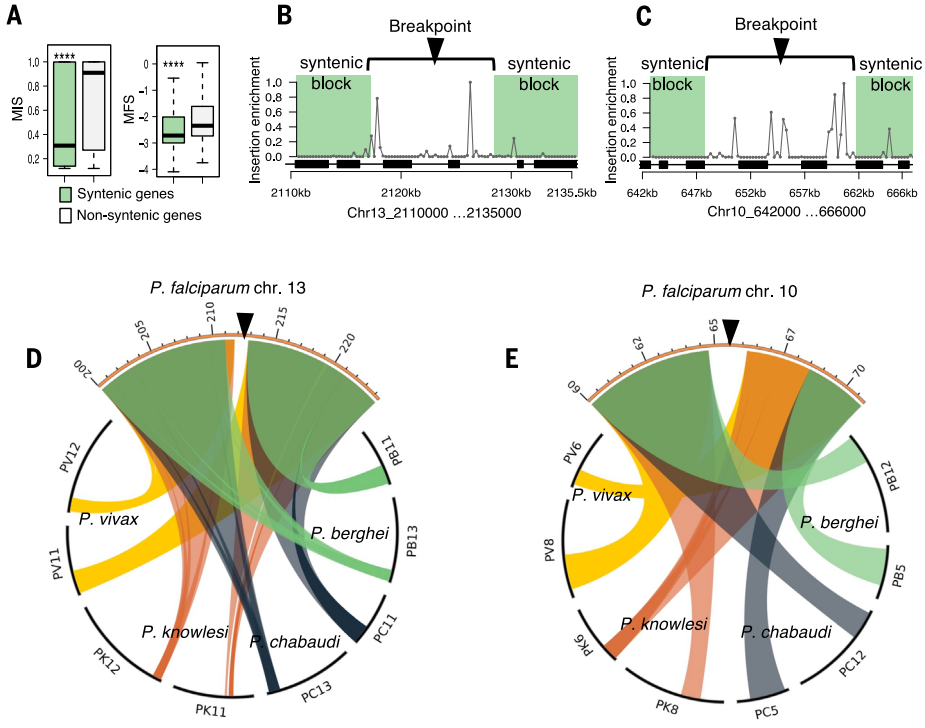

Fig. 4. Chromosomal syntenic breakpoints are enriched in dispensable genes. (**A**) Genes within conserved syntenic blocks have a significantly lower MIS and MFS (Wilcoxon $P < 2.2 \times 10^{-16}$). Syntenic genes or "syntenic block" is defined as at least three genes in the same order on the same chromosome as their orthologs in another species within a 25-kb search window. (**B** and **C**) Scatter plots show the insertion site enrichment along two syntenic breakpoints [chromosome 13 (Ch13), 2,110,000 to 2,135,000; Chr10, 642000 to 666000]. Each gap in synteny (white area) is enriched for *piggyBac* insertions while flanked by essential regions (green shading); black boxes represent the location of CDS. (**D** and **E**) Circos plots indicate the syntenic blocks of *P. falciparum* in relation to other *Plasmodium* spp. (*P. berghei*, *P. chabaudi*, *P. knowlesi*, and *P. vivax*).

genes of *P. falciparum* and *T. gondii* was weaker, indicating that genus-specific gene functions are enriched for dispensability. Overall, these comparisons show that although phenotype classifications from the large-scale mutagenesis screens in apicomplexan species are also broadly predictive of the *P. falciparum* phenotype classifications, the closer evolutionary relationship of *P. berghei* provides a higher level of sensitivity and specificity for the orthologs that could be disrupted (Fig. 5I and fig. S8F).

Consistent with this assessment that nonmutable genes represented core essential functions in *P. falciparum*, Gene Ontology (GO) enrichment analysis indicated that genes with functions associated with translation, RNA metabolism, and cell cycle control were more likely to be essential, whereas genes associated with protein phosphorylation, virulence factors, and transcription were more likely to be dispensable (Fig. 6A). Comparing the relative number of essential, versus dispensable, genes within specific GO biological processes, molecular functions, and cellular components provided a ranking of the essentiality of potential druggable targets and pathways (Fig. 6, A to C; fig. S9, A to C; and table S8). For example, nearly all genes annotated as being involved in ubiquitin-dependent degradation processes were experimentally defined as essential, whereas individual genes linked to microtubule motility and antigenic variation are experimentally defined as dispensable based on MIS. RNA metabolism and translation-related processes are also highly essential, supporting emerging evidence for the importance of posttranscriptional and -translational control (*30*).

Essentiality of the proteasome-degradation pathway

Recent genetic analysis of artemisinin-combination therapy resistance has linked drug resistance to cellular stress-response mechanisms involving the *P. falciparum* ubiquitin/proteasome system (*31*, *32*). Genes of the proteasome-degradation pathway were well represented in the *piggyBac* mutagenesis screen, and 54 of the 72 genes could be classified as essential genes according to our data (fig. S10A), further strengthening the priority of the proteasome degradation pathway as a high-value druggable target (*33*). We validated this link between artemisinin sensitivity and proteasome inhibition sensitivity using a set of single-insertion *piggyBac* mutants previously defined with chemogenomic profiling to be part of an artemisinin-sensitivity cluster, including a mutant of the K13 Kelch propeller gene (*16*, *34*). We found 10-fold increased sensitivity to the proteasome inhibitor Bortezomib in mutants of the artemisinin-sensitivity cluster, which is significantly different relative to wild-type NF54 or mutants with distinct chemogenomic profiles (fig. S10, B to E), providing additional support for the association between the ART (Artimisinin) mechanism of action and proteasome function.

Summary

Our genome-wide saturation mutagenesis screen in the major human pathogen *P. falciparum* has defined genes essential for parasite survival during the blood stage and provided critical functional data for prioritizing high-value drug targets and pathways. The complete characterization of the essential genome with high-throughput saturation mutagenesis will help open new frontiers for antimalarial therapeutic research. The methodology also opens the way for new systematic functional screens for other phenotypes, such as transmission and cytoadherence.

Materials and Methods

Parasite culture

All *P. falciparum* parasite NF54 and *piggyBac* mutants were cultured in complete RPMI 1640 with 5% hematocrit (medium containing 0.5% Albumax II, 0.25% sodium bicarbonate and 0.01 mg/ml gentamicin). All parasite cultures were maintained by standard methods (*35*).

piggyBac Transfection

High-efficiency transfection (96-well plate method) was carried out on NF54 schizonts purified by magnetic column (MiltyenyiBiotec, CS column) using a transposon plasmid (pLBacII-HDH, containing selection marker human *dhfr*) and a transposase-expressing helper plasmid (pDCTH) (*19*, *35*). RBCs were first loaded with plasmid DNA by electroporation using Gene PulserXCell+CE Module (BioRad). A total of 10 million schizonts, 1200 μg plasmid DNA and 600 μg helper plasmid DNA were used per 96-well plate to achieve maximal transfection efficiency. The drug WR99210 (final concentration 2.5 nM) was added to each plate for selecting transfected parasites, using a robot (Integra VIAFLO 96) to change media with drug every day for 5 days. Transfections were performed in batches over the course of 4 to 6 weeks. Each 96-well plate was cultured in triplicate and cryopreserved in duplicate. One hundred 96-well plates were used to generate the large pools for sequencing (fig. S1A).

Corrected 3 May 2018. See full text.

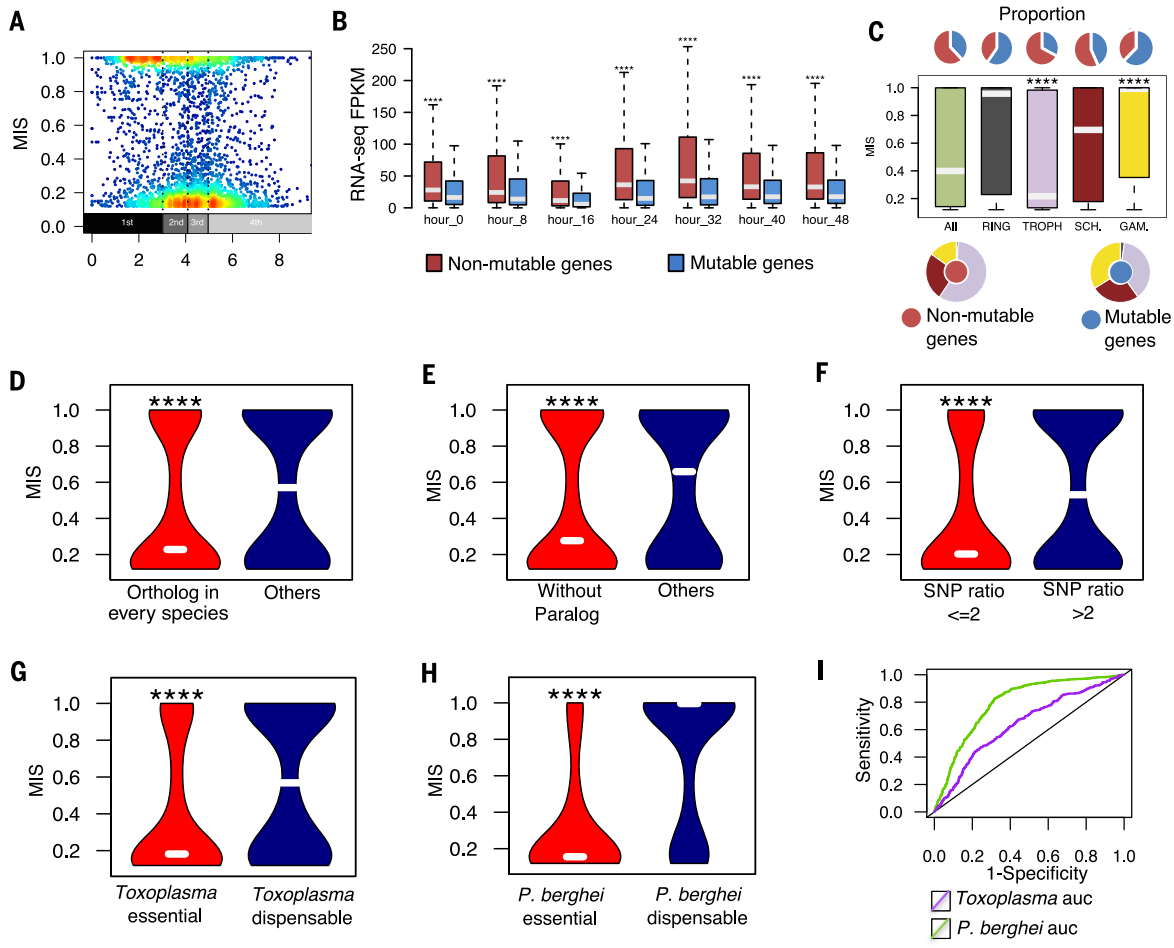

Fig. 5. Distinct biological process and evolutionary conservation segregate the tendency of dispensable and essential genes. (**A**) The genes with lowest FPKM expression value (first quantile) among different stages were enriched for dispensable genes (Wilcoxon $P < 2.2 \times 10^{-16}$ compared with other quantiles) (*26*). The expression level cut off is set at 20 FPKM. (**B**) Nonmutable essential genes had significantly higher expression value for blood-stage development. (**C**) The group of trophozoite-stage genes had the highest proportion of essential genes (red), whereas gametocyte genes had the highest proportion of dispensable genes (blue) (Wilcoxon $P < 1 \times 10^{-12}$). (**D** to **F**) Characteristics of essential genes significantly different from dispensable genes include (D) 1:1 ortholog conserved among *Plasmodium* spp., (E) absence of paralogs, and (F) reduced rate of nonsynonymous to synonymous single-nucleotide polymorphisms. Bars indicate the group median (Wilcoxon, $^{****}P < 2.2 \times 10^{-16}$). (**G** and **H**) Essential genes reported in (G) *Toxoplasma* and (H) *P. berghei* showed significantly lower MIS in this mutagenesis screen of *P. falciparum* (Wilcoxon, $^{****}P < 2.2 \times 10^{-16}$). (**I**) Plot of receiver operating characteristics (ROC) indicate the level of retention of essential genes across species. The MIS of *P. falciparum* more strongly correlates with the essentiality phenotype of *P. berghei* than *Toxoplasma*.

For maximum recovery of unique mutants, the transfected culture was distributed into 96-well plates by robot (200 µl each well) and grown under two rounds of drug selection. Wells were screened for parasites by PCR and Giemsa-stained thin blood films. >50% of wells became parasite-positive within three weeks. Each positive well with ≥9 unique mutants (one well = one "Mixed Population", or MP) was cryopreserved in duplicate (two 96 well plates). Additional 96-well plates were used to generate the pools that were then cultured in a T75 flask and harvested after two cycles growth by standard methods for genomic DNA isolation for QIseq (*17*). Although mutants grow at different rates, the pools can be expanded for at least 12 asexual life cycle generations ("cycles") without significant loss in detectable diversity. Importantly, each mutant pool can be regenerated and cloned from their original MPs.

Datasets of reference genomes, transcriptome data and epigenetics data

The NF54 reference genome can be downloaded from (ftp://ftp.sanger.ac.uk/pub/project/pathogens/Plasmodium/falciparum/NF54/Assembly/V1_morphed). The QIseq sequencing mapping followed previously published methods (*17*). Ortholog counts, paralog counts, and non-synonymous/synonymous (NonSyn/Syn) ratios can be downloaded from PlasmoDB (http://plasmodb.org/plasmo) (*36*). Previously published RNA-seq expression data (*26*, *37*) are used in computational analysis. Formaldehyde-Assisted Isolation of Regulatory Elements (FAIRE-seq) data of seven time points (0, 6, 12, 18, 24, 30 and 36 hour) were used to measure chromatin accessibility (*38*). The motif information of transcription factor ApiAP2 binding sites is available in previously published work (*39*). The genome synteny across five *Plasmodium* species is available in published work (*25*).

Identification of >38,000 mutants carrying piggyBac insertion

The QIseq sequencing generated a total of 3,301,112 raw reads. First, all the raw reads were filtered by the criteria of matching expected transposon target site "TTAA." This filtering step yielded 2,042,147 reads, which is >sixfold genome coverage. The insertion site QIseq signal was calculated as the reads count of the filtered QIseq reads. To compare the insertion signals

between different QIseq runs, we normalized for each insertion i as

$$S_i = \frac{c_i}{\sum_{j \in R} c_j} \times 250,000 \quad (1)$$

where S_j represents the signal of the insertions i with reads counts c_i in run R. All the *piggyBac* insertions with reads in both 5′ and 3′ ends were treated as true insertions by using an extremely high level of accuracy in target site (target motif TTAA ~ 99%). To identify true insertions with reads only in single 5′ or 3′ ends, we used a method that selected the most accurate signal cutoff based on the ratio of the number of input reads/ the number of output disrupted genes.

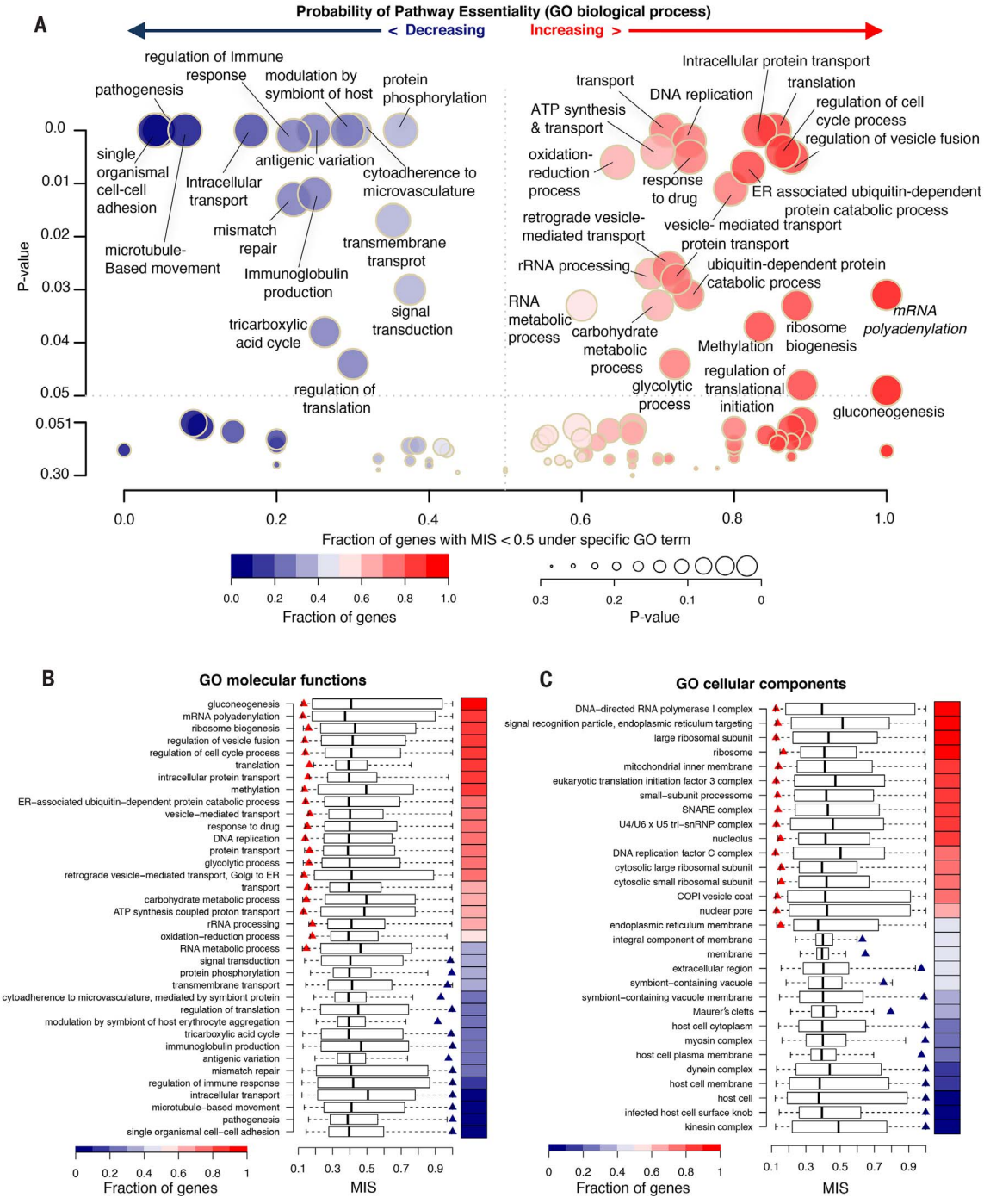

Fig. 6. Differentiating dispensable and essential genes and discovering high-priority druggable targets and pathways. (**A**) Functional annotations of biological processes are represented by the *P* value, and the *x* axis shows the fraction of the genes with MIS > 0.5. Each GO term is assigned a *P* value on the *y* axis to represent the tendency to be essential or dispensable. Essentiality is indicated on a spectrum of red (essential) to blue (dispensable) and circle sizes indicate the GO term enrichment. (**B** and **C**) Boxplot of (B) molecular processes and (C) cellular components shows the MIS distribution generated by 1000× sampling of the number of genes in the query GO-term category. Left (red) and right (blue) triangles indicate GO terms with significantly lower or higher MIS ($P < 0.05$ compared with background), respectively; the heatmap represents the essentiality defined as the fraction of genes per GO term with MIS > 0.5.

We computed the number of gene CDSs targeted by the insertions upper cutoff (i.e., more accurate). We noticed that there was a single large and sharp increase in the number of CDSs targeted by the insertions with reads number increasing from cutoff 2.0 to cutoff 2.3 ($P < 0.05$ compared with changing another cutoff) (fig. S2E). The result indicated a large amount of false positive may be included when setting cutoff ≥ 2.3. Therefore, the normalized reads count = 2.3 was set as the lower bound for identifying true insertions.

Mutagenesis saturation computational validation

To evaluate the levels of whole-genome mutagenesis and eventual saturation, we used a computational method based on sampling. First, a specific number of insertions were randomly extracted and the fraction of genome elements targeted were counted. This procedure was repeated 1000 times for each query insertion number in fig. S1C. A log-based curve was observed by plotting the mutational events and the median number of genome elements targeted by insertions. The plateauing of the curve at about 20,000 mutational events indicated that a very small number of new genome elements could be targeted even with very large amount of insertions. Importantly, the real data-based sampling curve was very similar to our independent mathematical predictions of Negative Binomial distributions prior to the start of the saturation mutagenesis experiments (fig. S1D). Together, both our mathematical model and real-data computational sampling show that >33,000 mutants represent saturation-level mutagenesis of the entire set of protein-encoding genes in the *P. falciparum* genome.

Sampling methods for accounting for fragment length differences and nucleoside composition bias

For genes in the *P. falciparum* genome, 5′ upstream and 3′ downstream intergenic regions displayed similar TTAA densities (median number of TTAA sites per 100 bp were 1.82 and 1.89, respectively). However, they have significantly different region length distributions (median values are 1681 bp and 926 bp in 5′ and 3′ direction, respectively; $P < 0.001$ Wilcoxon test). Therefore, there are different numbers of genomic TTAA sites in 5′ and 3′ intergenic regions, as an intrinsic feature of the *P. falciparum* genome. To account for this region-length and total-TTAA bias in our QIseq calculations, the TTAA sites in 3′ intergenic regions were sampled based on the TTAA number in 5′ intergenic regions, so that our comparison was based on two identical background target-site distributions. Distribution of insertions and TTAA sites (Fig. 1E) were plotted based on these sampling data.

MIS calculation

To quantify the mutability of every protein-coding gene in the *P. falciparum* genome, we first checked the number of *piggyBac* insertions located inside the gene CDS regions. To keep the criteria stringent, the insertions located on the very end (distance from insertion to TSS > 99% of the CDS length) of the CDS were not considered, due to a significantly higher number of insertions at the last 1% of the CDS compared with other regions of the CDS (fig. S2F). We calculated the initial score MIS of gene MS_g based on the equation

$$MS_g = \log\left(\frac{N_g + 1}{D_g}\right) \quad (2)$$

where N_g represents the number of insertions on gene g. D_g is the TTAA density of the gene g, which could be represented as the number of TTAA per kb of the CDS. We found that the MS could be decomposed into two mixed Gaussian distributions (fig. S11). We reasoned that dispensable and essential genes exhibit different MS distribution. Therefore, a binary variable π_g was used to model whether the gene g is dispensable or not: $\pi_g = 1$ corresponds to dispensable and vice versa. The probability of observing a MS_g of gene g is mixture of two Gaussian distributions:

$$P(MS_g) = \sum\nolimits_{\pi_g=1,0} P(\pi_g) N(MS_g|\mu_{\pi_g}, \sigma_{\pi_g})$$
$$\sum\nolimits_{\pi_g=1,0} P(\pi_g) = 1 \quad (3)$$

Subsequently, the EM algorithm was implemented to search for the optimized value of parameters. The posterior distribution after the EM optimization procedures could be calculated as:

$$P(\pi_g = 1|MS_g, \Theta) = \frac{P(\pi_g = 1) N(MS_g|\mu_{\pi_g=1}, \sigma_{\pi_g=1})}{\sum_{\pi_g=1,0} P(\pi_g) N(MS_g|\mu_{\pi_g}, \sigma_{\pi_g})} \quad (4)$$

where Θ is the parameter space. The MIS was defined as the posterior distribution to be dispensable.

MFS calculation

For the mutants that were subjected to competitive growth essay, we calculated MFS to represent the comparative growth fitness of a mutant. The QIseq sequencing reads distribution reflects the fitness of unique *piggyBac* mutants in the competitive-growth assays. The start and the end of the growth assay could be represented as t_0 and t. At the end of the assay, $a_{t,g}^{m,v}$ indicated the relative abundance of each mutant m, targeted into the CDS of gene g in sample v. Therefore, the abundance of the mutant of the gene g at the end of the assay could be represented as $\sum_{m \in v} a_{t,g}^{m,v}$. The $\sum_{m \in v} a_{t,g}^{m,v}$ was directly proportional to the QIseq reads number $\sum_{m \in v} r_{t,g}^{m,v}$. Here, $r_{t,g}^{m,v}$ represents the normalized reads number of mutant m targeting gene g on CDS, which is $\sum_{m \in v} a_{t,g}^{m,v} \sim \sum_{m \in v} r_{t,g}^{m,v}$. The QIseq reads starting with 'TTAA' were used to measure $r_{t,g}^{m,v}$. To normalize different $\sum_{m \in v} r_{t,g}^{m,v}$ in different sample v, the average value of $\sum_{m \in v} r_{t,g}^{m,v}$ was calculated as

$$\sum\nolimits_v \sum\nolimits_m r_{t,g}^{m,v} \Big/ \sum\nolimits_m I(m\ on\ g) \quad (5)$$

Here, $I(\cdot)$ is the indicator function. $\sum_m I(m\ on\ g)$ as the number of mutants targeting gene g in all samples. At the start of the assay t_0, the relative abundance of each mutant equal to the background TTAA density D_g. Finally, the MFS is calculated as:

$$MFS_g = \log\left[\frac{\sum_v \sum_m r_{t,g}^{m,v} \Big/ \sum_m I(m\ on\ g)}{D_g}\right] \quad (6)$$

Therefore, the MFS calculation based on individual mutant abundance is a proxy for competitive growth fitness in in vitro blood stage.

GO analysis

All the Gene Ontology (GO) terms were downloaded from (http://plasmodb.org/plasmo/) (27). For each specific GO term g, the MIS distribution in the term g could be represented as MIS_g. The number of genes in term g is Num_g. We asked whether the genes in the term g are more prone to be dispensable or essential. To answer this question, we compared the median value of MIS_g with sampled data distribution as background. The genes with the same number of Num_g were sampled out and represented as S_g. This procedure was repeated 1000 times and the median MIS of each $S_{g,t}$ ($t \in 1, 2, 3, \ldots 1000$) was calculated as $MIS_{S_{g,t}}$. The P value was calculated as

$$p_g = \begin{cases} \sum_{t=1}^{1000} I(MIS_g < MIS_{S_{g,t}})/1000 (MIS_g > 0.5) \\ \sum_{t=1}^{1000} I(MIS_g > MIS_{S_{g,t}})/1000 (MIS_g < 0.5) \end{cases} \quad (7)$$

Here, $I(\cdot)$ is the indicator function.

Half-maximal inhibitory concentration (IC_{50}) estimation

To calculate IC_{50}, the dose-response data (e.g., drug concentrations c_1, c_2, ...c_n and growth inhibition q_1, q_2, ... q_n) were used to fit a Hill Equation.

$$q = U + \frac{U - D}{1 + 10^{(c - \log C)B}} \quad (8)$$

where c was drug concentrations in logarithmic form. The parameter C was the estimate of IC_{50}. The goodness of fit was calculated from dose-response data and the Hill Equation.

REFERENCES AND NOTES

1. E. A. Ashley *et al.*, Spread of artemisinin resistance in *Plasmodium falciparum* malaria. *N. Engl. J. Med.* **371**, 411–423 (2014). doi: 10.1056/NEJMoa1314981; pmid: 25075834
2. C. J. Woodrow, N. J. White, The clinical impact of artemisinin resistance in Southeast Asia and the potential for future spread. *FEMS Microbiol. Rev.* **41**, 34–48 (2017). doi: 10.1093/femsre/fuw037; pmid: 27613271

3. M. J. Gardner *et al*., Genome sequence of the human malaria parasite *Plasmodium falciparum*. *Nature* **419**, 498–511 (2002). doi: 10.1038/nature01097; pmid: 12368864
4. M. Ghorbal *et al*., Genome editing in the human malaria parasite *Plasmodium falciparum* using the CRISPR-Cas9 system. *Nat. Biotechnol.* **32**, 819–821 (2014). doi: 10.1038/nbt.2925; pmid: 24880488
5. J. C. Wagner, R. J. Platt, S. J. Goldfless, F. Zhang, J. C. Niles, Efficient CRISPR-Cas9-mediated genome editing in *Plasmodium falciparum*. *Nat. Methods* **11**, 915–918 (2014). doi: 10.1038/nmeth.3063; pmid: 25108687
6. S. M. Sidik *et al*., A Genome-wide CRISPR Screen in toxoplasma identifies essential apicomplexan genes. *Cell* **166**, 1423–1435.e12 (2016). doi: 10.1016/j.cell.2016.08.019; pmid: 27594426
7. T. F. de Koning-Ward, P. R. Gilson, B. S. Crabb, Advances in molecular genetic systems in malaria. *Nat. Rev. Microbiol.* **13**, 373–387 (2015). doi: 10.1038/nrmicro3450; pmid: 25978707
8. S. T. Thibault *et al*., A complementary transposon tool kit for *Drosophila melanogaster* using P and piggyBac. *Nat. Genet.* **36**, 283–287 (2004). doi: 10.1038/ng1314; pmid: 14981521
9. M. J. Fraser, G. E. Smith, M. D. Summers, Acquisition of host cell DNA sequences by baculoviruses: Relationship between host DNA insertions and FP mutants of *Autographa californica* and *Galleria mellonella* nuclear polyhedrosis viruses. *J. Virol.* **47**, 287–300 (1983). pmid: 16789244
10. M. J. Fraser, J. S. Brusca, G. E. Smith, M. D. Summers, Transposon-mediated mutagenesis of a baculovirus. *Virology* **145**, 356–361 (1985). doi: 10.1016/0042-6822(85)90172-2; pmid: 2992159
11. L. C. Cary *et al*., Transposon mutagenesis of baculoviruses: Analysis of *Trichoplusia* ni transposon IFP2 insertions within the FP-locus of nuclear polyhedrosis viruses. *Virology* **172**, 156–169 (1989). doi: 10.1016/0042-6822(89)90117-7; pmid: 2549707
12. B. Balu, D. A. Shoue, M. J. Fraser Jr., J. H. Adams, High-efficiency transformation of Plasmodium falciparum by the lepidopteran transposable element piggyBac. *Proc. Natl. Acad. Sci. U.S.A.* **102**, 16391–16396 (2005). doi: 10.1073/pnas.0504679102; pmid: 16260745
13. B. Balu *et al*., CCR4-associated factor 1 coordinates the expression of *Plasmodium falciparum* egress and invasion proteins. *Eukaryot. Cell* **10**, 1257–1263 (2011). doi: 10.1128/EC.05099-11; pmid: 21803864
14. H. Ikadai *et al*., Transposon mutagenesis identifies genes essential for *Plasmodium falciparum* gametocytogenesis. *Proc. Natl. Acad. Sci. U.S.A.* **110**, E1676–E1684 (2013). doi: 10.1073/pnas.1217712110; pmid: 23572579
15. B. Balu *et al*., Atypical mitogen-activated protein kinase phosphatase implicated in regulating transition from pre-S-Phase asexual intraerythrocytic development of *Plasmodium falciparum*. *Eukaryot. Cell* **12**, 1171–1178 (2013). doi: 10.1128/EC.00028-13; pmid: 23813392
16. A. Pradhan *et al*., Chemogenomic profiling of Plasmodium falciparum as a tool to aid antimalarial drug discovery. *Sci. Rep.* **5**, 15930 (2015). doi: 10.1038/srep15930; pmid: 26541648
17. I. F. Bronner *et al*., Quantitative insertion-site sequencing (QIseq) for high throughput phenotyping of transposon mutants. *Genome Res.* **26**, 980–989 (2016). doi: 10.1101/gr.200279.115; pmid: 27197223
18. T. Hart *et al*., High-resolution CRISPR screens reveal fitness genes and genotype-specific cancer liabilities. *Cell* **163**, 1515–1526 (2015). doi: 10.1016/j.cell.2015.11.015; pmid: 26627737
19. B. Balu *et al*., piggyBac is an effective tool for functional analysis of the *Plasmodium falciparum* genome. *BMC Microbiol.* **9**, 83 (2009). doi: 10.1186/1471-2180-9-83; pmid: 19422698
20. Q. Zhang *et al*., Exonuclease-mediated degradation of nascent RNA silences genes linked to severe malaria. *Nature* **513**, 431–435 (2014). doi: 10.1038/nature13468; pmid: 25043062
21. R. Ménard *et al*., Circumsporozoite protein is required for development of malaria sporozoites in mosquitoes. *Nature* **385**, 336–340 (1997). doi: 10.1038/385336a0; pmid: 9002517
22. A. M. Bobenchik *et al*., *Plasmodium falciparum* phosphoethanolamine methyltransferase is essential for malaria transmission. *Proc. Natl. Acad. Sci. U.S.A.* **110**, 18262–18267 (2013). doi: 10.1073/pnas.1313965110; pmid: 24145416
23. N. M. B. Brancucci *et al*., Lysophosphatidylcholine regulates sexual stage differentiation in the human malaria parasite *Plasmodium falciparum*. *Cell* **171**, 1532–1544.e15 (2017). doi: 10.1016/j.cell.2017.10.020; pmid: 29129376
24. T. W. Kooij *et al*., A Plasmodium whole-genome synteny map: Indels and synteny breakpoints as foci for species-specific genes. *PLOS Pathog.* **1**, e44 (2005). doi: 10.1371/journal.ppat.0010044; pmid: 16389297
25. J. D. DeBarry, J. C. Kissinger, Jumbled genomes: Missing Apicomplexan synteny. *Mol. Biol. Evol.* **28**, 2855–2871 (2011). doi: 10.1093/molbev/msr103; pmid: 21504890
26. T. D. Otto *et al*., New insights into the blood-stage transcriptome of *Plasmodium falciparum* using RNA-Seq. *Mol. Microbiol.* **76**, 12–24 (2010). doi: 10.1111/j.1365-2958.2009.07026.x; pmid: 20141604
27. V. A. Blomen *et al*., Gene essentiality and synthetic lethality in haploid human cells. *Science* **350**, 1092–1096 (2015). doi: 10.1126/science.aac7557; pmid: 26472760
28. T. Wang *et al*., Identification and characterization of essential genes in the human genome. *Science* **350**, 1096–1101 (2015). doi: 10.1126/science.aac7041; pmid: 26472758
29. E. Bushell *et al*., Functional profiling of a *Plasmodium* genome reveals an abundance of essential genes. *Cell* **170**, 260–272.e8 (2017). doi: 10.1016/j.cell.2017.06.030; pmid: 28708996
30. S. S. Vembar, D. Droll, A. Scherf, Translational regulation in blood stages of the malaria parasite *Plasmodium* spp.: Systems-wide studies pave the way. *Wiley Interdiscip. Rev. RNA* **7**, 772–792 (2016). doi: 10.1002/wrna.1365; pmid: 27230797
31. C. Dogovski *et al*., Targeting the cell stress response of Plasmodium falciparum to overcome artemisinin resistance. *PLOS Biol.* **13**, e1002132 (2015). doi: 10.1371/journal.pbio.1002132; pmid: 25901609
32. A. Mbengue *et al*., A molecular mechanism of artemisinin resistance in *Plasmodium falciparum* malaria. *Nature* **520**, 683–687 (2015). doi: 10.1038/nature14412; pmid: 25874676
33. H. Li *et al*., Structure- and function-based design of *Plasmodium*-selective proteasome inhibitors. *Nature* **530**, 233–236 (2016). doi: 10.1038/nature16936; pmid: 26863983
34. W. C. Van Voorhis *et al*., Open source drug discovery with the malaria box compound collection for neglected diseases and beyond. *PLOS Pathog.* **12**, e1005763 (2016). doi: 10.1371/journal.ppat.1005763; pmid: 27467575
35. S. P. Maher, M. Zhang, B. Balu, J. H. Adams, in *Methods in Malaria Research*, K. Moll, A. Kaneko, A. Scherf, M. Wahlgren, Eds. (EVIMalaR, MR4/BEI Resources, 2013), chap. VII, pp. 391–396.
36. C. Aurrecoechea *et al*., EuPathDB: The eukaryotic pathogen database. *Nucleic Acids Res.* **41** (D1), D684–D691 (2013). doi: 10.1093/nar/gks1113; pmid: 23175615
37. M. J. López-Barragán *et al*., Directional gene expression and antisense transcripts in sexual and asexual stages of *Plasmodium falciparum*. *BMC Genomics* **12**, 587 (2011). doi: 10.1186/1471-2164-12-587; pmid: 22129310
38. N. Ponts *et al*., Nucleosome landscape and control of transcription in the human malaria parasite. *Genome Res.* **20**, 228–238 (2010). doi: 10.1101/gr.101063.109; pmid: 20054063
39. T. L. Campbell, E. K. De Silva, K. L. Olszewski, O. Elemento, M. Llinás, Identification and genome-wide prediction of DNA binding specificities for the ApiAP2 family of regulators from the malaria parasite. *PLOS Pathog.* **6**, e1001165 (2010). doi: 10.1371/journal.ppat.1001165; pmid: 21060817

ACKNOWLEDGMENTS

Funding: This work was supported by the Wellcome Trust grant 098051 (J.C.R.), the National Institutes of Health grants R01 AI094973, R01 AI117017 (J.H.A.), and F32 AI112271 (J.O.).
Author contributions: Transfection and cell culture was performed by M.Z., X.L., K.U., D.C., S.L., and J.S.; quantitative insertion-site sequencing was performed by M.Z., I.F.B., M.M., and J.B.; computational analysis was performed by C.W., M.Z., T.D.O., J.O., S.R.A., and R.H.Y.J.; writing group consisted of M.Z., C.W., T.D.O., J.O., J.C.R., R.H.Y.J., and J.H.A.; and the study was conceived and directed by J.C.R., R.H.Y.J., and J.H.A. **Competing interests:** U.S. patent 7932088 (26 April 2011), "High efficiency transformation of *Plasmodium falciparum* by the Lepidopteran transposon, *piggyBac*," is held by inventors J.H.A., M. J. Fraser Jr., B. Balu, and D. A. Shoue. The invention relates to use of *piggyBac* as a tool for genetic manipulation of the *Plasmodium* genome. **Data and materials availability:** All data and code to understand and assess the conclusions of this research are available in the main text and supplementary materials and are deposited into the European Nucleotide Archive. Accession numbers for individual experiments and libraries are listed in table S9. *piggyBac* transfection plasmids (MRA911/912) and mutants are deposited with the Malaria Research Reagent and Reference Repository (BEI Resources). *piggyBac* transfection plasmids and mutant parasites may be obtained directly from the authors at the University of South Florida, using a standard academic materials transfer agreement based on the Uniform Biological Material Transfer Agreement.

SUPPLEMENTARY MATERIALS

www.sciencemag.org/content/360/6388/eaap7847/suppl/DC1
Figs. S1 to S11
Tables S1 to S9
References (*41*)

14 September 2017; accepted 2 March 2018
10.1126/science.aap7847

RESEARCH ARTICLE SUMMARY

BIOMATERIALS

Fractal-like hierarchical organization of bone begins at the nanoscale

Natalie Reznikov, Matthew Bilton, Leonardo Lari, Molly M. Stevens,* Roland Kröger*

INTRODUCTION: The components of bone assemble hierarchically to provide stiffness and toughness. Deciphering the specific organization and relationship between bone's principal components—mineral and collagen—requires answers to three main questions: whether the association of the mineral phase with collagen follows an intrafibrillar or extrafibrillar pattern, whether the morphology of the mineral building blocks is needle- or platelet-shaped, and how the mineral phase maintains continuity across an extensive network of cross-linked collagen fibrils. To address these questions, a nanoscale level of three-dimensional (3D) structural characterization is essential and has now been performed.

RATIONALE: Because bone has multiple levels of 3D structural hierarchy, 2D imaging methods that do not detail the structural context of a sample are prone to interpretation bias. Site-specific focused ion beam preparation of lamellar bone with known orientation of the analyzed sample regions allowed us to obtain imaging data by 2D high-resolution transmission electron microscopy (HRTEM) and to identify individual crystal orientations. We studied higher-level bone mineral organization within the extracellular matrix by means of scanning TEM (STEM) tomography imaging and 3D reconstruction, as well as electron diffraction to determine crystal morphology and orientation patterns. Tomographic data allowed 3D visualization of the mineral phase as individual crystallites and/or aggregates that were correlated with atomic-resolution TEM images and corresponding diffraction patterns. Integration of STEM tomography with HRTEM and crystallographic data resulted in a model of 3D mineral morphology and its association with the organic matrix.

ON OUR WEBSITE

Read the full article at http://dx.doi.org/10.1126/science.aao2189

RESULTS: To visualize and characterize the crystallites within the extracellular matrix, we recorded imaging data of the bone mineral in two orthogonal projections with respect to the arrays of mineralized collagen fibrils. Three motifs of mineral organization were observed: "filamentous" (longitudinal or in-plane) and "lacy" (out-of-plane) motifs, which have been reported previously, and a third "rosette" motif comprising hexagonal crystals. Tomographic reconstructions showed that these three motifs were projections of the same 3D assembly. Our data revealed that needle-shaped, curved nanocrystals merge laterally to form platelets, which further organize into stacks of roughly parallel platelets separated by gaps of approximately 2 nanometers. These stacks of platelets, single platelets, and single acicular crystals coalesce into larger polycrystalline aggregates exceeding the lateral dimensions of the collagen fibrils, and the aggregates span adjacent fibrils as continuous, cross-fibrillar mineralization.

CONCLUSION: Our findings can be described by a model of mineral and collagen assembly in which the mineral organization is hierarchical at the nanoscale. First, the data reveal that mineral particles are neither exclusively needle- nor platelet-shaped, but indeed are a combination of both, because curved acicular elements merge laterally to form slightly twisted plates. This can only be detected when the organic extracellular matrix is preserved in the sample. Second, the mineral particles are neither exclusively intrafibrillar nor extrafibrillar, but rather form a continuous cross-fibrillar phase where curved and merging crystals splay beyond the typical dimensions of a single collagen fibril. Third, in the organization of the mineral phase of bone, a helical pattern can be identified. This 3D observation, integrated with previous studies of bone hierarchy and structure, illustrates that bone (as a material, as a tissue, and as an organ) follows a fractal-like organization that is self-affine. The assembly of bone components into nested, helix-like patterns helps to explain the paradoxical combination of enhanced stiffness and toughness of bone and results in an expansion of the previously known hierarchical structure of bone to at least 12 levels. ■

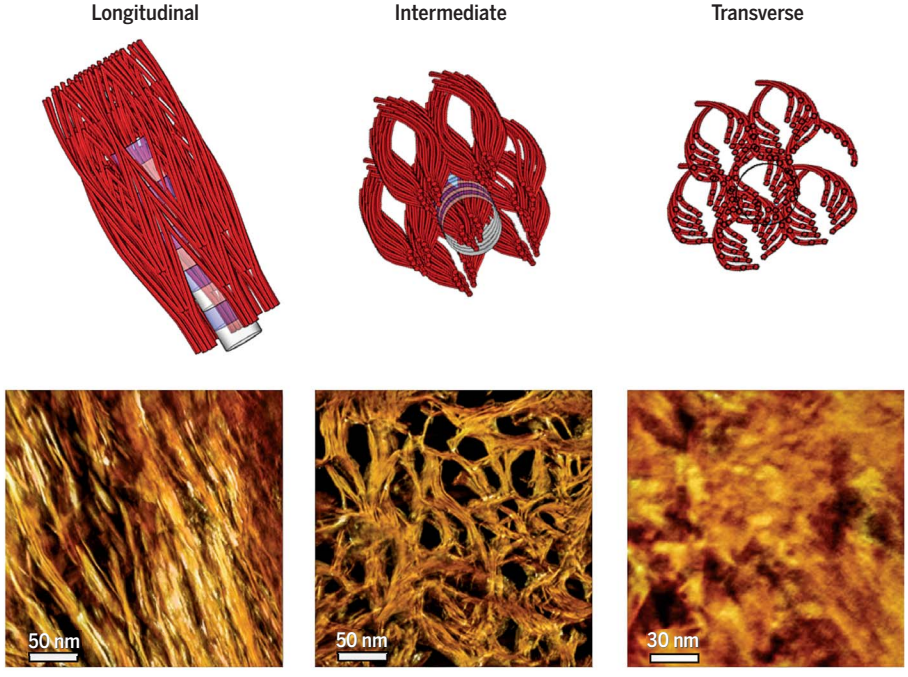

Proposed model of crystal organization in bone. Patterns specified by our model (top) are compared with projections of the STEM tomogram reconstructed from a STEM tilt series, showing the mineral organization in different directions (bottom).

The list of author affiliations is available in the full article online.
*Corresponding author. Email: roland.kroger@york.ac.uk (R.K.); m.stevens@imperial.ac.uk (M.M.S.)
Cite this article as N. Reznikov *et al.*, *Science* **360**, eaao2189 (2018). DOI: 10.1126/science.aao2189

RESEARCH ARTICLE

BIOMATERIALS

Fractal-like hierarchical organization of bone begins at the nanoscale

Natalie Reznikov,[1] Matthew Bilton,[2,3] Leonardo Lari,[2,4] Molly M. Stevens,[1]* Roland Kröger[2]*

The components of bone assemble hierarchically to provide stiffness and toughness. However, the organization and relationship between bone's principal components—mineral and collagen—has not been clearly elucidated. Using three-dimensional electron tomography imaging and high-resolution two-dimensional electron microscopy, we demonstrate that bone mineral is hierarchically assembled beginning at the nanoscale: Needle-shaped mineral units merge laterally to form platelets, and these are further organized into stacks of roughly parallel platelets. These stacks coalesce into aggregates that exceed the lateral dimensions of the collagen fibrils and span adjacent fibrils as continuous, cross-fibrillar mineralization. On the basis of these observations, we present a structural model of hierarchy and continuity for the mineral phase, which contributes to the structural integrity of bone.

Bone is a most impressive natural material that combines stiffness (for support and leverage) and toughness (for protection and impact resistance)—properties usually considered mutually exclusive. In bone, stiffness coexists with toughness by virtue of bone's hierarchical organization: Smaller structural units form larger structural units, which in turn are structured themselves in this manner into higher-order units.

In light of previous studies of bone structure analyzed at different scales, an informative and intriguing picture emerges. At the macroscopic level, most bones incorporate a helical motif in their anatomical shape. This helical motif can be recognized by the twisting of grooves and tuberosities along the shaft of the humerus, by the curvature of the clavicle, or by the course of a rib with respect to the body axis (*1*). These twisted or helical morphologies are easy to identify on robust bones that are well adapted to loading. In humans, multiple Haversian canals traverse compact bone at the millimeter level. They are roughly aligned with the longitudinal axis of the shaft. Indeed, they form helical arrays where each canal and its associated osteon lie along a screw-shaped trajectory with a roughly constant small pitch; this is presumably an adaptation to loading (*2*). At the micrometer level, the helical secondary osteons themselves are formed of concentric lamellae of mineralized collagen fibrils. These fibrillar arrays are inclined with respect to the central Haversian canal at an average angle of approximately 30°, thus forming an assembly of nested coils with alternating pitches (*3*). A single lamella in three dimensions often appears as a layer of bundles, each 2 to 3 μm in diameter, in which mineralized collagen fibrils twist around the bundle axis, just as filaments of a rope twist around its axis with a shallow pitch (*4*). At the nanometer level, the helical theme continues as quasi-hexagonal packing of triple helices of collagen into a fibril (*5*). Each collagen triple helix itself is a supercoil of single α-chain helices (*6*). This abridged overview of independently described helical motifs in bone highlights remarkable self-affinity of structure across 9 or 10 orders of magnitude (in mathematical terms, self-affinity is a less restricted notion than self-similarity). Indeed, in nature it is not uncommon to observe self-affine patterns (also called fractal-like), in which a part of the structure resembles larger entities and/or the whole structure (*7*). Many natural self-affine patterns are helical or spiral (*8*).

Existing evidence describing bone structural hierarchy indicates that below the submicrometer level, the helical pattern pertains only to the collagen component. For bone mineral alone, the paradigm of self-affinity is not obvious. Details of the architecture of both the organic and inorganic constituents of bone have become available with the advancement of x-ray diffraction and electron microscopy methodologies. The mineral of bone—carbonate-substituted hydroxyapatite—must occupy a preformed, osmotically crowded, covalently cross-linked organic niche. Before mineralization, the organic phase of bone is already assembled and is capable of the fine regulation of crystal nucleation and growth (*9*). Bone mineral is nano- and polycrystalline with a substantial degree of disorder and a considerable amount of substitution (*10*–*12*). These features lead to inherent difficulties in the interpretation of crystallographic data. Furthermore, x-ray–based methods require relatively large sampling volumes where the crystallographic observations are averaged and often isolated from their immediate structural context. Another characterization challenge is that bone apatite is associated with disordered or amorphous phases (*13*). These mineral phases, such as octacalcium phosphate (*14*) and amorphous calcium phosphate (*15*), are stabilized by noncollagenous proteins (*16*), citrate ions (*17*), and a rigid hydration shell (*18*). Therefore, the ripening of the crystals is inhibited especially where they interface with organic moieties (*19*). As a result, multiple mineral phases are thought to coexist in bone (*20*, *21*), which also complicates the interpretation of crystallographic studies. The complex structure of skeletal mineral often makes it difficult to prepare samples for electron microscopy imaging without causing specimen preparation artifacts such as disintegration, dehydration, and/or destabilization of metastable mineral phases (*22*). Finally, the three-dimensional (3D) structure of bone mineral, and thus the hierarchical structure, cannot be reconstructed exclusively on the basis of 2D information.

For these reasons, it is not surprising that diverse, sometimes conflicting views have evolved regarding bone mineral morphology and its relationships to the organic extracellular matrix. A number of predominantly electron microscopy–based studies identify the bone mineral building blocks as being acicular (needle-shaped) nanocrystals with diameters between 3 and 10 nm and a length of several hundred nanometers (*23*–*25*), or as platelets with a variety of dimensions ranging from 5 nm × 20 nm × 40 nm (*26*) to 100 nm in the largest dimension (*27*). Furthermore, there is apparent disagreement as to whether the mineral phase is growing in an intra- or extrafibrillar fashion (*28*)—a matter of great importance for the structural integrity of bone. Hence, there is no consensus on the fine details of bone mineral morphology and organization. Besides explaining its unique mechanical properties, a clearer understanding of the mineral-organic interface in the context of bone hierarchical structure will provide insight into skeletal pathologies, growth and development defects, diagenesis (postmortem modification over time), and the metabolic role of bone as an ion reservoir. The organization and relationships between mineral and the organic extracellular matrix are important in such diverse fields as osteology, endocrinology, forensic medicine, and archeology, and this information may additionally inspire the design of novel composite materials.

Our work aims to evaluate the mineral phase of bone in three dimensions, within its immediate structural framework, in such a way that preparation artifacts are minimized and the hierarchical context of bone structure is taken into consideration. Using advanced preparation methodology and high-resolution electron microscopy, we explain how earlier conflicting models can be reconciled and advanced by the findings presented here.

[1]Department of Materials, Department of Bioengineering and Institute for Biomedical Engineering, Faculty of Engineering, Imperial College London, London, UK. [2]Department of Physics, University of York, Heslington, York, UK. [3]4D LABS, Simon Fraser University, Burnaby, British Columbia, Canada. [4]York JEOL Nanocentre, Science Park, York, UK.
*Corresponding author. Email: roland.kroger@york.ac.uk (R.K.); m.stevens@imperial.ac.uk (M.M.S.)

Two-dimensional projections of the apatite mineral phase

Lamellar bone is the most common type of bone in a mature human skeleton. Mineralized collagen fibrils are ordered and tightly packed within a single lamella (*29*). On the micrometer scale, mineralized collagen fibrils can be considered to be roughly co-aligned, whereas their orientation changes more or less abruptly at the boundaries between adjacent lamellae.

By aligning a focused ion beam (FIB)–milled, electron-transparent specimen perpendicular to the lamellar boundaries, one can expect to observe the collagen fibrils with respect to the image plane in a wide range of orientations from edge-on views to in-plane views (*29*). We assumed that, using such specimen geometry, nearly in-plane and nearly edge-on arrays of mineralized collagen fibrils could be observed in the resulting cross sections (fig. S1). Interestingly, three distinct motifs of mineral organization were identified (Fig. 1).

Of the three revealed motifs of nanoscale bone organization, the first, in-plane motif (Fig. 1A) contains extended quasi-linear elements; we term this the "filamentous" motif. The characteristic banding pattern of type I collagen fibrils (the 67-nm D-periodicity) can be followed in this orientation, confirming that the fibrils are roughly aligned with the image plane. The filamentous mineral particles are roughly co-oriented with the D-periodicity (at an angular range of approximately ±20°) and therefore are aligned with the long axes of the collagen fibrils. However, the length of the mineral particles usually exceeds 67 nm, which suggests that they are not confined to a single period of the collagen fibril. Similar filamentous motifs have been reported previously (*30*–*32*). The second, "lacy" pattern (Fig. 1C) incorporates groups of concentrically curved, thin mineral particles surrounding irregular voids 30 to 50 nm in diameter. The third pattern of mineral particle arrangement is relatively dense and comprises left-handed "rosettes" with lateral crystal sizes between 5 and 10 nm. These rosettes of edge-on imaged particles are assembled in a quasi–closely packed pattern when the outlines of entire rosettes are considered. Overall, the lateral particle size distribution was found to be lognormal with an average particle diameter of 5.8 nm and a variation of ±1.4 nm.

Selected-area electron diffraction (SAED) patterns obtained from all three motifs are shown in Fig. 1, B, D, and F. All SAED patterns indicate polycrystallinity and are somewhat spotty in nature because of the limited number of refracting crystals in the analyzed volumes (SAED area diameter, 250 nm). The azimuthal intensity distribution is therefore not homogeneous, yet the radial intensity distribution clearly indicates the presence of apatite-related reflections and allows for the extraction of important crystallographic information. The filamentous motif shows a pair of arcs corresponding to the (002) plane-related reflection. The arc axis with respect to the center of the diffraction patterns is aligned with the texture of the filamentous motif, and the angular dispersions of both are in agreement. The systematic absence of (002) plane-related reflections in Fig. 1, D and F indicates that the crystallographic *c* axes are considerably tilted out of the plane of view, as would be expected if the mineralized collagen fibrils are out-of-plane.

Higher-magnification images of the three motifs are shown in Fig. 1, G to I. The crystallographic planes of mineral particles can be traced to about 5 nm laterally (in thickness, such as in Fig. 1I and to some extent in Fig. 1H) and to more than 100 nm longitudinally (e.g., Fig. 1G). Note that the individual crystals are not exactly straight in Fig. 1, A and G, but rather display bending, with curvature radii varying between 50 and 150 nm.

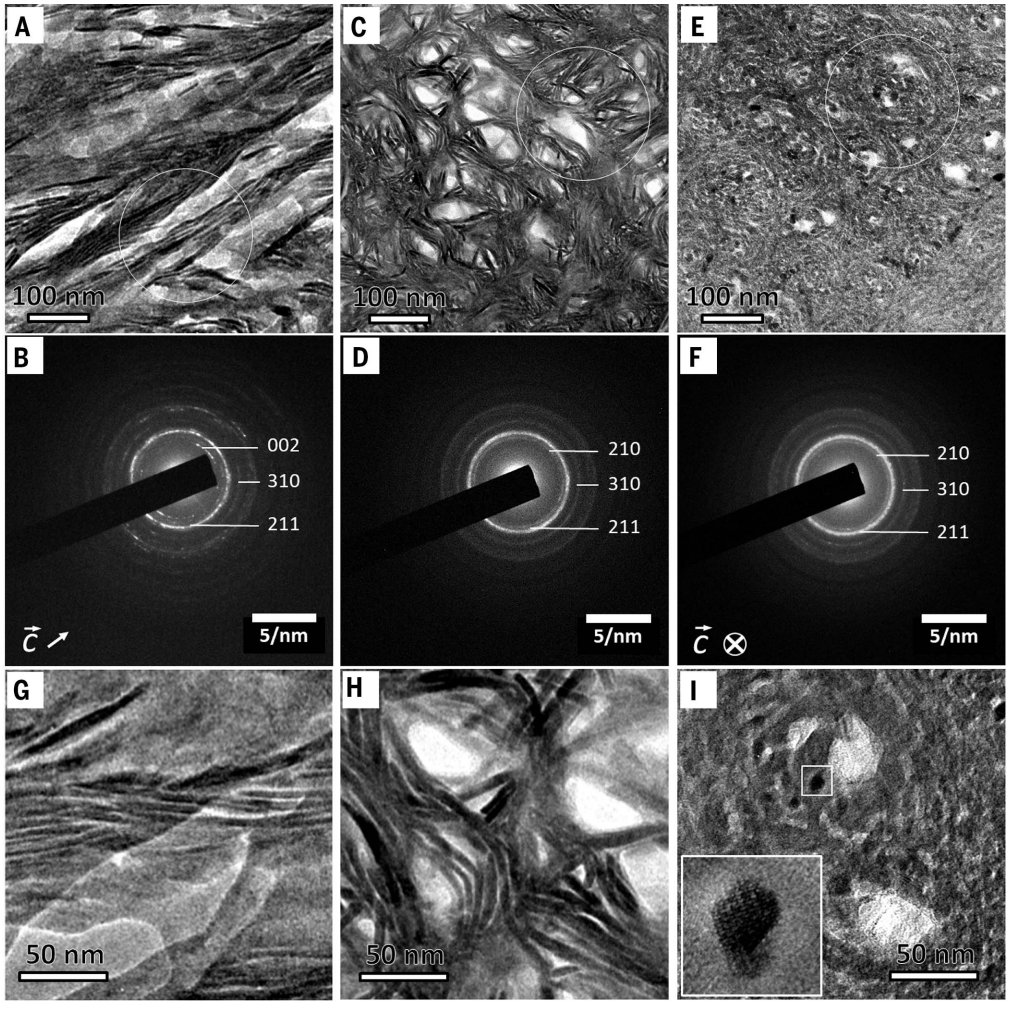

Fig. 1. Three projections of bone structure as observed by TEM and corresponding electron diffraction patterns. (**A**) The filamentous pattern shows curved crystals more than 100 nm in length. (**B**) Diffraction pattern from (A) shows well-defined (002) plane-related reflections, which are oriented in the direction of the elongated crystals. (**C**) The lacy pattern comprises groups of parallel, slightly bent crystals surrounding electron-transparent voids. (**D**) The absence of the (002) plane-related reflections indicates that the crystals' *c* axes are oriented out of plane. (**E**) Nested rosettes, a previously unknown pattern, show crystals of about 5 nm in size arranged into left-handed helices. (**F**) Corresponding diffraction pattern with (002) plane-related reflections being absent, similar to that in (D). (**G** to **I**) Higher magnification of the same motifs. (G) The filamentous motif. (H) The lacy motif. (I) The rosette motif. Note a nearly hexagonal outline of the dark crystallite in (I); the inset shows a HRTEM image of the area indicated by the small white square, and the white circles in (A), (C), and (E) indicate the areas from which the SAED patterns in (B), (D), and (F) were recorded.

As shown in Fig. 1, C and E, we found two motifs when the mineralized fibrils are observed in cross section. The observed lacy motif has been reported in (*12*, *28*–*31*, *33*, *34*), whereas the rosette motif has not previously been described. Each of the rosettes is a chain of hexagonally faceted crystals with clearly visible lattice fringes when imaged by high-resolution transmission electron microscopy (HRTEM) (Fig. 1I). Analysis of the lattice fringes shows that the long *c* axes of the crystals are approximately parallel to the zone axis (Fig. 1I and fig. S2). As a result, the *c*-axis orientation could be approximately indicated in the SAED pattern in Fig. 1B as in-plane and in Fig. 1F as out-of-plane, whereas the corresponding *a* and *b* axes are randomly distributed, as confirmed by the SAED patterns.

The lateral extension of the rosettes in the motif shown in Fig. 1E is between 100 and 120 nm, which is consistent with the diameter of collagen fibrils in bone. Furthermore, their close-packing arrangement is reminiscent of the quasi-hexagonal packing of bone collagen fibrils (*5*, *35*). These observations raise the question of how the same, presumably edge-on, projection can generate two distinct structural patterns.

Three-dimensional morphology of bone mineral

Tomographic tilt series were acquired from five FIB-milled sections, of which we present the results for two sections that at the 0° tilt angle revealed (i) a domain containing the filamentous and the lacy motifs simultaneously, and (ii) a domain containing exclusively the lacy motif. The lateral resolution of tomographic images exceeds the *z*-resolution because the *z*-axis dimension is reconstructed from tilted projections of an electron-transparent specimen. In tilted projections, the electron beam travels through a larger thickness than at the 0° tilt projection. For this reason, it was important to reconstruct 3D images from specimen areas containing in-plane and out-of-plane mineralized collagen fibrils. The resulting reconstructions were rendered and are shown in Figs. 2 and 3. *Z*-contrast imaging allows for a clear distinction of the mineral phase in the context of the organic matrix. However, the mass density variation attributable to the sequence of gap and overlap regions also makes it possible to observe the collagen D-periodicity simultaneously with the mineral phase, without the need for any staining agent.

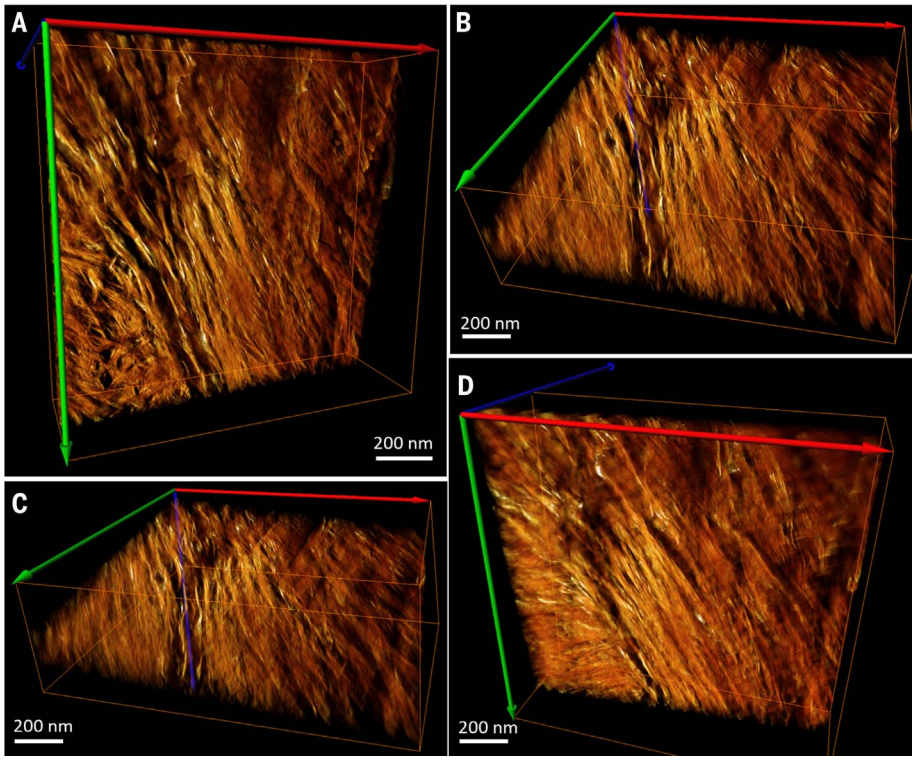

Fig. 2. Filamentous and lacy motifs: Reconstructed and rendered STEM tomogram in different projections of a FIB-milled specimen of mature human lamellar bone. (**A**) Sample showing mostly the filamentous pattern with a fragment of the lacy pattern in the bottom left corner; these patterns originate from two adjacent lamellae. (**B**) The same volume slightly tilted around the horizontal axis. (**C**) The same volume as in (A) tilted approximately 50° to 60° around the horizontal axis. (**D**) The same volume as in (A) tilted approximately −30° around the horizontal axis. Note the angular offset of approximately 60° between the crystallites of the neighboring motifs apparent in (C). Colored arrows indicate the axes of the reconstructed 3D volume orientation in space.

We collected tilt series of scanning transmission electron microscopy (STEM) images at tilt-angle increments of 2° through a tilt range of ±70°. The tilt series were reconstructed into 3D stacks (tomograms) with the use of a filtered back-projection algorithm applying the IMOD 4.9.0 software [http://bio3d.colorado.edu/imod/ (*36*)]. The volume-rendered tomograms are presented in movies S1 and S2. The 3D reconstructed volumes show the in-plane filamentous motif and/or the out-of-plane lacy motif. In the 3D view, both appear as assemblies of irregularly shaped, opaque, elongated mineral particles. Crystals in the filamentous motif are roughly aligned with the collagen fibrils that are identified by their D-periodicity (Fig. 2A). The lacy motifs display lens-shaped voids 20 to 50 nm in diameter; within the imaged volume, the size and distribution of these voids are far less than those of collagen fibrils observed in 3D studies of demineralized bone (*37*).

Having found two adjacent motifs (lacy and filamentous) at the boundary of two bone lamellae in the same tomogram, with the same thickness and imaged under identical conditions, we performed virtual reslicing of digitally isolated filamentous and lacy areas. This allowed us to examine whether these two motifs are projections of morphologically identical crystalline assemblies. Two cubic volumes, each of 100 nm × 100 nm × 100 nm size, were cropped from each area and globally labeled by applying a White TopHat algorithm (*38*)—a function used for en masse extraction of small features in digital image processing (Avizo 9.2, FEI, USA). The resulting binary cubic images were digitally resliced at 90° so that the original in-plane area would be viewed edge-on, and vice versa. Subsequently, all images comprising the resliced stack were overlaid into a single image (a digital projection) using average pixel values, and the brightness was adjusted. The resulting original and reciprocal projections of in-plane and out-of-plane arrays are presented in Fig. 4, demonstrating that essentially the lacy and filamentous motifs are different projections of the same 3D arrangement.

Besides demonstrating that lacy and filamentous motifs are different projections of identical structures, Fig. 4 also shows that the TopHat-labeling algorithm results in a reliable and feature-retaining segmentation of bone mineral. We used 3D rendering of individual mineral particle labels to study their morphology while avoiding the masking effect of the neighboring, coalescing labels. Separate mineral particles and their aggregates showing the least degree of confluence are shown in Fig. 5. Unobscured observation of highly irregular individual particles shows that there exist three hierarchical levels of mineral particle aggregation: lateral, stacked, and wedged, increasing in order of size (Table 1). The smallest entity above the noise level that could be labeled is an acicular particle with a shorter dimension of 5 nm and a longer dimension of at least 30 nm. These acicular particles are consistent with the dimensions of the crystalline domains observed by TEM (Fig. 1, A and G, filamentous motif). The

extended needles show bending, with a curvature of approximately 100 to 150 nm, similar to the values observed for the crystals constituting the lacy pattern in Fig. 1H. The angular distribution of the needles is in the range of up to ±20° relative to the main axis of the collagen fibrils in the original image (Fig. 2, filamentous portion in all panels), and thus they are similar to the azimuthal length of the (002) plane-related reflection arcs found in the diffraction patterns of the filamentous motif (Fig. 1B). These filaments aggregate laterally and form larger, platelet-shaped morphologies, and for that reason their maximal length cannot be reliably defined. The platelets often show longitudinal striations corresponding to the filament directions. Mostly, individual filaments are visible only at the fringes of a platelet (resembling the fingers of a hand), and in some cases these can be captured as self-standing entities. The platelet-shaped aggregates of acicular particles have two distinct features: (i) They form stacks of two to four parallel platelets separated by a well-defined uniform gap of about 2 nm, and (ii) the platelet-shaped aggregates often show a gentle twist along their longitudinal axis, resembling the shape of a fan blade. Finally, platelets and their stacks converge into larger aggregates in such a way that the gap between them becomes wedge-shaped. These largest aggregates exceed the dimensions of the D-period and the interfibrillar spaces observed in 3D images of demineralized collagen in bone (*29*). Note that only the smallest converging aggregates are presented here, and these illustrate the lower limit of their dimensions; it must be kept in mind that most of the aggregates are more extended than those shown in Fig. 5 and fig. S3. Apparently, these larger crystalline structures incorporating nested arrays of simpler acicular and platelet-shaped particles are not associated with only one collagen fibril, but rather they span several collagen fibrils, and can thus form an interlinked mineral network through cross-fibrillar mineralization (being both intrafibrillar and extrafibrillar).

A three-dimensional model of mineral assembly

We applied the information obtained from the 2D projections and the 3D electron tomography to construct a 3D model of the mineral phase, as shown in movie S3. By relating the facts that (i) there are three distinct projection patterns of crystalline assemblies, (ii) the crystals are slightly curved, (iii) the lacy pattern is already clearly visible when the filamentous projection is tilted by just 30° to 50° with respect to the fibrils' long axes, and (iv) the collagen helices are staggered in a superhelical fashion (*5*, *6*, *39*), we suggest that apatite crystals within a continuous collagenous matrix follow an asymmetrical, subtly splaying pattern of organization, as illustrated in Fig. 6. The individual curved acicular mineral particles are partly aligned with the long axes of the collagen fibrils. Because of their curvature and their longitudinal dimensions (≥100 nm), these acicular mineral particles also splay away from the fibril, thus providing space for an adjacent tier of acicular particles along the collagen fibril axis. Thus, an intercalated cross-fibrillar network is formed, in which the acicular units are associated with the collagen fibrils and with the extrafibrillar space, and are likely associated with the neighboring collagen fibrils. Of note, the propensity of fine apatite crystals to splay away from a constraining fibril has been previously reported in vitro (*40*). For the sake of illustration clarity, the model of curved splaying acicular units does not reflect the fact that they partly coalesce laterally to form thin platelets, but their coalescence can be clearly observed in the tomographic images. Therefore, the model here underestimates the amount of extrafibrillar

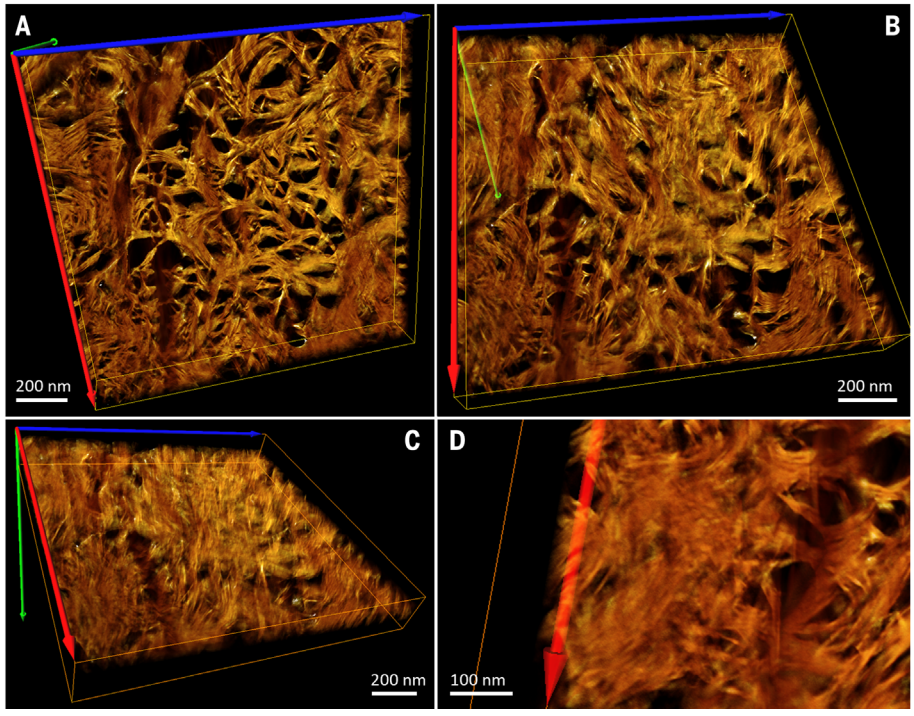

Fig. 3. Lacy motif: Reconstructed and rendered STEM tomogram in different projections of a FIB-milled specimen of mature human lamellar bone. (**A** to **C**) The same volume viewed vertically (A), tilted approximately 30° around the horizontal axis (B), and tilted approximately 60° around the horizontal axis (C). Note that in the right top corner of (C) the faint D-periodicity of collagen can be detected. (**D**) A fragment of the same sample in such an orientation that acicular projections of the crystallites appear, resembling the rosette pattern in Fig. 1E. Colored arrows indicate the axes of the reconstructed 3D-volume orientation in space.

Table 1. Description of hierarchically organized bone apatite crystals and their approximate sizes.

Structural entity	Morphology	Dimensions
Acicular crystal	Thin, subtly curved "fingers"	Base 5 nm, length 50 to 100 nm
Platelet	Irregular, flattened, formed of partly merging aligned acicular crystals; "hand with fingers"	Thickness 5 nm, width 20 to 30 nm, length 50 to 100 nm
Stacks of platelets	Two to four platelets separated by uniform gaps of 1 to 2 nm; "pressed-together hands"	Thickness 20 to 40 nm, width 20 to 40 nm, length 100 nm
Aggregates of stacks	Stacks of platelets and/or single platelets and/or individual acicular crystals coalescing at an angle	Complex irregular 3D shape, up to 200 to 300 nm

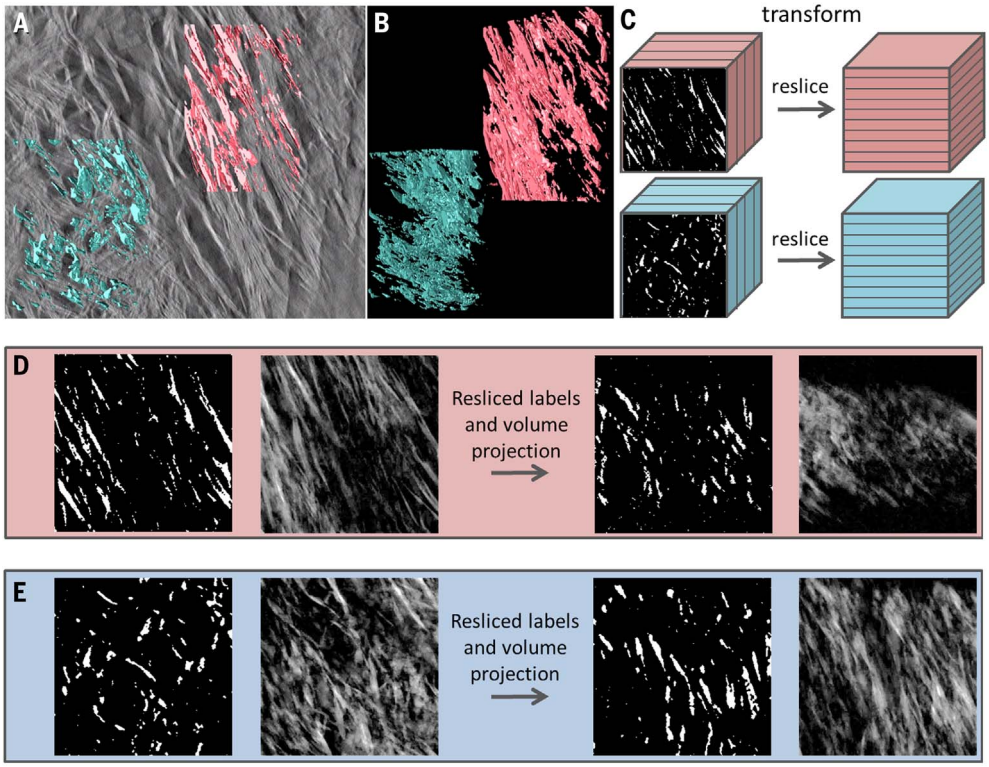

Fig. 4. Labeling algorithm and comparison of the lacy and filamentous patterns in bone in reciprocally oriented projections. (**A**) Tomogram slice with superimposed labels of the lacy (blue) and filamentous (pink) patterns. (**B**) Labeled volumes show extensively aggregated and coalesced elongated entities of variable size and irregular shape. (**C**) Volumes cropped to an identical size in all three dimensions are transformed in such a way that former *XY* planes now are *XZ* planes (i.e., the in-plane labels are viewed in the out-of-plane orientation, and vice versa). (**D**) Digital manipulation of the filamentous label field (from left to right): Original labels in a cubic stack are averaged in terms of pixel value to form a pseudo-2D image, which is similar to the corresponding area in (A). The resliced label field stack is averaged in terms of pixel value to form a pseudo-2D image in an orthogonal direction. (**E**) Digital manipulation of the lacy label field follows the same sequence of steps. Note the similarity of the resliced projected filamentous label field to the original lacy motif, and vice versa.

mineral. The subtle curvature of most acicular units, as noticeable in 2D and 3D images, is slightly accentuated in the model. The model viewed in the direction perpendicular to the collagen fibril axes (i.e., fibrils in-plane) is congruent with the filamentous motif and provides a good explanation for the angular distribution of the crystals of approximately 20° relative to the fibril axis. The same model viewed in the direction almost aligned with the fibril axes (i.e., fibrils roughly out-of-plane) produces a lacy motif with lens-shaped holes surrounded by parallel segments of curved filaments. Finally, the same model viewed exactly edge-on with respect to the collagen fibril axes results in concentric rosettes of cross-sections of the acicular units. To summarize, the same 3D structure—assembled arrays of curved, coarsely aligned acicular elements that splay away from one collagen fibril toward adjacent neighboring fibrils via the confined extrafibrillar space—explains the occurrence of all the motifs observed in 3D projections, as well as the 3D-rendered tomographic images.

The repercussions of this hierarchical mineral/collagen assembly pattern are manifold, affecting the mechanical properties of bone as well as the metabolic role of the carbonated apatite phase as a reservoir for mobilization and sequestration of inorganic ions (*41*). The uniform gaps between the platelet-shaped formations are known to contain disordered calcium phosphate, structural water (*42*, *43*), and possibly noncollagenous proteins (*44*) and polysaccharides (*19*). These unstructured sheaths maintain the uniform high aspect ratio of individual crystallites, which contribute to their flexibility and toughness as well as their reduced sensitivity to stress-induced crack formation—a feature characteristic for the mechanical behavior of high–aspect ratio structures, for example, of nanotubes or nanowhiskers (*45*). From the mechanical perspective of composite materials theory, a high aspect ratio of staggered filler units within the matrix, together with a high density of the filler units, both contribute to higher material strength and stiffness (*46*). Notably, in bone the high aspect ratio of the thin elongated crystals is purposefully maintained by the rigid layers of structural water between neighboring mineral particles (*42*, *43*, *47*), whereas the loss of structural water from bone tissue is associated with age-related decay of bone mechanical properties (*48*).

The mechanism by which acicular crystals merge to form platelets remains unclear. In concert with the theory of biomineralization occurring through an amorphous precursor stage (*49*, *50*), the crystallization of biological apatite could be expected to proceed along the path of least interference within a cross-linked collagenous matrix that is rich in mineralization inhibitors that regulate crystal growth. The formation of an ordered crystalline phase throughout the amorphous template can be locally disrupted by the presence of noncollagenous organic entities (*51*), substantial amounts of bound water and inorganic impurities (*14*, *17*), or prestress of the collagenous matrix (*52*). It remains unknown whether acicular crystals merge into platelets or whether thin prestressed platelets split into acicular crystals at their periphery. The interfacial role of water is mediated by numerous organic inclusions (*9*, *19*) and inorganic impurities (*14*), both of which can disrupt the long-range order of bone apatite.

The higher-level coalescence of stacks of platelets into larger wedged aggregates is an illustration of continuity of the mineral phase transversely spanning the dimensions of more than one collagen fibril. The collagenous matrix of bone is extensively cross-linked by intermolecular covalent bonds (*53*). In bone—as opposed to tendon, for example—it is difficult to discern individual collagen fibrils and their trajectories because they are all aligned in register. To examine the true length of individual collagen fibril segments, we performed manual labeling of demineralized bone collagen fibrils imaged by FIB scanning electron microscopy (FIB-SEM) in a digitally resliced edge-on orientation. Figure 7 and movie S4 show that individual fibrils can only be tracked along a segment length of 200 nm on average before they split or merge with other fibrils, thus effectively forming a continuous 3D network. Because individual fibrils are integrated into a continuous network, both fibril segments and extrafibrillar spaces are of a finite length, rarely exceeding a few hundred nanometers. It could be coincidental that the average segment length of the collagen network and the maximal size of a mineral aggregate are of similar values. However, it is possible that the longitudinal dimension of the extrafibrillar space serves as a limiting factor influencing the extent of mineral aggregation. Such a physical confinement is in accord with the need to keep mineral particles small in

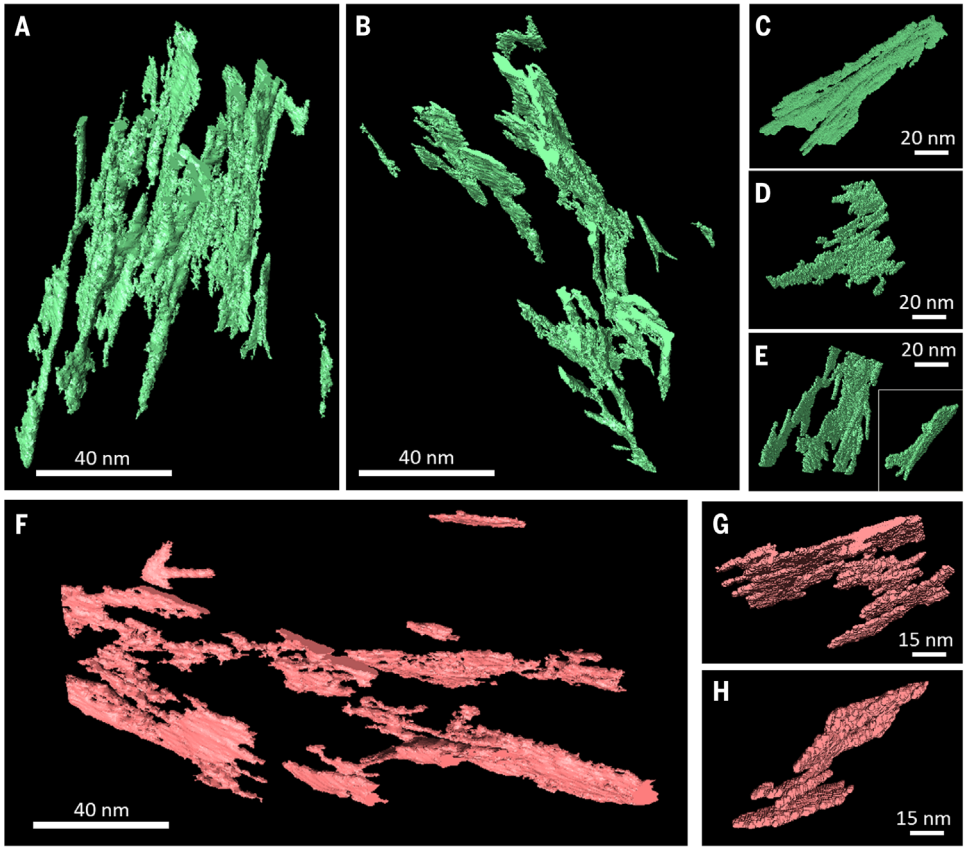

Fig. 5. Evaluation of the tomogram shown in Fig. 2. Individual labels were selected within the lacy pattern [(A) to (E)] and the filamentous pattern [(F) to (H)]. Only the mineral aggregates that showed the least degree of confluence with each other were selected. (**A** and **B**) The same 10 labels in situ, in two different projections. (**C** to **E**) Four of these 10 labels in individually adjusted projections to highlight their 3D shape. (**F** to **H**) Ten individual labels from the filamentous pattern; (G) and (H) show two of these in adjusted projections. There are three levels of confluence of mineral formations with each other: (i) lateral merging of needle-shaped entities into platelets; (ii) planar merging of platelet-shaped entities into stacks of two to four, with a uniform gap between them; and (iii) merging of adjacent stacks at an angle [like fan blades, especially obvious in (C), (E), and (H)] with a wedge-shaped clearance between them. Almost all labels in three dimensions show a delicate twist, especially visible in (B). The overall ratio of label density to total volume was the same in both samples (approximately 0.45 to 0.5).

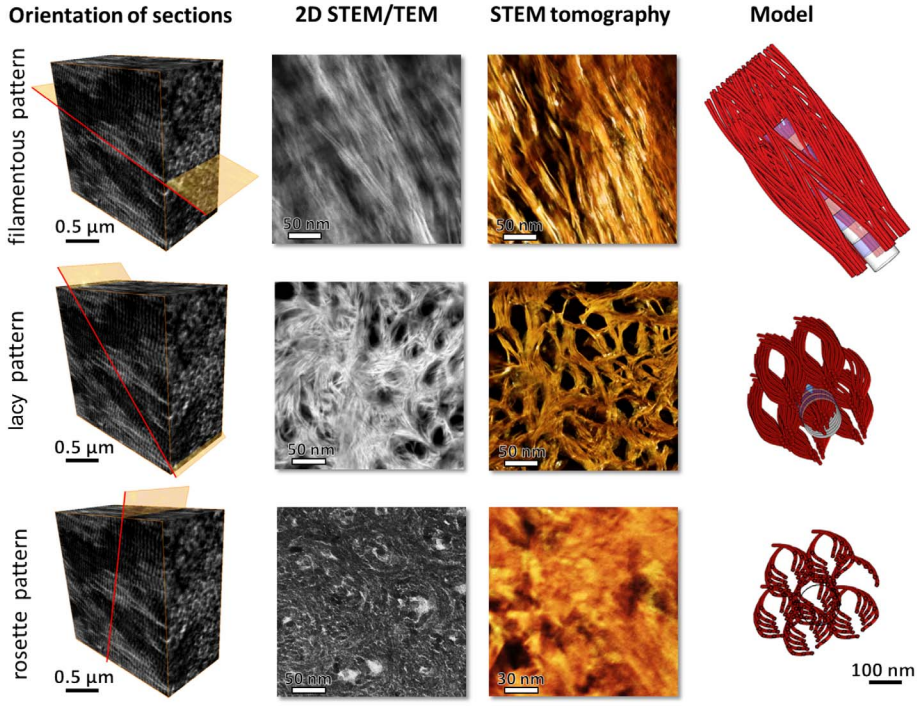

Fig. 6. Morphology and organization of crystals within mineralized collagenous matrix of bone, as seen in different orientations. A proposed model of crystal organization in bone is compared with 2D projections obtained from TEM and STEM (second column of panels) and the tomogram reconstructed from the STEM tilt series (amber-colored, third column of panels). The first column of panels shows the orientation of a thin specimen with respect to the ordered array of mineralized collagen fibrils in lamellar bone. The last column of panels features the same simplified 3D model of bone apatite crystals viewed in three different projections: in-plane, out-of-plane, and edge-on views. For the sake of clarity, the model drawing has fewer concentric tiers of curved filaments than it presumably would accommodate.

order to optimize material toughness. This observation is also consistent with the noticeable crystallite growth in bone observed in the process of diagenesis and postmortem decay of organic matter (*54*).

Although the mechanisms of collagen cross-linking into a continuous framework and the mechanisms of crystallite aggregation are obviously different, the final results converge to provide for the continuity of bone tissue's organic and inorganic components. The preservation of bone morphology at multiple scales has been previously demonstrated using specimens treated by deproteinization or demineralization in hydrated conditions (*55*, *56*).

The impact of morphology on effective mineral surface area

The small size of bone crystallites has been reported to contribute to the substantial surface area of mineral in the human skeleton, which is on the order of 0.1 km^2/kg (*57*–*59*) according to gas absorption experiments. The effective mineral surface area reportedly decreases at a temperature exceeding 300°C when the loss of bound water and charring of organic constituents occur, indicating crystal merging (*59*). To quantitatively compare the impact of the mineral morphology on the total surface area, we calculated the total crystallite specific surface area from

$$a_{i,tot} = 0.32\frac{A_i}{\rho_{AP}V_i} \quad (1)$$

where A_i and V_i are the area and volume of the crystal morphology, respectively, and ρ_{AP} is the density of the apatite phase. For platelet-shaped crystals, we find

$$a_{PL} = \frac{0.64}{\rho_{AP}}\left(\frac{1}{w}+\frac{1}{d}+\frac{1}{t}\right) \quad (2)$$

with average crystallite dimensions w, d, and t, whereas for the acicular morphology the surface per mass unit can be calculated from

$$a_{AC} \approx \frac{1.48}{\rho_{AP}d} \quad (3)$$

where d is, in this case, the acicular crystallite cross-sectional diameter.

Using an apatite density of 3190 kg/m^3 and a typical mineral content of the skeleton amounting to 32 weight percent (wt %) (*60*) [not to be confused with 67 wt % in mineralized extracellular matrix of bone (*61*) usually assumed for a dissected, defatted, dry specimen], these values were used to calculate the specific surface area for a thin platelet of 5 nm × 25 nm × 100 nm to be compared with the value obtained for acicular crystallites with cross-sectional diameter of 5 nm and length of 100 nm. We find that for an average-size human [having a total skeleton mass of roughly 10 kg, of which about 32% is ash (*60*)], the total surface area of the acicular bone crystallites is approximately 0.9 km^2 (for comparison, this is about twice the area of Vatican City and is consistent with the estimates based on gas adsorption measurements). In contrast, if the bone mineral geometry were plate-shaped, with the crystal size being 5 nm × 20 nm × 100 nm, the total surface area would be almost 40% lower, which is incongruent with the gas adsorption experiments. To validate the surface area dependence on imaging resolution, we calculated the surface-to-volume ratio of the 3D-rendered mineral as a function of pixel size. The original pixel size in the 3D tomographic images was 0.98 nm and it was digitally coarsened to 5 nm—a decrease of resolution where the acicular elements could not be clearly visualized but the plate-shaped aggregates could still be well defined. Interestingly, in the tomogram with the pixel size artificially coarsened from <1 nm to 5 to 6 nm, the surface-to-volume ratio was 40% lower relative to the original resolution (i.e., at which the acicular crystals were well resolved; see fig. S4).

Fractal-like hierarchical bone architecture

The hierarchical assembly of the organic and inorganic components of bone is implemented in a bottom-up manner through the interactions between cells and the extracellular matrix during growth, development, and maintenance. However, the paradigm of bone hierarchy was originally elaborated using a top-down approach by the English physician Clopton Havers, who in 1691 first distinguished five nested structural levels spanning from a bone's anatomy to its basic components: the "earth" (organic matter) and the "fixed salt" (inorganic matter) (*62*). Major methodological leaps have enriched our concept of bone hierarchy. The key review by Weiner and Wagner in 1998 described seven nested levels of organization (*63*). With the advent of nanoscale 3D imaging, nine hierarchical levels were defined in 2014 (*4*). The current understanding of the hierarchical structure of bone is that the organic and inorganic components blend at the submicrometer level to generate mineralized

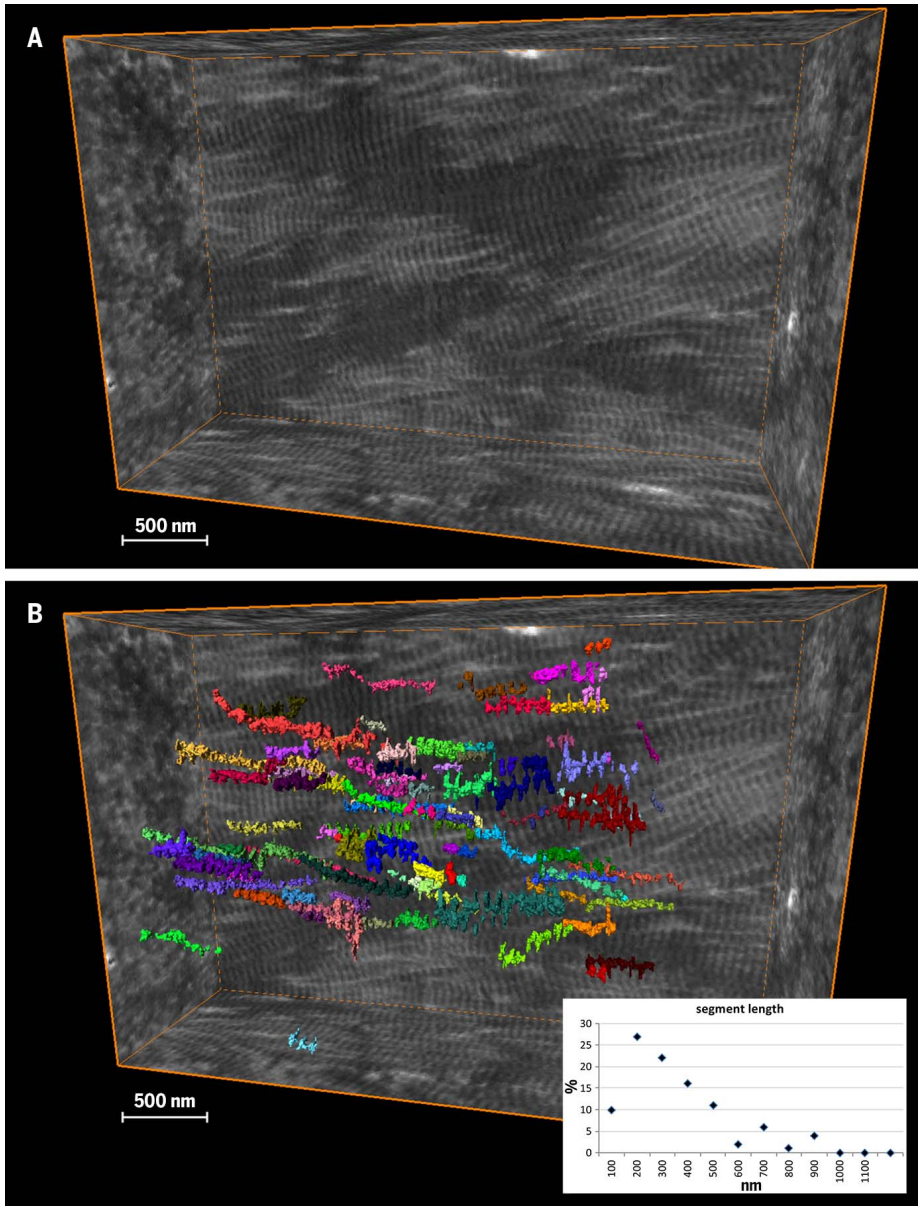

Fig. 7. Discernible segment length of collagen fibrils in the extracellular matrix of bone. (**A**) Reconstructed volume of demineralized and stained collagen fibrils in bone. (**B**) Individual fibrils color-labeled where they can be continuously traced in the edge-on view. Each of 100 labels is shown in a different color visualizing the distribution of segment lengths.

collagen fibrils, as shown in Fig. 8. The hierarchical and self-affine assembly of collagen as the major component of bone's organic phase has been demonstrated previously and is in accordance with the overall hierarchy of bone at the tissue and organ level, up to the macroscopic scale. The demonstration here of bone mineral as a separate hierarchical phase, although counterintuitive, is not at odds with the bigger picture, nor is the observation of the gentle curvature and cross-fibrillar low-pitch coiling of nanocrystals. We show that a helical motif repeats itself on every scale of bone architecture, and that this pertains to both collagen and mineral. Observations that crystals curve and bend are possible in light of the crystals' nanoscale-level high aspect ratio, their formation via an amorphous precursor stage, and their location within a prestressed hydrated matrix. The shallow-pitch helical morphology of bone mineral crystals is in accordance with the nested self-affine helical motifs found throughout the hierarchy of bone structure in general and gives rise to the identification of bone as a fractal-like structure.

As nature uses and reuses effective strategies (*64*), and as helical motifs are abundant in shells, horns, cones, and spider webs (*8*) among other biological structures, we suggest that the fractal-like organization (i.e., the self-affine helical motif occurring across multiple scales) is another way to further optimize bone structure-function relations over millions of years of evolutionary refinement.

Materials and methods

Samples and preparation

Our study focused on compact lamellar bone samples prepared from the proximal femur of two female individuals, 48 and 50 years old. The Imperial College Tissue Bank (application R13004) approved collection and research of excess human tissue from surgeries performed at Charing Cross Hospital, London. The proximal femur samples were collected from elective arthroplasty for osteoarthritis where prior written informed consent was obtained from the patient. The lower femoral necks, also referred to as the "calcar" area (compact bone tissue, generally not affected by the joint degenerative disease), were cut in two planes, along and across the long axis, so that compact bone osteons would be cut in both long and cross sections. The resulting sample sections were polished, and shallow ridges of osteonal lamellae were identified by optical microscopy. The polished bone samples were defatted in acetone and embedded in Epon (Electron Microscopy Sciences, USA) in vacuum; embedding in vacuum was conducted in order to fill bone porosities with a solid medium. The top surface of the embedded samples was exposed with a glass knife and a diamond knife to visualize osteonal lamellae as shallow ridges oriented in concentric circles (transverse osteon section) or as a parallel series (longitudinal osteon section).

Ion beam milling by FIB-SEM provides precise ablation of the mineralized substrate and controlled thinning of the area of interest until electron transparency is obtained. We prepared 100-nm-thick specimens by FIB milling and the lift-out technique, using a Helios Nanolab 600, FEI, USA, following an automated procedure (AutoTEM G2 software, FEI, Netherlands) at 30 keV. The real-time visual control of the milling and thinning processes in the FIB-SEM allows for the preparation of a TEM specimen in the desired orientation (perpendicular to the lamellar planes for both configurations) and sufficiently distanced from the osteocyte lacunae. Specimens were mounted on a semi-grid for thinning to obtain electron transparency (approximating a 100-nm section thickness) using current reduction from 0.46 nA to 28 pA, at 30 keV. Final polishing of the thinned samples was conducted at ion acceleration voltages of 16 keV and then 5 keV, using at the same time electron currents sufficient for visual control in order to gently remove surface unevenness, redeposited debris, and the products of local mineral amorphization. Using an appropriate sequence of decreasing voltage and current values prevents ion beam–related artifacts (*65*) and allows for the best possible preservation of the structural features of the sample, which is especially important for specimens containing organic-inorganic interfaces (*32*) and components sensitive to contact with water (*22*).

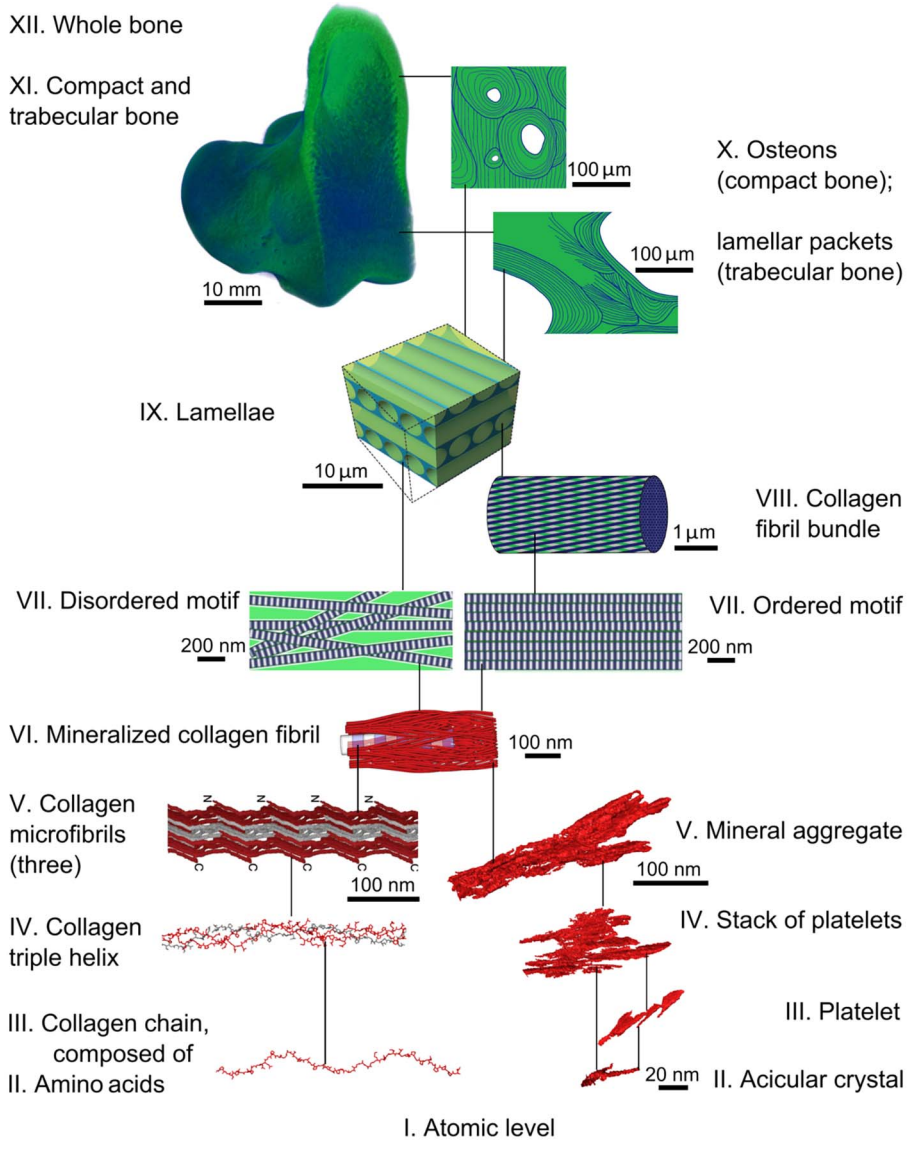

Fig. 8. A scheme of hierarchical organization in bone. For levels VII to XII (green), see Reznikov *et al*. (*4*, *29*, *71*). Both ordered and disordered motifs of lamellar bone comprise mineralized collagen fibrils (VI) that are 80 to 120 nm thick and form a continuous network. Collagen fibrils are composed of quasi–hexagonally packed microfibrils (V), each of which incorporates multiple staggered triple helices (IV) that in turn are formed from repetitive chains (III) of amino acids (II). Collagen levels V to II are discussed in detail by Orgel *et al*. (*5*, *35*, *39*, *72*, *73*). The inorganic component of the mineralized collagen fibrils (VI) itself incorporates several nested structural motifs, listed as follows in decreasing order of complexity: mineral aggregates (V), stacks of platelets (IV), platelets (III), and acicular crystals (II). [(V) copyright 2006, National Academy of Sciences, U.S.A.]

The TEM investigation of the ultrastructure of bone followed a two-pronged approach using bright-field and high-resolution TEM in conjunction with SAED to obtain and characterize 2D projections of the crystal structure. STEM tomography was used to identify the 3D assembly pattern particularly of the mineral phase in unmodified air-dried bone embedded in epoxy resin in vacuum.

Transmission electron microscopy

For 2D imaging of cross sections, we used a conventional JEOL 2011 TEM as well as a JEOL 2200 FS TEM operating in the STEM mode with a third-order probe aberration corrector and a high-angle annular dark field imaging detector (inner collection angle, 110 mrad). Both microscopes were operated at a 200-kV acceleration voltage. For diffraction pattern collection and high-resolution imaging, we notably found the use of an LaB_6 electron source beneficial compared to a field emission gun source because the lower spatial electron coherence minimizes damage by the electron beam.

The appropriate choice of imaging conditions for observing the details of the mineral/organic organization in bone constitutes a major challenge. For TEM analyses, low electron doses are required to avoid material ablation and redeposition during imaging (*66*). Generally, STEM allows for better contrast at low beam exposure compared to plane-view TEM, and is thus less prone to producing artifacts of this type (*66*). In addition, STEM provides directly interpretable contrast, and is therefore also preferable for tomography because plane-view TEM imaging depends strongly on Bragg contrast. Because the local contrast depends on the sample orientation, tomographic imaging is difficult and the achievable spatial resolution is limited. For this reason, STEM methodology is preferable over the TEM methodology for 3D tomographic imaging of polycrystalline samples such as bone.

STEM tomography

We used STEM in conjunction with a high angular annular dark field (HAADF) detector, an imaging approach sensitive to variations in the atomic number Z, thus enabling the simultaneous imaging of collagen and mineral phases in situ. Furthermore, tomographic sample tilting in the STEM mode allows 3D imaging with nanometer-level resolution (*67*), as required for the small dimensions of the apatite crystals.

Tomography was performed using an FEI Tecnai Osiris STEM (X-FEG Schottky field emitter) operated at 200 kV, 245 μA, using a Fischione 2020 advanced tomography holder with a previous data set obtained using manual tilt at a JEOL 2200 FS (*68*). The image size acquired at 0.5 nA was 2048 × 2048 pixels, with a total acquisition time of 2.15 s per frame as follows: area search (0.15 s), focus (0.5 s), exposure (1 s), and tracking (0.5 s), automated and equal for each frame. Data were acquired using the FEI Tecnai Osiris using the FEI Xplore3D and Inspect3D acquisition, post-alignment, and reconstruction software. To produce the resulting 3D volumes, the tilt series was then processed using the IMOD software package (http://bio3d.colorado.edu/imod/) using the filtered back-projection algorithm without applying fiducial markers. We subsequently used the FEI Avizo 9.2 software for 3D rendering and segmentation.

FIB-SEM tomography

The FIB-SEM tomography workflow is described in (*29*). Briefly, the bone sample was demineralized in parallel with mild fixation (*69*), conditioned with alcian blue to stabilize noncollagenous organic components, fixed with glutaraldehyde, and stained with osmium tetroxide (OTOTO protocol). The sample was high-pressure frozen and freeze-substituted, which preserves the dimensions and architecture as in the hydrated state. The sample was then embedded in Epon and sectioned, and imaging was performed using a dual-beam FEI Helios 600 Nanolab FIB-SEM operating in the serial-surface view mode with the slice thickness equal to the lateral resolution of the 2D images in the stack, being approximately 10 nm at 30 keV, 86 pA. The stack was aligned using Fiji (NIH, USA) (*70*). Labeling of individual collagen fibrils was carried out using the local threshold algorithm in Avizo 9.2, FEI, USA. For the current study, the stack of adult human osteonal lamellar bone (originally referred as M77) was used for collagen segment tracing. An area of well-aligned, ordered, nearly horizontal collagen fibrils within one lamella was selected. In the edge-on projection, a cross section of a fibril was labeled based on the local gradient and then traced in both directions until the same cross section could not be identified. In this manner, 100 collagen fibril segments were traced, their length was recorded in nanometers, and the distribution histogram of the segment length values was analyzed.

Specific surface area and crystallite morphologies

Mineral morphology in bone has important implications because of the resulting high surface area and its adsorption capacity, particularly for water molecules. The surface area of a single-crystal platelet having dimensions w, d, and t is

$$A_{\mathrm{PL}} = 2 \cdot (w \cdot d + w \cdot t + d \cdot t) \quad (4)$$

The volume of an individual platelet is

$$V_{\mathrm{PL}} = w \cdot d \cdot t \quad (5)$$

and the platelet mass is

$$M_{\mathrm{PL}} = \rho_{\mathrm{AP}} V_{\mathrm{PL}} \quad (6)$$

where ρ_{AP} is the mass density of the bone apatite. For an acicular crystal with hexagonal symmetry where the crystal length l is much larger than its lateral extension d, we find

$$A_{\mathrm{AC}} = 3 \cdot d \cdot l + \sqrt{27} \cdot \left(\frac{d}{2}\right)^2 \approx 3 \cdot d \cdot l \quad (7)$$

The volume of an individual (acicular) needle is

$$V_{\mathrm{AC}} = \frac{\sqrt{27}}{2} \cdot \left(\frac{d}{2}\right)^2 \cdot l \quad (8)$$

and the needle mass is

$$M_{\mathrm{AC}} = \rho_{\mathrm{AP}} V_{\mathrm{AC}} \quad (9)$$

To obtain the total surface area resulting from the specific geometries, it is necessary to multiply the surface area of the individual crystals by 0.32 (32 wt % mineral content) and the number of crystals constituting the mineral phase (which is the ratio of the total mineral mass divided by the mass of an individual crystal). Thus,

$$A_{\mathrm{i,tot}} = 0.32 \frac{M_{\mathrm{tot}}}{\rho_{\mathrm{AP}}} \frac{A_{\mathrm{i}}}{V_{\mathrm{i}}} \quad (10)$$

with the index representing either a plate-shaped or acicular geometry. This results in the following expressions for the total specific surface areas for both geometries:

$$A_{\mathrm{PL,tot}} = 0.64 \frac{M_{\mathrm{tot}}}{\rho_{\mathrm{AP}}} \left(\frac{1}{w} + \frac{1}{d} + \frac{1}{t}\right) \quad (11)$$

$$A_{\mathrm{AC,tot}} = 0.32 \frac{M_{\mathrm{tot}}}{\rho_{\mathrm{AP}}} \frac{24}{\sqrt{27} \cdot d} \quad (12)$$

The respective specific areas per mass a_{PL} and a_{AC} are given by the total areas divided by the total masses.

REFERENCES AND NOTES

1. T. A. Cook, *The Curves of Life, Being an Account of Spiral Formations and Their Application to Growth in Nature, to Science and to Art, With Special Reference to the Manuscripts of Leonardo Da Vinci* (Constable, London, 1914).
2. J. Heřt, P. Fiala, M. Petrtýl, Osteon orientation of the diaphysis of the long bones in man. *Bone* **15**, 269–277 (1994). doi: 10.1016/8756-3282(94)90288-7; pmid: 8068447
3. W. Wagermaier *et al.*, Spiral twisting of fiber orientation inside bone lamellae. *Biointerphases* **1**, 1–5 (2006). doi: 10.1116/1.2178386; pmid: 20408608
4. N. Reznikov, R. Shahar, S. Weiner, Bone hierarchical structure in three dimensions. *Acta Biomater.* **10**, 3815–3826 (2014). doi: 10.1016/j.actbio.2014.05.024; pmid: 24914825
5. J. P. R. O. Orgel, T. C. Irving, A. Miller, T. J. Wess, Microfibrillar structure of type I collagen in situ. *Proc. Natl. Acad. Sci. U.S.A.* **103**, 9001–9005 (2006). doi: 10.1073/pnas.0502718103; pmid: 16751282
6. J. P. R. O. Orgel *et al.*, The in situ supermolecular structure of type I collagen. *Structure* **9**, 1061–1069 (2001). doi: 10.1016/S0969-2126(01)00669-4; pmid: 11709170
7. B. Mandelbrot, How long is the coast of Britain? Statistical self-similarity and fractional dimension. *Science* **156**, 636–638 (1967). doi: 10.1126/science.156.3775.636; pmid: 17837158
8. D. W. Thompson, *On Growth and Form* (Cambridge Univ. Press, ed. 2, 1942).
9. A. George, A. Veis, Phosphorylated proteins and control over apatite nucleation, crystal growth, and inhibition. *Chem. Rev.* **108**, 4670–4693 (2008). doi: 10.1021/cr0782729; pmid: 18831570
10. F. Betts, N. C. Blumenthal, A. S. Posner, Bone mineralization. *J. Cryst. Growth* **53**, 63–73 (1981). doi: 10.1016/0022-0248(81)90056-7
11. J. C. Elliott, Hydroxyapatites and nonstoichiometric apatites. *Stud. Inorg. Chem.* **18**, 111–189 (1994). doi: 10.1016/B978-0-444-81582-8.50008-0
12. E. Bonucci, in *Advanced Topics on Crystal Growth*, S. O. Ferreira, Ed. (InTech, 2013), chap. 6.
13. J. Mahamid *et al.*, Bone mineralization proceeds through intracellular calcium phosphate loaded vesicles: A cryo-electron microscopy study. *J. Struct. Biol.* **174**, 527–535 (2011). doi: 10.1016/j.jsb.2011.03.014; pmid: 21440636
14. E. Davies *et al.*, Citrate bridges between mineral platelets in bone. *Proc. Natl. Acad. Sci. U.S.A.* **111**, E1354–E1363 (2014). doi: 10.1073/pnas.1315080111; pmid: 24706850
15. K. Chatzipanagis *et al.*, Crystallization of citrate-stabilized amorphous calcium phosphate to nanocrystalline apatite: A surface-mediated transformation. *CrystEngComm* **18**, 3170–3173 (2016). doi: 10.1039/C6CE00521G

16. D. E. Rodriguez *et al*., Multifunctional role of osteopontin in directing intrafibrillar mineralization of collagen and activation of osteoclasts. *Acta Biomater.* **10**, 494–507 (2014). doi: 10.1016/j.actbio.2013.10.010; pmid: 24140612
17. Y.-Y. Hu, A. Rawal, K. Schmidt-Rohr, Strongly bound citrate stabilizes the apatite nanocrystals in bone. *Proc. Natl. Acad. Sci. U.S.A.* **107**, 22425–22429 (2010). doi: 10.1073/pnas.1009219107; pmid: 21127269
18. J. D. Termine, A. S. Posner, Amorphous/crystalline interrelationships in bone mineral. *Calcif. Tissue Res.* **1**, 8–23 (1967). doi: 10.1007/BF02008070; pmid: 6060147
19. E. R. Wise *et al*., The organic-mineral interface in bone is predominantly polysaccharide. *Chem. Mater.* **19**, 5055–5057 (2007). doi: 10.1021/cm702054c
20. C. Jaeger *et al*., Investigation of the nature of the protein-mineral interface in bone by solid-state NMR. *Chem. Mater.* **17**, 3059–3061 (2005). doi: 10.1021/cm050492k
21. B. Wopenka, J. D. Pasteris, A mineralogical perspective on the apatite in bone. *Mater. Sci. Eng. C* **25**, 131–143 (2005). doi: 10.1016/j.msec.2005.01.008
22. C. Rey, C. Combes, C. Drouet, M. J. Glimcher, Bone mineral: Update on chemical composition and structure. *Osteoporos. Int.* **20**, 1013–1021 (2009). doi: 10.1007/s00198-009-0860-y; pmid: 19340505
23. H. Fernandez-Morán, A. Engström, Electron microscopy and x-ray diffraction of bone. *Biochim. Biophys. Acta* **23**, 260–264 (1957). doi: 10.1016/0006-3002(57)90327-X; pmid: 13412720
24. A. L. Arsenault, M. D. Grynpas, Crystals in calcified epiphyseal cartilage and cortical bone of the rat. *Calcif. Tissue Int.* **43**, 219–225 (1988). doi: 10.1007/BF02555138; pmid: 3145127
25. W. Traub, T. Arad, S. Weiner, Origin of mineral crystal growth in collagen fibrils. *Matrix* **12**, 251–255 (1992). doi: 10.1016/S0934-8832(11)80076-4; pmid: 1435508
26. M. J. Glimcher, Molecular biology of mineralized tissues with particular reference to bone. *Rev. Mod. Phys.* **31**, 359–393 (1959). doi: 10.1103/RevModPhys.31.359
27. S. Weiner, W. Traub, H. D. Wagner, Lamellar bone: Structure-function relations. *J. Struct. Biol.* **126**, 241–255 (1999). doi: 10.1006/jsbi.1999.4107; pmid: 10475685
28. E. A. McNally, H. P. Schwarcz, G. A. Botton, A. L. Arsenault, A model for the ultrastructure of bone based on electron microscopy of ion-milled sections. *PLOS ONE* **7**, e29258 (2012). doi: 10.1371/journal.pone.0029258; pmid: 22272230
29. N. Reznikov, R. Shahar, S. Weiner, Three-dimensional structure of human lamellar bone: The presence of two different materials and new insights into the hierarchical organization. *Bone* **59**, 93–104 (2014). doi: 10.1016/j.bone.2013.10.023; pmid: 24211799
30. E. McNally, F. Nan, G. A. Botton, H. P. Schwarcz, Scanning transmission electron microscopic tomography of cortical bone using Z-contrast imaging. *Micron* **49**, 46–53 (2013). doi: 10.1016/j.micron.2013.03.002; pmid: 23545162
31. B. A. Cressey, G. Cressey, A model for the composite nanostructure of bone suggested by high-resolution transmission electron microscopy. *Mineral. Mag.* **67**, 1171–1182 (2003). doi: 10.1180/0026461036760156
32. V. Jantou, M. Turmaine, G. D. West, M. A. Horton, D. W. McComb, Focused ion beam milling and ultramicrotomy of mineralised ivory dentine for analytical transmission electron microscopy. *Micron* **40**, 495–501 (2009). doi: 10.1016/j.micron.2008.12.002; pmid: 19157888
33. D. S. Bocciarelli, Morphology of crystallites in bone. *Calcif. Tissue Res.* **5**, 261–269 (1970). doi: 10.1007/BF02017554; pmid: 5433628
34. H. P. Schwarcz, The ultrastructure of bone as revealed in electron microscopy of ion-milled sections. *Semin. Cell Dev. Biol.* **46**, 44–50 (2015). doi: 10.1016/j.semcdb.2015.06.008; pmid: 26165821
35. J. P. R. O. Orgel, J. D. San Antonio, O. Antipova, Molecular and structural mapping of collagen fibril interactions. *Connect. Tissue Res.* **52**, 2–17 (2011). doi: 10.3109/03008207.2010.511353; pmid: 21182410
36. J. R. Kremer, D. N. Mastronarde, J. R. McIntosh, Computer visualization of three-dimensional image data using IMOD. *J. Struct. Biol.* **116**, 71–76 (1996). doi: 10.1006/jsbi.1996.0013; pmid: 8742726
37. N. Reznikov, R. Almany-Magal, R. Shahar, S. Weiner, Three-dimensional imaging of collagen fibril organization in rat circumferential lamellar bone using a dual beam electron microscope reveals ordered and disordered sub-lamellar structures. *Bone* **52**, 676–683 (2013). doi: 10.1016/j.bone.2012.10.034; pmid: 23153959
38. J. Serra, *Image Analysis and Mathematical Morphology* (Academic Press, 1983).
39. J. P. R. O. Orgel, A. V. Persikov, O. Antipova, Variation in the helical structure of native collagen. *PLOS ONE* **9**, e89519 (2014). doi: 10.1371/journal.pone.0089519; pmid: 24586843
40. M. J. Olszta *et al*., Bone structure and formation: A new perspective. *Mater. Sci. Eng. Rep.* **58**, 77–116 (2007). doi: 10.1016/j.mser.2007.05.001
41. N. Reznikov, J. A. M. Steele, P. Fratzl, M. M. Stevens, A materials science vision of extracellular matrix mineralization. *Nat. Rev. Mater.* **1**, 16041 (2016). doi: 10.1038/natrevmats.2016.41; pmid: 24193662
42. M. J. Duer, The contribution of solid-state NMR spectroscopy to understanding biomineralization: Atomic and molecular structure of bone. *J. Magn. Reson.* **253**, 98–110 (2015). doi: 10.1016/j.jmr.2014.12.011; pmid: 25797009
43. Y. Wang *et al*., Water-mediated structuring of bone apatite. *Nat. Mater.* **12**, 1144–1153 (2013). doi: 10.1038/nmat3787; pmid: 24193662
44. M. D. McKee, M. T. Kaartinen, in *Aging, Osteoporosis and Dental Implants*, G. Zarb, U. Lekholm, T. Albrektsson, H. Tenenbaum, Eds. (Quintessence, Carol Stream, IL, 2002), pp. 191–205.
45. S. Iijima, C. Brabec, A. Maiti, J. Bernholc, Structural flexibility of carbon nanotubes. *J. Chem. Phys.* **104**, 2089–2092 (1996). doi: 10.1063/1.470966
46. B. Bar-On, H. D. Wagner, New insights into the Young's modulus of staggered biological composites. *Mater. Sci. Eng. C* **33**, 603–607 (2013). doi: 10.1016/j.msec.2012.10.003; pmid: 25427462
47. M. A. Fernández-Seara, S. L. Wehrli, F. W. Wehrli, Diffusion of exchangeable water in cortical bone studied by nuclear magnetic resonance. *Biophys. J.* **82**, 522–529 (2002). doi: 10.1016/S0006-3495(02)75417-9; pmid: 11751339
48. J. S. Nyman, Q. Ni, D. P. Nicolella, X. Wang, Measurements of mobile and bound water by nuclear magnetic resonance correlate with mechanical properties of bone. *Bone* **42**, 193–199 (2008). doi: 10.1016/j.bone.2007.09.049; pmid: 17964874
49. L. B. Gower, Biomimetic model systems for investigating the amorphous precursor pathway and its role in biomineralization. *Chem. Rev.* **108**, 4551–4627 (2008). doi: 10.1021/cr800443h; pmid: 19006398
50. J. Mahamid *et al*., Mapping amorphous calcium phosphate transformation into crystalline mineral from the cell to the bone in zebrafish fin rays. *Proc. Natl. Acad. Sci. U.S.A.* **107**, 6316–6321 (2010). doi: 10.1073/pnas.0914218107; pmid: 20308589
51. M. D. McKee, M. Murshed, M. T. Kaartinen, in *Mineralized Tissues in Oral and Craniofacial Science: Biological Principles and Clinical Correlates*, L. K. McCauley, M. J. Somerman, Eds. (Wiley, 2012), pp. 99–109.
52. L. Bertinetti *et al*., Osmotically driven tensile stress in collagen-based mineralized tissues. *J. Mech. Behav. Biomed. Mater.* **52**, 14–21 (2015). doi: 10.1016/j.jmbbm.2015.03.010; pmid: 25862347
53. D. R. Eyre, I. R. Dickson, K. Van Ness, Collagen cross-linking in human bone and articular cartilage. Age-related changes in the content of mature hydroxypyridinium residues. *Biochem. J.* **252**, 495–500 (1988). doi: 10.1042/bj2520495; pmid: 3415669
54. T. Wess *et al*., Microfocus small angle X-ray scattering reveals structural features in archaeological bone samples: Detection of changes in bone mineral habit and size. *Calcif. Tissue Int.* **70**, 103–110 (2002). doi: 10.1007/s002230020045; pmid: 11870416
55. V. B. Rosen, L. W. Hobbs, M. Spector, The ultrastructure of anorganic bovine bone and selected synthetic hyroxyapatites used as bone graft substitute materials. *Biomaterials* **23**, 921–928 (2002). doi: 10.1016/S0142-9612(01)00204-6; pmid: 11771712
56. P.-Y. Chen, D. Toroian, P. A. Price, J. McKittrick, Minerals form a continuum phase in mature cancellous bone. *Calcif. Tissue Int.* **88**, 351–361 (2011). doi: 10.1007/s00223-011-9462-8; pmid: 21274705
57. J. M. Holmes, R. A. Beebe, Surface areas by gas adsorption on amorphous calcium phosphate and crystalline hydroxyapatite. *Calcif. Tissue Res.* **7**, 163–174 (1971). doi: 10.1007/BF02062604; pmid: 5560371
58. J. C. Elliott, Calcium phosphate biominerals. *Rev. Geochem. Mineral.* **48**, 427–453 (2002). doi: 10.2138/rmg.2002.48.11
59. A. S. Posner, R. A. Beebe, The surface chemistry of bone mineral and related calcium phosphates. *Semin. Arthritis Rheum.* **4**, 267–291 (1975). doi: 10.1016/0049-0172(75)90013-X; pmid: 1091977
60. H. H. Mitchell, T. S. Hamilton, F. R. Steggerda, H. W. Bean, The chemical composition of the adult human body and its bearing on the biochemistry of growth. *J. Biol. Chem.* **158**, 623 (1945).
61. J. D. Currey, *Bones: Structure and Mechanics* (Princeton Univ. Press, ed. 2, 2002).
62. C. Havers, *Osteologia Nova* (Samuel Smith, London, 1691).
63. S. Weiner, H. D. Wagner, The material bone: Structure-mechanical function relations. *Annu. Rev. Mater. Sci.* **28**, 271–298 (1998). doi: 10.1146/annurev.matsci.28.1.271
64. P. Pearce, *Structure in Nature Is a Strategy for Design* (MIT Press, 1990).
65. J. Mayer, L. A. Giannuzzi, T. Kamino, J. Michael, TEM sample preparation and FIB-induced damage. *MRS Bull.* **32**, 400–407 (2007). doi: 10.1557/mrs2007.63
66. D. B. Carlson, J. E. Evans, in *The Transmission Electron Microscope*, K. Maaz, Ed. (InTech, 2012), pp. 85–97.
67. P. A. Midgley, M. Weyland, 3D electron microscopy in the physical sciences: The development of Z-contrast and EFTEM tomography. *Ultramicroscopy* **96**, 413–431 (2003). doi: 10.1016/S0304-3991(03)00105-0; pmid: 12871805
68. L. Lari, I. Wright, E. D. Boyes, DIY tomography sample holder. *J. Phys. Conf. Ser.* **644**, 012013 (2015). doi: 10.1088/1742-6596/644/1/012013
69. M. D. McKee *et al*., Effects of fixation and demineralization on the retention of bone phosphoprotein and other matrix components as evaluated by biochemical analyses and quantitative immunocytochemistry. *J. Bone Miner. Res.* **6**, 937–945 (1991). doi: 10.1002/jbmr.5650060907; pmid: 1789141
70. J. Schindelin *et al*., Fiji: An open-source platform for biological-image analysis. *Nat. Methods* **9**, 676–682 (2012). doi: 10.1038/nmeth.2019; pmid: 22743772
71. N. Reznikov, H. Chase, V. Brumfeld, R. Shahar, S. Weiner, The 3D structure of the collagen fibril network in human trabecular bone: Relation to trabecular organization. *Bone* **71**, 189–195 (2015). doi: 10.1016/j.bone.2014.10.017; pmid: 25445457
72. J. P. R. O. Orgel, T. J. Wess, A. Miller, The in situ conformation and axial location of the intermolecular cross-linked non-helical telopeptides of type I collagen. *Structure* **8**, 137–142 (2000). doi: 10.1016/S0969-2126(00)00089-7; pmid: 10673433
73. J. P. R. O. Orgel, A. Eid, O. Antipova, J. Bella, J. E. Scott, Decorin core protein (decoron) shape complements collagen fibril surface structure and mediates its binding. *PLOS ONE* **4**, e7028 (2009). doi: 10.1371/journal.pone.0007028; pmid: 19753304

ACKNOWLEDGMENTS

We thank C. Boig for support with sample preparation; C. Vacar (FEI) for helpful discussions on tomogram segmentations; T. Roncal-Herrero for support with STEM imaging (R.K. and N.R.); J. O. P. Orgel (Illinois Institute of Technology), O. Smirnov (Petersburg Nuclear Physics Institute), S. Weiner (Weizmann Institute of Science), and M. D. McKee (McGill University) for critical reading of this manuscript; the direct-care teams at Charing Cross Hospital for consenting patients and collecting tissue samples; the patients who agreed to donate tissue for research; the Imperial College Healthcare National Health Service (NHS) staff; G. A. Thomas and Imperial College Tissue Bank staff who helped with the collection of the samples; R. L. Abel (Imperial College London) for sharing samples; J. Orgel for collagen panels III and IV in Fig. 8; and Harvey Flower Electron Microscopy Suite, Imperial College London, for using their characterization facilities. **Funding:** This work was carried out in the framework of the projects SMILEY (FP7-NMP-2012-SMALL-6-310637) and the UK Engineering and Physical Sciences Research Council (EPSRC) (grant EP/I001514/1), funding the Material Interface with Biology (MIB) consortium (R.K. and M.B.). M.B. acknowledges support from the 4D LABS shared research facility, which is supported by the Canada Foundation for Innovation (CFI), British Columbia Knowledge Development Fund (BCKDF), Western Economic Diversification Canada, and Simon Fraser University. M.M.S. acknowledges funding support from a Wellcome Trust Senior Investigator Award (098411/Z/12/Z) N.R. gratefully acknowledges support from the Value-In-People Award from the Wellcome Trust Institutional Strategic Support Fund (097816/Z/11/B). The Imperial College NHS Tissue Bank is funded by the National Institute for Health Research–Biomedical Research Centres (NIHR-BRC), UK. **Author contributions:** R.K. conceived the idea and planned the experiments. M.B., L.L., N.R., and R.K. carried out the experiments. N.R. and R.K. reconstructed and processed experimental data. R.K. generated the model presented. All authors discussed the results and contributed to the final manuscript. **Competing interests:** The authors declare no competing interests. **Data and materials availability:** Data are available online at DOI: 10.5281/zenodo.1196033 All (other) data needed to evaluate the conclusions in the paper are present in the paper or the supplementary materials.

SUPPLEMENTARY MATERIALS

www.sciencemag.org/content/360/6388/eaao2189/suppl/DC1
Figs. S1 to S4
Movies S1 to S4

27 June 2017; accepted 8 March 2018
10.1126/science.aao2189

RESEARCH ARTICLE

STRUCTURAL BIOLOGY

Activation mechanism of a human SK-calmodulin channel complex elucidated by cryo-EM structures

Chia-Hsueh Lee and Roderick MacKinnon*

Small-conductance Ca^{2+}-activated K^+ (SK) channels mediate neuron excitability and are associated with synaptic transmission and plasticity. They also regulate immune responses and the size of blood cells. Activation of SK channels requires calmodulin (CaM), but how CaM binds and opens SK channels has been unclear. Here we report cryo–electron microscopy (cryo-EM) structures of a human SK4-CaM channel complex in closed and activated states at 3.4- and 3.5-angstrom resolution, respectively. Four CaM molecules bind to one channel tetramer. Each lobe of CaM serves a distinct function: The C-lobe binds to the channel constitutively, whereas the N-lobe interacts with the S4-S5 linker in a Ca^{2+}-dependent manner. The S4-S5 linker, which contains two distinct helices, undergoes conformational changes upon CaM binding to open the channel pore. These structures reveal the gating mechanism of SK channels and provide a basis for understanding SK channel pharmacology.

Ca^{2+} is arguably one of the most crucial cellular signals, and it affects virtually every aspect of a cell. Gárdos first discovered a link between Ca^{2+} and K^+ permeability in 1958 when he recognized that Ca^{2+} can enhance the K^+ permeability of human erythrocytes (*1*). Since then, several studies have reported a similar "Gárdos effect" in various types of neurons (*2*). We now know that this effect is mediated by a family of Ca^{2+}-activated K^+ channels (*3*). These channels were historically cataloged as intermediate- or small-conductance Ca^{2+}-activated K^+ (SK) channels to distinguish them from the well-studied large-conductance Ca^{2+}-activated K^+ (BK) channels (*4*–*8*). Widely expressed in neurons of the central nervous system, SK channels contribute to the after-hyperpolarization following an action potential and mediate the intrinsic excitability of neurons (*9*). SK channels are also implicated in synaptic transmission and plasticity. In T lymphocytes, SK channels modulate the activation of immune responses (*7*, *10*, *11*). In erythrocytes, they regulate cell volume, and their dysfunction causes cell dehydration and hemolysis (*8*, *12*–*15*).

Given the physiological importance of SK channels, it is important to understand how they work at a molecular level. Although both SK and BK channels are activated by Ca^{2+}, their amino acid sequence identities are low, and their channel gating mechanisms are completely different. Ca^{2+} ions open BK channels directly, whereas Ca^{2+} ions open SK channels via calmodulin (CaM) (*4*, *16*). CaM opens SK channels in a cooperative manner with high Ca^{2+} sensitivity (median effective concentration, around 100 to 400 nM) (*4*–*7*, *17*). The structures of BK channels have been studied in molecular detail (*18*, *19*), but the Ca^{2+}-CaM gating mechanism of SK channels has remained a mystery. To understand the structural basis of gating in SK channels, we determined structures of a full-length human SK channel in closed and activated states by using single-particle cryo–electron microscopy (cryo-EM).

Characterization of a human SK4-CaM channel complex

After an initial screening of 25 SK proteins from different species by fluorescence-detection size-exclusion chromatography (*20*), we identified human SK4 (also known as IK, $K_{Ca}3.1$, KCNN4, or Gárdos channel) as a promising candidate for structural studies. We then expressed and purified human SK4 from mammalian cells. Purified full-length SK4 channels, although having a predicted molecular mass of 48 kDa, migrate at about 37 kDa by SDS–polyacrylamide gel electrophoresis (SDS-PAGE) (Fig. 1A). CaM was co-purified with the channel in both the presence and absence of Ca^{2+}. This observation suggests that Ca^{2+} is not necessary for the SK-CaM interaction and that CaM constitutively binds to the channel.

To examine the function of the purified SK4-CaM complex, we reconstituted it into liposomes and monitored K^+ flux by means of a fluorescence-based assay (*21*). Proteoliposomes were reconstituted with a high concentration of K^+ (150 mM KCl), then diluted into K^+-free solution while ionic strength was maintained with 150 mM NaCl. In the presence of Ca^{2+}, a fluorescence decrease was observed owing to K^+ efflux out of the liposomes (Fig. 1A), which could be inhibited using two different SK4 channel blockers, NS6180 and senicapoc (*22*, *23*). Thus, the purified

Laboratory of Molecular Neurobiology and Biophysics, The Rockefeller University, Howard Hughes Medical Institute, 1230 York Avenue, New York, NY 10065, USA.
***Corresponding author. Email: mackinn@rockefeller.edu**

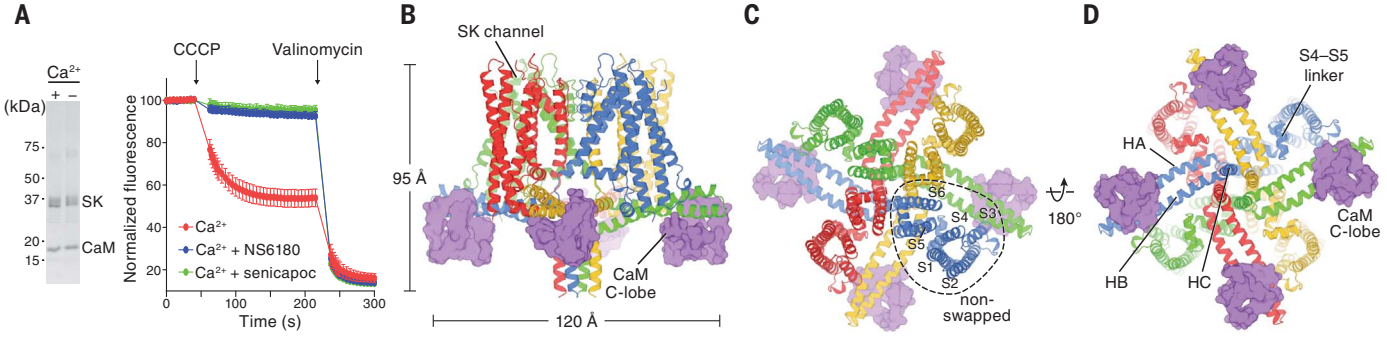

Fig. 1. Functional characterization and architecture of the Ca^{2+}-free SK-CaM channel complex. (**A**) Purified SK-CaM channel complex and fluorescence-based liposome flux assay. Left, SK-CaM complex in the presence or absence of Ca^{2+} (2 mM $CaCl_2$ or 5 mM EGTA), analyzed by SDS-PAGE. Right, SK-CaM complex–mediated flux. Fluorescence changes due to K^+ flux were monitored over time (mean ± SEM; n = 4 to 8). Proteoliposomes in the presence of 2 mM $CaCl_2$ showed robust flux, which could be blocked by 10 μM NS6180 or senicapoc. CCCP, carbonyl cyanide m-chlorophenylhydrazone. (**B** to **D**) Cryo-EM structure of the Ca^{2+}-free SK-CaM complex. Each channel subunit is shown in a different color. Purple, CaM C-lobe in surface representation.

SK4-CaM protein complex (hereafter referred to as SK-CaM) recapitulates the functional Ca^{2+}-activated K^+ efflux and pharmacological inhibition characteristic of native channels.

Architecture of Ca^{2+}-free SK-CaM channel complex

We first determined the structure of SK-CaM in the absence of Ca^{2+} to a resolution of 3.4 Å (figs. S1 and S2). We found that four SK subunits form a fourfold-symmetric tetramer that is ~95 Å in length and 120 Å in width when viewed from within the plane of the membrane (Fig. 1B). Transmembrane helices S5 and S6 form the ion channel pore, which is surrounded by membrane-embedded helices S1 to S4. The domain comprising these four helices interacts with the pore domain from the same subunit (Fig. 1C). This arrangement is similar to that of the BK channel (also known as Slo1) but different from that of domain-swapped K_v1 to K_v7 channels, where helices S1 to S4 interact with a neighboring pore domain (*18*, *24*, *25*).

At the C-terminal end of S6, the helix unwinds near the inner leaflet of the cell membrane. This allows the polypeptide to make a sharp turn before two helices, HA and HB, that run almost parallel to the membrane plane. HB is followed by the HC helix (Fig. 1D). The HC helices from four SK subunits make up a coiled coil located at the center of the channel, which is important for channel assembly and trafficking (*26*, *27*). Because this region of the channel is flexible, the local structure is not as well resolved as other regions, and the last 41 residues are invisible in the structure. Consistent with previous studies (*28*, *29*), the peripheral ends of HA and HB form the binding site for the CaM C-lobes, which are visible in the cryo-EM map (Fig. 1D). On the basis of light scattering and analytical ultracentrifugation experiments performed on CaMs and channel fragments, Halling *et al.* suggested that two to eight CaM molecules may bind to one channel (*30*). In the context of a full-length channel, we observed that one CaM binds to one SK subunit, resulting in four CaMs per channel tetramer.

Dynamic CaM N-lobe as a Ca^{2+} sensor

When C_4 symmetry was imposed during cryo-EM reconstruction, the CaM N-lobes of the channel complex exhibited poor density, which precluded model building of this portion of CaM (Fig. 1, B to D, and fig. S1C). This suggests that the N-lobes exhibit static disorder, consistent with high mobility in the absence of Ca^{2+}. When the structure was reconstructed without imposing symmetry, only one of the four CaM N-lobes was visible (fig. S1C). To analyze the static disorder of the CaM N-lobes further, we expanded the data set and reoriented each subunit onto a single position according to the C_4 point group (*31*). We then performed focused classification and subsequent refinement (fig. S3A). Through this strategy, three distinct conformations of CaM with improved N-lobe density were identified (Fig. 2).

In these reconstructions, the differences in the CaM C-lobes are subtle, resulting from a slight sliding along the HA and HB helices (fig. S3, B and C). In contrast, the CaM N-lobes exhibit large positional variations. It is evident that the N-lobe can swing from the periphery of the channel (Fig. 2, red) all the way to the center of the channel, close to the coiled coil (Fig. 2, blue). The N- and C-lobes of CaM are connected by a central linker, which has the capacity to maintain

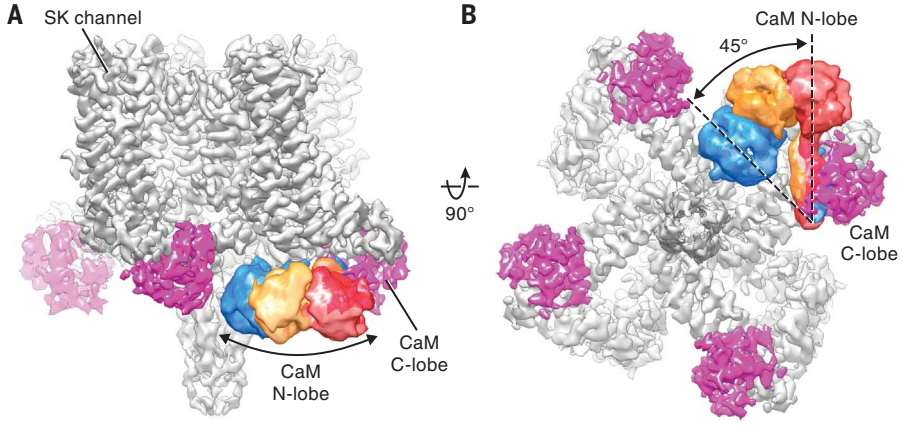

Fig. 2. Conformational dynamics of CaM N-lobe. (**A** and **B**) Cryo-EM reconstruction of the Ca^{2+}-free SK-CaM complex. CaM N-lobe densities (blue, yellow, and red) from three classes after focused classification are superimposed on the consensus 3.4-Å-resolution map.

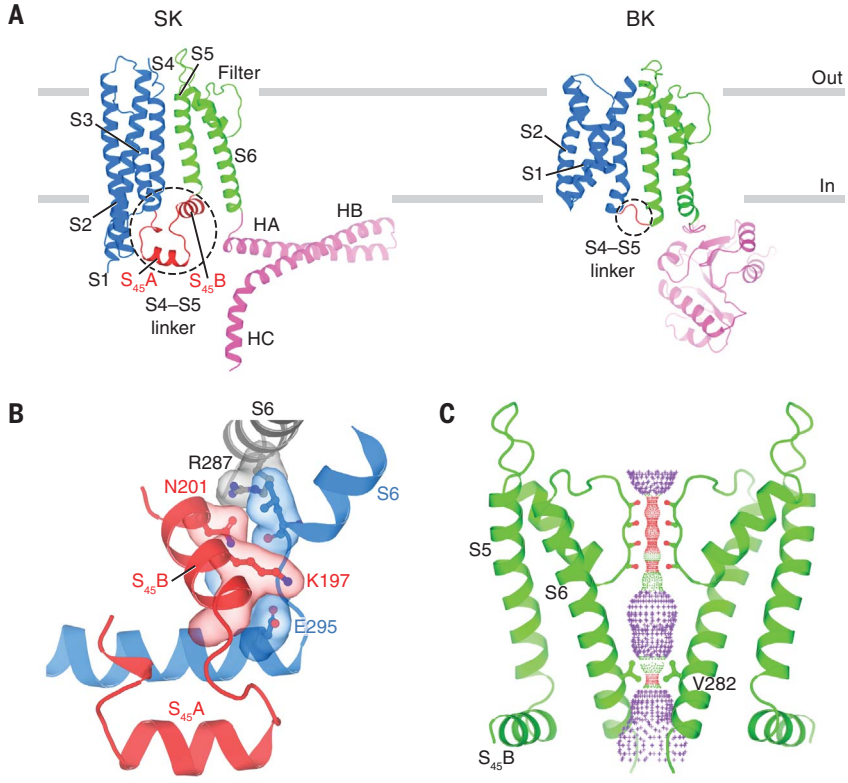

Fig. 3. Transmembrane domain and ion channel pore. (**A**) Comparison of single SK and BK subunits. Gray bars represent approximate boundaries of the membrane bilayer. For clarity, only part of the BK intracellular domain is shown (Protein Data Bank ID, 5TJI). (**B**) Interface between the $S_{45}B$ and S6 helices, shown in surface representation. Gray, S6 helix from the same subunit as $S_{45}B$. Blue, S6 and HA helices from an adjacent subunit. (**C**) Channel pore with only two subunits shown for clarity. Pore radius: red, <1.15 Å; green, 1.15 to 2.30 Å; purple, >2.30 Å. Throughout the figures, single-letter abbreviations for the amino acid residues are as follows: A, Ala; C, Cys; D, Asp; E, Glu; G, Gly; I, Ile; K, Lys; L, Leu; N, Asn; Q, Gln; R, Arg; S, Ser; T, Thr; V, Val; and Y, Tyr.

an α-helical structure or unwind into a loop, allowing CaM to adopt multiple conformations (*32*). Under Ca^{2+}-free conditions in SK-CaM, this flexible linker permits the N-lobe to undergo long-range, rigid-body–like motions, traveling from the bottom of the S2 helix to the bottom of the S4-S5 linker (Figs. 2B and 1D), while the C-lobe maintains its interaction with the HA and HB helices (fig. S3C). Previous mutagenesis experiments suggested that the two lobes of CaM serve distinct functions in the SK channel complex (*33*–*35*): The C-lobe interacts with SK channels in a Ca^{2+}-independent manner, whereas the N-lobe senses Ca^{2+} and gates the channel. Our structure supports these findings by demonstrating a permanent bound CaM C-lobe and a dynamic N-lobe. This molecular plasticity of the N-lobe seems ideal for rapid detection and response to local Ca^{2+} signals.

Transmembrane domain and ion conduction pore

Although the SK channel has a similar topology to the BK channel, we noticed two interesting differences. First, the S1 and S2 helices in SK are much longer than those in BK (*18*). Each about 60 Å in length, S1 and S2 in SK extend beyond the membrane boundary, into the cytoplasmic space (Fig. 3A). The second difference involves the S4-S5 linker, which in SK consists of two α-helices, $S_{45}A$ and $S_{45}B$, rather than the short turn observed in BK and other non–domain-swapped members of the six-transmembrane ion channel superfamily, including the K_v10 to K_v12, Slo2, and HCN channels (*18*, *36*–*39*). In voltage-gated ion channels—whether domain-swapped or not—the S4-S5 linker plays a critical role in channel gating by coupling movements of the voltage sensor to opening of the pore. But SK is voltage-insensitive (*5*, *6*, *17*). Its particular S4-S5 linker structure is apparently suited to confer CaM-mediated Ca^{2+} sensitivity to the SK channel gate.

$S_{45}B$ is wedged in between HA and S6, thus providing lateral contacts between the pore and the cytoplasmic structural elements that ultimately attach CaM to the channel (Fig. 3B). Hydrogen bonds formed between Lys^{197} on $S_{45}B$ and Glu^{295} on HA from a neighboring subunit, and between Asn^{201} on $S_{45}B$ and Arg^{287} on S6 from the same subunit, appear to "glue" these structural elements together. Mutations of Arg^{287}, possibly by interfering with this interaction, change the intrinsic open probability of SK channels in the absence of Ca^{2+} (*40*). The inter-subunit connectivity of this interface (each S4-S5 linker interacts structurally with S6 from two subunits) could be the structural underpinning of the high cooperativity of Ca^{2+} activation in SK (*4*–*7*, *17*).

In the absence of Ca^{2+}, the SK channel is functionally closed. The structure determined in the absence of Ca^{2+} also appears closed. Residues Val^{282} from each of the four S6 helices form a constricted gate with a radius less than 1 Å (Fig. 3C). This finding is in good agreement with studies that have used thiol-reactive methanethiosulfonate (MTS) reagents to assess the reactivity of site-directed cysteine residues placed along the S6 helix (*41*–*44*). Furthermore, it has been shown that replacement of Val^{282} by Gly produces a "leaky" channel that conducts current in the absence of Ca^{2+} (*45*). The structure also provides information on the molecular basis of the channelopathy known as hereditary xerocytosis, a type of hemolytic anemia associated with human SK4 mutations Val^{282}→Glu and Val^{282}→Met (*14*, *15*, *46*, *47*). These two gain-of-function mutations involve precisely that residue which forms the narrowest constriction within the pore of the closed SK channel.

Structures of Ca^{2+}-bound SK-CaM channel complex

To visualize an open conformation and understand how Ca^{2+} activation occurs, we determined the structure of the SK-CaM complex in the presence of Ca^{2+} to a resolution of 3.5 Å (figs. S4 and S5). We again observed that four CaMs bind to a channel tetramer (Fig. 4, A and B), just as in the Ca^{2+}-free state. However, the density for the CaM N-lobe was significantly improved relative to that in the Ca^{2+}-free structure, permitting the building of an entire CaM model. Ca^{2+} binding alters the conformation of the CaM N-lobe and causes it to attach firmly to the channel. The structure reveals several previously unidentified interactions between Ca^{2+}-bound CaM and the channel subunits. First, cytosolic portions of the S1 and S2 helices, which extend into the cytoplasmic space, directly contact CaM (Fig. 4, C and D). Such interactions provide a plausible justification for the extraordinary length of S1 and S2. Second, the N-lobe interacts with HA and HC from an adjacent subunit (Fig. 4, C and D, yellow subunit). Through these newly formed interactions, Ca^{2+}-bound CaM and the SK channel form an extensive interaction network, with each CaM molecule communicating with three channel subunits (Fig. 4, C and D, green, blue, and yellow subunits). This distributed interaction could potentially permit conformational changes brought about through the binding of one CaM N-lobe to influence the neighboring CaM molecules. It seems likely that this structural property could give rise, at least in part, to the high cooperativity that is characteristic of SK channel activation.

Two major differences between the full-length cryo-EM structure and the previously determined crystal structure of CaM in complex with channel fragments (HA, HB, and part of HC) (*29*) deserve attention. First, in the cryo-EM structure, the CaM N-lobe binding pocket recognizes $S_{45}A$, the first helix of the S4-S5 linker (Fig. 4, C and D), whereas in the crystal structure, the N-lobe binds to HC rather than $S_{45}A$ ($S_{45}A$ was not included in the crystallization construct). Many of the residues forming the HC binding site in the crystal structure are buried at the center of the coiled coil in the cryo-EM structure (fig. S6). The buried

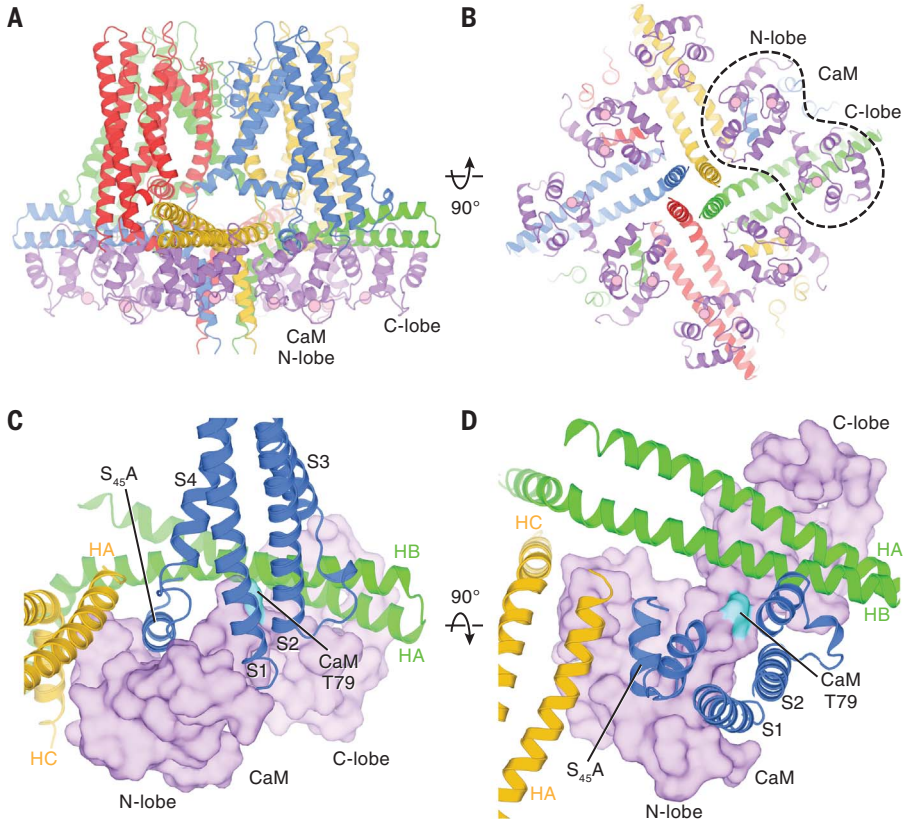

Fig. 4. Structure of the Ca^{2+}-bound SK-CaM channel complex. (**A** and **B**) Structure of the Ca^{2+}-bound SK-CaM channel complex, colored as in Fig. 1 (purple, CaM). Ca^{2+} ions are shown as pink spheres. (**C** and **D**) Interactions between CaM (surface representation) and SK subunits.

residues are therefore likely not accessible to the CaM N-lobe in the full-length channel. We conclude that $S_{45}A$ is the functional CaM N-lobe binding site.

Second, in the crystal structure, the channel fragments and CaMs form a dimeric, twofold-symmetric structure. On the basis of that observation, a mechanism was proposed in which channel activation breaks down the fourfold symmetry, causing the channel to become a twofold-symmetric dimer-of-dimers. This transition was proposed to generate a rotary force to open the channel (*29*). Although this was a reasonable idea given the structures of channel fragments, the full-length structure shows that the activated SK-CaM complex remains fourfold-symmetric throughout (Fig. 4, A and B, and fig. S4C).

Structural basis for channel activation

Although the amino acid sequence of $S_{45}A$ does not correspond to a known canonical CaM-binding motif (*48*), $S_{45}A$ is highly conserved, and residues directly facing the CaM N-lobe pocket (Ala, Ser, and Leu) are identical across the SK channel family (Fig. 5A), suggesting that this region is crucial to channel function. When the CaM N-lobe binds, it pulls the $S_{45}A$ helix downward and displaces it by 4 Å (as measured at the C-terminal end of $S_{45}A$) (Fig. 5B, activated state I). This in turn causes $S_{45}B$ to move outward, away from the pore axis. Because $S_{45}B$ is tightly coupled to the pore-lining S6 helix (Fig. 3B), this displacement of $S_{45}B$ expands the S6 helical bundle and enlarges the radius of the cytoplasmic pore entrance to 5 Å (Fig. 5, B and D). In addition, the channel gate formed by Val^{282} expands. Even after this expansion, the Val^{282} side chain still constricts the pore to a radius of ~1.6 Å (Fig. 5, C and D), which is too narrow to permit the flow of hydrated K^+ ions. In this activated state I, the channel is undergoing movements toward opening, although the pore appears to remain nonconductive. The existence of such a channel conformation is supported by functional studies, which indicate that the maximum channel-open probability of SK4 remains low (*49*, *50*), usually 0.1 to 0.3, at saturating concentrations of Ca^{2+}. Thus, even under maximal stimulation, the channel is still more often in a nonconductive conformation.

Through three-dimensional classification, we identified another activated state (Fig. 5, B to D, activated state II) and determined the corresponding structure at moderate resolution (4.7 Å) (figs. S4C and S7). Compared with activated state I, the CaM N-lobe binding more dramatically rearranges $S_{45}A$, $S_{45}B$, and S6 in state II. $S_{45}A$ and $S_{45}B$ are displaced by an additional 2 Å (Fig. 5B and fig. S7D), which causes S6 to move further away from the pore axis. This expands the channel gate at the level of Val^{282} to a radius of ~3.5 Å (Fig. 5, C and D), which would allow permeation of partially hydrated K^+ ions. State II is less populated than state I (fig. S4C), which is consistent with open probability measurements showing that activated channels occupy a conductive state with lower probability than they occupy the nonconductive states. These analyses reinforce the notion that activated state II likely represents an open, conductive state of SK channels, although future higher-resolution structures will be required to reach an unambiguous conclusion.

Our structures lead us to propose that the binding of the CaM N-lobe to $S_{45}A$ initiates channel activation. This proposal predicts that preventing the interaction between CaM and $S_{45}A$ would preclude channel opening. To test this prediction, we introduced a cysteine at position 181 on the $S_{45}A$ helix. Ser^{181} is located in the middle of $S_{45}A$ and points directly into the CaM N-lobe pocket. We reasoned that labeling this position with a negative-charged MTS reagent

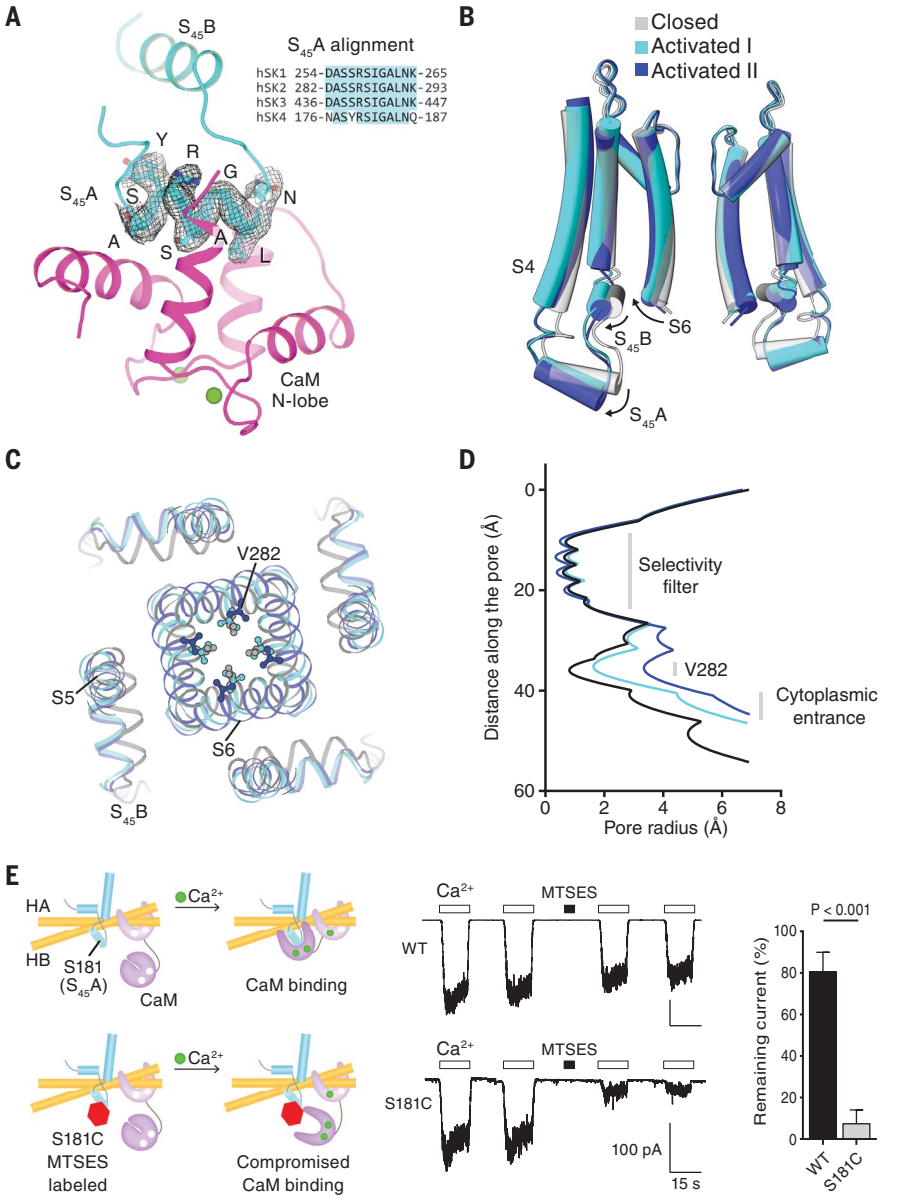

Fig. 5. Channel activation by Ca^{2+}-bound CaM. (**A**) Binding of CaM N-lobe to SK $S_{45}A$. The cryo-EM density of $S_{45}A$ is shown (from the 3.5-Å-resolution map of the Ca^{2+}-bound SK-CaM complex). Ca^{2+} ions are shown as green spheres. Inset, the amino acid sequence alignment of $S_{45}A$ from four human SK channel subtypes. The region highlighted in cyan is absolutely conserved. (**B**) Conformational changes in the S4-S5 linker and pore upon CaM N-lobe binding. Structures of different states are aligned at the selectivity filter. (**C**) Top-down view of conformational changes in the pore, shown from the extracellular side. (**D**) Radius of the pore in the activated states versus the closed state. The radius is plotted as a function of the distance along the pore axis. V282 defines the narrowest constriction site of the cytoplasmic gate. (**E**) Preventing channel activation by compromising the CaM N-lobe–$S_{45}A$ interaction. 10 μM Ca^{2+} or 2 mM MTSES was applied as indicated. Quantification of remaining currents after MTSES labeling is also shown (mean ± SD; n = 4 to 5; Student's t test). WT, wild type.

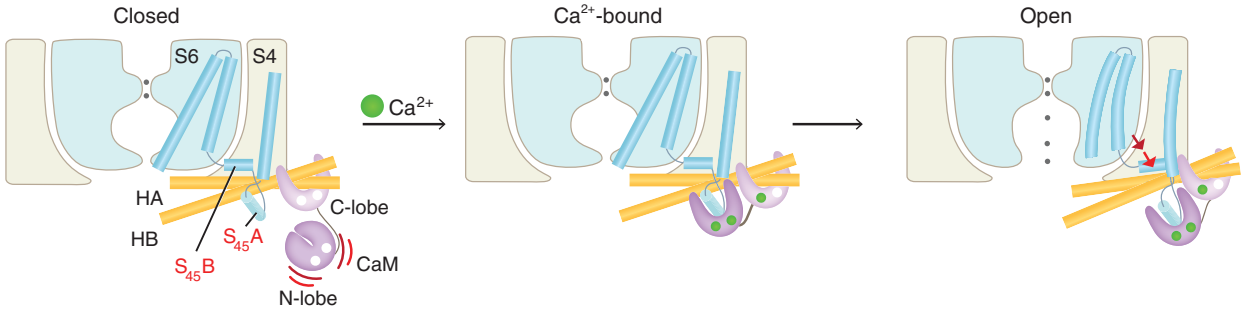

Fig. 6. Gating mechanism of the SK channel. In the absence of Ca^{2+} (left panel), the SK channel is closed. The CaM C-lobe stays associated with the channel, whereas the CaM N-lobe barely binds to the channel. The very flexible N-lobe can adopt multiple conformations, but its binding pocket remains closed (*60*, *61*). When Ca^{2+} binds to the CaM N-lobe (middle panel), the lobe rearranges into a more open conformation, allowing it to interact with $S_{45}A$. The N-lobe pulls the $S_{45}A$ helix downward, which displaces $S_{45}B$ away from the pore axis (right panel). This expands the S6 helical bundle and eventually opens the pore.

(MTSES) would reduce the affinity of the CaM N-lobe and thereby impede N-lobe binding (Fig. 5E). After exposure to MTSES, the current from the Ser^{181}→Cys mutant channels diminished significantly (7 ± 7% remaining current), whereas the current from wild-type channels showed only a small reduction (81 ± 9% remaining current). These results support the proposed role of the CaM N-lobe–$S_{45}A$ interaction in channel gating.

Discussion

On the basis of the structural and functional analyses presented here, we propose a new model for SK channel activation (Fig. 6). In the absence of Ca^{2+}, CaM preassociates with the channel through its C-lobe. Meanwhile, the CaM N-lobe maintains only weak interactions with the channel and is conformationally flexible. In this resting state, the channel pore is closed. In the presence of increasing Ca^{2+} concentrations, the CaM N-lobe binds to Ca^{2+}. This triggers a conformational change, which increases the affinity of the N-lobe for the $S_{45}A$ helix within the S4-S5 linker. Upon CaM binding, $S_{45}A$ is displaced downward (toward the cytoplasm), which causes $S_{45}B$ to move away from the pore axis. Such a movement rearranges the S6 helices, permitting the pore to open. As an aid to visualizing the structural transition of SK channel activation, we animated the CaM movement and the corresponding conformational changes in the SK channel upon Ca^{2+} binding. This animation illustrates how CaM opens the SK channel and encapsulates the activation model (movie S1).

Several studies have shown that the phosphorylation state of CaM regulates SK channel activity (*51*–*53*). When CaM is phosphorylated at position Thr^{79}, the apparent Ca^{2+} sensitivity of the SK channel is reduced, causing the channel to close more rapidly (*52*). One hypothesis to explain this is that Thr^{79} phosphorylation disrupts interactions between lipids and the SK-CaM complex (*53*). Our study provides a basis for interpreting these functional studies and perhaps for building on the hypothesis. Thr^{79} is positioned within the hinge that connects the CaM N- and C-lobes, which is wedged between S2 and HB and faces toward the lipid membrane (Fig. 4, C and D). The addition of a phosphate group to Thr^{79} would seem likely to influence the conformation of the surrounding channel subunits and/or influence lipid-channel interactions.

Riluzole, the first U.S. Food and Drug Administration–approved medication for amyotrophic lateral sclerosis, has been suggested to act through SK channels (*54*, *55*). Riluzole and related compounds (e.g., 1-EBIO) potentiate SK channel activity and are proposed, on the basis of crystal structures, to bind to the interface between the CaM N-lobe and HC (*56*–*59*). Because our results redefine the native CaM N-lobe binding interface, we suggest that SK channel potentiators may instead bind in between the CaM N-lobe and $S_{45}A$ (fig. S8). Such a possibility needs further exploration.

This study provides a plausible mechanism of SK channel activation and highlights the role of the S4-S5 linker in coupling Ca^{2+}-induced CaM binding to channel opening. Our structures also provide a foundation for the development of therapeutic agents targeting SK channels.

REFERENCES AND NOTES

1. G. Gárdos, *Biochim. Biophys. Acta* **30**, 653–654 (1958).
2. J. P. Adelman, *Channels* **10**, 1–6 (2016).
3. L. K. Kaczmarek *et al.*, *Pharmacol. Rev.* **69**, 1–11 (2017).
4. X. M. Xia *et al.*, *Nature* **395**, 503–507 (1998).
5. T. M. Ishii *et al.*, *Proc. Natl. Acad. Sci. U.S.A.* **94**, 11651–11656 (1997).
6. W. J. Joiner, L.-Y. Y. Wang, M. D. Tang, L. K. Kaczmarek, *Proc. Natl. Acad. Sci. U.S.A.* **94**, 11013–11018 (1997).
7. N. J. Logsdon, J. Kang, J. A. Togo, E. P. Christian, J. Aiyar, *J. Biol. Chem.* **272**, 32723–32726 (1997).
8. D. H. Vandorpe *et al.*, *J. Biol. Chem.* **273**, 21542–21553 (1998).
9. J. P. Adelman, J. Maylie, P. Sah, *Annu. Rev. Physiol.* **74**, 245–269 (2012).
10. M. D. Cahalan, K. G. Chandy, *Immunol. Rev.* **231**, 59–87 (2009).
11. S. Feske, H. Wulff, E. Y. Skolnik, *Annu. Rev. Immunol.* **33**, 291–353 (2015).
12. J. F. Hoffman *et al.*, *Proc. Natl. Acad. Sci. U.S.A.* **100**, 7366–7371 (2003).
13. R. Rapetti-Mauss *et al.*, *Blood* **126**, 1273–1280 (2015).
14. E. Glogowska, K. Lezon-Geyda, Y. Maksimova, V. P. Schulz, P. G. Gallagher, *Blood* **126**, 1281–1284 (2015).
15. I. Andolfo *et al.*, *Am. J. Hematol.* **90**, 921–926 (2015).
16. C. M. Fanger *et al.*, *J. Biol. Chem.* **274**, 5746–5754 (1999).
17. M. Köhler *et al.*, *Science* **273**, 1709–1714 (1996).
18. X. Tao, R. K. Hite, R. MacKinnon, *Nature* **541**, 46–51 (2017).
19. R. K. Hite, X. Tao, R. MacKinnon, *Nature* **541**, 52–57 (2017).
20. T. Kawate, E. Gouaux, *Structure* **14**, 673–681 (2006).
21. Z. Su, E. C. Brown, W. Wang, R. MacKinnon, *Proc. Natl. Acad. Sci. U.S.A.* **113**, 5748–5753 (2016).
22. D. Strøbæk *et al.*, *Br. J. Pharmacol.* **168**, 432–444 (2013).
23. J. W. Stocker *et al.*, *Blood* **101**, 2412–2418 (2003).
24. S. B. Long, E. B. Campbell, R. Mackinnon, *Science* **309**, 897–903 (2005).
25. J. Sun, R. MacKinnon, *Cell* **169**, 1042–1050.e9 (2017).
26. C. A. Syme *et al.*, *J. Biol. Chem.* **278**, 8476–8486 (2003).
27. D. Tuteja *et al.*, *Circ. Res.* **107**, 851–859 (2010).
28. R. Wissmann *et al.*, *J. Biol. Chem.* **277**, 4558–4564 (2002).
29. M. A. Schumacher, A. F. Rivard, H. P. Bächinger, J. P. Adelman, *Nature* **410**, 1120–1124 (2001).
30. D. B. Halling, S. A. Kenrick, A. F. Riggs, R. W. Aldrich, *J. Gen. Physiol.* **143**, 231–252 (2014).
31. S. H. W. Scheres, *Methods Enzymol.* **579**, 125–157 (2016).
32. H. Tidow, P. Nissen, *FEBS J.* **280**, 5551–5565 (2013).
33. J. E. Keen *et al.*, *J. Neurosci.* **19**, 8830–8838 (1999).
34. W.-S. Lee, T. J. Ngo-Anh, A. Bruening-Wright, J. Maylie, J. P. Adelman, *J. Biol. Chem.* **278**, 25940–25946 (2003).
35. W. Li, D. B. Halling, A. W. Hall, R. W. Aldrich, *J. Gen. Physiol.* **134**, 281–293 (2009).
36. R. K. Hite, R. MacKinnon, *Cell* **168**, 390–399.e11 (2017).
37. J. R. Whicher, R. MacKinnon, *Science* **353**, 664–669 (2016).
38. W. Wang, R. MacKinnon, *Cell* **169**, 422–430.e10 (2017).
39. C.-H. Lee, R. MacKinnon, *Cell* **168**, 111–120.e11 (2017).
40. W. Li, R. W. Aldrich, *Proc. Natl. Acad. Sci. U.S.A.* **108**, 5946–5953 (2011).
41. M. Simoes *et al.*, *J. Gen. Physiol.* **120**, 99–116 (2002).
42. A. Bruening-Wright, M. A. Schumacher, J. P. Adelman, J. Maylie, *J. Neurosci.* **22**, 6499–6506 (2002).
43. H. Klein *et al.*, *J. Gen. Physiol.* **129**, 299–315 (2007).
44. A. Bruening-Wright, W.-S. Lee, J. P. Adelman, J. Maylie, *J. Gen. Physiol.* **130**, 601–610 (2007).
45. L. Garneau *et al.*, *J. Biol. Chem.* **284**, 389–403 (2009).
46. R. Rapetti-Mauss, O. Soriani, H. Vinti, C. Badens, H. Guizouarn, *Haematologica* **101**, e431–e435 (2016).
47. A. Rivera *et al.*, *Am. J. Hematol.* **92**, E108–E110 (2017).
48. K. Mruk, B. M. Farley, A. W. Ritacco, W. R. Kobertz, *J. Gen. Physiol.* **144**, 105–114 (2014).
49. H. M. Jones *et al.*, *Channels* **1**, 80–91 (2007).
50. P. Morales *et al.*, *J. Gen. Physiol.* **142**, 37–60 (2013).
51. W. Bildl *et al.*, *Neuron* **43**, 847–858 (2004).
52. D. Allen, B. Fakler, J. Maylie, J. P. Adelman, *J. Neurosci.* **27**, 2369–2376 (2007).
53. M. Zhang *et al.*, *Nat. Chem. Biol.* **10**, 753–759 (2014).
54. Y.-J. Cao, J. C. Dreixler, J. J. Couey, K. M. Houamed, *Eur. J. Pharmacol.* **449**, 47–54 (2002).
55. M. Dimitriadi *et al.*, *J. Neurosci.* **33**, 6557–6562 (2013).
56. M. Zhang, J. M. Pascal, M. Schumann, R. S. Armen, J.-F. Zhang, *Nat. Commun.* **3**, 1021 (2012).
57. M. Zhang, J. M. Pascal, J.-F. Zhang, *Proc. Natl. Acad. Sci. U.S.A.* **110**, 4828–4833 (2013).
58. B. M. Brown, H. Shim, M. Zhang, V. Yarov-Yarovoy, H. Wulff, *Mol. Pharmacol.* **92**, 469–480 (2017).
59. Y.-W. Nam *et al.*, *Sci. Rep.* **7**, 17178 (2017).
60. M. Zhang, T. Tanaka, M. Ikura, *Nat. Struct. Biol.* **2**, 758–767 (1995).
61. H. Kuboniwa *et al.*, *Nat. Struct. Biol.* **2**, 768–776 (1995).

ACKNOWLEDGMENTS

We thank M. Ebrahim and J. Sotiris at the Evelyn Gruss Lipper Cryo-EM Resource Center of Rockefeller University for assistance with data collection and members of the MacKinnon and Jue Chen laboratories for helpful discussions. We gratefully acknowledge the support of NVIDIA Corporation with the donation of the Titan X Pascal GPU used for this research. **Funding:** This work was supported in part by National Institutes of Health grant GM43949. C.-H.L. is supported by the Jane Coffin Childs Memorial Fund fellowship (#61-1632). R.M. is an investigator of the Howard Hughes Medical Institute. **Author contributions:** C.-H.L. performed all experiments. C.-H.L. and R.M. analyzed the structures and wrote the manuscript. **Competing interests:** The authors declare no competing financial interests. **Data and materials availability:** Cryo-EM density maps of the SK-CaM complex have been deposited in the Electron Microscopy Data Bank under accession codes EMD-7537 (Ca^{2+}-free state), -7538 (Ca^{2+}-bound state I), and -7539 (Ca^{2+}-bound state II). Atomic coordinates have been deposited in the Protein Data Bank under accession codes 6CNM (Ca^{2+}-free state), 6CNN (Ca^{2+}-bound state I), and 6CNO (Ca^{2+}-bound state II).

SUPPLEMENTARY MATERIALS

www.sciencemag.org/content/360/6388/508/suppl/DC1
Materials and Methods
Figs. S1 to S8
Table S1
References (*62*–*80*)
Movie S1

8 January 2018; accepted 16 March 2018
10.1126/science.aas9466

REPORT

NANOMATERIALS

Tunable intraparticle frameworks for creating complex heterostructured nanoparticle libraries

Julie L. Fenton,* Benjamin C. Steimle,* Raymond E. Schaak†

Complex heterostructured nanoparticles with precisely defined materials and interfaces are important for many applications. However, rationally incorporating such features into nanoparticles with rigorous morphology control remains a synthetic bottleneck. We define a modular divergent synthesis strategy that progressively transforms simple nanoparticle synthons into increasingly sophisticated products. We introduce a series of tunable interfaces into zero-, one-, and two-dimensional copper sulfide nanoparticles using cation exchange reactions. Subsequent manipulation of these intraparticle frameworks yielded a library of 47 distinct heterostructured metal sulfide derivatives, including particles that contain asymmetric, patchy, porous, and sculpted nanoarchitectures. This generalizable mix-and-match strategy provides predictable retrosynthetic pathways to complex nanoparticle features that are otherwise inaccessible.

Nanoparticles (NPs) with compositional asymmetry and various types of morphologies and interfaces can be produced by top-down templating, surface patterning, and localized deposition (*1*–*6*). Because these approaches use planar surfaces to achieve the targeted complex features, only a relatively small number of NPs are produced compared with solution routes, which also can achieve size uniformity, morphology control, and tunable composition (*7*, *8*). However, for multicomponent nanostructures, each distinct combination of materials generally requires a "tour de force" synthetic effort. Reaction conditions must be rigorously fine-tuned, and unavoidable incompatibilities among the multiple components and reagents must be sidestepped, typically many times during the synthesis of a single nanoarchitecture (*9*, *10*). The robust modularity that characterizes molecular synthesis and top-down nanofabrication is largely absent from the approaches that are available to produce complex NP systems. Accordingly, the demand for complex nanostructures outpaces the synthetic methods available for obtaining them, and many high-value targets remain out of reach.

By analogy to the retrosynthetic framework through which complex molecules are synthesized, we deconstruct a target structure into smaller, synthetically tractable pieces and define a divergent synthesis strategy to access multicomponent NPs with arbitrary complexity. A key first step in this approach is to identify appropriate synthons that are simple, readily accessible, and can be rationally modified; we refer to these as first-generation (G-1) nanostructures. A structurally complex intraparticle framework of interfaces and junctions is then introduced in a predictable and generalizable manner to produce G-2 nanostructures, followed by systematic incorporation of a diverse library of materials at desired locations to produce higher-generation nanostructures. We selected $Cu_{1.8}S$ as a G-1 synthon because $Cu_{1.8}S$ NPs in a range of sizes and shapes can be routinely synthesized (*11*, *12*) and Cu^+ cations have high mobilities that facilitate partial or complete exchange with other cations (*13*–*19*). These characteristics allow a rich collection of materials and interfaces to be introduced in subsequent steps across a diverse range of morphologies. Transmission electron microscopy (TEM) images are shown in Fig. 1 for three distinct classes of $Cu_{1.8}S$ NPs—zero-dimensional (0D) spheres (Fig. 1A), 1D rods (Fig. 1B), and 2D plates (Fig. 1C); additional characterization data are included in fig. S1 of the supplementary materials.

To transform the G-1 nanostructures into more complex G-2 systems, various types of interfaces and junctions must be introduced to break the symmetry of the synthons and produce structurally complex intraparticle frameworks. We replaced a fraction of the Cu^+ cations in each of the G-1 $Cu_{1.8}S$ structures with Cd^{2+} or Zn^{2+} by applying the principles of nanocrystal (NC) cation exchange (*20*), intentionally arresting each reaction at various stages before it went to completion. TEM images and element maps generated from scanning TEM with energy dispersive spectroscopy (STEM-EDS) corresponding to the resulting G-2 NP library (Fig. 1) show that each type of G-2 NP has a distinct segmentation pattern and newly engineered internal interfaces between material components. The extent of cation exchange could be controlled by reaction time, which led to broad tunability of the intraparticle framework features. Spherical $Cu_{1.8}S$ NPs (Fig. 1A) reacted with Cd^{2+} to produce hemispherical CdS–$Cu_{1.8}S$ Janus particles (Fig. 1D), and reaction with Zn^{2+} formed two discrete ZnS domains in a layered, sandwich-like ZnS–$Cu_{1.8}S$–ZnS structure (Fig. 1E) (*15*). $Cu_{1.8}S$ nanorods (Fig. 1B) reacted with Cd^{2+} preferentially at the tips to generate CdS–$Cu_{1.8}S$ nanorods (Fig. 1F), whereas striped ZnS–$Cu_{1.8}S$ nanorods were the dominant products formed upon reacting with Zn^{2+} (Fig. 1G). Hexagonal $Cu_{1.8}S$ nanoplates (Fig. 1C) reacted with Cd^{2+} to produce large patches of CdS in a $Cu_{1.8}S$ matrix (Fig. 1H), whereas reaction with Zn^{2+} yielded a highly interdigitated network of ZnS and $Cu_{1.8}S$ with small, marbled filaments throughout (Fig. 1I). Despite the different interfacial structures, the overall sizes and shapes of the G-1 $Cu_{1.8}S$ synthons were retained in the G-2 structures (table S1).

Across the library of G-2 NPs in Fig. 1, exchange with Zn^{2+} generally resulted in the formation of a larger number of smaller ZnS regions within the intraparticle frameworks, whereas exchange with Cd^{2+} resulted in a smaller number of larger CdS regions. This behavior can be rationalized by considering differences in cation radius, lattice matching, and interfacial strain (*15*, *21*). Exchanging Cu^+ for the larger Cd^{2+} cation to form CdS requires a volume expansion of 14% relative to the comparable subunit of the $Cu_{1.8}S$ crystal structure (fig. S2), whereas exchange with the smaller Zn^{2+} cation requires a smaller (10%) volume contraction (*22*, *23*). Intraparticle phase segregation between CdS and $Cu_{1.8}S$ is expected to be greater than between ZnS and $Cu_{1.8}S$, resulting in fewer interfaces in the CdS–$Cu_{1.8}S$ systems relative to ZnS–$Cu_{1.8}S$, as observed. Additionally, the *a*-axis lattice parameters for comparable subunits of the hexagonal close-packed S lattices of $Cu_{1.8}S$ (3.87 Å) and ZnS (3.81 Å) are similar but differ substantially from CdS (4.13 Å), whereas the *c*-axis lattice parameters are closer for $Cu_{1.8}S$ (6.71 Å) and CdS (6.72 Å) than for ZnS (6.23 Å) (Fig. 1J) (*17*, *23*).

To minimize interfacial lattice distortion, exchange with Cd^{2+} propagated along the *a* direction of $Cu_{1.8}S$, which interfaced $Cu_{1.8}S$ and CdS along the closely lattice-matched *c* direction. In contrast, exchange with Zn^{2+} propagated along the *c* direction, which interfaced $Cu_{1.8}S$ and ZnS along the closely lattice-matched *a* direction. The high-resolution TEM (HRTEM) images of CdS–$Cu_{1.8}S$ Janus NPs and ZnS–$Cu_{1.8}S$–ZnS sandwich NPs, shown in fig. S3, confirmed the different crystallographic orientations within the NPs and helped to rationalize the distinct intraparticle frameworks that emerged from the various cation exchange reactions. Thus, ionic radii, lattice matching, and reaction time can be used to predict the number of segments. The extent of cation exchange, the corresponding sizes of the regions each material occupies within the intraparticle framework, and the interfacial area between the

Department of Chemistry and Materials Research Institute, The Pennsylvania State University, University Park, PA 16802, USA.
*These authors contributed equally to this work.
†Corresponding author. Email: res20@psu.edu

material components all can be rationally tuned while maintaining the key morphological features of the G-1 synthons.

The G-2 nanostructures contained a residual $Cu_{1.8}S$ region, as well as either CdS or ZnS (Fig. 1K). All three of these metal sulfides can be targeted by NC cation exchange reactions, but their different chemical driving forces in principle allow each region to be addressed selectively and independently. Cu^+ will diffuse faster than either Cd^{2+} or Zn^{2+} because of its lower charge density and higher mobility (*15*). Cu^+ is also a softer cation than either Cd^{2+} or Zn^{2+}, making its coordination with the soft phosphorus atom in trioctylphosphine (TOP), which is included in the reaction solution, more favorable than either of the divalent cations (*20*, *24*). Accordingly, the $Cu_{1.8}S$ regions of the G-2 CdS–$Cu_{1.8}S$ and ZnS–$Cu_{1.8}S$ nanostructures in Fig. 1 could be exchanged selectively, keeping the CdS or ZnS regions intact while introducing other materials into the remainder of the intraparticle framework. After reaction with Zn^{2+} in the presence of TOP, the G-2 CdS–$Cu_{1.8}S$ nanostructures (Fig. 2, A, C, and E) transformed into G-3 CdS–ZnS (Fig. 2, G, I, and K). Likewise, after reaction with Cd^{2+} in the presence of TOP, the G-2 ZnS–$Cu_{1.8}S$ nanostructures (Fig. 2, B, D, and F) transformed to G-3 ZnS–CdS (Fig. 2, H, J, and L). The G-3 products retained the overall morphologies and segmentation patterns defined by their G-1 and G-2 precursors, respectively, while containing barely detectable amounts (<3%) of residual Cu (figs. S7 and S8), based on

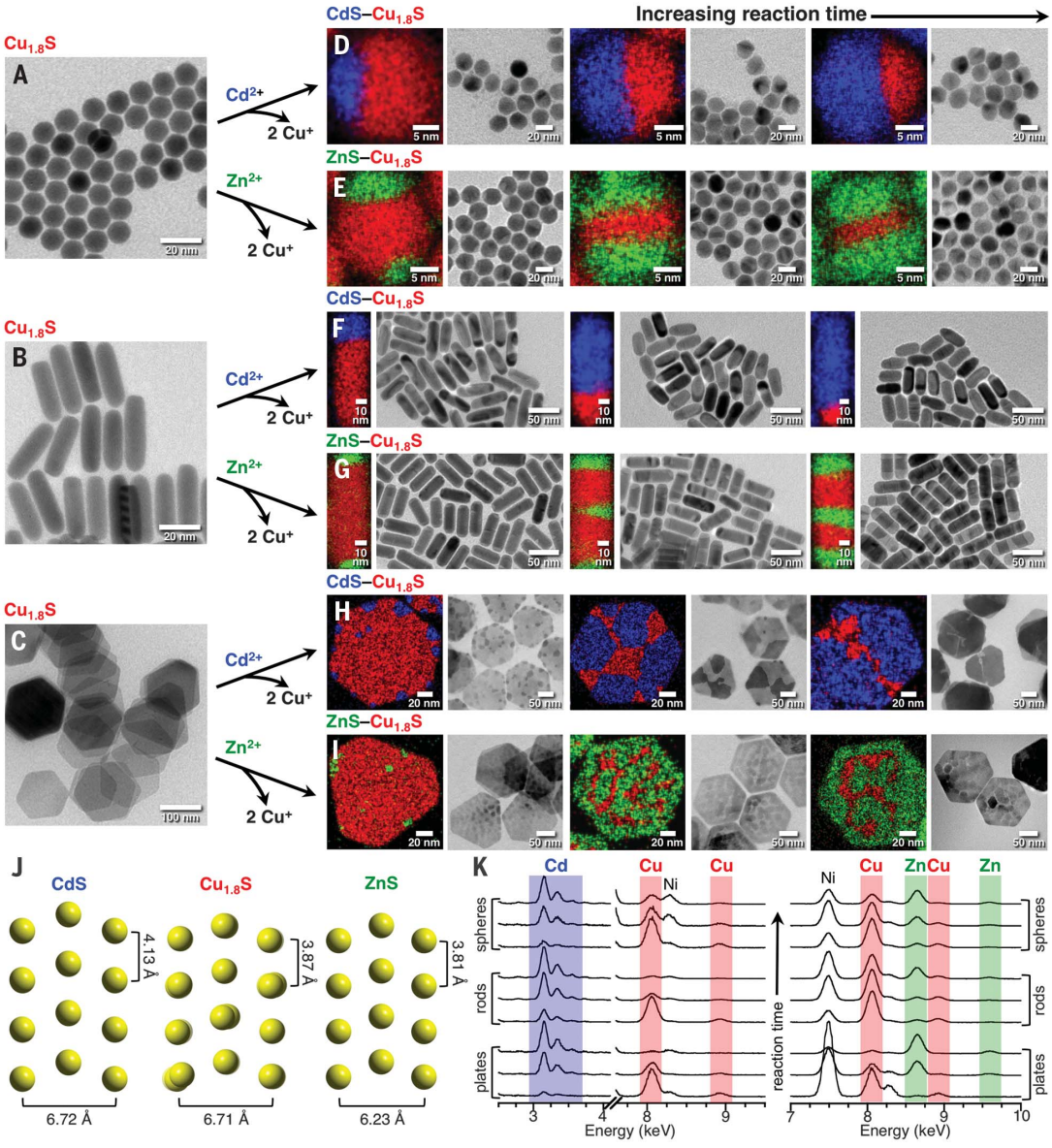

Fig. 1. Formation of G-2 nanostructures. $Cu_{1.8}S$ (**A**) spheres, (**B**) rods, and (**C**) hexagonal plates (shown in TEM images) are used as G-1 synthons for introducing diverse intraparticle frameworks through partial cation exchange with Cd^{2+} and Zn^{2+}. The resulting library of segmented G-2 nanostructures includes (**D**) hemispherical CdS–$Cu_{1.8}S$ Janus particles, (**E**) sandwich-like ZnS–$Cu_{1.8}S$–ZnS particles, (**F**) CdS–$Cu_{1.8}S$ capped rods, (**G**) ZnS–$Cu_{1.8}S$ striped rods, (**H**) CdS–$Cu_{1.8}S$ patchy plates, and (**I**) ZnS–$Cu_{1.8}S$ marbled plates. For each type of NP, the extent of partial cation exchange can be tuned by adjusting the reaction time. Three examples are shown for each type of nanostructure in (D) through (I). Each panel includes a TEM image and STEM-EDS element map. Cu, Cd, and Zn are shown in red, blue, and green, respectively. Crystal structure projections of wurtzite CdS, roxbyite $Cu_{1.8}S$, and wurtzite ZnS are shown in (**J**) to highlight the crystallographic relationships between the adjacent phases within the intraparticle frameworks. Selected regions of the EDS spectra for all samples are shown in (**K**). For the spheres, rods, and plates, the Cd and Zn signals increase as the reaction time increases, whereas the Cu signals decrease (fig. S4 and table S2). The Ni signal is from the Ni TEM grid.

analysis by energy-dispersive x-ray spectroscopy (EDS). Powder x-ray diffraction (XRD) confirmed the presence of each of the expected phases across all three generations of spherical nanostructures (figs. S9 and S10). The observed color changes were also consistent with those expected for the transformations of G-1 NPs into G-2 and G-3 nanostructures (fig. S11).

The resulting library of nanostructures in Fig. 2, G to L, represents six distinct classes of heterostructured CdS–ZnS isomers that have the same material components in different spatial and interfacial arrangements within colloidal NPs that maintain the uniform shapes and sizes defined by the G-1 $Cu_{1.8}S$ synthons. Although selected members of the G-2 CdS–$Cu_{1.8}S$ and ZnS–$Cu_{1.8}S$ NP library were chosen as representative examples for transformation into G-3 products, any of the other G-2 members from Fig. 1 could also be used to further expand the scope of accessible isomeric CdS–ZnS heterostructures.

The process that transformed G-1 $Cu_{1.8}S$ NPs into G-2 CdS–$Cu_{1.8}S$ and ZnS–$Cu_{1.8}S$ NPs and G-3 CdS–ZnS NPs was also extended to other materials systems through cation exchange with different metals; this step could be implemented at any stage of the reaction sequence. For example, the G-1 $Cu_{1.8}S$ nanorods underwent partial cation exchange with Co^{2+} and Ni^{2+} to produce G-2 CoS–$Cu_{1.8}S$ and Ni_9S_8–$Cu_{1.8}S$ striped nanorods (figs. S12 and S13). G-3 CoS–ZnS striped nanorods, formed by exchange of the $Cu_{1.8}S$ region of G-2 ZnS–$Cu_{1.8}S$ striped nanorods, are shown in figs. S12 and S14. Similarly, the residual Cu^+ in the G-2 CdS–$Cu_{1.8}S$ hexagonal plates exchanged with Co^{2+} to produce hexagonal plates of CoS with embedded CdS islands (figs. S12 and S14). Figure 2, M to R, shows the products formed by reacting the G-2 spherical CdS–$Cu_{1.8}S$ Janus NPs and ZnS–$Cu_{1.8}S$–ZnS sandwich structures with Co^{2+}, Mn^{2+}, and Ni^{2+} in the presence of TOP. The resulting library of G-3 nanostructures included CdS–CoS, CdS–MnS, and CdS–Ni_9S_8 Janus NPs and ZnS–CoS–ZnS, ZnS–MnS–ZnS, and ZnS–Ni_9S_8–ZnS sandwich structures.

The formation of diverse intraparticle frameworks can be decoupled from the integration of targeted materials in a predictive manner, but the modularity and scope of this approach to complex NP synthesis extends far beyond the G-2 and G-3 systems highlighted in Fig. 2. Any point in the reaction sequence can serve as a springboard to a more complex target through a rational and predictive mix-and-match process. In addition to cation exchange, several other classes of nanochemical reactions can be integrated, including seeded growth (*25*, *26*) and selective etching (*27*). Figure 3 highlights several examples of highly sophisticated nanostructures that would otherwise not be accessible. For example, G-2 ZnS–$Cu_{1.8}S$ striped nanorods (Fig. 3A) were transformed to G-3 ZnS–CdS striped nanorods (Fig. 3B), followed by reaction with Ag^+ to produce complex segmented nanorods that formed through regioselective cation exchange (Fig. 3C). Under these mild reaction conditions, Ag^+ should exchange with both ZnS and CdS (*28*). However, with a substoichiometric amount of Ag^+, cation exchange only occurred with Cd^{2+}, due to the more closely matched sizes of the Ag^+ and Cd^{2+} cations (*22*), and the ZnS regions remained intact. Alternatively, the $Cu_{1.8}S$ regions of the G-2 ZnS–$Cu_{1.8}S$ striped nanorods in Fig. 3A were partially etched in the presence of a trialkylphosphine and air (*27*). The nanorod products maintained the morphologies of the ZnS regions while adopting concave $Cu_{1.8}S$ regions, resulting in intricately sculpted ZnS–$Cu_{1.8}S$ NPs (Fig. 3D). Exchanging the remaining Cu^+ in the sculpted segments with Zn^{2+} transformed them to ZnS, resulting in a 1D NP composed entirely of ZnS but maintaining the complex sculpted morphology (Fig. 3E).

To further demonstrate the mix-and-match modularity of this synthetic framework, partial exchange of Cu^+ with Zn^{2+} was carried out on the

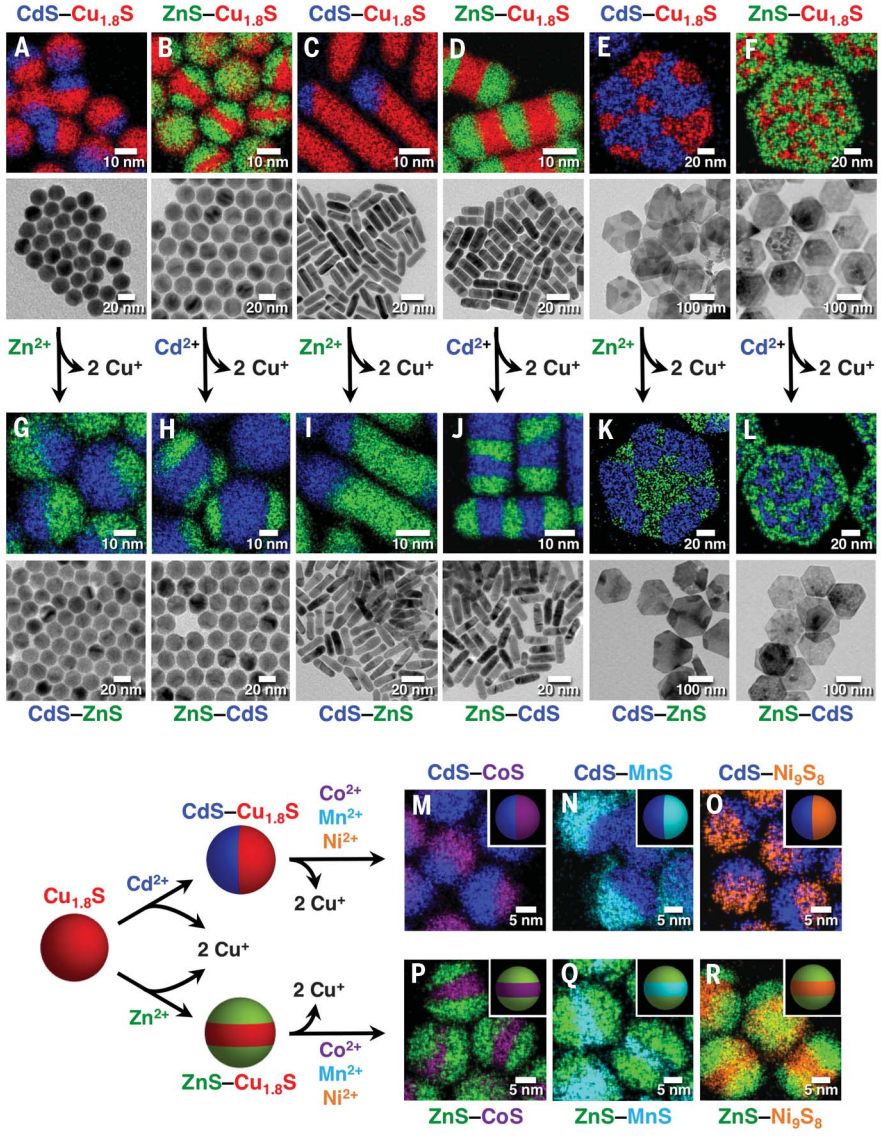

Fig. 2. Formation of G-3 nanostructures. G-2 (**A**) hemispherical CdS–$Cu_{1.8}S$ Janus particles, (**B**) sandwich-like ZnS–$Cu_{1.8}S$–ZnS particles, (**C**) CdS–$Cu_{1.8}S$ capped rods, (**D**) ZnS–$Cu_{1.8}S$ striped rods, (**E**) CdS–$Cu_{1.8}S$ patchy plates, and (**F**) ZnS–$Cu_{1.8}S$ marbled plates are transformed into (**G** to **L**) six distinct classes of heterostructured G-3 CdS–ZnS isomers via selective cation exchange of Cu^+ with Cd^{2+} or Zn^{2+}. Selective exchange of Cu^+ in the $Cu_{1.8}S$ regions of G-2 CdS–$Cu_{1.8}S$ Janus and ZnS–$Cu_{1.8}S$–ZnS sandwich particles with Co^{2+}, Mn^{2+}, and Ni^{2+} results in (**M**) CdS–CoS, (**N**) CdS–MnS, and (**O**) CdS–Ni_9S_8 Janus NPs and (**P**) ZnS–CoS–ZnS, (**Q**) ZnS–MnS–ZnS, and (**R**) ZnS–Ni_9S_8–ZnS sandwich particles. The G-3 NPs preserve the morphology of the G-1 $Cu_{1.8}S$ NPs and the intraparticle frameworks of the G-2 NPs while containing none of the original $Cu_{1.8}S$. STEM-EDS maps and TEM images are shown for each population of particles. Cu, Cd, Zn, Co, Mn, and Ni are shown in red, blue, green, purple, cyan, and orange, respectively. For additional characterization data, see figs. S5 to S8 and S12 to S15.

G-2 CdS–$Cu_{1.8}S$ Janus NPs shown in Fig. 3F. The product, shown in Fig. 3G, combined both Janus and sandwich features by replacing the top and bottom regions of the $Cu_{1.8}S$ hemisphere with ZnS while maintaining the hemisphere of CdS. The resulting NP contained one hemisphere of CdS and one hemisphere of a ZnS–$Cu_{1.8}S$–ZnS sandwich-type particle, and was further modified in multiple ways to produce complex derivative products. Selectively etching the $Cu_{1.8}S$ region produced a NP with a CdS hemisphere having two attached, noncontiguous ZnS domains (Fig. 3H). Alternatively, exchanging the Cu^+ with Co^{2+} transformed the central region to CoS, producing a (ZnS–CoS–ZnS)–CdS Janus NP (Fig. 3I). As yet another alternative, exchanging the Cu^+ with Cd^{2+} transformed the $Cu_{1.8}S$ region to CdS, resulting in a spherical CdS NP with two embedded regions of ZnS (Fig. 3J).

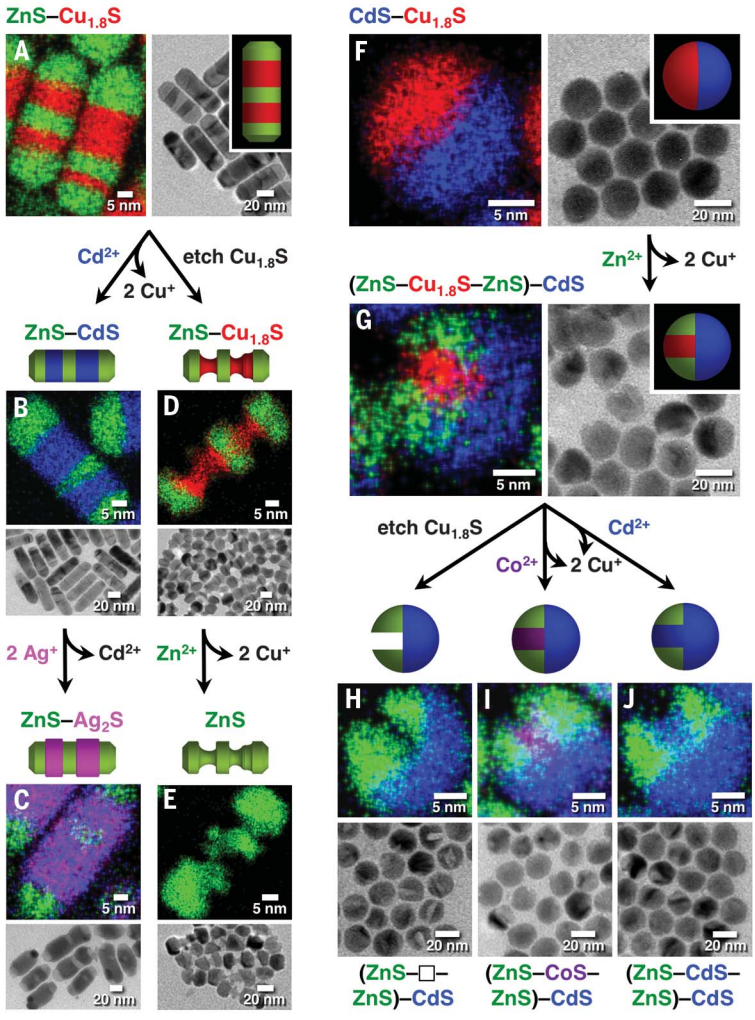

Fig. 3. Higher-generation nanostructures formed by rationally applying multiple exchange and/or etching steps. (**A**) G-2 ZnS–$Cu_{1.8}S$ striped rods react with Cd^{2+} to form (**B**) G-3 ZnS–CdS striped rods, which further react with Ag^+ to selectively target the CdS regions, forming (**C**) G-4 Ag_2S–ZnS striped rods. Alternatively, the $Cu_{1.8}S$ regions of the ZnS–$Cu_{1.8}S$ striped rods in (A) can be partially etched with TOP to form the sculpted ZnS–$Cu_{1.8}S$ rods shown in (**D**); the Cu^+ can then exchange with Zn^{2+} to replace the remaining $Cu_{1.8}S$ with ZnS, forming the complex sculpted rods in (**E**) that are composed entirely of ZnS. Partial exchange of Cu^+ in the $Cu_{1.8}S$ region of (**F**) G-2 CdS–$Cu_{1.8}S$ Janus NPs with Zn^{2+} results in the new type of particle shown in (**G**), which merges the features of partial Zn^{2+} and Cd^{2+} cation exchanges by retaining the CdS hemisphere while introducing sandwich-like ZnS caps on the $Cu_{1.8}S$ hemisphere. The remaining $Cu_{1.8}S$ in these complex (ZnS–$Cu_{1.8}S$–ZnS)–CdS Janus particles can be (**H**) etched to produce particles containing two noncontiguous ZnS domains on a CdS hemisphere or (**I**) replaced with CoS to form (ZnS–CoS–ZnS)–CdS Janus NPs. Alternatively, the Cu^+ of the $Cu_{1.8}S$ region of the (ZnS–$Cu_{1.8}S$–ZnS)–CdS Janus NPs can be exchanged with Cd^{2+} to form (**J**) (ZnS–CdS–ZnS)–CdS Janus NPs, which can also be described as a spherical CdS particle containing two distinct embedded regions of ZnS. STEM-EDS maps, TEM images, and drawings are shown for each population of NPs. Cu, Cd, Zn, Ag, and Co are shown in red, blue, green, pink, and purple, respectively. For additional characterization data, see figs. S16 to S18.

Other classes of nanostructured NPs could also be intentionally designed with this modular framework. For example, nanoscale spherical colloids lack compositional asymmetry, or valency, on their surfaces and hence are generally unable to facilitate directional or anisotropic interactions with other particles and/or surface-based chemical processes (*29*). Likewise, many targeted nanoscale architectures, including those for applications in photocatalytic water splitting, require deposition of NPs selectively on different regions of a central particle (*30*). Figure 4 shows multiple design strategies for achieving such features. The G-2 CdS–$Cu_{1.8}S$ Janus NPs had two distinct surfaces exposed, and Pt deposited selectively on the $Cu_{1.8}S$ region (Fig. 4A). The remaining Cu^+ in the CdS–$Cu_{1.8}S$–Pt NP was then exchanged with Cd^{2+} to transform the spherical particle entirely to CdS, forming asymmetrically functionalized CdS–Pt (Fig. 4B). The CdS–$Cu_{1.8}S$ intermediate introduced asymmetry that led to regioselective surface deposition of Pt. Au was then deposited on the exposed CdS surface to form asymmetric $(Au)_x$–CdS–Pt NPs (Fig. 4C). For comparison, direct deposition of Pt and/or Au onto spherical CdS particles resulted in Pt and Au NPs decorating the entire surface (fig. S20). To further expand the scope of regioselective functionalization, Au was deposited exclusively on the CdS patches of CdS–ZnS hexagonal plates (Fig. 4D).

As an additional design goal, introducing porosity into nanostructures increases surface area and is desirable for applications in catalysis (*31*, *32*), gas storage and separation (*33*), and batteries and supercapacitors (*34*), where chemical interactions with exposed surfaces must be maximized. By leveraging the diversity of accessible intraparticle frameworks, along with chemistry that can selectively etch $Cu_{1.8}S$ (*27*), a variety of porous NPs were produced. Two distinct pore sizes were incorporated into morphologically identical ZnS nanoplates by starting with two distinct intraparticle frameworks incorporated into ZnS–$Cu_{1.8}S$ precursors (Fig. 4, E and F).

This modular and divergent synthetic strategy allows us to reenvision the synthesis of multicomponent nanostructures by first carving a substructure of interfaces into a reactive nanoparticle synthon and then integrating desired materials, in mix-and-match fashion, at precise locations. Complex colloidal nanoarchitectures that would otherwise be inaccessible can now be designed and synthesized in a predictive manner. Combining these capabilities with a broader class of nanoparticle chemical transformation reactions will provide synthetic entryways into other materials systems, including oxides, metals, phosphides, and other chalcogenides (*20*, *35*–*37*). Such advances will enable the design and synthesis of the increasingly complex NP systems that are in demand across a wide range of application areas, including semiconductor-semiconductor interfaces for the controllable separation or confinement of excitons, anisotropic particles for

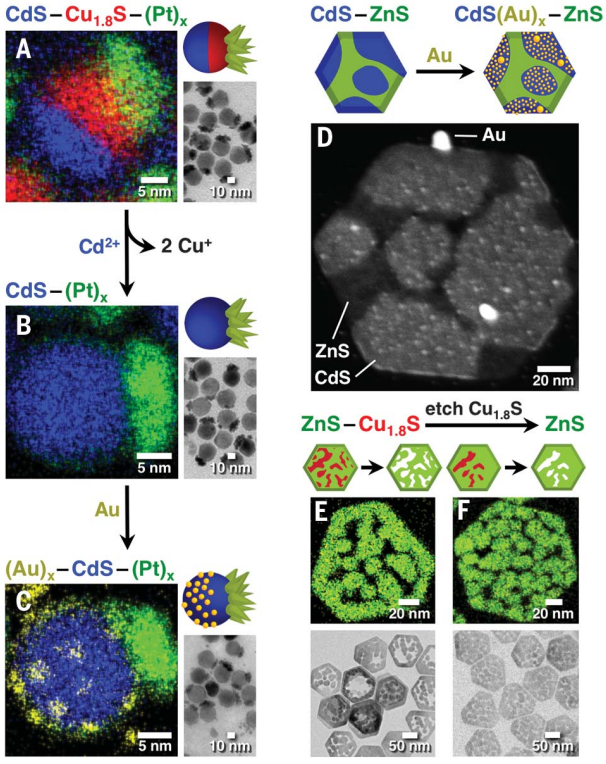

Fig. 4. Complex nanostructures formed by combining multiple cation exchange steps with regioselective deposition or etching. (**A**) Selective deposition of Pt on the $Cu_{1.8}S$ surface of a G-2 CdS–$Cu_{1.8}S$ Janus particle, followed by (**B**) subsequent exchange of the Cu^+ in the $Cu_{1.8}S$ hemisphere with Cd^{2+}, formed a spherical NP that was fully CdS while being asymmetrically functionalized with Pt on one side. (**C**) Further deposition of small Au NPs on the exposed CdS surface forms an asymmetric Au-CdS-Pt NP. In (A) to (C), Cu, Cd, Pt, and Au are shown in red, blue, green, and yellow, respectively. (**D**) Au NPs were selectively deposited on the CdS patches of a G-3 CdS–ZnS patchy hexagonal plate, as shown in the high-angle annular dark-field STEM image. (**E** and **F**) The $Cu_{1.8}S$ regions of ZnS–$Cu_{1.8}S$ marbled plates were selectively etched, forming the nanoporous ZnS plates shown in the TEM images and STEM-EDS maps. By tuning the reaction time in the initial partial cation exchange step that produces the ZnS–$Cu_{1.8}S$ marbled plates, the size of the nanopores in the resultant plates can also be tuned. In (D) to (F), Cu, Cd, Zn, and Au are shown in red, blue, green, and yellow, respectively. For additional characterization data, see figs. S19, S21, and S22.

nonlinear optics, and precision integration of semiconductors and catalysts for light-driven chemical transformations.

REFERENCES AND NOTES

1. P.-C. Chen *et al.*, *Science* **352**, 1565–1569 (2016).
2. A. G. Mark, J. G. Gibbs, T.-C. Lee, P. Fischer, *Nat. Mater.* **12**, 802–807 (2013).
3. X. Xu *et al.*, *ACS Nano* **11**, 10384–10391 (2017).
4. S. R. Nicewarner-Peña *et al.*, *Science* **294**, 137–141 (2001).
5. A. Nemiroski *et al.*, *ACS Nano* **8**, 11061–11070 (2014).
6. M. M. Hawkeye, M. J. Brett, *J. Vac. Sci. Technol. A* **25**, 1317–1335 (2007).
7. J. Park *et al.*, *Nat. Mater.* **3**, 891–895 (2004).
8. Y. Xia, Y. Xiong, B. Lim, S. E. Skrabalak, *Angew. Chem. Int. Ed.* **48**, 60–103 (2009).
9. J. M. Hodges, R. E. Schaak, *Acc. Chem. Res.* **50**, 1433–1440 (2017).
10. J. M. Hodges *et al.*, *Chem. Mater.* **29**, 106–119 (2017).
11. C. Coughlan *et al.*, *Chem. Rev.* **117**, 5865–6109 (2017).
12. Y. Zhai, M. Shim, *Chem. Mater.* **29**, 2390–2397 (2017).
13. V. Lesnyak, R. Brescia, G. C. Messina, L. Manna, *J. Am. Chem. Soc.* **137**, 9315–9323 (2015).
14. J. M. Luther, H. Zheng, B. Sadtler, A. P. Alivisatos, *J. Am. Chem. Soc.* **131**, 16851–16857 (2009).
15. D.-H. Ha *et al.*, *Nano Lett.* **14**, 7090–7099 (2014).
16. Y. Zhai, J. C. Flanagan, M. Shim, *Chem. Mater.* **29**, 6161–6167 (2017).
17. A. E. Powell, J. M. Hodges, R. E. Schaak, *J. Am. Chem. Soc.* **138**, 471–474 (2016).
18. J. L. Fenton, R. E. Schaak, *Angew. Chem. Int. Ed.* **56**, 6464–6467 (2017).
19. L. Mu, F. Wang, B. Sadtler, R. A. Loomis, W. E. Buhro, *ACS Nano* **9**, 7419–7428 (2015).
20. L. De Trizio, L. Manna, *Chem. Rev.* **116**, 10852–10887 (2016).
21. B. Sadtler *et al.*, *J. Am. Chem. Soc.* **131**, 5285–5293 (2009).
22. R. D. Shannon, C. T. Prewitt, *Acta Crystallogr. B* **25**, 925–946 (1969).
23. Y.-N. Xu, W. Y. Ching, *Phys. Rev. B Condens. Matter* **48**, 4335–4351 (1993).
24. J. Gui *et al.*, *Angew. Chem. Int. Ed. Engl.* **54**, 3683–3687 (2015).
25. T. Mokari, C. G. Sztrum, A. Salant, E. Rabani, U. Banin, *Nat. Mater.* **4**, 855–863 (2005).
26. S. Naskar *et al.*, *Chem. Mater.* **27**, 3159–3166 (2015).
27. A. Nelson, D.-H. Ha, R. D. Robinson, *Chem. Mater.* **28**, 8530–8541 (2016).
28. R. D. Robinson *et al.*, *Science* **317**, 355–358 (2007).
29. Z. Gong, T. Hueckel, G.-R. Yi, S. Sacanna, *Nature* **550**, 234–238 (2017).
30. S. Chen, T. Takata, K. Domen, *Nat. Rev. Mater.* **2**, 17050 (2017).
31. G. Prieto *et al.*, *Chem. Rev.* **116**, 14056–14119 (2016).
32. T. F. Jaramillo *et al.*, *Science* **317**, 100–102 (2007).
33. R. E. Morris, P. S. Wheatley, *Angew. Chem. Int. Ed.* **47**, 4966–4981 (2008).
34. L. Yu, H. B. Wu, X. W. D. Lou, *Acc. Chem. Res.* **50**, 293–301 (2017).
35. I. T. Sines, R. E. Schaak, *J. Am. Chem. Soc.* **133**, 1294–1297 (2011).
36. X. Xia, Y. Wang, A. Ruditskiy, Y. Xia, *Adv. Mater.* **25**, 6313–6333 (2013).
37. J. Park, H. Zheng, Y. W. Jun, A. P. Alivisatos, *J. Am. Chem. Soc.* **131**, 13943–13945 (2009).

ACKNOWLEDGMENTS

TEM imaging was performed in the Penn State Microscopy and Cytometry facility. HRTEM imaging, STEM imaging, and EDS mapping were performed at the Materials Characterization Laboratory of the Penn State Materials Research Institute. The authors thank K. Wang and J. L. Gray for assistance with TEM experiments and helpful discussions. **Funding:** This work was supported by the U.S. National Science Foundation under grant DMR-1607135. **Author contributions:** J.L.F., B.C.S., and R.E.S. conceived of the concept, designed the experiments, and wrote the paper; B.C.S. and J.L.F. synthesized and characterized the nanoparticles; J.L.F. performed HRTEM and STEM-EDS characterization. **Competing interests:** The authors declare no competing financial interests. **Data and materials availability:** All data needed to evaluate the conclusions in the paper are present in the paper or the supplementary materials.

SUPPLEMENTARY MATERIALS

www.sciencemag.org/content/360/6388/513/suppl/DC1
Materials and Methods
Figs. S1 to S22
Tables S1 to S5
References

21 November 2017; accepted 9 March 2018
10.1126/science.aar5597

MEMBRANES

Polyamide membranes with nanoscale Turing structures for water purification

Zhe Tan,[1] Shengfu Chen,[1] Xinsheng Peng,[2] Lin Zhang,[1]* Congjie Gao[1,3]

The emergence of Turing structures is of fundamental importance, and designing these structures and developing their applications have practical effects in chemistry and biology. We use a facile route based on interfacial polymerization to generate Turing-type polyamide membranes for water purification. Manipulation of shapes by control of reaction conditions enabled the creation of membranes with bubble or tube structures. These membranes exhibit excellent water-salt separation performance that surpasses the upper-bound line of traditional desalination membranes. Furthermore, we show the existence of high water permeability sites in the Turing structures, where water transport through the membranes is enhanced.

Alan Turing's 1952 paper (*1*), "The chemical basis of morphogenesis," theoretically analyzed how two chemical substances, activator and inhibitor (*2*) (Fig. 1A), can, under certain conditions, react and diffuse with each other to generate spatiotemporal stationary structures. Turing's ideas have profoundly influenced theoretical understanding of pattern formation in chemical (*3*) and biological (*4*, *5*) systems, but it was not until nearly 40 years after his paper was published that experimental evidence was obtained for the chlorite-iodide-malonic acid (CIMA) reaction (*6*, *7*). About 10 years later, stationary Turing states were also observed in the Belousov-Zhabotinsky (BZ) reaction microemulsion consisting of reverse micelles (*8*). Recently, a variety of two- and three-dimensional stationary structures were studied in chemical (*9*, *10*) and biological (*11*–*15*) systems.

Turing structures typically emerge in reaction-diffusion processes far from thermodynamic equilibrium (*1*), in which the diffusion coefficient of the inhibitor must be larger than that of the activator, resulting in the "local activation and lateral inhibition" phenomenon (Fig. 1B) that underlies diffusion-driven instability (*2*). However, this condition is not easily satisfied in homogeneous solutions, for most chemical reactions involve small molecules with similar or inappropriately differing diffusion coefficients. In the classic Turing systems, two main approaches have been developed to selectively control the effective diffusion coefficients of reactants: (i) Introduce a macromolecule that reversibly binds the activator, like starch or polyvinyl alcohol (PVA) in the CIMA reaction, and (ii) use a heterogeneous finely dispersed multiphase reaction system in which the activator resides in a low-mobility phase, such as when polar BZ reagents are confined within nanosized aqueous droplets (*6*–*10*). On the basis of theoretical analyses and experimental observations, we successfully applied these chemical and physical approaches to aqueous-organic interfacial polymerization and developed a facile route to generate nanoscale Turing structures with high water permeability under ambient conditions.

Interfacial polymerization is a reaction-diffusion process far from thermodynamic equilibrium (*16*). It is based on the Schotten-Baumann reaction, in which the irreversible polymerization of two fast-reacting multifunctional monomers occurs near the interface of two immiscible phases of a heterogeneous liquid system (*17*, *18*). This technique has been used to prepare reverse osmosis and nanofiltration membranes for large-scale and low-cost water purification applications (*19*, *20*). In a typical membrane synthesis (fig. S1), organic amines are dissolved in water while acyl chlorides are dissolved in an organic solvent, and a very thin insoluble polyamide (PA) membrane forms on top of a porous support (figs. S2 and S3). In our experiment, piperazine (PZ) is the activator, and trimesoyl chloride (TMC) is the inhibitor (Fig. 1C). The reaction is initiated when the top surface of a porous polysulfone (PSU) support containing an aqueous solution of the activator comes in contact with an organic solution of the inhibitor. Because the acyl chloride has very little solubility in water, the polymerization occurs predominantly on the organic side of the interface. Initially, the activator reacts with the locally available inhibitor in the reaction zone, later it diffuses to penetrate more deeply into the reaction zone, and finally, a cross-linked PA membrane forms across the region of pore openings of the PSU support (figs. S4 to S11 and table S1). This PA membrane formed by a conventional interfacial polymerization reaction is not of Turing type, for there are not appropriate differences between the diffusion coefficients of the activator and the inhibitor. During the reaction, the aqueous solution of the activator is confined within surface nanometer-sized pores of the PSU support, where physical obstruction blocks dispersed aqueous-phase movement and slows the activator transport. The diffusion coefficient of the organic molecules is around 10^{-5} cm^2 s^{-1}, whereas the diffusion of the dispersed aqueous phases in the organic phase can be as low as 10^{-6} cm^2 s^{-1} (fig. S12). When a certain amount of macromolecule, PVA, was added to the aqueous solution, it interacted with the activator via hydrogen bonding and increased solution viscosity, further reducing the diffusion rate of the activator (fig. S13). Through the synergetic effects of the physical obstruction and chemical interaction, the systems meet appropriate differences in the diffusion coefficients of the activator and inhibitor (*21*, *22*), leading to a diffusion-driven instability and generating nanoscale spotted (Fig. 1D) and striped (Fig. 1E) Turing structures.

Atomic force microscopy (AFM) measurements (Table 1) show that the surfaces of membranes with the nanoscale spotted (TS-I) and striped (TS-II) Turing structures are relatively rough and heterogeneous. The measured average root mean square roughnesses were 22 and 32 nm, respectively, which is quite different from that of traditional semiaromatic PA membrane (figs. S14 and S15 and table S2) with a relatively smooth and homogeneous surface (*23*). The spotted and striped structures have virtually the same height, whereas the surface area increase of TS-II is approximately two times greater than that of TS-I, suggesting that the continuous striped structures have a larger surface area relative to the discrete spotted structures in the scan area. To further investigate the nanoscale Turing structures, the membranes were characterized by scanning electron microscopy (SEM) and transmission electron microscopy (TEM) analyses. The SEM

Table 1. Surface properties of the Turing-type PA membranes. Comparison of the surface properties of the spotted and striped Turing structures. These results were acquired from AFM measurements over a scanning area of 5 μm by 5 μm. Reported are the averages and standard deviations.

Sample	AFM scans	Height (nm)	Root mean square roughness (nm)	Surface area increase (%)
TS-I	12	137 ± 34	21.7 ± 6.6	18.7 ± 5.3
TS-II	12	119 ± 21	32.2 ± 8.5	35.5 ± 9.7

[1]Key Laboratory of Biomass Chemical Engineering, College of Chemical and Biological Engineering, Zhejiang University, Hangzhou 310027, China. [2]School of Materials Science and Engineering, Zhejiang University, Hangzhou 310027, China. [3]National Engineering Research Center for Liquid Separation Membrane, Hangzhou 310012, China.
*Corresponding author. Email: linzhang@zju.edu.cn

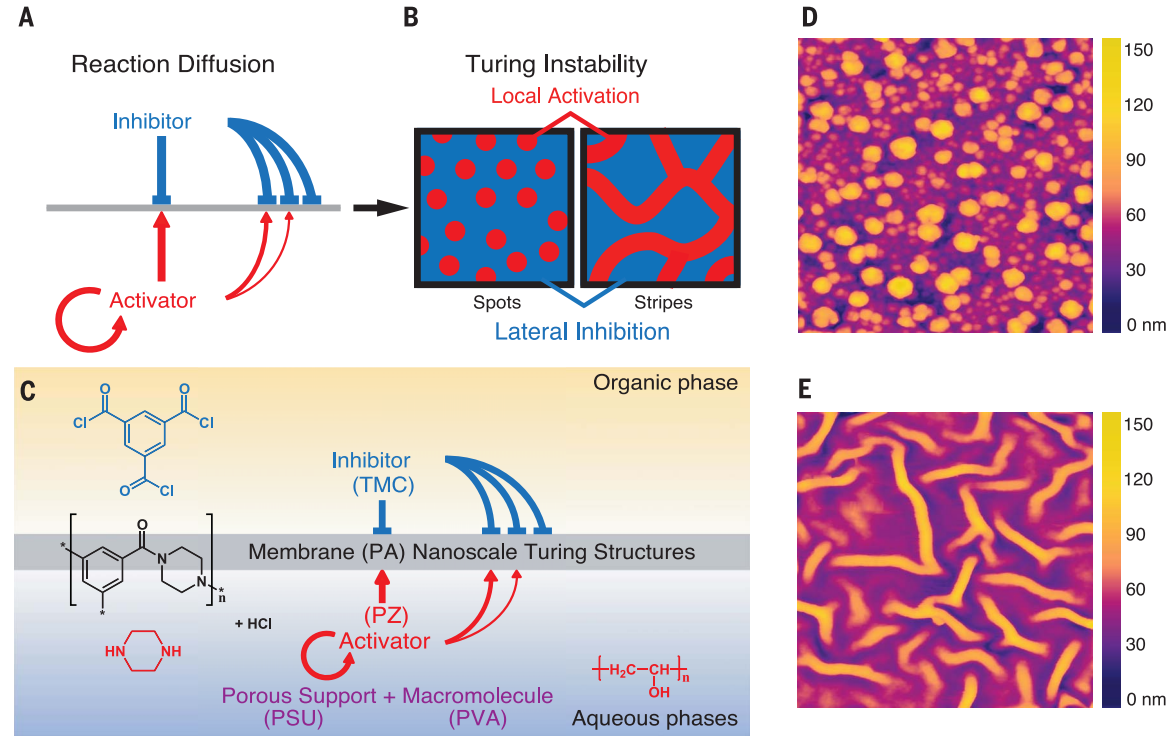

Fig. 1. Turing-type structures in interfacial polymerization. (**A**) Schematic diagram of activator-inhibitor interaction in a reaction-diffusion process. Reactions leading to Turing structures rely on competing activation (red) and inhibition (blue) kinetic pathways. (**B**) Spatial representation of local activation and lateral inhibition. In two dimensions, Turing structures generally consist of spots or stripes. (**C**) Schematic illustration of interfacial polymerization Turing system. The inhibitor (TMC) is dissolved in the organic phase (top), and the activator (PZ) and the macromolecule (PVA) are dissolved in the aqueous phases (bottom). The membrane (PA) with nanoscale Turing structures forms on the porous support (PSU). (**D** and **E**) AFM topography images of the Turing-type PA membranes. Bright yellow and orange regions correspond to the formed solid-state nanoscale Turing structures. Initial concentrations for nanoscale spots (D) are [TMC] = 6 mM, [PZ] = 28 mM, and [PVA] = 12 mM, and for nanoscale stripes (E), [TMC] = 8 mM, [PZ] = 23 mM, and [PVA] = 32 mM. Scan area is 2 μm by 2 μm.

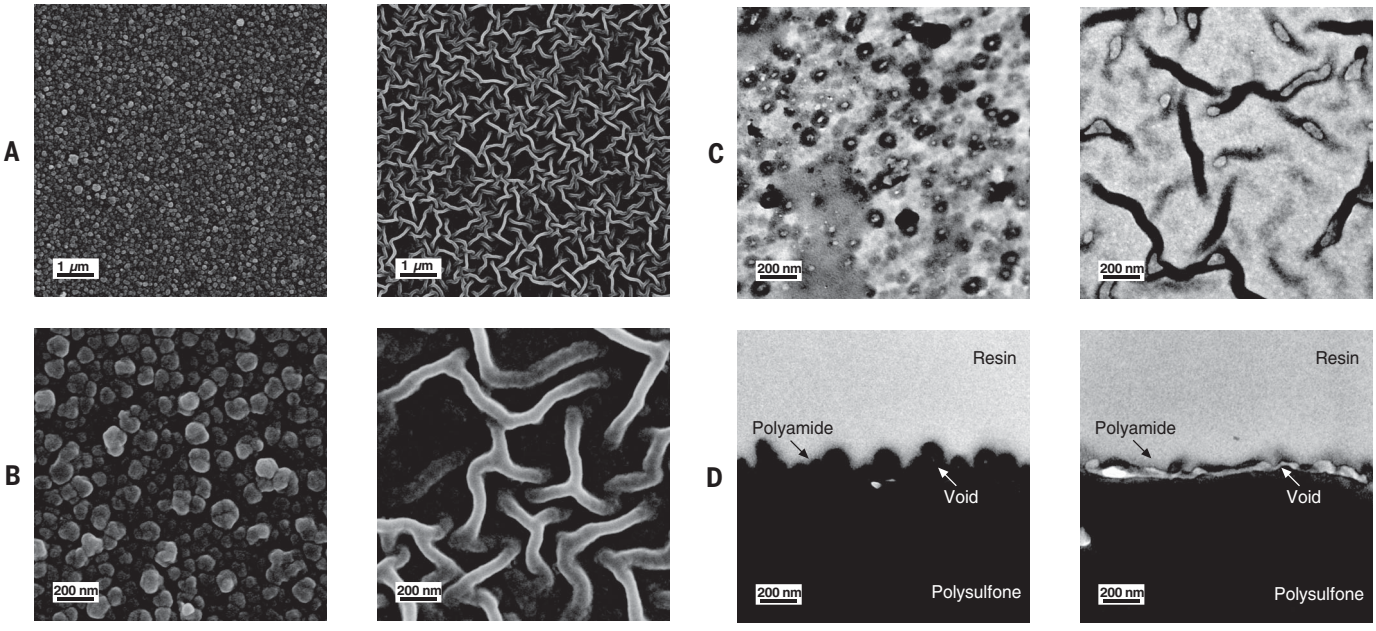

Fig. 2. Electron micrographs of the Turing-type PA membranes. (**A**) Low-magnification SEM images of the two membrane surfaces. (**B**) High-magnification SEM images of the two different structures. (**C** and **D**) Projected area TEM images (C) and cross-sectional TEM images (D), showing the internal characteristics and three-dimensional morphologies of the two structures.

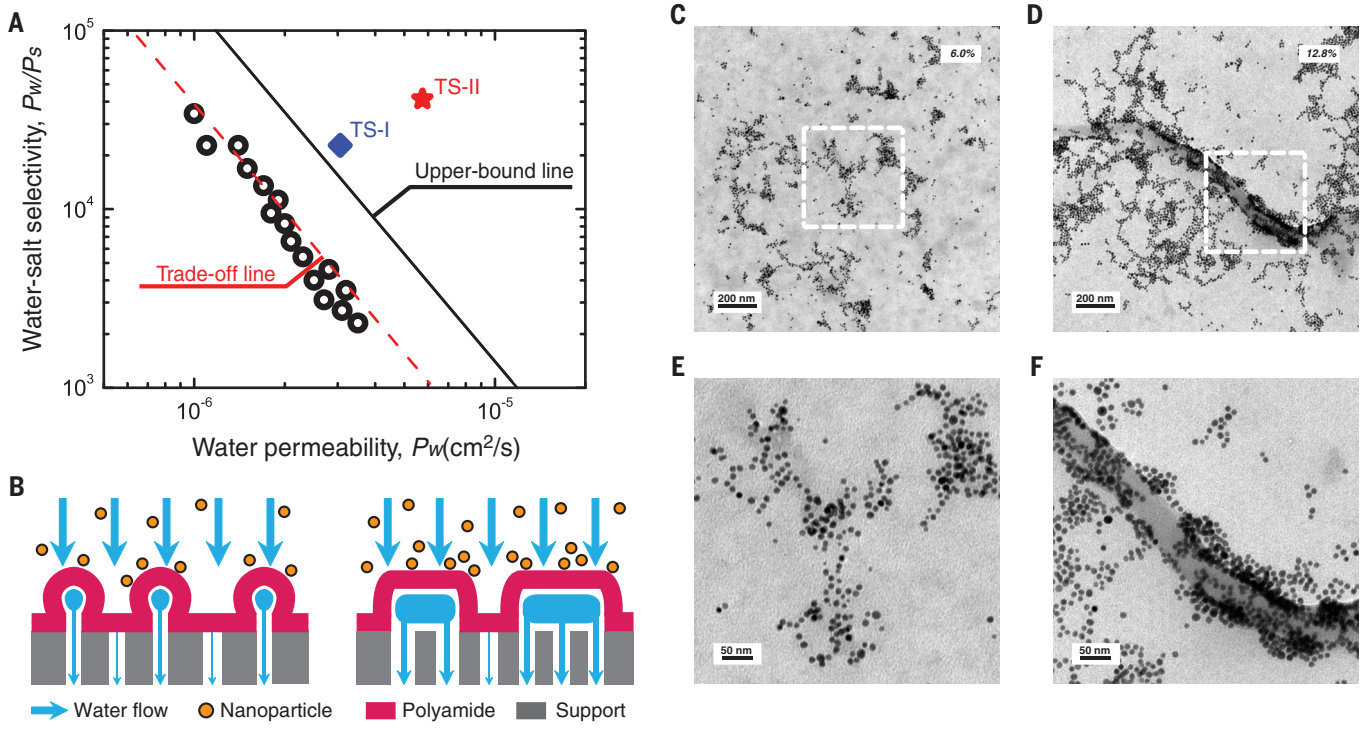

Fig. 3. Spatial distribution of water permeability sites in the Turing-type PA membranes. (**A**) Correlation between water permeability and water-salt selectivity for the Turing-type PA membranes [TS-I (blue diamond) and TS-II (red star)] and other nanofiltration membranes (open circles). These data were obtained from water-salt separation tests (2000 ppm $MgSO_4$, 25°C, 4.8 bar). The dashed red line is the permeability-selectivity trade-off for traditional semiaromatic PA membranes, and the solid black line is the empirical upper-bound relationship (*26*). P_s, salt permeability. (**B**) Schematic diagrams of the dynamic filtration experiments with GNPs and the transport of water across the Turing-type PA membranes. (**C** to **F**) Projected area TEM images showing nanoparticle deposition on the surfaces of the Turing-type PA membranes after 10-min filtration tests (1.0×10^{12} particles ml^{-1}, 25°C, 4.8 bar). In (C) and (D), GNP percent surface area coverage is given in the upper right corner of each image. In (E) and (F), high-resolution TEM images of outlined areas from (C) and (D), respectively, show spatial distribution of nanoparticle deposition patterns and Turing structures.

images show that both structures are uniformly distributed throughout the membranes (Fig. 2A), which is consistent with the corresponding AFM measurements. A closer look at the membrane surfaces (Fig. 2B) reveals that the nanoscale Turing structures generally consist of close-packed hexagonal arrays or interconnected labyrinthine networks (figs. S16 to S18), with diameters ranging between 60 and 80 nm (fig. S19). The TEM analyses not only present the external features on the surfaces of the membranes but also provide morphology information on the internal characteristics of the structures. Projected area (Fig. 2C) and cross-sectional TEM (Fig. 2D) micrographs show that there are two types of voids in the Turing structures, with diameters ranging from 30 to 40 nm (fig. S20). The thickness of the Turing-type PA membranes is about 20 nm or less, two times thinner than that of traditional semiaromatic PA membranes (*24*). In three dimensions, the Turing structures are bubble or tube shaped, like Turing patterns in the BZ microemulsion system (*25*).

We evaluated separation performance of the two membranes by saltwater desalination tests and explored structure-property relationships in these membranes for water purification. The water and salts transport data show that both membranes exhibit excellent separation performance, surpassing the water-salt separation upper-bound line (Fig. 3A) of traditional nanofiltration membranes (*26*). Counterintuitively, water permeability and water-salt selectivity are both high, in contrast to the trade-off behavior of traditional polymer membranes (tables S3 and S4), where higher water permeability invariably leads to lower water-salt selectivity (*27*). Additionally, tube-structured membrane TS-II exhibits higher water flux and similar salt rejections compared to that of bubble-structured membrane TS-I under the same test conditions (Table 2). The water flux of TS-II is as high as 125 liters m^{-2} $hour^{-1}$,

Table 2. Separation performance of the Turing-type PA membranes. The operating pressure was controlled at 4.8 bar, and the temperature was maintained at 25°C by a heat exchanger. The feed flow rate was 6 liters min^{-1}, and the concentrations of salts in the feed solutions were 2000 parts per million. All measurements were made 1 hour after starting the filtration to stabilize the membrane performance. The rejections were calculated on the basis of the electrical conductivities of feed and permeate solutions.

Solute	TS-I		TS-II	
	Flux (liters m^{-2} $hour^{-1}$)	Rejection (%)	Flux (liters m^{-2} $hour^{-1}$)	Rejection (%)
NaCl	64 ± 6	51.2 ± 2.3	124 ± 11	49.6 ± 2.0
$MgCl_2$	60 ± 5	88.1 ± 1.6	114 ± 12	91.2 ± 1.2
$CaCl_2$	58 ± 5	88.0 ± 1.5	117 ± 10	92.7 ± 1.5
$MgSO_4$	63 ± 7	98.5 ± 0.5	125 ± 14	99.2 ± 0.1
Na_2SO_4	61 ± 4	99.1 ± 0.2	119 ± 11	99.6 ± 0.1

which is approximately two times higher than that of TS-I. This result correlates well with the excess surface area ratio of the membranes, indicating that the Turing structures have a large effect on the water flux. On the basis of these observations, we hypothesized that there must be some specific sites with relatively higher water permeability in the Turing structures and that these high-permeability sites lead to membranes with an enhanced water transport property.

To verify this hypothesis, we used gold nanoparticles (GNPs) as probes in combination with microscopy methods to visually examine the spatial distribution of water permeability sites in the Turing-type membranes (Fig. 3B). GNPs are negatively charged under neutral conditions, and both membranes showed essentially the same surface charge behavior as GNPs (table S5). Consequently, for deposition to occur (figs. S21 and S22), drag forces had to overcome repulsive forces originating from nanoparticle-membrane electrostatic interactions (*28*, *29*). Projected area TEM micrographs revealed that the deposition of GNPs was not uniformly distributed across the membrane surfaces. Nanoparticle surface area coverage for TS-I and TS-II were 6.0 (Fig. 3C) and 12.8% (Fig. 3D), respectively. GNPs deposited in specific areas of the membrane surfaces and formed clusters, leaving other areas of the surfaces uncovered or with considerably fewer sparsely distributed GNPs (figs. S23 and S24 and tables S6 and S7). Most of GNPs were deposited around bubble (Fig. 3E) or tube structures (Fig. 3F), which provides visual evidence supporting the existence of relatively higher water permeability sites in the nanoscale Turing structures (figs. S25 and S26).

Our work demonstrates that Turing structures can be produced by interfacial polymerization when appropriate initial conditions are created. Microscopic characterization of the Turing-type membranes reveals that the spatial distribution of relatively higher water permeability sites agrees well with the corresponding Turing structures at the nanoscale. These unusual nanostructures, which are generated by diffusion-driven instability, enable outstanding transport properties in both water permeability and water-salt selectivity.

REFERENCES AND NOTES

1. A. M. Turing, *Philos. Trans. R. Soc. Lond. B Biol. Sci.* **237**, 37–72 (1952).
2. A. Gierer, H. Meinhardt, *Kybernetik* **12**, 30–39 (1972).
3. G. Nicolis, I. Prigogine, *Self-organization in Nonequilibrium Systems* (Wiley, 1977).
4. H. Meinhardt, *Models of Biological Pattern Formation* (Academic Press, 1982).
5. J. D. Murray, *Mathematical Biology* (Springer, 1989).
6. V. Castets, E. Dulos, J. Boissonade, P. De Kepper, *Phys. Rev. Lett.* **64**, 2953–2956 (1990).
7. Q. Ouyang, H. L. Swinney, *Nature* **352**, 610–612 (1991).
8. V. K. Vanag, I. R. Epstein, *Phys. Rev. Lett.* **87**, 228301 (2001).
9. J. Horváth, I. Szalai, P. De Kepper, *Science* **324**, 772–775 (2009).
10. T. Bánsági Jr., V. K. Vanag, I. R. Epstein, *Science* **331**, 1309–1312 (2011).
11. S. Sick, S. Reinker, J. Timmer, T. Schlake, *Science* **314**, 1447–1450 (2006).
12. S. Kondo, T. Miura, *Science* **329**, 1616–1620 (2010).
13. P. Müller *et al*., *Science* **336**, 721–724 (2012).
14. R. Sheth *et al*., *Science* **338**, 1476–1480 (2012).
15. J. Raspopovic, L. Marcon, L. Russo, J. Sharpe, *Science* **345**, 566–570 (2014).
16. P. W. Morgan, *Condensation Polymers: By Interfacial and Solution Methods* (Interscience, New York, 1965).
17. E. L. Wittbecker, P. W. Morgan, *J. Polym. Sci., Polym. Phys. Ed.* **40**, 289–297 (1959).
18. P. W. Morgan, S. Kwolek, *J. Polym. Sci., Polym. Phys. Ed.* **40**, 299–327 (1959).
19. J. E. Cadotte, R. S. King, R. J. Majerle, R. J. Petersen, *J. Macromol. Sci. Chem.* **15**, 727–755 (1981).
20. R. J. Petersen, *J. Membr. Sci.* **83**, 81–150 (1993).
21. L. J. Schwartz, C. L. DeCiantis, S. Chapman, B. K. Kelley, J. P. Hornak, *Langmuir* **15**, 5461–5466 (1999).
22. J. M. Petit, X. X. Zhu, P. M. Macdonald, *Macromolecules* **29**, 70–76 (1996).
23. C. Y. Tang, Y. N. Kwon, J. O. Leckie, *Desalination* **242**, 168–182 (2009).
24. F. A. Pacheco, I. Pinnau, M. Reinhard, J. O. Leckie, *J. Membr. Sci.* **358**, 51–59 (2010).
25. I. R. Epstein, B. Xu, *Nat. Nanotechnol.* **11**, 312–319 (2016).
26. G. M. Geise, H. B. Park, A. C. Sagle, B. D. Freeman, J. E. McGrath, *J. Membr. Sci.* **369**, 130–138 (2011).
27. H. B. Park, J. Kamcev, L. M. Robeson, M. Elimelech, B. D. Freeman, *Science* **356**, eaab0530 (2017).
28. L. Song, M. Elimelech, *J. Colloid Interface Sci.* **173**, 165–180 (1995).
29. C. Y. Tang, J. O. Leckie, *Environ. Sci. Technol.* **41**, 4767–4773 (2007).

ACKNOWLEDGMENTS

We thank X. A. Zhao for helpful discussions and L. He, J. Hong, N. H. Rong, S. D. Shen, H. Wang, Y. Xu, M. J. Yu, and H. J. Zhang for technical assistance. **Funding**: This work was supported by the National Natural Science Foundation of China (nos. 51578485 and 21671171) and the National Basic Research Program of China (no. 2015CB655303). **Author contributions**: Z.T. performed the experiments. Z.T., S.F.C., X.S.P., and L.Z. designed the experiments and analyzed the data. All authors discussed the results and wrote the manuscript. **Competing interests**: L.Z., Z.T., and S.F.C. are inventors on patent application 201810120316.x submitted by Zhejiang University, which covers Turing-type polyamide membranes. **Data and materials availability**: All data are available in the manuscript or in the supplementary materials.

SUPPLEMENTARY MATERIALS

www.sciencemag.org/content/360/6388/518/suppl/DC1
Materials and Methods
Supplementary Text
Figs. S1 to S26
Tables S1 to S7
References (*30*–*39*)

1 December 2017; accepted 21 March 2018
10.1126/science.aar6308

SURFACE CHEMISTRY

Real-space and real-time observation of a plasmon-induced chemical reaction of a single molecule

Emiko Kazuma,[1] Jaehoon Jung,[2] Hiromu Ueba,[3] Michael Trenary,[4] Yousoo Kim[1]*

Plasmon-induced chemical reactions of molecules adsorbed on metal nanostructures are attracting increased attention for photocatalytic reactions. However, the mechanism remains controversial because of the difficulty of direct observation of the chemical reactions in the plasmonic field, which is strongly localized near the metal surface. We used a scanning tunneling microscope (STM) to achieve real-space and real-time observation of a plasmon-induced chemical reaction at the single-molecule level. A single dimethyl disulfide molecule on silver and copper surfaces was dissociated by the optically excited plasmon at the STM junction. The STM study combined with theoretical calculations shows that this plasmon-induced chemical reaction occurred by a direct intramolecular excitation mechanism.

Localized surface plasmon (LSP) resonances of metal nanostructures can focus light near the metal surface to sizes below the diffraction limit (*1*), and the generated localized electric field can be used for near-field optical spectroscopies (*2*, *3*). In addition, LSPs facilitate highly efficient conversion of solar energy in photovoltaics (*4*, *5*) and photocatalysts (*5*, *6*). In particular, plasmon-induced chemical reactions of molecules adsorbed on metal nanostructures are attracting increased attention as photocatalysts (*7*, *8*) that can form bonds (*9*–*13*) or dissociate them (*13*–*16*). An indirect hot-electron transfer mechanism (Fig. 1A) (*7*, *8*) has been invoked for these reactions. Electron-hole pairs are generated in the metal nanostructures by nonradiative decay of the LSP (*7*, *17*, *18*), and the hot electrons transfer to form a transient negative ion (TNI) state of the adsorbed molecule (*7*). Recently, plasmon-induced dissociations of O_2 (*14*) and H_2 (*15*) molecules were observed and explained by a mechanism in which the dissociation reactions proceed through vibrational excitation after the transfer of hot electrons generated TNI states.

We propose a direct intramolecular excitation mechanism (Fig. 1B) on the basis of direct observation of a plasmon-induced chemical reaction of a single molecule. The LSP resonantly excites electrons from the occupied state to the unoccupied state in the electronic structure of an adsorbate. Single molecules in the strongly localized plasmonic field near the metal surface can be observed in real space and real time. We successfully made such observations through experimental studies with the LSP excited within the nanogap between a metal substrate and a Ag tip of a scanning tunneling microscope (STM).

Figure 2, A and B, illustrates our experimental scheme for investigating the plasmon-induced chemical reaction with the STM. Dimethyl disulfide [$(CH_3S)_2$] was selected as a target molecule for the plasmon-induced chemical reaction. To excite the LSP optically, the Ag tip with a curvature radius of ~60 nm (fig. S1) was positioned over the bare metal surface, and the sample bias voltage (V_s) and tunneling current (I_t) were set to 20 mV and 0.2 nA, respectively. Tunneling electrons at a bias of 20 mV cannot excite vibrational modes related to any kind of reaction, such as rotation, desorption, or dissociation of the molecule (*19*, *20*).

The LSP generates a strong electric field in the nanogap (Fig. 2C and fig. S2). Figure 2, D and E, shows the spatial distribution of isolated $(CH_3S)_2$ molecules on Ag(111) before and after the excitation of the LSP with p-polarized light at 532 nm. Although individual $(CH_3S)_2$ molecules appear as elliptical protrusions in the STM images, some molecules near the tip position were transformed into two identical ball-shaped protrusions after the excitation of the LSP (fig. S3). The dissociated chemical species have the same appearance as CH_3S molecules obtained by injecting tunneling electrons into a $(CH_3S)_2$ molecule (*19*–*21*). This implies that the S–S bond in $(CH_3S)_2$ was dissociated by the LSP. Notably, other reactions, such as rotation or desorption, were not observed.

The dissociation ratio (N/N_0), which we defined as the number of $(CH_3S)_2$ molecules (N) after LSP excitation divided by the number of preadsorbed molecules (N_0), was measured for quantitative analyses. Figure 2F shows plots of $\ln(N/N_0)$ as a function of the irradiation time (t) in the four areas depicted with concentric rings (Fig. 2B). The linearity of the plots shows that the dissociation, $(CH_3S)_2 \rightarrow 2CH_3S$, is a first-order reaction. The slopes of the lines in Fig. 2F determine the dissociation rate constant (k). The rate constant was largest in area one and decreased with lateral distance from the tip (Fig. 2G). We calculated the electromagnetic field intensity in the nanogap (E_{gap}) (Fig. 2C) using the Ag tip with a curvature radius of 60 nm and a cone angle of 15° estimated from the scanning electron microscopy images shown in fig. S1 (see the supplementary text and fig. S2). The lateral distribution of E_{gap} is also shown in Fig. 2G. From comparison of k with E_{gap}, we conclude that the plasmon-induced dissociation has a strong correlation with the electric field intensity of the optically excited LSP.

To explore a plausible mechanism for the plasmon-induced dissociation, we first examined the wavelength (λ) dependence of the dissociation yield on Ag(111) (fig. S3). The rate constant divided by the number of incident photons per second is equivalent to the yield of plasmon-induced dissociation (Y_{LSP}). The wavelength at the maximum intensity of Y_{LSP} (λ_{Max}) and the threshold wavelength of Y_{LSP} (λ_{Th}) obtained in area one (Fig. 3A) were ~532 nm (~2.33 eV) and ~780 nm (~1.59 eV), respectively. The plasmon-induced dissociation of $(CH_3S)_2$ was also examined on a Cu(111) substrate (Fig. 3B and fig. S4), which has a different electronic structure and plasmonic properties. The Y_{LSP} λ spectrum for Cu(111) had λ_{Max} = ~670 nm (~1.85 eV) and λ_{Th} = ~980 nm (~1.27 eV).

In contrast, the photodissociation yield (Y_{photon}) measured when the sample was exposed to light with the tip retracted by more than 2 μm from the surface exhibited peak and threshold wavelengths at ~450 nm (~2.76 eV) and ~635 nm (~1.95 eV) on Ag(111) and ~450 and ~670 nm on Cu(111), respectively. Our previous work (*21*) revealed that photodissociation of the S–S bond in $(CH_3S)_2$ molecules adsorbed on Ag(111) and Cu(111) surfaces occurs through direct electronic excitation from the highest occupied molecular orbital (HOMO)– to the lowest unoccupied molecular orbital (LUMO)–derived orbitals of $(CH_3S)_2$, that is, from the nonbonding lone pair–type orbitals on the S atoms (n_S) to the antibonding orbital localized at the S–S bond (σ^*_{SS}) (supplementary text).

The hybridization between $(CH_3S)_2$ and the metal substrate reduced the optical energy gap into the range of visible light. Furthermore, LUMO-derived molecular states with less overlap with the metal substrate were formed, which resulted in longer excited-state lifetimes than would be the case for strong overlap with the substrate. Thus, photodissociation occurs through the direct excitation between the frontier MOs, and the shape of the Y_{photon} λ spectra reflected the densities of states (DOSs) of both the HOMO and LUMO (fig. S5). In contrast, the Y_{LSP} λ spectra had a shape similar to that of the simulated E_{gap} λ spectra (Fig. 3C) in the wavelength regions where photodissociation occurs. This similarity indicates that the LSP was an excitation source and that the Y_{LSP} strongly depended on the energy profiles of the LSP. A similar wavelength

[1]Surface and Interface Science Laboratory, RIKEN, Wako, Saitama 351-0198, Japan. [2]Department of Chemistry, University of Ulsan, 93 Daehak-ro, Nam-gu, Ulsan 680-749, Republic of Korea. [3]Graduate School of Science and Engineering, University of Toyama, Toyama 930-8555, Japan. [4]Department of Chemistry, University of Illinois at Chicago, Chicago, IL 60607, USA.
*Corresponding author. Email: ykim@riken.jp

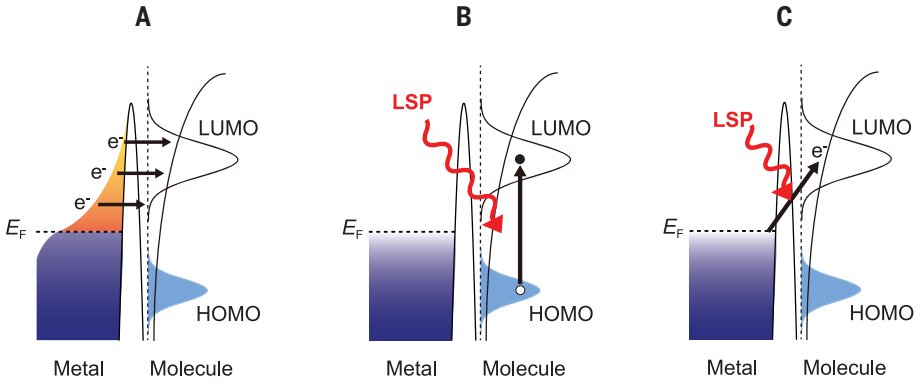

Fig. 1. Excitation mechanisms for plasmon-induced chemical reactions. (**A**) Indirect hot-electron transfer mechanism. Hot electrons (e^-) generated via nonradiative decay of an LSP transferred to form the TNI states of the molecule. (**B**) Direct intramolecular excitation mechanism. The LSP induces direct excitation from the occupied state to the unoccupied state of the adsorbate. (**C**) Charge transfer mechanism. The electrons are resonantly transferred from the metal to the molecule.

dependence on Ag and Cu was also observed in the enhancement of surface-enhanced Raman scattering (SERS) intensities (*22*). In addition, the maximum intensity of Y_{LSP} on Ag(111) and Cu(111) was ~400 and ~300 times as high as that of Y_{photon}, respectively, which was caused by the strong enhancement of the electric field by the LSP (Fig. 3C).

In the indirect hot-electron transfer mechanism (Fig. 1A), the Y_{LSP} is determined both by the energy distribution of hot electrons and by the DOSs of the LUMOs. Energy distributions of hot electrons and holes generated by the decay of LSPs are sensitive to the electronic band structure of metals (*17*, *18*). If the energy of the LSPs was lower than the threshold energy for direct interband transitions of the metals, both electrons and holes would be equitably distributed from zero to the energy of the LSP through phonon-assisted transitions (*18*). In contrast, at

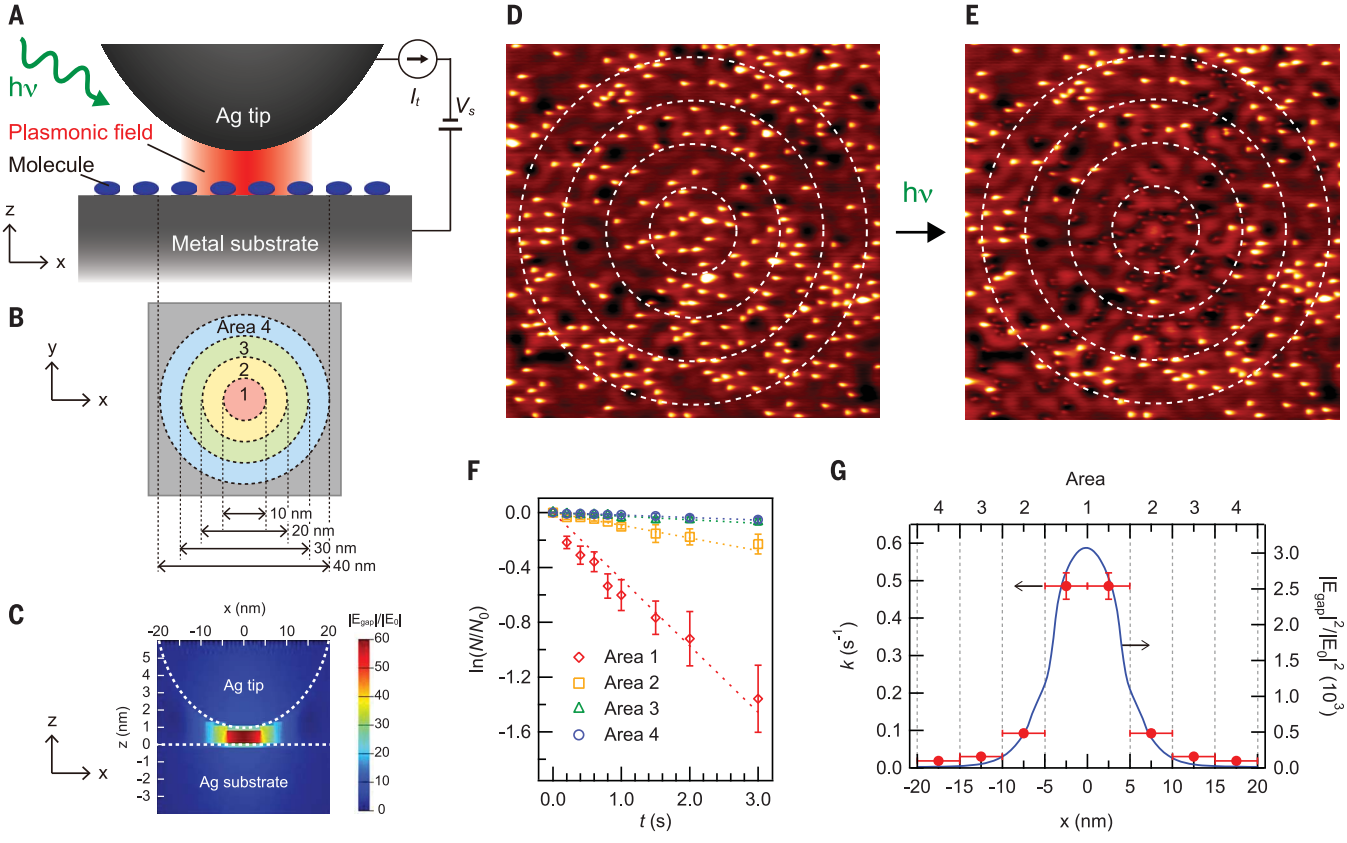

Fig. 2. Real-space investigations of the plasmon-induced chemical reaction. (**A**) Schematic illustration of the experiment for the real-space investigation of the plasmon-induced chemical reaction in the nanogap between a Ag tip and a metal substrate. The tip was positioned over the metal surface during light irradiation with the feedback loop turned on to maintain the gap distance. The V_s and I_t were kept at 20 mV and 0.2 nA. hν, Planck's constant (*h*) multiplied by frequency (ν). (**B**) Division of the STM image into four areas depicted with 10-nm wide concentric rings for analysis. (**C**) Simulated spatial distribution of the electric field at the 1-nm gap under p-polarized light at 532 nm. E_0, incident electric field. Topographic STM images of $(CH_3S)_2$ molecules on Ag(111) (**D**) before and (**E**) after irradiation with p-polarized light at 532 nm (~7.6 × 10^{17} photons cm^{-2} s^{-1}, 2 s) (V_s = 20 mV, I_t = 0.2 nA, 43 nm by 43 nm). The tip was positioned at the center of area one during light irradiation. (**F**) Time dependence of the dissociation ratio (N/N_0) under irradiation with p-polarized light at 532 nm (~5.9 × 10^{16} photons cm^{-2} s^{-1}) in the four areas shown in (B). Each data point represents the average of results from six trials. The dotted lines denote single exponential functions fitted to the data points [$\ln(N/N_0) = -kt$]. Error bars indicate SD. (**G**) The rate constant *k* obtained at areas one through four and the calculated lateral profile of electric field intensity at 0.1 nm above the substrate surface (z = 0.1 nm) under 533-nm light. x = 0 nm corresponds to the center of the tip.

higher energies, direct transitions dominate, and the relative probability density of hot carriers dramatically increases.

If the plasmon-induced dissociation of $(CH_3S)_2$ occurred through hot-electron transfer, the Y_{LSP} λ spectra would have exhibited a step change at the threshold energy of the interband transition at ~3.0 and ~2.0 eV for Ag and Cu, respectively (*23*), and increased at the higher energies, because the LUMO states are distributed broadly above the Fermi level (E_F) (fig. S5). In addition, the hot electrons generated by the direct transitions of Cu have a broad energy distribution above E_F (*18*) and can be transferred into the LUMO states, resulting in the excitation of vibrational modes lying along the reaction coordinate. However, the expected spectral change at the threshold energy of the interband transition of the metal was not observed. Moreover, the overall shapes of the Y_{LSP} λ spectra reflected not only the shape of the E_{gap} λ spectra (Fig. 3C) but also the shape of the Y_{photon} λ spectra, that is, the energy distribution of the DOSs for both the HOMO (n_S) and the LUMO (σ^*_{SS}) (Fig. 3, A and B). Thus, we could exclude the indirect hot-electron transfer mechanism for this plasmon-induced dissociation. Furthermore, hot-hole transfer in Cu, where hot holes are much more energetic than hot electrons (*17*, *18*), could also be excluded by the shape of the Y_{photon} λ spectrum. We conclude that the LSP efficiently induces and enhances the dissociation reaction through the same reaction pathway as photodissociation ($n_S \rightarrow \sigma^*_{SS}$), on the basis of the direct intramolecular excitation mechanism (Fig. 1B).

The Y_{LSP} λ spectra also had tails extending to longer wavelengths where photodissociation never occurred. This finding suggests that the LSP also enabled direct intramolecular excitation from the MO in-gap states near E_F (supplementary text and figs. S5 to S7) to σ^*_{SS} ($MO_{in\text{-}gap} \rightarrow \sigma^*_{SS}$), as well as the HOMO-LUMO transition ($n_S \rightarrow \sigma^*_{SS}$). The computationally estimated energy gaps between E_F and the edge of the LUMO state are ~1.0 and ~0.80 eV on Ag(111) and Cu(111), respectively (fig. S5). This model is consistent with the threshold energy of the Y_{LSP} on Ag(111) being greater than that on Cu(111). Dissociation was also apparently induced by direct intramolecular excitation of $MO_{in\text{-}gap} \rightarrow \sigma^*_{SS}$. The DOS of the in-gap states is much smaller than that of the frontier electronic states (figs. S5 to S7), and thus the direct excitation of $MO_{in\text{-}gap} \rightarrow \sigma^*_{SS}$ is expected to be a much less efficient process than that of HOMO-LUMO transition ($n_S \rightarrow \sigma^*_{SS}$). However, the LSP generated a strong electric field localized at the interface between the adsorbate and the metal and enabled dissociation even through inefficient excitation pathways ($MO_{in\text{-}gap} \rightarrow \sigma^*_{SS}$).

A charge transfer from metals to molecules (Fig. 1C) was proposed to explain chemical enhancement effects in SERS (*24*–*26*) on the basis of LSPs. The Raman intensities of pyridine molecules adsorbed on coinage metals such as Ag, Cu, and Au were enhanced by electron transfer from the highest occupied state (the valence shell s orbital) of the metal near the E_F to the unoccupied MOs (*24*, *25*). In addition, the charge transfer mechanism was invoked recently to describe a plasmon-induced chemical transformation (*27*) in which the electrons near the E_F of plasmonic metal nanoparticles were transferred to adsorbed molecules. In the plasmon-induced dissociation of $(CH_3S)_2$, the charge transfer from near the E_F to σ^*_{SS} ($E_F \rightarrow \sigma^*_{SS}$) was also taken into account to explain the tails of the Y_{LSP} λ spectra in the low-energy region because the energy gaps between E_F and σ^*_{SS} were about 1.0 to 2.0 eV and 0.8 to 1.5 eV on Ag(111) and Cu(111), respectively (fig. S5).

Real-time observation with an STM allowed us to measure the rates of plasmon-induced chemical reactions for single molecules, thereby providing insights into the elementary reaction pathways that cannot be accessed by conventional spectroscopies and the analyses of Y_{LSP} λ spectra. I_t is highly sensitive to the change in the gap distance (*d*) (*28*), and thus real-time information can be collected by tracing I_t under light irradiation (Fig. 4A). Figure 4B shows the current trace when the STM tip was positioned over a target molecule adsorbed on Ag(111) and exposed to p-polarized light at 532 nm. A sudden drop of I_t reflected the change in *d* from d_1 to d_2 (Fig. 4A) caused by molecular dissociation, and the dissociation rate was determined by the inverse of the time required for the plasmon-induced dissociation (t_R).

Notably, no reaction could be induced with tunneling electrons at a V_s of 20 mV, and thermal expansion of the tip was negligible because I_t was stable on the metal surface under light irradiation (fig. S8). The gap distance *d* (Fig. 4C) is controlled by I_t, where $I_t \propto V_s \exp(-Ad\sqrt{\Phi})$ (V_s = 20 mV; *A*, coefficient; and Φ, barrier height). We investigated the dependence of *d* on the dissociation rate ($1/t_R$) at the single-molecule level (Fig. 4C and fig. S9). We note that $1/t_R$ exhibited *d* dependence similar to that of the calculated electric field intensity (Fig. 4D and fig. S10). This relation indicates that the reaction is caused by the LSP and suggests that the reactivity is determined by the coupling between the electric field of the LSP and a transition dipole moment of the molecule.

In the indirect hot-electron transfer mechanism, the reactions are initiated from the TNI states formed by the hot-electron transfer to molecules via an inelastic electron tunneling (IET) process (*8*) (Fig. 1A). We can obtain further knowledge of reaction pathways initiated from the TNI states formed by electron transfer from the metal to the molecule via the IET process with the STM (*19*, *20*). In addition, the IET process examined with the STM enables us to describe the elementary processes of vibrational or electronic excitation resulting in molecular motion or reaction, which reflects the local DOS of the adsorbed molecules (*28*). Both the hot electrons of the LSP and the tunneling electrons had a broad energy distribution from the E_F to the energy of the LSP (*17*, *18*) and the applied V_s, respectively (fig. S11). Thus, the reaction pathways in the same energy regions should be the same regardless of the excitation source: hot electrons or tunneling electrons. Rotation (Fig. 4E) and dissociation (Fig. 4F) of $(CH_3S)_2$ on Ag(111) were induced through vibrational excitation with inelastically tunneled electrons at energies higher than ~0.28 and ~0.36 eV, respectively (Fig. 4G). Dissociation occurred through vibrational excitation of the C–H

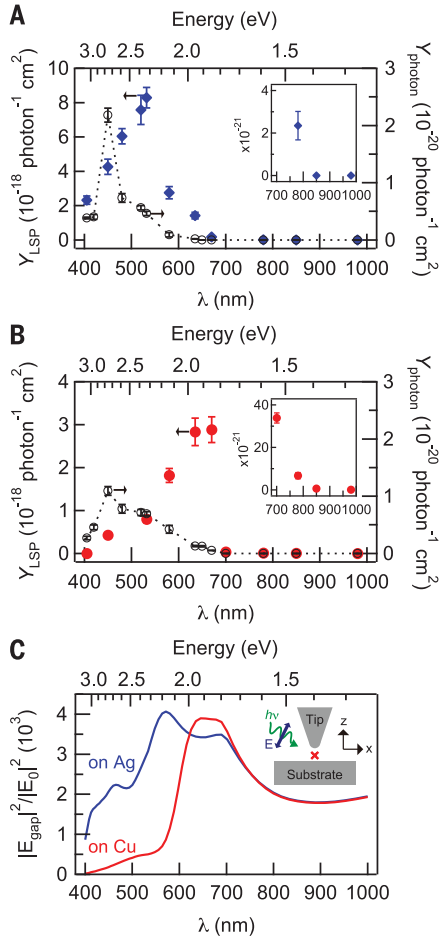

Fig. 3. Wavelength dependence of the plasmon-induced chemical reaction and of the plasmonic electric field. Wavelength dependence of Y_{LSP} of $(CH_3S)_2$ molecules on (**A**) Ag(111) (blue diamonds) and (**B**) Cu(111) (red circles). Insets in (A) and (B) show Y_{LSP} for 700 to 980 nm. Each data point represents the average of results from six trials. The photodissociation yields without the excitation of the LSP [Y_{photon}, previously reported in (*21*)] (black circles) are also shown. The yield is determined from *k* divided by the number of incident photons per second (~6.0 × 10^{16} to 6.5 × 10^{16} photons cm^{-2} s^{-1} for both plasmon-induced dissociation and photodissociation). Error bars indicate SD. (**C**) Calculated electric field intensity for a 1-nm gap between a Ag tip and the metal substrates under p-polarized light. The simulated point is *z* = 0.1 nm above the substrate surfaces and *x* = 0 nm.

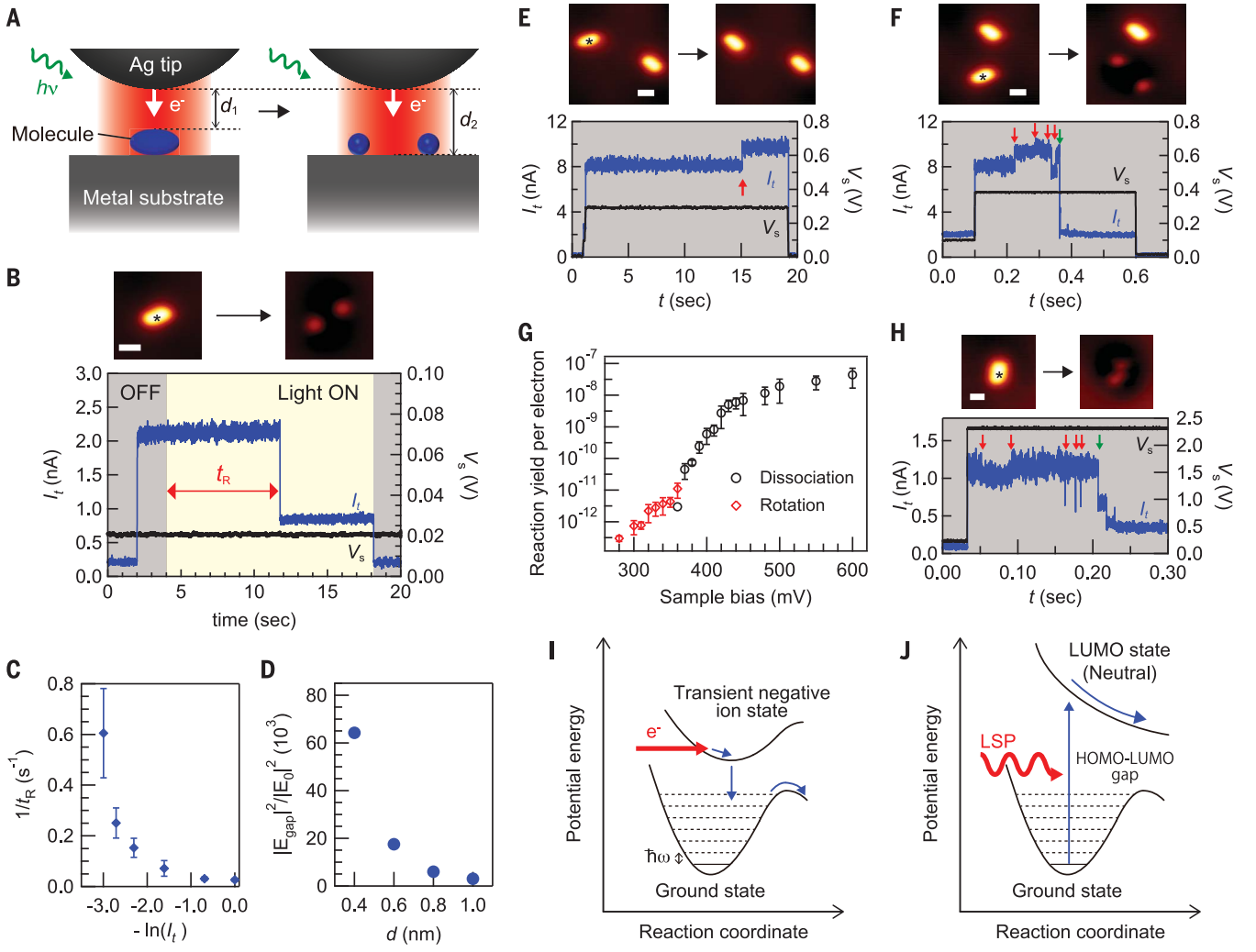

Fig. 4. Real-time STM results for the plasmon-induced chemical reaction and IET-induced reactions of a single molecule. (**A**) Schematic illustration of the real-time observation of the plasmon-induced chemical reaction. (**B**) Current trace for detecting the dissociation event for the target molecule (STM images) on Ag(111) induced by the LSP excited with p-polarized light at 532 nm (~2.7 × 10^{15} photons cm^{-2} s^{-1}). The Ag tip was positioned above the molecule marked by the asterisk in the STM image. The fixed gap resistance (V_s = 20 mV and I_t = 2.0 nA) was applied and the feedback loop was turned off to maintain the tip height at t = 2.0 s. Light irradiation started at t = 4.0 s. The light was turned off and the feedback loop was turned on at t = 18 s. The tunneling conditions at t = 0 to 2.0 s and 18 to 20 s are V_s = 20 mV and I_t = 0.2 nA. The time required for the plasmon-induced dissociation (t_R) is directly read from the current trace. (**C**) Gap distance d dependence of the dissociation rate ($1/t_R$) obtained under p-polarized light at 532 nm (~1.3 × 10^{15} photons cm^{-2} s^{-1}). Each data point represents the average of results for 12 molecules. Error bars indicate SD. (**D**) Gap distance dependence of the calculated electric field intensity at 532 nm. The simulated point is z = 0.1 nm above the substrate surface and x = 0 nm. (**E** to **H**) IET-induced reactions in the dark. Current trace was measured on the molecules with the feedback loop turned off. The tunneling conditions were (E) V_s = 0.30 V and I_t = 8.0 nA, (F) 0.38 V and 8.0 nA, and (H) 2.3 V and 1.0 nA. The current changes indicated by red and green arrows correspond to rotation and dissociation, respectively. (G) Action spectrum for the rotation and dissociation of the $(CH_3S)_2$ molecules induced by injecting tunneling electrons. The initial current was set to 8.0 nA. Each data point represents the average of results from 16 trials. Error bars indicate SD. At 360 mV, the dissociation and the rotation occurred 1 time and 15 times in 16 trials, respectively. The scale bars in the STM images in (B), (E), (F), and (H) are 0.5 nm. Schematic illustrations of the potential energy surface for the plasmon-induced chemical reactions on the basis of (**I**) the indirect hot-electron transfer mechanism and (**J**) the direct intramolecular excitation mechanism are shown. $\hbar\omega$, Planck's constant h divided by 2π ($\hbar$) multiplied by the angular frequency (ω).

stretch mode (*19*) and a combination of the C–H stretch and the S–S stretch modes (*20*). Moreover, dissociation induced with tunneling electrons was accompanied by rotation, which resulted in small changes in I_t followed by its sudden drop (Fig. 4F). Rotation before dissociation was also observed in the dissociation of O_2 on Pt(111) through vibrational excitation via the IET process with an STM (*29*).

We conclude that the energy of the TNI states formed by electron transfer from the metal to the molecule was dissipated to the vibrationally excited states according to the nondissociative potential energy surface (Fig. 4I and fig. S12), which resulted in both rotation and dissociation of $(CH_3S)_2$, and rotation is a precursor for dissociation. The small changes of I_t caused by rotation before its sudden drop were also observed for the dissociation reaction induced with tunneling electrons at 2.3 V (Fig. 4H) and 2.0 and 1.0 V (fig. S13), an energy region almost equal to that of the hot electrons of the LSP excited with light at 532, 620, and 1240 nm, respectively. Thus, the IET process through vibrational excitation at the lower energy region is always included in the reaction pathway when the electrons are distributed from the E_F to the upper energy level, which

is higher than the vibrational energies of the ground state.

If the plasmon-induced dissociation proceeded through vibrational excitation, current changes caused by rotation should appear before the dissociation. However, changes in I_t before the sudden drop were not observed (Fig. 4B and fig. S9). This difference excluded the hot-electron–mediated process, which always involved vibrational excitation in the TNI state (Fig. 4I), as an elementary pathway for the plasmon-induced dissociation of $(CH_3S)_2$. By considering the mechanistic insight obtained from the Y_{LSP} λ spectra (Fig. 3), we concluded that the plasmon-induced dissociation of $(CH_3S)_2$ occurred through the direct dissociation pathway from neutral excited states generated by direct intramolecular excitation (Fig. 4J). In addition, if the potential energy surface of the excited state formed by charge transfer from the metal states to σ^*_{SS} was dissociative for the S–S bond cleavage (fig. S12C), the charge transfer mechanism could also contribute to the plasmon-induced dissociation in the low-energy region (supplementary text). However, it is difficult to quantify the contribution of the charge transfer mechanism, because the excited state formed by charge transfer (fig. S12C) cannot be simply described in the STM experiment because of the broad energy distribution of the tunneling electrons.

The LUMOs of $(CH_3S)_2$ were weakly hybridized with the metal substrates (*21*). The weak hybridization suppressed the relaxation of the excited state and thus allowed access to the dissociative potential energy surface from the neutral excited state (Fig. 4J), which was theoretically predicted for the photodissociation of $(CH_3S)_2$ molecules in the gas phase (*30*). In contrast, the MOs of O_2 and H_2, for which plasmon-induced dissociation was explained by the indirect hot-electron transfer mechanism, were strongly hybridized with metal substrates (*14*, *15*). This suggests that the degree of hybridization between MOs and metals plays a crucial role in the plasmon-induced chemical reactions.

Our real-space and real-time STM study combined with theoretical calculations revealed that the plasmon-induced dissociation of the S–S bond in a single $(CH_3S)_2$ molecule on Ag and Cu surfaces occurred principally by the direct intramolecular excitation to the LUMO state of the antibonding S–S (σ^*_{SS}) orbital through a decay of the optically excited LSP in the nanogap between the Ag tip and the metal surface. The present results underline that the plasmon-induced chemical reactions of the molecule with the electronic states less hybridized with metals are explained by the direct intramolecular excitation mechanism but not by the indirect hot-electron transfer mechanism. These findings provide deep insights into the interaction between LSPs and molecules at metal surfaces for designing efficient plasmon-induced photocatalysis in a highly controlled fashion.

REFERENCES AND NOTES

1. J. A. Schuller *et al*., *Nat. Mater.* **9**, 193–204 (2010).
2. J. N. Anker *et al*., *Nat. Mater.* **7**, 442–453 (2008).
3. R. Zhang *et al*., *Nature* **498**, 82–86 (2013).
4. H. A. Atwater, A. Polman, *Nat. Mater.* **9**, 205–213 (2010).
5. C. Clavero, *Nat. Photonics* **8**, 95–103 (2014).
6. Q. Zhang, E. Uchaker, S. L. Candelaria, G. Cao, *Chem. Soc. Rev.* **42**, 3127–3171 (2013).
7. M. L. Brongersma, N. J. Halas, P. Nordlander, *Nat. Nanotechnol.* **10**, 25–34 (2015).
8. S. Linic, U. Aslam, C. Boerigter, M. Morabito, *Nat. Mater.* **14**, 567–576 (2015).
9. Y. F. Huang *et al*., *J. Am. Chem. Soc.* **132**, 9244–9246 (2010).
10. H. Zhu, X. Ke, X. Yang, S. Sarina, H. Liu, *Angew. Chem. Int. Ed.* **49**, 9657–9661 (2010).
11. E. M. van Schrojenstein Lantman, T. Deckert-Gaudig, A. J. G. Mank, V. Deckert, B. M. Weckhuysen, *Nat. Nanotechnol.* **7**, 583–586 (2012).
12. L. Kang *et al*., *Chem. Commun.* **49**, 3389–3391 (2013).
13. Z. Zhang, T. Deckert-Gaudig, P. Singh, V. Deckert, *Chem. Commun.* **51**, 3069–3072 (2015).
14. P. Christopher, H. Xin, S. Linic, *Nat. Chem.* **3**, 467–472 (2011).
15. S. Mukherjee *et al*., *Nano Lett.* **13**, 240–247 (2013).
16. Z. Zhang, S. Sheng, H. Zheng, H. Xu, M. Sun, *Nanoscale* **6**, 4903–4908 (2014).
17. R. Sundararaman, P. Narang, A. S. Jermyn, W. A. Goddard 3rd, H. A. Atwater, *Nat. Commun.* **5**, 5788 (2014).
18. A. M. Brown, R. Sundararaman, P. Narang, W. A. Goddard 3rd, H. A. Atwater, *ACS Nano* **10**, 957–966 (2016).
19. M. Ohara, Y. Kim, S. Yanagisawa, Y. Morikawa, M. Kawai, *Phys. Rev. Lett.* **100**, 136104 (2008).
20. K. Motobayashi, Y. Kim, M. Ohara, H. Ueba, M. Kawai, *Surf. Sci.* **643**, 18–22 (2016).
21. E. Kazuma, J. Jung, H. Ueba, M. Trenary, Y. Kim, *J. Am. Chem. Soc.* **139**, 3115–3121 (2017).
22. B. Chase, B. Parkinson, *J. Phys. Chem.* **95**, 7810–7813 (1991).
23. H. Ehrenreich, H. R. Philipp, *Phys. Rev.* **128**, 1622–1629 (1962).
24. H. Ueba, *Surf. Sci.* **131**, 347–366 (1983).
25. D. Wu *et al*., *J. Phys. Chem. C* **112**, 4195–4204 (2008).
26. M. Osawa, N. Matsuda, K. Yoshii, I. Uchida, *J. Phys. Chem.* **98**, 12702–12707 (1994).
27. C. Boerigter, U. Aslam, S. Linic, *ACS Nano* **10**, 6108–6115 (2016).
28. Y. Kim, K. Motobayashi, T. Frederiksen, H. Ueba, M. Kawai, *Prog. Surf. Sci.* **90**, 85–143 (2015).
29. B. C. Stipe, M. A. Rezaei, W. Ho, *Science* **280**, 1732–1735 (1998).
30. C. Luo, W. Du, X. Duan, J. Liu, Z. Li, *Chem. Phys. Lett.* **469**, 242–246 (2009).

ACKNOWLEDGMENTS

We appreciate Y. Hasegawa for supporting the preparation of Ag tips. We thank J. Yoshinobu for helpful discussions. **Funding:** The present work was supported in part by a Grant-in-Aid for Scientific Research (A) (15H02025), a Grant-in-Aid for Young Scientists (B) (16K17862), and the RIKEN postdoctoral researchers (SPDR) program. J.J. acknowledges the financial support of the National Research Foundation under the Next Generation Carbon Upcycling Project (grant 2017M1A2A2043144) of the Ministry of Science and Information and Communication Technology, Republic of Korea. H.U. was supported by Ministry of Education, Culture, Sports, Science and Technology Grants-in-Aid for Scientific Research (KAKENHI) grant C-2539000, which allows him to continue to work after retirement from the University of Toyama. M.T. acknowledges support from a grant from the NSF (CHE-1464816). We are grateful for the use of the HOKUSAI-GreatWave supercomputer system of RIKEN. **Author contributions:** E.K. designed and carried out the experiments and the finite-difference time-domain calculations. J.J. carried out the density functional theory calculations. E.K., J.J., H.U., M.T., and Y.K. contributed to the interpretation of the results and wrote the manuscript. Y.K. planned and supervised the project. **Competing interests:** The authors declare no competing financial interests. **Data and materials availability:** All data are presented in the main text and supplementary materials.

SUPPLEMENTARY MATERIALS

www.sciencemag.org/content/360/6388/521/suppl/DC1
Materials and Methods
Supplementary Text
Figs. S1 to S13
Table S1
References (*31*–*51*)

13 June 2017; resubmitted 15 August 2017
Accepted 7 March 2018
10.1126/science.aao0872

METALLURGY

Enhanced thermal stability of nanograined metals below a critical grain size

X. Zhou,[1,2] X. Y. Li,[1]* K. Lu[1]*

The limitation of nanograined materials is their strong tendency to coarsen at elevated temperatures. As grain size decreases into the nanoscale, grain coarsening occurs at much lower temperatures, as low as ambient temperatures for some metals. We discovered that nanometer-sized grains in pure copper and nickel produced from plastic deformation at low temperatures exhibit notable thermal stability below a critical grain size. The instability temperature rises substantially at smaller grain sizes, and the nanograins remain stable even above the recrystallization temperatures of coarse grains. The inherent thermal stability of nanograins originates from an autonomous grain boundary evolution to low-energy states due to activation of partial dislocations in plastic deformation.

Refining grains of metals into the nanometer scale may greatly enhance their strength and hardness (*1*). But the introduced high density of grain boundaries (GBs) provides a strong driving force for grain coarsening accompanied by property degradation. The instability temperature, which marks the onset of grain coarsening, decreases substantially for nanometer-sized grains in metals (*1*–*3*). In some nanograined metals, such as Cu, coarsening occurs even at ambient temperatures (*1*, *4*). The inherent thermal instability is an "Achilles' heel" of nanograined materials and hinders technological applications at elevated temperatures. The temperature response also complicates the processing of nanograined metals for further structure refinement and property enhancements (*1*).

Grain coarsening in polycrystals is basically a GB migration process, which can be inhibited by various alloy methods. Coarsening kinetics can be suppressed by pinning GBs with a second-phase drag, a solute or impurity drag, or by chemical ordering (*5*–*8*). Lowering GB energy by solute segregation may reduce the thermodynamic driving force for coarsening and hence stabilize the nanograins as well, as observed in FeP, Ni-P, and Pd-Zr systems (*9*–*11*). But these alloy-based approaches may unavoidably influence, and often deteriorate, mechanical, physical, or chemical properties of nanograined materials. Stabilizing nanograined structures in pure metals without alloying is technically challenging.

Recent experimental results showed elevated thermal stabilities of nanolaminated structures in several pure metals with low-energy interfaces, such as twin boundaries or low-angle boundaries (*12*, *13*), relative to nanograined structures with conventional high-angle GBs. Apparently, reduced interfacial excess energy is effective to stabilize nanostructures in pure metals (*1*). Nevertheless, generating three-dimensional nanograins in pure metals with every GB in a low-energy state is practically very difficult. We discovered an autonomous structural evolution in GBs toward low-energy states in pure Cu and Ni as the grain sizes were reduced below a critical value by plastic deformation. This evolution led to notable thermal stability in nanograins, for which the apparent instability temperature was even higher than that for coarse grains.

We processed coarse-grained oxygen-free Cu bar specimens with a purity of 99.97% by using a surface mechanical grinding treatment (SMGT) in liquid nitrogen to generate a gradient nanograined surface layer (*14*) (table S1). After the treatment, randomly oriented grains with an average transversal size of ~40 ± 2 nm and an aspect ratio of 1.7 were formed in the topmost surface layer (Fig. 1, A and B). Using longitude-sectional transmission electron microscopy (TEM) measurements, we found that the transversal grain sizes increased gradually with increasing depth, to about 70 nm at a 20-μm depth and 200 nm at an ~150-μm depth. We observed deformed coarse-grained structures adherent on the deformation-free core in the depth span of 150 to 500 μm.

We found weak {111}<110> texture in the surface layer of the as-prepared SMGT Cu sample with the use of electron diffraction analysis under TEM and electron backscattered diffraction (EBSD). The fraction of material with this texture changed slightly from 37.3% at the topmost surface level to 31.5% at a 40-μm depth (*14*) (fig. S5). We examined possible processing-induced contamination in the surface layer with the use of TEM–energy-dispersive spectroscopy and electron energy loss spectroscopy. The composition remained constant with increasing depth, and we did not detect impurities such as carbon and oxygen deeper than 0.5 μm from the processed surface in Cu (*14*) (fig. S4). The compositional stability resulted from performing the SMGT process in liquid nitrogen, which suppressed the atomic diffusion of elements. We removed the measurement data for the topmost 1-μm-thick layer from our analysis to avoid any potential contamination and surface effects.

We examined the grain size effects on thermal stability with the use of scanning electron microscopy (SEM) observations of the gradient nanograined specimens annealed at various temperatures for 30 min (Fig. 1A and fig. S1) (*14*). As annealing temperatures exceeded 373 K, sporadic coarsened grains began to appear in the subsurface layer in a depth span of 20 to 50 μm, where the original grains were 70 to 110 nm in size. At higher temperatures, coarsening became more evident and the coarsening layer thickened. At 453 K, the upper front of the coarsening layer migrated slightly upward and the lower front migrated downward to ~120 μm deep, where the initial grain sizes were ~175 nm. The grain size and nanohardness profiles we measured along increasing depths for the annealed samples showed an obvious softening corresponding to the coarsening in the subsurface layer (Fig. 1F). The higher the annealing temperature, the lesser the hardness and the larger the depth span of the coarsening layer, consistent with SEM observations.

Coarsening should start with the topmost, smallest grains instead of the subsurface layers. We were surprised to find coarsening begin in a different part of our sample. More notably, we did not detect any grain coarsening under SEM in the top 20-μm-thick surface layer that we annealed below 453 K (Fig. 1, A and D). We observed no obvious change in either the morphology or the size of the nanograins after annealing (the average transversal size was 43 ± 2 nm after annealing at 433 K) (Fig. 1C) with the use of TEM characterization. Under the same annealing conditions, the submicrometer-sized grains in deep layers coarsened into micrometer-sized grains. The hardness of the nanograined top layer we measured remained unchanged after annealing, verifying the TEM and SEM results. The nanograins were stable as annealed at 433 K even for 12 hours (*14*) (fig. S3). Clearly, the degree of thermal stability of the nanograins in the top layer was higher, rather than lower, than that of the submicrometer-sized grains.

As annealing temperatures exceeded 453 K, large grains appeared in the top surface layer (Fig. 1, A and E), most of them elongated, more than 10 μm long in parallel to the surface, and a few micrometers thick. These large grains were recrystallization products of the nanograins, but their morphologies were distinct from those of the coarsened grains underneath. Increasing the annealing temperature caused more recrystallized grains to form. These grains were embedded in the nanograins and were attached to the underneath coarsened grains, located in the interior of the nanograined layer, or found in the topmost surface layer (Fig. 1, A and E). We frequently

[1]Shenyang National Laboratory for Materials Science, Institute of Metal Research, Chinese Academy of Sciences, 72 Wenhua Road, Shenyang 110016, China. [2]School of Materials Science and Engineering, University of Science and Technology of China, Hefei 230026, China.
*Corresponding author. Email: xyli@imr.ac.cn (X.Y.L.); lu@imr.ac.cn (K.L.)

observed nanograined layers sandwiched with recrystallized grains. We were surprised that some nanograins remained stable even after annealing at 623 K (*14*), about 230 K higher than the coarsening temperature for the submicrometer-sized grains in the same sample. We found a general trend in that the smaller grains closer to the surface were more resistant to recrystallization. As the annealing temperature exceeded 623 K, no nanograins survived and the top surface layer fully recrystallized.

Several lines of observational evidence indicated that the nanograins in the top surface layer were more thermally stable than the larger grains. This relationship differs fundamentally from the traditional view of the "smaller less-stable" trend with regard to thermal stability. This difference is not from surface contaminations or texture effects, as we found no change in chemical composition and texture across the grain size regime (*14*). Recrystallization of nanograins at the topmost surface level before those in the interior is an indicator of negligible contamination at the processed surface. For further verification, we used the same SMGT process but with lower strain rates and a higher temperature (173 K) to prepare submicrometer-sized grains in the top surface layer (Fig. 2). Annealing this gradient submicrometer-grained sample above 433 K, we found grain coarsening onset at the top surface with the smallest grains and in the subsurface layer (Fig. 2B). At higher annealing temperatures, the coarsening continued throughout a surface layer that was more than 100 μm thick (Fig. 2C). These results support our discovery that the marked thermal stability of the surface nanograins is a grain size effect rather than a result of processing-induced contamination.

We annealed a number of individual specimens by heating them directly to preset temperatures and holding at those temperatures for 30 min (*14*) (fig. S1) to determine the grain-coarsening temperature as a function of initial grain size in Cu samples (Fig. 3A) (*15*–*21*). We found that for grain sizes above 70 nm, the coarsening temperature drops with decreasing size, in agreement with the reported trend for nanograined Cu processed from different plastic deformation routes. Grains below 70 nm exhibit distinct stability. Smaller nanograins become more stable, and their instability temperature rises up to $0.45T_m$ (T_m is the equilibrium melting point), which is even higher than that of the recrystallization temperatures of coarse-grained Cu (usually below $0.4T_m$). The instability temperature for 40-nm grains in the topmost surface layer (623 K) is about 290 K higher than that for Cu grains with comparable sizes prepared from inert gas condensation (~333 K), which falls in line with the conventional trend.

We performed the same experiments with gradient nanograined Ni samples (99.5% purity) prepared with the use of SMGT. As we observed in Cu, nanograins in the top surface layer exhibited much higher stability against annealing than the submicrometer-sized grains in the subsurface layer (Fig. 4, A and B). The sizes and morphologies of the nanograins remained stable even after annealing at 873 K (Fig. 4, C to E). Under the same annealing conditions, micrometer-sized grains were formed in the subsurface layer with initial grain sizes larger than 90 nm. The variation of grain coarsening temperature with initial grain size in Ni was similar to that in Cu. The instability temperature of nanograins in Ni can be as high as 1173 K (~$0.68T_m$) (*14*) (fig. S2), which is much higher than the recrystallization temperature of coarse-grained Ni (Fig. 4F) (*13*, *22*, *23*).

Generally, the driving force for recrystallization and coarsening of the nanograins is stored energy in the forms of dislocations and GBs. We measured this energy by differential scanning calorimetry (DSC) (*14*). We cut foil specimens with nanograins and submicrometer-sized grains at different depths from the as-prepared Cu sample. Upon heating, an exothermic peak due to

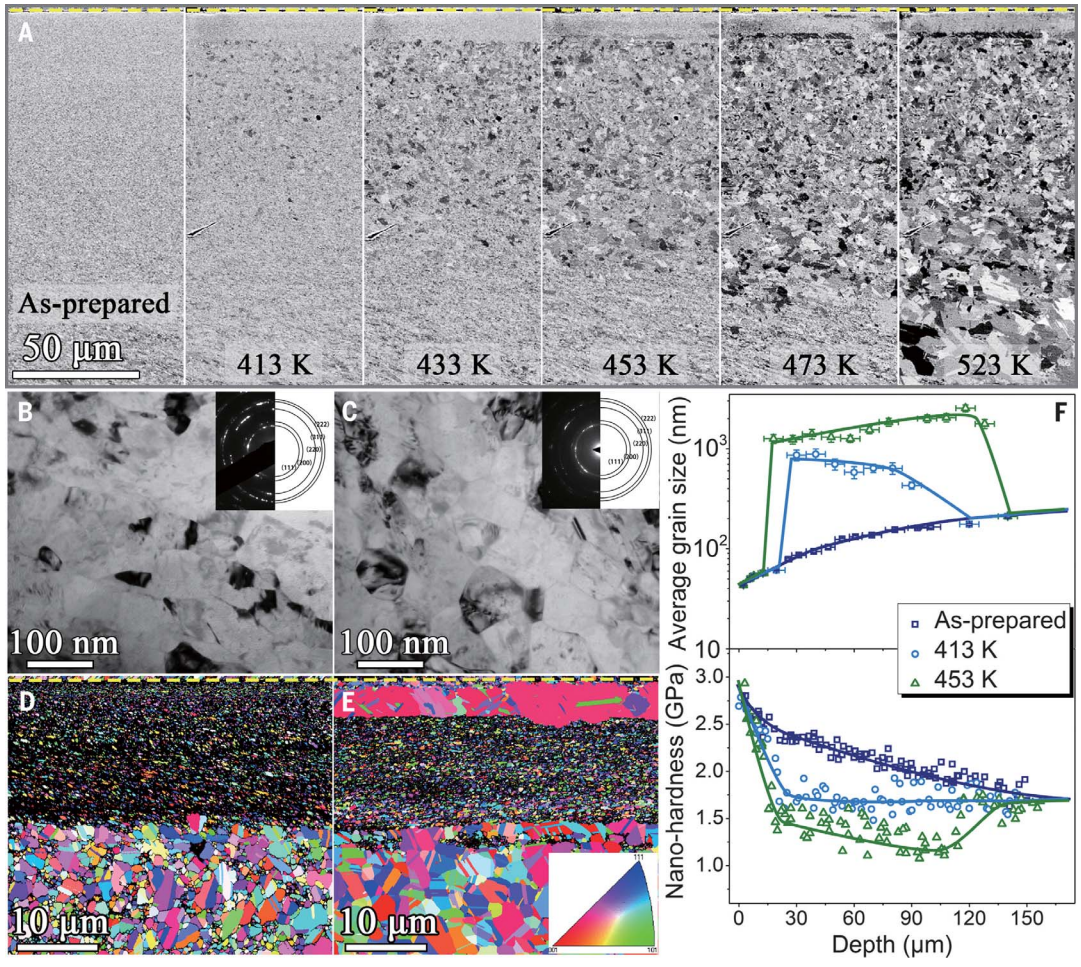

Fig. 1. Annealing-induced structure changes in the gradient nanograined structure in pure Cu. (**A**) Cross-sectional SEM images of the as-prepared gradient nanograined Cu sample (left) and samples after ex situ annealing at various temperatures (as indicated) for 30 min. Dotted lines represent the treated surface. Cross-sectional bright-field TEM images with selected area electron diffraction patterns (insets) for the nanograins at a depth of 2 μm from the surface in the as-prepared sample (**B**) and a sample annealed at 433 K for 30 min (**C**). Typical cross-sectional EBSD images of the top surface layer in the Cu samples annealed at 433 K (**D**) and 473 K (**E**) for 30 min. (**F**) Variations of average grain size and nanohardness along increasing depths from the surface in the as-prepared and the as-annealed Cu samples treated at 413 and 453 K for 30 min. Error bars indicate the variation range of measured statistic grain sizes within a depth span.

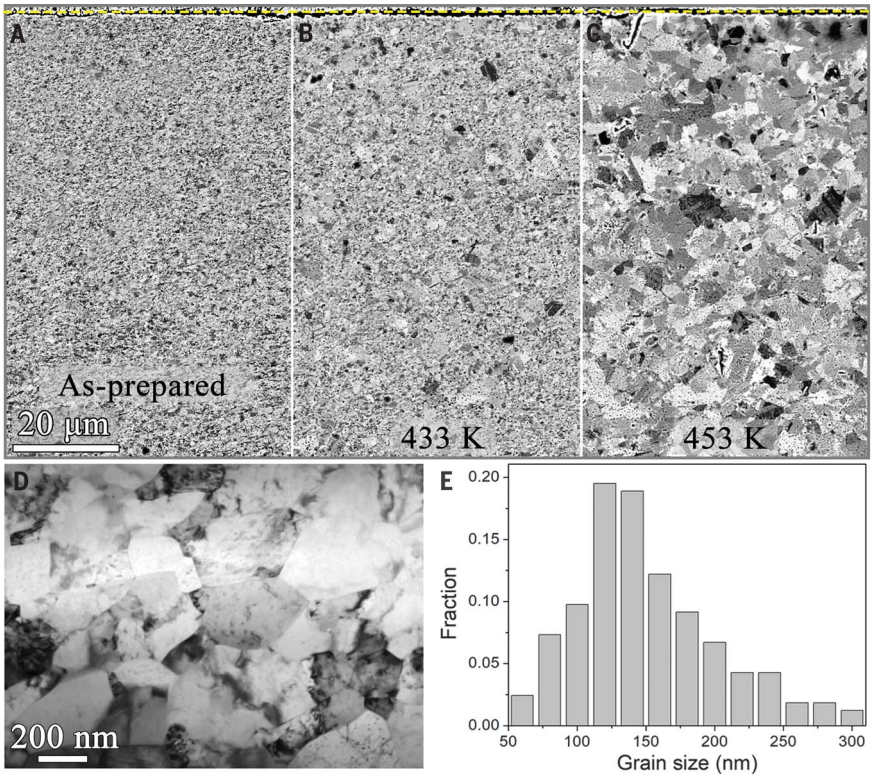

Fig. 2. Annealing-induced coarsening of submicrometer grains in the top surface layer in Cu. Cross-sectional SEM images of the as-prepared gradient submicrometer-grained Cu sample (**A**) and samples after annealing at 433 K (**B**) and 453 K (**C**) for 30 min. Dotted lines represent the treated surface. (**D**) A bright-field TEM image of the top surface layer. (**E**) Corresponding grain size distribution, with an average size of 140 nm.

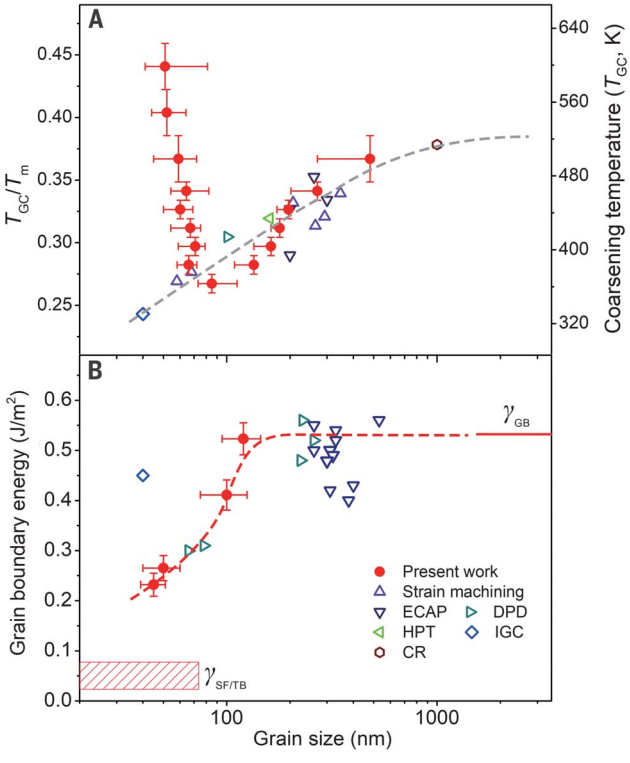

Fig. 3. Grain size dependence of instability temperature and GB energy in Cu. Measured grain coarsening (instability) temperature (T_{GC}) (**A**) and GB excess energy (**B**) as a function of average grain size in Cu. Literature data for Cu processed with different techniques [strain machining (*15*), equal-channel angle pressing (ECAP) (*16*, *17*, *24*, *25*), dynamic plastic deformation (DPD) (*18*), high-pressure torsion (HPT) (*19*), cold rolling (CR) (*20*), and inert gas condensation (IGC) (*21*)] are included. Conventional GB energies (γ_{GB}) and energies for stacking faults and twin boundaries ($\gamma_{SF/TB}$) of Cu are indicated. Error bars in (A) indicate the variation range of measured instability temperatures within a grain size span. Error bars in (B) indicate the variation range of measured GB energies within the grain size span.

recrystallization and grain coarsening of the nanostructures appeared. With the measured enthalpy release and grain size changes, specific GB excess energy was determined to be ~0.52 ± 0.03 J/m^2 (minor contributions of other defects were ignored) for an average grain size of 125 nm. This value is consistent with the conventional GB energy for Cu (*21*, *24*, *25*) and for submicrometer-grained Cu produced from plastic deformation. For grain sizes of ~50 nm, we obtained GB energies of 0.23 to 0.27 J/m^2, only half of conventional GB energy but consistent with that in nanograined Cu prepared from plastic deformation (*18*). From the available GB energy data for Cu processed with different plastic deformation techniques, we noticed an obvious drop in GB energy as grain sizes decreased below ~100 nm (Fig. 3B). This seems analogous to the observation that more stable interfaces with low excess energy were formed during extreme plastic straining in bimetal nanoscale multilayer films (*26*).

We found a reasonable correlation between the critical grain sizes for the GB energy drop and the thermal stability change (Fig. 3, A and B) when measurement errors in grain size were taken into account. A drop in GB energy means a reduced driving force for recrystallization, consistent with the enhanced thermal stability of nanograins below a critical size. Our measured GB energy for a size of ~50 nm is much lower than that for comparable grain sizes prepared from inert gas condensation (0.45 J/m^2) (*21*) but is in good accord with the difference in thermal stability we observed.

The GB energy drop we observed at small grain sizes may be inferred from the grain refinement mechanism and the GB relaxation process during plastic deformation. Because of the high strain rates and low temperatures, plastic deformation in the top surface layer of the SMGT samples is dominated by the formation of stacking faults and twin boundaries. In terms of the grain refinement mechanism discussed previously in the literature (*27*, *28*), most nanograins were formed from fragmentation or shear banding of the lamellar bundles of nanoscale twins and stacking faults, generating plenty of GBs that are in low-energy configurations, analogous to those in the nanograined Cu produced from dynamic plastic deformation (*18*). TEM observations of the SMGT Ni samples showed that the fraction of grains containing twins or stacking faults in the top surface layer is much higher than that in deep layers (*14*) (fig. S6).

In addition, plastic straining may trigger relaxation of GBs in nanograins so that GB structures transform into a lower energy state via GB dissociation processes (*29*–*31*). Simulations and experimental investigations on a range of tilt GBs in several face-centered cubic metals indicated that dissociation of GBs occurs by emission of stacking faults (*29*). This provides a general mode of GB relaxation, especially in metals with low stacking fault energies, such as Cu. Similar processes are anticipated in high–stacking fault energy metals such as Ni under high shear stress, as in our process. Formation of nanometer-scale

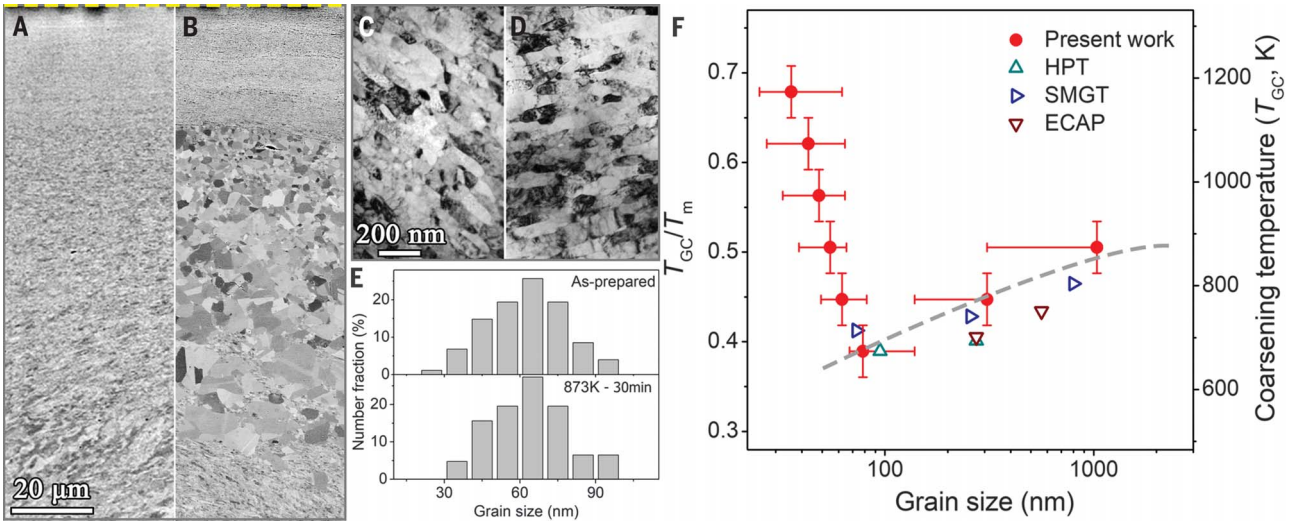

Fig. 4. Annealing-induced structure changes in the gradient nangrained structure in pure Ni. Cross-sectional SEM images of the as-prepared gradient nanograined Ni sample (**A**) and a sample after annealing at 873 K for 30 min (**B**). Dotted lines represent the treated surface. Typical bright-field cross-sectional TEM images of the nanograins (at a depth of ~25 μm from the surface) in the as-prepared state (**C**) and after annealing at 873 K (**D**) and the corresponding grain size distributions (**E**). (**F**) Measured grain coarsening temperature as a function of average grain size in Ni. Literature data for Ni processed with different techniques [HPT (*22*), ECAP (*23*), and SMGT (*13*)] are included. Error bars indicate the variation range of measured instability temperatures within a grain size span.

twins from a GB is also able to lower the GB energy state, as it has been observed that atomic diffusion in Cu is obviously slowed along the GBs adjacent to the triple point where they meet a twin boundary (*32*). Formation of stacking faults or twins from GBs, both with evolving emissions of partial dislocations, may induce GB relaxation to lower energy states and stabilization.

Dislocation activity is grain size dependent. Full dislocation activity may be inhibited at very small grain sizes as partial dislocation activity becomes more favorable. In terms of the Orowan relation (*33*), the resolved shear stress required for expansion of a dislocation loop with a diameter of D is $\tau_{RSS} = \frac{\mu b}{D}$, where μ is the shear modulus and b is the Burgers vector of dislocation. Full dislocation multiplication requires that Frank-Read–type sources have a minimum grain size (D^*) at the yield strength (σ_y) of

$$D^* = \frac{\mu b}{\sigma_y(D^*)/m}$$

where $1/m$ is the average Schmid factor for polycrystals ($m = 3$). In terms of the yield strength of the nanograined Cu, the calculated critical size is D^* = 70 nm [which is very close to that reported by Legros *et al.* (*34*)]. This would mean that as Cu grain sizes become smaller than 70 nm, full dislocation is inhibited and partial dislocation activity becomes dominant in the deformation of most grains, hence enhancing the GB relaxation process. This behavior is exactly what we observed, as both the GB energy drop and the enhanced thermal stability in nanograined Cu appeared around this critical size. As the GB relaxation process is triggered by plastic deformation, it may not happen in the nanograined metals produced from inert gas condensation, which possess high GB energy and hence poor thermal stability (Fig. 3).

The discovery of the marked thermal stability of nanograins in Cu and Ni is important for understanding the nature of GBs at the nanoscale and their response to external thermal and mechanical stimuli. Stabilizing nanograins is also vital for developing stable nanostructured metals and alloys for high-temperature applications.

REFERENCES AND NOTES

1. K. Lu, *Nat. Rev. Mater.* **1**, 16019 (2016).
2. C. C. Koch, R. O. Scattergood, K. A. Darling, J. E. Semones, *J. Mater. Sci.* **43**, 7264–7272 (2008).
3. C. C. Koch, *J. Mater. Sci.* **42**, 1403–1414 (2007).
4. Y. Huang *et al.*, *Mater. Sci. Eng. A* **656**, 55–66 (2016).
5. J. Weissmüller, *Nanostruct. Mater.* **3**, 261–272 (1993).
6. R. Kirchheim, *Acta Mater.* **50**, 413–419 (2002).
7. P. C. Millett, R. P. Selvam, A. Saxena, *Acta Mater.* **55**, 2329–2336 (2007).
8. T. Chookajorn, H. A. Murdoch, C. A. Schuh, *Science* **337**, 951–954 (2012).
9. F. Liu, R. Kirchheim, *J. Cryst. Growth* **264**, 385–391 (2004).
10. K. Boylan, D. Ostrander, U. Erb, G. Palumbo, K. T. Aust, *Scr. Metall. Mater.* **25**, 2711–2716 (1991).
11. B. K. VanLeeuwen, K. A. Darling, C. C. Koch, R. O. Scattergood, B. G. Butler, *Acta Mater.* **58**, 4292–4297 (2010).
12. X. Zhang, A. Misra, *Scr. Mater.* **66**, 860–865 (2012).
13. X. C. Liu, H. W. Zhang, K. Lu, *Science* **342**, 337–340 (2013).
14. See supplementary materials.
15. C. Saldana, A. H. King, S. Chandrasekar, *Acta Mater.* **60**, 4107–4116 (2012).
16. Y. Zhang, J. T. Wang, C. Cheng, J. Q. Liu, *J. Mater. Sci.* **43**, 7326–7330 (2008).
17. N. Lugo, N. Llorca, J. J. Suñol, J. M. Cabrera, *J. Mater. Sci.* **45**, 2264–2273 (2010).
18. Y. Zhang, N. R. Tao, K. Lu, *Acta Mater.* **56**, 2429–2440 (2008).
19. P. Jenei, J. Gubicza, E. Y. Yoon, H. S. Kim, J. L. Lábár, *Compos. Part A Appl. Sci. Manuf.* **51**, 71–79 (2013).
20. Z. N. Mao *et al.*, *Mater. Sci. Eng. A* **674**, 186–192 (2016).
21. A. Kumpmann, B. Günther, H. D. Kunze, *Mater. Sci. Eng. A* **168**, 165–169 (1993).
22. H. W. Zhang, X. Huang, R. Pippan, N. Hansen, *Acta Mater.* **58**, 1698–1707 (2010).
23. S. V. Divinski, G. Reglitz, M. Wegner, M. Peterlechner, G. Wilde, *J. Appl. Phys.* **115**, 113503 (2014).
24. O. F. Higuera-Cobos, J. M. Cabrera, *Mater. Sci. Eng. A* **571**, 103–114 (2013).
25. C. F. Gu, C. H. J. Davies, *Mater. Sci. Eng. A* **527**, 1791–1799 (2010).
26. I. J. Beyerlein *et al.*, *Proc. Natl. Acad. Sci. U.S.A.* **111**, 4386–4390 (2014).
27. K. Wang, N. R. Tao, G. Liu, J. Lu, K. Lu, *Acta Mater.* **54**, 5281–5291 (2006).
28. W. L. Li, N. R. Tao, K. Lu, *Scr. Mater.* **59**, 546–549 (2008).
29. J. D. Rittner, D. N. Seidman, K. L. Merkle, *Phys. Rev. B* **53**, R4241–R4244 (1996).
30. P. M. Derlet, H. Van Swygenhoven, A. Hasnaoui, *Philos. Mag.* **83**, 3569–3575 (2003).
31. R. G. Hoagland, S. M. Valone, *Philos. Mag.* **95**, 112–131 (2015).
32. K. C. Chen, W. W. Wu, C. N. Liao, L. J. Chen, K. N. Tu, *Science* **321**, 1066–1069 (2008).
33. E. Orowan, in *Symposium on Internal Stresses in Metals and Alloys* (Institute of Metals, 1948), p. 451.
34. M. Legros, B. R. Elliott, M. N. Rittner, J. R. Weertman, K. J. Hemker, *Philos. Mag. A* **80**, 1017–1026 (2000).

ACKNOWLEDGMENTS

We thank F. H. Duan for technical assistance with DSC experiments. **Funding:** This work was supported by the Ministry of Science and Technology of China (grants 2012CB932201 and 2017YFA0204401), the National Science Foundation of China (grant 51231006), and the Chinese Academy of Sciences (grant zdyz201701). **Author contributions:** X.Y.L. and K.L. initiated the study; X.Z. and X.Y.L. performed the experiments; X.Z., X.Y.L., and K.L. analyzed the results; and X.Y.L. and K.L. wrote the paper. **Competing interests:** We declare no competing financial interests. **Data and materials availability:** All data are available in the main text or the supplementary materials.

SUPPLEMENTARY MATERIALS

www.sciencemag.org/content/360/6388/526/suppl/DC1
Materials and Methods
Figs. S1 to S6
Table S1

7 December 2017; accepted 26 March 2018
10.1126/science.aar6941

NEUROSCIENCE

Piezo2 channel–Merkel cell signaling modulates the conversion of touch to itch

Jing Feng,[1] Jialie Luo,[1] Pu Yang,[1] Junhui Du,[2] Brian S. Kim,[1,3,4] Hongzhen Hu[1]*

The somatosensory system relays many signals ranging from light touch to pain and itch. Touch is critical to spatial awareness and communication. However, in disease states, innocuous mechanical stimuli can provoke pathologic sensations such as mechanical itch (alloknesis). The molecular and cellular mechanisms that govern this conversion remain unknown. We found that in mice, alloknesis in aging and dry skin is associated with a loss of Merkel cells, the touch receptors in the skin. Targeted genetic deletion of Merkel cells and associated mechanosensitive Piezo2 channels in the skin was sufficient to produce alloknesis. Chemogenetic activation of Merkel cells protected against alloknesis in dry skin. This study reveals a previously unknown function of the cutaneous touch receptors and may provide insight into the development of alloknesis.

Chronic pruritus or itch is an increasingly common and debilitating problem in the elderly. Age-related dry skin is strongly associated with alloknesis, whereby the sensation of itch is evoked by innocuous mechanical stimulation such as light touch. We adapted the well-established von Frey technique to mechanically irritate the skin of young and aged mice (2 months and >24 months of age, respectively) at varying levels of mechanical force. Mechanical stimulation ranging from 0.02 to 0.16 g evoked scratching behavior in aged mice in a manner not observed in young mice (Fig. 1A and movies S1 and S2). In contrast, acute itch in response to classical pruritogens such as histamine (His) or chloroquine (CQ) was unaffected by aging (Fig. 1, B and C). Mechanical pain (2.0 g von Frey hair force) and thermal pain responses did not reveal any differences in aged mice relative to young mice (fig. S1).

Recent studies have identified a subpopulation of neuropeptide Y (NPY)–positive interneurons that are innervated by hairy-skin low-threshold mechanoreceptors (LTMRs) and critically regulate mechanical itch in the spinal cord (*1*). To investigate whether aging also affects the firing properties of LTMRs, we analyzed the firing patterns of different types of cutaneous fibers by means of ex vivo skin-nerve recordings (*2*–*6*). In marked contrast to the sustained firing of type I slowly adapting (SAI) afferents in young mice, skin-nerve preparations from the aged mice displayed truncated static firing, which was classified as intermediately adapting (IA) responses (Fig. 1, E and F) (*4*). The firing rates of SAI afferents elicited by a range of mechanical force from 1 to 150 mN were significantly reduced starting from 50 mN (Fig. 1, D and E), and the firing threshold of SAI afferents was markedly increased in aged mice versus young mice (Fig. 1G). Spike counts in both dynamic and static phases were also markedly reduced in aged mice (Fig. 1, H and I). However, comparable firing properties of rapidly adapting (RA), A delta (Aδ), and C LTMRs were evident between aged and young mice (figs. S2 to S4). The overall proportions of Aβ fiber subtypes and conduction velocities were also similar in the two groups (fig. S5). Although the spinal NPY-expressing interneurons were reported to selectively receive mechanosensory inputs only from hairy skin (*1*), we found no significant difference in firing properties between the SAI fibers innervating hairy and glabrous skin in either young or aged mice (fig. S6), which suggests that both NPY^+ and unidentified NPY^- inhibitory interneurons likely receive inputs from SAI afferents.

Because Merkel cells in the epidermis and SAI afferents make "synapse-like" contacts and encode unique SAI firing patterns (*3*, *4*, *7*–*9*), we speculated that Merkel cells may act upstream and thus may be implicated in the selective attenuation of the SAI responses in the setting of aging-associated alloknesis. We therefore used immunofluorescent staining to determine the numbers and morphology of Merkel cells in aged skin. There were significantly fewer Merkel cells in the epidermal mechanosensory touch domes of aged mice (Fig. 1, J and K). In contrast, the afferent ending structures in the touch domes were intact and comparable between the aged and young mice (Fig. 1, J and L). Given that Merkel cells are specifically required for sustained action potential firing of touch-dome afferents (*8*), the loss of Merkel cells in aging skin may promote alloknesis.

We thus used the well-established acetone-ether-water (AEW) model, which recapitulates dry skin itch as observed in elderly patients and manifests alloknesis (*10*–*13*). AEW-treated mice displayed enhanced alloknesis relative to water-treated control mice starting from day 3, and the alloknesis score reached a plateau at day 5 (Fig. 2A). The number of Merkel cells was markedly reduced in the AEW-treated mice relative to control mice, whereas the total length of the nerve fibers was comparable between the two groups (Fig. 2, B to D). We next investigated whether the loss of Merkel cells affects the SAI responses by targeted recording from touch-dome afferents. The touch-dome afferents from the AEW-treated mice also displayed markedly different firing pattern of IA responses versus the SAI responses in water-treated mice (Fig. 2, E and H). Although the conduction velocities of SAI afferents were comparable in both groups (fig. S7), touch-dome afferents from the AEW-treated mice displayed significantly higher firing thresholds (Fig. 2, F and G) and fewer firing counts in both dynamic and static phases (Fig. 2, I and J).

To directly test the contribution of Merkel cells in regulating alloknesis, we measured mechanical itch in Merkel cell–deficient $K14^{Cre}$; $Atoh1^{f/f}$ mice (*4*, *14*). These mice showed significantly increased scratching in response to mild von Frey filament stimulations when compared with Cre^- littermate control mice (Fig. 3A). Neither acute itch responses induced by intradermal injections of His and CQ nor evoked mechanical and thermal pain responses were altered in the $K14^{Cre}$; $Atoh1^{f/f}$ mice (fig. S8).

We then tested whether activation of Merkel cells could act on the same pathways that would suppress alloknesis. By crossing the $Atoh1^{CreERT}$; *Ai9* reporter mice with *Gq*-coupled *DREADD* (designer receptors exclusively activated by designer drugs) mice, we generated mice in which Merkel cells could be selectively activated by chemogenetic stimulation (*15*). After tamoxifen induction, the $Atoh1^{CreERT}$; *Ai9* reporter mice showed strong expression of tdTomato in the Merkel cells but not other structures such as sensory nerve endings (fig. S9). The DREADD ligand clozapine N-oxide (CNO) elicited a rapid intracellular Ca^{2+} concentration ($[Ca^{2+}]_i$) response in the tdTomato-positive Merkel cells in the enlargement segment of freshly isolated whisker hair follicles from Cre^+ mice but not Cre^- *Atoh1-Gq-DREADD* mice (Fig. 3B). Treatment with CNO significantly increased the firing frequency (Fig. 3, C and D), especially the static phase of SAI firing, in response to mechanical stimulation forces in the skin-nerve preparations from the AEW-treated Cre^+ mice but not Cre^- *Atoh1-Gq-DREADD* mice (Fig. 3G). This finding suggests that activation of *Gq-DREADDs* in spared Merkel cells promotes sustained firing of the SAI afferents in the AEW-treated mice. We therefore tested whether broad chemogenetic activation of Merkel cells could suppress alloknesis in the *Atoh1-Gq-DREADD* mice by measuring mechanical itch at day 5 after AEW treatment. Indeed, the administration of CNO significantly suppressed alloknesis

[1]Department of Anesthesiology, Center for the Study of Itch, Washington University School of Medicine, St. Louis, MO 63110, USA. [2]Department of Pathology and Immunology, Baylor College of Medicine, Houston, TX 77030, USA. [3]Department of Dermatology, Center for the Study of Itch, Washington University School of Medicine, St. Louis, MO 63110, USA. [4]Deparment of Pathology and Immunology, Washington University School of Medicine, St. Louis, MO 63110, USA.
*Corresponding author. Email: hongzhen.hu@wustl.edu

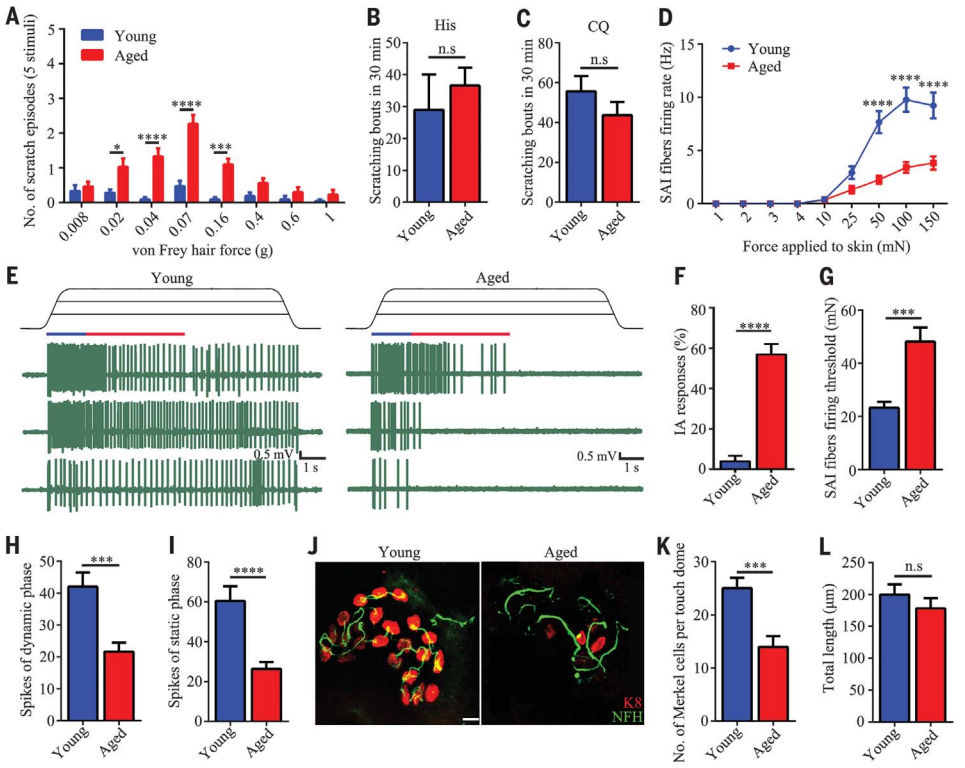

Fig. 1. Alloknesis in aged mice is correlated with a decline in SAI responses and reduced numbers of touch-dome Merkel cells. (**A**) Alloknesis scores in young (n = 7) and aged (n = 10) mice. (**B** and **C**) Scratching responses to intradermal injections of His (B) and CQ (C) in young (n = 8) and aged (n = 8) mice. (**D**) Firing rates of SAI fibers from young (23 units) and aged (38 units) mice. (**E**) Touch-dome afferents firing in young and aged mice. Top, ramp-and-hold displacements (50, 100, and 150 mN); bottom, corresponding spike trains. Blue and red lines indicate dynamic and static phases. (**F**) Proportion of IA responses from young (4.0 ± 2.6%) and aged (56.9 ± 5.1%) mice; n = 7 mice for each group. (**G**) Firing threshold of SAI fibers from young (25.8 ± 2.5 mN, n = 23) and aged (47.4 ± 6.8 mN, n = 38) mice. (**H**) Maximum number of spikes in the dynamic phases; n = 23 from young mice (42.0 ± 4.4 counts), n = 38 from aged mice (21.9 ± 2.9 counts). (**I**) Maximum number of spikes in the static phases; n = 23 from young mice (60.5 ± 7.3 counts), n = 38 from aged mice (26.4 ± 3.5 counts). (**J**) Confocal images of keratin-8 (K8, red) and neurofilament heavy polypeptide (NFH, green) costaining in a single touch dome. Scale bar, 10 μm. (**K**) Merkel cell numbers in each touch dome of young (25.1 ± 1.9, n = 30) and aged (14.0 ± 2.0, n = 30) mice. (**L**) Length of NFH$^+$ fiber innervating touch domes of young (200.2 ± 15.8 μm, n = 30) and aged (178.2.0 ± 16.2 μm, n = 30) mice. Data are presented as mean ± SEM. *P < 0.05, ***P < 0.001, ****P < 0.0001 [Student t test in (A) to (C), (H), (I), (K), and (L); two-way analysis of variance (ANOVA) with Bonferroni post hoc analysis in (D); Fisher's exact test in (F); Mann-Whitney U test in (G)]; n.s, not significant.

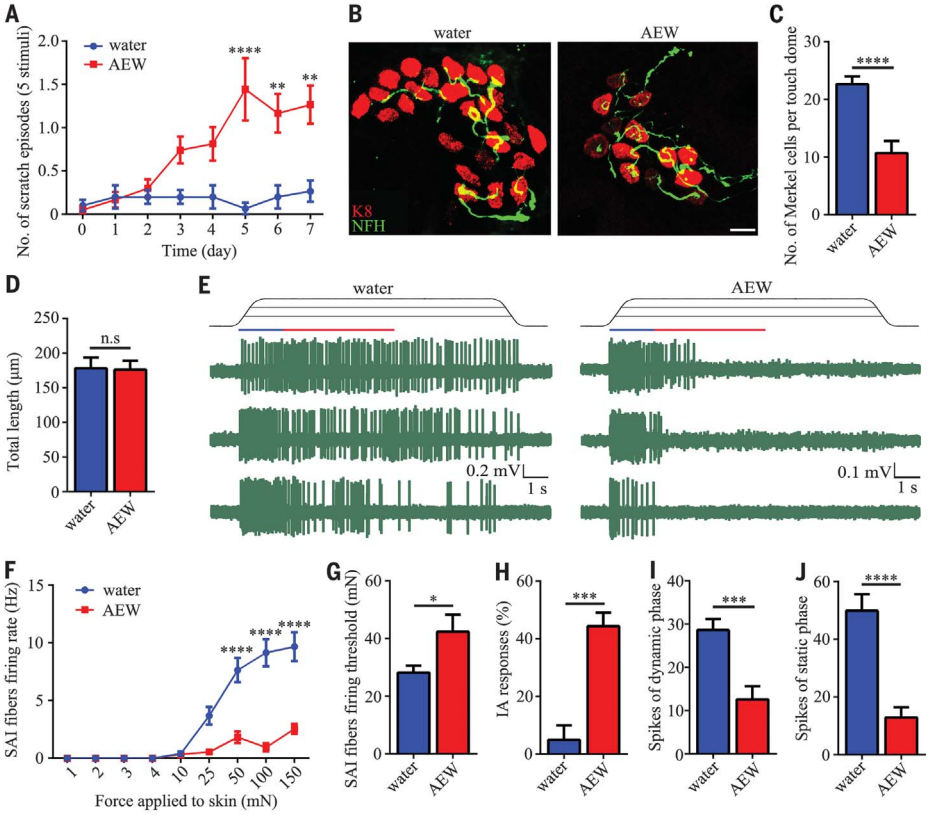

Fig. 2. Alloknesis in a mouse model of dry skin is correlated with a decline in SAI responses and reduced numbers of touch-dome Merkel cells. (**A**) Time course of alloknesis in mice treated with AEW (n = 10) or water (n = 10). (**B**) Confocal images of K8 (red) and NFH (green) costaining in a single touch dome. Scale bar, 10 μm. (**C**) Merkel cell numbers in touch domes of water-treated (22.6 ± 1.3, n = 26) and AEW-treated (9.6 ± 1.9, n = 26) mice. (**D**) Length of NFH$^+$ fiber innervating touch domes of water-treated (178.3 ± 15.4 μm, n = 26) and AEW-treated (176.4 ± 13.0 μm, n = 26) mice. (**E**) Firing traces of SAI afferents in response to mechanical stimulations (50, 100, and 150 mN) in water-treated and AEW-treated mice. (**F**) Firing rates of SAI fibers from water-treated (n = 17 units) and AEW-treated (n = 19 units) mice. (**G**) Firing threshold of SAI afferents of water-treated (29.3 ± 2.5 mN, n = 20) and AEW-treated (44.4 ± 8.1 mN, n = 19) mice. (**H**) Proportion of IA responses of water-treated (5.0 ± 5.0%, n = 5) and AEW-treated (41.7 ± 4.8%, n = 5) groups. (**I**) Maximum number of spikes in the dynamic phases (water-treated, 28.6 ± 2.5 counts, n = 20; AEW-treated, 13.6 ± 4.3 counts, n = 19). (**J**) Maximum number of spikes in the static phases (water-treated, 50.0 ± 5.8 counts, n = 20; AEW-treated, 9.5 ± 2.3 counts, n = 19). Data are presented as mean ± SEM. *P < 0.05, **P < 0.01, ***P < 0.001, ****P < 0.0001 [two-way ANOVA with Bonferroni post hoc analysis in (A) and (F); Student t test in (C), (D), (I), and (J); Mann-Whitney U test in (G); Fisher's exact test in (H)].

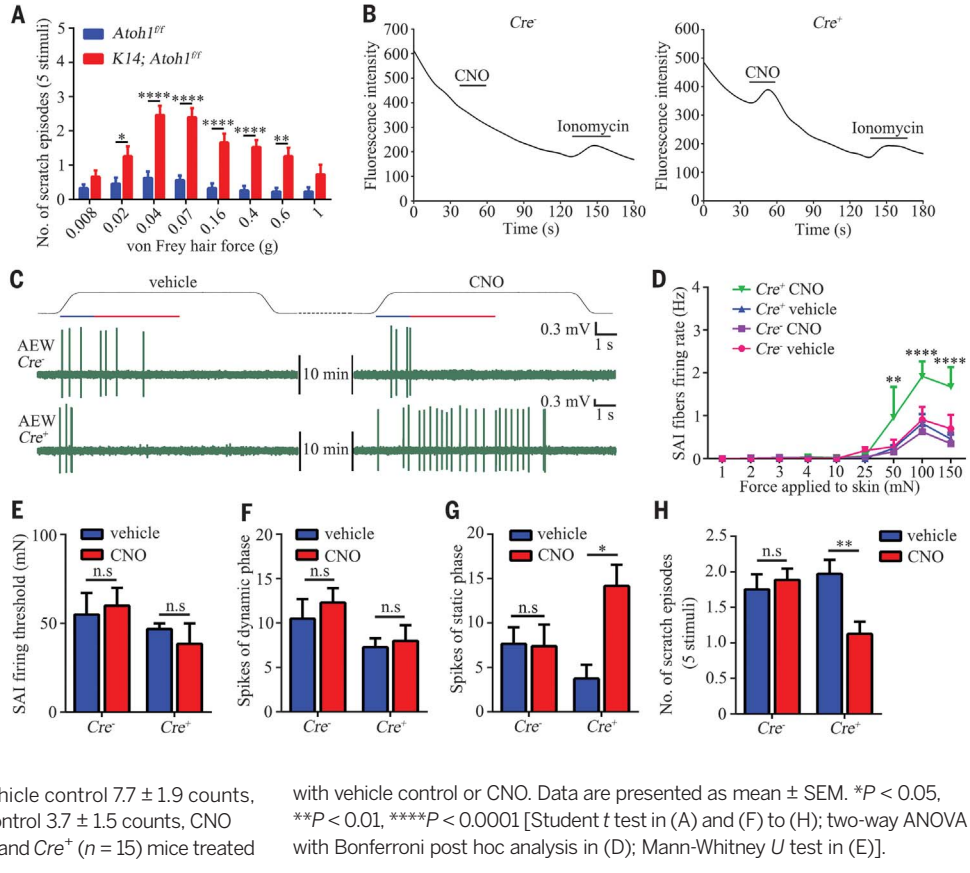

Fig. 3. Chemogenetic activation of Merkel cells is sufficient to modulate alloknesis. (**A**) Alloknesis score in Merkel cell–deficient *K14^{Cre}; Atoh1$^{f/f}$* mice (n = 10) and wild-type littermates (n = 10). (**B**) Traces showing that 300 μM CNO elicited $[Ca^{2+}]_i$ responses in tdTomato-positive Merkel cells in hair follicles isolated from *Cre*$^+$ but not *Cre*$^-$ mice. Ionomycin (10 μM) was used as positive control; n = 25 hair follicles from 5 mice. (**C**) Firings of SAI afferents of AEW-treated *Cre*$^-$ and *Cre*$^+$ mice in response to 100-mN mechanical stimulation in the absence and presence of 300 μM CNO. (**D**) Firing rates of SAI fibers of AEW-treated *Cre*$^-$ (n = 10 units) and *Cre*$^+$ (n = 5 units) mice in response to increased forces of mechanical stimulation in the absence and presence of 300 μM CNO. (**E**) Firing threshold of SAI afferents of AEW-treated *Cre*$^-$ and *Cre*$^+$ mice in the absence and presence of 300 μM CNO (*Cre*$^-$ n = 10, vehicle control 55.0 ± 12.2 mN, CNO 60.0 ± 10.0 mN; *Cre*$^+$ n = 5, vehicle control 46.9 ± 3.1 mN, CNO 38.5 ± 11.5 mN). (**F**) Maximum number of spikes in the dynamic phases (n = 5 *Cre*$^-$ mice, vehicle control 10.5 ± 2.2 counts, CNO 12.3 ± 1.6 counts; n = 5 *Cre*$^+$ mice, vehicle control 7.3 ± 1.0 counts, CNO 8.0 ± 1.8 counts). (**G**) Maximum number of spikes in the static phases (n = 5 *Cre*$^-$ mice, vehicle control 7.7 ± 1.9 counts, CNO 7.4 ± 2.4 counts; n = 5 *Cre*$^+$ mice, vehicle control 3.7 ± 1.5 counts, CNO 14.2 ± 2.4 counts). (**H**) Alloknesis of *Cre*$^-$ (n = 15) and *Cre*$^+$ (n = 15) mice treated with vehicle control or CNO. Data are presented as mean ± SEM. *P < 0.05, **P < 0.01, ****P < 0.0001 [Student t test in (A) and (F) to (H); two-way ANOVA with Bonferroni post hoc analysis in (D); Mann-Whitney U test in (E)].

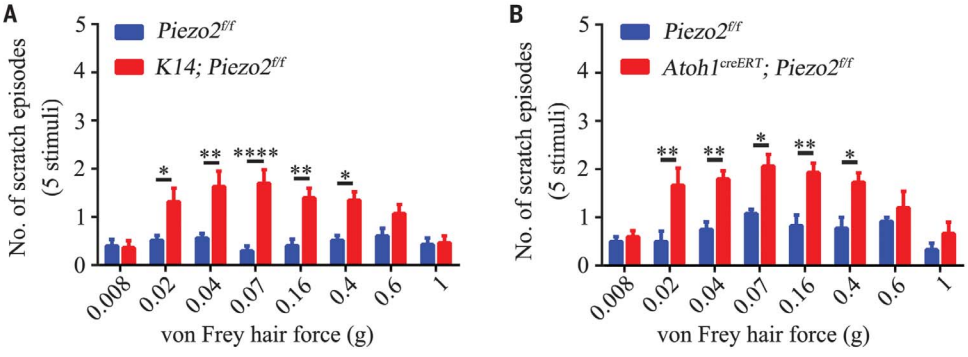

Fig. 4. Genetic ablation of Piezo2 function in Merkel cells produces alloknesis. (**A**) Alloknesis score in *K14^{Cre}; Piezo2$^{f/f}$* mice (n = 10) and wild-type *Piezo2$^{f/f}$* littermates (n = 10). (**B**) Alloknesis score in *Atoh1^{CreERT}; Piezo2$^{f/f}$* mice (n = 5) and wild-type *Piezo2$^{f/f}$* littermates (n = 4). Data are presented as mean ± SEM. *P < 0.05, **P < 0.01, ****P < 0.0001 (Student t test).

in *Cre*$^+$ *Atoh1-Gq-DREADD* mice when compared with vehicle. The alloknesis score was comparable between the vehicle-injected and CNO-injected *Cre*$^-$ littermates (Fig. 3H).

The mechanosensitive ion channel Piezo2 is a canonical light-touch receptor expressed by cutaneous Merkel cells (*16*) and is required for normal SAI responses (*4*, *8*). We directly tested whether Piezo2 was involved in the modulation of mechanical itch in the skin. *Cre*$^+$ *K14^{Cre}; Piezo2$^{f/f}$* mice displayed markedly increased alloknesis to low mechanical stimulation relative to *Cre*$^-$ mice (Fig. 4A). We then specifically ablated Piezo2 function in Merkel cells by crossing *Atoh1^{CreERT}* with *Piezo2$^{f/f}$* mice. *Cre*$^+$ but not *Cre*$^-$ mice showed significantly increased mechanical itch behavior after tamoxifen induction (Fig. 4B). In contrast, itch responses induced by His or CQ were comparable between *Cre*$^-$ and *Cre*$^+$ *K14^{Cre}; Piezo2$^{f/f}$* mice and *Atoh1^{CreERT}; Piezo2$^{f/f}$* mice (fig. S10, A, B, E, and F). Neither mechanical nor thermal pain responses were altered in the *K14^{Cre}; Piezo2$^{f/f}$* and *Atoh1^{CreERT}; Piezo2$^{f/f}$* mice (fig. S10, C, D, G, and H).

Our results show that cutaneous Piezo2 channel–Merkel cell signaling is critical in modulating the conversion of touch to itch, and is evidently required for the normal function of peripheral mechanoreceptors that convert mechanical stimuli from the skin to the spinal cord; in turn, these stimuli may control the activity of both NPY$^+$ and NPY$^-$ inhibitory interneurons (*1*) (fig. S11). Our findings may also offer an explanation for the loss of mechanical itch gating under aging and chronic itch conditions.

REFERENCES AND NOTES

1. S. Bourane *et al.*, *Science* **350**, 550–554 (2015).
2. J. Du, M. Koltzenburg, S. M. Carlton, *Pain* **89**, 187–198 (2001).
3. S. H. Woo *et al.*, *Nature* **509**, 622–626 (2014).
4. S. Maksimovic *et al.*, *Nature* **509**, 617–621 (2014).
5. K. L. Marshall *et al.*, *Cell Rep.* **17**, 1719–1727 (2016).
6. S. A. Wellnitz, D. R. Lesniak, G. J. Gerling, E. A. Lumpkin, *J. Neurophysiol.* **103**, 3378–3388 (2010).
7. R. Ikeda *et al.*, *Cell* **157**, 664–675 (2014).
8. S. H. Woo, E. A. Lumpkin, A. Patapoutian, *Trends Cell Biol.* **25**, 74–81 (2015).
9. L. Li *et al.*, *Cell* **147**, 1615–1627 (2011).
10. T. Akiyama *et al.*, *J. Invest. Dermatol.* **132**, 1886–1891 (2012).
11. T. Miyamoto, H. Nojima, T. Shinkado, T. Nakahashi, Y. Kuraishi, *Jpn. J. Pharmacol.* **88**, 285–292 (2002).
12. J. Luo *et al.*, *J. Allergy Clin. Immunol.* **141**, 608–619.e7 (2018).
13. T. G. Berger, M. Shive, G. M. Harper, *J. Am. Med. Assoc.* **310**, 2443–2450 (2013).

14. E. G. Reed-Geaghan *et al*., *J. Neurosci.* **36**, 4362–4376 (2016).
15. B. L. Roth, *Neuron* **89**, 683–694 (2016).
16. S. S. Ranade *et al*., *Nature* **516**, 121–125 (2014).

ACKNOWLEDGMENTS

We thank B. Duan, Y. Yan, and Z. F. Chen for helpful discussion; M. Hoshinoa, E. A. Lumpkin, and B. U. Hoffman for the *Atoh1*^{CreERT} mouse line; and N. F. Shroyer and R. D. Newberry for the *Atoh1*$^{f/f}$ mouse line. **Funding:** Supported by NIH grants R01GM101218 and R01DK103901, Washington University School of Medicine Digestive Disease Research Core Center (NIDDK grant P30 DK052574), and NIH grants R01AR070116 and K08AR065577 (B.S.K.). **Author contributions:** H.H. conceived and supervised the study; J.F. and H.H. designed the research; J.F. performed the behavior tests, calcium imaging, and immunostaining; J.F. and H.H. contributed to the movie recordings; J.F., J.D., and J.L. performed the skin-nerve recordings; J.F., J.L., P.Y., and H.H. analyzed the data; and J.F., B.S.K., and H.H. wrote the paper. All authors discussed and revised the manuscript. **Competing interests:** None declared. **Data and materials availability:** The data that support the findings of this study are available within the article and supplementary materials.

SUPPLEMENTARY MATERIALS

www.sciencemag.org/content/360/6388/530/suppl/DC1
Materials and Methods
Figs. S1 to S11
Movies S1 and S2

22 November 2017; accepted 7 March 2018
10.1126/science.aar5703

PLANT SCIENCE

CORNICHON sorting and regulation of GLR channels underlie pollen tube Ca^{2+} homeostasis

Michael M. Wudick,[1,2] Maria Teresa Portes,[1,2] Erwan Michard,[1,2] Paul Rosas-Santiago,[3] Michael A. Lizzio,[1] Custódio Oliveira Nunes,[1,2] Cláudia Campos,[2] Daniel Santa Cruz Damineli,[1] Joana C. Carvalho,[2] Pedro T. Lima,[2] Omar Pantoja,[3] José A. Feijó[1,2]*

Compared to animals, evolution of plant calcium (Ca^{2+}) physiology has led to a loss of proteins for influx and small ligand–operated control of cytosolic Ca^{2+}, leaving many Ca^{2+} mechanisms unaccounted for. Here, we show a mechanism for sorting and activation of glutamate receptor–like channels (GLRs) by CORNICHON HOMOLOG (CNIH) proteins. Single mutants of pollen-expressed *Arabidopsis thaliana* GLRs (*At*GLRs) showed growth and Ca^{2+} flux phenotypes expected for plasma membrane Ca^{2+} channels. However, higher-order mutants of *At*GLR3.3 revealed phenotypes contradicting this assumption. These discrepancies could be explained by subcellular *At*GLR localization, and we explored the implication of *At*CNIHs in this sorting. We found that *At*GLRs interact with *At*CNIH pairs, yielding specific intracellular localizations. *At*CNIHs further trigger *At*GLR activity in mammalian cells without any ligand. These results reveal a regulatory mechanism underlying Ca^{2+} homeostasis by sorting and activation of *At*GLRs by *At*CNIHs.

Plants use Ca^{2+} signaling despite lacking many components known to control the cytosolic Ca^{2+} concentration in mammalian cells (*1*). The gene family encoding glutamate receptor–like channels (GLRs) has been implicated in Ca^{2+} transport in various settings, namely, male gamete function (*2*, *3*), stomatal closure (*4*), immunity (*5*), wound signaling (*6*), and root initiation (*7*). Evolutionary diversification of this family in Arabidopsis (*AtGLR*) resulted in 20 genes, distributed into three clades (*8*). To study *AtGLR* function in pollen tubes, whose growth and function depend on Ca^{2+} influx (*9*), we used reverse genetics, generating multiple *AtGLR* mutants (fig. S1, A and B).

In general, pollen tubes carrying *At*GLR mutations showed conspicuous branching (Fig. 1, A to D), preceded by emergence of a new Ca^{2+} gradient, which reestablished the gradient onto the growing tip (Fig. 1, F and G, and movie S1). We also observed that sperm cells were typically shunted into the growing branch (Fig. 1E), suggesting that tip Ca^{2+} signaling established growth polarity and guided sperm nuclei toward the growing tip, thereby providing a basis for the unaffected fertility of most mutants.

We measured extracellular net Ca^{2+} fluxes of growing pollen tube tips using a Ca^{2+}-selective vibrating probe. Tubes from *glr1.2*, *glr2.1*, *glr1.1/glr1.2*, *glr1.2/glr1.4-1*, and *glr1.2/1.4-1/2.2/3.3-1* mutants showed only half the flux of wild type (Fig. 1H, lower panel). Lower cytosolic Ca^{2+} concentrations in tip and shank were found in *glr1.1/glr1.2* tubes (Fig. 1I) as quantified with the ratiometric Ca^{2+} sensor Yellow Cameleon 3.6 (YC3.6) (*2*, *10*), supporting the view of *At*GLRs as plasma membrane channels (*1*). Additionally, *glr1.2/glr1.4* pollen tubes were shorter than those of wild type (~100 μm; Fig. 1J and fig. S2A), suggesting that mutations in *AtGLR*s affect various pollen-mediated phenotypes. Mutations that did not alter Ca^{2+} fluxes often experienced genetic compensation. For instance, in *glr1.1/1.4-1* pollen, *AtGLR1.2* mRNA was overexpressed (fig. S1C).

A diminished growth rate did not correlate with Ca^{2+} flux reductions. Double and triple mutants involving *AtGLR3.3* showed greater Ca^{2+} fluxes than mutants not involving *AtGLR3.3*. Whereas *glr1.2* alone decreased Ca^{2+} flux, the *glr1.2/3.3* double mutant restored it. Nonetheless, in all mutant combinations, pollen tubes grew more slowly than wild type (Fig. 1H, upper panel). Thus, a correlation between Ca^{2+} influx and growth (*11*) did not hold. Cluster analysis revealed a group of mutants with wild-type or higher Ca^{2+} fluxes but slower-than-normal growth rates, composed of double or triple mutants that include *AtGLR3.3* (fig. S2B). We defined a "Ca^{2+} use growth efficiency" metric as the ratio of growth rate to Ca^{2+} flux (Fig. 1K). In mutants involving *glr3.3*, this efficiency decreased as a result of high fluxes, and we hypothesized that mechanisms other than channel conductance could regulate Ca^{2+} homeostasis.

So far, *At*GLRs, like their mammalian counterparts, have been assumed to localize to the plasma membrane (*1*, *7*). However, the antagonistic effects of *glr1.2* and *glr3.3* could be explained by their localization in different membranes. Therefore, we analyzed the subcellular localization of *At*GLR3.3 and *At*GLR2.1, the *At*GLR most highly expressed in pollen. *At*GLR2.1-GFP (green fluorescent protein) localized to the complex vacuolar system (Fig. 2A and fig. S2, C to F), whereas *At*GLR3.3-GFP localized to the sperm plasma membrane and endomembranes but was undetectable in the pollen tube plasma membrane (Fig. 2B and fig. S2, G to I), indicating that the secretory pathway must sort and target both *At*GLRs.

We queried a membrane-based interactome database (*12*) for *CORNICHON* homologs, because they mediate the trafficking of ionotropic glutamate receptors (iGluRs) in animal cells (*13*). Arabidopsis contains five *CORNICHONS* (*AtCNIH1-5*; fig. S3, A and D). *At*CNIH1 interacted with various *At*GLRs (*12*). *At*CNIH1-5 all share characteristic features, including a *cornichon* motif (fig. S3, A and B) and an "IFRTL"-like Sec24-interacting motif (fig. S3, A, B, E, and F). RNA of all *AtCNIHs* was detected in pollen, being highest for *AtCNIH4* (fig. S3C). Both *At*CNIH1 and *At*CNIH4 interact with *At*GLR3.3 (Fig. 2C). In other species, CORNICHONS are essential for sorting and trafficking proteins from the endoplasmic reticulum (ER). We confirmed this for *At*CNIHs by complementing the *erv14p*Δ yeast *Saccharomyces cerevisiae* (*Sc*) CORNICHON mutant (*14*) and observing tolerance toward Na^+ and *Sc*Nha1p localization (Fig. 2F and fig. S3G). Plasma membrane localization of *Sc*Nha1p in the *erv14p*Δ mutant was rescued by *At*CNIH1, 3, and 4, but not by *At*CNIH2 or 5, and restored Na^+ tolerance to wild-type levels, permitting growth on 800 mM NaCl.

In pollen, red fluorescent protein–tagged *At*CNIHs (RFP-*At*CNIHs) localized to endomembranes and punctate structures (Fig. 2, D and E, and fig. S4, A to C) that colocalized with markers for the ER (fig. S4, L to S) but not the cis or medial Golgi (fig. S4, D to K). We also observed pollen tube plasma membrane localization of RFP-*At*CNIH4 (Fig. 2E) and RFP-*At*CNIH3 (fig. S4C). The presence of *At*CNIHs in ER foci (Fig. 2, D and E) was consistent with their localization at ER exit sites (ERES) (*15*). Indeed, *At*CNIHs colocalized with the ERES marker *At*Sec24 (fig. S4, T to W). *cnih1*, *cnih4*, and the double *cnih1/cnih4* mutants (fig. S5, A and B) showed reduced pollen tube tip Ca^{2+} fluxes but wild-type–like growth rates (fig. S5, C and D).

We next analyzed the impact of *At*CNIHs on cargo trafficking. Although *At*GLR3.3-GFP localized to sperm in *cnih1* or *cnih4* pollen (Fig. 3, A and B), it accumulated in reticulate and punctate structures in *cnih1/cnih4* (Fig. 3C) and other *cnih* double mutants (fig. S6, A to E). Neither overexpression of *At*GLR3.3-GFP in *cnih1* and *cnih4* pollen, nor its endomembrane retention in *cnih1/cnih4* mutants, changed the Ca^{2+} flux phenotypes observed in corresponding lines lacking *At*GLR3.3-GFP (fig. S7A). Confirming a role in ER sorting, *At*GLR2.1-GFP was similarly retained in endomembranes in *cnih1/cnih4*, but not in any single mutant (fig. S6, F to H).

We next addressed the *At*CNIH cargo specificity in wild type and *cnih1/cnih4* by comparing two P-type ATPases (adenosine triphosphatases) with comparable intramembrane domain topology.

[1]University of Maryland Department of Cell Biology and Molecular Genetics, 0118 Bioscience Research Building, 4066 Campus Drive, College Park, MD 20742-5815, USA. [2]Instituto Gulbenkian de Ciência, Rua da Quinta Grande 6, Oeiras, 2780-156, Portugal. [3]Instituto de Biotecnología, Universidad Nacional de Autónoma de México, Cuernavaca, Morelos 62250, México.
***Corresponding author. Email: jfeijo@umd.edu**

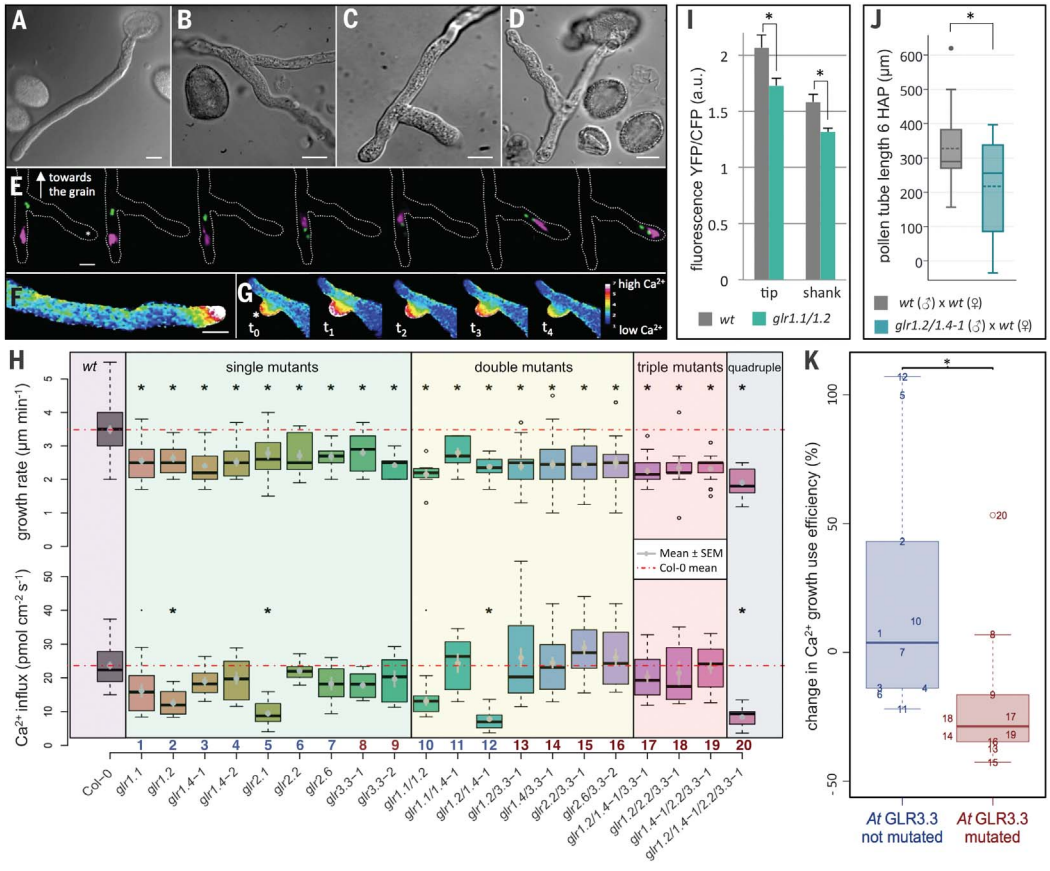

Fig. 1. Characterization of *At*GLR loss-of-function lines. Differential interference contrast images of wild-type (**A**), *glr1.4-1* (**B**), *glr3.3-1* (**C**), and *glr1.4-1/3.3-1* (**D**) pollen. (**E**) Time-lapse series of migrating vegetative (magenta) and sperm (green) nuclei in a branching *glr3.3-1* tube. The tube outline is dotted; the asterisk indicates the growing branch. (**F**) Steep Ca^{2+} gradient in an YC3.6-expressing wild-type pollen tube with highest Ca^{2+} concentration ($[Ca^{2+}]$) at the tip. (**G**) Time series (t_0 to t_4, movie S1) of a branching YC3.6-expressing *glr1.4-1* tube with oscillatory $[Ca^{2+}]$ at the newly emerging tip (asterisk). Bars, 10 µm. (**H**) Pollen tube growth rate (upper panel) and Ca^{2+} influx (lower panel) across the tip plasma membrane of wild-type (Col-0) and *glr* mutants. Dot-dashed lines represent wild-type means of growth rate or Ca^{2+} influx, respectively. $^*P < 0.05$, $\cdot P < 0.1$. (**I**) YC3.6-measured cytosolic Ca^{2+} signatures (YFP/CFP fluorescence values) were significantly lower in *glr1.1/1.2* than in wild type, both at the tip ($^*P < 0.05$) and shank ($^*P < 0.05$). (**J**) Average length of wild-type and *glr1.2/glr1.4-1* pollen tubes 6 hours after pollination (HAP, $n = 15$) on wild-type pistils. Asterisk indicates significant difference from wild type ($P < 0.05$); dotted line represents mean. (**K**) Comparison of normalized growth rates/fluxes, in mutants with (*At*GLR3.3 not mutated) or without *At*GLR3.3 (*At*GLR3.3 mutated). Numbers refer to the lines in Fig. 1H. $^*P < 0.01$.

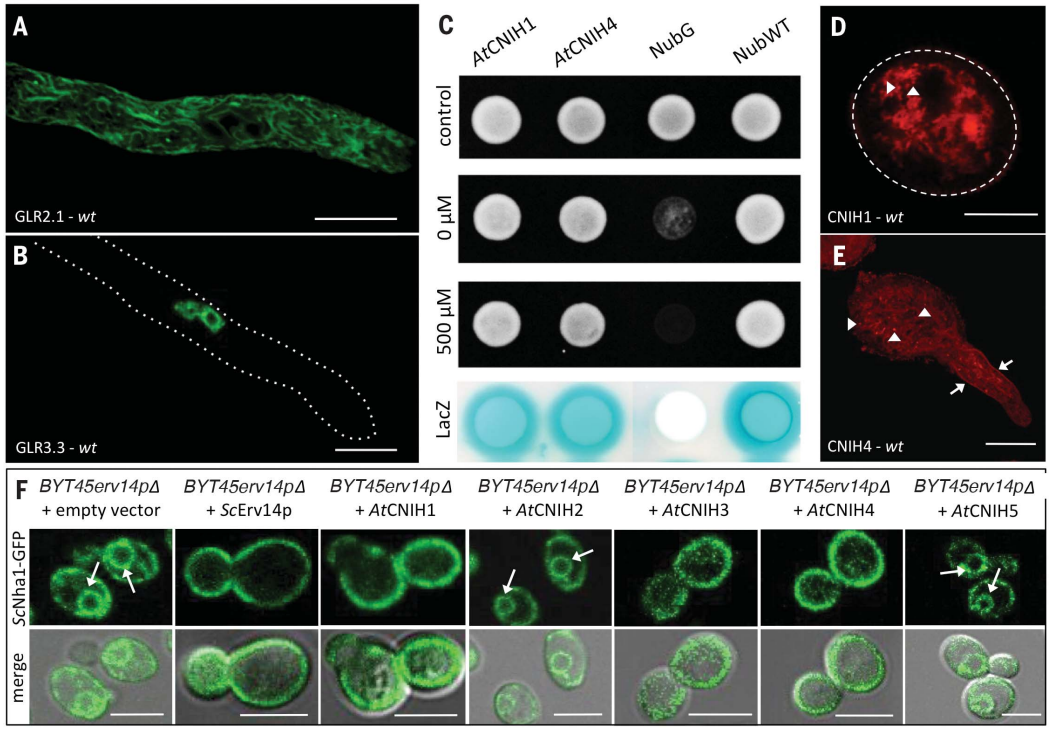

Fig. 2. Subcellular localization of *At*GLRs and *At*CNIHs, their interaction, and functional yeast complementation. Wild-type (*wt*) pollen tubes expressing *At*GLR2.1-GFP (**A**) or *At*GLR3.3-GFP (**B**) localizing to the tonoplast or sperm cell plasma membrane and endomembranes, respectively. Tube contour indicated by dotted line. (**C**) Yeast mating-based split ubiquitin system (mbSUS) assay revealing interaction on control (row 1) or selective media (rows 2 and 3) of *At*GLR3.3/*At*CNIH1 (column 1) or *At*CNIH4 (column 2) in the absence (0 µM) or presence (500 µM) of methionine. Negative (NubG) and positive controls (NubWT) are in columns 3 and 4, respectively. *At*GLR3.3/*At*CNIH1 and *At*GLR3.3/*At*CNIH4 interactions were corroborated by *LacZ* activation (bottom row). (**D**) RFP-*At*CNIH1 and (**E**) RFP-*At*CNIH4 labeling ER exit site–like structures (ERES, arrowheads), and the tube plasma membrane [(E), arrows]. Bars, 10 µm. (**F**) Fluorescence (upper row) and merged bright-field images (lower row) of an *BYT45ervp*Δ yeast expressing *Sc*Nha1p-GFP and cotransformed with the *At*CNIHs. Arrows indicate the peri-nuclear ER. Bars, 5µm.

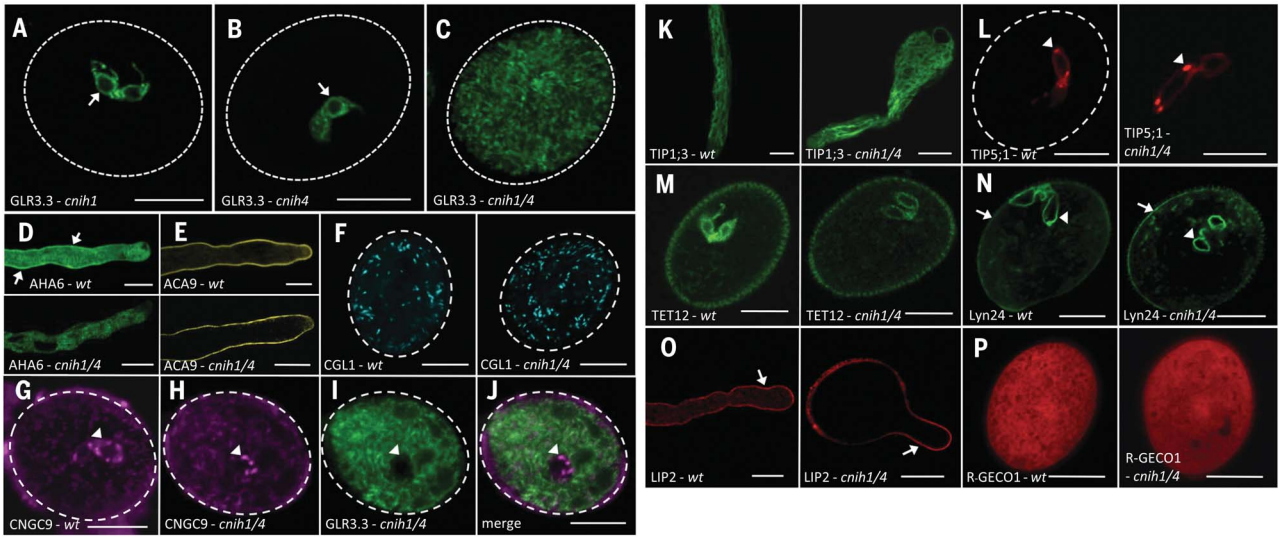

Fig. 3. Expression of *At*GLR3.3-GFP and reference proteins in control and *cnih* pollen. (**A**) *cnih1* and (**B**) *cnih4* pollen expressing *At*GLR3.3-GFP in sperm cells (arrows). (**C**) *At*GLR3.3-GFP localization in *cnih1/cnih4* pollen, labeling endomembranes. (**D**) Expression of *At*AHA6-GFP or (**E**) *At*ACA9-YFP in wild-type (*wt*, upper panels) or *cnih1/cnih4* pollen (lower panels). (**F**) Localization of the cis or medial Golgi marker *At*CGL1-CFP in wild-type (*wt*, left panel) and *cnih1/cnih4* pollen (right panel). Expression of mCherry-*At*CNGC9 in wild-type (*wt*) (**G**) or *cnih1/cnih4* pollen (**H**) coexpressing *At*GLR3.3-GFP (**I**). (**J**) Corresponding merged image. (**K**) Expression of *At*TIP1;3-GFP, (**L**) *At*TIP5;1-mCherry, (**M**) *At*TET12-GFP, (**N**) *Mus musculus* Lyn24 (*Mm*Lyn24-GFP), (**O**) *At*LIP2-RFP, and (**P**) R-GECO1 in wild-type (*wt*, left panels) and *cnih1/cnih4* pollen (right panels). Arrows indicate the tube plasma membrane, arrowheads the sperm cells. Bars, 10 μm.

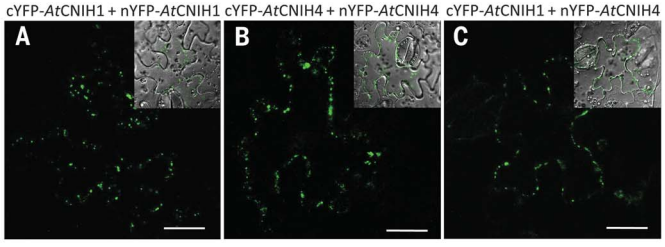

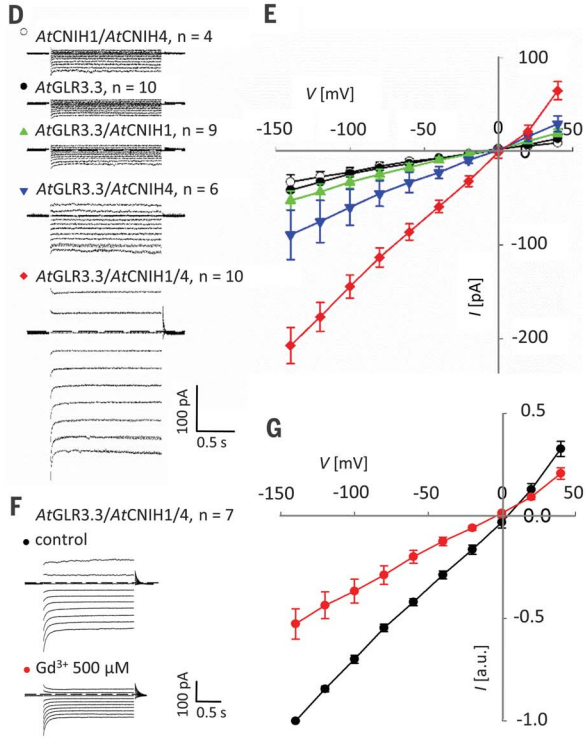

Fig. 4. Interaction of *At*CNIH1/*At*CNIH4 and their effect on *At*GLR3.3 current properties. Transient tobacco epidermis leaf expression of cYFP-*At*CNIH1 + nYFP-*At*CNIH1 (**A**) and cYFP-*At*CNIH4 + nYFP-*At*CNIH4 (**B**) caused YFP fluorescence reconstitution, indicating the formation of homomers (A and B) or heteromers (**C**). Insets represent merged bright-field/fluorescence images. Bars, 20 μm. (**D**) Typical currents in COS-7 cells expressing *At*CNIHs, *At*GLR3.3, or a combination thereof. (**E**) Stationary current/voltage relationships from recordings shown in (D). (**F**) Typical currents recorded in cells coexpressing *At*GLR3.3 and *At*CNIH1/*At*CNIH4 in bath solution (control) or after Gd^{3+} addition (Gd^{3+} 500 μM). (**G**) Stationary normalized current/voltage relationships from recordings shown in (F). Error bars represent SE.

Similarly to *At*GLR2.1 and 3.3, the autoinhibited H^+-ATPase 6 (*At*AHA6-GFP) was retained in endomembranes in *cnih1/cnih4* (Fig. 3D), whereas the autoinhibited Ca^{2+}-ATPase 9 (*At*ACA9-YFP) was unaffected in this (Fig. 3E) or other *cnih* double mutants (fig. S6, I and J), suggesting cargo specificity for pairs of *At*CNIHs. Indeed, marker proteins for the cis or medial Golgi (Fig. 3, F to J, and fig. S6, K to M), vegetative and sperm vacuoles (Fig. 3, K and L), and coat protein complex II (COPII) vesicles (fig. S6, N and O) remained correctly targeted in *cnih1/cnih4* pollen, as were proteins with *At*GLR3.3-like localization (Fig. 3, M to O), or a cytoplasmic protein (Fig. 3P). Thus, ER sorting of certain integral membrane proteins, but not of other soluble or membrane-attached proteins, was dependent on *At*CNIH pairs. Although we found that *At*CNIH homomers may be formed (Fig. 4, A and B), *At*GLR trafficking was dependent on the formation of *At*CNIH heteromers (Fig. 4C and fig. S6, P to R).

We next challenged *At*CNIH regulation of *At*GLR channel activity, as documented for animal glutamate receptors (*13*). Patch-clamp experiments in COS-7 cells expressing *At*CNIH1, *At*CNIH4, *At*GLR3.3, or *At*CNIH1/*At*GLR3.3 revealed control-like currents (Fig. 4, D and E, and fig. S7B). However, cells coexpressing *At*GLR3.3/*At*CNIH4 showed larger currents, and coexpression of *At*GLR3.3/*At*CNIH1/*At*CNIH4 led to a twofold increase, even without ligand (Fig. 4, D and E). Currents were ohmic-like, Gd^{3+}-sensitive, and without selectivity for Na^+ over Ca^{2+}, as revealed by the reversal potential close to 0 mV, despite asymmetric solutions (pipette: 150 mM Na^+; bath: 20 mM Ca^{2+}, 10 mM Na^+; Fig. 4, E to G). We next addressed *At*CNIH specificity for eliciting currents by using *At*GLR3.2, a pollen tube–expressed *At*GLR3.3 homolog. Coexpressing *At*GLR3.2 with either *At*CNIH1 or *At*CNIH4 yielded activation of currents similar to those for *At*GLR3.3/*At*CNIH1/*At*CNIH4 (fig. S7, C to F), albeit up to fivefold higher than the currents measured for any other *At*GLR in heterologous systems (*7*, *16*). In COS-7, *At*GLR3.2 plasma membrane localization was independent of *At*CNIH1 or 4 (fig. S7, G to H), suggesting they were more relevant for channel activity than targeting in this system.

We conclude that *At*CNIHs are essential for sorting, trafficking, and localizing *At*GLRs in planta, and the interaction between proteins of these two families enhances *At*GLR channel activity. These additive effects support increased cationic currents driven by *At*GLRs at a magnitude not previously observed (*2*, *7*, *16*). Ionic selectivity of *At*GLRs is not understood, but *Physcomitrella patens* GLR1 (*Pp*GLR1) conducts Ca^{2+} (*3*). Multiple mechanisms linked to cytosolic Ca^{2+} homeostasis may contribute to the phenotypes that we observed. Some *At*GLR members, like *At*GLR1.2, may work as plasma membrane Ca^{2+} channels, but we posit that sorting of other *At*GLRs to internal Ca^{2+} reservoirs (ER, vacuole, mitochondria) contributes to cytosolic Ca^{2+} homeostasis. When perturbed by multiple mutations, Ca^{2+} homeostasis is disrupted and growth is affected. Therefore, our results suggest that specific *At*CNIHs regulate quantity, location, and activity of *At*GLRs, affecting the concentration of cytosolic Ca^{2+} and, by interacting with other protein families, possibly the concentration of different ions (*15*).

REFERENCES AND NOTES

1. K. H. Edel, E. Marchadier, C. Brownlee, J. Kudla, A. M. Hetherington, *Curr. Biol.* **27**, R667–R679 (2017).
2. E. Michard *et al.*, *Science* **332**, 434–437 (2011).
3. C. Ortiz-Ramírez *et al.*, *Nature* **549**, 91–95 (2017).
4. D. Kong *et al.*, *Cell Reports* **17**, 2553–2561 (2016).
5. M. Kwaaitaal, R. Huisman, J. Maintz, A. Reinstädler, R. Panstruga, *Biochem. J.* **440**, 355–365 (2011).
6. S. A. R. Mousavi, A. Chauvin, F. Pascaud, S. Kellenberger, E. E. Farmer, *Nature* **500**, 422–426 (2013).
7. E. D. Vincill, A. E. Clarin, J. N. Molenda, E. P. Spalding, *Plant Cell* **25**, 1304–1313 (2013).
8. R. Davenport, *Ann. Bot.* **90**, 549–557 (2002).
9. E. Michard, A. A. Simon, B. Tavares, M. M. Wudick, J. A. Feijó, *Plant Physiol.* **173**, 91–111 (2017).
10. D. S. C. Damineli, M. T. Portes, J. A. Feijó, *J. Exp. Bot.* **68**, 3267–3281 (2017).
11. J. A. Feijó *et al.*, *BioEssays* **23**, 86–94 (2001).
12. A. M. Jones *et al.*, *Science* **344**, 711–716 (2014).
13. S. C. Haering, D. Tapken, S. Pahl, M. Hollmann, *Membranes* **4**, 469–490 (2014).
14. J. Powers, C. Barlowe, *Mol. Biol. Cell* **13**, 880–891 (2002).
15. P. Rosas-Santiago *et al.*, *J. Exp. Bot.* **66**, 2733–2748 (2015).
16. D. Tapken *et al.*, *Sci. Signal.* **6**, ra47 (2013).

ACKNOWLEDGMENTS

We thank L. Boavida, F. Brandizzi, A. Costa, U. Grossniklaus, J. Harper, M. Iwano, I. Heilmann, M. Palmgren, L.-J. Qu, and Y. Zhang for sharing materials; S. Wolniak and N. Andrews for sharing facilities; A. Beaven for assisting image acquisition; A. David and T. Maié for lab help; L. Boavida for discussions; and A. A. Simon for reviewing the manuscript. **Funding:** NSF (MCB 1616437/2016 and MCB1714993/2017), UMD, and FCT (PTDC/BEX-BCM/0376/2012, PTDC/BIA-PLA/4018/2012) to J.A.F.; CONACYT (220085) and DGAPA-UNAM (IN-203817) to O.P.; and postdoctoral fellowships SFRH/PD/70739/2010 and SFRH/PD/70820/2010 to M.M.W. and M.T.P., respectively.
Author contributions: M.M.W. contributed to the conceptualization, methodology, validation, formal analysis, investigation, resources, data curation, writing, editing, supervision, and vizualization. M.T.P. and E.M. contributed to the methodology, validation, formal analysis, investigation, data curation, writing, reviewing, and visualization. P.R.-S. contributed to the methodology, validation, investigation, resources, reviewing, and visualization. M.A.L. contributed to the methodology, investigation, resources, reviewing, and visualization. C.C. contributed to the methodology, investigation, resources, and review. C.O.N., J.C.C., and P.T.L. contributed to the methodology, validation, investigation, and review. D.S.C.D. contributed to the conceptualization, methodology, software, validation, formal analysis, data curation review, and visualization. O.P. contributed to methodology, review, supervision, and funding aquisition. J.A.F. contributed to the conceptualization, methodology, writing, editing, supervision, project administration, and funding aquisition. **Competing interests:** None declared. **Data and materials availability:** Accession numbers for all genes referred to in this manuscript and all data needed to evaluate the conclusions in the paper are present in the paper or the supplementary materials.

SUPPLEMENTARY MATERIALS

www.sciencemag.org/content/360/6388/533/suppl/DC1
Materials and Methods
Supplementary Text
Figs. S1 to S7
Table S1
Movie S1
References (*17*–*47*)

4 December 2017; accepted 14 March 2018
10.1126/science.aar6464

NEUROSCIENCE

The threshold for conscious report: Signal loss and response bias in visual and frontal cortex

Bram van Vugt,[1]* Bruno Dagnino,[1]* Devavrat Vartak,[1]* Houman Safaai,[2,3]† Stefano Panzeri,[3] Stanislas Dehaene,[4,5] Pieter R. Roelfsema[1,6,7]†

Why are some visual stimuli consciously detected, whereas others remain subliminal? We investigated the fate of weak visual stimuli in the visual and frontal cortex of awake monkeys trained to report stimulus presence. Reported stimuli were associated with strong sustained activity in the frontal cortex, and frontal activity was weaker and quickly decayed for unreported stimuli. Information about weak stimuli could be lost at successive stages en route from the visual to the frontal cortex, and these propagation failures were confirmed through microstimulation of area V1. Fluctuations in response bias and sensitivity during perception of identical stimuli were traced back to prestimulus brain-state markers. A model in which stimuli become consciously reportable when they elicit a nonlinear ignition process in higher cortical areas explained our results.

Understanding how conscious perception arises in the brain is a major challenge for neuroscience. Experimentally, one approach consists of comparing the neuronal activity evoked by identical weak stimuli, which are sometimes perceived and sometimes remain subliminal. Previous experiments have shown that subliminal stimuli elicit considerable activity in many brain areas, including the prefrontal cortex (*1*), raising the question of why this activity is insufficient for conscious report (*2*).

The classical model that describes how weak stimuli are perceived or missed is signal detection theory (SDT) (*3*). It posits that stimuli elicit a stochastic signal, which has to reach a threshold for perception (Fig. 1A). Stimuli that fail to reach the threshold are missed. In the absence of a stimulus, the signal usually stays below the threshold (correct rejection) but may cross the threshold on occasion, giving rise to a false alarm. According to SDT, a higher threshold decreases the number of false alarms but also increases the number of misses.

SDT does not specify the brain processes that determine the variability of the stimulus-induced signal nor the mechanism that determines the threshold. By contrast, global neuronal workspace theory (GNWT) (*1*, *4*) proposes that stimuli reach awareness by propagating to the higher levels of the cerebral cortex, where they can lead to "ignition," a nonlinear event that causes information about a brief stimulus to become sustained and broadcasted back through recurrent interactions between many brain areas (Fig. 1B) (*5*). According to GNWT, there are two reasons why a stimulus may fail to become consciously accessible. First, the propagation of activity to higher levels may be too weak. Second, global ignition may fail—for example, if the system is refractory because another stimulus caused ignition or if attention is diverted (*1*). Combining insights from SDT and GNWT (*6*, *7*), we hypothesized that the SDT threshold might equal the amount of neural activity required for ignition. Furthermore, the stochasticity in signal strength might relate to variations in the propagation of activity from lower to higher cortical levels, possibly caused by fluctuations in prestimulus brain state.

We trained monkeys to detect low-contrast stimuli and recorded multiunit activity (MUA) in areas V1 and V4 of the visual cortex and in the dorsolateral prefrontal cortex (dlPFC) in order to examine the fate of identical subliminal and supraliminal stimuli. We asked the following questions: (i) Where in the visual hierarchy do subliminal signals get lost? (ii) Which neuronal mechanisms underlie the threshold for reporting a stimulus? (iii) What are the internal sources of fluctuations that allow a fixed stimulus to either cross or fail to cross the threshold?

The monkeys directed their gaze to a fixation point, and on half of the trials, we presented a 2° low-contrast circle as stimulus in the neurons' receptive field (RF) for 50 ms (Fig. 1C). After a delay of 450 ms, introduced to prevent reflexive eye movements (*8*), the monkey reported the stimulus by making a saccade to its previous location. In the absence of a stimulus, the monkey made a saccade to another, smaller gray circle (the reject dot). Accuracy on such stimulus-absent trials was high (~5 to 10% of false alarms). We adjusted the contrast on stimulus-present trials close to the threshold of perception, at an accuracy of ~80% (supplementary materials, materials and methods). The contrast threshold (θ_{High}; accuracy of 80%) varied with stimulus eccentricity between 2.5 and 7% (fig. S1, A to C). To examine perception of very weak stimuli, we also defined a second threshold, θ_{Low}, associated with an accuracy of 40% and categorized stimulus strength into three categories: easy (contrast > θ_{High}), intermediate (θ_{Low} < contrast < θ_{High}), and difficult (contrast < θ_{Low}) (Fig. 1D). We normalized the neuronal responses to the activity elicited by a high-contrast stimulus (supplementary materials, materials and methods).

Stimuli with higher contrasts elicited more activity than did stimuli with lower contrasts (time window 0 to 300 ms after stimulus onset, *t* tests, all $P < 10^{-3}$) (Fig. 1E). Within each strength category, we compared neuronal activity between hits and misses with identical stimulus contrast (supplementary materials, materials and methods). Hits elicited stronger activity in V1, V4, and the dlPFC than did misses, at every difficulty level (window 0 to 300 ms, paired *t* tests, all areas and categories $P < 0.01$) (Fig. 2A and fig. S2, example recording sites). Hence, during misses information is lost during the propagation of visual information to higher cortical areas. In the dlPFC and, to a lesser extent, areas V4 and V1, the extra neuronal activity for hits was maintained until the saccade (time window 300 to 500 ms, all areas and categories $P < 0.05$) (Fig. 2 and fig. S3).

To determine the locus of the information loss, we computed the miss fraction—the percentage of activity remaining for nonreported stimuli ($Activity_{Miss}/Activity_{Hit}$* 100%, time window 0 to 300 ms) (Fig. 2B). For the difficult stimuli, the miss fraction was 46% in area V1 and 14% in V4, implying a substantial loss of activity before V1 and a further loss between V1 and V4 [significant difference between miss fractions in V1 and V4, $t_{46} = 2.5$, $P < 0.01$, number of recording sites in V1 (N_{V1}) = 27, $N_{V4} = 26$]. For the intermediate and easy stimuli, the miss fractions were much higher (around 60 and 80%, respectively) and did not differ significantly between V1 and V4 (for both, $P > 0.05$), indicating substantial propagation of neural activity for misses. Now, however, extra activity was lost between V4 and the dlPFC, both for the intermediate (62 versus 33%, $t_{50} = 3.4$, $P < 0.05$, $N_{V4} = 33$, $N_{dlPFC} = 19$) and easy stimuli (83 versus 22%, $t_{49} = 4.0$, $P < 10^{-3}$, $N_{V4} = 34$, $N_{dlPFC} = 17$). Thus, subliminal stimuli can be lost at different stages of bottom-up signal propagation, depending on their strength.

The activity levels in V1 and V4 on easy miss trials (Fig. 2A, right, red curves) were at least as strong as those on difficult hit trials (Fig. 2A, left, green curves). Hence, the neuronal activity level in these areas does not fully predict stimulus detection. In the dlPFC, however, the activity

[1]Department of Vision and Cognition, Netherlands Institute for Neuroscience, Meibergdreef 47, 1105 BA Amsterdam, Netherlands. [2]Department of Neurobiology, Harvard Medical School, Boston, MA 02115, USA. [3]Neural Computation Laboratory, Istituto Italiano di Tecnologia, 38068 Rovereto, Italy. [4]Cognitive Neuroimaging Unit, Commissariat à l'Énergie Atomique et aux Énergies Alternatives, Direction des Sciences du Vivant/Institut d'Imagerie Biomédicale, INSERM, NeuroSpin Center, Université Paris-Sud and Université Paris-Saclay, 91191 Gif-sur-Yvette, France. [5]Collège de France, 75005 Paris, France. [6]Department of Integrative Neurophysiology, Center for Neurogenomics and Cognitive Research, Vrije Universiteit, Amsterdam, Netherlands. [7]Department of Psychiatry, Academic Medical Center, Amsterdam, Netherlands.
*These authors contributed equally to this work.
†Corresponding author. Email: p.roelfsema@nin.knaw.nl (P.R.R.); houman_safaai@hms.harvard.edu (H.S.)

elicited by hits was stronger at all contrast levels than that elicited by misses, implying that these neurons predicted conscious report in a more categorical manner, which is presumably related to the planning of an eye movement toward the neurons' RF. These results were consistent between monkeys (fig. S4).

In the absence of a stimulus, neuronal activity also differed between false alarms and correct rejections (Fig. 2A). In the dlPFC and area V4, neuronal activity was higher on false-alarm trials (time window 200 ms before saccade; dlPFC, $t_{27} = 4.5$, $P < 10^{-3}$; V4, $t_{36} = 4.8$, $P < 10^{-3}$), with a trend in the same direction in area V1 ($t_{34} = 1.8$, $P = 0.07$). The extra activity on false-alarm trials

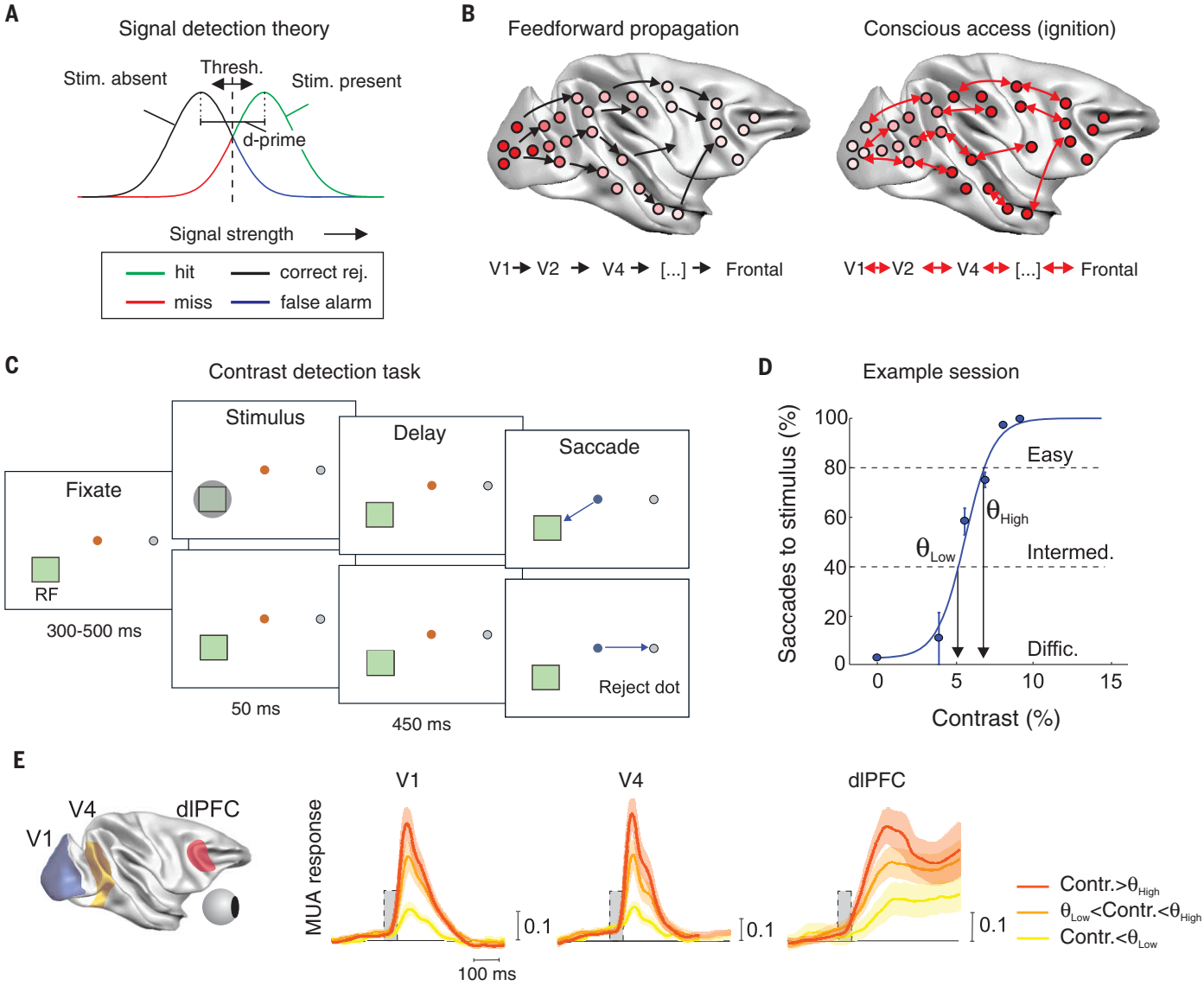

Fig. 1. Visual perception at low contrast. (**A**) SDT holds that stimuli need to cause an internal signal strength larger than a threshold to be perceived and reported. The internal signal strength is stochastic, and false alarms result if the signal crosses the threshold in the absence of a stimulus. In SDT, the subject's bias can be changed by shifting the threshold. A high threshold makes the subject more conservative, and a low threshold makes the subject less conservative, in his "target present" judgments. *d*-prime is a measure of the subject's sensitivity. It corresponds to the distance between the distributions of signal strength for stimulus-present and stimulus-absent trials, measured in units of the standard deviation. (**B**) According to GNWT, sensory activity first needs to be propagated to the higher stages of the cortical hierarchy. If it is strong enough, it can access awareness by causing "global ignition," a process that enables maintenance and sharing of information about the stimulus between cortical processors, manifested by an increase in activity. (**C**) Contrast detection task. On half of the trials, a low-contrast 2° circle stimulus was presented for 50 ms after 300 to 500 ms of fixation. On the other half of the trials, there was no stimulus. After a delay of 450 ms, the monkey reported the stimulus by making a saccade to its previous location and the absence of the stimulus by making a saccade to a smaller gray circle (reject dot). (**D**) Psychometric detection curve for an example session in monkey B. We determined two thresholds, θ_{Low} (accuracy of 40%) and θ_{High} (accuracy of 80%), based on the psychometric function. (**E**) MUA elicited in V1, V4, and the dlPFC by means of easy (contrast > θ_{High}), intermediate (θ_{Low} < contrast < θ_{High}), and difficult stimuli (contrast < θ_{Low}). The activity was averaged across all recording sites per brain region. The numbers of sites—N_{Easy}, $N_{Intermed}$, and N_{Diff}—in area V1 were 33, 25, and 23; in V4 were 36, 34, and 29; and in the dlPFC were 17, 20, and 14, respectively. The vertical scale bar is in units of normalized activity because the MUA at all sites was normalized to the response elicited by a high-contrast stimulus (supplementary materials, materials and methods, and fig. S8). The shaded areas represent ± SEM.

was already present in a 300-ms time window before stimulus onset in all areas (for all, $P < 0.05$), suggesting that increased cortical excitation is a prestimulus brain-state marker that predicts false alarms. We therefore computed the area under the receiver-operating curve (AUROC). An AUROC of 0.5 indicates no predictive power, and a value of 1 indicates perfect prediction. We obtained AUROCs of 0.52, 0.52, and 0.57 in areas V1 and V4 and the dlPFC, respectively (300 ms time window) (Fig. 3A, striped green MUA bars). The AUROC values around the time that a stimulus could have been presented, known as "choice probabilities," were higher (striped black bars). On stimulus-present trials, we focused on trials of intermediate difficulty level, for which we had enough trials, and obtained relatively low prestimulus AUROCs (V1, 0.52; V4, 0.50; and dlPFC, 0.51). Again, choice probabilities after stimulus presentation were higher (0 to 300 ms after stimulus onset; V1, 0.71; V4, 0.71; and dlPFC, 0.74; for all, $P < 0.01$) (Fig. 3A, solid black bars).

We next asked whether fluctuations in the prestimulus brain state were related to variations in stimulus detection. We therefore also evaluated several markers that might predict perceptual report, including the diameter of the pupil (Pu); its time derivative (ΔPu) (*9*); the power in the α, β, and low or high γ bands of the local field potential (*10*, *11*); and the time that the monkeys took to initiate a new trial, which is informative about their motivation. When considered individually, all markers gave weak predictions (Fig. 3A). We linearly combined prestimulus brain-state measures into a joint measure J (supplementary materials, materials and methods), which predicted perceptual outcome with an accuracy close to 60% (V1, 0.59; V4, 0.58; and dlPFC, 0.58; for all, $P < 0.001$). To examine the influence of J on neuronal activity, we selected all trials from the highest and lowest quintile of the J distribution across trials. A higher value for J was associated with higher prestimulus activity and a stronger visual response in all three areas (Fig. 3C). High J values also caused a slight increase in the false-alarm rate (Fig. 3B).

SDT distinguishes between fluctuations in signal strength and response bias. The bias determines the false alarm rate, and we computed another combination of prestimulus brain-state parameters, bias (B), which predicted false alarms with AUROC values around 0.6 (V1, 0.60; V4, 0.62; and dlPFC, 0.61; for all, $P < 0.01$) (Fig. 3, A and B). Higher B values were associated with extra prestimulus firing in all three areas in stimulus-present (not used to define B) (Fig. 3D) and stimulus-absent trials (fig. S5).

In SDT, accuracy also depends on d-prime, the distance between the stimulus-present and -absent distributions of signal strength (Fig. 1A). Our comparison between hit and miss trials (Fig. 2) suggested that there was variability in the propagation of neuronal activity to higher cortical levels. However, J did not have an isolated effect on d-prime because it also influenced the false-alarm rate. We therefore devised a third linear combination of prestimulus brain-state measures to index sensitivity (S), designed to discriminate hits from misses without influencing the false-alarm rate (Fig. 3, A and B, and supplementary materials, materials and methods). A high S value increased visually driven activity, especially in the higher areas, in accordance with an influence on the efficiency of activity propagation to higher levels (Fig. 3E). Hence, we identified separable influences of prestimulus brain state on the subject's response bias and sensitivity. Bias B relates to an increase in ongoing activity, whereas sensitivity S relates to an increase in the efficiency of signal propagation (Fig. 3F).

We interpreted our results in terms of variation in signal propagation from area V1 to V4 and then onward to the PFC, but visual information can reach higher areas through multiple routes, some of which bypass area V1 (*12*). To specifically demonstrate the role of V1-to-V4 propagation and its failures around the threshold of perception, we activated area V1 with electrical microstimulation while recording from V4. The monkeys reported a phosphene—an illusory light percept at the RF of the stimulated neurons (*13*)—elicited in V1 with five pulses (200 Hz) while we varied stimulation strength (Fig. 4A). We determined two thresholds for the stimulation current (Fig. 4B; the distribution of θ_{High} is shown in fig. S1D) and recorded MUA in V4 from neurons with RFs that overlapped with those of the stimulated V1 neurons (Fig. 4C, right) for a total of 84 V1-V4 pairs (58 in monkey B and 26 in monkey C).

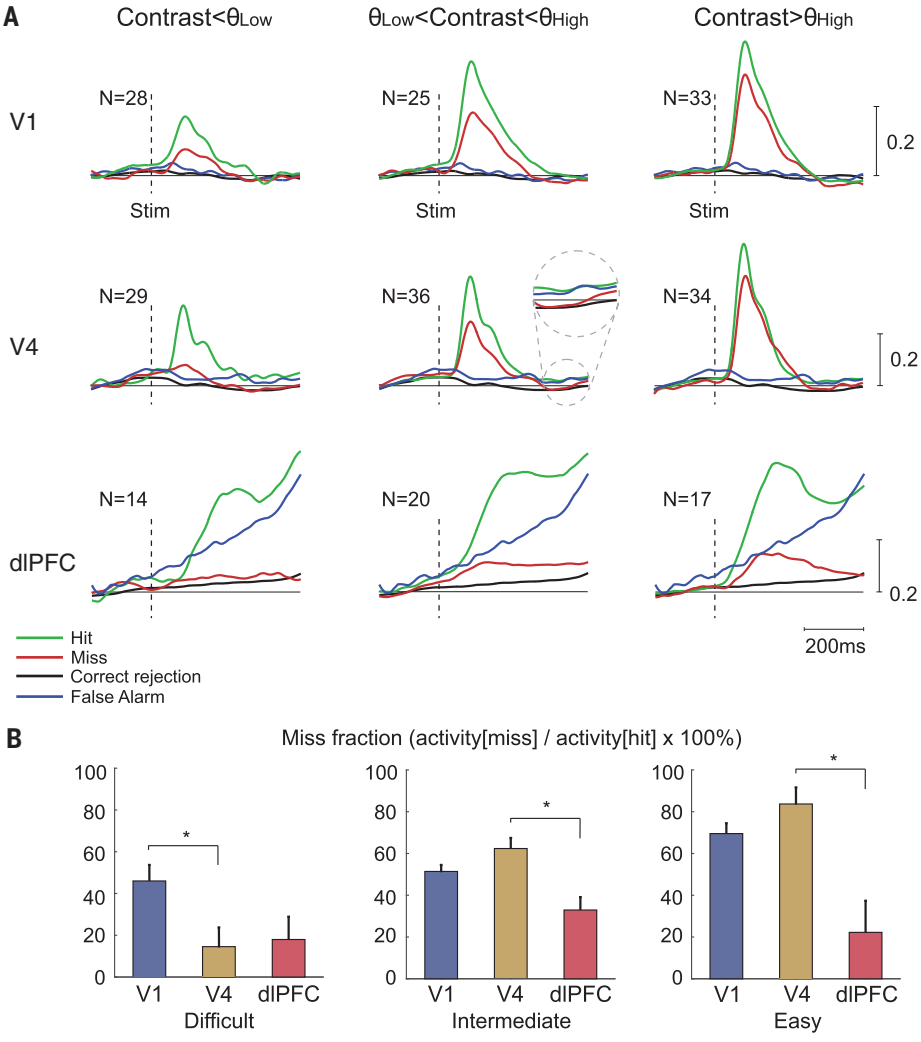

Fig. 2. Activity in areas V1 and V4 and the dlPFC in the contrast-detection task. (**A**) Activity averaged across all recording sites in (top) V1, (middle) V4, and (bottom) dlPFC by contrasts lower than θ_{Low} (difficult; left), between θ_{Low} and θ_{High} (intermediate; middle), and higher than θ_{High} (easy; right) for contrast-matched hits (green curves) and misses (red curves). The black curves indicate average activity on trials in which the monkeys correctly reported the absence of a stimulus, and the blue curves indicate activity on trials with false alarms. (Inset) The influence of choice on late V4 activity in one of the conditions. (**B**) Miss fraction ($Activity_{Miss}/Activity_{Hit} \times 100\%$) in V1 (blue bars), V4 (yellow bars), and the dlPFC (red bars) for the different stimulus categories (time window, 0 to 300 ms after stimulus onset).

Consistent with the propagation hypothesis, V1 microstimulation elicited V4 activity, with a temporal profile that resembled the response elicited by a visual stimulus, and higher V1 currents increased the V4 response (for all, $P < 0.05$) (Fig. 4C and fig. S6). Furthermore, V4 activity was larger on hit trials than on miss trials at all current strengths (time window from 0 to 150 ms after stimulus onset; paired t test, all Ps $< 10^{-6}$) (Fig. 4D and fig. S6C). Hence, the efficiency of activity propagation from V1 to V4 predicts perceptual report. The miss fraction increased from 16% in difficult trials to 42% in intermediate trials and to 83% in easy trials (Fig. 4E) (t tests; for all, Ps $< 10^{-3}$; N_{Low} = 47, $N_{Intermediate}$ = 41, N_{High} = 67), implying that for the stronger electrical stimuli, information could still be lost at processing levels higher than that of area V4. Indeed, V4 activity on easy miss trials was stronger than on difficult hit trials, confirming that although correlated with the hit probability, the amplitude of the V4 response does not fully predict whether a stimulus will enable conscious report.

Can a simple mathematical model of hierarchically arranged areas reproduce these findings? The model's architecture was based on previous modeling studies (*14*) and contained the lateral geniculate nucleus and four hierarchically arranged cortical areas (Fig. 4F). We represented the population of neurons in each area with a single, stochastic Ornstein-Uhlenbeck process so that only five variables described the evolution of the network state during simulated trials, one for each brain region. The model contained feedforward connections, self-connections within the areas, and feedback connections. The reciprocal connections between the parietal and frontal cortex were relatively strong so that activity exceeding a threshold in these areas became self-sustained (Fig. 4I, ignition, and supplementary materials). The model produced a realistic psychometric function, with increased accuracy for higher contrasts (Fig. 4G). The activity of the model units was

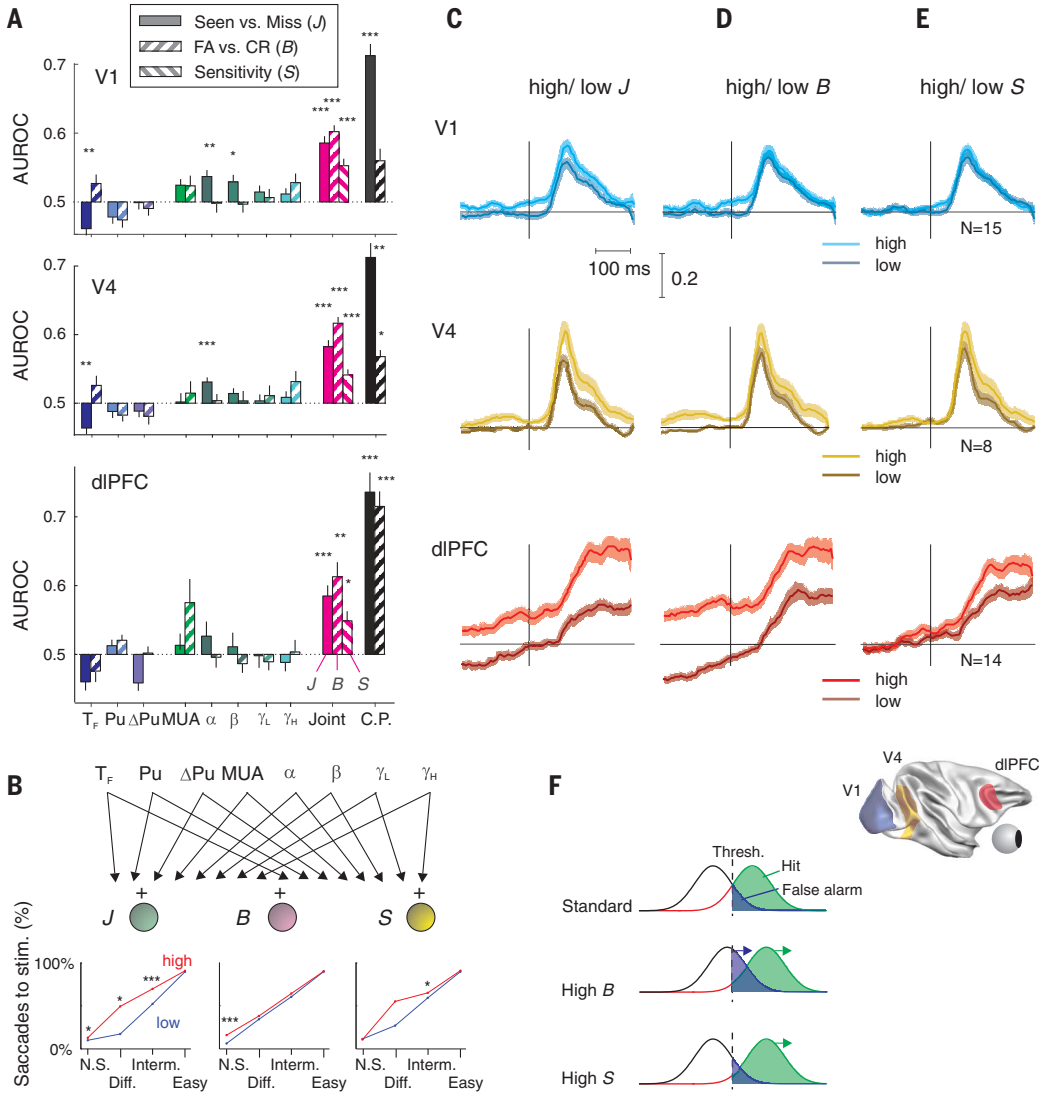

Fig. 3. Influence of prestimulus brain state on neuronal activity and choice. (**A**) Behavioral and neurophysiological markers of prestimulus brain state that predict the animal's choice. Predictive value was quantified as the AUROC. Results of experiments in which we recorded activity in areas V1 and V4 and the dlPFC are shown at top, middle, and bottom, respectively. Positive AUROCs indicate that a higher value of the marker predicts a higher probability of hits or false alarms. T_F, time between the appearance of the fixation point and the moment that the monkey directed gaze to the fixation point; Pu, pupil diameter; ΔPu, change in pupil diameter; MUA, prestimulus MUA; α, power from 5 to 15 Hz; β, 15 to 25 Hz; γ_L, 25 to 40 Hz; γ_H, 40 to 80 Hz; Joint, combination of markers best distinguishing between hits and misses (*J*), correct rejections and false alarms (*B*), and a measure that discriminates between hits and misses with a minimal influence on the false alarm rate (*S*) [schematic in (B)]; C.P., choice probability based on MUA in the stimulus-presentation time window. Solid bars indicate hits versus misses. Striped bars indicate false alarms versus correct rejections. *$P < 0.05$, **$P < 0.01$, ***$P < 0.001$, one-tailed t test with Holm-Bonferroni correction. (**B**) *J*, *B*, and *S* were based on linear combinations of prestimulus brain-state markers. (Bottom) Influence of *J*, *B*, and *S* on the probability of reporting stimulus present on no-stimulus trials (N.S., false alarms) and stimulus-present trials (hits) at the three difficulty levels, comparing lowest (blue) and highest quintiles (red). (**C**) Neuronal activity (smoothed with a 40-ms window) on stimulus-present trials within the highest quintile (lighter shades) and lowest quintile (darker shades) of the distribution of *J*. The shaded regions indicate ± SEM as determined with bootstrapping. (**D** and **E**) Activity on stimulus-present trials within higher and lower quintiles of *B* (D) and *S* (E) during the prestimulus epoch. *B* was defined on the basis of stimulus-absent trials but is applied here to sort stimulus-present-trials. (**F**) High values of *B*, which increase the false-alarm rate, are associated with higher firing rates throughout the trial, causing neurons to be closer to the threshold of ignition. High values of *S* are associated with more efficient propagation of neuronal activity to higher processing levels, increasing the separation between the distributions of signal strength on target-present and target-absent trials.

remarkably similar to that recorded in the monkeys (Fig. 4I and fig. S7; compare with Fig. 2), and weak stimuli tended to get lost at lower levels than did stronger stimuli (fig. S7D). Once ignition occurred at the higher levels, the feedback connections from frontal and parietal regions to the visual cortex caused a small increase in activity in areas V1 and V4 after the stimulus had disappeared, just as in the data in the epoch before the saccade (Fig. 2 and fig. S3A). The model also accounted for the profile of neuronal activity on trials without a stimulus. In a fraction of these trials, stochastic fluctuations in activity caused spontaneous ignitions at variable time points, giving rise to false alarms. When averaged across trials, time-locked

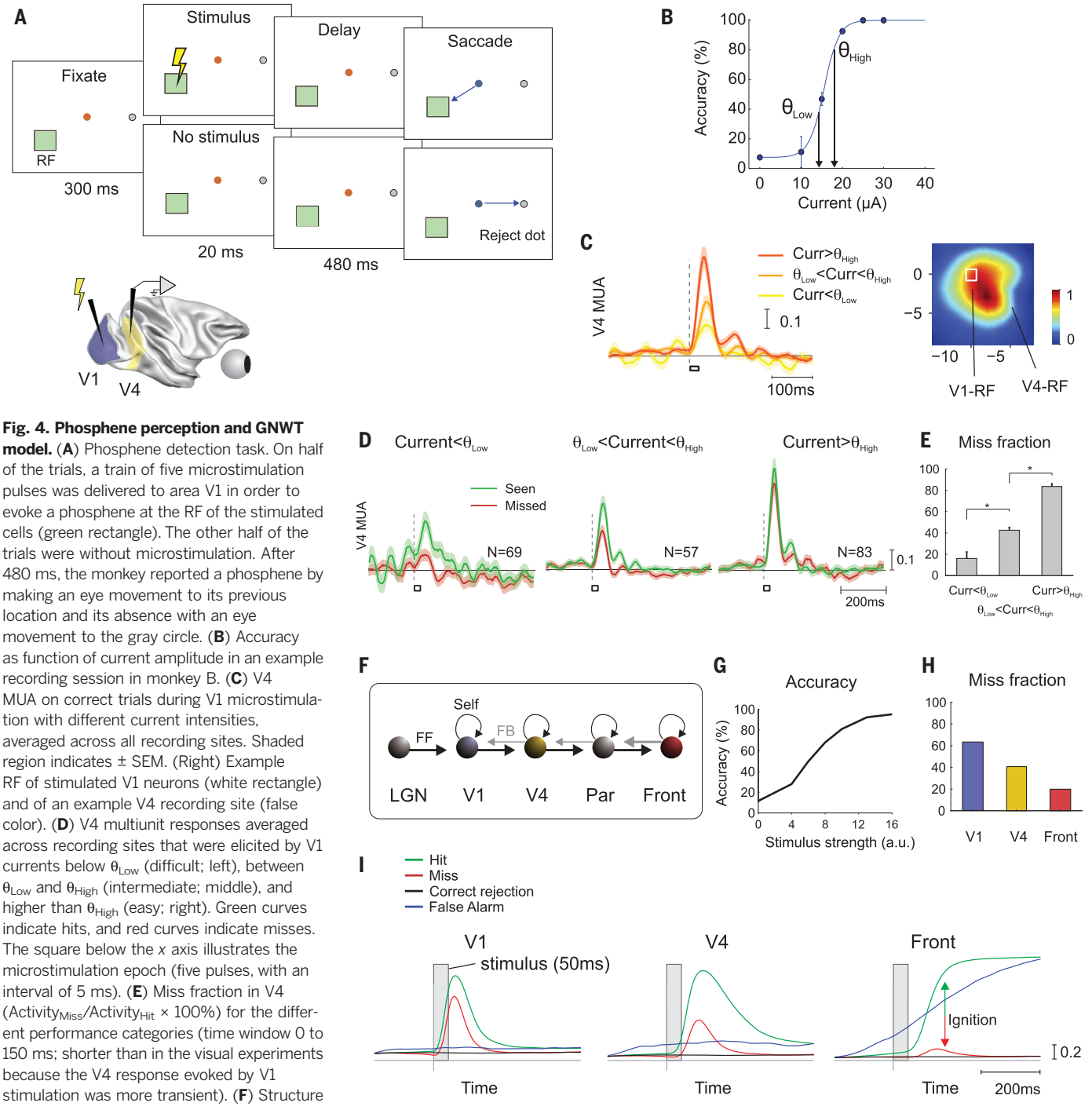

Fig. 4. Phosphene perception and GNWT model. (**A**) Phosphene detection task. On half of the trials, a train of five microstimulation pulses was delivered to area V1 in order to evoke a phosphene at the RF of the stimulated cells (green rectangle). The other half of the trials were without microstimulation. After 480 ms, the monkey reported a phosphene by making an eye movement to its previous location and its absence with an eye movement to the gray circle. (**B**) Accuracy as function of current amplitude in an example recording session in monkey B. (**C**) V4 MUA on correct trials during V1 microstimulation with different current intensities, averaged across all recording sites. Shaded region indicates ± SEM. (Right) Example RF of stimulated V1 neurons (white rectangle) and of an example V4 recording site (false color). (**D**) V4 multiunit responses averaged across recording sites that were elicited by V1 currents below θ_{Low} (difficult; left), between θ_{Low} and θ_{High} (intermediate; middle), and higher than θ_{High} (easy; right). Green curves indicate hits, and red curves indicate misses. The square below the *x* axis illustrates the microstimulation epoch (five pulses, with an interval of 5 ms). (**E**) Miss fraction in V4 ($Activity_{Miss}/Activity_{Hit}$ × 100%) for the different performance categories (time window 0 to 150 ms; shorter than in the visual experiments because the V4 response evoked by V1 stimulation was more transient). (**F**) Structure of the GNWT model. The visual stimulus activated the lateral geniculate nucleus (LGN), and feedforward connections (FF) propagated activity from the visual cortex (areas V1 and V4) to the parietal and frontal cortex. Self-connections were within the areas, and feedback connections (FB) propagated activity from higher back to lower areas. (**G**) Probability of target-present response as function of stimulus strength. a.u., arbitrary units. (**H**) Miss fractions are lower at higher cortical levels, indicating that more activity is lost on the miss trials. (**I**) Activity elicited in model V1, V4, and frontal cortex (compare with Fig. 2A). When the activity in the frontal cortex of the model reaches a threshold level of activity, it can sustain itself (ignition, red and green arrows) because of the strong reciprocal connectivity with the parietal cortex. Activity dies down if this threshold activity level is not reached and the stimulus is missed. The black curves indicate activity for correct rejections, and the blue curves indicate activity for false alarms.

to trial onset, these spontaneous ignitions led to a ramping of activity, just as in the dlPFC of monkeys (Fig. 2A). On these trials, feedback to areas V1 and V4 also caused slightly higher activity levels than on trials with correct rejections, just as observed in the monkey visual cortex (Fig. 2A).

Overall, our results provide new insights into why a fixed stimulus sometimes leads to a conscious report and sometimes remains subliminal and inspire unification of SDT and GNWT. Both data and model support the concept of multiple bottlenecks for conscious access: Weak stimuli tend to get lost at early processing levels, whereas stronger stimuli may transiently activate frontal cortex but still fail to reach the threshold for reportability. For conscious detection to occur in the model, stimuli must elicit a threshold level of prefrontal activity that is sufficient for ignition; stimuli that fail to reach this level are missed. Ignition corresponds to a self-sustained pattern of neuronal activity at the higher processing levels. Because of the variability of neuronal activity, the ignition threshold is occasionally reached on stimulus-absent trials, so that a false alarm occurs. The model proposes that ignition is caused by strong reciprocal interactions between the parietal and frontal cortex, in accordance with studies demonstrating that anesthesia weakens these interactions (*15*).

In our study, V1 activity was weaker on miss than on hit trials, in accordance with previous work (*16*), but our findings differ from results in the primary somatosensory cortex of monkeys in which neuronal responses did not predict the perception of weak tactile stimuli (*17*). Here too, however, V1 and V4 activity also did not fully predict perceptual report because neuronal activity evoked by missed visual or electrical stimuli could be at least as strong as that elicited by stimuli that were reported, implying information loss in downstream areas. By contrast, the activity level in the dlPFC categorically predicted perceptual report, implying that dlPFC lies at or beyond the stage that determines the reporting threshold.

We note a few limitations of our experiments. First, they were not aimed at revealing all of the brain regions that contribute to conscious reportability; although we focused on dlPFC neurons that contribute to eye movement planning, a broader set of high-level regions, linked by bidirectional connections, is likely to contribute to the postulated global work space. Other cortical regions—upstream from the dlPFC and including, for example, the temporal (*18*–*20*) and parietal cortex (*21*, *22*)—also exhibit extra activity if a stimulus reaches awareness, suggesting that they take part in conscious perception. Second, our design did not dissociate the brain regions required for conscious experience from those involved in conscious access and reportability (*23*). Because our goal was to investigate the mechanism of reportability and its fluctuations, we needed an explicit behavioral report in order to sort otherwise identical trials according to their subjective detection. It has been proposed that PFC activity mainly reflects conscious reporting (*24*, *25*). Although this account may suffice for the present results, PFC neurons also selectively represent consciously perceived stimuli during binocular flash suppression even if there is no need for report (*26*).

The higher brain regions provided feedback to areas V1 and V4, where the initial responses were driven by the stimulus, but later activity was stronger if the animals reported the stimulus (Fig. 2). A previous functional magnetic resonance imaging (fMRI) study observed a comparable increase of neuronal activity in early visual cortex when subjects reported a stimulus (*27*), but the fMRI signal did not differentiate between hits and false alarms, as though it was blind to stimulus presentation. The difference with the present results may be caused by the nature of the fMRI signal, which is insensitive to fine-grained timing but sensitive to processes other than spiking activity, such as synaptic activity of feedback connections (*28*, *29*).

SDT stipulates an undefined source of signal fluctuations across trials. We found that part of this variability arises before stimulus onset. Various markers of prestimulus brain state could be combined to predict stimulus detection with accuracies greater than 60%. Additional measures of prestimulus brain state may further increase predictive power, although part of the unpredictability may be caused by the intrinsic stochasticity of neuronal activity, which was an essential ingredient of the model (Fig. 4F). It proved possible to define linear combinations of prestimulus brain-state markers with independent information about the subject's response bias and sensitivity. A bias to report target present was associated with a higher baseline firing rate across different brain regions, bringing neurons closer to the threshold for ignition (Fig. 3). By contrast, a higher sensitivity was associated with an improved propagation of neuronal activity to higher processing levels, increasing the difference in activity levels between target-present and target-absent trials at the processing stage that determines the threshold for ignition. Although our study did not address the brain mechanisms that influence the prestimulus firing rate and the quality of signal propagation, previous studies have established relations between pupil size and the frequency bands of the electroencephalography and the tone of neuromodulators such as noradrenaline (*9*) and acetylcholine (*30*). Future studies could examine whether the activity of these neuromodulatory systems indeed exerts separable influences on the animals' bias and sensitivity when stimuli are near the threshold of conscious perception.

REFERENCES AND NOTES

1. S. Dehaene, J.-P. Changeux, *Neuron* **70**, 200–227 (2011).
2. L. Weiskrantz, *Consciousness Lost and Found* (Oxford Univ. Press, Oxford, 1998).
3. D. M. Green, J. A. Swets, *Signal Detection Theory and Psychophysics* (Wiley, 1966).
4. B. J. Baars, *Trends Cogn. Sci.* **6**, 47–52 (2002).
5. V. A. F. Lamme, P. R. Roelfsema, *Trends Neurosci.* **23**, 571–579 (2000).
6. J. R. King, S. Dehaene, *Philos. Trans. R. Soc. Lond. B Biol. Sci.* **369**, 20130204 (2014).
7. Y. Ko, H. Lau, *Philos. Trans. R. Soc. London B Biol. Sci.* **367**, 1401–1411 (2012).
8. A. V. Belopolsky, A. F. Kramer, J. Theeuwes, *J. Cogn. Neurosci.* **20**, 2285–2297 (2008).
9. J. Reimer *et al.*, *Neuron* **84**, 355–362 (2014).
10. V. Wyart, C. Tallon-Baudry, *J. Neurosci.* **29**, 8715–8725 (2009).
11. L. Iemi, M. Chaumon, S. M. Crouzet, N. A. Busch, *J. Neurosci.* **37**, 807–819 (2017).
12. M. C. Schmid *et al.*, *Nature* **466**, 373–377 (2010).
13. E. M. Schmidt *et al.*, *Brain* **119**, 507–522 (1996).
14. S. Dehaene, J.-P. Changeux, *PLOS Biol.* **3**, e141 (2005).
15. U. Lee *et al.*, *Anesthesiology* **118**, 1264–1275 (2013).
16. C. Palmer, S.-Y. Cheng, E. Seidemann, *J. Neurosci.* **27**, 8122–8137 (2007).
17. V. de Lafuente, R. Romo, *Nat. Neurosci.* **8**, 1698–1703 (2005).
18. G. Avidan *et al.*, *J. Neurophysiol.* **87**, 3102–3116 (2002).
19. L. Fisch *et al.*, *Neuron* **64**, 562–574 (2009).
20. R. Q. Quiroga, R. Mukamel, E. A. Isham, R. Malach, I. Fried, *Proc. Natl. Acad. Sci. U.S.A.* **105**, 3599–3604 (2008).
21. F. Siclari *et al.*, *Nat. Neurosci.* **20**, 872–878 (2017).
22. W. X. Herman *et al.*, *Cereb. Cortex* 10.1093/cercor/bhx327 (2018).
23. C. Koch, M. Massimini, M. Boly, G. Tononi, *Nat. Rev. Neurosci.* **17**, 307–321 (2016).
24. S. Frässle, J. Sommer, A. Jansen, M. Naber, W. Einhäuser, *J. Neurosci.* **34**, 1738–1747 (2014).
25. N. Tsuchiya, M. Wilke, S. Frässle, V. A. F. Lamme, *Trends Cogn. Sci.* **19**, 757–770 (2015).
26. T. I. Panagiotaropoulos, G. Deco, V. Kapoor, N. K. Logothetis, *Neuron* **74**, 924–935 (2012).
27. D. Ress, D. J. Heeger, *Nat. Neurosci.* **6**, 414–420 (2003).
28. A. Maier *et al.*, *Nat. Neurosci.* **11**, 1193–1200 (2008).
29. N. K. Logothetis, J. Pauls, M. Augath, T. Trinath, A. Oeltermann, *Nature* **412**, 150–157 (2001).
30. L. Pinto *et al.*, *Nat. Neurosci.* **16**, 1857–1863 (2013).

ACKNOWLEDGMENTS

Funding: The work was supported by Nederlandse Organisatie voor Wetenschappelijk Onderzoek (Brain and Cognition grant 433-09-208 and ALW grant 823-02-010) and the European Union Seventh Framework Program (Marie-Curie Action PITN-GA-2011-290011 "ABC," grant agreement 7202070 "Human Brain Project," and European Research Council grant agreement 339490 "Cortic_al_gorithms") awarded to P.R.R.; S.P. was supported by Fondation Bertarelli, and S.D. was supported by the Canadian Institute for Advanced Research. **Author contributions:** P.R.R., B.v.V., and B.D. conceived the study; B.v.V., B.D. and D.V. collected the data; H.S., S.P., and P.R.R. designed the analysis of prestimulus brain state; S.D. constructed the model with input from P.R.R.; B.v.V. and P.R.R. wrote the paper; and all authors commented on it. **Competing interests:** The authors declare no competing financial interests. **Data and materials availability:** The data and the computer code used to analyze the data are available for download and curated at the Human Brain Project Joint Platform (https://object.cscs.ch/v1/AUTH_227176556f3c4bb38df9feea4b91200c/hbp-data-000789/index.html). Correspondence and requests for materials should be addressed to P.R.R. or H.S.

SUPPLEMENTARY MATERIALS

www.sciencemag.org/content/360/6388/537/suppl/DC1
Materials and Methods
Table S1
Figs. S1 to S9
References (*31*–*52*)
Matlab Files S1 and S2
Instruction Files S1 and S2

10 December 2017; accepted 9 March 2018
Published online 22 March 2018
10.1126/science.aar7186

SYSTEMS BIOLOGY

Morphogen gradient reconstitution reveals Hedgehog pathway design principles

Pulin Li,[1]* Joseph S. Markson,[1]* Sheng Wang,[1] Siheng Chen,[1] Vipul Vachharajani,[1] Michael B. Elowitz[1,2]†

In developing tissues, cells estimate their spatial position by sensing graded concentrations of diffusible signaling proteins called morphogens. Morphogen-sensing pathways exhibit diverse molecular architectures, whose roles in controlling patterning dynamics and precision have been unclear. In this work, combining cell-based in vitro gradient reconstitution, genetic rewiring, and mathematical modeling, we systematically analyzed the distinctive architectural features of the Sonic Hedgehog pathway. We found that the combination of double-negative regulatory logic and negative feedback through the PTCH receptor accelerates gradient formation and improves robustness to variation in the morphogen production rate compared with alternative designs. The ability to isolate morphogen patterning from concurrent developmental processes and to compare the patterning behaviors of alternative, rewired pathway architectures offers a powerful way to understand and engineer multicellular patterning.

During development and regeneration, tissue patterning unfolds with astonishing precision in space and time. Diffusible signaling molecules known as morphogens provide a key patterning mechanism. Morphogens are secreted by sender cells and form concentration gradients that are interpreted by cognate signaling pathways in receiver cells to generate distinct cell fate domains (*1*). Morphogen-sensing pathways have diverse regulatory architectures that actively process intracellular signals and modulate the abundance of extracellular morphogens (*2*, *3*). However, the roles of these features in pattern formation have generally remained unclear. To address this gap, we developed a system to reconstitute patterning in cell culture and used it to directly compare the patterning behaviors of natural and rewired morphogen pathways (Fig. 1A).

We focused on the Hedgehog (HH) pathway, a classic long-range morphogen system that is implicated in developmental diseases and cancer (*4*). Unlike other morphogen pathways, in which ligands positively activate their receptors, the HH pathway uses a distinctive "double-negative" activation mechanism (Fig. 1B): Unliganded PTCH receptors suppress intracellular pathway activity, and this suppression is relieved by HH ligand binding. Furthermore, by sequestering HH, PTCH receptors also modulate the ligand's extracellular spatial distribution. The combination of these intracellular and extracellular activities makes PTCH effectively bifunctional (*5*). Lastly, HH signaling up-regulates PTCH expression, generating negative feedback through both inhibition of intracellular signaling and sequestration of extracellular ligands (*6*–*8*). Despite much work, the functional rationale for this pathway architecture has largely remained obscure.

We reconstituted HH signaling gradients in NIH 3T3 cells, which transduce HH signals without differentiating and do not naturally express HH ligands (*9*). We generated an inducible sender line by placing the wild-type Sonic Hedgehog (*Shh)* coding sequence under the control of a 4-hydroxytamoxifen (4-OHT)–inducible system (Fig. 1C). We also engineered a receiver cell line containing a synthetic construct in which GBS (GLI-binding site) sequences recognized by the downstream transcription factor GLI drive the expression of nuclear-localized H2B-Citrine fluorescent protein (*10*, *11*). Reporter expression responded to SHH in a dose-dependent manner and correlated with endogenous SHH pathway targets (fig. S1). Diluting sender cells in a 1000-fold excess of receivers produced radial gradients of SHH signaling extending from single sender cells, reaching a limiting size of about four or five cell diameters (80 to 100 μm) over a time span of 60 hours (Fig. 1D). Additionally, to mimic quasi–one-dimensional contexts, such as limb buds, neural tubes, and *Drosophila* wing discs (*12*), we used a cell culture insert system to plate senders and receivers in adjacent, contiguous regions (Fig. 1E). In this configuration, gradients extended more than ~200 μm. These results show that SHH signaling gradients with sizes comparable to naturally occurring gradients can be generated by coculturing synthetic senders and receivers in vitro.

In principle, SHH gradients could form through diffusion of ligands in the liquid medium or through lateral movement of ligands within the cell layer (as by diffusion in the extracellular matrix or transport along filopodia) (*13*–*16*). To distinguish between these two possibilities, we analyzed gradient formation on a laboratory rocker, which should disrupt media-based gradients. However, rocking had no effect on gradients (Fig. 1F). In a second experiment, we cultured senders and receivers on coverslip fragments separated by a 30-μm gap. This gap, which is much shorter than the gradient length, was sufficient to prevent activation of receivers by senders (Fig. 1G). In contrast, when the coverslips were directly adjacent (no gap), the gradient formed normally. Both experiments indicate that, under these conditions, the SHH gradient forms predominantly through movement within the cell layer, requiring cell-cell contact or continuous extracellular matrix (*17*). In addition, cell migration and division have minimal effects on gradient formation owing to their low rates in this context, but they could play more substantial roles in natural contexts (fig. S2, B to D).

The ability to reconstitute gradient formation in cell culture enabled us to explore the functional implications of the SHH pathway architecture. We first focused on the unusual double-negative logic of the core pathway (Fig. 1B) by eliminating the feedback on PTCH (table S1) to create a simpler, "open-loop" receiver cell line (Fig. 2A). We knocked out both endogenous *Ptch1* alleles and integrated a copy of *Ptch1* under a doxycycline (Dox)–inducible promoter (fig. S3). Coculturing this open-loop cell line adjacent to sender cells allowed us to observe the dynamics of open-loop gradient formation across a matrix of SHH and PTCH expression levels (Fig. 2, B to D; fig. S4, A and B; and movies S1 and S2). Analysis of the resulting movies revealed that elevating the SHH production rate increased gradient amplitude and extended the length scale, whereas elevating the PTCH production rate had the opposite effect (Fig. 2D and fig. S4C). Gradient length scale and amplitude specifically depended on the ratio of SHH and PTCH production rates (Fig. 2E and fig. S4D).

To understand this ratiometric behavior, we constructed a minimal mathematical model of the core pathway (fig. S5A). This model assumes that free PTCH promotes production of the repressor form of GLI (GLIR), which in turn inhibits target gene expression. Binding of PTCH to HH inactivates both proteins, decreasing GLIR production. We fit the model to experimental data for a range of SHH production rates at a single PTCH level (fig. S5, B to D, and table S2) (*17*). The model recapitulated ratiometric length-scale and amplitude control across a broad range of PTCH expression levels (Fig. 2F and fig. S5E). Further analysis revealed that double-negative regulatory logic is sufficient for ratiometric control (*17*). This behavior was preserved when additional factors, such as the activating form of GLI, were incorporated (fig. S6) (*18*). Together, these results show that control of gradient properties is shared by both senders (through the SHH production rate) and receivers (through the PTCH production rate) in the open-loop configuration.

[1]Division of Biology and Biological Engineering, California Institute of Technology, Pasadena, CA 91125, USA. [2]Howard Hughes Medical Institute and Department of Applied Physics, California Institute of Technology, Pasadena, CA 91125, USA.
*These authors contributed equally to this work.
†Corresponding author. Email: melowitz@caltech.edu

Ratiometric control provides robustness to correlated changes in SHH and PTCH expression that preserve their ratio, but it implies sensitivity to perturbations in these parameters individually. Deletion of one SHH allele has no obvious phenotype in mice (*19*). Although it is not known whether gene dosage directly affects the level of secreted SHH, this nevertheless suggests that the system may have intrinsic mechanisms to buffer variations in the morphogen production rate.

We hypothesized that negative feedback resulting from the highly conserved, SHH-dependent up-regulation of PTCH expression could provide robustness to SHH expression level (*20*–*22*). To represent this feedback in the model, we introduced a GLI-dependent PTCH production term, with a single new parameter for feedback strength, defined as the amount of PTCH expression for a given level of signaling (Fig. 3A and fig. S7). In simulations, the PTCH feedback had three effects. First, it enhanced the robustness of gradient amplitude and length scale to variations in ligand production rate (Fig. 3B). Second, it accelerated the approach to steady state (Fig. 3C). Third, it preserved the relatively linear gradient shape as HH production rate increased, whereas the open-loop gradients became increasingly plateau-like (Fig. 3, D and E). Linear profiles have been suggested to maximize the extent of the "useful" region for patterning multiple cell fate domains (*23*).

To understand what features of PTCH produce these advantageous effects, we considered alternative

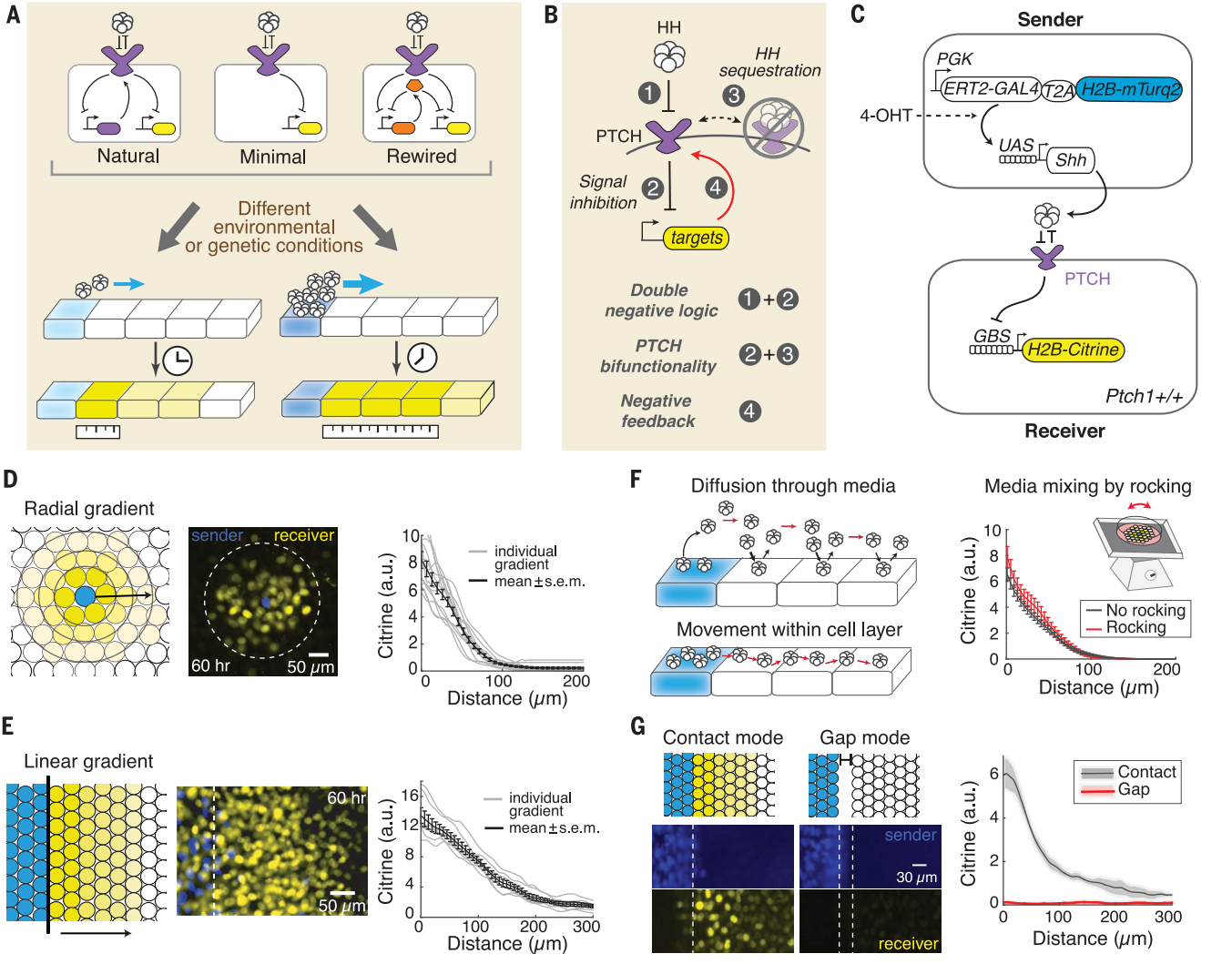

Fig. 1. In vitro reconstitution of morphogen signaling gradients. (**A**) Reconstitution enables quantitative analysis of the spatiotemporal patterning dynamics, including length scale (ruler) and speed (clock), generated by natural morphogen pathways, as well as by minimal and rewired variants. The sensitivity of circuit variants to perturbations, such as changes in ligand production, can also be determined. The various components of the schematic are clarified in the subsequent panels. (**B**) The distinctive combination of architectural features in the Hedgehog (HH) pathway. (**C**) Sender and receiver cell lines for reconstituting the SHH signaling gradient in wild-type NIH 3T3 cells. Senders constitutively expressing GAL4 fused to a mutant estrogen receptor (ERT2) and mTurquoise2 (mTurq2) fused to histone 2B (H2B) produce SHH upon induction with 4-hydroxytamoxifen (4-OHT). An 8×GLI-binding sequence (GBS) driving H2B-Citrine expression reports pathway activity in receivers. (**D** and **E**) Reconstituting SHH signaling gradients in radial and linear geometries. Blue and yellow cells (schematic) represent senders and receivers, respectively, and the varying opacity of the yellow shading corresponds to the level of intracellular pathway activity. Arrows indicate the direction of gradient propagation. In the radial gradients [n = 13 (D)], all activation was due to a single sender cell (blue, near the center of the dashed circle that indicates the gradient's outer edge). In the linear gradients [n = 7 (E)], the white dashed line indicates the boundary between sending and receiving fields. (**F** and **G**) Ligand transport requires continuous cell or extracellular matrix contact. In principle, ligand transport could involve bulk diffusion through the medium [upper schematic in (F)] or lateral movement within the cell layer [lower schematic in (F)]. Gradient formation is unaffected by rocking that should disturb bulk diffusion [n = 8 (F)] and is blocked by a 30-μm gap between senders and receivers [n = 5 (G)]. Error bars (F) and shading (G), SEM. a.u., arbitrary units.

feedback schemes mediated by hypothetical PTCH-like proteins possessing subsets of its features (Fig. 3A and fig. S7, A and B). Feedback through a protein denoted "I," possessing only PTCH's intracellular signal inhibition activity, provided amplitude robustness but exacerbated length-scale sensitivity (Fig. 3B and figs. S7, C and D, and S8). On the other hand, feedback through a protein denoted "E," possessing only PTCH's ligand-binding activity, provided length-scale but not amplitude robustness [consistent with studies of self-enhanced ligand degradation (*21*)]. Furthermore, simply coexpressing I and E together in a single "uncoupled" model was not sufficient to reproduce the benefits of the PTCH feedback (Fig. 3, B to E, and fig. S7, C and D). A model in which I and E were physically tethered, but where the intracellular activity persisted even when the extracellular domain was bound to ligand, also did not provide PTCH-like robustness (fig. S9D). Thus, the bifunctional nature of PTCH—specifically, its ability to switch between intracellular inhibition (ligand-free) and extracellular sequestration (ligand-bound) states—is essential for the robustness provided by this feedback mechanism. The coupling of multiple functions in the same protein has similarly been shown to promote robustness in other biological contexts (*24*).

The differences between PTCH and uncoupled feedbacks can be understood in terms of their divergent responses to high ligand concentrations (fig. S8). In both models, high ligand levels can deplete the extracellular feedback component (E or PTCH). With the PTCH feedback, this simultaneously reduces the intracellular activity, which in turn activates the pathway, replenishing PTCH and thereby continuing to limit ligand penetration. In contrast, in the uncoupled model, depletion of E does not directly reduce I; this results in a disproportionate accumulation of I, which blocks replenishment of E by suppressing signaling. In this way, the uncoupled model fails to keep up with increasing ligand expression levels. The benefit of the PTCH feedback compared with the uncoupled feedback persists even if the I and E feedback strengths are independently fine-tuned (fig. S9, A to C). These qualitative differences among feedback models are preserved in models that incorporate the activator form of GLI, positive feedback on GLI expression, or temporal adaptation through GLI down-regulation (figs. S6 and S10 to S12).

To experimentally test the prediction that the PTCH feedback improves the speed and robustness of gradient formation, we designed a synthetic feedback (SynFB) pathway in which SHH signaling up-regulates PTCH1 expression (Fig. 4A). We placed the Tet3G activator under SHH signaling control by using an additional copy of the GBS promoter (Fig. 1C and fig. S1A). The SynFB design mimics the natural PTCH1 feedback but allows continuous modulation of feedback strength through Dox concentration, from an

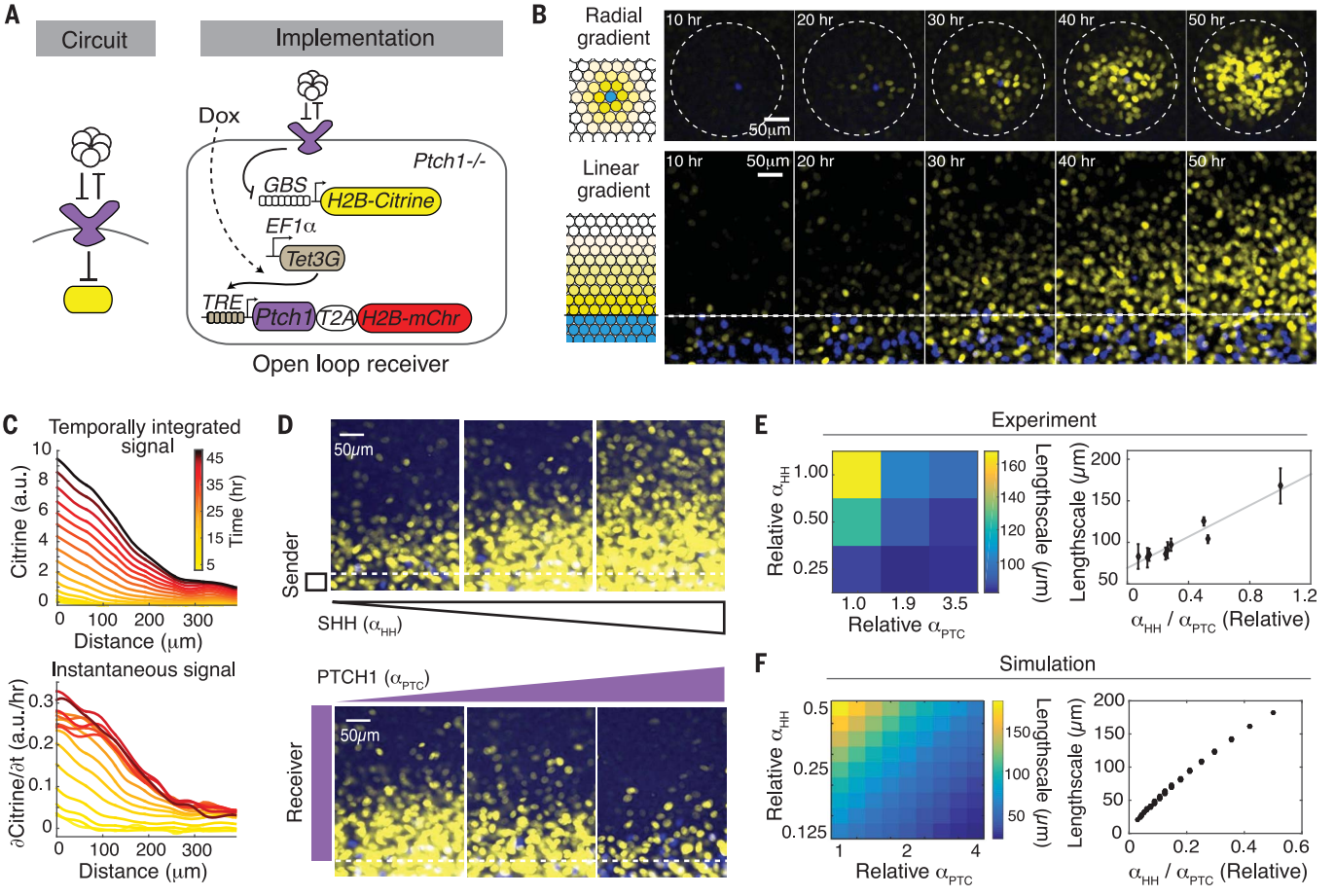

Fig. 2. Open-loop SHH pathway architecture produces gradients sensitive to variations in key parameters. (**A**) Engineering open-loop receiver cells. Both *Ptch1* alleles in wild-type receivers were deleted and replaced by ectopic *Ptch1* under Tet-3G control, enabling graded tuning of PTCH1 abundance with doxycycline (Dox), indicated by coexpression of mCherry (mChr). (**B**) Time-lapse images of representative radial and linear SHH signaling gradients. Dashed lines are as in Fig. 1. (**C**) Quantifying spatiotemporal dynamics of linear signaling gradients. Total fluorescence (upper plot) reflects the time-integrated pathway activity (mean of $n = 8$). The time derivative of Citrine (lower plot) approximates instantaneous pathway activity over space and time (fig. S1C). (**D**) Signaling gradient sensitivity to variations in SHH and PTCH1 production rates (α_{HH} and α_{PTC}, respectively). α_{HH} was increased by varying the sender density (upper panel), whereas α_{PTC} was increased in the receivers by varying the Dox concentration (lower panel). (**E**) The ratio of α_{HH} to α_{PTC} determines gradient length scale, defined by the distance at which the signal drops to $1/e$ of the amplitude. The α_{HH}/α_{PTC} ratio also controls gradient amplitude, defined by the signaling strength in the cells closest to the boundary (fig. S4D). Error bars, SEM. (**F**) A simple model recapitulates the ratiometric dependence of gradient properties on α_{HH} and α_{PTC} (fig. S5E). Relative α_{HH} is an arbitrary unit.

open-loop regime to a strong closed-loop regime exceeding the feedback strength of wild-type 3T3 cells (fig. S13, A to C). Movies of gradient formation in the SynFB cell line revealed that the PTCH feedback accelerated the approach to steady state, made both the amplitude and the length scale of the signaling gradient less sensitive to variations in ligand production rates, and improved the linearity of the gradient (Fig. 4, B to D; fig. S13, D to F; and movies S3 to S6). Furthermore, the magnitude of improvement increased with the strength of the feedback (fig. S13D). These results are consistent with model predictions.

As a further test of the model, we constructed a cell line incorporating a synthetic intracellular feedback (Fig. 4E). We substituted a PTCH mutant, PTCH1$^{\Delta Loop2}$, which is unable to bind ligand, for wild-type PTCH1 in SynFB (*25*) (Fig. 4E and fig. S14). As predicted by the model, these cells produced gradients whose amplitudes were more robust to ligand production rate and whose length scales and shapes were more sensitive (Fig. 4E and fig. S13F). Together, these results demonstrate that the PTCH feedback architecture has the remarkable capability of both reducing gradient sensitivity to variations in ligand production rates and accelerating the approach to steady state, providing a functional rationale for this highly conserved feature of the HH pathway (*6*–*8*).

Spatial patterning is an active process in which the dynamics of the morphogen and those of its signaling pathway are intertwined. Compared with analysis of embryos, reconstitution of morphogen gradient formation in vitro provides several advantages: It avoids interference from other processes and pathways (isolation), permits quantitative control of key parameters, allows rewiring of regulatory interactions, and facilitates straightforward analysis of patterning dynamics in space and time. In this case, reconstitution revealed how the distinctive combination of features in the HH pathway provides a compact, elegant design solution to the challenge of rapidly generating robust gradients (Fig. 4F and fig. S9C). Future work should help to extend the bottom-up approach developed here to more complex phenomena by incorporating downstream signal interpretation circuits (*26*) and integrating with additional, concurrent, morphogenetic patterning processes (*27*).

The HH architecture contrasts sharply with that of other morphogen pathways, such as BMP (bone morphogenetic protein) or FGF (fibroblast growth factor), in which ligands activate receptors,

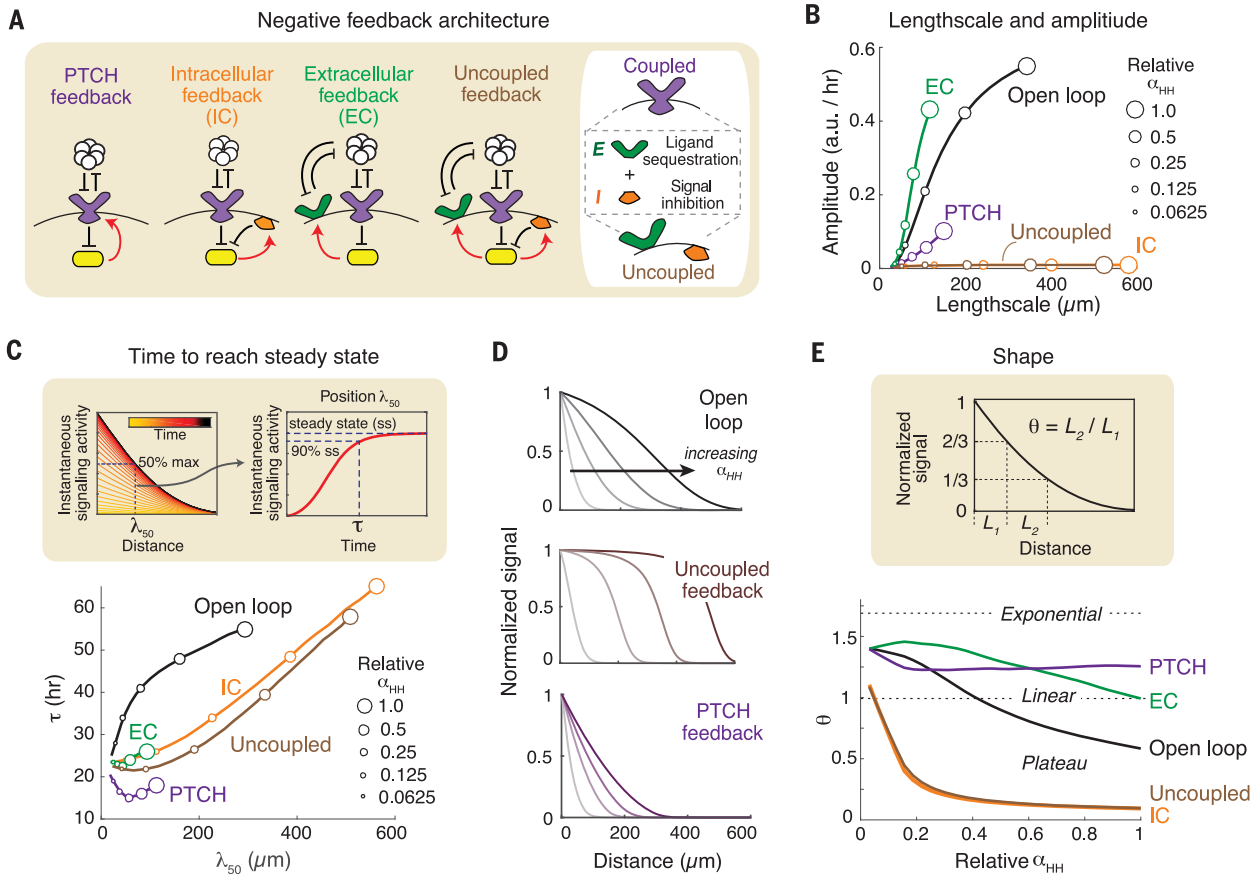

Fig. 3. Mathematical modeling shows that the PTCH feedback improves patterning performance by physically coupling intracellular and extracellular activities. (**A**) A negative feedback can act intracellularly by inhibiting signaling (IC feedback) or extracellularly by sequestering ligand (EC feedback). These functionalities can coexist, implemented either through separate molecules (uncoupled feedback) or through a bifunctional molecule such as PTCH (PTCH feedback). (**B**) Steady-state gradient length scale and amplitude as a function of α_{HH} (marker size) for different models. The feedback strengths for the IC and EC models were fine-tuned so that the amplitude or length scale, respectively, matches that of the PTCH feedback at relative α_{HH} = 0.0625. Those same feedback strengths were used for the uncoupled model, but the qualitative differences between those models hold across all nonzero feedback strengths (figs. S7, C and D, and S9, A and B). The same feedback strengths were used for (C) to (E). (**C**) Time to reach steady state (τ) for each model as a function of α_{HH} and λ_{50}, the position at which steady-state signal activity equals 50% of the amplitude. τ is the first time point at which signal activity reaches 90% of its steady-state value at λ_{50} (schematic). (**D**) Amplitude-normalized signaling gradient profiles for the open-loop, uncoupled, and PTCH feedback models at different relative values of α_{HH} (0.0625, 0.25, 0.50, and 1.0) show distinct trends in length scale and shape. (**E**) Only the PTCH feedback maintains a constant gradient shape with increasing α_{HH}. The shape factor θ equals the ratio of the width of the second third of the gradient (L_2) to the width of the first third of the gradient (L_1) (schematic).

which in turn activate intracellular effectors. These "double-positive" architectures should exhibit a different dependence on ligand and receptor levels (*17*). Compared with the HH pathway, receptor feedback appears to be less pervasive in these systems, provoking the question of whether they possess alternative mechanisms to achieve similar patterning capabilities, or whether they are optimized for distinct spatiotemporal behaviors (*28*). The approaches developed here should provide general insights into the performance trade-offs among different morphogen systems and establish a platform for designing synthetic circuits that genetically program cells to self-pattern into spatially organized tissues.

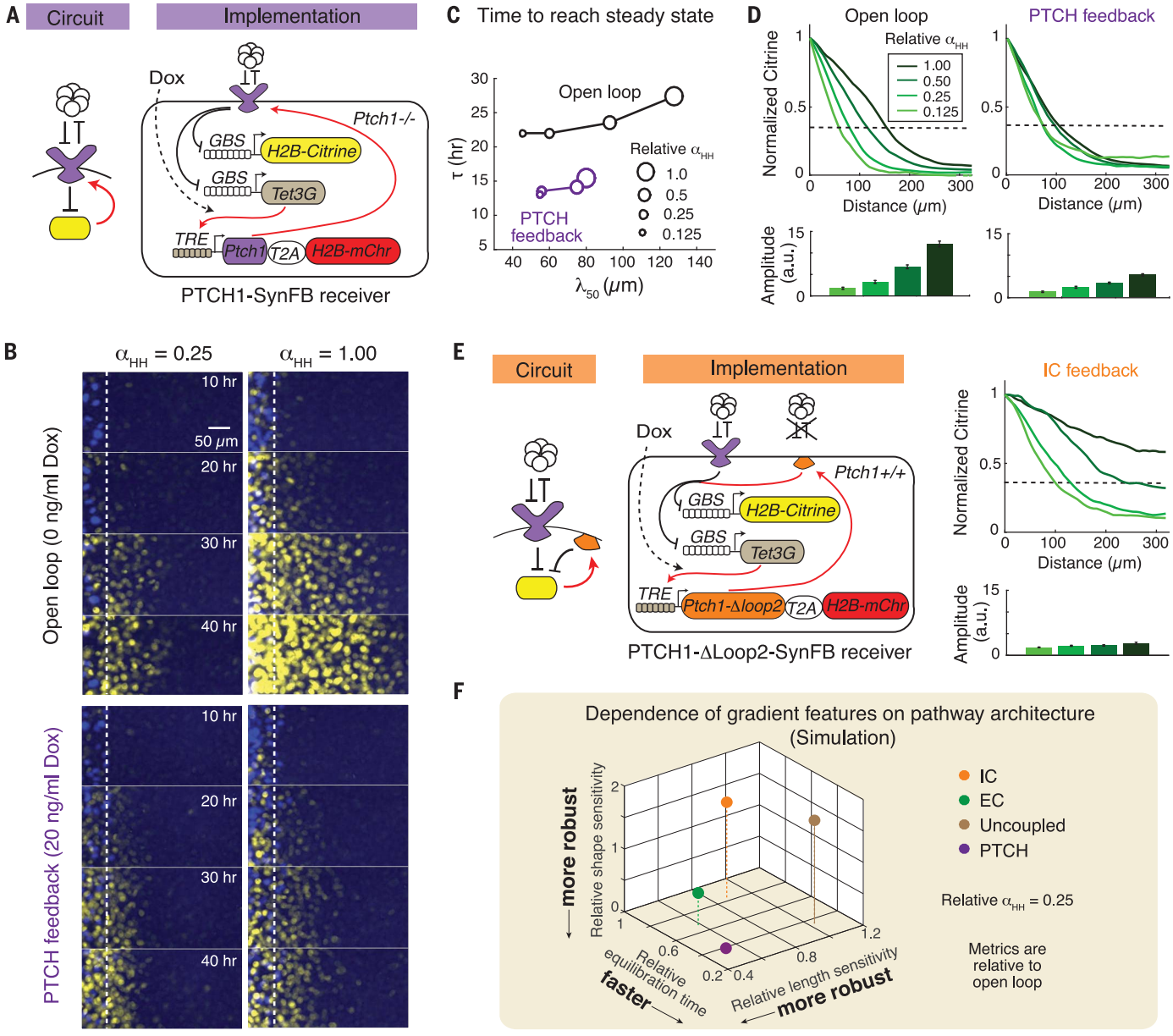

Fig. 4. The PTCH feedback simultaneously improves gradient speed and robustness. (**A**) A synthetic PTCH1 feedback loop (red), whose strength is tunable with Dox, was introduced in *Ptch1*$^{-/-}$ receiver cells to generate the PTCH1-SynFB cell line. At 0 ng/ml Dox, the basal activity of the *TRE* promoter produces sufficient PTCH1 to suppress pathway activity in the absence of SHH. (**B**) Temporal evolution of PTCH1-SynFB signaling gradients (yellow) with (20 ng/ml Dox) or without (0 ng/ml Dox) PTCH1 feedback. Sender cells (blue) remain throughout the experiment but are visually obscured by increasing Citrine expression. (**C**) PTCH1-SynFB accelerates the approach to steady state at λ_{50} (defined in Fig. 3C). (**D**) Profile of PTCH1-SynFB signaling gradients, with (right; 20 ng/ml Dox) or without (left; 0 ng/ml Dox) PTCH1 feedback, at 42.5 hours after 100 nM 4-OHT induction. Gradient profiles are normalized to their own amplitudes to show differences in length scale (distance at which the dashed line is crossed) and shape. Bar plots show amplitudes (mean ± SEM; n = 7 each). (**E**) A SynFB circuit was introduced in wild-type receiver cells to generate the PTCH1-ΔLoop2-SynFB cell line (left). PTCH1$^{\Delta Loop2}$ lacks the HH-binding domain but has the same capability as PTCH to suppress intracellular signaling (fig. S14). This IC feedback circuit enables robust gradient amplitude at the cost of greatly flattened shape and exacerbated length-scale sensitivity to α_{HH} (right). (**F**) Summary of the performance of different feedback architectures (simulation results). The distinctive, conserved architectural features of the HH pathway combine to enhance the speed and robustness of signaling gradient formation. Performance is measured relative to that of the open-loop model at relative α_{HH} = 0.25, which has a value of 1 in each dimension (fig. S9C shows plots at other α_{HH} values).

REFERENCES AND NOTES

1. K. W. Rogers, A. F. Schier, *Annu. Rev. Cell Dev. Biol.* **27**, 377–407 (2011).
2. N. Perrimon, A. P. McMahon, *Cell* **97**, 13–16 (1999).
3. M. Freeman, *Nature* **408**, 313–319 (2000).
4. J. Briscoe, P. P. Thérond, *Nat. Rev. Mol. Cell Biol.* **14**, 416–429 (2013).
5. Y. Chen, G. Struhl, *Cell* **87**, 553–563 (1996).
6. L. Milenkovic, L. V. Goodrich, K. M. Higgins, M. P. Scott, *Development* **126**, 4431–4440 (1999).
7. J. Jeong, A. P. McMahon, *Development* **132**, 143–154 (2005).
8. L. V. Goodrich, R. L. Johnson, L. Milenkovic, J. A. McMahon, M. P. Scott, *Genes Dev.* **10**, 301–312 (1996).
9. J. Taipale *et al*., *Nature* **406**, 1005–1009 (2000).
10. N. Balaskas *et al*., *Cell* **148**, 273–284 (2012).
11. D. Sprinzak *et al*., *Nature* **465**, 86–90 (2010).
12. A. D. Lander, Q. Nie, F. Y. M. Wan, *Dev. Cell* **2**, 785–796 (2002).
13. M. Bischoff *et al*., *Nat. Cell Biol.* **15**, 1269–1281 (2013).
14. X. Zeng *et al*., *Nature* **411**, 716–720 (2001).
15. T. A. Sanders, E. Llagostera, M. Barna, *Nature* **497**, 628–632 (2013).
16. P.-T. Chuang, T. B. Kornberg, *Curr. Opin. Genet. Dev.* **10**, 515–522 (2000).
17. Materials and methods and supplementary text are available as supplementary materials.
18. M. Cohen *et al*., *Nat. Commun.* **6**, 6709 (2015).
19. C. Chiang *et al*., *Nature* **383**, 407–413 (1996).
20. N. Rosenfeld, M. B. Elowitz, U. Alon, *J. Mol. Biol.* **323**, 785–793 (2002).
21. A. Eldar, D. Rosin, B.-Z. Shilo, N. Barkai, *Dev. Cell* **5**, 635–646 (2003).
22. B.-Z. Shilo, N. Barkai, *Dev. Cell* **40**, 429–438 (2017).
23. G. Tkačik, J. O. Dubuis, M. D. Petkova, T. Gregor, *Genetics* **199**, 39–59 (2015).
24. Y. Hart, U. Alon, *Mol. Cell* **49**, 213–221 (2013).
25. J. Briscoe, Y. Chen, T. M. Jessell, G. Struhl, *Mol. Cell* **7**, 1279–1291 (2001).
26. J. Briscoe, S. Small, *Development* **142**, 3996–4009 (2015).
27. N. Perrimon, C. Pitsouli, B.-Z. Shilo, *Cold Spring Harb. Perspect. Biol.* **4**, a005975 (2012).
28. Y. E. Antebi, N. Nandagopal, M. B. Elowitz, *Curr. Opin. Syst. Biol.* **1**, 16–24 (2017).

ACKNOWLEDGMENTS

We thank J. Briscoe and A. McMahon for DNA constructs and helpful discussion, Y. Antebi for data analysis programs and discussion of modeling, J. Bois for advice on model simulation, Z. Singer for cloning ERT2-GAL4, F. Tan for suggesting the rocker experiment, and the Elowitz laboratory for discussion. We also thank U. Alon, N. Barkai, P. Beachy, A. Eldar, J. Garcia-Ojalvo, L. Goentoro, E. Hui, P. Jordan, B. Shilo, B. Shraiman, and D. Sprinzak for discussion and feedback. **Funding:** The work was funded by the Howard Hughes Medical Institute (M.B.E.), American Cancer Society Postdoc Fellowship 127270-PF-15-032-01-DDC (P.L.), NICHD (Eunice Kennedy Shriver National Institute of Child Health and Human Development) Pathway to Independence Career Award K99HD087532 (P.L.), NIH Ruth Kirschstein National Research Service Award F32 AR067103 (J.S.M.), Institute for Collaborative Biotechnologies contract W911NF-09-D-0001 through the U.S. Army Research Office, and BBSRC (UK Biotechnology and Biological Sciences Research Council)–NSF award 1546197. The RNA-sequencing work was supported by the Millard and Muriel Jacobs Genetics and Genomics Laboratory at the California Institute of Technology. **Author contributions:** P.L. and M.B.E. conceived the project and designed the experiments. P.L., S.W., and V.V. performed the experiments. P.L., J.S.M., and S.W. analyzed the experimental data. J.S.M., P.L., and S.C. developed the mathematical models. P.L., J.S.M., and M.B.E. wrote the paper. **Competing interests:** The authors declare no competing interests. **Data and materials availability:** Original data, Matlab code, DNA constructs, and cell lines are available upon request.

SUPPLEMENTARY MATERIALS

www.sciencemag.org/content/360/6388/543/suppl/DC1
Materials and Methods
Supplementary Text
Figs. S1 to S14
Tables S1 to S4
References (*29*–*52*)
Movies S1 to S6

14 June 2017; accepted 22 March 2018
Published online 5 April 2018
10.1126/science.aao0645

PALEOGENOMICS

Pleistocene North African genomes link Near Eastern and sub-Saharan African human populations

Marieke van de Loosdrecht,[1] Abdeljalil Bouzouggar,[2,3]*† Louise Humphrey,[4] Cosimo Posth,[1] Nick Barton,[5] Ayinuer Aximu-Petri,[6] Birgit Nickel,[6] Sarah Nagel,[6] El Hassan Talbi,[7] Mohammed Abdeljalil El Hajraoui,[2] Saaïd Amzazi,[8] Jean-Jacques Hublin,[3] Svante Pääbo,[6] Stephan Schiffels,[1] Matthias Meyer,[6] Wolfgang Haak,[1]† Choongwon Jeong,[1]*† Johannes Krause[1]*†

North Africa is a key region for understanding human history, but the genetic history of its people is largely unknown. We present genomic data from seven 15,000-year-old modern humans, attributed to the Iberomaurusian culture, from Morocco. We find a genetic affinity with early Holocene Near Easterners, best represented by Levantine Natufians, suggesting a pre-agricultural connection between Africa and the Near East. We do not find evidence for gene flow from Paleolithic Europeans to Late Pleistocene North Africans. The Taforalt individuals derive one-third of their ancestry from sub-Saharan Africans, best approximated by a mixture of genetic components preserved in present-day West and East Africans. Thus, we provide direct evidence for genetic interactions between modern humans across Africa and Eurasia in the Pleistocene.

Under typical conditions (i.e., aside from intermittent greening periods), the Sahara desert poses an ecogeographic barrier for human migration between North and sub-Saharan Africa (*1*). Sub-Saharan Africa is home to the most deeply divergent genetic lineages among present-day humans (*2*), and the general view is that all Eurasians mostly descend from a single group of humans that dispersed outside of sub-Saharan Africa around 50,000 to 100,000 years before the present (yr B.P.) (*3*). This group likely represented only a small fraction of the genetic diversity within Africa, most closely related to a Holocene East African group (*4*). Present-day North Africans share a majority of their ancestry with present-day Near Easterners but not with sub-Saharan Africans (*5*). Thus, from a genetic perspective, present-day North Africa is largely a part of Eurasia. However, the temporal depth of this genetic connection between the Near East and North Africa is poorly understood and has been estimated only indirectly from present-day mitochondrial DNA (mtDNA) variation (*6*, *7*).

Owing to challenging conditions for DNA preservation, relatively few ancient genomes have been recovered from Africa. Genome-wide data from 23 individuals have been reported from South and East Africa, with the oldest dating back to 8100 yr B.P. (*4*, *8*, *9*). In North Africa, a genomic study of Egyptian mummies from the first millennium BCE showed that the genetic connection between the Near East and North Africa was established by that time (*5*). However, the genetic affinity of North African populations at a greater time depth has remained unknown.

Here we present genome-wide data from seven individuals, directly dated between 15,100 and 13,900 calibrated years before present (cal. yr B.P.) (table S1), from Grotte des Pigeons near Taforalt in eastern Morocco (*10*). These genomic data provide a critical reference point to help explain the deep genetic history of North Africa and the broader Middle East (Fig. 1). The Taforalt individuals are associated with the Later Stone Age Iberomaurusian culture, whose origin is debated. These individuals may have descended either directly from the manufacturers of the preceding Middle Stone Age technologies (Aterian or local West African bladelet technologies) or from an exogenous population with ties to the Upper Paleolithic technocomplexes of the Near East or Southern Europe (*10*, *11*).

For nine Taforalt individuals (table S2), we created double-indexed single-stranded DNA libraries (*12*) for next-generation sequencing of DNA isolated from petrous bones. We then used in-solution capture probes (*13*) to enrich libraries for the whole mitochondrial genome and ~1,240,000 single-nucleotide polymorphisms (SNPs) in the nuclear genome (*14*). The DNA fragments obtained from seven individuals, six genetic males and one female, had postmortem degradation characteristics typical of ancient DNA (tables S3 to S5 and fig. S6). We reconstructed the mitochondrial genomes of all seven individuals (102× to 1701× coverage, unmerged libraries; table S4) while maintaining a low level of contamination from the DNA of modern humans (1 to 8%; table S4). For the nuclear data analysis, in which ancient DNA is more susceptible to contamination than in mitochondrial analyses, we analyzed five individuals (four males and one female) on the basis of coverage (table S3, merged libraries) and negligible modern human contamination for males (1.7 to 2.5%; table S5). For each individual, we randomly chose a single base per site as a haploid genotype. We intersected our new data with data from a panel of worldwide present-day populations, genotyped on the Affymetrix Human Origins array for ~600,000 markers, as well as ancient genomic data covering Europe, the Near East, and sub-Saharan Africa (*4*, *8*, *15*–*17*). The final data set includes 593,124 intersecting autosomal SNPs with 183,041 to 544,232 SNP positions covered for each of the five individuals (table S3). For group-based analyses involving other ancient individuals, we adopted the population labels from the original studies (*4*, *16*). We found an overall high genetic relatedness between the Taforalt individuals, suggesting a strong population bottleneck (fig. S26).

We analyzed the genetic affinities of the Taforalt individuals by performing principal components analysis and model-based clustering of worldwide data (Fig. 2). When projected onto the top principal components of African and west Eurasian populations, the Taforalt individuals form a distinct cluster in an intermediate position between present-day North Africans [e.g., Amazighes (Berbers), Mozabites, and Saharawis] and East Africans (e.g., Afars, Oromos, and Somalis) (Fig. 2A). Consistently, we find that all males with sufficient nuclear DNA preservation carry Y haplogroup E1b1b1a1 (M-78; table S16). This haplogroup occurs most frequently in present-day North and East African populations (*18*). The closely related E1b1b1b (M-123) haplogroup has been reported for Epipaleolithic Natufians and Pre-Pottery Neolithic Levantines (Levant_N) (*16*). Unsupervised genetic clustering also suggests a connection of Taforalt to the Near East. The three major components that make up the Taforalt genomes are maximized in early Holocene Levantines, East African hunter-gatherer Hadza from north-central Tanzania, and West Africans (number of genetic clusters K = 10; Fig. 2B). In contrast, present-day North Africans have smaller sub-Saharan African components with minimal Hadza-related contribution (Fig. 2B).

We calculated outgroup f_3 statistics of the form f_3(Taforalt, X; Mbuti) across worldwide ancient and present-day test populations. Consistent with previous analyses, we find that ancient Near Eastern populations, especially Epipaleolithic Natufians and early Neolithic Levantines, show the highest

[1]Department of Archaeogenetics, Max Planck Institute for the Science of Human History (MPI-SHH), Jena, Kahlaische Strasse 10, D-07745, Germany. [2]Origin and Evolution of *Homo sapiens* in Morocco Research Group, Institut National des Sciences de l'Archéologie et du Patrimoine, Hay Riad, Madinat Al Irfane, Angle rues 5 et 7, Rabat-Instituts, 10 000 Rabat, Morocco. [3]Department of Human Evolution, Max Planck Institute for Evolutionary Anthropology (MPI-EVA), Leipzig, Deutscher Platz 6, D-04103, Germany. [4]Department of Earth Sciences, The Natural History Museum, London SW7 5BD, UK. [5]Institute of Archaeology, University of Oxford, 36 Beaumont Street, Oxford OX1 2PG, UK. [6]Department of Evolutionary Genetics, Max Planck Institute for Evolutionary Anthropology (MPI-EVA), Leipzig, Deutscher Platz 6, D-04103, Germany. [7]Faculté des Sciences, Campus d'Al Qods, Université Mohammed Premier, B.P. 717 Oujda, Morocco. [8]Mohammed V University, Avenue Ibn Batouta, Rabat, Morocco.
***Corresponding author. Email: krause@shh.mpg.de (J.K.); jeong@shh.mpg.de (C.J.); bouzouggar@eva.mpg.de (A.B.)**
†These authors contributed equally to this work.

outgroup f_3 values with Taforalt (Fig. 3A). This is confirmed by f_4 symmetry statistics of the form f_4(Chimpanzee, Taforalt; NE_1, NE_2) that measure a relative affinity of a pair of Near Eastern (NE) groups to Taforalt. A positive value indicates that NE_2 is closer than NE_1 to Taforalt. We consistently find positive f_4 values when the NE_2 group is Natufian or Levant_N and the NE_1 group is representative of other populations [z score = 2.2 to 11.0 standard error (SE); table S6]. Congruent to the outgtoup-f_3 results, the Natufian population shows higher affinity to Taforalt than does the Levant_N group (z score = 2.2 SE; table S6). This indicates that the early Holocene Levantine populations, overlapping with or postdating our Taforalt individuals by up to 6000 years (*16*), are most closely related to the Taforalt group, among Near Eastern populations. Next, we evaluated whether the Taforalt individuals have sub-Saharan African ancestry by calculating f_4(Chimpanzee, X; Natufian, Taforalt). We observe significant positive f_4 values for all sub-Saharan African groups and significant negative values for all Eurasian populations, supporting a substantial contribution from sub-Saharan Africa (Fig. 3B). West Africans, such as Mende and Yoruba, most strongly pull out the sub-Saharan African ancestry in Taforalt (Fig. 3B and figs. S15 and S16).

We investigated whether two first-hand proxies, Natufians and West Africans, are sufficient to explain the Taforalt gene pool or whether a more complex admixture model is required. We thus tested whether Natufians could be a sufficient proxy for the Eurasian ancestry in Taforalt without explicit modeling of its African ancestry (fig. S18). This line of investigation was inspired by proposed archaeological connections between the Iberomaurusian and Upper Paleolithic cultures in Southern Europe, either via the Strait of Gibraltar (*19*) or Sicily (*20*). If this connection is true, both the Upper Paleolithic European and Natufian ancestries will be required to explain the Taforalt gene pool. For our admixture modeling with the program qpAdm (*16*), we chose outgroups that can distinguish sub-Saharan African, Natufian, and Paleolithic European ancestries but are blind to differences between sub-Saharan African lineages (*11*). A two-way admixture model, comprising Natufian and sub-Saharan African populations, does not significantly deviate from our data (χ^2 $P \geq 0.128$), with 63.5% Natufian and 36.5% sub-Saharan African ancestry, on average (table S8). Adding Paleolithic European lineages as a third source only marginally increased the model fit (χ^2 $P = 0.019$ to 0.128; table S9). Consistently, by using the qpGraph package (*21*), we find that a mixture of Natufian and Yoruba reasonably fits the Taforalt gene pool ($|z| \leq 3.7$; fig. S19 and table S10). Adding gene flow from Paleolithic Europeans does not improve the model fit and provides an ancestry contribution estimate of 0% (fig. S19). We thus find no evidence of gene flow from

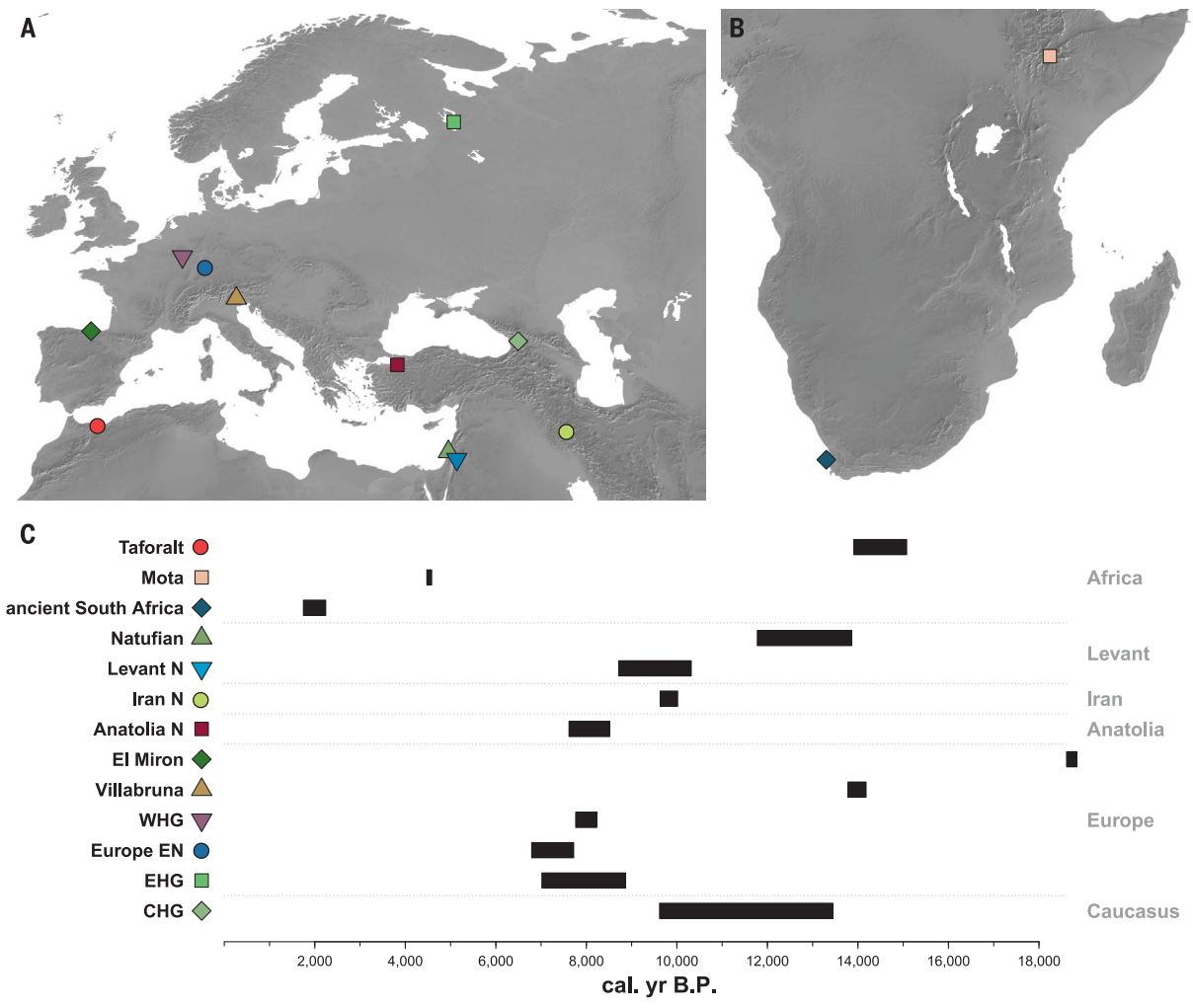

Fig. 1. Spatiotemporal locations of the Taforalt and other ancient genomes. (**A** and **B**) Geographic locations of representative ancient genomes from West Eurasia and Africa included in our analysis. The Pleistocene Taforalt site is denoted by a red circle. (**C**) The date range of each ancient group is marked by black bars, representing the range of 95% confidence intervals of radiocarbon dates across all dated individuals (cal. yr B.P. on the *x* axis). Group labels are taken from previous studies reporting each ancient genome (*4*, *16*, *27*). N, Neolithic; WHG, Western European hunter-gatherers; EHG, Eastern European hunter-gatherers; CHG, Caucasus hunter-gatherers.

Paleolithic Europeans into Taforalt within the resolution of our data.

We further characterized the sub-Saharan African–related ancestry in the Taforalt individuals by using f_4 statistics in the form f_4(Chimpanzee, African; Yoruba/Mende, Natufian). We find that Yoruba or Mende and Natufians are symmetrically related to two deeply divergent outgroups, an ancient South African group from 2000 yr B.P. (aSouthAfrica) and Mbuti Pygmy, respectively ($|z| \leq 1.564$ SE; table S11). Because f_4 statistics are linear under admixture, we expect the Taforalt population not to be any closer to these outgroups than Yoruba or Natufians if the two-way admixture model is correct. However, we find

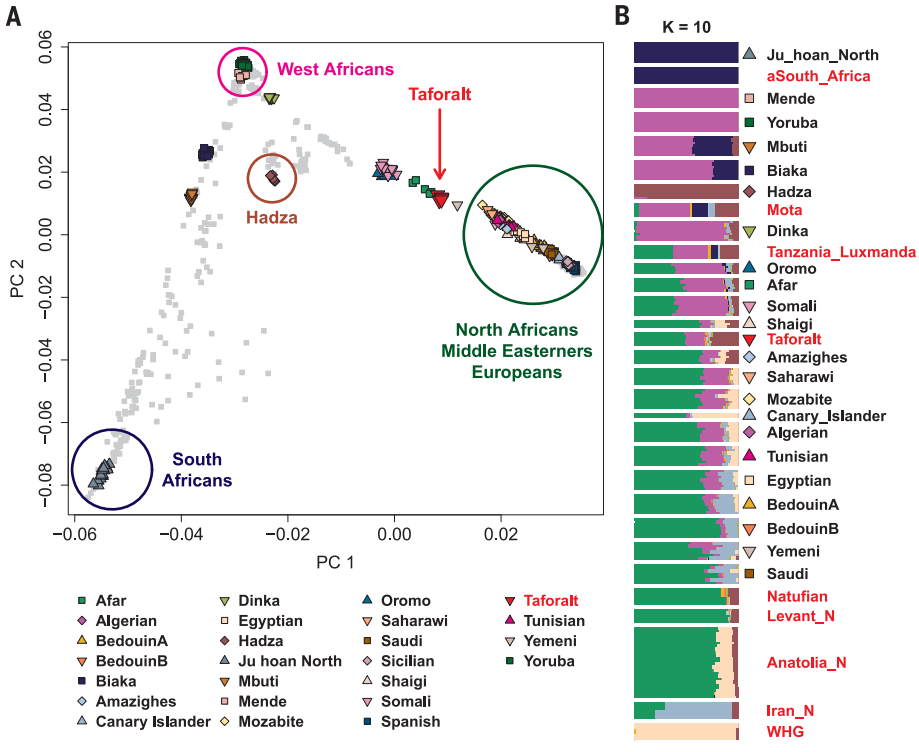

Fig. 2. Summary of the genetic profile of the Taforalt individuals. (**A**) The top two principal components (PCs) calculated from present-day African, Near Eastern, and Southern European individuals from 72 populations. The Taforalt individuals are projected thereon (red inverted triangles), and selected present-day populations are denoted by various colored symbols. Labels for other populations (denoted by small gray squares) are provided in fig. S8. (**B**) ADMIXTURE analysis results of chosen African and Middle Eastern populations (K = 10). Ancient individuals are labeled in red. Major ancestry components in Taforalt individuals are maximized in early Holocene Levantines (green), West Africans (purple), and East African Hadza (brown). The ancestry component prevalent in pre-Neolithic Europeans (beige) is absent in Taforalt.

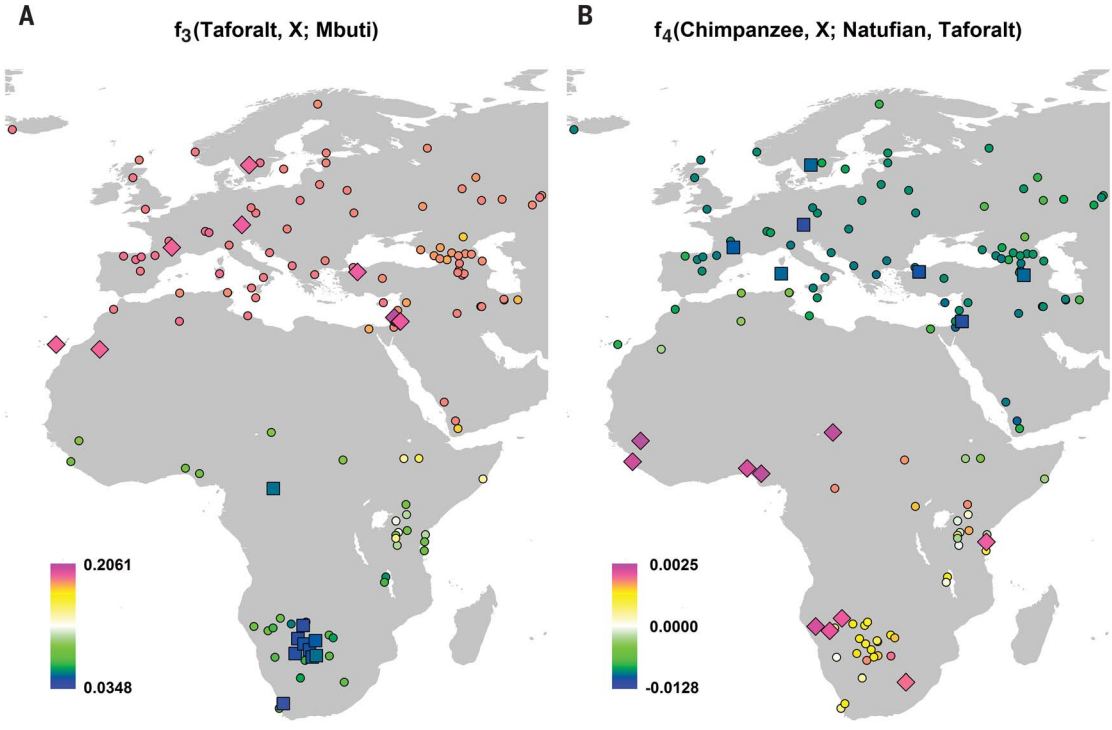

Fig. 3. Geographic distribution of the genetic affinity of the Taforalt group with worldwide populations. (**A**) Mean shared genetic drift with the Taforalt group, as measured by outgroup f_3 statistics in the form f_3 (Taforalt, X; Mbuti). Warm colors denote populations genetically close to Taforalt. Large diamonds and squares represent the 10 highest and lowest f_3 values, respectively. Early Holocene Levantine groups (Natufians and Neolithic Levantines) show the highest affinity with Taforalt. The statistics and their associated SEs for the top 30 signals are presented in fig. S14. (**B**) Extra genetic affinity with the Taforalt group in comparison to Natufians, as measured by f_4 statistics in the form f_4(Chimpanzee, X; Natufian, Taforalt). Large diamonds and squares represent the 10 most positive and negative f_4 values, respectively. Sub-Saharan Africans show high positive values, with West African Yoruba and Mende having the highest values, supporting the presence of sub-Saharan African ancestry in Taforalt individuals. In contrast, all Eurasian populations are genetically closer to Natufians than to the Taforalt group. The statistics and their associated SEs for the top 30 signals are presented in fig. S16.

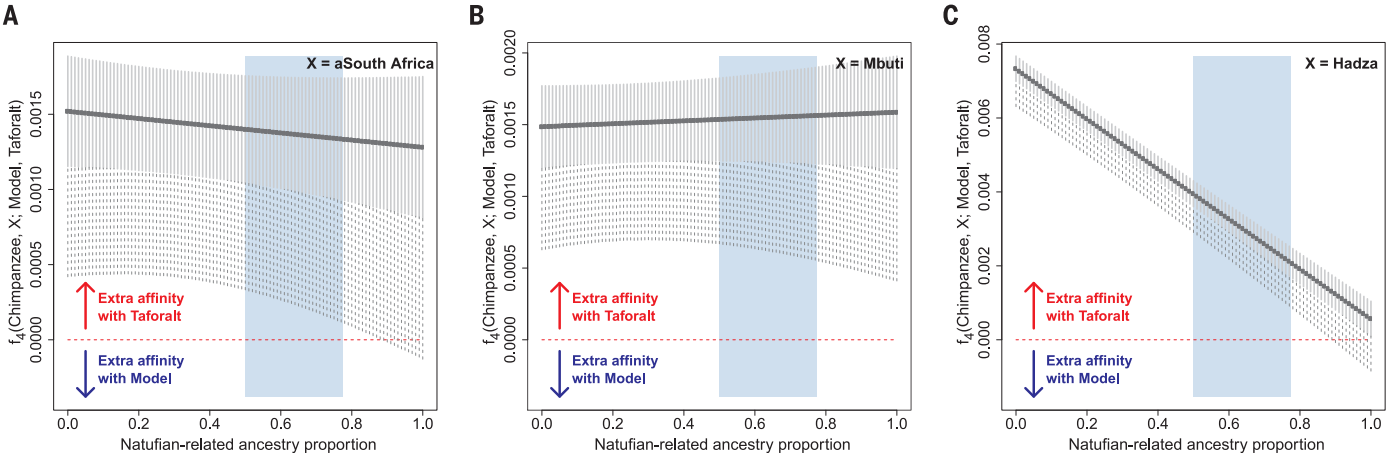

Fig. 4. Relative genetic affinity of representative sub-Saharan African groups to a mixture of Yoruba and Natufians in comparison to the Taforalt group. We measured f_4 statistics in the form f_4(Chimpanzee, African; Yoruba+Natufian, Taforalt) by using (**A**) aSouthAfrica, (**B**) Mbuti, and (**C**) Hadza as the African group. The f_4 statistics were calculated for the proportions of Natufian-related ancestry ranging from 0 to 100% in increments of 1%. The blue rectangle marks a plausible range of Natufian ancestry proportion, estimated by our qpAdm modeling [0.637 ± (2 × 0.069)]. Gray solid and dotted lines represent ±1 and −3 SE ranges, respectively. SEs were calculated by 5-centimorgan block jackknife method.

instead that the Taforalt group is significantly closer to both outgroups (aSouthAfrica and Mbuti) than any combination of Yoruba and Natufians ($z \geq 2.728$ SE; Fig. 4). A similar pattern is observed for the East African outgroups Dinka, Mota, and Hadza (table S11 and fig. S20). These results can only be explained by Taforalt harboring an ancestry that contains additional affinity with South, East, and Central African outgroups. None of the present-day or ancient Holocene African groups serve as a good proxy for this unknown ancestry, because adding them as the third source is still insufficient to match the model to the Taforalt gene pool (table S12 and fig. S21). However, we can exclude any branch in human genetic diversity more basal than the deepest known one represented by aSouthAfrica (*4*) as the source of this signal: it would result in a negative affinity to aSouthAfrica, not a positive one as we find (Fig. 4). Both an unknown archaic hominin and the recently proposed deep West African lineage (*4*) belong to this category and therefore cannot explain the Taforalt gene pool.

Mitochondrial consensus sequences of the Taforalt individuals belong to the U6a (six individuals) and M1b (one individual) haplogroups (*15*), which are mostly confined to present-day populations in North and East Africa (*7*). U6 and M1 have been proposed as markers for autochthonous Maghreb ancestry, which might have been originally introduced into this region by a back-to-Africa migration from West Asia (*6*, *7*). The occurrence of both haplogroups in the Taforalt individuals proves their pre-Holocene presence in the Maghreb. We used the BEAST v1.8.1 package (*24*) to analyze the seven ancient Taforalt individuals in combination with four Upper Paleolithic European mtDNA genomes (*22*, *23*) and present-day individuals belonging to U6 and M1 (*7*). By using a human mtDNA mutation rate inferred from tip calibration of ancient mtDNA genomes (*23*), we obtained divergence estimates for U6 at 37,000 yr B.P. (40,000 to 34,000 yr B.P. for 95% highest posterior density, HPD) and M1 at 24,000 yr B.P. (95% HPD: 29,000 to 20,000 yr B.P.) (table S15). Our estimated dates are considerably more recent than those of a study using present-day data only (45,000 ± 7000 yr B.P. for U6 and 37,000 ± 7000 yr B.P. for M1) (*7*) but are similar to those of Pennarun *et al.* (*25*). Moreover, we observed an asynchronous increase in the effective population size for U6 and M1 (fig. S24), which suggests that the demographic histories of these North and East African haplogroups do not coincide and might have been influenced by multiple expansions in the Late Pleistocene (*25*). Notably, the diversification of haplogroups U6a and M1 found for Taforalt is dated to ~24,000 yr B.P. (fig. S23), which is close in time to the earliest known appearance of the Iberomaurusian culture in Northwest Africa [25,845 to 25,270 cal. yr B.P. at Tamar Hat (*26*)].

The relationships of the Iberomaurusian culture with those of the preceding Middle Stone Age, including the local backed bladelet technologies in Northeast Africa, and the Epigravettian in Southern Europe have been questioned (*13*). The genetic profile of Taforalt suggests substantial Natufian-related and sub-Saharan African–related ancestries (63.5 and 36.5%, respectively) but not additional ancestry from Epigravettian or other Upper Paleolithic European populations. Therefore, we provide genomic evidence for a Late Pleistocene connection between North Africa and the Near East, predating the Neolithic transition by at least four millennia, while rejecting the hypothesis of a potential Epigravettian gene flow from Southern Europe into northern Africa, within the resolution of our data. Archaeogenetic studies on additional Iberomaurusian sites will be critical to evaluate the representativeness of Taforalt for the Iberomaurusian gene pool. We speculate that the Natufian-related ancestral population may have been widespread across North Africa and the Near East, associated with microlithic backed bladelet technologies that started to spread out in this area by at least 25,000 yr B.P. [(*10*) and references therein]. However, given the absence of ancient genomic data from a similar time frame for this broader area, the epicenter of expansion, if any, for this ancestral population remains unknown.

Although the oldest Iberomaurusian microlithic bladelet technologies are found earlier in the Maghreb than their equivalents in northeastern Africa (Cyrenaica) and the earliest Natufian in the Levant, the complex sub-Saharan ancestry in Taforalt makes our individuals an unlikely proxy for the ancestral population of later Natufians who do not harbor sub-Saharan ancestry. An epicenter in the Maghreb is plausible only if the sub-Saharan African admixture into Taforalt either postdated the expansion into the Levant or was a locally confined phenomenon. Alternatively, placing the epicenter in Cyrenaica or the Levant requires an additional explanation for the observed archaeological chronology.

REFERENCES AND NOTES

1. I. S. Castañeda *et al.*, *Proc. Natl. Acad. Sci. U.S.A.* **106**, 20159–20163 (2009).
2. B. M. Henn *et al.*, *Proc. Natl. Acad. Sci. U.S.A.* **108**, 5154–5162 (2011).
3. S. Mallick *et al.*, *Nature* **538**, 201–206 (2016).
4. P. Skoglund *et al.*, *Cell* **171**, 59–71.e21 (2017).
5. V. J. Schuenemann *et al.*, *Nat. Commun.* **8**, 15694–15704 (2017).
6. A. M. González *et al.*, *BMC Genomics* **8**, 223–234 (2007).
7. A. Olivieri *et al.*, *Science* **314**, 1767–1770 (2006).
8. M. Gallego Llorente *et al.*, *Science* **350**, 820–822 (2015).
9. C. M. Schlebusch *et al.*, *Science* **358**, 652–655 (2017).
10. R. N. Barton *et al.*, *J. Hum. Evol.* **65**, 266–281 (2013).
11. See supplementary materials.
12. M.-T. Gansauge *et al.*, *Nucleic Acids Res.* **45**, e79 (2017).
13. Q. Fu *et al.*, *Proc. Natl. Acad. Sci. U.S.A.* **110**, 2223–2227 (2013).
14. Q. Fu *et al.*, *Nature* **524**, 216–219 (2015).
15. E. R. Jones *et al.*, *Nat. Commun.* **6**, 8912–8919 (2015).
16. I. Lazaridis *et al.*, *Nature* **536**, 419–424 (2016).
17. M. Raghavan *et al.*, *Nature* **505**, 87–91 (2014).
18. F. Cruciani *et al.*, *Mol. Biol. Evol.* **24**, 1300–1311 (2007).
19. P. Pallary, in *Mémoires de la Société Historique Algérienne* (Jourdan, 1909), vol. 3.

20. G. Camps, *Les Civilisations Préhistoriques de l'Afrique du Nord et du Sahara* (Doin, 1974).
21. N. Patterson *et al.*, *Genetics* **192**, 1065–1093 (2012).
22. M. Hervella *et al.*, *Sci. Rep.* **6**, 25501–25505 (2016).
23. C. Posth *et al.*, *Curr. Biol.* **26**, 827–833 (2016).
24. A. J. Drummond, A. Rambaut, *BMC Evol. Biol.* **7**, 214 (2007).
25. E. Pennarun *et al.*, *BMC Evol. Biol.* **12**, 234–245 (2012).
26. J. T. Hogue, R. Barton, *Quat. Int.* **413**, 62–75 (2016).
27. Q. Fu *et al.*, *Nature* **534**, 200–205 (2016).

ACKNOWLEDGMENTS

We thank H. Temming and A. Le Cabec (MPI-EVA) for CT scanning and G. Brandt, A. Wissgott, F. Aron, M. Burri, C. Freund, and R. Stahl (MPI-SHH) for DNA sequencing. **Funding:** This work was supported by the Max Planck Society, Institut National des Sciences de l'Archéologie et du Patrimoine (Protars grant P32/09-CNRST), the Natural Environment Research Council (grants EFCHED NER/T/S/2002/00700 and RESET NE/E015670/1), the Leverhulme Trust (grant F/08 735/F), the British Academy, Oxford University (Fell Fund, Boise and Meyerstein), the Natural History Museum (Human Origins Research Fund), and the Calleva Foundation. **Author contributions:** J.K., A.B., J.J.-H., and L.H. conceived of the study. A.B., L.H., N.B., and J.-J.H. provided archaeological material and input for the archaeological interpretation. M.v.d.L., B.N., and S.N. performed laboratory work with the help of A.A.-P. and M.M. M.v.d.L., C.J., C.P., and W.H. analyzed data. M.v.d.L., C.J., J.K., C.P., A.B., L.H., N.B., and M.M. wrote the manuscript with input from all coauthors. **Competing interests:** A.B. keeps an additional affiliation with the MPI-EVA; this institute supported his excavation efforts and worked with him on the site. This is also reflected in the coauthorship of J.J.-H., director of MPI-EVA. The authors declare no competing interests. **Data and materials availability:** Genomic data (BAM format) are available through the Sequence Read Archive (accession number SRP132033) and consensus mitogenome sequences (FASTA format) in GenBank (accession numbers MG936619 to MG936625).

SUPPLEMENTARY MATERIALS

www.sciencemag.org/content/360/6388/548/suppl/DC1
Supplementary Text
Figs. S1 to S26
Tables S1 to S16
References (*28–114*)

21 December 2017; accepted 28 February 2018
Published online 15 March 2018
10.1126/science.aar8380

STRUCTURAL BIOLOGY

Structure of the DASH/Dam1 complex shows its role at the yeast kinetochore-microtubule interface

Simon Jenni[1] and Stephen C. Harrison[1,2]*

Kinetochores connect mitotic-spindle microtubules with chromosomes, allowing microtubule depolymerization to pull chromosomes apart during anaphase while resisting detachment as the microtubule shortens. The heterodecameric DASH/Dam1 complex (DASH/Dam1c), an essential component of yeast kinetochores, assembles into a microtubule-encircling ring. The ring associates with rodlike Ndc80 complexes to organize the kinetochore-microtubule interface. We report the cryo–electron microscopy structure (at ~4.5-angstrom resolution) of a DASH/Dam1c ring and a molecular model of its ordered components, validated by evolutionary direct-coupling analysis. Integrating this structure with that of the Ndc80 complex and with published interaction data yields a molecular picture of kinetochore-microtubule attachment, including how flexible, C-terminal extensions of DASH/Dam1c subunits project and contact widely separated sites on the Ndc80 complex rod and how phosphorylation at previously identified sites might regulate kinetochore assembly.

Kinetochore linkages between chromosomes and spindle microtubules (MTs) persist despite rapid gain and loss of tubulin subunits during cell division (*1*). The capacity to follow cycles of polymerization and depolymerization without dissociation is an important and puzzling property of the kinetochore-MT interface. The puzzle is particularly evident for "point-centromere" kinetochores of budding yeast, each of which connects a single MT with a small (~125 to 200 base pairs) and well-defined centromere (*2*, *3*). Although motor proteins participate during an initial, side-on attachment to MTs (*4*), the energy for chromosome movement during anaphase comes from the guanosine triphosphatase (GTPase) activity of tubulin and the polymerization-depolymerization events it governs (*5*–*7*).

Stable association with the plus end of a MT while the MT lengthens and shortens depends most directly on two essential molecular components of the budding-yeast kinetochore—the heterotetrameric Ndc80 complex (Ndc80c) and the heterodecameric DASH/Dam1 complex (DASH/Dam1c). Ndc80c is an end-to-end, rodlike assembly of two heterodimers (Ndc80-Nuf2 and Spc24-Spc25), with a ~580-Å-long coiled-coil shaft and small, globular domains at either end (*8*, *9*). It establishes the principal kinetochore axis, by associating with the MT at its Ndc80-Nuf2 end and with chromosome-proximal substructures at its Spc24-Spc25 end. A single kinetochore contains multiple copies of Ndc80c; the most recent estimates from quantitative fluorescence microscopy and biochemistry are in the range of 6 to 10 (*10*–*12*).

DASH/Dam1c is a more compact structure that assembles into a ring encircling the MT, organizing the Ndc80c rods and potentially other kinetochore components (*13*, *14*). Ring formation under physiological conditions in vitro by recombinant DASH/Dam1c requires MTs, and at high enough concentrations, DASH/Dam1c rings (or helical spirals) decorate the entire MT length. The limited abundance of the 10 subunits in yeast cells indicates that kinetochores in vivo have no more than one or two DASH/Dam1c rings (table S1) (*15*). DASH/Dam1c and Ndc80c interact with each other in addition to their separate interactions with MTs (*16*). Specific phosphorylation regulates most of these contacts, suggesting that a DASH/Dam1c-Ndc80c assembly controls both the timing of end-on attachment and the mechanical coupling of chromosome separation to MT shortening (*17*, *18*). DASH/Dam1c is not present in metazoans, which instead have the three-protein Ska complex (*19*). The two complexes appear to have analogous functions (*20*–*22*).

Multiple sequence alignments and secondary-structure predictions (*23*) allowed us to identify likely α-helical regions in the 10 DASH/Dam1c subunits and to make corresponding truncations in all of them (table S2). We prepared multigene expression vectors containing these truncated subunits, individually and in various combinations (see materials and methods and fig. S1) and analyzed the integrity of the expressed complexes by affinity purification and gel electrophoresis (fig. S2, A and B). We did so for nine fungal species in addition to *Saccharomyces cerevisiae* (table S3 and fig. S2C). A 115-kDa *Chaetomium thermophilum* DASH/Dam1c construct, comprising the 10 subunits, crystallized as hexagonal rods, but Bragg peaks extended only to very low resolution (60 to 40 Å) (fig. S2, D to J). The apparent unit-cell dimensions (table S4) suggested that the crystallized DASH/Dam1c had formed rings or helical spirals, like those observed when it has assembled around MTs (*13*, *24*, *25*). Dynamic light scattering (DLS) and negative-stain electron microscopy (EM) showed that *C. thermophilum* DASH/Dam1c assembled into tubes upon incubation with increasing concentrations of monovalent salts (for example, sodium formate or ammonium formate), consistent with the high-salt conditions that gave the crystals.

For cryo–electron microscopy (EM), we locked assembled DASH/Dam1c with bifunctional cross-linkers in high-salt buffer and purified the tubes by size exclusion chromatography in low salt (fig. S3). The tubes are one-dimensional (1D) crystals formed by alternate stacking of DASH/Dam1c rings with 17 protomers (C_{17} symmetry, fig. S4). Poor long-range order limited the resolution of an initial helical reconstruction (fig. S5). We therefore carried out a symmetric reconstruction at 6.5-Å resolution of individual DASH/Dam1c double rings, by masking images and reference volumes (fig. S6). At this stage, we validated our reconstruction by tilt-pair analysis, which also established the correct enantiomer (fig. S7). We then independently refined sets of four adjacent protomers in a ring ("asymmetric refinement" in FREALIGN), improving the nominal resolution to 4.5 Å (fig. S6). 3D classification did not yield better maps, presumably because selecting particles from stacks had eliminated bad ones and because the rings in a stack have a continuum of small structural distortions or variations.

We built a de novo DASH/Dam1c molecular model into the asymmetric reconstruction. We could obtain a reliable model because the structure consists mostly of α helices, which are well resolved at 4.5-Å resolution and for which more than one large side chain can establish correct sequence register for the rest of the helix (fig. S8). After an initial manual build, we used RosettaCM (*26*) to find low-energy conformations that fit the density map and then refined the structure with PHENIX (*27*). We validated the model by predicting molecular contacts within DASH/Dam1c by direct-coupling analysis (DCA) of residue coevolution (*28*). For this purpose, we identified and annotated all DASH/Dam1c genes from about 1300 fungal genomes as input for the DCA (see materials and methods). Figure S9 shows residue pairs with the highest coupling scores mapped onto our molecular model. The analysis confirmed the subunit assignment and sequence register. DCA has successfully predicted folded-protein structure (*29*); its application to validating residue assignments is likely to be a powerful tool for interpreting cryo-EM maps, when a suitably large and diverse set of sequences is available. The final model contains amino acid residues for Ask1 (residues 13 to 78), Dad1 (18 to 76), Dad2 (25 to 95, 109 to 116), Dad3 (18 to 82), Dad4 (3 to 70), Dam1 (53 to 107), Duo1 (49 to 121), Hsk3 (22 to 77), Spc19 (7 to 112), and Spc34 (3 to

[1]Department of Biological Chemistry and Molecular Pharmacology, Harvard Medical School, 250 Longwood Avenue, Boston, MA 02115, USA. [2]Howard Hughes Medical Institute, Harvard University, 250 Longwood Avenue, Boston, MA 02115, USA.
*Corresponding author. Email: harrison@crystal.harvard.edu

48, 112 to 199). Data collection and model statistics are provided in table S5.

DASH/Dam1c is a 160-Å-long, rod-shaped complex, with two coiled-coil arms that merge in the middle, where a protruding domain extends roughly perpendicular to the arms (Fig. 1). The overall shape agrees well with a published, low-resolution envelope of the *S. cerevisiae* complex (*24*). Both coiled-coil domains are parallel five-helix bundles, with the N termini of the subunits at the distal ends of the arms, generally consistent with previous assignments (*30*). Arm I contains Ask1, Dad2, Dad4, Hsk3, and the N-proximal segment of Spc19; arm II contains Dad3, Duo1, Dad1, Dam1, and the N-proximal segment of Spc34. The subunits of the two five-helix bundles interdigitate in the middle of the complex, forming what was called, at low resolution, a "central domain." The C-terminal halves of Spc19 and Spc34 form the base and extension of the protrusion domain. Part of the base, formed by Spc34, is not α helical; it is less conserved, and probably flexible. We did not attempt to model it (fig. S10A).

A layer of buried hydrophobic amino acid side chains lines the core of the central domain (fig. S10B), and hydrophobic residues also line the interiors of the two arms. The structure shows that removal of any of the 10 subunits would expose hydrophobic patches and probably induce degradation of DASH/Dam1c in the cell. Indeed, omitting Hsk3 from coexpression disrupts arm I, leading to dissociation of Ask1, Dad2, and Dad4 and leaving a hexameric complex of the remaining subunits. Similarly, omitting Dam1 disrupts arm II so that Duo1, Dad1, and Dad3 no longer associate with the complex (*31*).

Apart from the protrusion domain, the DASH/Dam1c heterodecamer has approximate internal twofold symmetry relating the left and right arms (Fig. 1B). Each subunit in one arm has a corresponding subunit in the other arm, with similar organization and 3D conformation. Sequence analysis has shown homology between some DASH/Dam1c subunits (*20*). Our structure shows that each subunit has a structural paralog, and we can assign the five pairs as Ask1-Dad3, Dad2-Duo1, Dad4-Dad1, Hsk3-Dam1, and Spc19-Spc34. Contemporary DASH/Dam1c may thus have evolved from one or more gene duplication events.

The stacking interactions between rings in our in vitro assembled tubes are probably adventitious contacts resulting from the high protein and high salt concentrations that allow tube

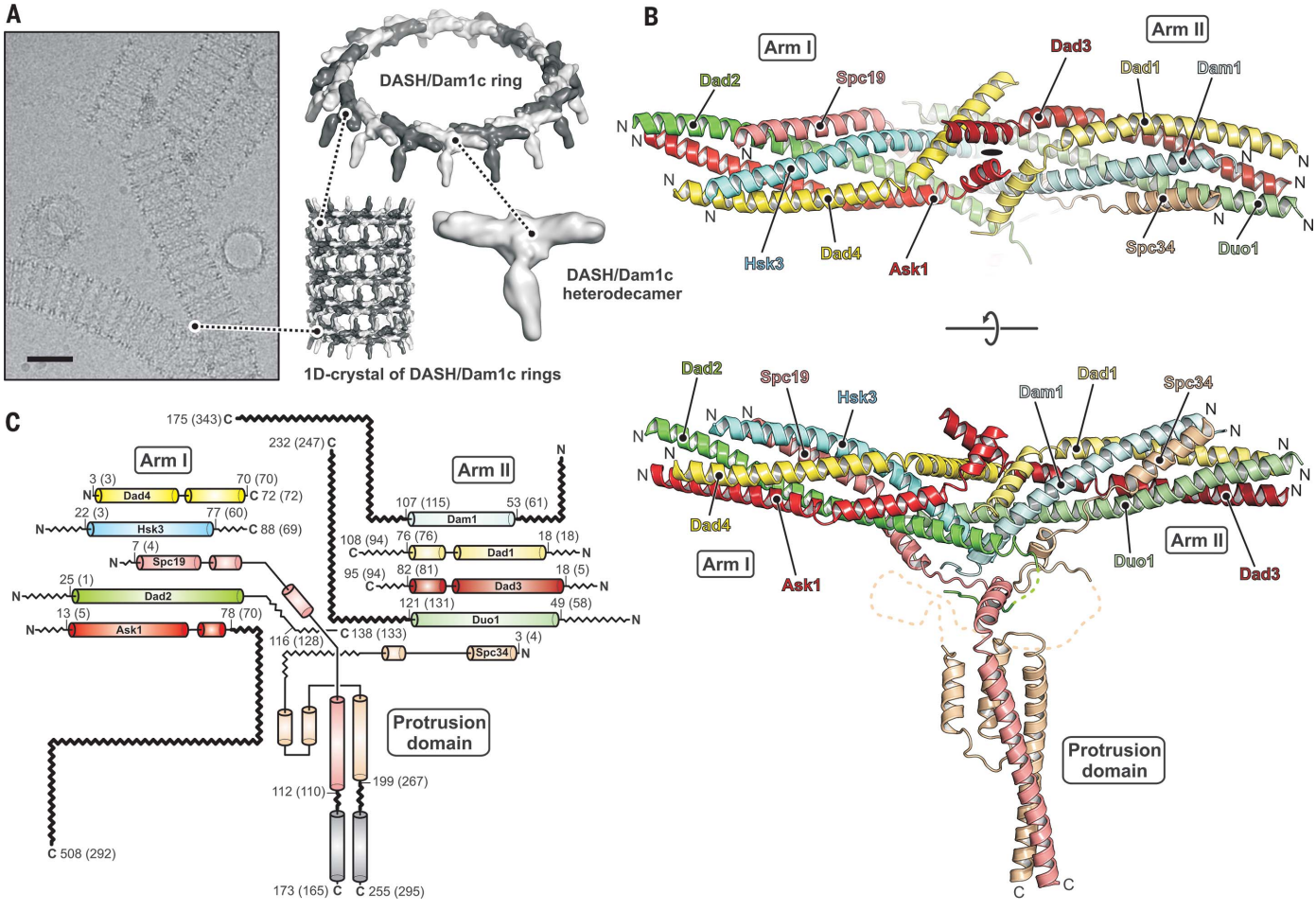

Fig. 1. Cryo-EM structure of the DASH/Dam1c heterodecamer. (**A**) Cryo–electron micrograph of DASH/Dam1c helical tubes (1D crystals) in vitreous ice recorded at 1.9-μm defocus. Scale bar, 50 nm. 1D crystals formed by sequential stacking of DASH/Dam1c rings, composed of 17 heterodecamers. (**B**) Ribbon diagram of the DASH/Dam1c structure with subunits colored: Ask1 (red), Dad2 (green), Dad4 (yellow), Hsk3 (cyan), Spc19 (salmon), Dad3 (brick red), Duo1 (pale green), Dad1 (pale yellow), Dam1 (pale cyan), and Spc34 (tan). On top, the view of the complex is along the approximate twofold symmetry axis. N, N terminus; C, C terminus. (**C**) Secondary-structure diagram. The same color scheme is used as in (B). α Helices are shown as cylinders. The first and last residue numbers included in the model are shown (numbers in parentheses are the corresponding residues in *S. cerevisiae*). C-terminal residue numbers of all subunits are shown. α Helices not modeled in the structure, but inferred from secondary-structure prediction, are shown in gray. Zigzag lines show flexible loops, N- and C-terminal extensions that were not included in the expression construct or observed in the cryo-EM map (functionally important termini of Dam1, Duo1, Ask1, and Spc19-Spc34 are in bold). The description of a previous low-resolution structure identified arm I as the "top rod" and arm II as the "bottom rod" (*24*).

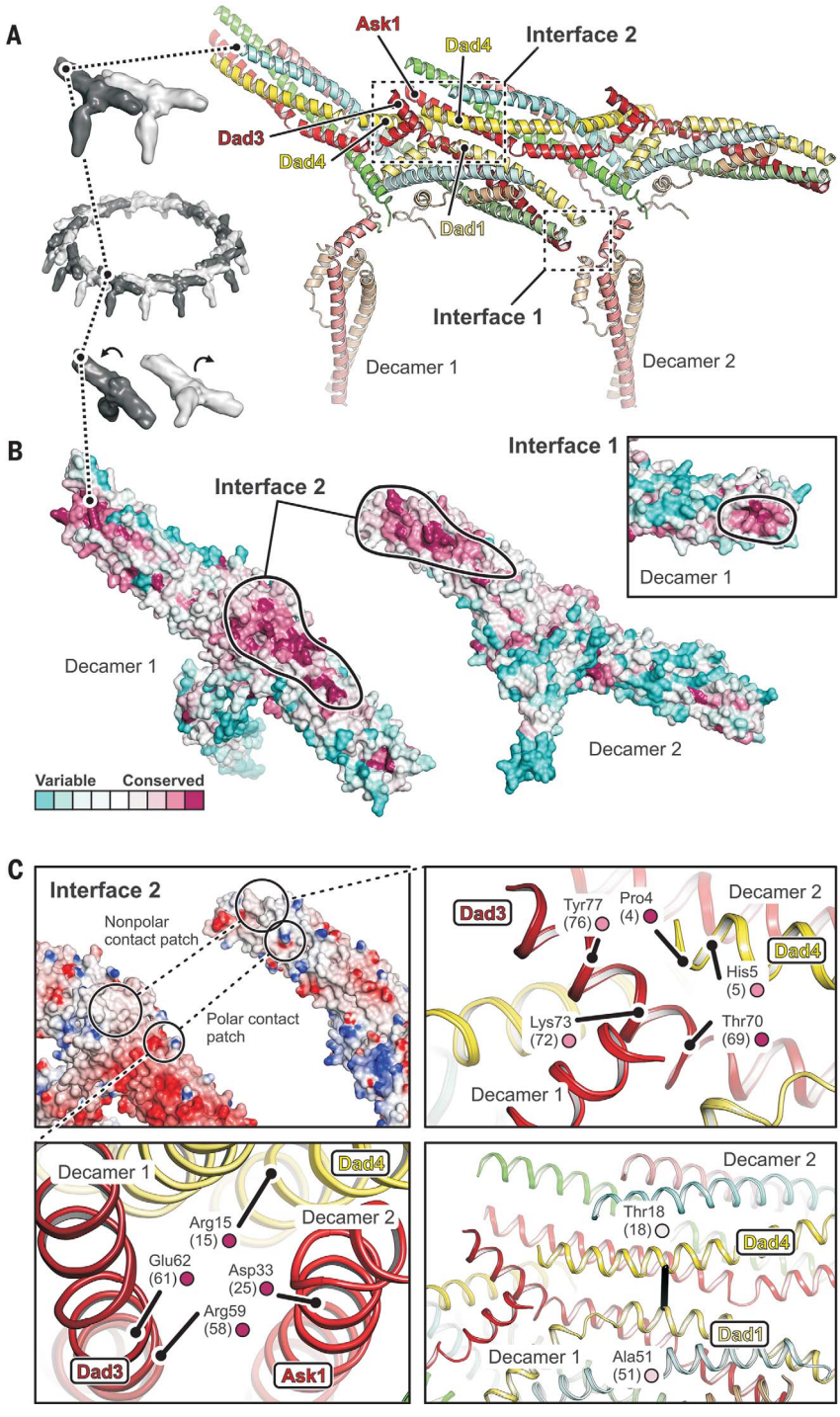

Fig. 2. Structural basis of DASH/Dam1c oligomerization. (**A**) Close-up view of two adjacent protomers (labeled decamers 1 and 2) within the DASH/Dam1c ring. Interfaces 1 and 2 are identified by dashed-line boxes. The subunits are colored as in Fig. 1. (**B**) Surface residue conservation of DASH/Dam1c in the fungal kingdom. Conservation scores were calculated with ConSurf (*46*) and mapped onto our structure. The protomers are flipped open, exposing interface 2. Black lines surround the intercomplex binding footprints. The inset shows a close-up view of interface 1 for decamer 1 only. (**C**) Interface 2 has patches of polar and hydrophobic contacts. Top left, surface representation of the two protomers, colored according to the electrostatic potential, as calculated with DelPhi (*47*). Bottom left, close-up view of the polar contact patch. Relevant amino acids are labeled with residue numbers (*S. cerevisiae* numbers in parentheses) and conservation score [small circle, color as in (B)]. Top right, close-up view of the hydrophobic patch. Bottom right, interface molecular contact inferred from DCA of residue coevolution, shown as a black line.

formation and crystallization. There is good evidence, however, that the formation of lateral interactions between protomers within a ring is the physiological mechanism of DASH/Dam1c oligomerization: (i) The same relative heterodecamer orientation (Fig. 2A) is present in a low-resolution reconstruction of a *S. cerevisiae* DASH/Dam1c dimer (*24*), (ii) the diameter of the ring is very similar to that of the ring formed by *S. cerevisiae* DASH/Dam1c (*25*) and consistent with the requirement that it surround a MT, (iii) surface amino acid residues involved in the lateral intercomplex interactions are conserved (Fig. 2B), and (iv) we detect coevolution of residues in the intercomplex interface (Fig. 2C, bottom right).

There are two interfaces between DASH/Dam1c heterodecamers within the lateral, interprotomer contacts. At interface 2, arm I of one complex (decamer 2) binds the central domain and proximal parts of arm II of an adjacent complex (decamer 1). At interface 1, the base of the protrusion domain of decamer 2 engages the arm II tip of an adjacent decamer 1 (Fig. 2A). From our multiple amino acid sequence alignments, we calculated DASH/Dam1c residue conservation scores within the fungal kingdom. Figure 2B shows that the highest conservation scores of surface residues overlap with the footprints of the oligomerization interfaces. At interface 2 (Fig. 2C, top left), we find a tight cluster of charged residues where Ask1 (Asp^{33}) and Dad4 (Arg^{15}) of decamer 2 face Dad3 (Arg^{59}, Glu^{62}) of decamer 1 (Fig. 2C, bottom left); these four residues have the highest conservation scores. Moreover, conserved Pro^{4} at the tip of the Dad4 helix (decamer 2) contacts a patch of hydrophobic residues (Thr^{70}, Lys^{73}, Ala^{74}, Tyr^{77}) at the end of the Dad3 helix (decamer 1) (Fig. 2C, top right). Because we could not model part of the base of the protrusion domain, folded from Spc34 sequence, we could not analyze specific interactions at interface 1.

Under our experimental conditions, 17 *C. thermophilum* DASH/Dam1c protomers polymerized into a ring with an outer diameter of 560 Å, about twice that of a MT (Fig. 3A). The ring has one protomer more than the 16-membered rings reported for the *S. cerevisiae* complex (*25*). Insertion of an additional DASH/Dam1c does not substantially change the diameter of the ring (fig. S11A), which could vary among species. Even within a species, there may be some variation from ring to ring in the number of protomers. When encircling a MT, the gap between the MT lattice surface and DASH/Dam1c is about 60 Å. Oligomerization interfaces 1 and 2 determine the relative orientation of adjacent protomers; ring closure defines their orientation with respect to the MT.

Near the N terminus of Dam1, phosphorylation of Ser^{20} (in *S. cerevisiae)* by Ipl1/Aurora B inhibits cooperative binding of DASH/Dam1c to MTs (*17*, *32*). The location of the Dam1 N terminus, on the outside of the ring (Fig. 3B, center right), suggests that Ser^{20} phosphorylation could modulate DASH/Dam1c oligomerization either by destabilizing an interaction with a

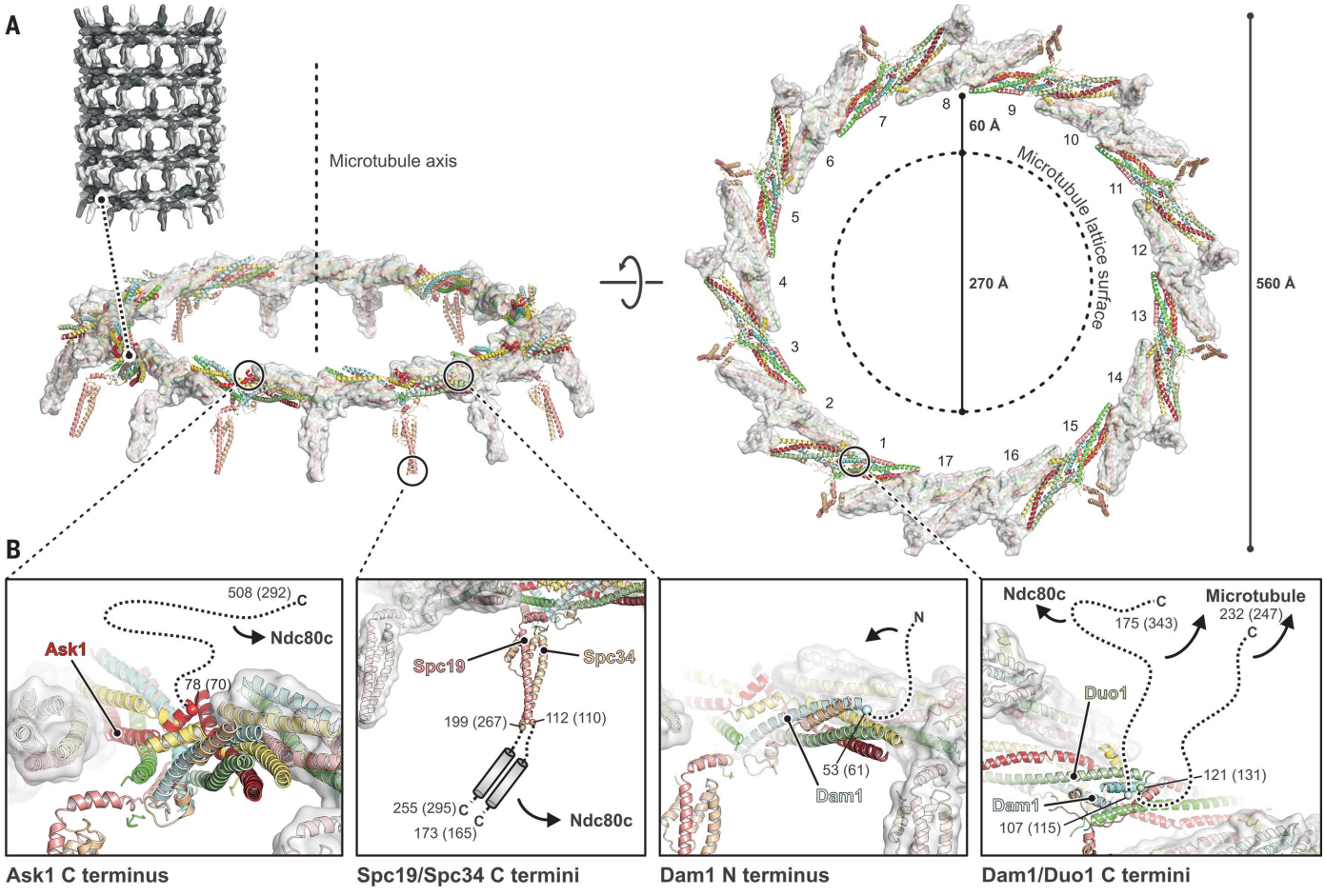

Fig. 3. The DASH/Dam1c ring with flexible extensions. (**A**) Structure of the 17-membered ring. Heterodecamers are shown as ribbons and colored as in Fig. 1. Protomers are alternately shown with transparent surface. The MT axis (side view, left) and lattice surface (top view, right) are shown as a vertical and circular dashed line, respectively. (**B**) Close-up views of the anchor points on the ring [circled in (A)], from which flexible extensions project. α-Carbon atoms of terminal amino acids modeled in the cryo-EM map are shown as spheres with residue numbers (*S. cerevisiae* numbers in parentheses). Flexible extensions are drawn schematically as dotted lines, except for Spc19 and Spc34 (center left panel), for which we indicate a C-terminal heterodimeric coiled coil based on secondary-structure prediction and molecular contacts inferred from DCA of residue coevolution.

neighboring protomer or by stabilizing an autoinhibitory interaction within the same protomer. The phosphorylation site is conserved among budding yeast (data S1), and the length of the Dam1 N-terminal extension could accommodate either option.

Flexible polypeptide extensions that link partner protein complexes are a general feature of kinetochore architecture (*33*, *34*). Apart from ring formation, in which DASH/Dam1c cores interact directly, contacts with both MT and Ndc80c are through subunit extensions predicted to be conformationally variable (Fig. 1C and data S1). Although these extensions were either omitted from our construct or undefined (owing to flexibility) in the cryo-EM map, the structure of the DASH/Dam1c core and its orientation with respect to the MT together determine the directions in which the flexible extensions project and, hence, their likely contacts.

The structure of the DASH/Dam1c ring also suggests how to interpret three sets of contact points, detected by chemical cross-linking of Ndc80c with Dam1, Ask1, and Spc34, respectively (*35*), leading to the interactions illustrated by arrows in Fig. 3B and to the model for the MT-proximal components of the yeast kinetochore shown in Fig. 4. The lengths of the C-terminal extensions of Dam1, Ask1, and Spc34 and the directions in which they project permit all three Ndc80c contacts to be established with a single DASH/Dam1c ring (Fig. 4B). The molecular organization of this assembly is also consistent with the assumption that a DASH/Dam1c ring encircles a MT plus end with curled protofilaments, as observed in tomographic reconstructions of kinetochore MTs (*36*).

The C-terminal halves of Dam1 and Duo1 bridge the gap between the DASH/Dam1c ring and the MT and contact the MT surface (*31*, *37*). The points from which the Dam1 and Duo1 extensions emanate are next to each other on the inside of the ring (Fig. 3B, right). Their proximity explains the extensive cross-linking of Dam1 and Duo1 C-terminal extensions with each other (*37*, *38*). Both also cross-link to tubulin at positions on the outer surface of a MT (*37*). Low-resolution density, likely from Dam1 and Duo1, is present in the reconstruction of a MT-encircling, DASH/Dam1c ring from *S. cerevisiae* (fig. S11B) (*24*, *25*). The long Dam1 C-terminal projection in *S. cerevisiae* cross-links to Ndc80 (*35*) and, hence, has a dual role (Fig. 3B, right). The site of cross-linking, a hairpin at the junction between the Ndc80 globular head and the coiled-coiled shaft, is also the site of a deletion that affects chromosome segregation (*18*). When Ndc80c attaches to a MT, this loop is close to the MT surface (*39*). Because of the high symmetry of the DASH/Dam1c ring, however, the same Dam1 subunit need not participate in both MT and Ndc80 contacts at the same time. In some fungal species, including *C. thermophilum*, the C-terminal extension of Dam1 may not be long enough to extend from a DASH/Dam1c ring to the Ndc80 globular head (data S1).

The Ask1 C-terminal extension projects from the outside of the ring (Fig. 3B, left). Its contact on the Ndc80-Nuf2 shaft (*35*), possibly also involving residues of the "Ndc80 loop" (*16*), is well

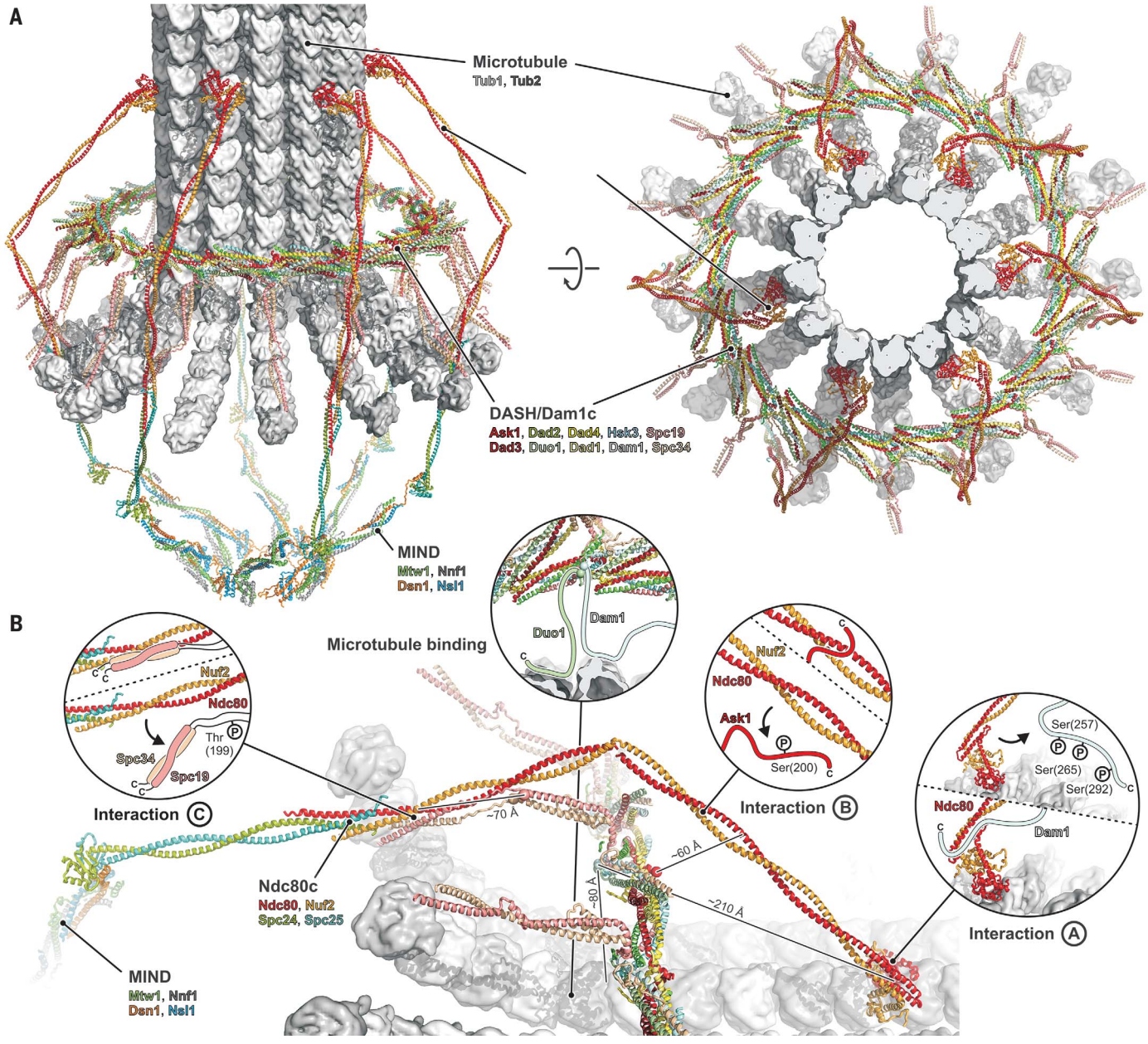

Fig. 4. Model of the yeast kinetochore-MT interface. (**A**) Overview from the side (left) and top (right). (**B**) Close-up view and interactions of DASH/Dam1c with the MT and Ndc80c. Approximate distances between the attachments of the flexible extensions on the DASH/Dam1c ring and their target sites, defined by cross-linking, are shown. Interactions A, B, and C are between Ndc80c and DASH/Dam1c subunits Dam1, Ask1, and Spc34-Spc19, respectively. *S. cerevisiae* residues known to be phosphorylated by Ipl1/Aurora B are shown in the magnified views, and arrows indicate release of Ndc80c binding upon phosphorylation. P, phosphate.

within reach of the Ask1 C-terminal extension, which would emerge from just beneath the Ndc80c shaft as positioned in Fig. 4. The Spc19 and Spc34 C-terminal extensions project from the tip of the protrusion domain. Secondary-structure prediction (data S1) and the second-highest peak in our Spc19-Spc34 molecular contact map from DCA suggest that a heterodimeric Spc19-Spc34 coiled coil is flexibly tethered to the structured protrusion domain by two short linkers (Fig. 3B, center left). The observed cross-link toward the C terminus of Nuf2 (*35*), near the junction with Spc24-Spc25, and binding of *S. cerevisiae* Spc19 residues 128 to 165 and Nuf2 residues 399 to 429 (*40*) then set the polarity of the DASH/Dam1c ring with respect to the MT, with the protrusion pointing toward the plus end. As the C-terminal Spc19-Spc34 binding module is anchored to the structured core of the DASH/Dam1c ring through a relatively short linker, the Ndc80-Nuf2 coiled-coil shaft probably bends around the DASH/Dam1c ring, perhaps near the position of the Ndc80 loop, bringing the Spc24-Spc25 tip of Ndc80c closer to the kinetochore central axis where it binds the MIND adaptor complex (Fig. 4A).

DASH/Dam1c and Ndc80c are both essential for kinetochore-MT attachments that are stable enough to withstand the forces generated by MT depolymerization (*41*, *42*). A rigid DASH/Dam1c ring that interacts through flexible extensions with the MT and Ndc80c has several potential functional advantages: (i) Junctions created by a flexible peptide extension that fits into a specific docking site can adapt to different relative orientations of the partner complexes, as required by

variable stoichiometry and unmatched symmetry in the kinetochore (for example, a 13-protofilament MT surrounded by a 16- or 17-protomer DASH/Dam1c ring and six to eight Ndc80 complexes). (ii) These junctions allow distinct interactions at different stages of mitosis: Budding-yeast kinetochores first attach to the lateral surface of a MT, along which they migrate toward the spindle pole. DASH/Dam1c is dispensable at this stage, but it is necessary for the transition to stable end-on attachments (*4*). Adaptability of the DASH/Dam1c contacts with Ndc80c is probably a functional requirement for this process. (iii) Peptide segments facilitate regulation of the assembly state and interaction affinities by posttranslational modifications in DASH/Dam1c (*17*, *43*). Unfolded and extended polypeptides are good substrates for kinases and other modifying enzymes, as they fit readily into the enzymatic active sites. Ipl1/Aurora B phosphorylation of DASH/Dam1c subunits switches off the interactions of all three sets with Ndc80c (Fig. 4B) (*35*) to reset MT attachments during activation of the spindle checkpoint. (iv) Docked-peptide interactions are generally of modest strength, so that individual contacts dissociate and rebind rapidly, allowing a disassembling agent, such as the Ipl1 kinase, to access the DASH/Dam1c peptide segments for modification and to release the kinetochore from the MT. (v) Multiple weak contacts, flexible distance constraints, and incommensurate symmetries enable the organized assembly of Ndc80c and DASH/Dam1c to track the plus end of a depolymerizing MT by stochastic, "hand-over-hand" biased diffusion. The role of the DASH/Dam1c ring as a structural organizer of Ndc80c is central to this process. (vi) Coordinated structural changes in the cagelike structure of the kinetochore, made possible by flexibility of the DASH/Dam1c-Ndc80c interactions (and of linkages in other parts of the assembly), may be part of the tension-sensing mechanism implicated in setting and releasing the mitotic spindle assembly checkpoint. Compliance of the overall structure can reposition components in response to tension and convert force into changes in molecular proximity.

The molecularly detailed model of the kinetochore-MT connection in budding yeast (Fig. 4), derived from the DASH/Dam1c and Ndc80c structures and from the constraints of published biochemical and genetic data, unifies two proposals for how the energy released by MT depolymerization drives chromosome separation at anaphase (*44*, *45*). One model invokes biased diffusion, in which rapid, asynchronous association and dissociation of multiple, flexible contacts allows any individual contact to break and form again further along the shortening MT. The other invokes a conformational wave (for example, protofilament curling) that actively pushes the kinetochore in the direction of shortening. Protofilament curling against a closed ring probably exerts force directly, but MT contacts, from the Dam1-Duo1 extensions and from the organized set of Ndc80 complexes, must break and reform to allow MT shortening to progress. Thus, docking and undocking of flexible connections between defined subunits can allow a kinetochore to track the end of the MT through cycles of growth and shrinkage.

REFERENCES AND NOTES

1. S. Biggins, *Genetics* **194**, 817–846 (2013).
2. S. Furuyama, S. Biggins, *Proc. Natl. Acad. Sci. U.S.A.* **104**, 14706–14711 (2007).
3. M. Winey *et al.*, *J. Cell Biol.* **129**, 1601–1615 (1995).
4. K. Tanaka, E. Kitamura, Y. Kitamura, T. U. Tanaka, *J. Cell Biol.* **178**, 269–281 (2007).
5. E. L. Grishchuk, J. R. McIntosh, *EMBO J.* **25**, 4888–4896 (2006).
6. D. E. Koshland, T. J. Mitchison, M. W. Kirschner, *Nature* **331**, 499–504 (1988).
7. J. D. Tytell, P. K. Sorger, *J. Cell Biol.* **172**, 861–874 (2006).
8. R. R. Wei, P. K. Sorger, S. C. Harrison, *Proc. Natl. Acad. Sci. U.S.A.* **102**, 5363–5367 (2005).
9. C. Ciferri *et al.*, *J. Biol. Chem.* **280**, 29088–29095 (2005).
10. P. Aravamudhan, I. Felzer-Kim, A. P. Joglekar, *Curr. Biol.* **23**, 770–774 (2013).
11. P. Aravamudhan, I. Felzer-Kim, K. Gurunathan, A. P. Joglekar, *Curr. Biol.* **24**, 1437–1446 (2014).
12. G. Pekgöz Altunkaya *et al.*, *Curr. Biol.* **26**, 2370–2378 (2016).
13. J. J. Miranda, P. De Wulf, P. K. Sorger, S. C. Harrison, *Nat. Struct. Mol. Biol.* **12**, 138–143 (2005).
14. S. Westermann *et al.*, *Mol. Cell* **17**, 277–290 (2005).
15. S. Ghaemmaghami *et al.*, *Nature* **425**, 737–741 (2003).
16. J. F. Maure *et al.*, *Curr. Biol.* **21**, 207–213 (2011).
17. I. M. Cheeseman *et al.*, *Cell* **111**, 163–172 (2002).
18. F. Lampert, C. Mieck, G. M. Alushin, E. Nogales, S. Westermann, *J. Cell Biol.* **200**, 21–30 (2013).
19. A. A. Jeyaprakash *et al.*, *Mol. Cell* **46**, 274–286 (2012).
20. J. J. E. van Hooff, B. Snel, G. J. P. L. Kops, *Genome Biol. Evol.* **9**, 1295–1303 (2017).
21. P. L. Janczyk *et al.*, *Dev. Cell* **41**, 438–449.e4 (2017).
22. D. K. Cheerambathur *et al.*, *Dev. Cell* **41**, 424–437.e4 (2017).
23. G. Yachdav *et al.*, *Nucleic Acids Res.* **42** (W1), W337–W343 (2014).
24. H. W. Wang *et al.*, *Nat. Struct. Mol. Biol.* **14**, 721–726 (2007).
25. V. H. Ramey *et al.*, *Mol. Biol. Cell* **22**, 457–466 (2011).
26. Y. Song *et al.*, *Structure* **21**, 1735–1742 (2013).
27. P. D. Adams *et al.*, *Acta Crystallogr. D Biol. Crystallogr.* **66**, 213–221 (2010).
28. F. Morcos *et al.*, *Proc. Natl. Acad. Sci. U.S.A.* **108**, E1293–E1301 (2011).
29. T. A. Hopf *et al.*, *Cell* **149**, 1607–1621 (2012).
30. V. H. Ramey *et al.*, *Mol. Biol. Cell* **22**, 4335–4342 (2011).
31. J. J. Miranda, D. S. King, S. C. Harrison, *Mol. Biol. Cell* **18**, 2503–2510 (2007).
32. D. R. Gestaut *et al.*, *Nat. Cell Biol.* **10**, 407–414 (2008).
33. Y. N. Dimitrova, S. Jenni, R. Valverde, Y. Khin, S. C. Harrison, *Cell* **167**, 1014–1027.e12 (2016).
34. S. Jenni, Y. N. Dimitrova, R. Valverde, S. M. Hinshaw, S. C. Harrison, *Cold Spring Harb. Symp. Quant. Biol.* 10.1101/sqb.2017.82.033738 (2017).
35. J. O. Kim *et al.*, *eLife* **6**, e21069 (2017).
36. J. R. McIntosh *et al.*, *J. Cell Biol.* **200**, 459–474 (2013).
37. T. Legal, J. Zou, A. Sochaj, J. Rappsilber, J. P. Welburn, *Open Biol.* **6**, 150237 (2016).
38. A. Zelter *et al.*, *Nat. Commun.* **6**, 8673 (2015).
39. G. M. Alushin *et al.*, *Nature* **467**, 805–810 (2010).
40. Y. Wang *et al.*, *Mol. Biol. Cell* **23**, 3911–3922 (2012).
41. J. F. Tien *et al.*, *J. Cell Biol.* **189**, 713–723 (2010).
42. F. Lampert, P. Hornung, S. Westermann, *J. Cell Biol.* **189**, 641–649 (2010).
43. J. A. Latham, R. J. Chosed, S. Wang, S. Y. Dent, *Cell* **146**, 709–719 (2011).
44. C. L. Asbury, J. F. Tien, T. N. Davis, *Trends Cell Biol.* **21**, 38–46 (2011).
45. C. L. Asbury, *Biology (Basel)* **6**, 15 (2017).
46. H. Ashkenazy *et al.*, *Nucleic Acids Res.* **44** (W1), W344–W350 (2016).
47. L. Li *et al.*, *BMC Biophys.* **5**, 9 (2012).

ACKNOWLEDGMENTS

We thank C. Xu (University of Massachusetts Medical School) for instructing S.J. in cryo-EM; C. Hong, Z. Yu (Janelia Research Campus), M. Chambers, and Z. Li (Harvard Medical School) for help with data collection; S. Hinshaw (Harvard Medical School) for valuable comments on the manuscript; A. Bellemare and A. Tsang (Concordia University) for providing *C. thermophilum* cDNA; A. Rohou, T. Grant, and N. Grigorieff (Janelia Research Campus) for helpful discussions and a prerelease version of FrealignX; and the Northeastern Collaborative Access Team (NE-CAT) beamline staff for help with x-ray data collection. MycoCosm sequence data were produced by the U.S. Department of Energy (DOE) Joint Genome Institute (www.jgi.doe.gov) in collaboration with the user community. **Funding:** Some of the research was conducted at the Advanced Photon Source (APS), on the NE-CAT beamlines, funded by NIH grant P41 GM103403; the Pilatus 6M detector on beam line 24-ID-C is funded by NIH-ORIP HEI grant S10 RR029205. APS is operated for the DOE Office of Science by Argonne National Laboratory under contract no. DE-AC02-06CH11357. S.J. was a Howard Hughes Medical Institute (HHMI) Fellow of the Damon Runyon Cancer Research Foundation (DRG-2004-09). S.C.H. is an Investigator in the HHMI. **Author contributions:** S.J. conceived experimental strategies, designed experiments, carried out experiments, performed computations, and wrote the paper; S.C.H. proposed overall project and some experimental strategies and wrote the paper. **Competing interests:** None declared. **Data and materials availability:** The cryo-EM symmetric and asymmetric reconstructions are deposited in the Electron Microscopy Data Bank (EMDB accession numbers EMD-7446, EMD-7469). The DASH/Dam1c structure is deposited in the Protein Data Bank (PDB accession number 6CFZ).

SUPPLEMENTARY MATERIALS

www.sciencemag.org/content/360/6388/552/suppl/DC1
Materials and Methods
Figs. S1 to S11
Tables S1 to S6
References (*48*–*99*)
Movie S1
Data S1 and S2

1 December 2017; accepted 15 March 2018
10.1126/science.aar6436

IMMUNOLOGY

C1q restrains autoimmunity and viral infection by regulating CD8$^+$ T cell metabolism

Guang Sheng Ling,[1] Greg Crawford,[1] Norzawani Buang,[1] Istvan Bartok,[1] Kunyuan Tian,[1] Nicole M. Thielens,[2] Isabelle Bally,[2] James A. Harker,[1] Philip G. Ashton-Rickardt,[1] Sophie Rutschmann,[1] Jessica Strid,[1] Marina Botto[1]*

Deficiency of C1q, the initiator of the complement classical pathway, is associated with the development of systemic lupus erythematosus (SLE). Explaining this association in terms of abnormalities in the classical pathway alone remains problematic because C3 deficiency does not predispose to SLE. Here, using a mouse model of SLE, we demonstrate that C1q, but not C3, restrains the response to self-antigens by modulating the mitochondrial metabolism of CD8$^+$ T cells, which can themselves propagate autoimmunity. C1q deficiency also triggers an exuberant effector CD8$^+$ T cell response to chronic viral infection leading to lethal immunopathology. These data establish a link between C1q and CD8$^+$ T cell metabolism and may explain how C1q protects against lupus, with implications for the role of viral infections in the perpetuation of autoimmunity.

Systemic lupus erythematosus (SLE) is an autoimmune condition that develops as a result of complex genetic and environmental interactions. B and CD4$^+$ T cell abnormalities are well known features of SLE (*1*), but the role of CD8$^+$ T lymphocytes remains poorly understood. Transcriptomic data suggest that a CD8$^+$ T cell signature can predict disease outcome (*2*, *3*).

There is evidence for a strong association between SLE and complement C1q deficiency (*4*). Previous work has shown that C1q deficiency leads to the ineffective clearance of apoptotic cells and consequently enhanced exposure to self-antigens, which facilitate autoimmunity (*5*). However, there are multiple pathways, including those mediated by C3, through which apoptotic cell clearance occurs (*6*). This suggests that the contribution of C1q is redundant and the "waste disposal" hypothesis (*5*) is inadequate to fully explain why C1q deficiency, and not C3 deficiency, is associated with autoimmunity. Alternative, but not mutually exclusive, hypotheses have been proposed (*7*). However, an explanation for this strong association in terms of classical complement pathway abnormalities alone remains unsatisfactory. Given that there is evidence that C1q has multiple roles that are independent of complement activation (*8*), we searched for an alternative function that could explain why C1q is so critical for maintaining self-tolerance.

Chronic graft-versus-host-disease (cGvHD) is a well-established inducible model of SLE. We used the bm12-cGvHD model (*9*) and injected splenocytes from B6(C)-*H2-Ab1*^{bm12}/KhEgJ (bm12) mice into coisogenic C57BL/6 (B6) recipients lacking C1q (*C1qa*$^{-/-}$) or C3 (*C3*$^{-/-}$). Lupus autoantibody levels were similar at disease onset (weeks 0–4), but increased at later time points only in the *C1qa*$^{-/-}$ mice (Fig. 1A). At week 10, *C1qa*$^{-/-}$ mice displayed more severe glomerulonephritis and increased glomerular deposition of immunoglobulin G (IgG) and C3 (Fig. 1B). They also had splenomegaly with higher percentages of germinal center B cells, follicular helper T cells (T_{FH}), activated CD4$^+$ and CD8$^+$ T cells than the wild-type (WT) and *C3*$^{-/-}$ counterparts (fig. S1). During the course of the disease there were no differences in blood B and CD4$^+$ T cell activation between experimental groups, but the proportion of activated CD44^{hi}CD62L$^-$CD8$^+$ T cells in the *C1qa*$^{-/-}$ mice was increased with a relative expansion of KLRG1$^+$IL-7R$^-$ short-lived effector cells (SLECs) and a corresponding reduction in KLRG1$^-$IL-7R$^+$ memory precursor effector cells (MPECs) (Fig. 1C) (*10*). Consistent with the alterations in blood, cGvH-treated *C1qa*$^{-/-}$ mice had early (from week 1) splenic CD8$^+$ T cell abnormalities, whereas the initial B and CD4$^+$ T cell responses were similar to WT and *C3*$^{-/-}$ animals (fig. S1). Furthermore, the in vitro restimulation of *C1qa*$^{-/-}$ CD8$^+$ T cells resulted in increased interferon-γ (IFN-γ) and granzyme B expression and fewer IL-2$^+$ cells (fig. S2), indicating that the lack of C1q, but not of C3, resulted in CD8$^+$ T cell responses skewed toward an effector phenotype. To determine whether bystander inflammation or self-antigen stimulation promoted CD8$^+$ T cell activation during bm12-cGvH induction, naïve CD8$^+$ T cells from B6.CD45.1$^+$ and ovalbumin (OVA)–specific T cell receptor (TCR) transgenic (OT-I) mice were cotransferred into B6.CD45.2$^+$ animals, which were challenged with bm12 splenocytes. Donor CD45.1$^+$CD8$^+$ T cells expanded and became activated like the host CD45.2$^+$CD8$^+$ T cells, whereas pentamer$^+$ OT-I cells remained quiescent (fig. S3), suggesting that TCR engagement by self-antigen was required.

CD8α$^+$ dendritic cells (DCs) cross-present apoptotic cell-associated antigens to CD8$^+$ T cells (*11*). However, the cross-priming by CD8α$^+$ DCs in *C1qa*$^{-/-}$ animals was not impaired (fig. S4, A to C). Furthermore, after cGvH induction, the number and phenotype of CD8α$^+$ DCs was unaffected by C1q deficiency (fig. S4, D and E). We then depleted CD8$^+$ T cells to demonstrate their direct contribution to the autoimmune response in cGvHD. Although similar autoantibody levels were initially detected in all groups (Fig. 1D), from week 4 onwards, CD8$^+$ T cell-depleted *C1qa*$^{-/-}$ mice displayed a progressive decline in lupus-associated autoantibodies, whereas total IgG levels remained unaffected (Fig. 1D). CD8$^+$ T cell-depleted *C1qa*$^{-/-}$ mice also showed reduced glomerular deposition of IgG and C3 compared with nondepleted mice (Fig. 1E). Thus, these data suggest that CD8$^+$ T cells are responsible for perpetuating the lupus-like disease observed in cGvH-treated *C1qa*$^{-/-}$ mice.

To explore whether C1q also modulates CD8$^+$ T cell immunity during infections, we used lymphocytic choriomeningitis virus (LCMV) models. *C1qa*$^{-/-}$ mice, subjected to acute LCVM-Armstrong (Arm) infection, had an aberrant effector LCMV-specific CD8$^+$ T cell response at day 8 (Fig. 2A and fig. S5A), but did not show markedly different memory and recall responses (fig. S5, B to D). We next used the chronic LCMV-clone 13 (Cl13) model where an exaggerated effector immune response can cause lethal lung immunopathology (*12*). When compared with WT mice, Cl13-infected *C1qa*$^{-/-}$ mice experienced greater body weight loss and had to be culled at day 11 (Fig. 2B). Examination of *C1qa*$^{-/-}$ lung tissue showed edema that was absent in the controls (Fig. 2C and fig. S6A). Consistent with a vigorous CD8$^+$ T cell response, *C1qa*$^{-/-}$ mice showed increased LCMV-specific gp33$^+$ and gp276$^+$CD8$^+$ T cell populations (Fig. 2D and fig. S6B). On day 8, when *C1qa*$^{-/-}$ mice still had numbers of LCMV-specific CD8$^+$ T cells comparable to WT animals, virus-specific *C1qa*$^{-/-}$ CD8$^+$ T cells were functionally overreactive, with enhanced degranulation and cytokine production (Fig. 2, E and F). Consistent with an enhanced CD8$^+$ T cell response, serum viral loads were lower in Cl13-infected *C1qa*$^{-/-}$ mice compared with WT mice (Fig. 2G). Moreover, the up-regulation of PD-1 expression was similar in WT and *C1qa*$^{-/-}$ LCMV–specific CD8$^+$ T cells, indicating that C1q deficiency did not impair the PD-1 signaling pathway (Fig. 2H). These findings demonstrate that C1q plays a pivotal role in regulating effector CD8$^+$ T cell responses in both autoimmunity and viral infection.

Complement can mediate its cellular effects via both extracellular and intracellular pathways (*13*). To explore how C1q affect CD8$^+$ T cells, we cotransferred naïve CD8$^+$ T cells, isolated from B6.CD45.1$^+$ and *C1qa*$^{-/-}$.CD45.2$^+$ mice into B6.CD45.1$^+$.CD45.2$^+$ mice, which were challenged with bm12 CD4$^+$ T cells one day later. C1q-sufficient and C1q-deficient donor CD8$^+$ T cells showed similar expansion and activation,

[1]Faculty of Medicine, Imperial College London, London W12 ONN, UK. [2]University Grenoble Alpes, CEA, CNRS, IBS, F-38000 Grenoble, France.
*Corresponding author. Email: m.botto@imperial.ac.uk

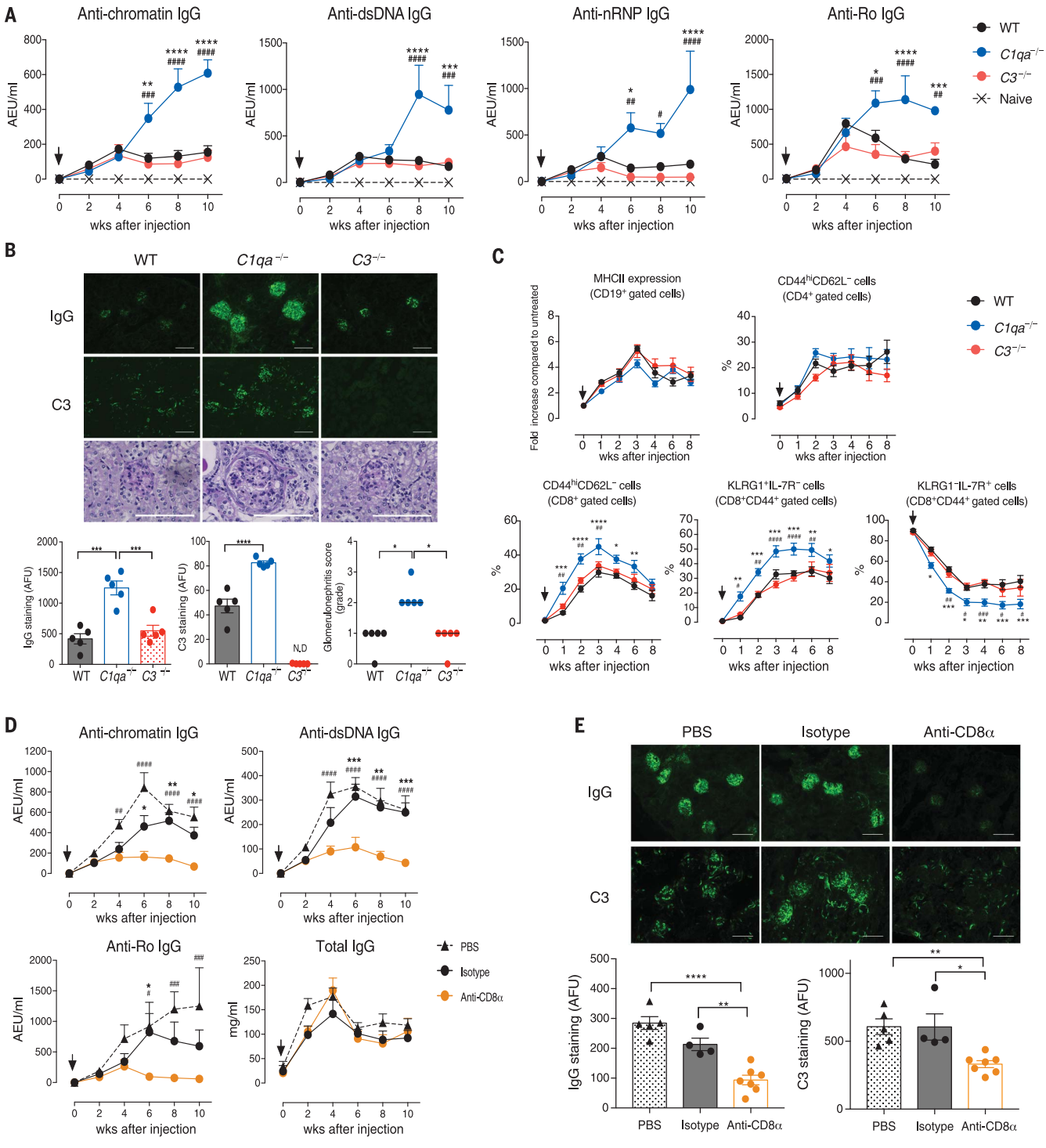

Fig. 1. Autoimmune features and CD8$^+$ T cell response in *C1qa*$^{-/-}$ mice after bm12-cGvH induction. (**A**) Autoantibody levels after bm12 injection (arrows) (n = 5 mice per group). (**B**) IgG, C3, and periodic acid–Schiff (PAS) staining of kidney sections at week 10. Quantification of glomerular IgG and C3 deposition expressed as arbitrary fluorescence units (AFU). ND, not detectable. Glomerulonephritis score: 0 to 4, bars indicate the median; *P < 0.05; Kruskal-Wallis H test. (**C**) Flow cytometric analysis of blood cells after cGvH induction (arrows) (n = 8 to 10 mice per group). (**D** and **E**) *C1qa*$^{-/-}$ mice were administrated phosphate-buffered saline (PBS), antibody to CD8α (anti-CD8α), or isotype-matched IgG2b antibody (n = 4 to 7 mice per group). (D) Autoantibody and IgG levels after cGvH induction (arrows). (E) Images and quantification of glomerular IgG and C3 deposition at week 10. *P < 0.05, **P < 0.01, ****P < 0.001; one-way analysis of variance (ANOVA) [(B) and (E)]; *P < 0.05, **P < 0.01, ***P < 0.005, ****P < 0.0001 (WT versus *C1qa*$^{-/-}$), $^{\#}P$ < 0.05, $^{\#\#}P$ < 0.01, $^{\#\#\#}P$ < 0.005, $^{\#\#\#\#}P$ < 0.0001 (*C1qa*$^{-/-}$ versus *C3*$^{-/-}$) two-way ANOVA [(A) and (C)]; *P < 0.05, **P < 0.01, ***P < 0.005 (isotype versus anti-CD8α), $^{\#\#}P$ < 0.01, $^{\#\#\#}P$ < 0.005, $^{\#\#\#\#}P$ < 0.0001 (PBS versus anti-CD8α) two-way ANOVA (D). Data are mean ± SEM unless indicated otherwise; pooled results of two experiments (C); representative of two [(D) and (E)] or three [(A) and (B)] experiments. Scale bars, 100 μm [(B) and (E)].

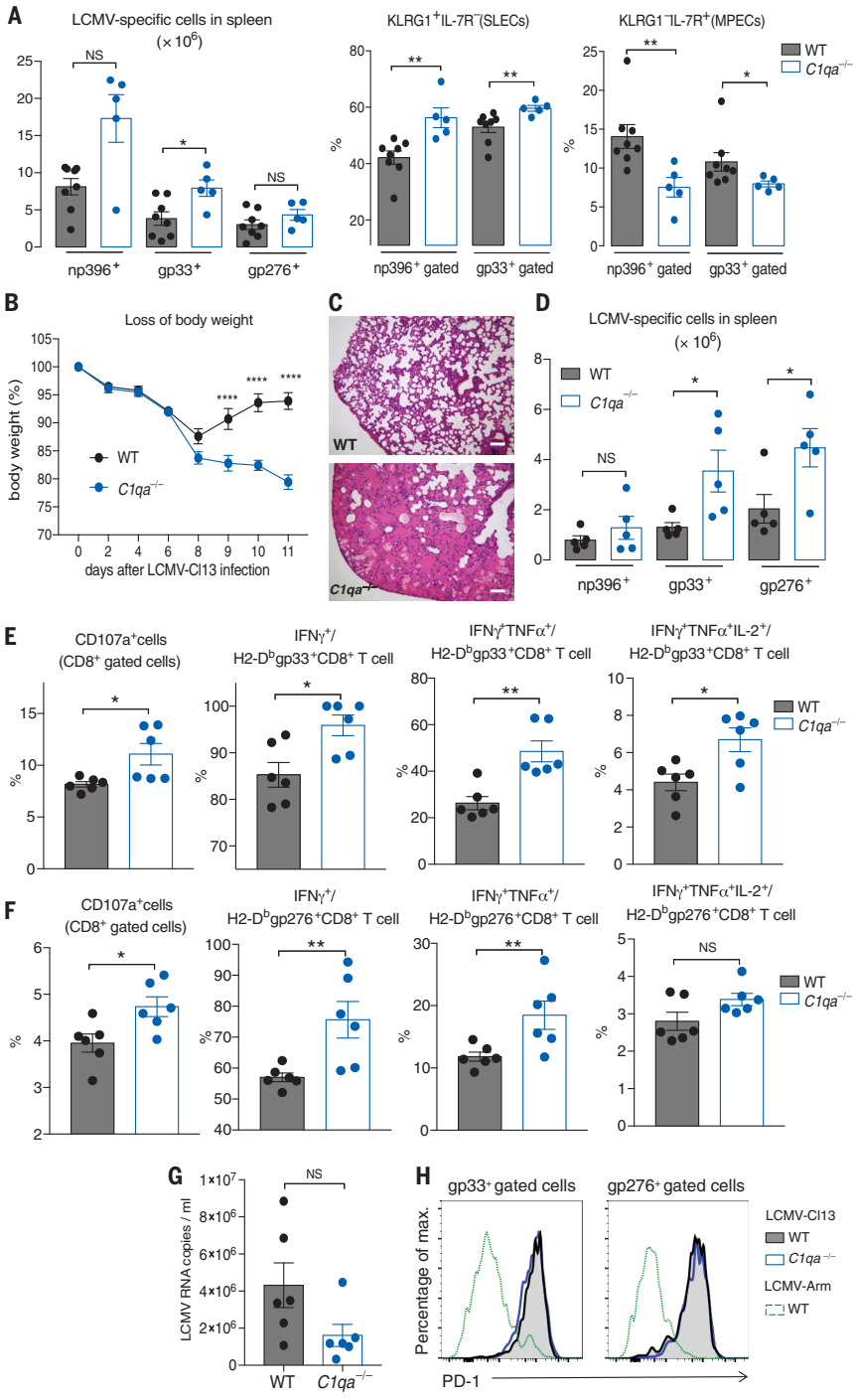

Fig. 2. Essential role for C1q in chronic LCMV infection. (**A**) Numbers of splenic np396$^+$, gp33$^+$, and gp276$^+$ CD8$^+$ T cells and proportions of SLECs and MPECs among LCMV-specific CD8$^+$ T cells in LCMV-Arm–infected WT and *C1qa*$^{-/-}$ mice at day 8 (n = 5 to 8 mice per group). (**B** to **G**) Analysis of WT and *C1qa*$^{-/-}$ mice infected with LCMV-Cl13. (B) Percentage of body weight loss (n = 5 mice per group). (C) Representative lung histology on day 11. Scale bars, 100 μm. (D) Numbers of splenic LCMV-specific CD8$^+$ T cells at day 11 (n = 5 mice per group). [(E) and (F)] Percentages of CD8$^+$ T cells positive for CD107a and the proportion of LCMV-specific CD8$^+$ T cells producing IFN-γ, tumor necrosis factor–α (TNF-α), and interleukin-2 (IL-2) after incubation with LCMV gp33 peptide (E) or gp276 peptide (F) at day 8 (n = 6 mice per group). (G) Serum viral load measured using quantitative polymerase chain reaction (PCR). (**H**) PD-1 expression on LCMV-specific CD8$^+$ T cells at day 8 after LCMV-Cl13 and LCMV-Arm. NS, not significant; *P < 0.05, **P < 0.01, ****P < 0.0001; unpaired Student's t test [(A) and (D) to (F)]; two-way ANOVA (B). Data are mean ± SEM and representative of two experiments.

suggesting a cell-extrinsic effect of C1q (fig. S7). We corroborated this using the lymphopenia-induced proliferation model by cotransferring carboxyfluorescein diacetate succinimidyl ester (CFSE)–labeled CD8$^+$ and CD4$^+$ T cells from B6.CD45.1$^+$ mice into irradiated B6.CD45.2$^+$ and *C1qa*$^{-/-}$.CD45.2$^+$ mice. Fourteen days later, donor B6.CD45.1$^+$CD8$^+$ T cells showed greater proliferation and activation in *C1qa*$^{-/-}$.CD45.2$^+$ recipients, whereas the cotransferred B6.CD45.1$^+$CD4$^+$ T cells were unaffected (Fig. 3A and fig. S8A). As in the bm12-cGvHD model, C1q operated independently of C3 (fig. S8B). Lymphopenia-induced T cell expansion is triggered by low-affinity interactions (*14*). Analysis of OT-I proliferation with OVA peptides of different affinities showed that C1q had an inhibitory effect only in response to partial (T4) and weak (G4) agonists but not to a strong (N4) ligand (fig. S8C). Similarly, C1q inhibited human CD8$^+$ T cell activation, proliferation, and cytotoxic functions under suboptimal stimulation (fig. S9). C1q was detected mainly on activated CD8$^+$ T cells (mouse and human) (Fig. 3B and fig. S10A) and almost exclusively on MPECs (Fig. 3C). Preincubation with the globular C1q region, but not with the collagen tail, inhibited C1q binding in a dose-dependent manner (fig. S10, B and C), indicating that C1q recognizes activated CD8$^+$ T cells through its globular domain. Correspondingly, expression of the globular C1q receptor (p32/gC1qR) (*15*), a mitochondrial molecule present on the surface of several immune cells (fig. S11A), was increased on activated mouse and human CD8$^+$ T cells (fig. S11, B and C). Consistent with the preferential binding of C1q to MPECs (Fig. 3C), cGvH-treated *C1qa*$^{-/-}$ MPECs expressed lower levels of the anti-apoptotic factor Bcl-2 and higher levels of Blimp-1, a repressor that promotes cytotoxic T functions (*16*), than WT MPECs (Fig. 3D and fig. S12, A and B). Furthermore, the proportion of *C1qa*$^{-/-}$ MPECs, but not SLECs, secreting granzyme B was higher compared with WT cells (fig. S12C). Abnormal Bcl-2 expression in *C1qa*$^{-/-}$ mice suggests that C1q may influence MPEC viability. In cGvH-treated *C1qa*$^{-/-}$ mice, MPECs, but not SLECs, displayed a higher rate of bromodeoxyuridine (BrdU) decay compared with WT animals (Fig. 3E), indicating a more rapid turnover of this subpopulation. Moreover, the percentage of *C1qa*$^{-/-}$ MPECs expressing active caspase 3/7 was higher (Fig. 3F and fig. S12D). Altogether, these findings suggest that C1q controls the programming and survival of MPECs through its globular domain.

CD8$^+$ T cells undergo major metabolic changes upon activation (*17*). CD44$^+$CD62L$^+$CD8$^+$ (MPECs) and CD44$^+$CD62L$^-$CD8$^+$ (SLECs) T cells from cGvH-treated *C1qa*$^{-/-}$ animals exhibited similar extracellular acidification rate (ECAR) and basal oxygen consumption rate (OCR) when compared with WT cells. However, *C1qa*$^{-/-}$ MPECs, but not SLECs, had impaired mitochondrial spare respiratory capacity (SRC) (Fig. 4, A to C). SRC has been shown to correlate with mitochondrial mass (*17*), and MitoTracker staining showed reduced mitochondrial content in *C1qa*$^{-/-}$ MPECs compared

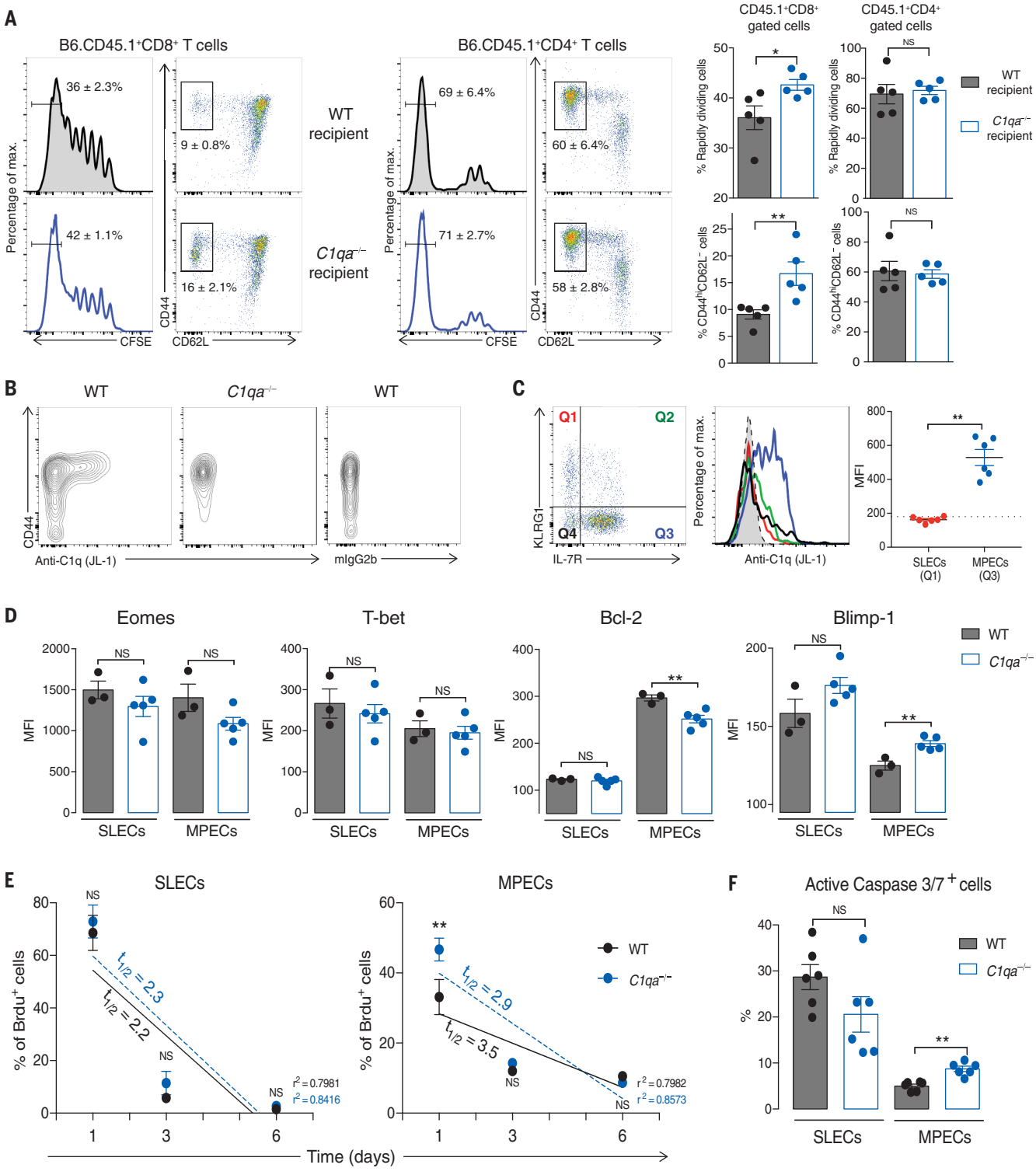

Fig. 3. C1q selectively regulates MPEC programming and survival. (**A**) Analysis of CFSE$^+$CD45.1$^+$CD8$^+$ and CD45.1$^+$CD4$^+$T cells cotransferred in sublethally irradiated CD45.2$^+$ WT or *C1qa*$^{-/-}$ hosts (n = 5 mice per group). Percentages of activated and fast proliferating donor T cell subsets in spleen on day 14. (**B**) Flow cytometric gating of C1q staining on blood CD8$^+$ T cells at day 14 after cGvHD. (**C**) KLRG1 and IL-7R expression in WT CD44$^+$CD8$^+$ T cells (left); histogram of C1q staining (middle) and quantification (right) on MPECs and SLECs. Dotted line indicates mean fluorescence intensity (MFI) of isotype control. Each symbol represents a mouse. (**D**) Expression of transcription factors in splenic SLECs and MPECs from WT and *C1qa*$^{-/-}$ mice 2 weeks after cGvH induction (n = 3 to 5 mice per group). (**E**) Decay of Brdu$^+$ SLECs and Brdu$^+$ MPECs over 6 days (from day 11 after cGvH induction) in WT and *C1qa*$^{-/-}$ mice. Half-life times ($t_{1/2}$) of the decay and the r^2 value of the linear regressions are indicated (n = 6 mice per group). (**F**) Fractions of splenic SLECs and MPECs caspase 3/7$^+$ at week 3 after cGvHD (n = 6 mice per group). NS, not significant; *P < 0.05, **P < 0.01; unpaired Student's t test [(A), (C), (D), and (F)]; two-way ANOVA (E). Data are mean ± SEM and representative of three experiments.

with WT MPECs (Fig. 4D). The addition of C1q increased the MitoTracker staining (Fig. 4E) and up-regulated the expression of mitochondrial biogenesis genes, such as *Tfam* and *Ppargc1b*, in IL-15–differentiated memory-committed OT-I cells but not in IL-2–differentiated effector-like cells (Fig. 4F). Consistent with a C1q-dependent pathway regulating MPEC mitochondrial biogenesis, in vitro metabolic conditions favoring a MPEC molecular profile (*18*) promoted p32/gC1qR surface expression on activated $CD8^+$ T cells (Fig. 4G and fig. S13). The internalization of surface-bound C1q occurred via an endocytic pathway (fig. S14), and C1q colocalized with p32/gC1qR in the mitochondria (Fig. 4H).

Altogether, these data link C1q to the metabolic reprogramming and regulation of activated $CD8^+$ T cells and lead us to propose a new paradigm

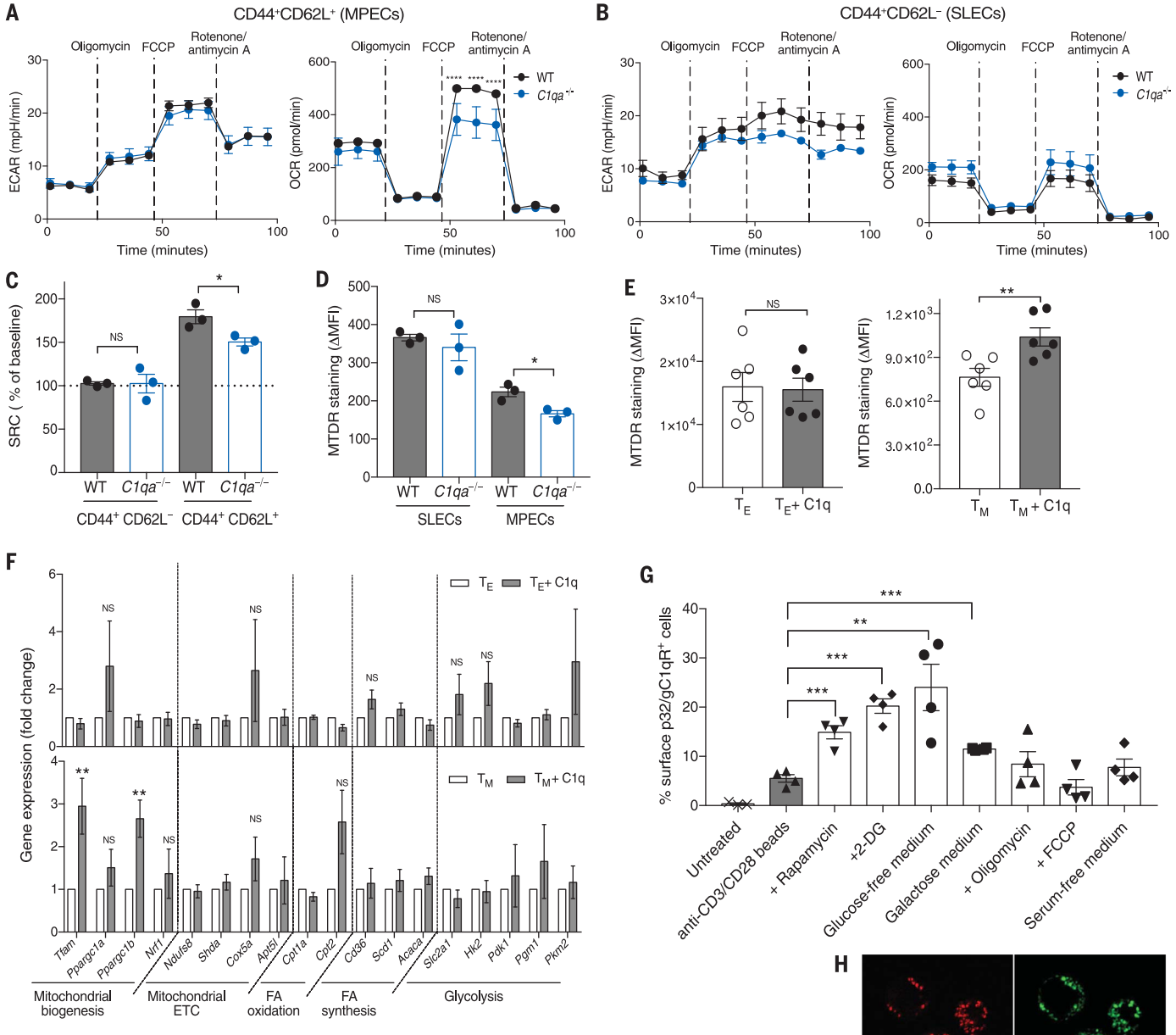

Fig. 4. C1q regulates mitochondrial metabolism in MPECs. (**A** and **B**) ECAR and OCR under basal conditions and after mitochondrial inhibitors in sorted splenic $CD8^+$ T cells from WT and *C1qa*$^{-/-}$ mice 2 weeks after cGvHD. Curve shows mean ± SEM of four technical replicates of pooled samples from four animals. Data are representative of three experiments. (**C**) SRC of the $CD8^+$ T cell subsets, as in (A) and (B). Each symbol represents a biological replicate. (**D**) MTDR staining in SLECs and MPECs 2 weeks after cGvHD (n = 3 mice per group). (**E**) MTDR staining of in vitro IL-2 (T_E) and IL-15 (T_M)–differentiated OT-I cells with and without hC1q (n = 6 mice per group). (**F**) Mitochondrial gene expression in T_E and T_M cells with and without hC1q (n = 5 mice per group). (**G**) Percentages of activated $CD8^+$ T cells expressing p32/gC1qR under different metabolic conditions (n = 4 mice per group). (**H**) Confocal images of T_M cells cultured with hC1q, stained with MitoTracker (red), anti-C1q (green), anti-p32/gC1qR (cyan), and 4′,6-diamidino-2-phenylindole (DAPI) (blue). Scale bar, 5 μm. NS, not significant; *P < 0.05, **P < 0.01, ***P < 0.005, ****P < 0.0001; two-way ANOVA [(A) and (B)], unpaired Student's t test [(C) to (G)]. Data are mean ± SEM and representative of three experiments [(D) to (G)]. FCCP, fluorocarbonylcyanide phenylhydrazone; ΔMFI = MFI − FMO (fluorescence minus one); MTDR, MitoTracker deep red; 2DG, 2-deoxyglucose.

for the protective role of C1q in SLE: C1q limits tissue damage and autoimmunity by acting as a "metabolic rheostat" for effector $CD8^+$ T cells that are capable of propagating autoimmunity through the generation of unique autoantigen fragments by granzyme B (*19*, *20*) (fig. S15). The role of $CD8^+$ T cells in SLE has been largely overlooked and remains poorly characterized, with conflicting findings in human and animal studies (*20*–*24*), perhaps reflecting a changing role of these cells at different stages of the disease. By uncovering the role of effector $CD8^+$ T cells in a lupus-like disease associated with C1q deficiency, our data demonstrate that an aberrant effector $CD8^+$ T cell response to viral infection may autoamplify the breakdown of self-tolerance. This is in addition to molecular mimicry and the bystander activation of autoreactive T cells (*25*). Furthermore, very little is known about the metabolic profile of $CD8^+$ T cells in SLE. Because a $CD8^+$ T cell transcriptional signature can predict the clinical outcome (*2*, *3*), it is conceivable that metabolic abnormalities in these cells play a key role. Our study showing that C1q, a key lupus susceptibility gene in humans, can influence the mitochondrial metabolism of $CD8^+$ T cells demonstrates this link. As p32/gC1qR is ubiquitously present in mitochondria and is indispensable for mitochondrial function (*26*), we hypothesize that the surface expression of p32/gC1qR coupled with another receptor may determine the specificity of the cellular effect(s) mediated by C1q. Thus, our findings describe a new paradigm to explain how C1q may prevent lupus flares and highlight the importance of the interplay between complement and immunometabolism in autoimmunity.

REFERENCES AND NOTES

1. G. C. Tsokos, M. S. Lo, P. Costa Reis, K. E. Sullivan, *Nat. Rev. Rheumatol.* **12**, 716–730 (2016).
2. E. F. McKinney, J. C. Lee, D. R. Jayne, P. A. Lyons, K. G. Smith, *Nature* **523**, 612–616 (2015).
3. E. F. McKinney *et al*., *Nat. Med.* **16**, 586–591 (2010).
4. A. P. Manderson, M. Botto, M. J. Walport, *Annu. Rev. Immunol.* **22**, 431–456 (2004).
5. M. J. Walport, *Nat. Genet.* **25**, 135–136 (2000).
6. M. Martin, A. M. Blom, *Immunol. Rev.* **274**, 218–232 (2016).
7. K. B. Elkon, D. M. Santer, *Curr. Opin. Immunol.* **24**, 665–670 (2012).
8. N. M. Thielens, F. Tedesco, S. S. Bohlson, C. Gaboriaud, A. J. Tenner, *Mol. Immunol.* **89**, 73–83 (2017).
9. R. A. Eisenberg, C. S. Via, *J. Autoimmun.* **39**, 240–247 (2012).
10. S. M. Kaech, W. Cui, *Nat. Rev. Immunol.* **12**, 749–761 (2012).
11. S. Zelenay *et al*., *J. Clin. Invest.* **122**, 1615–1627 (2012).
12. D. L. Barber *et al*., *Nature* **439**, 682–687 (2006).
13. S. Freeley, C. Kemper, G. Le Friec, *Immunol. Rev.* **274**, 16–32 (2016).
14. A. Khoruts, J. M. Fraser, *Immunol. Lett.* **98**, 23–31 (2005).
15. B. Ghebrehiwet, E. I. Peerschke, *Mol. Immunol.* **41**, 173–183 (2004).
16. R. M. Welsh, *Immunity* **31**, 178–180 (2009).
17. M. D. Buck, D. O'Sullivan, E. L. Pearce, *J. Exp. Med.* **212**, 1345–1360 (2015).
18. M. Sukumar *et al*., *J. Clin. Invest.* **123**, 4479–4488 (2013).
19. L. Casciola-Rosen, F. Andrade, D. Ulanet, W. B. Wong, A. Rosen, *J. Exp. Med.* **190**, 815–826 (1999).
20. P. Blanco *et al*., *Arthritis Rheum.* **52**, 201–211 (2005).
21. K. Kis-Toth *et al*., *Arthritis Rheumatol.* **68**, 164–173 (2016).
22. L. Couzi *et al*., *Arthritis Rheum.* **56**, 2362–2370 (2007).
23. E. Mozes, L. D. Kohn, F. Hakim, D. S. Singer, *Science* **261**, 91–93 (1993).
24. E. Mozes, J. Lovchik, H. Zinger, D. S. Singer, *Lupus* **14**, 308–314 (2005).
25. D. R. Getts, E. M. Chastain, R. L. Terry, S. D. Miller, *Immunol. Rev.* **255**, 197–209 (2013).
26. M. Yagi *et al*., *Nucleic Acids Res.* **40**, 9717–9737 (2012).

ACKNOWLEDGMENTS

We thank the staff of the Imperial Central Biomedical Services for the care of the animals. We thank L. Lawrence for histological processing of the samples, H. T. Cook for histological analysis, N. Shaikh for technical support, D. Carling and G. Chennell for Seahorse analysis, C. Reis e Sousa for providing the OVA mouse embryonic fibroblasts, and E. Simpson for critical reading of the paper. **Funding:** This work was supported by the Wellcome Trust (grant reference number 108008/Z/15/Z) (to M.B.). J.A.H. is a recipient of a Wellcome Trust and Royal Society Sir Henry Dale Fellowship (101372/Z/13/Z). We also acknowledge a contribution from the National Institute for Health Research (NIHR) Biomedical Research Centre based at Imperial College Healthcare NHS Trust and Imperial College London. The views expressed are those of the author(s) and not necessarily those of the NHS, the NIHR, or the Department of Health. **Author contributions:** G.S.L. performed the experiments with assistance from G.C., I.Bar., Z.B., K.T., and S.R.; N.M.T., I.Bal., and P.G.A-R. provided key reagents; J.A.H. and J.S. assisted with data analysis and interpretation; M.B. supervised and conceived the project; and M.B. and G.S.L. wrote the paper. All authors commented on the manuscript. **Competing interests:** Authors declare no competing interests. **Data and materials availability:** All data are available in the main text or the supplementary materials.

SUPPLEMENTARY MATERIALS

www.sciencemag.org/content/360/6388/558/suppl/DC1
Materials and Methods
Figs. S1 to S15
References (*27*–*38*)

22 July 2017; resubmitted 15 December 2017
Accepted 14 March 2018
10.1126/science.aao4555

Present your work to the world

Are you a representative of the upcoming generation of thought leaders in your field? Together we look forward to your application for the new Sartorius & *Science* Prize for Regenerative Medicine & Cell Therapy.

Apply now!

www.passionforscience.com/prize

The Sartorius & *Science* Prize for Regenerative Medicine & Cell Therapy

Awarded by sartorius Science

eppendorf & Science

PRIZE FOR NEURO BIOLOGY

2017 Winner
Flavio Donato, Ph.D.
Kavli Institute
Norwegian University of
Science and Technology

For research on how neural networks mature during development to represent space in the brain

Application Deadline
June 15, 2018

Call for Entries

Eppendorf & Science Prize for Neurobiology
The annual Eppendorf & Science Prize for Neurobiology is an international award which honors young scientists for their outstanding contributions to neurobiological research based on methods of molecular and cell biology. The winner and finalists are selected by a committee of independent scientists, chaired by *Science's* Senior Editor, Dr. Peter Stern. To be eligible, you must be 35 years of age or younger.

As the Grand Prize Winner, you could be next to receive
> Prize money of US$25,000
> Publication of your work in *Science*
> Full support to attend the Prize Ceremony held in conjunction with the Annual Meeting of the Society for Neuroscience in the USA
> 10-year AAAS membership and online subscription to *Science*
> Complimentary products worth US$1,000 from Eppendorf
> An invitation to visit Eppendorf in Hamburg, Germany

It's easy to apply! Learn more at:

www.eppendorf.com/prize

eppendorf Science AAAS

eppendorf & Science

PRIZE FOR NEURO BIOLOGY

2017 年获奖者
Flavio Donato, Ph.D.
卡弗里研究所
挪威科技大学

专注发育期间神经网络成熟如何构建大脑空间的研究

申请截止日期
2018 年 6 月 15 日

欢迎参选

Eppendorf & Science 神经生物学奖
一年一度的 Eppendorf & Science 神经生物学奖是一项国际奖项，授予用分子与细胞生物学方法在神经生物学领域取得非凡成果的青年科学家。冠军及入围候选人均是由《Science》杂志高级编辑 Peter Stern 博士领衔的独立科学家所组成的委员会评出。年龄不超过 35 岁的科学家可以申请参选。

您可能就是下一位获奖者并获得：
> $25,000 美元奖金
> 获奖论文发表在《Science》杂志上
> 得以全额资助参与美国神经科学协会年会和颁奖仪式
> 10 年 AAAS 会员和《Science》电子期刊
> 赠送价值 $1,000 美元的 Eppendorf 产品
> 获邀参观 Eppendorf 位于德国汉堡的总部

申请非常容易！
要了解更多信息，请登陆：

www.eppendorf.com/prize

eppendorf Science AAAS

eppendorf & Science

PRIZE FOR NEURO BIOLOGY

2017 Winner
Flavio Donato, Ph.D.
Kavli Institute
Norwegian University of
Science and Technology

For research on how neural networks mature during development to represent space in the brain

申込期限
2018年6月15日

Call for Entries

Eppendorf & Science for Neurobiology
Eppendorf & Science神経生物学賞は、分子生物学や細胞生物学に基づく神経生物学研究において、卓越した貢献をなされた若手科学者に贈呈している国際賞です。最終選考選出者ならびに受賞者は、Science誌編集主任Dr. Peter Sternをはじめとする科学者達の独立委員会によって選出されます。35歳までの研究者が応募条件できます。

As the Grand Prize Winner, you could be next to receive
> 賞金：25,000米ドル
> Science誌に研究内容を掲載
> 米神経科学学会年次総会に併せて開催される授賞式への参加を全面サポート
> 10年間のAAAS会員資格およびScience誌のオンライン購読権
> 1,000米ドル相当のエッペンドルフ製品を提供
> ドイツ、ハンブルクのエッペンドルフ本社にご招待

応募は簡単です！ 詳しくはこちら：

www.eppendorf.com/prize

eppendorf Science AAAS

CALL FOR PAPERS

SCIENCE PARTNER JOURNALS

spj.ScienceMag.org/research

Research

OFFICIAL JOURNAL OF CAST

An Open Access Journal

Research is a comprehensive, interdisciplinary, and selective **Open Access journal from the China Association of Science and Technology (CAST)**, published quarterly and distributed by the **American Association for the Advancement of Science (AAAS)**. *Research* provides an international platform for academic exchange, research collaboration, and technological advancements. The journal will publish fundamental research in the life and physical sciences as well as important findings or issues in engineering and applied science.

The Science Partner Journals (SPJ) program was established by AAAS, the nonprofit publisher of the *Science* family of journals. The SPJ program features high-quality, online-only open access publications produced in collaboration with international research institutions, foundations, funders and societies. Through these collaborations, AAAS expands its efforts to communicate science broadly and for the benefit of all people by providing top-tier international research organizations with the technology, visibility and publishing expertise that AAAS is uniquely positioned **to offer as the world's largest general science membership society**.

Freeze Dryer

The Freezemobile freeze dryer from SP Scientific is designed to provide a convenient, flexible solution for high-quality preparation of peptides, proteins, plant materials, and organic tissue. Offered in 25-L and 35-L condenser sizes, the unit offers the largest capacity commercially available for manifold/flask freeze dryers. With a –85°C condenser to suit optimized removal of a wide variety of solvents, it can be configured for your exact processing requirements, and allows you to add or remove individual samples without interrupting workflow. Featuring an extensive range of single- and multitiered horizontal "T"-type manifolds, the Freezemobile can dry multiple flasks simultaneously. To improve the laboratory operating environment, it can also be supplied with a low-noise, oil-free vacuum pump.

SP Scientific
For info: 800-431-8232
www.spscientific.com/freezemobile

NGC Fraction Collector

The NGC Fraction Collector from Bio-Rad allows researchers to choose how to collect and when to access their fractions. The system can be triggered to collect based on slope, percent of buffer from pump B, pH, and detector signals. Front-to-back dispensing provides easy access to fractions before method completion for faster downstream analysis. Researchers can also choose the type of collection vessel they prefer for each phase of a method, including deep-well plates, tubes, bottles, and carboys (with prep-rack adaptors for large-scale purification). Adding two new fraction collectors to each NGC System can further expand capacity. A highly efficient benchtop Peltier cooling module saves lab space and preserves the integrity of temperature-sensitive biomolecules. An optional enclosure protects samples from environmental conditions while allowing full access during a run. Because the enclosure is optional, the same fraction collector can also be used for reverse-phase chromatography applications.

Bio-Rad
For info: 800-424-6723
www.bio-rad.com/ngcfc

Automation Workstation

Tecan's Fluent Gx Automation Workstation offers the flexibility to meet a host of laboratory needs—clinical diagnostics, next-generation sequencing, and nucleic acid purification—and provides the advanced security features required for regulated applications in clinical, GCP, GLP, GMP, and QC facilities. The Fluent Gx combines the powerful liquid-handling and workflow benefits already familiar to Fluent users—fast, precise processing, high on-deck workload capacities, and intuitive operation—with a suite of software features needed to comply with rigorous regulatory requirements, including FDA 21 CFR Part 11. These advanced features not only ensure regulatory compliance, but simplify day-to-day activities in busy laboratories and enhance productivity.

Tecan
For info: +41-(0)-44-922-81-11
www.tecan.com/fluentgx

Automated Incubator

BioSpa 8 Automated Incubator links BioTek readers and imagers together with washers and dispensers, for full workflow automation of up to eight microplates or other labware. It can automate your processes, from ELISA tests to long-term live-cell assays. Temperature and CO_2/O_2 control, plus humidity monitoring and lid handling, ensure an ideal environment for cell cultures during all experiment stages, with minimal manual intervention required. BioSpa's software records and reports session timelines and environmental conditions, while customizable text and email alerts assure confidence during long- and short-term runs. Link a washer or dispenser and a plate reader or imager for start-to-finish workflow automation.

BioTek
For info: 888-451-5171
www.biotek.com

Liquid-Handling System

dragonfly discovery liquid-handling technology from TTP Labtech has been produced to provide researchers a standard platform where they can easily develop and screen complex assays in a robust, cost-effective manner. The platform enables rapid and reliable low-volume dispensing (200 nL and upwards) from a positive-displacement disposable pipette with 4-mL capacity and 96-, 384-, and 1,536-well compatibility, allowing assays to be developed directly in high-density plate format using a common platform. dragonfly discovery not only significantly reduces assay development time, but also facilitates a more seamless transition from development to screening. Additionally, it permits researchers to deploy experiment design as part of assay development—a particularly beneficial feature for complex cellular assays.

TTP Labtech
For info: 617-494-9794
ttplabtech.com

Microplate Mover

Increase throughput, storage capacity, and operational flexibility with the Orbitor RS Microplate Mover. Extensive vertical reach allows multiple stacked or high-density instruments to be loaded in a small footprint, and a bidirectional telescoping arm provides superior reach, improved user safety, and unlimited base rotations within a 360° workspace. Novice users appreciate the Orbitor's numerous safety features. The arm of the mover includes an overhead gripper—with variable force control, the Orbitor will stop with the slightest contact, and plate detection in the gripper eliminates the hassles of dropped and spoiled samples. Orbitor solutions can easily be upgraded in the field, either with multiple devices for operation pooling, or with sample preparation instrumentation. There's also a wide selection of storage options, from random access and stacked storage to storage carousels.

Thermo Fisher Scientific
For info: 800-955-6288
www.thermofisher.com

Electronically submit your new product description or product literature information! Go to www.sciencemag.org/about/new-products-section for more information.

Newly offered instrumentation, apparatus, and laboratory materials of interest to researchers in all disciplines in academic, industrial, and governmental organizations are featured in this space. Emphasis is given to purpose, chief characteristics, and availability of products and materials. Endorsement by *Science* or AAAS of any products or materials mentioned is not implied. Additional information may be obtained from the manufacturer or supplier.

FORCEFORSCIENCE.ORG

STAND TOGETHER
Be a Force for Science

GET THE FACTS

Understand the science behind the issues that matter.

FOLLOW AAAS ADVOCACY

Champion public discussion and evidence-based policy.

TAKE ACTION

Learn ways you can become an advocate and stand up for science.

AMERICAN ASSOCIATION FOR THE ADVANCEMENT OF SCIENCE

AAAS

NEW ENGLAND BioLabs® Inc.

be INSPIRED
drive DISCOVERY
stay GENUINE

We've spread our wings.

Monarch® Nucleic Acid Purification Kits Now available for DNA & RNA

Designed with sustainability in mind, Monarch® Nucleic Acid Purification Kits are the perfect complement to many molecular biology workflows. Available for DNA & RNA purification, with buffers and columns available separately, Monarch kits are optimized for excellent performance, convenience and value. Quickly and easily recover highly pure, intact DNA and RNA in minutes. Available kits include:

- Monarch Plasmid Miniprep Kit
- Monarch DNA Gel Extraction Kit
- Monarch PCR & DNA Cleanup Kit (5 µg)
- **NEW** MONARCH TOTAL RNA MINIPREP KIT – optimized for use with a variety of sample types, including cells, tissues, blood, and more

Make the change and migrate to Monarch today.

Interested in trying a sample of our new Monarch Total RNA Miniprep Kit?

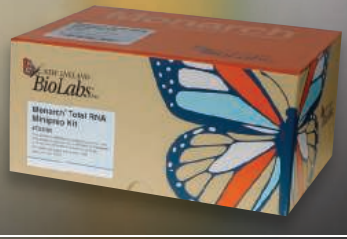

Learn more at
NEBMonarch.com

Science Careers

SCIENCE CAREERS ADVERTISING

For full advertising details, go to ScienceCareers.org and click For Employers, or call one of our representatives.

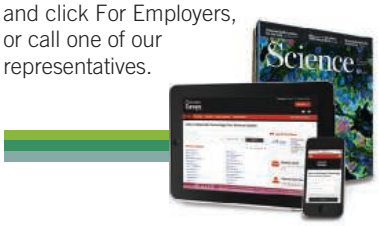

AMERICAS

+1 202 326-6577
+1 202 326-6578
advertise@sciencecareers.org

EUROPE, INDIA, AUSTRALIA, NEW ZEALAND, REST OF WORLD

+44 (0) 1223 326527
advertise@sciencecareers.org

CHINA, KOREA, SINGAPORE, TAIWAN, THAILAND

+86 131 4114 0012
advertise@sciencecareers.org

JAPAN

+81 3-6459-4174
advertise@sciencecareers.org

CUSTOMER SERVICE

AMERICAS

+1 202 326-6577

REST OF WORLD

+44 (0) 1223 326528

advertise@sciencecareers.org

All ads submitted for publication must comply with applicable U.S. and non-U.S. laws. *Science* reserves the right to refuse any advertisement at its sole discretion for any reason, including without limitation for offensive language or inappropriate content, and all advertising is subject to publisher approval. *Science* encourages our readers to alert us to any ads that they feel may be discriminatory or offensive.

ScienceCareers
FROM THE JOURNAL SCIENCE AAAS

ScienceCareers.org

Step up your job search with *Science* Careers

- Access thousands of job postings
- Sign up for job alerts
- Explore career development tools and resources

Search jobs on **ScienceCareers.org** today

ScienceCareers
FROM THE JOURNAL SCIENCE AAAS

Biological Sciences at Peking University

Biological Sciences at PKU aspires to advance education and research in the broad spectrum of life sciences through learning, discovery, and multidisciplinary team science. As one of the oldest biology departments in China, our education and research span a wide spectrum of subjects, from single molecules and individual cells in the laboratory to endangered animals in our Conservation Biology Field Stations. Our overarching missions are: (1) To encourage students to achieve academic excellence through an interdisciplinary curriculum, inquiry-based learning and extracurricular activities, so that they can explore and develop their full potential; and to educate students to be responsible citizens and leaders who can be called upon to serve society; (2) To encourage and respect the creativity of individuals, to generate new knowledge and ideas through innovative research and discovery; and to disseminate new discoveries for the benefit of education, scientific development and human health; (3) To build long-term sustainable research programs by encouraging teamwork and collaborative efforts, and to focus on cutting-edge research through multidisciplinary recruitment and national/international collaborations.

We have benefited from significant increases in the national budget for education and research, as well as new and flexible national recruitment programs and policies. The size of our faculty has nearly doubled in the past 10 years, while the number of annual citations of our publications has increased more than 20 times. Among the 78 principal investigators (PIs), 5 are members of the Chinese Academy of Sciences, 3 are members of the American Academy of Sciences, 10 are Cheung Kong Scholars, 21 have been designated as National Natural Science Foundation Distinguished Young Scholars, and 6 and 17 are recent "1000 Talents" and "1000 Young Talents" recruits, respectively. In addition, we house 3 National and Ministry of Education Key Laboratories. Our user-friendly core facility provides essential services and supports for our research community. The 2018 QS World University Subject Rankings ranked Biological Sciences at PKU 38th in the world.

Here we highlight some major achievements in the research areas we are pushing forward at PKU:

Regenerative medicine: Regenerative medicine holds great promise for treating challenging diseases such as diabetes and neurodegenerative disorders. One major question in regenerative medicine is how to generate pluripotent stem cells that can give rise to any desired cell type of the body for clinical applications. Professor Hongkui Deng achieved a groundbreaking milestone by using small molecules to reprogram somatic cells into pluripotent stem cells, establishing a fundamentally new, chemical-based method of manipulating cellular identity and functionality. Using a new chemical cocktail, his group established mouse and human extended pluripotent stem (EPS) cells that possessed both embryonic and extra-embryonic developmental potential, a key functional feature of totipotency. These pioneering undertakings provide new resources for regenerative medicine, as well as deep insight into cell fate regulation and developmental potency.

Anti-virus infection: Viral infection causes major global public health problems. In an attempt to decipher the molecular mechanisms of host defense against viral infection, Dr. Zhengfan Jiang' s team identified several critical genes required for innate immune activation by viruses, and revealed molecular mechanisms governing the coordination among viral infection-induced cytokine production, inflammation and apoptotic cell death. They also discovered that a trace amount of Mn++ can alert cells to viral infection via sensitization and activation of the cGAS-STING pathway. These findings provide new ideas for reestablishment of homeostasis of the host immune system after a viral infection.

Maintaining genomic stability: Within each round of the cell cycle, all genomic DNA must be accurately replicated and packed into the nucleosome in order to propagate the gene expression state and cell identity to daughter cells. Dr. Li Qing' s group revealed a novel mechanism that couples DNA replication with nucleosome assembly. They established that replication protein A binds directly with histone H3-H4 in a process mediated by multiple histone chaperones and promotes nucleosome assembly on nascent DNA. Dr. Kong Daochun' s group discovered that fission yeast protein Sap1 is a DNA replication initiation protein that directly participates in assembling the pre-replication complex. ATP-dependent helicase/nuclease DNA2 functions during the S-phase checkpoint to prevent fork reversal, thus stabilizing stalled replication forks during replication stress. These achievements have advanced our knowledge on chromatin replication, epigenetic inheritance and genome stability. Such knowledge may help in preventing replication errors and genome instability in precancerous cells.

Genome editing: Genome editing technology has profoundly impacted biomedical research and the pharmaceutical industry by enabling efficient and precise genetic modifications. Dr. Wensheng Wei and his team have focused on the development of various genome editing tools, especially for high-throughput functional genomics. After establishing one of the first functional CRISPR screening methods for identification of protein-coding genes, they subsequently developed a series of new approaches for investigating long noncoding RNAs, topologically active chromatin hubs, and functional domain mapping at single-amino-acid resolution. Wei and his team aim to facilitate the development of better therapeutics by generating and dissecting functional big data in biological contexts to provide critical insight into disease mechanisms.

Plant biology: Unlike animals, the sperm cells of the angiosperm are unable to swim

and have to be transported in pollen tubes as cargo to female gametes to accomplish fertilization. Professor LiJia Qu' s group recently revealed the precise regulatory mechanism underlying the control of pollen tube integrity and rupture. They demonstrated that a receptor complex receives RALF4/19 autocrine peptide signals secreted from the pollen tube to maintain pollen tube integrity. However, after pollen tubes arrive at the ovule, the same receptor complex now receives ovule-produced RALF34 and triggers pollen tube rupture, thus releasing sperm cells for fertilization. This exciting study substantially advances our understanding of how and when a pollen tube maintains its integrity.

In addition to basic research and scientific publications, our faculty has also contributed significantly to society through various outreach and educational programs, national and international forums, as well as through advisory roles for local and central governments on environmental and conservation policies. That our faculty, staff, students and alumni carry a tremendous sense of pride, belonging and responsibility is the most important foundation of Biological Sciences and the driving force for our future growth. Feel free to contact us:

Website: http://bio.pku.edu.cn/en/
Email: hqf@pku.edu.cn

The School of Advanced Agricultural Sciences at Peking University

In late 2014, at a critical stage of rural reform and transformation in China, Peking University formally launched a brand new school: the School of Advanced Agricultural Sciences (SAAS). Benefiting from the existing research and educational disciplines at Peking University, including natural sciences, social sciences, and humanities, the mission of this new school is to become a new international hub in modern agricultural research and the cultivation of professional talents in agriculture and related fields. The initial plan of SAAS is to develop four disciplines, including plant genetics and development, agricultural biotechnology, food nutrition and safety, and agricultural economics and management. In 2017, the school collaborated with Shangdong Province and set out to establish an associated institute in Weifang branch campus (a leading agricultural zone in Shangdong): the Research Institute of Advanced Agricultural Sciences.

In January 2018, Professor Zhihong Xu, academician of the Chinese Academy of Sciences (CAS) and the Third World Academy of Sciences (TWAS), was appointed as the first dean of SAAS. Under his direction, the School is endeavoring to accomplish its mission and goal of constructing a world-class institution of advanced agricultural technologies and management.

Since its founding, SAAS has recruited 10 full-time faculty members in the field of agricultural economics and has another 24 adjunct faculty members, most of them from the School of Life Sciences at Peking University, in the field of plant genetics and development. The school has developed curriculums for undergraduates and graduates in the fields of agricultural sciences and agricultural economics, and has taken in two classes of PhD candidates since 2016.

Among its full-time faculty, Professor Xingwang Deng, a former Yale University endowed professor and member of the US National Academy of Sciences, is renowned internationally for his research on "plant responses to light environments" . Since returning to China, he has dedicated himself to developing new agricultural sciences and biotechnologies, such as the molecular base of plant heterosis and the new generation of hybrid breeding technology for rice and wheat. His team was the winner of both the Creative Research Group grant award from the National Natural Science Foundation of China (NSFC) in 2016 and the National Key Research and Development Program award from the Ministry of Sciences and Technology (MOST).

Jianhua Lin, the President of PKU, appointed Prof. Xu as Dean of SAAS.

Prof. Deng gave a plenary talk at Molecular Plant Breeding Conference 2017.

Prof. Huang gave a plenary talk at T20 Argentina 2018 Inception Workshop, Buenos Aires.

Professor Jikun Huang, fellow of TWAS for the advancement of science in developing countries and Honorary Life Member of the International Association of Agricultural Economists (IAAE), is another world-renowned scholar in agricultural economics. He is the founder and director of the China Center for Agriculture Policy (CCAP), which was the first winner of the Creative Research Group grant award from NSFC in 2001. He has conducted a wide range of research in agricultural and rural development and generated an enormous impact on academics and policy makers domestically and internationally.

To enhance our research and teaching capacities, the school is actively recruiting new faculty members for its facility on the main campus of Peking University as well as its Shandong-branch research institute for all relevant disciplines at all ranks. The school welcomes both research and education collaboration from China and the rest of world. More information is available on the website: http://www.saas.pku.edu.cn/. You may also inquire for information or send an application through the following contact:

Contact Person: Ms. Qian Wan
Email Address: stellawan@pku.edu.cn
Mailing Address: the 4th Floor, Wangkezhen Building, Peking University, No. 5 Yiheyuan Road, Haidian District, Beijing 100871

VIRGINIA COMMONWEALTH UNIVERSITY

VCU

POSTDOCTORAL RESEARCH POSITIONS AVAILABLE

Virginia Commonwealth University School of Medicine

Postdoctoral positions are available for talented scientists to be part of exciting projects directed by Dr. Sarah Spiegel, Chair of Biochemistry and Molecular Biology, Virginia Commonwealth University School of Medicine, Richmond, VA. We study the functions of the bioactive sphingolipid metabolite sphingosine-1-phosphate in novel signaling pathways important for inflammation and cancer (see *Nature*. **510:**58, 2014). Additional information about the Spiegel laboratory that includes publications is found at https://www.ncbi.nlm.nih.gov/myncbi/browse/collection/40908097/?sort=date&direction=ascending

Candidates must have a Ph.D., or M.D., or M.D.-Ph.D. and should have experience in biochemistry, molecular biology, or other relevant fields. Must be a U.S. citizen or have legal permanent resident status. For highly qualified individuals with postdoctoral experience, appointments as Instructor or Research Assistant Professor will be considered.

Submit a cover letter with curriculum vitae, and three reference letters by email to: **Dr. Sarah Spiegel (sarah.spiegel@vcuhealth.org)** and cc **michael.maceyka@vcuhealth.org**.

University of Pittsburgh Tenure-track Faculty Positions in the Department of Structural Biology

The University of Pittsburgh is conducting a broad faculty candidate search for creative individuals who use structural and biophysical methods to address fundamental biomedical questions. The ideal candidate will be motivated to explore applications of his or her structural expertise to disease related questions. We particularly encourage individuals with research activities in cryo-electron microscopy/tomography for in situ structural biology to apply. At present, the cryo-EM facility in the Department comprises 3 Thermo Fisher (FEI) microscopes – a Polara equipped with a Falcon 3 DED camera and Gatan US4000 and Orius CCD cameras; a TF20 equipped with a TVIPS XF416 camera and two Gatan 626 cryoholders; and a T12 equipped with Gatan US 1000 and Orius CCD cameras. The University has funding to replace the Polara with a Krios 3Gi instrument. Additional accessory instrumentation is also available. The department also possesses dedicated computing resources suitable for handling and storing large datasets.

Applications at any rank are invited.

The University of Pittsburgh is the fifth most highly ranked domestic institution of higher education in terms of NIH funding, and a very wide spectrum of collaborative opportunities exists. The research resources in the Department of Structural Biology and the intellectual environment at the University are truly extraordinary, from state-of-the-art instrumentation to expert support and creative investigators.
Successful applicants are expected to develop and lead independent research programs that address important problems in biomolecular systems of wide scientific and medical interest.

Competitive salaries and start-up packages will be offered. Applicants should hold PhD and/or MD or equivalent degrees and have demonstrable expertise and scholarly achievement in structural biology or biophysics. Proposed starting date is October 1, 2018 or thereafter. In order to ensure full consideration, applications must be received by **August 31, 2018**.

Application materials including the candidate's curriculum vitae, the names and contact information for three references, and a brief statement of research interests should be sent to: **Dean Duncan, Administrator, Department of Structural Biology, 1050 BST3, 3501 5th Avenue, Pittsburgh, PA 15260; dxd8@pitt.edu**

EEO/AA/M/F/Vets/Disabled.

By **Paul R. Sanberg**

Finding reward in risk

I was in my first full professorship, spending long hours in the lab and focused on publishing my research. I was doing everything I had been taught to do in a traditional academic setting, exactly the way I had been taught to do it. I loved my field and was proud of my work. I should have been happy to have come this far. I was the only one in my family to have earned a bachelor's degree, and a career as an academic researcher was far beyond what I had ever imagined when I was younger. Yet I had to acknowledge that I was a little bored with the routine that had been my life since graduate school.

Life has a habit of throwing curveballs, and at about that time I was offered a chance to move from my stable post at the University of Cincinnati to a nontenured research faculty appointment at Brown University. There I would help start a spinoff company to advance cell therapies for Parkinson's disease and diabetes. For the first time, I could translate my laboratory work into real-world impact, and the idea of delivering treatments directly to otherwise hopeless patients spoke to me on a deep level. Giving up a tenured position and the kind of financial security my parents could have never imagined was risky, but the potential financial rewards that the startup offered made the choice easier. It also helped that I was young and had few responsibilities.

"All these faculty members wanted to embrace their inventive side."

So I made the leap. In an old brick building on the banks of the Providence River, three mentors—an investor and startup founder, a university administrator, and an academic researcher—showed me how to combine the rigor of scientific discovery with a determination to develop practical solutions for real-world problems. They also encouraged me to file for patents, which made a bold personal statement: My ideas had value beyond academia.

But as much as I enjoyed the pace and challenge of that entrepreneurial experience, I also missed many aspects of traditional university research, including collaborating with other faculty members and publishing and presenting my work. I wanted to bring these two passions together. This desire led me to my next gamble a few years later: As the startup went public, I left the company—and my Ivy League appointment—for a little-known public university not yet 40 years old. There I could have the best of both worlds. I would lead a laboratory conducting basic and translational research, and my superiors would support me in patenting new technologies and launching startups.

The combination worked for me as a tenured scientist. But I discovered that more junior faculty members had less freedom. The University of South Florida (USF), despite its youth, had traditional tenure and promotion practices. I heard distressing stories: the faculty member who was denied a promotion because she was spending too much time on an invention, the physics professor whose department chair discouraged him from starting a company because it would take time away from traditional research and publishing.

When I became a senior research administrator, I found that the challenge was even greater than I had realized. I hosted a lunch for any USF faculty members who held a U.S. patent, expecting maybe a dozen people would show up. More than 100 did. All these faculty members wanted to embrace their inventive side, but the traditional academic environment constrained them. That was the beginning of the National Academy of Inventors, which I went on to establish in collaboration with the U.S. Patent and Trademark Office. It has since blossomed into an international organization to recognize and celebrate the contributions of academic inventors.

Over the intervening years, USF's senior leadership updated the university's promotion and tenure guidelines to credit faculty members who patent inventions and create startups, offering one model for how universities can promote both basic research and applied entrepreneurship. I hope that other institutions will develop their own models, and that the days of having to choose between being a traditional academic scientist or a future-focused inventor are coming to an end. ■

Paul R. Sanberg is the senior vice president for research, innovation, and knowledge enterprise at the University of South Florida in Tampa and the founder and president of the National Academy of Inventors.

ILLUSTRATION: ROBERT NEUBECKER